BNL-90299-2009-BC, CERN-PH-TH-2009-112, FERMILAB-PUB-09-323-T, LAL 09-111,
MPP-2009-88, MZ-TH/09-22, MKPH-T-09-14, SLAC-R-926, TUM-HEP-728/09, WSU-HEP-0902

Flavor Physics in the Quark Sector

M. Antonelli [a] D. M. Asner [b] D. Bauer [c] T. Becher [d] M. Beneke [e]
A. J. Bevan [f] M. Blanke [g,h] C. Bloise [a] M. Bona [i] A. Bondar [j] C. Bozzi [k]
J. Brod [ℓ] A.J. Buras [g] N. Cabibbo [m,n] A. Carbone [o] G. Cavoto [m]
V. Cirigliano [p] M. Ciuchini [q] J. P. Coleman [r] D. P. Cronin-Hennessy [s]
J. P. Dalseno [t] C. H. Davies [u] F. Di Lodovico [f] J. Dingfelder [v] Z. Dolezal [w]
S. Donati [x,y] W. Dungel [z] G. Eigen [aa] U. Egede [c] R. Faccini [m,n]
T. Feldmann [g] F. Ferroni [m,n] J. M. Flynn [cf] E. Franco [m] M. Fujikawa [ab]
I. K. Furić [cd] P. Gambino [ac,ad] E. Gardi [ae] T. J. Gershon [af] S. Giagu [m,n]
E. Golowich [ag] T. Goto [t] C. Greub [bf] C. Grojean [i] D. Guadagnoli [g]
U. A. Haisch [ah] R. F. Harr [ai] A. H. Hoang [h] T. Hurth [i,r] G. Isidori [a]
D. E. Jaffe [aj] A. Jüttner [ak] S. Jäger [g] A. Khodjamirian [aℓ] P. Koppenburg [c]
R. V. Kowalewski [am] P. Krokovny [t] A. S. Kronfeld [d] J. Laiho [an]
G. Lanfranchi [a] T. E. Latham [af] J. Libby [ap] A. Limosani [aq]
D. Lopes Pegna [ar] C. D. Lu [as] V. Lubicz [q,at] E. Lunghi [d] V. G. Lüth [r]
K. Maltman [av] W. J. Marciano [aj] E. C. Martin [ao] G. Martinelli [m,n]
F. Martinez-Vidal [aw] A. Masiero [ay,az] V. Mateu [h] F. Mescia [ba]
G. Mohanty [af,bb] M. Moulson [a] M. Neubert [bc] H. Neufeld [bd] S. Nishida [t]
N. Offen [be] M. Palutan [a] P. Paradisi [g] Z. Parsa [aj] E. Passemar [bf] M. Patel [i]
B. D. Pecjak [bh] A. A. Petrov [ai] A. Pich [aw] M. Pierini [i] B. Plaster [bi]
A. Powell [bs] S. Prell [bj] J. Rademaker [ce] M. Rescigno [m] S. Ricciardi [bk]
P. Robbe [i,bg] E. Rodrigues [u] M. Rotondo [ay] R. Sacco [f] C. J. Schilling [bℓ]
O. Schneider [bm] E. E. Scholz [d] B. A. Schumm [cc] C. Schwanda [z]
A. J. Schwartz [bn] B. Sciascia [a] J. Serrano [bg] J. Shigemitsu [bo] I. J. Shipsey [cb]
A. Sibidanov [j,a] L. Silvestrini [m] F. Simonetto [az] S. Simula [q] C. Smith [bf,bp]
A. Soni [aj] L. Sonnenschein [i,bq] V. Sordini [br] M. Sozzi [x,y] T. Spadaro [a]
P. Spradlin [bs] A. Stocchi [bg] N. Tantalo [bt] C. Tarantino [q,at] A. V. Telnov [ar]
D. Tonelli [d] I. S. Towner [bu] K. Trabelsi [t] P. Urquijo [aq]
R. S. Van de Water [aj] R. J. Van Kooten [bw] J. Virto [m,n] G. Volpi [x,y]
R. Wanke [bx] S. Westhoff [bp] G. Wilkinson [bs] M. Wingate [by] Y. Xie [ae]

J. Zupan [i,bz,ca]

[a] *INFN LNF, Via Enrico Fermi 40, 00044 Frascati, Italy*
[b] *Carleton University, 1125 Colonel By Drive, Ottawa, ON, Canada K1S 5B6*
[c] *Imperial College London, London, SW7 2AZ, United Kingdom*
[d] *Fermi National Accelerator Laboratory, P.O. Box 500 Batavia, IL 60510-5011, USA*
[e] *Institut für Theoretische Physik E, RWTH Aachen University, 52056, Germany*
[f] *Queen Mary, University of London, E1 4NS, United Kingdom*
[g] *Technische Universität München, Excellence Cluster Universe, Boltzmannstraße 2, 85748 Garching, Germany*
[h] *Max-Planck-Institut für Physik, Foehringer Ring 6, 80805 München, Germany*
[i] *CERN CH-1211 Geneve 23, Switzerland*
[j] *Budker Institute of Nuclear Physics, 11, Prosp. Akademika Lavrentieva Novosibirsk 630090, Russian Federation*
[k] *INFN Sez. di Ferrara, Polo Scientifico e Tecnologico. Edificio C. Via Saragat, 1. 44100 Ferrara, Italy*
[ℓ] *Universität Karlsruhe, Liefer- und Besuchsanschrift: Kaiserstraße 12 - 76131 Karlsruhe Germany*
[m] *INFN Sez. di Roma, Piazzale Aldo Moro, 2 00185 Roma, Italy*
[n] *Universitá di Roma 'Sapienza', Dipartimento di Fisica, Piazzale Aldo Moro, 5 00185, Roma, Italy*
[o] *INFN Sez. di Bologna, Via Irnerio 46, I-40126 Bologna, Italy*
[p] *Los Alamos National Laboratory, Los Alamos, NM 87545, USA*
[q] *INFN Sez. di Roma Tre, Via della Vasca Navale, 84 00146 Roma, Italy*
[r] *SLAC National Accelerator Laboratory, 2575 Sand Hill Road, Menlo Park, CA 94025, USA*
[s] *University of Minnesota, Minneapolis, Minnesota 55455, USA*
[t] *High Energy Accelerator Research Organization (KEK), 1-1 Oho, Tsukuba, Ibaraki 305-0801 Japan*
[u] *University of Glasgow, Glasgow G12 8QQ, United Kingdom*
[v] *Physikalisches Institut Freiburg, Hermann-Herder-Str.3, 79104 Freiburg, Germany*
[w] *IPNP, Charles University in Prague, Faculty of Mathematics and Physics, V Holesovickach 2, 180 00 Prague 8, Czech Republic*
[x] *Dipartimento di Fisica, Universitá di Pisa, Largo Pontecorvo 3, 56126 Pisa, Italy*
[y] *INFN Sez. di Pisa, Edificio C - Polo Fibonacci Largo B. Pontecorvo, 3 - 56127 Pisa , Italy*
[z] *Institute of High Energy Physics, A-1050 Vienna, Austria*
[aa] *Dept. of Physics, University of Bergen, Allegaten 55, 5007 Bergen, Norway*
[ab] *Nara Women's University, Nara, Japan*
[ac] *INFN Sez. di Torino, Via Pietro Giuria 1, 10125 Torino, Italy*
[ad] *Dip. di Fisica Teorica, Univ. di Torino, Via Pietro Giuria 1, 10125 Torino, Italy*
[ae] *University of Edinburgh, Edinburgh EH9 3JZ, United Kingdom*
[af] *Department of Physics, University of Warwick, Coventry CV4 7AL, United Kingdom*
[ag] *University of Massachusetts, Amherst, Massachusetts 01003, USA*
[ah] *Johannes Gutenberg-Universität, 55099 Mainz, Germany*
[ai] *Wayne State University, Detroit, MI 48202, USA*
[aj] *Brookhaven National Laboratory, Upton, P.O. Box 5000 Upton, NY 11973-5000, USA*
[ak] *Institut für Theoretische Kernphysik, Johannes-Gutenberg Universität Mainz, Johann-Joachim-Becher Weg 45, 55099 Mainz, Germany*
[aℓ] *Universität Siegen, Walter Flex Str.3, Emmy Noether Campus, D-57068 Siegen, Germany*
[am] *University of Victoria, Victoria, British Columbia, Canada V8W 3P6*
[an] *Washington University, St. Louis, Missouri 63130, USA*
[ao] *University of California at Irvine, Irvine, California 92697, USA*
[ap] *Indian Institute of Technology Madras, IITM Post Office, Chennai, 600032, India*
[aq] *The University of Melbourne, The School of Physics, Victoria 3010, Australia*
[ar] *Princeton University, Princeton, New Jersey 08544, USA*
[as] *Institute of High Energy Physics, Chinese Academy of Sciences, 19B YuquanLu, Shijingshan District, Beijing, 100049, China*
[at] *Universitá di Roma Tre, Dipartimento di Fisica 'E. Amaldi', Via della Vasca Navale 84, 00146 Roma, Italy*
[au] *Stanford University, Stanford, CA 94309, USA*
[av] *York University, Toronto, ON M3J 1P3, Canada*

[aw] *IFIC, Universitat de Valencia-CSIC, E-46071 Valencia, Spain*
[ay] *INFN Sez. di Padova, Via F. Marzolo 8, 35131 Padova, Italy*
[az] *Universitá di Padova, Dipartimento di Fisica, Via F. Marzolo 8, 35131 Padova, Italy*
[ba] *Universitat de Barcelona, Facultat de Fisica, Departament ECM & ICC, E-08028 Barcelona, Spain*
[bb] *Tata Institute of Fundamental Research, Homi Bhabha Road, Mumbai 400 005, India*
[bc] *Institut für Physik, Johannes Gutenberg Universität, Mainz, Staudingerweg 7, 55128, Germany*
[bd] *Faculty of Physics, University of Vienna, Boltzmanngasse 5, A-1090, Wien, Austria*
[be] *Laboratoire de Physique Theorique, CNRS/Univ. Paris-Sud 11 (UMR 8627), F-91405 Orsay, France*
[bf] *Institute for theoretical physics, University of Bern, Sidlerstrasse 5, 3012 Bern, Switzerland*
[bg] *Laboratoire del Accelerateur Lineaire, Université Paris 11, UMR 8607, Batiment 200 91898 Orsay cedex, France*
[bh] *THEP, Johannes Gutenberg-Universität, 55099 Mainz, Germany*
[bi] *University of Kentucky, Lexington, KY 40506, USA*
[bj] *Iowa State University, Ames, Iowa 50011-3160, USA*
[bk] *STFC Rutherford Appleton Laboratory, Chilton, Didcot, OX11 0QX, United Kingdom*
[bℓ] *University of Texas at Austin, Austin, Texas 78712, USA*
[bm] *Ecole Polytechnique Federale de Lausanne (EPFL), CH 1015 (Centre Est) Lausanne, Switzerland*
[bn] *University of Cincinnati, P.O. Box 210011, Cincinnati, Ohio 45221, USA*
[bo] *Ohio State University, Columbus, Ohio 43210, USA*
[bp] *Universität Karlsruhe, Institut für Theoretische Teilchenphysik, D-76128 Karlsruhe, Germany*
[bq] *Laboratoire de Physique Nucleaire et de Hautes Energies, LPNHE - Tour 43 Rez-de-chaussoe - 4 place Jussieu - 75252 PARIS CEDEX*
[br] *ETH Zurich, HG Raemistrasse 101 8092 Zurich Switzerland*
[bs] *University of Oxford, Oxford, United Kingdom*
[bt] *INFN Sezione di Roma 'Tor Vergata' Via della Ricerca Scientifica, 1 00133 Roma - Italy*
[bu] *Physics Department, Queen's University, Kingston, Ontario K7L 3N6, Canada*
[bw] *Indiana University, Bloomington, IN 47405, USA*
[bx] *Universität Mainz, Institut für Physik, 55099 Mainz, Germany*
[by] *University of Cambridge, DAMTP, Wilberforce Road, Cambridge CB3 0WA, United Kingdom*
[bz] *Jozef Stefan Institute, Jamova cesta 39, 1000 Ljubljana, Slovenia*
[ca] *University of Ljubljana, Kongresni trg 12, 1000 Ljubljana, Slovenija*
[cb] *Purdue University, West Lafayette, IN 47907, USA*
[cc] *University of California at Santa Cruz, Institute for Particle Physics, Santa Cruz, California 95064, USA*
[cd] *University of Florida, Gainesville, FL 32611, USA*
[ce] *University of Bristol, Bristol, BS8 1TL, United Kingdom*
[cf] *School of Physics & Astronomy, University of Southampton, Southampton SO17 1BJ, United Kingdom*

Abstract

In the past decade, one of the major challenges of particle physics has been to gain an in-depth understanding of the role of quark flavor. In this time frame, measurements and the theoretical interpretation of their results have advanced tremendously. A much broader understanding of flavor particles has been achieved, apart from their masses and quantum numbers, there now exist detailed measurements of the characteristics of their interactions allowing stringent tests of Standard Model predictions. Among the most interesting phenomena of flavor physics is the violation of the CP symmetry that has been subtle and difficult to explore. In the past, observations of CP violation were confined to neutral K mesons, but since the early 1990s, a large number of CP-violating processes have been studied in detail in neutral B mesons. In parallel, measurements of the couplings of the heavy quarks and the dynamics for their decays

in large samples of K, D, and B mesons have been greatly improved in accuracy and the results are being used as probes in the search for deviations from the Standard Model.

In the near future, there will be a transition from the current to a new generation of experiments, thus a review of the status of quark flavor physics is timely. This report is the result of the work of the physicists attending the 5^{th} CKM workshop, hosted by the University of Rome "La Sapienza", September 9-13, 2008. It summarizes the results of the current generation of experiments that is about to be completed and it confronts these results with the theoretical understanding of the field which has greatly improved in the past decade.

Key words:
PACS:

Contents

1. Introduction

In the past decade, one of the major challenges of particle physics has been to gain an in-depth understanding of the role of quark flavor. In this time frame, measurements and the theoretical interpretation of their results have advanced tremendously. A much broader understanding of flavor particles has been achieved, apart from their masses and quantum numbers, there now exist detailed measurements of the characteristics of their interactions allowing stringent tests of Standard Model predictions.

Among the most interesting phenomena of flavor physics is the violation of the CP symmetry that has been subtle and difficult to explore. In the past, observations of CP violation were confined to neutral K mesons, but since the early 1990s, a large number of CP-violating processes have been studied in detail in neutral B mesons. In parallel, measurements of the couplings of the heavy quarks and the dynamics for their decays in large samples of K, D, and B mesons have been greatly improved in accuracy and the results are being used as probes in the search for deviations from the Standard Model.

In the near future, there will be a transition from the current to a new generation of experiments, thus a review of the status of quark flavor physics is timely. This report is the result of the work of the physicists attending the 5^{th} CKM workshop, hosted by the University of Rome "La Sapienza", September 9-13, 2008. It summarizes the results of the current generation of experiments that is about to be completed and it confronts these results with the theoretical understanding of the field which has greatly improved in the past decade.

In this section the basic formalism of the study of the quark couplings will be introduced and the relationship between CKM matrix elements and observables will be discussed. The last paragraph will then detail the plan of the report and the content of the rest of the sections.

1.1. *CKM matrix and the Unitarity Triangle*

The unitary CKM matrix [1, 2] connects the *weak eigenstates* (d', s', b') and the corresponding *mass eigenstates* d, s, b (in both basis the up-type mass matrix is diagonal and the up-type quarks are unaffected by this transformation):

$$\begin{pmatrix} d' \\ s' \\ b' \end{pmatrix} = \begin{pmatrix} V_{ud} & V_{us} & V_{ub} \\ V_{cd} & V_{cs} & V_{cb} \\ V_{td} & V_{ts} & V_{tb} \end{pmatrix} \begin{pmatrix} d \\ s \\ b \end{pmatrix} \equiv \hat{V}_{\rm CKM} \begin{pmatrix} d \\ s \\ b \end{pmatrix} . \quad (1)$$

The CKM matrix contains all the flavor-changing and CP-violating couplings of the Standard Model.

Several parameterizations of the CKM matrix have been proposed in the literature. This report will use the standard parametrization [3] recommended by the Particle Data

Group [4]. We also introduce the generalization of the Wolfenstein parametrization [5] presented in [6] and discuss its connection to the Unitarity Triangle parameters.

1.1.1. *Standard parametrization*

With $c_{ij} = \cos\theta_{ij}$ and $s_{ij} = \sin\theta_{ij}$ $(i, j = 1, 2, 3)$, the standard parametrization is given by:

$$\hat{V}_{\rm CKM} = \begin{pmatrix} c_{12}c_{13} & s_{12}c_{13} & s_{13}e^{-i\delta} \\ -s_{12}c_{23} - c_{12}s_{23}s_{13}e^{i\delta} & c_{12}c_{23} - s_{12}s_{23}s_{13}e^{i\delta} & s_{23}c_{13} \\ s_{12}s_{23} - c_{12}c_{23}s_{13}e^{i\delta} & -s_{23}c_{12} - s_{12}c_{23}s_{13}e^{i\delta} & c_{23}c_{13} \end{pmatrix}, \tag{2}$$

where δ is the phase necessary for CP violation. c_{ij} and s_{ij} can all be chosen to be positive and δ may vary in the range $0 \le \delta \le 2\pi$. However, measurements of CP violation in K decays force δ to be in the range $0 < \delta < \pi$, as the sign of the relevant hadronic parameter is fixed.

From phenomenological studies we know that s_{13} and s_{23} are small numbers: $\mathcal{O}(10^{-3})$ and $\mathcal{O}(10^{-2})$, respectively. Consequently, to a very good accuracy,

$$s_{12} \simeq |V_{us}|, \quad s_{13} \simeq |V_{ub}|, \quad s_{23} \simeq |V_{cb}|. \tag{3}$$

Thus these three parameters can be extracted from tree level decays mediated by the transitions $s \to u$, $b \to u$ and $b \to c$, respectively. The remaining parameter, the phase δ, is responsible for the violation of the CP symmetry. It can clearly be extracted from CP-violating transitions but also from CP-conserving ones using three-generation unitarity, through the construction of the Unitarity Triangle, as discussed below.

1.1.2. *Wolfenstein parametrization and its generalization*

The absolute values of the elements of the CKM matrix show a hierarchical pattern with the diagonal elements being close to unity, the elements $|V_{us}|$ and $|V_{cd}|$ being of order 0.2, the elements $|V_{cb}|$ and $|V_{ts}|$ of order $4 \cdot 10^{-2}$ whereas $|V_{ub}|$ and $|V_{td}|$ are of order $5 \cdot 10^{-3}$. The Wolfenstein parametrization [5] exhibits this hierarchy in a transparent manner. It is an approximate parametrization of the CKM matrix in which each element is expanded as a power series in the small parameter $\lambda \sim |V_{us}| \approx 0.22$,

$$\hat{V} = \begin{pmatrix} 1 - \dfrac{\lambda^2}{2} & \lambda & A\lambda^3(\varrho - i\eta) \\ -\lambda & 1 - \dfrac{\lambda^2}{2} & A\lambda^2 \\ A\lambda^3(1 - \varrho - i\eta) & -A\lambda^2 & 1 \end{pmatrix} + \mathcal{O}(\lambda^4)\,, \tag{4}$$

and the set (3) is replaced by

$$\lambda, \qquad A, \qquad \varrho, \qquad \text{and} \quad \eta\,. \tag{5}$$

Because of the smallness of λ and the fact that for each element the expansion parameter is actually λ^2, this is a rapidly converging expansion.

The Wolfenstein parametrization is certainly more transparent than the standard parametrization. However, if one requires sufficient level of accuracy, the terms of $\mathcal{O}(\lambda^4)$ and $\mathcal{O}(\lambda^5)$ have to be included in phenomenological applications. This can be done in

many ways [6]. The point is that since (4) is only an approximation the *exact* definition of the parameters in (5) is not unique in terms of the neglected order $\mathcal{O}(\lambda^4)$. This situation is familiar from any perturbative expansion, where different definitions of expansion parameters (coupling constants) are possible. This is also the reason why in different papers in the literature different $\mathcal{O}(\lambda^4)$ terms in (4) can be found. They simply correspond to different definitions of the parameters in (5). Since the physics does not depend on a particular definition, it is useful to make a choice for which the transparency of the original Wolfenstein parametrization is not lost.

In this respect a useful definition adopted by most authors in the literature is to go back to the standard parametrization (2) and to *define* the parameters $(\lambda, A, \varrho, \eta)$ through [6]

$$\lambda \equiv s_{12}\,, \qquad A\lambda^2 \equiv s_{23}\,, \qquad A\lambda^3(\varrho - i\eta) \equiv s_{13}e^{-i\delta} \tag{6}$$

to *all orders* in λ. It follows that

$$\varrho = \frac{s_{13}}{s_{12}s_{23}}\cos\delta, \qquad \eta = \frac{s_{13}}{s_{12}s_{23}}\sin\delta. \tag{7}$$

The expressions (6) and (7) represent simply the change of variables from (3) to (5). Making this change of variables in the standard parametrization (2) we find the CKM matrix as a function of $(\lambda, A, \varrho, \eta)$ which satisfies unitarity exactly. Expanding next each element in powers of λ we recover the matrix in (4) and in addition find explicit corrections of $\mathcal{O}(\lambda^4)$ and higher order terms. Including $\mathcal{O}(\lambda^4)$ and $\mathcal{O}(\lambda^5)$ terms we find

$$\hat{V} = \begin{pmatrix} 1 - \dfrac{1}{2}\lambda^2 - \dfrac{1}{8}\lambda^4 & \lambda + \mathcal{O}(\lambda^7) & A\lambda^3(\varrho - i\eta) \\ -\lambda + \dfrac{1}{2}A^2\lambda^5[1 - 2(\varrho + i\eta)] & 1 - \dfrac{1}{2}\lambda^2 - \dfrac{1}{8}\lambda^4(1 + 4A^2) & A\lambda^2 + \mathcal{O}(\lambda^8) \\ A\lambda^3(1 - \overline{\varrho} - i\overline{\eta}) & -A\lambda^2 + \dfrac{1}{2}A\lambda^4[1 - 2(\varrho + i\eta)] & 1 - \dfrac{1}{2}A^2\lambda^4 \end{pmatrix} \tag{8}$$

where

$$\overline{\varrho} \simeq \varrho(1 - \frac{\lambda^2}{2}) + \mathcal{O}(\lambda^4), \qquad \overline{\eta} = \eta(1 - \frac{\lambda^2}{2}) + \mathcal{O}(\lambda^4). \tag{9}$$

An all-order definition of $\overline{\varrho}$ and $\overline{\eta}$ will be given in the next section. We emphasize here that by definition the expression for V_{ub} remains unchanged relative to the original Wolfenstein parametrization and the corrections to V_{us} and V_{cb} appear only at $\mathcal{O}(\lambda^7)$ and $\mathcal{O}(\lambda^8)$, respectively. The advantage of this generalization of the Wolfenstein parametrization is the absence of relevant corrections to V_{us}, V_{cd}, V_{ub} and V_{cb} and an elegant change in V_{td} which allows a simple connection to the Unitarity Triangle parameters, as discussed below.

1.1.3. *Unitarity Triangle*

The unitarity of the CKM matrix implies various relations between its elements. In particular, we have

$$V_{ud}V_{ub}^* + V_{cd}V_{cb}^* + V_{td}V_{tb}^* = 0. \tag{10}$$

Phenomenologically this relation is very interesting as it involves simultaneously the elements V_{ub}, V_{cb} and V_{td} which are under extensive discussion at present. Other relevant unitarity relations will be presented as we proceed.

The relation (10) can be represented as a *unitarity triangle* in the complex plane. The invariance of (10) under any phase-transformations implies that the corresponding

triangle is rotated in the plane under such transformations. Since the angles and the sides (given by the moduli of the elements of the mixing matrix) in this triangle remain unchanged, they are phase convention independent and are physical observables. Consequently they can be measured directly in suitable experiments. One can construct five additional unitarity triangles [7, 8] corresponding to other orthogonality relations, like the one in (10). Some of them should be useful when the data on rare and CP violating decays improve. The areas (A_Δ) of all unitarity triangles are equal and related to the measure of CP violation $J_{\rm CP}$ [9]: $\mid J_{\rm CP} \mid = 2 \cdot A_\Delta$.

The relation (10) can be represented as the triangle in the complex plane as shown in Fig. 1, where

$$\overline{\varrho} + i\overline{\eta} \equiv \overrightarrow{\rm CA} = -\frac{V_{ub}^* V_{ud}}{V_{cb}^* V_{cd}} \tag{11}$$

and

$$\overrightarrow{\rm AB} = -\frac{V_{tb}^* V_{td}}{V_{cb}^* V_{cd}} = 1 - \overline{\varrho} - i\overline{\eta}\,,$$
$$\overrightarrow{\rm CB} = 1\,. \tag{12}$$

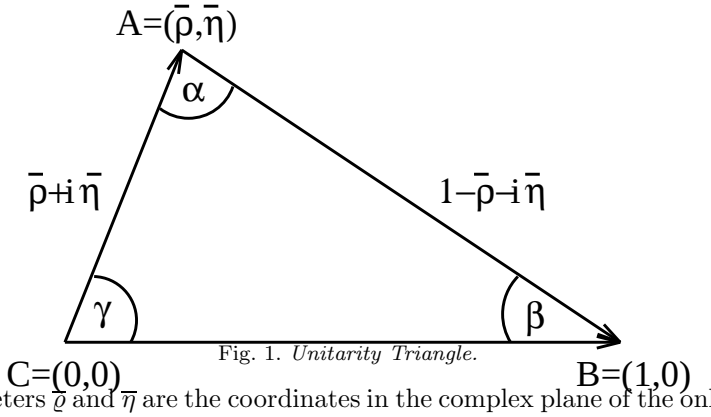

Fig. 1. *Unitarity Triangle.*

The parameters $\overline{\varrho}$ and $\overline{\eta}$ are the coordinates in the complex plane of the only non-trivial apex of the Unitarity Triangle. Using their definition in Eq. (11), the exact relation to the parameters ϱ and η as given in Eq. (6) can be easily found and reads

$$\varrho + i\eta = \sqrt{\frac{1-A^2\lambda^4}{1-\lambda^2}}\,\frac{\overline{\varrho}+i\overline{\eta}}{1-A^2\lambda^4(\overline{\varrho}+i\overline{\eta})} \simeq \left(1+\frac{\lambda^2}{2}\right)(\overline{\varrho}+i\overline{\eta}) + \mathcal{O}(\lambda^4)\,. \tag{13}$$

Phenomenological analyses of the Unitarity Triangles constrain the values of $\overline{\varrho}$ and $\overline{\eta}$. These can be translated to constraints on ϱ and η using Eq. (13) and then to the standard parametrization using Eq. (6). All recent analyses determine the $\hat{V}_{CKM}$ matrix elements in this way, using no expansion whatsoever.

Let us collect useful formulae related to the Unitarity Triangle:

– We can express $\sin(2\alpha_i)$, $\alpha_i = \alpha, \beta, \gamma$, in terms of $(\overline{\varrho}, \overline{\eta})$ using simple trigonometric formulae:

$$\sin(2\alpha) = \frac{2\overline{\eta}(\overline{\eta}^2 + \overline{\varrho}^2 - \overline{\varrho})}{(\overline{\varrho}^2+\overline{\eta}^2)((1-\overline{\varrho})^2+\overline{\eta}^2)}, \tag{14}$$

$$\sin(2\beta) = \frac{2\overline{\eta}(1-\overline{\varrho})}{(1-\overline{\varrho})^2+\overline{\eta}^2}, \tag{15}$$

$$\sin(2\gamma) = \frac{2\overline{\varrho}\overline{\eta}}{\overline{\varrho}^2 + \overline{\eta}^2}\,. \tag{16}$$

– The lengths of AC and AB, denoted by R_b and R_t respectively, are given by

$$R_b \equiv \frac{|V_{ub}^* V_{ud}|}{|V_{cb}^* V_{cd}|} = \sqrt{\overline{\varrho}^2 + \overline{\eta}^2} \simeq (1 - \frac{\lambda^2}{2})\frac{1}{\lambda}\left|\frac{V_{ub}}{V_{cb}}\right|, \tag{17}$$

$$R_t \equiv \frac{|V_{tb}^* V_{td}|}{|V_{cb}^* V_{cd}|} = \sqrt{(1-\overline{\varrho})^2 + \overline{\eta}^2} \simeq \frac{1}{\lambda}\left|\frac{V_{td}}{V_{cb}}\right|\,. \tag{18}$$

– The unitarity relation (10) can be rewritten as

$$R_b e^{i\gamma} + R_t e^{-i\beta} = 1\,. \tag{19}$$

– The angle α can be obtained through the relation

$$\alpha + \beta + \gamma = \pi\,. \tag{20}$$

– In the standard parametrization, the angles β and γ of the unitarity triangle are approximately related to the complex phases of the CKM matrix elements V_{td} and V_{ub} respectively. In particular,

$$V_{td} \simeq |V_{td}|e^{-i\beta}\,, \quad V_{ub} \simeq |V_{ub}|e^{-i\gamma}\,. \tag{21}$$

1.2. *Plan of the report*

The goal of the latest generation of flavor experiments has been not only the measurement of the angles and sides of the unitarity triangles, but the measurement of as many redundant observables sensitive to the parameters of the unitarity triangle. On one side in fact the consistency of this plethora of measurements is a signal that the CP-violation mechanism is fully understood, on the other side possible deviations from the Standard Model would spoil such a consistency. Sensitivity to "New Physics" is therefore proportional to the accuracy we are able to achieve on the Unitarity Triangle. Finally, in case New Physics is observed, the Standard Model Unitarity Triangle will have to be measured by means of a subset of observables , those that are not influenced by New Physics itself, namely tree dominated processes.

In this report, we first describe general theoretical (Sec. 2) and experimental (Sec. 3) tools. Next, the single measurements are described and averaged whenever possible. In particular Sec. 4 discusses the measurements of the Cabibbo Angle, Sec. 5 the measurement of $|V_{cx}|$ and $|V_{ub}|$ in semileptonic decays. Rare decays and measurements of $|V_{td}|$ and $|V_{ub}|$ are detailed in Sec. 6, while Sec. 7 reports on the mixing and lifetime related measurements, including the time-dependent measurements of the phases of the mixing diagram, both for B_d and B_s mesons. All other measurements of angles of the Unitarity Triangle are described in Sec. 8 and 9: the former shows a large number of measurements of the γ angle in tree dominated processes, while the latter comprises several techniques to measure α, β, and γ in charmless B decays.

These measurements are interpreted altogether in Sec. 10. First the results of global fits to all observables under the assumption that there is no deviation from the Standard Model is presented. This fit returns a very accurate measurement of the position of the apex of the unitarity triangle. Next, the redundancy of the measurements is exploited to test the possibility of deviations from the Standard Model both in model independent frames and under specific New Physics scenarios.

2. Theory Primers

This section contains the description of theretical tools that are common to different fields of flavor physics and that will therefore be used as starting point in the subsequent sections.

2.1. *Effective Weak Hamiltonians*

Flavor-changing hadron transitions are multi-scale processes conveniently studied using the operator product expansion (OPE) [10,11]. They involve at least two different energy scales: the electroweak scale, given for instance by the W boson mass M_W, relevant for the flavor-changing weak transition, and the scale of strong interactions $\Lambda_{\rm QCD}$, related to the hadron formation. Using the OPE, these processes can be described by effective weak Hamiltonians where the W boson and all heavier particles are eliminated as dynamical degrees of freedom from the theory [12–16]. These Hamiltonians are given by the first term of an expansion in renormalized local operators of increasing dimensions suppressed by inverse powers of the heavy scale.

The OPE realizes the scale separation between short-distance (high-energy) and long-distance (low-energy) physics. The scale μ at which the local operators are renormalized sets the threshold between the two regimes. The effect of particles heavier than M_W enters only through the Wilson coefficients, namely the effective couplings multiplying the operators of the Hamiltonian. Short-distance strong-interaction effects are also contained in the Wilson coefficients and can be computed using renormalization-group improved perturbation theory. Indeed, Wilson coefficients obey a renormalization group equation (RGE) allowing to resum large logs of the form $\alpha_s(\mu)^{n+m}\log(M_W/\mu)^n$ to all orders in n. The leading order (LO) resummation corresponds to $m=0$, the next-to-leading order (NLO) one to $m=1$, and so on. Since the Wilson coefficients depend on short distance physics only, they behave as effective couplings in the Hamiltonians. They can be calculated once and for all, i.e. for any external state used to compute the Hamiltonian matrix elements. Indeed, the complete definition of an effective weak Hamiltonian requires the choice of the operators and the computation of the corresponding Wilson coefficients.

The dependence on external states, as well as long-distance strong-interaction effects, is included in the hadronic matrix elements of the local operators and must be evaluated with a non-perturbative technique (lattice QCD, QCD sum rules, QCDF, SCET, etc.). As non-perturbative methods can typically compute matrix elements of local operators, this is a major motivation for using the effective weak Hamiltonians.

We now illustrate the procedure to define the effective weak Hamiltonians and to compute the Wilson coefficients discussing the case of $\Delta F=1$ transitions, namely processes where the quark flavor quantum numbers change by one unit.

The starting point is a generic S matrix element given by the T-product of two weak charged currents computed in the Standard Model (in the following called *full* theory to distinguish it from the *effective* theory defined by the effective weak Hamiltonian)

$$\langle F|S|I\rangle = \int d^4x D^{\mu\nu}\,(x,M_W)\,\langle F|T\Big(J^{\rm cc}_\mu(x),J^{cc\,\dagger}_\nu(0)\Big)|I\rangle\,, \tag{22}$$

where $\langle F|$ and $|I\rangle$ are the generic final and initial states and

$$J_\mu^{\rm cc}(x) = \frac{g}{\sqrt{2}} \sum_{j=1}^{3} \left[\left(\sum_{i=1}^{2} V_{u^i d^j} \bar{u}_L^i(x) \gamma_\mu d_L^j(x) \right) + \bar{e}_L^j(x) \gamma_\mu \nu_L^j(x) \right] , \tag{23}$$

where V is the Cabibbo-Kobayashi-Maskawa (CKM) matrix [1, 2], $u^i = \{u, c\}$ [1], $d^i = \{d, s, b\}$, $e^i = \{e, \mu, \tau\}$, $\nu^i = \{\nu_e, \nu_\mu, \nu_\tau\}$ and the subscript L denotes the left-handed component of the field.

Given that, using for instance the Feynman gauge,

$$D^{\mu\nu}(x, M_W) = \int \frac{d^4q}{(2\pi)^4} e^{-iq\cdot x} \frac{-g^{\mu\nu}}{q^2 - M_W^2 + i\varepsilon} = \delta(x) \frac{g^{\mu\nu}}{M_W^2} + \dots , \tag{24}$$

the two weak currents go at short distances in the large M_W limit. Thus the S matrix element can be expanded in terms of local operators and gives

$$\langle F|iS|I\rangle = 4 \frac{G_F}{\sqrt{2}} \sum_i C_i(\mu) \langle F|Q_i(\mu)|I\rangle + \dots , \tag{25}$$

where G_F is the Fermi constant $G_F/\sqrt{2} = g^2/8M_W^2$. The dots represent subdominant terms suppressed by powers of Q^2/M_W^2 where Q is the typical energy scale of the process under study ($\Lambda_{\rm QCD}$ for light hadron decays, m_b for B decays, etc.).

The OPE in Eq. (25) is valid for all possible initial and final states. This allows for the definition of the effective weak Hamiltonian, given by the operator relation

$$\mathcal{H}_W^{\Delta F=1} = 4 \frac{G_F}{\sqrt{2}} \sum_i C_i(\mu) Q_i(\mu) = 4 \frac{G_F}{\sqrt{2}} \boldsymbol{Q}^T(\mu) \cdot \boldsymbol{C}(\mu) . \tag{26}$$

The $Q_i(\mu)$ are local, dimension-six operators renormalized at the scale μ and the $C_i(\mu)$ are the corresponding Wilson coefficients. The set of operators $Q_i(\mu)$ forms a complete basis for the OPE. This set contains all the linearly-independent, dimension-six operators with the same quantum numbers of the original weak current product, usually reduced by means of the equations of motion (although off-shell basis can also be considered). In practice, the operators generated by the expansion of the *full* amplitude (in the so-called "matching" procedure described below) must be complemented by the additional operators generated by the renormalization procedure. Notice that, in the absence of QCD (and QED) corrections, the effective Hamiltonian in Eq. (26) reduces to the Fermi theory of weak interactions. For instance, from the leptonic part of the charged currents, one finds

$$\mathcal{H}_{\rm Fermi} = \frac{G_F}{\sqrt{2}} \bar{e} \gamma^\mu (1 - \gamma_5) \nu_e \bar{\nu}_\mu \gamma_\mu (1 - \gamma_5) \mu , \tag{27}$$

i.e. the Fermi Hamiltonian describing the muon decay.

For quark transitions, gluonic (and photonic) radiative corrections to amplitudes computed in terms of local operators produce ultraviolet divergences which are not present in the full theory. This implies that the local operators Q_i need to be renormalized and depend on the renormalization scale μ. Therefore μ-dependent Wilson coefficients must be introduced to cancel this dependence.

Provided that one choses a large enough renormalization scale $\mu \gg \Lambda_{\rm QCD}$, short-distance QCD (and QED) corrections to the Wilson coefficients can be calculated using a renormalization-group-improved perturbation theory, resumming classes of large logs

[1] The top quark is not included as we are building an effective theory valid for energies below M_W.

potentially dangerous for the perturbative expansion. All non-perturbative effects are confined in the matrix elements of the local operators. Their calculation requires a non-perturbative technique able to compute matrix elements of operators renormalized at the scale μ. In the case of leptonic and semi-leptonic hadron decays, the hadronic effects are confined to the matrix elements of a single current which can be conveniently written using meson decay constants (for matrix elements between one hadron and the vacuum) or form factors (for matrix elements between two hadron states) as for example

$$\begin{aligned}
&\langle 0|\bar{d}_L\gamma^\mu\gamma_5 u_L|\pi^+(q)\rangle = if_\pi q^\mu\,,\\
&\langle \pi^0(p')|\bar{s}_L\gamma^\mu d_l|K^0(p)\rangle = f_+^0(q^2)(p+p')^\mu + f_-^0(q^2)(p-p')^\mu\,, \quad q^2=(p-p')^2\,. \qquad (28)
\end{aligned}$$

Appearing in different processes, they can be computed using non-perturbative techniques or measured in one process and used to predict the others. Predictions for non-leptonic decays, on the other hand, usually require non-perturbative calculations. Data-driven strategies are possible in cases where many measurements related by flavor symmetries are available.

The determination of Wilson coefficients at a given order in perturbation theory requires two steps: (*i*) the *matching* between the full theory and the effective Hamiltonian at a scale $M \sim O(M_W)$ and (*ii*) the RGE evolution from the matching scale M down to the renormalization scale μ.

Let's discuss the second point first. Since $\mathcal{H}_W^{\Delta F=1}$ in Eq. (26) is independent of μ, i.e. $\mu^2\frac{d}{d\mu^2}\mathcal{H}_W^{\Delta F=1}=0$, the Wilson coefficients $\boldsymbol{C}(\mu)=(C_1(\mu),C_2(\mu),\dots)$ must satisfy the RGE

$$\mu^2\frac{d}{d\mu^2}\boldsymbol{C}(\mu) = \frac{1}{2}\hat{\gamma}^T\boldsymbol{C}(\mu)\,, \qquad (29)$$

which can be conveniently written as

$$\left(\mu^2\frac{\partial}{\partial\mu^2}+\beta(\alpha_s)\frac{\partial}{\partial\alpha_s}-\frac{1}{2}\hat{\gamma}^T(\alpha_s)\right)\boldsymbol{C}(\mu)=0\,, \qquad (30)$$

where

$$\beta(\alpha_s)=\mu^2\frac{d\alpha_s}{d\mu^2} \qquad (31)$$

is the QCD β function and

$$\hat{\gamma}(\alpha_s)=2\hat{Z}^{-1}\mu^2\frac{d}{d\mu^2}\hat{Z} \qquad (32)$$

is the operator anomalous dimension matrix. The matrix $\hat{Z}$ of the renormalization constants is defined by the relation connecting the bare operators $\boldsymbol{Q}^B$ to the renormalized ones $\boldsymbol{Q}(\mu)$

$$\boldsymbol{Q}(\mu)=\hat{Z}^{-1}(\mu,\alpha_s)\boldsymbol{Q}^B\,. \qquad (33)$$

The solution of the system of linear differential equations (30) is found by introducing a suitable evolution matrix $U(\mu,M_W)$ and by imposing an appropriate set of initial conditions, usually called matching conditions. The coefficients $\boldsymbol{C}(\mu)$ are given by [2]

$$\boldsymbol{C}(\mu)=\hat{U}(\mu,M)\boldsymbol{C}(M)\,, \qquad (34)$$

[2] The problem of the thresholds due to the presence of heavy quarks with a mass $M_W \gg m_Q \gg \Lambda_{\rm QCD}$ will be discussed below.

with

$$\hat{U}(m_1, m_2) = T_{\alpha_s} \exp\left(\int_{\alpha_s(m_1)}^{\alpha_s(m_2)} \frac{d\alpha_s}{\beta(\alpha_s)} \hat{\gamma}^T(\alpha_s) \right) . \tag{35}$$

T_{α_s} is the ordered product with increasing couplings from right to left.

The matching conditions are found by imposing that, at $\mu = M \sim O(M_W)$, the matrix elements of the original T-product of the currents coincide, up to terms suppressed by inverse powers of M_W, with the corresponding matrix elements of $\mathcal{H}_W^{\Delta F=1}$. To this end, we introduce the vector $\boldsymbol{T}$ defined by the relation

$$i\langle\alpha|S|\beta\rangle = 4\frac{G_F}{\sqrt{2}}\langle\alpha|\boldsymbol{Q}^T|\beta\rangle_0 \cdot \boldsymbol{T}(M_W, m_t; \alpha_s) + \dots \tag{36}$$

where $\langle\alpha|\boldsymbol{Q}^T|\beta\rangle_0$ are matrix elements of the operators computed at the tree level and the dots denote power-suppressed terms. The vector $\boldsymbol{T}$ contains the dependence on heavy masses and has a perturbative expansion in α_s [3] On dimensional basis, $\boldsymbol{T}$ can only be a function of m_t/M_W and of $\log(p^2/M_W^2)$ where p generically denotes the external momenta.

We also introduce the matrix $\hat{M}(\mu)$ such that

$$\begin{aligned}\langle\alpha|\mathcal{H}_W^{\Delta F=1}|\beta\rangle &= 4\frac{G_F}{\sqrt{2}}\langle\alpha|\boldsymbol{Q}^T(\mu)|\beta\rangle\boldsymbol{C}(\mu) \\ &= 4\frac{G_F}{\sqrt{2}}\langle\alpha|\boldsymbol{Q}^T|\beta\rangle_0\hat{M}^T(\mu;\alpha_s)\boldsymbol{C}(\mu) .\end{aligned} \tag{37}$$

In terms of $\boldsymbol{T}$ and $\hat{M}$, the matching condition

$$i\langle\alpha|S|\beta\rangle = \langle\alpha|\mathcal{H}_W^{\Delta F=1}|\beta\rangle \tag{38}$$

fixes the value of the Wilson coefficients at the scale M as

$$\boldsymbol{C}(M) = [\hat{M}^T(M;\alpha_s)]^{-1}\boldsymbol{T}(M_W, m_t; \alpha_s) . \tag{39}$$

As the full and the effective theories share the same infrared behavior, the dependence on the external states on which the matching conditions are imposed drops in Eq. (39), so that any matrix element can be used, even off-shell ones (with some caution), provided the *same* external states are used for computing matrix elements in both theories. Notice that the matching can be imposed at any scale M such that large logs do not appear in the calculation of the Wilson coefficients at that scale, i.e. $\alpha_s \log(M/M_W) \ll 1$.

Equation (34) is correct if no threshold corresponding to a quark mass between μ and M_W is present. Indeed, as α_s, $\hat{\gamma}$ and $\beta(\alpha_s)$ depend on the number of "active" flavors, it is necessary to change the evolution matrix $\hat{U}$ defined in Eq. (35), when passing quark thresholds. The general case then corresponds to a sequence of effective theories with a decreasing number of "active" flavors. By "active" flavor, we mean a dynamical massless ($\mu \gg m_q$) quark field. The theory with k "active" flavors is matched to the one with $k+1$ "active" flavors at the threshold. This procedure changes the solution for the Wilson coefficients. For instance, if one starts with five "active" flavors at the scale M_W and chooses $m_c \ll \mu \ll m_b$, the Wilson coefficients become

$$\boldsymbol{C}(\mu) = W[\mu, M_W]\boldsymbol{C}(M_W) = \hat{U}_4(\mu, m_b)\hat{T}_{45}\hat{U}_5(m_b, M_W)\boldsymbol{C}(M_W) . \tag{40}$$

[3] For simplicity, we discuss QCD corrections only. QED corrections can be considered as well and are included in a similar way.

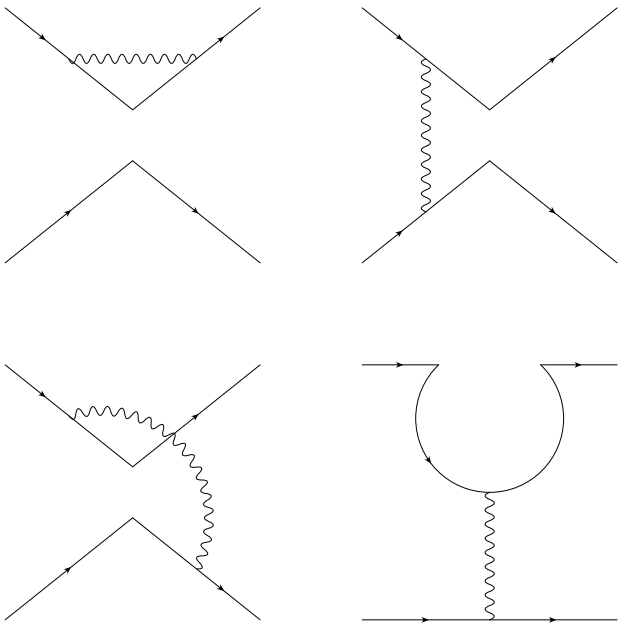

Fig. 2. One-loop correction to the $\Delta F = 1$ effective weak Hamiltonian.

The matrix $\hat{T}_{45}$ matches the four and five flavor theories so that the Wilson coefficients are continuous across the threshold. The inclusion of the charm threshold proceeds along the same lines.

So far we have presented the formal solution of the matching and the RGE for the Wilson coefficients. In practice, we can calculate the relevant functions (β, $\hat{\gamma}$, $\hat{M}$, $\boldsymbol{T}$, etc.) in perturbation theory only. At the LO, one has

$$\beta(\alpha_s) = -\frac{\alpha_s^2}{4\pi}\beta_0 + \dots\,, \quad \hat{\gamma} = \frac{\alpha_s}{4\pi}\hat{\gamma}^{(0)} + \dots \quad \boldsymbol{T} = T^{(0)} + \dots\,, \quad \hat{M} = \hat{1} + \dots\,, \tag{41}$$

so that the LO Wilson coefficients read

$$\boldsymbol{C}_{\rm LO}(\mu) = \left(\frac{\alpha_s(M)}{\alpha_s(\mu)}\right)^{\hat{\gamma}^{(0)T}/2\beta_0} \boldsymbol{T}^0\,. \tag{42}$$

The explicit solution can be found in the basis where the LO anomalous dimension matrix $\hat{\gamma}^{(0)}$ is diagonal. To go beyond the LO, we have to expand the relevant functions to higher order in α_s. Discussing the details on higher order calculations goes beyond the purpose of this primer. They can be found in the original literature cited in the following presentation of the actual effective Hamiltonians for $\Delta F = 1$ and $\Delta F = 2$ transitions.

2.1.1. $\Delta F = 1$ *effective weak Hamiltionians*

Even restricting to processes which change each flavor number by no more than one unit, namely $\Delta F = 1$ transitions, several effective Hamiltonians can be introduced. We start considering the Hamiltonian relevant for transtions with $\Delta B = 1$, $\Delta C = 0$, $\Delta S = -1$:

$$\mathcal{H}_W^{\Delta B=1\,,\Delta C=0\,,\Delta S=-1} = 4\frac{G_F}{\sqrt{2}}\Big(\lambda_c^s\big(C_1(\mu)Q_1^c(\mu)+C_2(\mu)Q_2^c(\mu)\big) \\ +\lambda_u^s\big(C_1(\mu)Q_1^u(\mu)+C_2(\mu)Q_2^u(\mu)\big)-\lambda_t^s\sum_{i=3}^{10}C_i(\mu)Q_i(\mu)\Big)\,, \tag{43}$$

where the $\lambda_q^s = V_{qb}^* V_{qs}$ and the operator basis is given by

$$\begin{aligned}
Q_1^q &= \bar{b}_L^\alpha\gamma^\mu q_L^\alpha\,\bar{q}_L^\beta\gamma_\mu s_L^\beta & Q_2^q &= \bar{b}_L^\alpha\gamma^\mu q_L^\beta\,\bar{q}_L^\beta\gamma_\mu s_L^\alpha \\
Q_3 &= \bar{b}_L^\alpha\gamma^\mu s_L^\alpha\sum_q\bar{q}_L^\beta\gamma_\mu q_L^\beta & Q_4 &= \bar{b}_L^\alpha\gamma^\mu s_L^\beta\sum_q\bar{q}_L^\beta\gamma_\mu q_L^\alpha \\
Q_5 &= \bar{b}_L^\alpha\gamma^\mu s_L^\alpha\sum_q\bar{q}_R^\beta\gamma_\mu q_R^\beta & Q_6 &= \bar{b}_L^\alpha\gamma^\mu s_L^\beta\sum_q\bar{q}_R^\beta\gamma_\mu q_R^\alpha \\
Q_7 &= \frac{3}{2}\bar{b}_L^\alpha\gamma^\mu s_L^\alpha\sum_q e_q\bar{q}_R^\beta\gamma_\mu q_R^\beta & Q_8 &= \frac{3}{2}\bar{b}_L^\alpha\gamma^\mu s_L^\beta\sum_q e_q\bar{q}_R^\beta\gamma_\mu q_R^\alpha \\
Q_9 &= \frac{3}{2}\bar{b}_L^\alpha\gamma^\mu s_L^\alpha\sum_q e_q\bar{q}_L^\beta\gamma_\mu q_L^\beta & Q_{10} &= \frac{3}{2}\bar{b}_L^\alpha\gamma^\mu s_L^\beta\sum_q e_q\bar{q}_L^\beta\gamma_\mu q_L^\alpha
\end{aligned} \tag{44}$$

The sum index q runs over the "active" flavors, α, β are color indices and e_q is the electric charge of the quark q. Besides Q_1, which come from the matching, the above operators are generated by gluon and photon exchanges in the Feynman diagrams of fig. 2. In particular, Q_2^q is generated by current–current diagrams while Q_3–Q_6 and Q_7–Q_{10} are generated by gluon and photon penguin diagrams respectively. Notice that the choice of the operator basis in not unique. Different possibilities have been considered in the literature [17–23].

The operators basis includes the ten independent operators in Eq. (44) in the five-flavor effective theory. Below the bottom threshold, the following relation holds

$$Q_{10} - Q_9 - Q_4 + Q_3 = 0\,, \tag{45}$$

so that the independent operators become nine. The basis is further reduced in the three-flavor theory, i.e. below the charm threshold, due to the additional relations

$$Q_4 - Q_3 - Q_2 + Q_1 = 0\,, \qquad Q_9 - \frac{3}{2}Q_1 + \frac{1}{2}Q_3 = 0\,. \tag{46}$$

For $b \to s$ transitions with a photon or a lepton pair in the final state, additional dimension-six operators must be included in the basis, namely

$$\begin{aligned}
Q_{7\gamma} &= \frac{e}{16\pi^2}m_b\bar{b}_L^\alpha\sigma^{\mu\nu}F_{\mu\nu}s_L^\alpha \\
Q_{8g} &= \frac{g_s}{16\pi^2}m_b\bar{b}_L^\alpha\sigma^{\mu\nu}G_{\mu\nu}^A T^A s_L^\alpha \\
Q_{9V} &= \frac{1}{2}\bar{b}_L^\alpha\gamma^\mu s_L^\alpha\,\bar{l}\gamma_\mu l \\
Q_{10A} &= \frac{1}{2}\bar{b}_L^\alpha\gamma^\mu s_L^\alpha\,\bar{l}\gamma_\mu\gamma_5 l
\end{aligned} \tag{47}$$

where $G_{\mu\nu}^A$ ($F_{\mu\nu}$) is the gluon (photon) field strength tensor and T^A are the $SU(3)$ generators. They contribute an additional term to the Hamiltonian in Eq. (44) so that,

up to doubly Cabibbo-suppressed terms and neglecting the electroweak penguin operators Q_7–Q_{10}, the effective weak Hamiltonian for these processes reads

$$\mathcal{H}_W = -4\frac{G_F}{\sqrt{2}}\lambda_t^s\Big(\sum_{i=1}^{6} C_i(\mu)Q_i(\mu) + C_{7\gamma}(\mu)Q_{7\gamma}(\mu) + C_{8g}(\mu)Q_{8g}(\mu) \\ + C_{9V}(\mu)Q_{9V}(\mu) + C_{10A}(\mu)Q_{10A}(\mu)\Big)\,, \tag{48}$$

with $Q_{1,2} = Q_{1,2}^c$ defined in Eq. (44).

At present, the $\Delta F = 1$ effective weak Hamiltonian in Eq. 44, including electroweak penguin operators (Q_7–Q_{10} in Eq. (44)), is known at the NNLO in α_s [24] and at the NLO in α_e [25,26]. The effective Hamiltonian in Eq. (48) has been fully computed at the NNLO in the strong coupling constant [27–30].

Effective weak Hamiltonians for other transtions can be obtained by trivial changes in the quark fields and in the CKM matrix elements entering eqs. (44) and (44). In particular

$$\begin{aligned}
&\Delta B = 1\,, \Delta C = 0\,, \Delta S = 0 : s \to d \\
&\Delta B = 0\,, \Delta C = 0\,, \Delta S = 1 : b \to s\,, s \to d \\
&\Delta B = 0\,, \Delta C = 1\,, \Delta S = 0 : b \to c\,, s \to u\,, c \to s\,, u \to d\,.
\end{aligned} \tag{49}$$

In other cases, for instance $\Delta B = 1$, $\Delta C = -1$, $\Delta S = 0$ transitions, the Hamiltonian has a simpler structure, namely

$$\mathcal{H}_W^{\Delta B=1,\,\Delta C=-1,\,\Delta S=0} = 4\frac{G_F}{\sqrt{2}}V_{cb}^* V_{ud}\Big(C_1(\mu)Q_1'(\mu) + C_2(\mu)Q_2'(\mu)\Big) \tag{50}$$

with

$$Q_1' = \bar{b}_L^\alpha \gamma^\mu c_L^\alpha\, \bar{u}_L^\beta \gamma_\mu d_L^\beta, \quad Q_2' = \bar{b}_L^\alpha \gamma^\mu c_L^\beta\, \bar{u}_L^\beta \gamma_\mu d_L^\alpha\,. \tag{51}$$

Only current–current operators enter this Hamiltonian. Penguin operators are not generated as the considered transitions involve four different flavors. Other Hamiltonians share this feature and can be obtained from eqs. (50) and (51) with the following replacements

$$\begin{aligned}
&\Delta B = 1\,, \Delta C = 1\,, \Delta S = 0 : c \to u\,, u \to c \\
&\Delta B = 1\,, \Delta C = -1\,, \Delta S = -1 : d \to s \\
&\Delta B = 1\,, \Delta C = 1\,, \Delta S = -1 : c \to u\,, u \to c\,, d \to s \\
&\Delta B = 0\,, \Delta C = -1\,, \Delta S = 1 : b \to s \\
&\Delta B = 0\,, \Delta C = 1\,, \Delta S = 1 : b \to s\,, c \to u\,, u \to c\,.
\end{aligned} \tag{52}$$

Clearly the (omitted) Hermitean-conjugate terms in the Hamiltonians mediate transitions with opposite ΔF.

Notice that physics beyond the SM could change not only the Wilson coefficients through the matching conditions, but also the operator basis where new spinor and color structures may appear. Indeed the most general $\Delta F = 1$ basis contains a large number of operators making it hardly useful. On the other hand, a possible definition of the class of new physics models with minimal flavor violation is that these models produce only real corrections to the SM Wilson coefficients without changing the operator basis of the effective weak Hamitonian [31].

2.1.2. $\Delta F = 2$ *effective weak Hamiltionians*

The $\Delta F = 2$ effective weak Hamiltionians are simpler than the $\Delta F = 1$ ones. In the SM, the operator basis includes one operator only. For example, the $\Delta S = 2$ effective Hamiltonian is commonly written as

$$\mathcal{H}_W^{\Delta S=2} = \frac{G_F^2}{4\pi^2} M_W^2 \Big(\lambda_c^2 \eta_1 S_0(x_c) + \lambda_t^2 \eta_2 S_0(x_t) + \lambda_t \lambda_c \eta_3 S_0(x_t, x_c) \Big) \hat{Q}_s \tag{53}$$

where $\lambda_q = V_{qs}^* V_{qd}$, the functions S_0 of $x_q = m_q^2/M_W^2$ come from the LO matching conditions, the coefficents η_i account for the RGE running and NLO effects. Starting from the dimension-six operator

$$Q_s = \bar{s}_L \gamma_\mu d_L \, \bar{s}_L \gamma^\mu d_L \, . \tag{54}$$

$\hat{Q}_s$ is defined as $\hat{Q}_s = K(\mu) Q_s(\mu)$, where $K(\mu)$ is the appropriate short-distance factor which makes $\hat{Q}$ independent of μ [32]. The matrix element of this operator between K^0 and $\bar{K}^0$ is parameterised in terms of the RG-invariant bag parameter $\hat{B}_K$ (see Sec. 7).

The Hamiltonian in Eq. (53) describes only the short-distance part of the $\Delta S = 2$ amplitude. Long-distance contributions generated by the exchange of hadronic states are also present. These contributions break the OPE producing additional terms which are diffcult to estimate. This is the case of the K^0–$\bar{K}^0$ mass difference ΔM_K which therefore cannot be reliably predicted. On the other hand, the CP-violation parameter ϵ_K, related to $\mathrm{Im}\langle \bar{K}^0 | \mathcal{H}_W^{\Delta S=2} | K^0 \rangle$, is short-distance dominated and thus calculable.

Concerning $\Delta B = 2$ transitions, namely the B_d^0–$\bar{B}_d^0$ and B_s^0–$\bar{B}_s^0$ mixing amplitudes, virtual top exchange gives the dominant contributions in the SM. Therefore these amplitudes are short-distance dominated and described by matrix elements of the Hamiltonian

$$\mathcal{H}_W^{\Delta B=2} = \frac{G_F^2}{4\pi^2} M_W^2 (\lambda_t^q)^2 \eta_2 S_0(x_t) \hat{Q}_b^q \tag{55}$$

where

$$Q_b^q = \bar{b}_L \gamma_\mu q_L \, \bar{b}_L \gamma^\mu q_L \, , \qquad q = \{d, s\} \, , \tag{56}$$

and $\hat{Q}_b^q$ is defined similarly to the $\Delta S = 2$ case in terms of the bag-parameter $\hat{Q}_b^q$ (see Sec. 7).

At present, $\Delta F = 2$ effective Hamiltonians are known at the NLO in the strong coupling constants [33–35].

It is worth noting that, unlike $\Delta F = 1$ Hamiltonians, generic new physics contributions to $\Delta F = 2$ transitions generate few additional operators allowing for model-independent studies of $\Delta F = 2$ processes where the Wilson coefficients at the matching scale are used as new physics parameters [36].

Finally, we mention that the absorbtive part of $\Delta F = 2$ amplitudes, related to the neutral mesons width differences, can also be calculated using an OPE applied to the rates rather than to the amplitudes. We refer the interested reader to Sec. 7. for details on this calculation.

2.2. *Factorization*

In the previous section it was shown how to integrate out physics at the electroweak scale, resulting in 10 four-fermion operators O_1-O_{10}. In order to measure the decay rates or CP-asymmetries in non-leptonic decays of a B meson to two light pseudoscalar mesons

(either π or K), one needs information about the matrix elements of these operators between the initial B meson and the given final state. The nature of the strong interaction implies that these matrix elements can not be calculated perturbatively, and one either has to resort to non-perturbative methods to calculate these matrix elements or extract them from data.

In order to determine the required matrix elements from data and still obtain information about the electroweak physics requires to have more experimental input than unknown matrix elements. It has been known for a long time that in the $B \to \pi\pi$ system there are more measurements than non-perturbative parameters, which allows to measure some fundamental parameters of the CKM matrix [37]. However, of the 8 possible measurements, only 6 have been made to this point, one of which still has very large uncertaities. Thus, in practice, even in the $\pi\pi$ system some additional information is required in order to have detailed information about the electroweak phases. The situation is worse once we include Kaons in the final state, and without using additional theoretical information, there are more unknown parameters than there are measurements.

Factorization utilizes an expansion in $\Lambda_{\rm QCD}/m_b$ in order to simplify the required matrix elements, resulting in new relations in the limit $\Lambda_{\rm QCD}/m_b \to 0$. Theoretically, this limit can be taken using diagrammatic factorization techniques (QCD factorization) [38–40] or, equivalently, soft-collinear effective theory (SCET) [41–44], together with heavy quark effective theory (HQET). Before detailing how the factorization theorems arise in the effective field theory approach, we give a simple physical picture of factorization, known as color transparency.

As discussed above, the decay $B \to M_1 M_2$ is described by the matrix elements of local four-fermion operators, allowing the b quark to decay to three light quarks. Two of these quarks will form the meson M_1, while the meson M_2 is formed from the third light quark together with the spectator quark of the B meson. The dominant contribution to a given decay arises from operators for which the two light quark forming M_1 are in a color singlet configuration.These two quarks in a color singlet configuration will only interact non-perturbatively with the remaining system once their separation is of order $1/\Lambda_{\rm QCD}$. Due to the large energy $E \sim m_b/2$ of the light mesons, this separation only occurs when the two quarks are a distance $d \sim E_\pi/\Lambda_{\rm QCD}^2$ from the origin of the decay, and therefore out of the reach $d \sim 1/\Lambda_{\rm QCD}$ of the non-perturbative physics of the B meson. Thus, the non-perturbative dynamics of one of the two mesons is independent of the rest of the system. Since the second light meson requires the spectator quark of the B meson, no such factorization should be expected.

Using effective field theory methods allows to prove this intuitive result rigorously, while at the same time allowing in principle to go beyond the leading order result in $\Lambda_{\rm QCD}/m_b$. The first step in the factorization proof is to separate the different energy scales in the system, by constructing the correct effective field theory. In the rest frame of the B meson, the two light mesons decay back-to-back with energy $m_B/2$, and we label the directions of the two mesons by four-vectors n and $\bar{n}$. To describe these two energetic mesons we require collinear quark and gluon fields which are labeled by the direction of flight n or $\bar{n}$ of the meson. We will call the collinear quark fields $\chi_{n/\bar{n}}$ and $A_{n/\bar{n}}$, respectively. In order to describe the heavy B meson, we require soft heavy quark and soft light quark and gluon fields, which we call h_s, q_s and A_s, respectively. Since it is the two light quarks in the n direction that form the meson M_1, we will also write $M_n \equiv M_1$ and $M_{\bar{n}} \equiv M_2$.

The important property of SCET/HQET that allows to prove the factorization theorem is that to leading order in $\Lambda_{\rm QCD}/m_b$ the collinear fields in the different directions do not interact with one another. Furthermore, all interactions between collinear and soft fields can be removed from the Lagrangian by redefining the collinear fields to be multiplied by a soft Wilson line Y_n, which depends on the direction n of the collinear field it belongs to. Since all interactions between the different sectors disappear at leading order, the Lagrangian can be written as

$$\mathcal{L}_{\rm eff} = \mathcal{L}_n + \mathcal{L}_{\bar{n}} + \mathcal{L}_s + \mathcal{O}(\Lambda_{\rm QCD}/m_b)\,. \tag{57}$$

The 4-quark operators O_i describing the decay of the heavy b quark are matched onto operators in the effective field theory, which are constructed out of the collinear and soft fields. This allows to write written as

$$O_i = C_i \otimes O_i^{n\bar{n}} = C_i \otimes \left[\bar{h}_s \Gamma_i Y_{\bar{n}} \chi_{\bar{n}}\right] \left[\bar{\chi}_n Y_n^\dagger \Gamma_i Y_n \chi_n\right]. \tag{58}$$

Here C_i denotes the Wilson coefficient of the operators and describes the physics occurring at the scale m_b, and the different operators are distinguished by their Dirac and color structure Γ_i. The symbol $\otimes$ denotes a convolution between the Wilson coefficients and operators, which is due to the fact that the Wilson coefficients can depend on the large energies of the light quarks. Note that if the two collinear quarks in the n direction form a color singlet (meaning Γ_i is color singlet), then we can use the unitarity of Wilson lines $Y_n^\dagger Y_n = 1$ to write

$$O_i = C_i \otimes \left[\bar{h}_s \Gamma_i Y_{\bar{n}} \chi_{\bar{n}}\right] \left[\bar{\chi}_n \Gamma_i \chi_n\right]. \tag{59}$$

Since the Wilson lines Y_n describe the coupling of the collinear fields χ_n to the rest of the system, their cancellation is the field theoretical realization of the physical picture given before.

The absence of interactions between the fields in the n direction from the rest of the system can be used to separate the matrix element of the operators O_i as

$$\begin{aligned}\langle M_n M_{\bar{n}} | O_i | B_s\rangle &= C_i \otimes \langle M_n M_{\bar{n}} | O_i^{n\bar{n}} | B_s\rangle = C_i \otimes \langle M_n | \bar{\chi}_n \Gamma_i \chi_n | 0\rangle \langle M_{\bar{n}} | h_s \Gamma_i Y_{\bar{n}} \chi_{\bar{n}} | B_s\rangle \\ &= C_i \otimes \phi_{M_n} \otimes \zeta_{BM_{\bar{n}}}\,.\end{aligned} \tag{60}$$

Here ϕ_M denotes the light cone distribution function of the meson M, while ζ_{BM} denotes the matrix element describing the $B \to M$ transition. Thus, the matrix element of the required operators factor into a convolution of a perturbatively calculable Wilson coefficient C_i, a matrix element describing the $B \to M_2$ transition, as well as the wave function of the meson M_1. The wave functions of the light pseudoscalar mesons have been measured in the past and are known relatively well, and some of the $B \to M_2$ matrix elements can be measured in semileptonic B decays. Thus, much information for the matrix elements of the operators O_i can be measured in other processes, allowing to use the non-leptonic data on to extract information about the weak scale physics.

There are several different approaches to understanding factorization and they go by the names QCD Factorization (QCDF) [38–40], perturbative QCD (PQCD) [45–50] and soft-collinear effective theory (SCET) [51–53] in the literature. All three approaches agree with everything discussed up to this point, and the main differences arises when trying to factorize the matrix elements ζ_{BM} further. This can be achieved by matching onto a

Table 1
Comparison of the different approaches to Factorization

	SCET	QCDF	PQCD
Expansion in $\alpha_s(\mu_i)$	No	Yes	Yes
Singular convolutions	N/A	New parameters	"Unphysical" k_T
Charm Loop	Non-perturbative	Perturbative	Perturbative
Number of paramterers	Most	Middle	Least

second effective theory which integrates out physics at the scale $\mu_i \sim \sqrt{\Lambda_{\rm QCD} m_b}$, which allows to write

$$\zeta_{BM} = J \otimes \phi_B \otimes \phi_M \,. \tag{61}$$

Here J is a matching coefficient that can be calculated perturbatively in an expansion in $\alpha_s(\mu_i)$. A naive calculation of this function J unfortunately leads to a singular convolution with the wave functions ϕ_M and ϕ_B, and it is the resolution of this problem that separates the different approaches. The SCET approach to factorization simply never performs the second step of the factorization theorem and uses directly the results in Eq. (60) but requiring the most experimental information. The PQCD results regulate the singular convolution with an unphysical transverse momentum of the light meson. These results are therefore on less solid theoretical footing, but require the least amount of experimental input. QCDF uses a mixture of both approaches and only uses Eq. (61) in cases where no singular convolutions are obtained. Note however, that for power corrections included into QCDF a different logic is used and a new non-perturbative parameter is included to parameterize singular convolutions.

Besides the differences in the treatment of singular convolutions, there are also differences in how matrix elements of operators containing charm quarks are treated. The theoretical question is whether such contributions can be calculated perturbatively or if they lead to new non-perturbative effects. The SCET approach does not attempt to calculate these matrix elements perturbatively, while QCDF and PQCD do use perturbation theory. The differences between the different approaches are summarized in Tab. 1.

2.3. *Lattice QCD*

The tools explained in the previous two sections are used to separate the physical scales of flavor physics into the weak scale, the heavy-quark scale, and the nonperturbative QCD scale. At the short distances of the first two, QCD effects can be treated with perturbation theory, as part of the evaluation of the Wilson coefficients. At longer distances, where QCD confines, perturbative QCD breaks down: to obtain the hadronic matrix elements of the operators, one must tackle nonperturbative QCD.

In some cases general features of field theory—symmetry, analyticity and unitarity, the renormalization group—are enough. For example, using the fact that QCD preserves CP one can show that the nonperturbative hadronic amplitude drops out of the CP asymmetry for a process like $B \to \psi K_S$. Another set of examples entails using one process to "measure" the hadronic matrix element, and then using this "measurement" in other, more intriguing, processes.

In general, however, one would like to compute hadronic matrix elements. The end objective is to see whether new physics lurks at short distances, so it is essential that one start with the QCD Lagrangian. Any approach will involve some approximation and compromise—QCD is too hard otherwise, so it is just as essential that any uncertainties be systematically reducible and under quantifiable control.

One method that has these aims is based on lattice gauge theory, which provides a mathematically sound definition of the gauge theory. In QCD, or any quantum field theory, anything of interest can be related to a correlation function

$$\langle O_1(x_1)O_2(x_2)\cdots O_n(x_n)\rangle = \frac{1}{Z}\int \prod_{x,\mu} dA_\mu(x) \prod_x d\bar{q}(x)dq(x)\, O_1(x_1)O_2(x_2)\cdots O_n(x_n)\, e^{-S}, \tag{62}$$

where the $O_i(x)$ are local, color singlet operators built out of quark fields q, antiquark fields $\bar{q}$, and gluon fields A_μ, and S is the classical action. The normalization factor Z is defined so that $\langle 1\rangle = 1$. For brevity, color, flavor, and (for q, $\bar{q}$) Dirac indices are implied but not written out. As it stands, Eq. (62) requires a definition of the products over the continuous spacetime label x. A mathematically sound way to do so is to start with a discrete spacetime variable, labeling the sites of a four-dimensional spacetime lattice. The idea goes back to Heisenberg, but for QCD and other gauge theories, the key came when Wilson showed how to incorporate local gauge invariance with the lattice [54]. If the lattice has $N_S^3 \times L_4$ sites, the spatial size of the finite volume is $L = N_S a$, where a is the lattice spacing, and temporal extent $L_4 = N_4 a$.

The lattice regulates the ultraviolet divergences that appear in quantum field theory and reduces the mathematical problem to one similar to statistical mechanics. Familiar perturbation theory can be derived starting with lattice field theory, but many other theoretical tools from condensed matter theory are available [55]. In the years after Wilson's paper there were, for example, many attempts to calculate hadron masses with strong coupling expansions.

If the lattice has a finite extent, then the system defined by Eq. (62) has a finite, albeit large, number of degrees of freedom. That means that the integrals can, in principle, be evaluated on a computer. In the rest of this report all applications of lattice QCD use this approach. In this section we provide a summary of the methods and a guide to estimate the inevitable errors that enter when mounting large-scale computing.

To start, let us leave the quarks and antiquarks aside and consider how many gluonic integration variables are needed. One would like the lattice spacing a to be smaller than a hadron, and the spatial volume should be large enough to contain at least one hadron. A desirable target is then $N_S = L/a = 32$, which is typical by now, and some groups use even larger lattices. For reasons explained below, the temporal extent N_4 is often taken to be 2 or 3 times larger than N_S. Taking the gluon's 8 colors and the 4-fold Lorentz index into account, the functional integral has $8 \times 4 \times 32^3 \times 64 \sim 10^8$ dimensions. This is practical with Monte Carlo methods, generating an ensemble of random values of the fields and replacing the right-hand side of Eq. (62) with

$$\langle O_1(x_1)O_2(x_2)\cdots O_n(x_n)\rangle = \frac{1}{C}\sum_c w(A^{(c)})\, O_1(x_1)O_2(x_2)\cdots O_n(x_n), \tag{63}$$

where the weight w for the cth configuration is specified below, and C is chosen so that $\langle 1\rangle = 1$. If the weight e^{-S} in Eq. (62) is real and positive, then the random fields can be

generated with distribution e^{-S}, in which case the weights are field independent. This is called importance sampling, and without it numerical lattice field theory is impractical.

In Minkowski space the weight is actually a phase factor $e^{iS_{\rm M}}$. That means that the weight fluctuates wildly, leading to enormous cancellations that are impossible to deal with numerically. For that reason, numerical LQCD calculations are carried out in Euclidean space or, equivalently, with imaginary time. With this restriction it remains straightforward to compute hadron masses and many matrix elements. If, however, the coordinates x_i in the original correlation function must have timelike or lightlike separation, then the function lies beyond current computational techniques.

Fermions, such as quarks, are special for several reasons. To impose the Pauli exclusion principle, the quark fields are Grassman numbers, *i.e.*, they anticommute with each other, $q_i q_j = -q_j q_i(1 - \delta_{ij})$. The integration is a formal procedure called Berezin integration. Fortunately, in cases of practical interest, the integration can be carried out by hand. The quark part of the action takes the form

$$S_{\bar{q}q} = \sum_{ij} \bar{q}_j \, M_{ji} q_i, \tag{64}$$

where i and j are multi-indices for spacetime, spin, color, and flavor. The matrix M is some lattice version of the Dirac operator. It is easy to show that

$$\int \prod_{ij} d\bar{q}_j dq_i e^{-S_{\bar{q}q}} = \det M. \tag{65}$$

Similarly, if quark fields appear in the operators, each instance of $q_i \bar{q}_j$ is replaced, using the Wick contraction, by the quark propagator M^{-1}_{ij}. The determinant and M^{-1} both depend on the gauge field; we simply carry out the quark and antiquark integration by hand and the gluon integration with the Monte Carlo, now with weight $\det M \, e^{-S_{\rm gauge}}$. The computation of M^{-1}_{ij} is demanding and the computation of $\det M$ is very demanding.

Another peculiar feature of fermions is an obstacle to realizing chiral symmetry on the lattice [56, 57], often called the fermion doubling problem, because a simple nearest-neighbor version of the Dirac operator leads to a 16-fold duplication of states. As a consequence, several formulations of lattice fermions are used in numerical lattice QCD. With staggered fermions [58, 59] some of the doubling remains, but a subset of the chiral symmetry is preserved. With Wilson fermions [60] all doubling is removed, but all of the (softly broken) chiral symmetries are explicitly broken. The Ginsparg-Wilson relation [61], which is derived from the renormalization group, shows how to preserve a remnant of chiral symmetry. Specific solutions are the fixed-point action [62,63], domain-wall fermions [64–67], and the overlap [68,69]. In the approaches satisfying the Ginsparg-Wilson relation, the chiral transformation turns out to depend on the gauge field [70]. From a theoretical perspective these are the most attractive, but from a practical perspective the staggered and Wilson formulations are numerically faster.

To obtain a finite problem, numerical lattice QCD uses a finite spacetime volume, so one must specify boundary conditions. In most cases, one identifies the field with itself, up to a phase:

$$q(x + L_\mu e_\mu) = e^{i\theta_\mu} q(x), \tag{66}$$

where e_μ is a unit vector and L_μ is the total extent, both in the μ direction. If $\theta_\mu = 0$ this is called a periodic boundary condition; if $\theta_\mu = \pi$ this is called an antiperiodic boundary condition; and otherwise this is called a twisted boundary condition [71, 72]

(although "twisted boundary condition" has other meanings too [73]). In a finite volume, the spectrum is discrete. The allowed 3-momenta are

$$\boldsymbol{p} = \frac{\boldsymbol{\theta}}{L} + \frac{2\pi}{L}\boldsymbol{n}, \tag{67}$$

where $\boldsymbol{n}$ is a vector of integers. One should bear in mind the discrete momentum follows from the finite volume, *not* the lattice itself. For one-particle states finite-volume effects are exponentially suppressed in periodic and antiperiodic [74], as well as (partially) twisted [75], boundary conditions. For multi-particle states the boundary effects are larger and more interesting [76], as discussed for $K \to \pi\pi$ in Ref. [77].

To determine the CKM matrix we need the matrix elements of the electroweak Hamiltonian derived in Sec. 2.1. In most cases, we are interested in transitions with at most one hadron in the initial or final state. These quantities are determined from 2- and 3-point correlation functions, as follows. A first step is to determine the mass. Let O be an operator with the quantum numbers (J^{PC}, etc.) of the state of interest. For large temporal extent L_4, and temporal separation $x_4 > 0$, the 2-point correlation function

$$\langle O(x) O^\dagger(0)\rangle = \langle 0|\hat{O}(x)\hat{O}^\dagger(0)|0\rangle, \tag{68}$$

where $|0\rangle$ is the QCD vacuum state and the hat indicates an operator in Hilbert space. Because these calculations are in Euclidean space, the time dependence of the annihilation operator is

$$O(x) = e^{x_4 \hat{H}} \hat{O} e^{-x_4 \hat{H}}, \tag{69}$$

where $\hat{H}$ is the Hamiltonian. In deriving Eq. (68) the eigenvalue of $\hat{H}$ in $|0\rangle$ is set to zero. Inserting a complete set of eigenstates of $\hat{H}$ into Eq. (68), one has

$$\langle O(x) O^\dagger(0)\rangle = \sum_n \langle 0|\hat{O} e^{-x_4 \hat{H}}|n\rangle\langle n|\hat{O}^\dagger|0\rangle = \sum_n e^{-x_4 E_n} |\langle n|\hat{O}^\dagger|0\rangle|^2, \tag{70}$$

where E_n is the energy of the nth state. If $|n\rangle$ is a single-particle state with zero 3-momentum, this energy is the mass. Taking x_4 large enough the state with the lowest-lying mass dominates, and this is how masses are computed in lattice QCD: evaluate the left-hand side of Eq. (70) with Monte Carlo techniques, and fit the right-hand side to a sum of exponentials.

Now suppose that one would like to consider the case where one is interested in a simple matrix element, one where an operator from the effective Hamiltonian annihilates the hadron. One can obtain the matrix element by computing another 2-point correlation function,

$$\langle J(x) O^\dagger(0)\rangle = \langle 0|\hat{J}(x)\hat{O}^\dagger(0)|0\rangle = \sum_n e^{-x_4 E_n} \langle 0|\hat{J}|n\rangle\langle n|\hat{O}^\dagger|0\rangle. \tag{71}$$

With the energies and overlaps $\langle n|\hat{O}^\dagger|0\rangle$ from the mass calculation, this calculation yields the transition matrix elements $\langle 0|\hat{J}|n\rangle$.

Most of the transitions of interest in flavor physics involve mesons, so it is worth illustrating how the quark propagators M^{-1} come in. For the charged Kaon, for example, we take the operator $O = \bar{s}\gamma_5 u$, and the 2-point function is computed via

$$\langle \bar{s}\gamma_5 u(x)\bar{u}\gamma_5 s(0)\rangle = -\langle \mathrm{tr}[G_u(x,0)\gamma_5 G_s(0,x)\gamma_5]\rangle_A, \tag{72}$$

where the trace is over color and Dirac indices, the average on the right-hand side is over gluon fields, and the quark propagator $G_f(x,y)$ is the solution of

$$\sum_x M(w,x)G_f(x,y) = \delta_{wy} \tag{73}$$

for flavor f, with color and Dirac indices implied. For the decay of a Kaon to leptons, the transition operator $J = \bar{s}\gamma_4\gamma_5 u$, and the computation of Eq. (71) simply replaces the first γ_5 on both sides of Eq. (72) with $\gamma_4\gamma_5$.

In neutral meson mixing and in semileptonic and radiative decays one encounters hadronic matrix elements with one hadron in both the initial and final states. For these one computes a 3-point correlation function,

$$\langle O_f(x)J(y)O_i^\dagger(0)\rangle = \sum_{mn} e^{-(x_4-y_4)E_{fm}} e^{-y_4 E_{in}} \langle 0|\hat{O}_f|fm\rangle\langle fm|\hat{J}|in\rangle\langle in|\hat{O}_i^\dagger|0\rangle. \tag{74}$$

The energies E_{fm}, E_{in} and amplitudes $\langle 0|\hat{O}_f|fm\rangle$, $\langle in|\hat{O}_i^\dagger|0\rangle$ are computed from 2-point functions, so the 3-point function yields $\langle fm|\hat{J}|in\rangle$. As before, for mesons (and baryons) the left-hand side is computed by contracting quark and antiquark fields in favor of quark propagators.

Hadron masses and decay amplitudes computed with lattice QCD depend on the bare gauge coupling and the bare quark masses, $1 + n_f$ free parameters, if n_f flavors are relevant to the problem at hand. The bare gauge coupling is related to the lattice spacing via renormalization. Thus, all dimensional quantities are really ratios of the quantity of interest compared to some fiducial quantity with dimensions of mass. This standard mass should be one that is either not very sensitive to the quark masses, such as some of the mass splitting in quarkonium, or whose mass dependence is seen to be under good control, such as f_π. The bare quark masses are fixed through the simplest hadron masses: m_π^2 and m_K^2 for the light and strange quarks, and the D_s and B_s or η_c and Υ masses for charmed and bottom quarks.

In computational physics it is important to know how to estimate uncertainties. In lattice QCD uncertainties arise, in principal, from the nonzero lattice spacing and the finite volume. In practice, the algorithms for computing $\det M$ and M^{-1} slow down as the quark masses are reduced. Consequently, the calculations cited elsewhere in this report are based on simulations with light quark masses that are higher than those of the up and down quarks in nature. Also in practice, one must be careful with heavy quarks, because the ultraviolet cutoff of currently available lattices, $1/a$ or π/a, is not (much) higher than the b-quark mass.

Fortunately, all these uncertainties may be assessed and quantified with effective field theories. (For a review of lattice QCD developed from this perspective, see [78].) For the so-called chiral extrapolation, lattice practitioners use chiral perturbation theory (χPT) to extend the reach from feasible light quark masses down to the physical up- and down-quark masses. This is the same χPT discussed in Sec. 2.4, although some practical considerations differ. Often applications of χPT to lattice QCD incorporate the leading discretization effects of the lattice. A chiral extrapolation entails a fit to numerical lattice-QCD data, and the associated uncertainty is estimated from a combination of quantitative measures, like goodness of fit, and qualitative considerations, such as the smallness of the quark mass and the effect of higher-order terms. In addition, χPT can be used to estimate finite-size effects, because the largest ones typically stem from processes in which a virtual pion is emitted, traverses the (periodic) boundary, and is then reabsorbed [74, 79, 80].

Discretization effects can be understood and controlled with the Symanzik effective field theory [81, 82]. The central Ansatz here is that lattice gauge theory is described by a continuum effective field theory. For QCD

$$\mathcal{L}_{\rm LGT} \doteq \mathcal{L}_{\rm QCD} + \sum_i a^{\dim \mathcal{L}_i - 4} K_i \mathcal{L}_i, \tag{75}$$

where the sum runs over operators $\mathcal{L}_i$ of dimension 5 or higher, and the power of a follows from dimensional analysis. The coefficient K_i subsumes short-distance effects, analogously to the Wilson coefficients in Sec. 2.1. The right-hand side of Eq. (75) is a tool to analyze the left-hand side or, more precisely, numerical data generated with the lattice Lagrangian $\mathcal{L}_{\rm LGT}$. If a is small enough, the higher dimensional operators may be treated as perturbations, leading to two key insights. The first is to justify an extrapolation in a to the continuum limit. More powerfully, if one can show for any (expedient) observable that, say, all the dimension-5 K_i vanish, then one knows that they vanish for all processes. The systematic reduction of the first several K_i is known as the Symanzik improvement program. With chirally symmetric actions, the dimension-5 K_i vanish by symmetry, so these are automatically $\mathrm{O}(a)$ improved.

For heavy quarks it is often the case that $m_Q a \not\ll 1$ and, hence, special care is needed. It is often said that lattice gauge theory breaks down, but it is more accurate to say that the most straightforward application of the Symanzik effective theory breaks down. For most calculations relevant to the CKM unitarity triangle, it is simpler to use HQET as a theory of cutoff effects [83–85]. This is possible because every (sensible) approach to heavy quarks on the lattice enjoys the same static limit and heavy-quark symmetries. So the same set-up as in Sec. 2.2 is possible, just with different short-distance structure—because the lattice changes short distance. Analogously to Symanzik, one can set up an improvement program. Now, however, the approach to the continuum limit is not so simple as $O(a)$ or $O(a^2)$. Nevertheless, most serious calculations with heavy-quarks use this formalism, or something equivalent, to estimate heavy-quark discretization effects. For further details on techniques for heavy quarks, see [86]. A more recent development is to map out the $m_Q a$ dependence in finite volume [87, 88], where both $m_Q a \ll 1$ and $m_Q a \approx 1$ are feasible (cf. Sec. 5).

One uncertainty that is not amenable to effective field theory (and is, therefore, devilish to quantify) stems from the so-called quenched approximation [89, 90]. It corresponds to replacing the computationally demanding $\det M$ in the weight by 1 and attempting to compensate by shifts in the bare gauge coupling and bare quark masses. Physically this corresponds to keeping valence quarks but treating sea quarks as a dielectric medium. This approximation is, by now, a historical artifact. All calculations that aspire to play a role in flavor physics now have either $n_f = 2$ or $2 + 1$ flavors of sea quarks. In both cases the 2 light quarks are taken as light as possible, as a basis for chiral extrapolation. For $2+1$ the third flavor is tuned to have the mass of the strange quark, whereas $n_f = 2$ means that the strange quark is quenched. A comparison of quenched and 2+1 flavor QCD is shown in Fig. 3, adapted from Ref. [91].

The results shown in Fig. 3, and many quoted in the rest of this report, have been obtained with staggered sea quarks [92, 93], which provide the least computationally demanding method for computing $\det M$ [94]. A drawback in this method is that staggered quarks come in four species, and a single quark flavor is simulated with $[\det_4 M]^{1/4}$ [95], where the subscript emphasizes the number of species in the determinant. There are con-

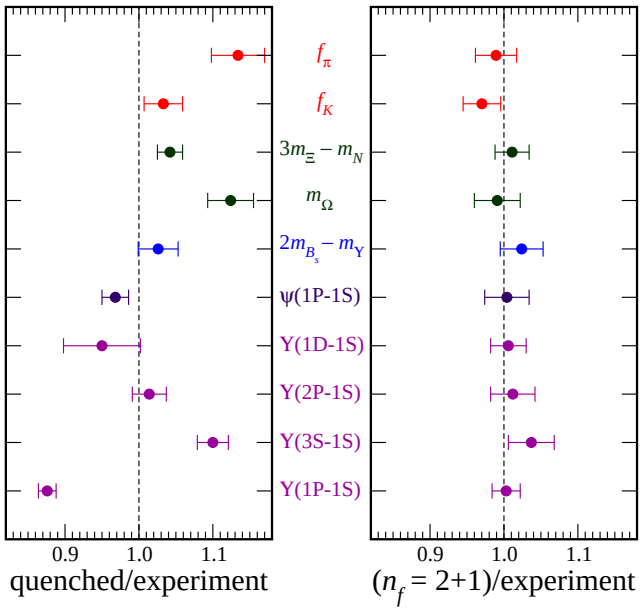

Fig. 3. Comparison of quenched and 2+1 flavor lattice QCD, plotting the ratio of calculated results to laboratory measurements [91]. The quenched results deviate by as much as 10–15%—not bad for a strongly-coupled field theory, but not good enough for flavor physics. With 2+1 flavors of sea quarks, however, the agreement is at the few-percent level.

cerns whether the fourth root really yields QCD in the continuum limit, although all published criticisms [96–98] have been refuted [99,100]. The theoretical arguments [101,102] in favor of this procedure are still being digested, although there is a significant body of supporting circumstantial evidence [103–105]. Whatever one thinks of the rooted staggered sea, it should be clear that these calculations should be confirmed. Other methods for sea quarks are accumulating sufficiently high statistics, so one can anticipate competitive results not only with staggered sea quarks [106], but also with Symanzik-improved Wilson sea quarks [107, 108], twisted-mass Wilson sea quarks [109], domain-wall sea quarks [110], and overlap sea quarks [111].

Calculations with 2 flavors of sea quarks have an uncertainty from quenching the strange quark. The error incurred may be as large as 3–5%, but is again hard to pin down. In many cases, for example the Ω^- mass, no significant effect is seen. When using 2-flavor results in this report, we take the original authors' estimates of the error for quenching the strange quark. If they have omitted this line from the error budget, we then assign a conservative 5% error.

Numerical lattice QCD has developed over the past thirty years, and much of the literature has aimed to develop numerical methods. Such work is not limited to algorithm development, but also to demonstrate how a phenomenologically relevant calculation could or should be carried out. Inevitably, some papers straddle the middle ground between development and mature results, with the consequence that some interesting papers have incomplete error budgets. Where such results are used later in the report, we try to account for omitted uncertainties in a rational way.

2.4. *Chiral Perturbation Theory*

Chiral perturbation theory (ChPT) is the effective field theory describing strong and electroweak interactions of the light pseudo-scalar mesons (π, K, η) at low energy, in a regime where standard perturbative methods are inapplicable [112–114]. ChPT relies on our understanding of the chiral symmetry of QCD in the limit of massless light quarks ($m_u = m_d = m_s = 0$), its spontaneous symmetry breaking according to the pattern $SU(3)_L \times SU(3)_R \to SU(3)_V$ and its explicit breaking due to non-vanishing quark masses.

In the massless limit $m_q = 0$, the QCD Lagrangian for light quarks ($q^\top = (u, d, s)$)

$$\mathcal{L}_{\rm QCD} = -\frac{1}{4}\, G^a_{\mu\nu} G^{\mu\nu}_a + i\, \bar{q}_L \gamma^\mu D_\mu q_L + i\, \bar{q}_R \gamma^\mu D_\mu q_R - \bar{q}_L\, m_q\, q_R - \bar{q}_L\, m_q\, q_L \tag{76}$$

is invariant under global independent $SU(3)_L \times SU(3)_R$ transformations of the left- and right-handed quarks in flavor space: $q_{L,R} \to g_{L,R}\; q_{L,R}\,,\; g_{L,R} \in SU(3)_{L,R}$. The absence of $SU(3)$ multiplets of opposite parity in the hadronic spectrum suggests that the chiral group $G = SU(3)_L \times SU(3)_R$ is spontaneously broken to the diagonal subgroup $H = SU(3)_V$, i.e. the symmetry is realized à la Nambu-Goldstone [115–117]. According to Goldstone's theorem [115] then, the spectrum of QCD should contain an octet of pseudoscalar massless bosons, in one to one correspondence to the broken symmetry generators. These are identified with the π, K, and η mesons, which would be massless in the exact chiral limit of $m_{u,d,s} = 0$, but acquire a finite mass in the real world due to explicit chiral symmetry breaking induced by $m_q \neq 0$. Pions, Kaons, and eta remain, however, the lowest lying hadronic excitations. The existence of a gap separating π, K, η from the rest of the spectrum makes it possible to build an effective theory involving only Goldstone modes.

The basic building blocks of the effective theory are the Goldstone fields φ. Intuitively, the massless Goldstone modes describe excitations of the system along the directions in field space that connect degenerate vacuum configurations (think about the circle of minima in a "Mexican-hat" potential). Mathematically, this means that the Goldstone fields parametrize the elements $u(\varphi)$ of the coset space $SU(3)_L \times SU(3)_R / \; SU(3)_V$ [118, 119]. The transformation of φ under G is determined by the action of G on the elements $u(\varphi)$ of the coset space

$$u(\varphi) \to u(\varphi') = g_R u(\varphi) h(g,\varphi)^{-1} = h(g,\varphi) u(\varphi) g_L^{-1} \tag{77}$$

where $g = (g_L, g_R) \in G$. The explicit form of $h(g,\varphi) \in SU(3)_V$ will not be needed here. An explicit parametrization of $u(\varphi)$ is given by

$$u(\varphi) = \exp\left\{ \frac{i}{\sqrt{2}F} \varphi \right\}, \tag{78}$$

with

$$\varphi = \begin{pmatrix} \frac{1}{\sqrt{2}}\,\pi^0 + \frac{1}{\sqrt{6}}\,\eta_8 & \pi^+ & K^+ \\ \pi^- & -\frac{1}{\sqrt{2}}\,\pi^0 + \frac{1}{\sqrt{6}}\,\eta_8 & K^0 \\ K^- & \bar{K}^0 & -\frac{2}{\sqrt{6}}\,\eta_8 \end{pmatrix}.$$

The structure of the effective Lagrangian $\mathcal{L}_{\rm eff}$ is determined by chiral symmetry and the discrete symmetries of QCD. $\mathcal{L}_{\rm eff}$ has to be invariant under chiral transformations, up to explicit symmetry breaking terms that transform like the quark mass term in the QCD Lagrangian (76). As a consequence, $\mathcal{L}_{\rm eff}$ is organized as an expansion in powers of (i) derivatives (momenta) of the Goldstone fields and (ii) light quark masses (m_q). Since the meson masses squared are proportional to the quark masses, the two expansions are related ($m_q \sim O(M_M^2) \sim O(p^2)$) and the mesonic effective chiral Lagrangian takes the form

$$\mathcal{L}_{\rm eff} = \sum_{n\geq 1} \mathcal{L}_{2n} \ , \qquad\qquad \mathcal{L}_{2n} \sim O(p^{2n}) \ . \tag{79}$$

The power counting parameter is given by the ratio $p^2 \sim p_{\rm ext}^2/\Lambda_\chi^2$ of a typical external momentum (or quark mass) over the intrinsic scale Λ_χ, set by the lightest non-Goldstone states ($\Lambda_\chi \sim 1$ GeV). To each order in the expansion, the effective Lagrangian contains a number of low-energy constants (LECs) not fixed by symmetry consideration, encoding underlying QCD dynamics.
The leading order effective Lagrangian reads (in terms of $U(\varphi) = u(\varphi)^2$),

$$\mathcal{L}_2 = \frac{F^2}{4}\ {\rm Tr}\left[\partial_\mu U\, \partial^\mu U + 2B\, m_q \left(U + U^\dagger\right)\right] \tag{80}$$

where $m_q = {\rm diag}(m_u, m_d, m_s)$ and the trace is performed over the $SU(3)$ indices. The dimensionful constants F and B are related to the pion decay constant and the quark condensate by $F_\pi = F\,(1 + O(m_q))$ and $\langle 0|\bar{u}u|0\rangle = -F^2\, B\,(1 + O(m_q))$. $\mathcal{L}_2$ contains the Gell-Mann-Oaks-Renner [120] and Gell-Mann-Okubo [121,122] mass relations and allows one to calculate physical processes, such as $\pi\pi$ scattering, to $O(p^2)$ in terms of just F_π and M_M^2 ($M_\pi^2 = B(m_u + m_d)$, ...).

The power of the effective field theory approach is that it allows to systematically improve the calculations of low-energy processes by considering higher-order terms in the momentum/light-quark-mass expansion. As shown by Weinberg [112], at any given order in this expansion only a finite number of couplings in (79) appear. For instance at $O(p^4)$ a given amplitude receives contributions only from: (i) tree-level diagrams with one insertion from $\mathcal{L}_4$; (ii) one-loop diagrams with all vertices from $\mathcal{L}_2$. The loop diagrams perturbatively unitarize the theory and introduce physical infrared singularities due to pseudoscalar meson intermediate states (the chiral logs, $\sim m_q \log m_q$). However, loops also introduce ultraviolet divergences. Using a regularization compatible with chiral symmetry, the counterterms necessary to absorb the divergences must have the same form as the terms present in $\mathcal{L}_4$: thus, one loop divergences simply renormalize the LECs of $O(p^4)$. This argument generalizes to any order in the low-energy expansion: the effective theory is renormalizable order by order in the low-energy expansion.

The finite parts of the LECs can be fitted to experiment or extracted by matching to lattice QCD results (or other, less systematic approximations to non-perturbative QCD dynamics). The accuracy of a given calculation is bounded by the size of higher order terms in the low-energy expansion. State of the art calculations in the strong sector go up to $O(p^6)$ [123].

To illustrate the general features discussed above, we report here the expression of the the pion decay constant to $O(p^4)$ [114]

$$F_\pi = F\left[1 - 2\mu_\pi - \mu_K + \frac{8B}{F^2}\Big(\hat{m}\, L_5^r(\mu) + (m_u + m_d + m_s) L_4^r(\mu)\Big)\right]. \qquad (81)$$

Here $\mu_P = M_P^2/(32\pi^2 F^2)\log(M_P^2/\mu^2)$, $M_\pi^2 = B(m_u + m_d)$, $M_K = B(m_s + \hat{m})$, and $\hat{m} = 1/2(m_u + m_d)$. Moreover, μ is the renormalization scale and $L_{4,5}^r(\mu)$ are two finite scale-dependent LECs. This expression illustrates the appearance of calculable chiral logarithms (with unambiguous coefficients) as well as polynomial terms in the quark masses multiplied by a priori unknown coefficients. Expressions of this type are used to extrapolate lattice QCD results from unphysical quark masses to the physical point. Nowadays, this is one of the most relevant applications of ChPT in CKM physics. An important recent development in this area is the use of $SU(2)$ ChPT [110,124], in which Kaons are treated as external massive fields, to study the extrapolation of Kaon amplitudes in $m_{u,d}$ (see Sec. 4.4.4 for discussion and applications)

The framework presented above describes the strong interactions of Goldstone modes. It has been extended in several directions, highly relevant to CKM physics, to include:
- non-leptonic weak interactions of Goldstone modes ($\Delta S = 1, 2$) [125–128];
- interactions of soft Goldstone modes with heavy particles (heavy mesons [129,130] and baryons [131,132]);
- interaction of Goldstone modes with external electromagnetic fields and weak gauge bosons (this is achieved by adding external sources that couple to quark bilinears in the QCD Lagrangian [113,114]);
- other dynamical fields in the low-energy theory, such as photons [133] and light leptons [134] (the amplitudes are expanded to $O(e^2 p^{2n})$, e being the electromagnetic coupling).

2.5. *Beyond the Standard Model*

Despite its impressive phenomenological success, the SM should be regarded as a low-energy effective theory. Viewing the SM as an effective theory poses two main questions: which is the *energy scale* and which are the *interactions and symmetries properties* of the new degrees of freedom. So far we have no unambiguous answer for both these questions; however, a strong theoretical prejudice for new degrees of freedom around the TeV scale follows from a natural stabilization of the mechanism of electroweak symmetry breaking. In this perspective, low-energy flavor physics provide a powerful tool to address the second question, and in particular to explore the symmetries properties of the new degrees of freedom.

In order to describe New Physics (NP) effects in flavor physics we can follow two main strategies, whose virtues and limitations can be summarised as follows:
- *Generic Effective Field Theory (EFT) approaches.*
  Assuming the new degrees to be heavier than SM fields, we can integrate them out and describe NP effects by means of a generalization of the Fermi Theory: the SM Lagrangian becomes the renormalizable part of a more general local Lagrangian which includes an infinite tower of higher-dimensional operators, constructed in terms of SM fields and suppressed by inverse powers of an effective scale $\Lambda_{\rm NP} > M_W$.
  This general bottom-up approach allows us to analyse all realistic extensions of the SM in terms of a limited number of parameters (the coefficients of the higher-dimensional

operators). The drawback of this method is the impossibility to establish correlations of NP effects at low and high energies: the scale $\Lambda_{\rm NP}$ defines the cut-off of the EFT. However, correlations among different low-energy processes can be established implementing specific symmetry properties on the EFT, such as the Minimal Flavor Violation hypothesis (see Sec. 2.5.1). The experimental tests of such correlations allow us to test/establish general features of the new theory which holds independently of the dynamical details of the model. In particular, B, D and K decays are extremely useful in determining the flavor-symmetry breaking pattern of the NP model.

– *Explicit Ultraviolet completions.*
The generic EFT approach is somehow the opposite of the standard top-down strategy, where a given NP theory –and a specific set of parameters– are employed to evaluate possible deviations from the SM. The top-down approach usually allows us to establish several correlations, both at low energies and between low- and high-energy observables. In the following we will discuss in some detail this approach in the case of Minimal Supersymmetric extension of the SM (see Sec. 2.5.2). The price to pay of this strategy is the loss of generality. This is quite a high price given our limited knowledge about the physics above the electroweak scale.

2.5.1. *Model-independent approaches and the MFV hypothesis*

The NP contributions should naturally induce large effects in processes which are severely suppressed in the SM, such as meson-antimeson mixing ($\Delta F = 2$ amplitudes) or flavor-changing neutral-current (FCNC) rare decays. Up to now there is no evidence of deviations from the SM in these processes and this implies severe bounds on the effective scale of various dimension-six operators in the EFT approach. For instance, the good agreement between SM expectations and experimental determinations of K^0–$\bar{K}^0$ mixing leads to bounds above 10^4 TeV for the effective scale of $\Delta S = 2$ operators, i.e. well above the few TeV range suggested by a natural stabilization of the electroweak-symmetry breaking mechanism.

The apparent contradiction between these two determinations of Λ is a manifestation of what in many specific frameworks (supersymmetry, technicolor, etc.) goes under the name of *flavor problem*: if we insist on the theoretical prejudice that new physics has to emerge in the TeV region, we have to conclude that the new theory possesses a highly non-generic flavor structure. Interestingly enough, this structure has not been clearly identified yet, mainly because the SM (the low-energy limit of the new theory), doesn't possess an exact flavor symmetry. Within a model-independent approach, we should try to deduce this structure from data, using the experimental information on FCNC transitions to constrain its form.

2.5.1.1. *Generic bounds on loop-mediated amplitudes.* In several realistic NP models we can neglect non-standard effects in all cases where the corresponding effective operator is generated at the tree-level within the SM. This general assumption implies that the experimental determination of the CKM matrix via tree-level processes is free from the contamination of NP contributions. Using this determination we can unambiguously predict meson-antimeson mixing and FCNC amplitudes within the SM. Comparing these predictions with data allows to derive general constraints on NP which holds in a wide class of models.

The most constrained sector is the one of $\Delta F = 2$ transitions, where almost all the interesting amplitudes have been measured with good accuracy. An updated analysis of the present constraints from these measurements will be presented in Sec. 10.2. The main conclusions that can be drawn form this analysis can be summarized as follows:

– In all the three accessible short-distance amplitudes (K^0–$\bar{K}^0$, B_d–$\bar{B}_d$, and B_s–$\bar{B}_s$) the magnitude of the new-physics amplitude cannot exceed, in size, the SM short-distance contribution. The latter is suppressed both by the GIM mechanism and by the hierarchical structure of the CKM matrix. As a result, new-physics models with TeV-scale flavored degrees of freedom and $\mathcal{O}(1)$ flavor-mixing couplings are essentially ruled out. For instance, considering a generic $\Delta F = 2$ effective Lagrangian of the form

$$\mathcal{L}^{\Delta F=2} = \sum_{i \neq j} \frac{c_{ij}}{\Lambda^2} (\bar{d}^i_L \gamma^\mu d^j_L)^2 \ , \tag{82}$$

where d^i denotes a generic down-type quark ($i = 1, 2, 3$) and c_{ij} are dimensionless couplings, the condition $|\mathcal{A}^{\Delta F=2}_{\rm NP}| < |\mathcal{A}^{\Delta F=2}_{\rm SM}|$ implies

$$\Lambda < \frac{3.4 \text{ TeV}}{|V^*_{ti} V_{tj}|/|c_{ij}|^{1/2}} \approx \begin{cases} 9 \times 10^3 \text{ TeV} \times |c_{sd}|^{1/2} \\ 4 \times 10^2 \text{ TeV} \times |c_{bd}|^{1/2} \\ 7 \times 10^1 \text{ TeV} \times |c_{bs}|^{1/2} \end{cases} \tag{83}$$

– In the case of B_d–$\bar{B}_d$ and K^0–$\bar{K}^0$ mixing, which are both well measured, there is still room for a new-physics contribution comparable to the SM one. However, this is possible only if the new-physics contribution is aligned in phase with respect to the SM amplitude. The situation is quite different in the case of B_s–$\bar{B}_s$ mixing, where present measurements allow a large non-standard CP violating phase.

As we will discuss in the following, a natural mechanism to reconcile the stringent bounds in Eq. (83) with the expectation $\Lambda \sim$ few TeV is obtained with the Minimal Flavor Violation hypothesis.

2.5.1.2. *Minimal Flavor Violation.* A very reasonable, although quite pessimistic, solution to the flavor problem is the so-called Minimal Flavor Violation (MFV) hypothesis. Under this assumption, flavor-violating interactions are linked to the known structure of Yukawa couplings also beyond the SM. As a result, non-standard contributions in FCNC transitions turn out to be suppressed to a level consistent with experiments even for $\Lambda \sim$ few TeV. One of the most interesting aspects of the MFV hypothesis is that it can naturally be implemented within the EFT approach to NP. The effective theories based on this symmetry principle allow us to establish unambiguous correlations among NP effects in various rare decays. These falsifiable predictions are the key ingredients to identify in a model-independent way which are the irreducible sources of flavor symmetry breaking.

The MFV hypothesis consists of two ingredients [135]: i) a *flavor symmetry* and ii) a set of *symmetry-breaking terms*. The symmetry is defined from the SM Lagrangian in absence of Yukawa couplings. This is invariant under a large gbobal symmetry of flavor transformations: $\mathcal{G}_q \otimes \mathcal{G}_\ell \otimes U(1)^5$, where

$$\mathcal{G}_q = SU(3)_{Q_L} \otimes SU(3)_{U_R} \otimes SU(3)_{D_R} \ , \qquad \mathcal{G}_\ell = SU(3)_{L_L} \otimes SU(3)_{E_R} \ . \tag{84}$$

The $SU(3)$ groups refer to a rotation in flavor space (or a flavor mixing) among the three families of basic SM fields: the quark and lepton doublets, Q_L and L_L, and the three singlets U_R, D_R and E_R. Two of the five $U(1)$ groups can be identified with the total baryon and lepton number (not broken by the SM Yukawa interaction), while an independent $U(1)$ can be associated to the weak hypercharge. Since hypercharge is gauged and involves also the Higgs field, it is more convenient not to include it in the flavour group, which would then be defined as $\mathcal{G}_{\rm SM} = \mathcal{G}_\ell \otimes U(1)^4$ [136].

Within the SM this large global symmetry, and particularly the SU(3) subgroups controlling flavor-changing transitions, is explicitly broken by the Yukawa interaction

$$\mathcal{L}_Y = \bar{Q}_L Y_D D_R H + \bar{Q}_L Y_U U_R H_c + \bar{L}_L Y_E E_R H \ + \ \text{h.c.} \tag{85}$$

The most restrictive hypothesis we can make to *protect* in a consistent way quark-flavor mixing beyond the SM is to assume that Y_D and Y_U are the only sources of $\mathcal{G}_q$ breaking also in the NP model. To implement and interpret this hypothesis in a consistent way, we can assume that $\mathcal{G}_q$ is a good symmetry, promoting $Y_{U,D}$ to be non-dynamical fields (spurions) with non-trivial transformation properties under this symmetry

$$Y_U \sim (3, \bar{3}, 1)_{\mathcal{G}_q} \ , \qquad Y_D \sim (3, 1, \bar{3})_{\mathcal{G}_q} \ . \tag{86}$$

If the breaking of the symmetry occurs at very high energy scales at low-energies we would only be sensitive to the background values of the Y, i.e. to the ordinary SM Yukawa couplings. Employing the effective-theory language, we then define that an effective theory satisfies the criterion of Minimal Flavor Violation in the quark sector if all higher-dimensional operators, constructed from SM and Y fields, are invariant under CP and (formally) under the flavor group $\mathcal{G}_q$ [135].

According to this criterion one should in principle consider operators with arbitrary powers of the (dimensionless) Yukawa fields. However, a strong simplification arises by the observation that all the eigenvalues of the Yukawa matrices are small, but for the top one, and that the off-diagonal elements of the CKM matrix are very suppressed. Y As a consequence, in the limit where we neglect light quark masses, the leading $\Delta F = 2$ and $\Delta F = 1$ FCNC amplitudes get exactly the same CKM suppression as in the SM:

$$\mathcal{A}(d^i \to d^j)_{\rm MFV} = (V_{ti}^* V_{tj}) \ \mathcal{A}_{\rm SM}^{(\Delta F=1)} \left[1 + a_1 \frac{16\pi^2 M_W^2}{\Lambda^2}\right] \ , \tag{87}$$

$$\mathcal{A}(M_{ij} - \bar{M}_{ij})_{\rm MFV} = (V_{ti}^* V_{tj})^2 \mathcal{A}_{\rm SM}^{(\Delta F=2)} \left[1 + a_2 \frac{16\pi^2 M_W^2}{\Lambda^2}\right] \ . \tag{88}$$

where the $\mathcal{A}_{\rm SM}^{(i)}$ are the SM loop amplitudes and the a_i are $\mathcal{O}(1)$ real parameters. The a_i depend on the specific operator considered but are flavor independent. This implies the same relative correction in $s \to d$, $b \to d$, and $b \to s$ transitions of the same type.

As pointed out in Ref. [31], within the MFV framework several of the constraints used to determine the CKM matrix (and in particular the unitarity triangle) are not affected by NP. In this framework, NP effects are negligible not only in tree-level processes but also in a few clean observables sensitive to loop effects, such as the time-dependent CPV asymmetry in $B_d \to J/\Psi K_{L,S}$. Indeed the structure of the basic flavor-changing coupling in Eq. (88) implies that the weak CPV phase of B_d–$\bar{B}_d$ mixing is $\arg[(V_{td}V_{tb}^*)^2]$, exactly as in the SM. This construction provides a natural (a posteriori) justification of why no NP effects have been observed in the quark sector: by construction, most of the clean observables measured at B factories are insensitive to NP effects in the MFV framework.

Table 2
Bounds on the scale of new physics for some representative $\Delta F = 2$ [36] and $\Delta F = 1$ [137] MFV operators (assuming effective coupling $1/\Lambda^2$).

Operator	Λ_i@95% prob. [TeV]	Observables
$H^\dagger \left(\bar{D}_R \lambda_d \lambda_{\rm FC} \sigma_{\mu\nu} Q_L\right) (eF_{\mu\nu})$	6.1	$B \to X_s\gamma$, $B \to X_s \ell^+\ell^-$
$\frac{1}{2}(\bar{Q}_L Y_U Y_U^\dagger \gamma_\mu Q_L)^2$	5.9	ϵ_K, Δm_{B_d}, Δm_{B_s}
$\left(\bar{Q}_L \lambda_{\rm FC} \gamma_\mu Q_L\right) (\bar{E}_R \gamma_\mu E_R)$	2.7	$B \to X_s \ell^+\ell^-$, $B_s \to \mu^+\mu^-$

In Tab. 2 we report a few representative examples of the bounds on the higher-dimensional operators in the MFV framework. As can be noted, the built-in CKM suppression leads to bounds on the effective scale of new physics not far from the TeV region. These bounds are very similar to the bounds on flavor-conserving operators derived by precision electroweak tests. This observation reinforces the conclusion that a deeper study of rare decays is definitely needed in order to clarify the flavor problem: the experimental precision on the clean FCNC observables required to obtain bounds more stringent than those derived from precision electroweak tests (and possibly discover new physics) is typically in the $1\% - 10\%$ range.

Although the MFV seems to be a natural solution to the flavor problem, it should be stressed that we are still very far from having proved the validity of this hypothesis from data.[4] A proof of the MFV hypothesis can be achieved only with a positive evidence of physics beyond the SM exhibiting the flavor-universality pattern (same relative correction in $s \to d$, $b \to d$, and $b \to s$ transitions of the same type) predicted by the MFV assumption.

The idea that the CKM matrix rules the strength of FCNC transitions also beyond the SM has become a very popular concept in the recent literature and has been implemented and discussed in several works. It is worth stressing that the CKM matrix represents only one part of the problem: a key role in determining the structure of FCNCs is also played by quark masses, or by the Yukawa eigenvalues. In this respect, the MFV criterion illustrated above provides the maximal protection of FCNCs (or the minimal violation of flavor symmetry), since the full structure of Yukawa matrices is preserved. At the same time, this criterion is based on a renormalization-group-invariant symmetry argument, which can be implemented independently of any specific hypothesis about the dynamics of the new-physics framework. The only difference between weakly- and strongly-iteracting theories at the TeV scale is that in the latter case the expansion in powers of the Yukawa spurions cannot be truncated to the first non-trivial terms [139,140] (leaving more freedom for non-negligible effects also in up-type FCNC amplitudes [140]). This model-independent structure does not hold in most of the alternative definitions of MFV models that can be found in the literature. For instance, the definition of Ref. [141] (denoted constrained MFV, or CMFV) contains the additional requirement that the effective FCNC operators playing a significant role within the SM are the only relevant ones also beyond the SM. This condition is realized only in weakly coupled theories at the TeV scale with only one light Higgs doublet, such as the MSSM with small $\tan\beta$. It does not hold in several other frameworks, such as Higgsless models, or the MSSM with large $\tan\beta$.

[4] In the EFT language we can say that there is still room for sizable new sources of favour symmetry breaking beside the SM Yukawa couplings [138].

2.5.1.3. *MFV at large* $\tan\beta$. If the Yukawa Lagrangian contains only one Higgs field, we can still assume that the Yukawa couplings are the only irreducible breaking sources of $\mathcal{G}_q$, but we can change their overall normalization.

A particularly interesting scenario is the two-Higgs-doublet model where the two Higgses are coupled separately to up- and down-type quarks:

$$\mathcal{L}_Y^{2HDM} = \bar{Q}_L Y_D D_R H_D + \bar{Q}_L Y_U U_R H_U + \bar{L}_L Y_E E_R H_D \ + \ \text{h.c.} \tag{89}$$

This Lagrangian is invariant under an extra U(1) symmetry with respect to the one-Higgs Lagrangian in Eq. (85): a symmetry under which the only charged fields are D_R and E_R (charge $+1$) and H_D (charge -1). This symmetry, denoted U_{PQ}, prevents tree-level FCNCs and implies that $Y_{U,D}$ are the only sources of $\mathcal{G}_q$ breaking appearing in the Yukawa interaction (similar to the one-Higgs-doublet scenario). Coherently with the MFV hypothesis, we can then assume that $Y_{U,D}$ are the only relevant sources of $\mathcal{G}_q$ breaking appearing in all the low-energy effective operators. This is sufficient to ensure that flavor-mixing is still governed by the CKM matrix, and naturally guarantees a good agreement with present data in the $\Delta F = 2$ sector. However, the extra symmetry of the Yukawa interaction allows us to change the overall normalization of $Y_{U,D}$ with interesting phenomenological consequences in specific rare modes.

The normalization of the Yukawa couplings is controlled by the ratio of the vacuum expectation values (vev) of the two Higgs fields, or by the parameter $\tan\beta = \langle H_U\rangle/\langle H_D\rangle$. For $\tan\beta \gg 1$ the smallness of the b quark and τ lepton masses can be attributed to the smallness of $1/\tan\beta$ rather than to the corresponding Yukawa couplings. As a result, for $\tan\beta \gg 1$ we cannot anymore neglect the down-type Yukawa coupling. Moreover, the $\mathrm{U}(1)_{\mathrm{PQ}}$ symmetry cannot be exact: it has to be broken at least in the scalar potential in order to avoid the presence of a massless pseudoscalar Higgs. Even if the breaking of $\mathrm{U}(1)_{\mathrm{PQ}}$ and $\mathcal{G}_q$ are decoupled, the presence of $\mathrm{U}(1)_{\mathrm{PQ}}$ breaking sources can have important implications on the structure of the Yukawa interaction, especially if $\tan\beta$ is large [135, 142–144]. We can indeed consider new dimension-four operators such as

$$\epsilon\ \bar{Q}_L Y_D D_R (H_U)^c \qquad \text{or} \qquad \epsilon\ \bar{Q}_L Y_U Y_U^\dagger Y_D D_R (H_U)^c\ , \tag{90}$$

where ϵ denotes a generic MFV-invariant $\mathrm{U}(1)_{\mathrm{PQ}}$-breaking source. Even if $\epsilon \ll 1$, the product $\epsilon \times \tan\beta$ can be $\mathcal{O}(1)$, inducing large corrections to the down-type Yukawa sector:

$$\epsilon\ \bar{Q}_L Y_D D_R (H_U)^c \ \xrightarrow{vev}\ \epsilon\ \bar{Q}_L Y_D D_R \langle H_U\rangle = (\epsilon \times \tan\beta)\ \bar{Q}_L Y_D D_R \langle H_D\rangle\ . \tag{91}$$

Since the b-quark Yukawa coupling becomes $\mathcal{O}(1)$, the large-$\tan\beta$ regime is particularly interesting for helicity-suppressed observables in B physics.

One of the clearest phenomenological consequences is a suppression (typically in the $10-50\%$ range) of the $B \to \ell\nu$ decay rate with respect to its SM expectation [145, 146]. Potentially measurable effects in the $10-30\%$ range are expected also in $B \to X_s\gamma$ [147, 148] and ΔM_{B_s} [149, 150]. The most striking signature could arise from the rare decays $B_{s,d} \to \ell^+\ell^-$ whose rates could be enhanced over the SM expectations by more than one order of magnitude [151–153]. An enhancement of both $B_s \to \ell^+\ell^-$ and $B_d \to \ell^+\ell^-$ respecting the MFV relation $\Gamma(B_s \to \ell^+\ell^-)/\Gamma(B_d \to \ell^+\ell^-) \approx |V_{ts}/V_{td}|^2$ would be an unambiguous signature of MFV at large $\tan\beta$ [137].

2.5.2. *The Minimal Supersymmetric extension of the SM (MSSM)*

The MSSM is one of the most well-motivated and definitely the most studied extension of the SM at the TeV scale. For a detailed discussion of this model we refer to the specialised literature (see e.g. Ref. [154]). Here we limit our self to analyse some properties of this model relevant to flavor physics.

The particle content of the MSSM consist of the SM gauge and fermion fields plus a scalar partner for each quark and lepton (squarks and sleptons) and a spin-1/2 partner for each gauge field (gauginos). The Higgs sector has two Higgs doublets with the corresponding spin-1/2 partners (higgsinos) and a Yukawa coupling of the type in Eq. (89). While gauge and Yukawa interactions of the model are completely specified in terms of the corresponding SM couplings, the so-called soft-breaking sector [5] of the theory contains several new free parameters, most of which are related to flavor-violating observables. For instance the 6×6 mass matrix of the up-type squarks, after the up-type Higgs field gets a vev ($H_U \to \langle H_U \rangle$), has the following structure

$$\tilde{M}_U^2 = \begin{pmatrix} \tilde{m}_{Q_L}^2 & A_U \langle H_U \rangle \\ A_U^\dagger \langle H_U \rangle & \tilde{m}_{U_R}^2 \end{pmatrix} \; + \; \mathcal{O}\left(m_Z, m_{\rm top}\right) \; , \tag{92}$$

where $\tilde{m}_{Q_L}$, $\tilde{m}_{U_R}$, and A_U are 3×3 unknown matrices. Indeed the adjective *minimal* in the MSSM acronyms refers to the particle content of the model but does not specify its flavor structure.

Because of this large number of free parameters, we cannot discuss the implications of the MSSM in flavor physics without specifying in more detail the flavor structure of the model. The versions of the MSSM analysed in the literature range from the so-called Constrained MSSM (CMSSM), where the complete model is specified in terms of only four free parameters (in addition to the SM couplings), to the MSSSM without R parity and generic flavor structure, which contains a few hundreds of new free parameters.

Throughout the large amount of work in the past decades it has became clear that the MSSM with generic flavor structure and squarks in the TeV range is not compatible with precision tests in flavor physics. This is true even if we impose R parity, the discrete symmetry which forbids single s-particle production, usually advocated to prevent a too fast proton decay. In this case we have no tree-level FCNC amplitudes, but the loop-induced contributions are still too large compared to the SM ones unless the squarks are highly degenerate or have very small intra-generation mixing angles. This is nothing but a manifestation in the MSSM context of the general flavor problem illustrated in Sec. 2.5.1.

The flavor problem of the MSSM is an important clue about the underling mechanism of supersymmetry breaking. On general grounds, mechanisms of SUSY breaking with flavor universality (such as gauge mediation) or with heavy squarks (especially in the case of the first two generations) tends to be favoured. However, several options are still open. These range from the very restrictive CMSSM case, which is a special case of

[5] Supersymmetry must be broken in order to be consistent with obsevations (we do not observe degenerate spin partners in nature). The soft breaking terms are the most general supersymmetry-breaking terms which prserve the nice ultraviolet properties of the model. They can be divided into two main classes: 1) mass terms which break the mass degeneracy of the spin partenrs (e.g. sfermion or gaugino mass terms); ii) trilinear couplings among the scalar fields of the theory (e.g. sfermion-sfermion-Higgs couplings).

MSSM with MFV, to more general scenarios with new small but non-negligible sources of flavor symmetry breaking.

2.5.2.1. *Flavor Universality, MFV, and RGE in the MSSM.* Since the squark fields have well-defined transformation properties under the SM quark-flavor group $\mathcal{G}_q$, the MFV hypothesis can easily be implemented in the MSSM framework following the general rules outlined in Sec. 2.5.1.2.

We need to consider all possible interactions compatible with i) softly-broken supersymmetry; ii) the breaking of $\mathcal{G}_q$ via the spurion fields $Y_{U,D}$. This allows to express the squark mass terms and the trilinear quark-squark-Higgs couplings as follows [135, 155]:

$$\tilde{m}^2_{Q_L} = \tilde{m}^2 \left(a_1 \mathbb{1} + b_1 Y_U Y_U^\dagger + b_2 Y_D Y_D^\dagger + b_3 Y_D Y_D^\dagger Y_U Y_U^\dagger + b_4 Y_U Y_U^\dagger Y_D Y_D^\dagger + \ldots \right) ,$$
$$\tilde{m}^2_{U_R} = \tilde{m}^2 \left(a_2 \mathbb{1} + b_5 Y_U^\dagger Y_U + \ldots \right) , \qquad A_U = A \left(a_3 \mathbb{1} + b_6 Y_D Y_D^\dagger + \ldots \right) Y_U , \quad (93)$$

and similarly for the down-type terms. The dimensionful parameters $\tilde{m}$ and A, expected to be in the range few 100 GeV – 1 TeV, set the overall scale of the soft-breaking terms. In Eq. (93) we have explicitly shown all independent flavor structures which cannot be absorbed into a redefinition of the leading terms (up to tiny contributions quadratic in the Yukawas of the first two families), when $\tan\beta$ is not too large and the bottom Yukawa coupling is small, the terms quadratic in Y_D can be dropped.

In a bottom-up approach, the dimensionless coefficients a_i and b_i should be considered as free parameters of the model. Note that this structure is renormalization-group invariant: the values of a_i and b_i change according to the Renormalization Group (RG) flow, but the general structure of Eq. (93) is unchanged. This is not the case if the b_i are set to zero, corresponding to the so-called hypothesis of *flavor universality*. In several explicit mechanism of supersymmetry breaking, the condition of flavor universality holds at some high scale M, such as the scale of Grand Unification in the CMSSM (see below) or the mass-scale of the messenger particles in gauge mediation (see Ref. [156]). In this case non-vanishing $b_i \sim (1/4\pi)^2 \ln M^2/\tilde{m}^2$ are generated by the RG evolution. As recently pointed out in Ref. [157, 158], the RG flow in the MSSM-MFV framework exhibit quasi infra-red fixed points: even if we start with all the $b_i = \mathcal{O}(1)$ at some high scale, the only non-negligible terms at the TeV scale are those associated to the $Y_U Y_U^\dagger$ structures.

If we are interested only in low-energy processes we can integrate out the supersymmetric particles at one loop and project this theory into the general EFT discussed in the previous sections. In this case the coefficients of the dimension-six effective operators written in terms of SM and Higgs fields (see Tab. 2) are computable in terms of the supersymmetric soft-breaking parameters. The typical effective scale suppressing these operators (assuming an overall coefficient $1/\Lambda^2$) is $\Lambda \sim 4\pi\tilde{m}$. Looking at the bounds in Tab. 2, we then conclude that if MFV holds, the present bounds on FCNCs do not exclude squarks in the few hundred GeV mass range, i.e. well within the LHC reach.

2.5.2.2. *The CMSSM framework.* The CMSSM, also known as mSUGRA, is the supersymmetric extension of the SM with the minimal particle content and the maximal number of universality conditions on the soft-breaking terms. At the scale of Grand Unification ($M_{\rm GUT} \sim 10^{16}$ GeV) it is assumed that there are only three independent soft-breaking terms: the universal gaugino mass ($\tilde{m}_{1/2}$), the universal trilinear term (A),

and the universal sfermion mass ($\tilde{m}_0$). The model has two additional free parameters in the Higgs sector (the so-called μ and B terms), which control the vacuum expectation values of the two Higgs fields (determined also by the RG running from the unification scale down to the electroweak scale). Imposing the correct W- and Z-boson masses allow us to eliminate one of these Higgs-sector parameters, the remaining one is usually chosen to be $\tan\beta$. As a result, the model is fully specified in terms of the three high-energy parameters $\{\tilde{m}_{1/2}, \tilde{m}_0, A\}$, and the low-energy parameter $\tan\beta$.[6] This constrained version of the MSSM is an example of a SUSY model with MFV. Note, however, that the model is much more constrained than the general MSSM with MFV: in addition to be flavor universal, the soft-breaking terms at the unification scale obey various additional constraints (e.g. in Eq. (93) we have $a_1 = a_2$ and $b_i = 0$).

In the MSSM with R parity we can distinguish five main classes of one-loop diagrams contributing to FCNC and CP violating processes with external down-type quarks. They are distinguished according to the virtual particles running inside the loops: W and up-quarks (i.e. the leading SM amplitudes), charged-Higgs and up-quarks, charginos and up-squarks, neutralinos and down-squarks, gluinos and down-squarks. Within the CMSSM, the charged-Higgs and chargino exchanges yield the dominant non-standard contributions.

Given the low number of free parameters, the CMSSM is very predictive and phenomenologically constrained by the precision measurements in flavor physics. The most powerful low-energy constraint comes from $B \to X_s\gamma$. For large values of $\tan\beta$, strong constraints are also obtained from $B_s \to \mu^+\mu^-$, ΔM_s and from $B(B \to \tau\nu)$. If these observables are within the present experimental bounds, the constrained nature of the model implies essentially no observable deviations from the SM in other flavor-changing processes. Interestingly enough, the CMSSM satisfy at the same time the flavor constraints and those from electroweak precision observables for squark masses below 1 TeV (see e.g. [159, 160]).

In principle, within the CMSSM the relative phases of the free parameters leads to two new observable CP-violating phases (beside the CKM phase). However, these phases are flavor-blind and turn out to be severely constrained by the experimental bounds on the electric dipole moments. In particular, the combination of neutron and electron edms forces these phases to be at most of $\mathcal{O}(10^{-2})$ for squark masses masses below 1 TeV. Once this constraints are satisfied, the effects of these new phases in the B, D and K systems are negligible.

2.5.2.3. *The Mass Insertion Approximation in the general MSSM.* Flavor universality at the GUT scale is not a general property of the MSSM, even if the model is embedded in a Grand Unified Theory. If this assumption is relaxed, new interesting phenomena can occur in flavor physics. The most general one is the appearance of gluino-mediated one-loop contributons to FCNC amplitudes [161, 162].

The main problem when going beyond simplifying assumptions, such as flavor universality of MFV, is the proliferation in the number of free parameters. A useful model-independent parameterization to describe the new phenomena occurring in the gen-

[6] More precisely, for each choice of $\{\tilde{m}_{1/2}, \tilde{m}_0, A, \tan\beta\}$ there is a discrete ambiguity related to the sign of the μ term.

Table 3
Upper bounds at 95% C.L. on the dimensionless down-type mass-insertion parameters (see text) for squark and gluino masses of 350 GeV (from Ref. [167]).

$\lvert(\delta^d_{12})_{LL,RR}\rvert < 1\cdot 10^{-2}$	$\lvert(\delta^d_{12})_{LL=RR}\rvert < 2\cdot 10^{-4}$	$\lvert(\delta^d_{12})_{LR}\rvert < 5\cdot 10^{-4}$	$\lvert(\delta^d_{12})_{RL}\rvert < 5\cdot 10^{-4}$
$\lvert(\delta^d_{13})_{LL,RR}\rvert < 7\cdot 10^{-2}$	$\lvert(\delta^d_{13})_{LL=RR}\rvert < 5\cdot 10^{-3}$	$\lvert(\delta^d_{13})_{LR}\rvert < 1\cdot 10^{-2}$	$\lvert(\delta^d_{13})_{RL}\rvert < 1\cdot 10^{-2}$
$\lvert(\delta^d_{23})_{LL}\rvert < 2\cdot 10^{-1}$	$\lvert(\delta^d_{23})_{RR}\rvert < 7\cdot 10^{-1}$	$\lvert(\delta^d_{23})_{LL=RR}\rvert < 5\cdot 10^{-2}$	$\lvert(\delta^d_{23})_{LR,RL}\rvert < 5\cdot 10^{-3}$

eral MSSM with R parity conservation is the so-called mass insertion (MI) approximation [163]. Selecting a flavor basis for fermion and sfermion states where all the couplings of these particles to neutral gauginos are flavor diagonal, the new flavor-violating effects are parametrized in terms of the non-diagonal entries of the sfermion mass matrices. More precisely, denoting by Δ the off-diagonal terms in the sfermion mass matrices (i.e. the mass terms relating sfermions of the same electric charge, but different flavor), the sfermion propagators can be expanded in terms of $\delta = \Delta/\tilde{m}^2$, where $\tilde{m}$ is the average sfermion mass. As long as Δ is significantly smaller than $\tilde{m}^2$ (as suggested by the absence of sizable deviations form the SM), one can truncate the series to the first term of this expansion and the experimental information concerning FCNC and CP violating phenomena translates into upper bounds on these δ's [164].

The major advantage of the MI method is that it is not necessary to perform a full diagonalization of the sfermion mass matrices, obtaining a substantial simplification in the comparison of flavor-violating effects in different processes. There exist four type of mass insertions connecting flavors i and j along a sfermion propagator: $(\Delta_{ij})_{LL}$, $(\Delta_{ij})_{RR}$, $(\Delta_{ij})_{LR}$ and $(\Delta_{ij})_{RL}$. The indices L and R refer to the helicity of the fermion partners.

In most cases the leading non-standard amplitude is the gluino-exchange one, which is enhanced by one or two powers of the ratio $(\alpha_{\rm strong}/\alpha_{\rm weak})$ with respect to neutralino- or chargino-mediated amplitudes. When analysing the bounds, it is customary to consider one non-vanishing MI at a time, barring accidental cancellations. This procedure is justified a posteriori by observing that the MI bounds have typically a strong hierarchy, making the destructive interference among different MIs rather unlikely. The bound thus obtained from recent measurements in B and K physics [7] are reported in Tab. 3. [8] The bounds mainly depend on the gluino and on the average squark mass, scaling as the inverse mass (the inverse mass square) for bounds derived from $\Delta F = 2$ ($\Delta F = 1$) observables.

The only clear pattern emerging from these bounds is that there is no room for sizable new sources of flavor-symmetry breaking. However, it is too early to draw definite conclusions since some of the bounds, especially those in the 2-3 sector, are still rather weak. As suggested by various authors (see e.g.), the possibility of sizable deviations

[7] The bounds on the 1-2 sector are obtained from the measurements of ΔM_K, ε and ε'/ε. In particular ΔM_K and ε bound the real and imaginary part of the product $(\delta^d_{12}\delta^d_{12})$, while ε'/ε puts a bound on $\mathrm{Im}(\delta^d_{12})$. The bounds on the 1-3 sector are obtained from ΔM_{B_d} (modulus) and the CP violating asymmetry in $B \to J/\Psi K$ (phase). The bounds on the $2-3$ sector are derived mainly from ΔM_{B_s}, $B \to X_s\gamma$ and $B \to X_s\ell^+\ell^-$.

[8] The leading $\Delta F = 1$ and $\Delta F = 2$ gluino-mediated amplitudes in the MI approximation can be found in Ref. [164]. In the $\Delta F = 2$ case also the NLO QCD corrections to effective Hamiltonian are known [165]. A more complete set of supersymmetric amplitudes in the MI approximation, including chargino-mediated relevant in the large-tan β limit, can be found in Ref. [166].

from the SM in the 2-3 sector could fit well with the large 2-3 mixing of light neutrinos, in the context of a unification of quark and lepton sectors [168, 169].

2.5.3. *Non-supersymmetric extensions of the Standard Model*

We conclude this chapter outlining two of the general features of flavor physics appearing in non-supersymmetric extensions of the Standard Model, without entering the details of specific theories.

In models with generic flavor structure, the most stringent constraints on the new flavor-violating couplings are tipically derived from Kaon physics (as it also happens for the bounds in Tab. 3). This is a consequence of the high suppression, within the SM, of short-distance dominated FCNC amplitudes between the first two families:

$$\mathcal{A}(s \to d)_{\rm SM} = \mathcal{O}(\lambda^5) \ , \qquad \mathcal{A}(b \to d)_{\rm SM} = \mathcal{O}(\lambda^3) \ , \qquad \mathcal{A}(b \to s)_{\rm SM} = \mathcal{O}(\lambda^2) \ . \quad (94)$$

As a result, a natural place to look for sizable deviations from the SM are rare decays $K \to \pi\nu\bar{\nu}$ and $K_L \to \pi^0\ell^+\ell^-$ (see for instance the expectations for these decays in the *Littlest Higgs model* without [170] and with [171–174]) T-parity. These decays allow us to explore the sector of $\Delta F = 1$ $s \to d$ transitions, that so far is only loosely tested.

An interesting alternative to MFV, which naturally emerges in models with *Extra Space-time Dimensions* (or models with strongly interacting dynamics at the TeV scale), is the hypothesis of hierarchical fermion profiles [175–179] (which is equivalent to the hypothesis of hierarchical kinetic terms [180]). Contrary to MFV, this hypothesis (often denoted as NMFV or RS-GIM mechanism) is not a symmetry principle but a dynamical argument: light fermions are weakly coupled to the new TeV dynamics, with a strength inversely proportional to their Yukawa coupling (or better the square root of their SM Yukawa coupling). Also in the case the most significant constraints are derived from Kaon physics. However, in this case the stringent constraints from ϵ_K and ϵ'_K generically disfavour visible effects in other observables, although it is still possible to have some effect, in particular in the phase of the B_s mixing amplitude [181, 182]. In view of the little CP problem in the kaon, several modifications of the quark-flavor sector of warped extra-dimensional models have been proposed. Most of them try to implement the notion of MFV into the RS framework [183–185] by using flavor symmetries. The downside of these constructions is that they no longer try to explain the fermion mass hierarchy, but only accommodate it with the least amount of flavor structure, making this class of models hard to probe via flavor precision tests.

3. Experimental Primers

This section contains all the relevant information on experiments and experimental techniques which are needed throughout the report.

3.1. *Overview of experiments*

3.1.1. *Kaon experiments*

In recent years, many experiments have been performed to precisely measure many Kaon decay parameters. Branching ratios (BR's) for main, subdominant, and rare decays, lifetimes, parameters of decay densities, and charge asymmetries have been measured

with unprecedented accuracy for K_S, K_L, and $K^{\pm}$. Different techniques have been used, often allowing careful checks of the results from experiments with independent sources of systematic errors.

In the approach of NA48 [186] at the CERN SPS and KTeV [187] at the Fermilab Tevatron, Kaons were produced by the interactions of intense high-energy proton beams on beryllium targets (see Tab. 4). Both experiments were designed to measure the direct CP violation parameter $\mathrm{Re}(\varepsilon'/\varepsilon)$ via the double ratio of branching fractions for K_S and K_L decays to $\pi^+\pi^-$ and $\pi^0\pi^0$ final states. In order to confirm or disprove the conflicting results of the former-generation experiments, NA31 [188] and E-731 [189], the goal was to reach an uncertainty of a few parts in 10^4. This not only requires intense K_L beams, so as to guarantee the observation of at least 10^8 decays of the rarest of the four modes, i.e., $K_L \to \pi^0\pi^0$; it also made it necessary to achieve a high level of cancelation of the systematic uncertainties for K_L and K_S detection, separately for neutral and charged decay modes, as well as rejection of the order of 10^6 for the most frequent K_L backgrounds, $K_L \to 3\pi^0$ and $K_L \to \pi\ell\nu$.

In both setups, the target producing the K_L beam is the origin of coordinates. K_L's are transported by a $\sim$ 100-m long beam line, with magnetic filters to remove unwanted particles and collimators to better define the Kaon-beam direction, to a fiducial decay volume (FV). The FV is surrounded by veto detectors, for rejecting decay products emitted at large angles and therefore with relatively low energy; this is particularly useful for the rejection of $K_L \to 3\pi^0$ background. The FV is followed by a tracker to measure the charge, multiplicity, and momentum of charged decay products, and by a fast scintillator hodoscope to provide the first-level trigger and determine the event time. The tracking resolution σ_p/p is $(4 \oplus p[\mathrm{GeV}]/11) \times 10^{-3}$ for NA48 and $(1.7 \oplus p[\mathrm{GeV}]/14) \times 10^{-3}$ for KTeV. In the downstream (forward) region, both experiments use fine-granularity, high-efficiency calorimeters to accurately measure multiplicity and energy of photons and electrons for the identification of $K_L \to 2\pi^0$. The KTeV calorimeter is made of pure CsI, while the NA48 calorimeter is made of liquid krypton. The energy resolution σ_E/E is $3.2\%/\sqrt{E[\mathrm{GeV}]} \oplus 9\%/E[\mathrm{GeV}] \oplus 0.42\%$ for NA48 and $2\%\sqrt{E[\mathrm{GeV}]} \oplus 0.4\%$ for KTeV. Behind the calorimeter, the detectors are completed by calorimeters for muon detection. Different methods are used for the production of a K_S beam. In NA48, a channeling crystal bends a small and adjustable fraction of protons that do not interact in the K_L target to a dedicated beam line; these protons are then transported and collimated to interact with a second target located few meters before the FV, thus producing a K_S/K_L beam with momentum and direction close to those of the K_L beam, so that most of K_S decays are in the FV. K_S decays are identified by tagging protons on the secondary beam line using time of flight. In KTeV, two K_L beams are produced at the first target, with opposite transverse momenta in the horizontal direction, and a thick regenerator is placed in one of the two beams to produce K_S, again a few meters before the FV. K_S and K_L decays are distinguished by their different transverse position on the detector. In both setups, one measures decays from a K_L beam with $<\sim 10^{-6}$ contamination from K_S, and from an enriched-K_S beam contaminated by a K_L component, which is determined very precisely during analysis.

The KTeV experiment at Fermilab underwent different phases. The E-799 KTeV phase-I used the apparatus of the E-731 experiment [189], upgraded to handle increased K_L fluxes and to study multibody rare K_L and π^0 decays. In phase-II of E-799, a new beam line and a new detector were used, including a new CsI calorimeter and a new tran-

Table 4
Typical beam parameters for K production in the NA48, KTeV, ISTRA+, and E787/E949 experiments.

Experiment	proton energy (GeV)	K, spill/cycle	K momentum	Beam type
NA48	450	1.5×10^{12}, 2.4 s/14.4 s	(70–170) GeV	K_S–K_L
NA48/1	400	5×10^{10}, 4.8 s/16.2 s	(70–170) GeV	K_S
NA48/2	400	7×10^{11}, 4.8 s/16.8 s	60 GeV	$K^{\pm}$
KTeV	450–800	3×10^{12}, 20 s/60 s	(40–170) GeV	K_S–K_L, K_L
ISTRA+	70	3×10^{6}, 1.9 s/9.7 s	25 GeV	K^-
E787	24	4–7$\times 10^{6}$, 1.6 s/3.6 s	710/730/790 MeV, stopped	K^+
E949	21.5	3.5$\times 10^{6}$, 2.2 s/5.4 s	710 MeV, stopped	K^+

sition radiation detector, thus allowing a sensitivity of 10^{-11} on the BR of many K_L decay channels and improving by large factors the accuracy on the ratio of BR's of all of the main K_L channels. Finally, using the E-832 experimental configuration $\mathrm{Re}(\varepsilon'/\varepsilon)$ was measured to few parts in 10^{-4} [187]. The NA48 program involved different setups as well. After operating to simultaneously produce K_L's and K_S's, the beam parameters were optimized in the NA48/1 phase to produce a high-intensity K_S beam for the study of rare K_S decays, reaching the sensitivity of 10^{-10} for some specific channels and especially improving knowledge on those with little background from the accompanying K_L decay to the same final state. Subsequent beam and detector upgrades, including the insertion of a Cerenkov beam counter ("NA48/2 setup") allowed production of simultaneous unseparated charged Kaon beams for the measurement of CP violation from the charge asymmetry in the Dalitz densities for three-pion decays [190]. The NA48/2 phase allowed the best present sensitivities for many rare $K^{\pm}$ decays to be reached, with BR's as low as 10^{-8} and improved precision for the ratios of BR's of the main $K^{\pm}$ channels. A recent run made in 2007 by the NA62 collaboration using the NA48/2 setup was dedicated to a precision measurement of the ratio $\Gamma(K_{e2})/\Gamma(K_{\mu 2})$. A future experiment is foreseen at the CERN SPS for the measurement of the ultra-rare decay $K^+ \to \pi^+ \nu\overline{\nu}$ with a 10% accuracy [191, 192].

An unseparated charged Kaon beam was also exploited for study of charged Kaon decay parameters with the ISTRA+ detector [193] at the U-70 proton synchrotron in IHEP, Protvino, Russia. A beam (see Tab. 4), with $\sim 3\%$ K^- abundance is analyzed by a magnetic spectrometer with four proportional chambers and a particle identification is provided by three Cerenkov counters. The detector concept is similar to those presented above, with the tracking of charged decay products provided by drift chambers, drift tubes, and proportional chambers and with the calorimetry for photon vetoing at large angle or energy measurement at low angle performed by lead-glass detectors.

A different approach for the study of the ultra-rare $K \to \pi\nu\overline{\nu}$ decay and the search for lepton-flavor violating transitions was taken by the E787 [194–196] and E949 [197] experiments at the Alternating Gradient Synchrotron (AGS) of the Brookhaven National Laboratory. Charged Kaons were produced by 24-GeV protons interacting on a fixed target. A dedicated beam line transported, purified and momentum selected Kaons. The beam (see Tab. 4) had adjustable momenta from 670 MeV to 790 MeV and a ratio of Kaons to pions of $\sim 4/1$.

The detector design was optimized to reach sensitivities of the order of 10^{-10} on the

BR's for decays of $K^{\pm}$ to charged particles, especially lepton-flavor violating decays, such as $K \to \pi\mu e$: for this purpose, redundant and independent measurements for particle identification and kinematics were provided, as well as efficient vetoing for photons. The beam was first analyzed by Cerenkov and wire-chamber detectors, and later slowed down by a passive BeO degrader and an active lead-glass radiator, the Cerenkov light of which was used to veto pions and early K decays. Kaons were then stopped inside an active target made of scintillating fibers. The charged decay products emitted at large angle were first analyzed in position, trajectory, and momentum by a drift chamber; their range and kinetic energy was then measured in a Range Stack alternating plastic scintillator with passive material. The readout of the Range Stack photomultipliers was designed to record times and shapes of pulses up to 6.4 μs after the trigger, thus allowing the entire chain of $\pi \to \mu \to e$ decays to be detected and allowing clean particle identification. The detector was surrounded by electromagnetic calorimeters for hermetic photon vetoing: a lead/scintillator barrel and two CsI-crystal endcaps. Two lead/scintillating-fiber collars allowed vetoing of charged particles emitted at small angles. Using this setup, the best sensitivity to date was obtained for the BR for $K \to \pi\nu\nu$, reaching the 10^{-10} level.

Precision studies of K_S, K_L, and $K^{\pm}$ main and subdominant decays were performed with a different setup using the KLOE detector at the DAΦNE. DAΦNE, the Frascati ϕ factory, is an e^+e^- collider working at $\sqrt{s} \sim m_\phi \sim 1.02$ GeV. ϕ mesons are produced essentially at rest with a visible cross section of ~ 3.1 μb and decay into K_SK_L and K^+K^- pairs with BR's of $\sim 34\%$ and $\sim 49\%$, respectively. During KLOE data taking, which started in 2001 and concluded in 2006, the peak luminosity of DAΦNE improved continuously, reaching $\sim 2.5 \times 10^{32}$ cm^{-2} s^{-1} at the end. The total luminosity integrated at the ϕ peak is ~ 2.2 fb^{-1}, corresponding to ~ 2.2 (~ 3.3) billion $K^0\overline{K^0}$ (K^+K^-) pairs.

Kaons get a momentum of ~ 100 MeV/c which translates into a low speed, $\beta_K \sim 0.2$. K_S and K_L can therefore be distinguished by their mean decay lengths: $\lambda_S \sim 0.6$ cm and $\lambda_L \sim 340$ cm. K^+ and K^- decay with a mean length of $\lambda_\pm \sim 90$ cm and can be distinguished from their decays in flight to one of the two-body final states $\mu\nu$ or $\pi\pi^0$.

The Kaon pairs from ϕ decay are produced in a pure $J^{PC} = 1^{--}$ quantum state, so that observation of a K_L (K^+) in an event signals, or tags, the presence of a K_S (K^-) and vice versa; highly pure and nearly monochromatic K_S, K_L, and $K^{\pm}$ beams can thus be obtained and exploited to achieve high precision in the measurement of absolute BR's.

The analysis of Kaon decays is performed with the KLOE detector, consisting essentially of a drift chamber, DCH, surrounded by an electromagnetic calorimeter, EMC. A superconducting coil provides a 0.52 T magnetic field. The DCH [198] is a cylinder of 4 m in diameter and 3.3 m in length, which constitutes a fiducial volume for K_L and $K^{\pm}$ decays extending for $\sim 0.5\lambda_L$ and $\sim 1\lambda_\pm$. The momentum resolution for tracks at large polar angle is $\sigma_p/p \leq 0.4\%$. The invariant mass reconstructed from the momenta of the two pion tracks of a $K_S \to \pi^+\pi^-$ decay peaks around m_K with a resolution of $\sim$800 keV, thus allowing clean K_L tagging. The c.m. momenta reconstructed from identification of 1-prong $K^{\pm} \to \mu\nu, \pi\pi^0$ decay vertices in the DC peak around the expected values with a resolution of 1–1.5 MeV, thus allowing clean and efficient $K^{\mp}$ tagging.

The EMC is a lead/scintillating-fiber sampling calorimeter [199] consisting of a barrel and two endcaps, with good energy resolution, $\sigma_E/E \sim 5.7\%/\sqrt{\mathrm{E(GeV)}}$, and excellent time resolution, $\sigma_T = 54$ ps$/\sqrt{\mathrm{E(GeV)}} \oplus 50$ ps. About 50% of the K_L's produced reach the EMC, where most interact. A signature of these interactions is the presence of an

Table 5
Accelerator parameters of the B-Factories. The design parameters are given for PEP-II and KEK-B. The final running parameters for CESR are given.

	CESR	KEK-B		PEP-II	
		LER	HER	LER	HER
Energy (GeV)	5.29	3.5	8.0	3.1	9.0
Collision mode	2 mrad	$11mrad$		Head-on	
Circumference (m)	768	3018		2199	
β_x^*/β_y^* (cm)	100/1.8	100/1	100/1	37.5/1.5	75/3
ξ_x^*/ξ_y^*	0.03/0.06	0.05/0.05		0.03/0.03	
$\epsilon_x^*/\epsilon_y^*$ (πrad $-$ nm)	210/1	19/0.19	19/0.19	64/2.6	48.2/1.9
relative energy spread (10^{-4})	6.0	7.7	7.2	9.5	6.1
Total Current (A)	0.34	2.6	1.1	2.14	0.98
number of bunches	45	5120		1658	
RF Frequency (MHz)/ Voltage (MV)	500/5	508/22	508/48	476/9.5	476/17.5
number of cavities	4	28	60	10	20

high-energy cluster not connected to any charged track, with a time corresponding to a low velocity: the resolution on β_K corresponds to a resolution of $\sim$ 1 MeV on the K_L momentum. This allows clean K_S tagging. The timing capabilities of the EMC are exploited to precisely reconstruct the position of decay vertices of K_L and $K^\pm$ to π^0's from the cluster times of the emitted photons, thus allowing a precise measurement of the K_L and $K^\pm$ lifetimes.

With this setup, KLOE reached the best sensitivity for absolute BR's of the main $K^\pm$, K_L, and K_S channels (dominating world data in the latter case) and improved the knowledge of semileptonic decay rate densities and lifetimes for $K^\pm$ and K_L.

3.1.2. *B Factories*

The high statistics required to perform precise flavor physics with B mesons has been accomplished by B-Factories colliding electrons and positrons at the energy of the $\Upsilon(4S)$ resonance ($e^+e^- \to \Upsilon(4S)B\overline{B}$): CESR at LEPP (Cornell, USA), PEP-II [200] at SLAC (Stanford, USA) and KEK-B [201] at KEK (Tsukuba, Japan). Measurements that exploit the evolution of the observables with the decay time of the mesons also require asymmetric beams in order to ensure a boost to the produced mesons.

To this aim PEP-II (KEK-B) collide 3.1 (3.5) GeV positrons on 9.0 (8.0) GeV electrons, thus achieving a boost $\beta\gamma = 0.56(0.43)$. The other design parameters of the B-Factories are listed in Tab: 5. The design instantaneous luminosities were 10^{33}, 3×10^{33}, and $1 \times 10^{34}\,\mathrm{cm}^{-2}\,\mathrm{s}^{-1}$ for CESR, PEP-II and KEK-B, respectively.

The accelerator performances have actually overcome the design: CESR has ceased its operations as B-Factory in 1999 with a peak luminosity $\mathcal{L} = 1.2 \times 10^{33}\ \mathrm{cm}^{-2}\,\mathrm{s}^{-1}$, PEP-II has ended its last run in April 2008 with a peak luminosity of $12 \times 10^{33}\,\mathrm{cm}^{-2}\,\mathrm{s}^{-1}$ and KEK-B, which is still operational and awaits an upgrade (Super-KEK-B), has achieved a luminosity as high as $1.7 \times 10^{34}\ \mathrm{cm}^{-2}\,\mathrm{s}^{-1}$. The total collected luminosities are 15.5, 553 and 895 fb^{-1} for CESR, PEP-II and KEK-B, respectively.

The detectors installed on these accelerators, CLEO-II/II.V/III[9] [202–206] at CESR, BaBar [207] at PEP-II and Belle [208] at KEK-B, are multipurpose and require exclusive and hermetic reconstruction of the decay products of all generated particles. To this aim the following requirements must be met: (1) accurate reconstruction of charged-particle trajectories; (2) precise measurement of neutral particle energies; and (3) good identification of photons, electrons, muons, charged Kaons, K^0_S mesons and K^0_L mesons.

The most challenging experimental requirement is the detection of the decay points of the short-lived B mesons. CLEO, BaBar and Belle use double-sided silicon-strip detectors allowing full tracking of low-momentum tracks. Four, three and five cylindrical layers are used at CLEO, Belle and BaBar, respectively. To minimize the contribution of multiple scattering, these detectors are located at small radii close to the interaction point. For tracking outside the silicon detector, and the measurement of momentum, all experiments use conventional drift chambers with a helium-based gas mixture to minimize multiple scattering and synchrotron radiation backgrounds.

The other difficult requirement for the detectors is the separation of Kaons from pions. At high momentum, this is needed to distinguish topologically identical final states such as $B^0 \to \pi^+\pi^-$ and $B^0 \to K^+\pi^-$ from one another. At lower momenta, particle identification is essential for B flavor tagging.

Three different approaches to high-momentum particle identification have been implemented, all of which exploit Cerenkov radiation. At CLEO a proximity focusing RICH with CH_4/TEA as the photosensitive medium and LiF as the radiator. The system relies on an expansion gap between the radiator and photon detector to separate the Cherenkov light without the use of additional focusing elements. The RICH has good K-π separation for charged tracks above 700 MeV/c; below this momenta dE/dx measurements in the drift chamber are used for particle identification.

At Belle, aerogel is used as a radiator. Blocks of aerogel are read out directly by fine-mesh phototubes that have high gain and operate reliably in a 1.5-Tesla magnetic field. Because the threshold momentum for pions in the aerogel is 1.5 GeV/c, below this momentum K/π separation is carried out using high-precision time-of-flight (TOF) scintillators with a resolution of 95 ps. The aerogel and TOF counter system is complemented by dE/dx measurements in the central drift chamber. The dE/dx system provides K/π separation below 0.7 GeV/c and above 2.5 GeV/c in the relativistic rise region.

At BaBar, Cerenkov light is produced in quartz bars and then transmitted by total internal reflection to the outside of the detector through a water tank to a large array of phototubes where the ring is imaged. The detector is called DIRC (Detector of Internally Reflected Cerenkov light). It provides particle identification for particles above 700 MeV/c. Additional particle identification is provided by dE/dx measurements in the drift chamber and the five-layer silicon detector.

To detect photons and electrons, all detectors use large arrays of CsI(Tl) crystals located inside the coil of the magnet. In BABAR and Belle, another novel feature is the use of resistive plate chambers (RPC) inserted into the steel return yoke of the magnet. This detector system is used for both muon and K^0_L detection. At CLEO the iron return yoke of the solenoid is instrumented with plastic streamer counters to identify muons.

[9] The detector went through several major upgrades during its lifetime. In this section only the final configuration, CLEO-III, is described. The size of the $\Upsilon(4S)$ data-sets collected were 4.7 fb^{-1}, 9.0 fb^{-1}, 9.1 fb^{-1} with CLEO-II, CLEO-II.V and CLEO-III, respectively.

Table 6
Accelerator parameters of τ-charm factories.

	BEPC	CESR-c	BEPC-II
Max. energy (GeV)	2.2	2.08	2.3
Collision mode	Head-on	$\pm$3.3 mrad	22 mrad
Circumference (m)	240	768	240
β_x^*/β_y^* (cm)	120/5	94/1.2	100/1.5
ξ_x^*/ξ_y^* (10^{-4})	350/350	420/280	400/400
$\epsilon_x^*/\epsilon_y^*(\pi$ rad $-$ nm)	660/28	120/3.5	144/2.2
relative energy spread (10^{-4})	5.8	8.2	5.2
Total Current (A)	0.04	0.072	0.91
number of bunches	1	24	93
RF Frequency (MHz)/ Voltage (MV)	200/0.6-1.6	500/5	500/1.5
number of cavities	4	4	2

To read out the detectors, BABAR uses electronics based on digital pipelines and incurs little or no dead-time. Belle uses charge-to-time (Q-to-T) converters that are then read out by multihit time-to-digital counters (TDCs). This allows a uniform treatment of timing and charge signals. Details of the CLEO data-acquisition system can be found in Ref. [204]; the system can handle trigger rates of 1 kHz well above the normal operating conditions (100 Hz).

3.1.3. *τ-charm Factories*

Recently there have been two accelerators that have been operating near the τ-charm threshold: BEPC at IHEP (Beijing, China) and CESR-c [209] at LEPP (Cornell, USA). The center-of-mass-energy ranges covered are $3.7 - 5.0$ GeV and $3.97 - 4.26$ GeV by BEPC and CESR-c, respectively. The peak instantaneous luminosities achieved are 12.6×10^{30} cm^{-2} s^{-1} and 76×10^{30} cm^{-2} s^{-1}. The other parameters of BEPC and CESR-c are given in Tab. 6.

At CESR-c the CLEO-III detector, described in Sec. 3.1.2, was modified for lower energy data-taking and renamed CLEO-c [209]. The principal differences were the reduction of the magnetic field from 1.5 T to 1 T and the replacement of the silicon vertex detector by a six-layer inner drift chamber. Both these modifications improved the reconstruction of low momentum tracks. CLEO-c collected 27 million $\psi(2S)$ events, 818 pb^{-1} of integrated luminosity at the $\psi(3770)$ and 602 pb^{-1} of integrated luminosity at a center-of-mass energy of 4.17 GeV. The latter data set includes a over half a million $D_s\overline{D}_s^*$ events.

The most recent detector installed on BEPC is BES-II [210, 211]. BES-II collected samples of 58 million J/ψ and 14 million $\psi(2S)$ events. In addition, an energy scan was performed between center-of-mass energies 3.7 to 5.0 GeV to determine both R and the resonances parameters of the higher-mass charmonium states. BES-II tracking was performed by a drift chamber surrounding a straw tube vertex detector. [10] A scintillating

[10] The vertex detector was originally operated at Mark III.

time-of-flight detector with 180 ps resolution is used for particle identification along with $\mathrm{d}E/\mathrm{d}x$ measurements in the drift chamber. There are sampling electromagnetic-shower counters in the barrel and endcap made from layers of streamer tubes sandwiched between lead absorbers. Outside the 0.4 T solenoid the iron flux return is instrumented with proportional tubes to detect muons.

BEPC and BES-III have recently undergone significant upgrades (see for example [212]). The BEPC-II accelerator has a design luminosity 100 times greater than BEPC with a peak of 10^{33} $\mathrm{cm}^{-2}\,\mathrm{s}^{-1}$. The other parameters of BEPC-II are given in Tab. 6. The BES-III detector has the following components: a He-based drift-chamber, a time-of-flight system with $\sim$100 ps resolution, a CsI(Tl) crystal calorimeter, a 1 T superconducting solenoid and the return yoke is instrumented with RPCs for muon identification. BES-III began taking data in the summer of 2008 and a $\psi(2S)$ data sample of 10 pb^{-1} has already been collected. The collection of unprecedented samples of J/ψ, $\psi(2S)$ and D mesons produced just above open-charm threshold are expected in the coming years.

3.1.4. *Hadron Colliders*

High energy proton-(anti)proton collisions offer superb opportunities for beauty and charm physics due to large production cross section and, in contrast to electron-positron colliders running at the $\Upsilon(4S)$, the possibility of studying all species of b-mesons and baryons. Present generation experiments, CDF and D0 operate at the Fermilab Tevatron providing $p\overline{p}$ collisions at $\sqrt{s} = 1.96\,\mathrm{TeV}$ in the Run II started in 2002, while experiments at the soon to be operated LHC collider at CERN will study proton-proton collisions at $\sqrt{s} = 14\,\mathrm{TeV}$. The Tevatron collides $p\overline{p}$ bunches every 396 ns, corresponding to an average of 2 inelastic collisions per crossing at a luminosity of $\mathcal{L} = 1 \times 10^{32}\,\mathrm{cm}^{-2}\mathrm{s}^{-1}$, typical of the data used to produce the physics results discussed here. More recently Tevatron provided peak luminosities in excess of $3 \times 10^{32}\,\mathrm{cm}^{-2}\mathrm{s}^{-1}$, and delivered in total 6.5 fb^{-1}as of this writing.

The cross section for centrally produced b-hadrons has been measured with a variety of techniques at Tevatron and found to be consistent with NLO theoretical calculations: an early measurement using inclusive J/ψ down to $P_T = 0$ in the rapidity range $|y| < 0.6$ found $\sigma(p\overline{p} \to b{+}X) = 17.6{\pm}0.4(\mathrm{stat.})\ ^{+2.5}_{-2.3}(\mathrm{sys.})\ \mu\mathrm{b}$ [213], while a more recent one using fully reconstructed $B^+ \to J/\psi K^+$ measured $\sigma(p\overline{p} \to B^+ + X, P_T > 6\ \mathrm{GeV}/c,\ |y| \leq 1) = 2.78 \pm 0.24\ \mu\mathrm{b}$ [214] which gives more of an idea of the usable cross-section for central detectors like CDFII and $D0$. The fragmentation fraction of b-quarks in $B_{u,d}$ and B_s mesons has been measured to be consistent at Tevatron and at LEP, with roughly 1 B_s meson produced every 4 B^+ or B^0, while the rate of b-baryons has been reported to be higher at Tevatron with a possible mild P_T dependence [215].

The huge production rate for heavy flavored particles has to be contrasted, however, with the overwhelming inelastic proton-(anti)proton interaction rate which is typically three order of magnitudes higher. This poses a fundamental experimental challenge for detectors ad hadron colliders, which needs to devise trigger strategies in order to be able to record as pure a signal as possible while discarding uninteresting events.

The Tevatron experiments exploit conceptually similar, multi-purpose central detectors with a cylindrical symmetry around the beam axis, in contrast the dedicated future experiment at LHC collider (LHCb) employs a radically different forward geometry, in order to exploit the rapidly increasing $b\overline{b}$ cross section at high rapidity.

Key elements in the design of detectors for heavy flavor physics at hadron colliders are: large magnetic spectrometers for charged particle momentum measurements; precision vertex detectors for proper decay time determination and signal separation, low energy electron and muon identification for triggering, flavor tagging, and identification of rare leptonic decays; high rate capability for data acquisition and trigger systems. Additionally π-K identification is crucial for flavor tagging and signal separation, and, thus, a significant part of the design of the dedicated LHCb detector, while in central muti-purpose detectors limited particle id is available with the exception of CDF-II which benefits from dE/dx and TOF measurements. In the following we will briefly describe the CDF [213] and D0 [216] detectors relevant for the experimental results discussed in this report.

CDF and D0 detectors

The CDF-II detector spectrometer is built around an axially symmetric Central Outer Tracker (COT), a open-cell drift chamber that provides charged track identification and measurement of the momentum transverse to the $p\bar{p}$ beams (p_T) in the central region($|\eta| \leq 1.2$) for tracks with $p_T > 400\,\mathrm{MeV}/c$. The active volume of the COT covers extends from a radius of 40 to 140 cm, with up to 96 axial and stereo measurement points inside a superconducting solenoid that provides a 1.4 T axial magnetic field. D0 Central Fiber Tracker fills a significant smaller space inside a 2 T solenoid, 20 to 50 cm, with 16000 channel organized in 8 alternating axial and stereo layers each providing a doublet of measurement points. The p_T resolution is found to be $\delta_{p_T}/p_T \sim 0.001 \cdot p_T(\,\mathrm{GeV}/c)$ in the CDF tracker. This results in precise invariant mass reconstruction which provides excellent signal-to-background ratio for fully reconstructed B and D decay modes.

Tracks found in the central tracker are extrapolated inward and matched to hits in silicon microvertex detectors in both CDF and D0. The CDF detector (SVX II + ISL) uses double sided silicon microstrip technology providing tracking information in the r-ϕ and r-z planes in the pseudo-rapidity range $|\eta| < 2$. The detector has up to 7 layers of double-sided silicon at radial distances ranging from 2.5 cm to 28 cm from the beamline.

Within the SVX is the innermost single-sided, radiation hard silicon layer (Layer 00), which is mounted directly onto the beam pipe at a radius of 1.35 to 1.62 cm [217]. The impact parameter resolution of the tracking system with, and without, the inclusion of Layer 00 is shown in Figure 4. The impact parameter resolution for high p_T charged tracks is $\sim 25\mu m$ taking in to account the $32\mu m$ contribution from the transverse size of the interaction region [217].

D0 silicon microstrip tracker (SMT) is composed of cylindrical barrels with 4 layers of double-sided detectors interspersed with disks in the central part, and complemented with large forward disk at both ends, a design optimized for tracking up to $|\eta| < 3$. In addition, in 2006 a new innermost layer (Layer 0) was installed inside the existing detector. This has improved the impact parameter resolution and will prevent the expected performance degradation due to radiation damage of the innermost SMT layer during the rest of the Tevatron run [218].

The silicon vertex detectors are crucial for precise decay length determination of b decays in time dependent measurement. Moreover the 3D vertex reconstruction allowed by the combined r-ϕ and r-z measurements provides efficient background rejection against the large background of prompt events.

Particle identification in CDF is provided by dE/dx in the central drift chamber and a time-of-flight (TOF) system consisting of 216 scintillator bars located between the COT

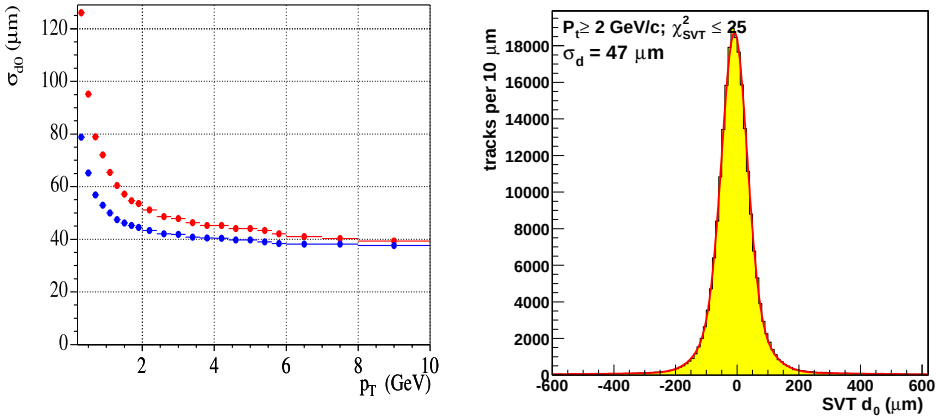

Fig. 4. CDF impact parameter resolution tracking tracks with Layer 00 hits (blue points) and without Layer 00 hits (red points.) a) and Silicon Vertex Trigger (SVT) impact parameter distribution for a generic sample of tracks b).

and the solenoid [219]. The TOF, with a resolution of around 110 ps, provides at least 2σ K/π separation for $p_T < 1.5$ GeV/c. For $p_T > 2.0$ GeV/c, the separation provided by dE/dx between pions and Kaons is equivalent to $1.4\,\sigma$ between two Gaussians while the separation for pions and electrons is $2.5\,\sigma$ at $p_T = 1.5$ GeV/c.

Outside the solenoid are electromagnetic and hadronic calorimeters covering the pseudo-rapidity region $|\eta| < 3.5$ in CDF and up to$|\eta| < 4.0$ in D0.

Muon detectors are located behind the hadron calorimeters, The CDF muon systems are segmented into four components, the Central Muon system (CMU) provides coverage for $|\eta| < 0.6$ and $p_T > 1.5$ GeV/c and sits behind $\sim$5.5 interaction lengths (λ) of material primarily consisting of the iron of the hadronic calorimeter. The Central Muon upgrade (CMP) sits behind an additional 60 cm, $\sim 3\lambda$ of steel, providing identification for muons with $p_T > 3.0\,\mathrm{GeV}/c$ in $|\eta| < 0.6$, with higher purity than muons identified only in the CMU. The Central Muon extension (CMX) consists of eight layers drift chambers arranged in conic sections and provides coverage for $0.6 < |\eta| < 1.1$ and $p_T > 2.0$ GeV/c, and is located behind absorber material corresponding to ~ 6 up to ~ 10 interaction lengths. The D0 muon system sits outside of a thick absorber (> 10 λ), and consists of a layer of tracking detectors and scintillation trigger counters inside a 1.8 T iron toroid, followed by two additional layers outside the toroid. The muon coverage extends to $|\eta| = 2$. Magnet polarities are regularly reversed during data collection, thus providing an important way to control charge dependent effects in muon reconstruction that might affect semileptonic asymmetry measurement.

Triggers

Data acquisition and trigger system for experiments at hadron colliders have to sustain an extremely high collision rate, 7.6(40) MHz at Tevatron(LHC), and reduce it to approximately 100-1000 Hz of interesting events that can be saved permanently for physics analysis, thus providing rejection factor $> 10^4$ against uninteresting proton-(anti)proton collisions. The most straightforward way to achieve such a goal is to design electron and muon based triggers, using single or multi-lepton signatures, that allow to select signif-

icantly pure samples of heavy flavor decays thanks to the large semileptonic branching ratios, or by isolating final states containing e.g. J/ψ. Rate is controlled primarily with lepton transverse momentum requirement, that has to be kept as low as possible in order to maximize signal efficiency. Inclusive electron and muon selection with a threshold of 6-8 GeV/c are typical at Tevatron. Much lower thresholds are possible for events with two leptons, approaching the minimum detectable transverse momentum in each detector (2 GeV/c at Tevatron).

This strategy has been implemented by all the present and forthcoming experiments and provided the majority of the result for rare decays and lifetime measurements at Tevatron in the last decade. A clear limitation of this approach is that it lacks the ability to select fully hadronic decays of b-hadrons. In the context of CKM-related physics the latter are important for the study of either 2 body charmless decays, or $B \to DK$ decays involved in the measurement of the angle γ in tree processes, and, most importantly, for selecting large samples of fully reconstructed $\overline{B}_s \to D_s^+\pi^-$ and $\overline{B}_s \to D_s^+\pi^+\pi^-\pi^+$ that lead to the first observation of $B_s^0 - \overline{B}_s^0$ mixing in 2006 [220]. To overcome this limitation the CDF collaboration pioneered the technique of online reconstruction of charged tracks originating from decay vertexes far from the collision point due to the significant boost and lifetime of B-mesons produced at high energy hadron colliders. The key innovation introduced for Run II in the CDF trigger was in fact the Silicon Vertex Trigger (SVT) [221] processor. At the second level of the trigger system, information from the silicon vertex detector is combined with tracks reconstructed at the first level trigger in the drift chamber. High resolution SVT-tracks are then provided within the latency of $\approx 20\,\mu$s, and are used to select events characterized by two tracks with high impact parameter and vertex decay length greater than 200 μm, thus providing a rejection factor of 100-1000 while maintaining a significant efficiency for B decays. The impact parameter resolution of the SVT, shown in Figure 4, is approximately $50\,\mu$m, which includes a contribution of $32\,\mu$m from the width of the $p\bar{p}$ interaction region. It has to be noted, however, that selecting events based upon decay length information, introduces an important inefficiency at small values of proper decay time. We will describe how this bias has been incorporated in the analysis in Section 3.2.3.

3.2. *Common experimental tools*

In the following the most relevant experimental techniques for flavor physics will be briefly discussed. Time dependent measurements require excellent vertexing and flavor tagging capabilities, crucial in the latter case is particle identification and π-K separation. Finally noise suppression, recoil tagging technique and Dalitz-plot analysis techniques will be discussed.

3.2.1. *Time-dependent measurements*

It is possible to measure phases of the CKM matrix elements, and therefore CP violating quantities, by exploiting the different time evolution of the two mass eigenstates of the B_0 meson system, B_L and B_H. At B-Factories, where a B_0 meson is produced coherently with its antiparticle, the probability density function of observing a B decay into a flavor eigenstate (called B_{tag}) and for whom $\eta = -1(+1)$ if B^0 ($\overline{B}^0$) and the other one, called B_{reco}, in a given final state f at times that differ by Δt is

$$f_\eta(\Delta t) = \frac{\Gamma}{4}\,\mathrm{e}^{-\Gamma|\Delta t|}\left\{1+\eta\left[S\sin\Delta m\Delta t - C\cos\Delta m\Delta t\right]\right\}, \tag{95}$$

where the decay width difference between the two mass eigenstates is neglected, Δm is the mass difference,

$$S = \frac{2Im\lambda}{1+|\lambda|^2} \qquad\qquad C = \frac{1-|\lambda|^2}{1+|\lambda|^2}, \tag{96}$$

and

$$\lambda = -\frac{|\langle B^0|\,\mathcal{H}_{\Delta B=2}\,|\overline{B}^0\rangle|}{\langle B^0|\,\mathcal{H}_{\Delta B=2}\,|\overline{B}^0\rangle}\frac{\langle f|\,\mathcal{H}_{\Delta B=1}\,|\overline{B}^0\rangle}{\langle f|\,\mathcal{H}_{\Delta B=1}\,|B^0\rangle}. \tag{97}$$

Depending on the choice of the final state f, S can be related to different phases of the CKM matrix elements. In particular if f is a flavor eigenstate then $\lambda = 0$ and $C = 1$ and $S = 0$, no phase can be measured but there is sensitivity to Δm; likewise if f is a CP eigenstate, λ is a pure phase and this is usually the cleanest configuration to measure CP violation parameters, although all non-zero values of λ allow such measurements.

At hadron colliders the same considerations apply, a part from the fact that Δt measures the time between the B meson production and its decay and that $\eta = -1(+1)$ for an initially produced B^0 ($\overline{B}^0$). The initial B flavor can be measured either by observing the decay products of the other hadron with a b quark in the event, or by utilizing information on the jet of particles the B meson is contained into.

There are therefore three key ingredients in these measurements: the identification of the flavor of the meson produced in association with the one reconstructed in the channel f (the so-called B-tagging), the measurement of Δt which requires the reconstruction of the decay vertex of at least one B meson (both mesons in the case of B-factories), and the reconstruction of the B meson in the final state f with the least possible background.

The experimental uncertainties on these quantities alter the probability density function of the measured quantities, function which is used in the likelihood fits implemented to perform these measurements. Instead of Eq. 95 one can then write

$$f_\eta(\Delta t) = \frac{\Gamma}{4}\,\mathrm{e}^{-\Gamma|\Delta t_{true}|}\left\{1+\eta\mathcal{D}\left[S\sin\Delta m\Delta t_{true} - C\cos\Delta m\Delta t_{true}\right]\right\}\otimes\mathcal{R}(\Delta t-\Delta t_{true})+f_\eta^{bkg}(\Delta t), \tag{98}$$

where $\otimes$ indicates the convolution, $\mathcal{D} = 1-p_w$ is the tagging dilution (p_w is the probability of incorrectly tagging a meson), R is the vertexing resolution function, and f_η^{bkg} is the probability density function for the background.

The next sections describe the techniques adopted for tagging, vertexing reconstruction and background rejection and the means available to estimate the quantities that enter into Eq. 98.

3.2.2. *B Flavor Tagging*

One of the key components in the measurement of neutral B meson flavor oscillations or time dependent CP asymmetries is identifying the flavor of the B meson (containing a $\bar{b}$ antiquark) or $\bar{B}$ meson (containing a b quark) at production, in the case of incoherent mixing at hadronic colliders, or at the moment the other b-meson decays in the case of $B^0\overline{B}^0$ from $\Upsilon(4S)$. We refer to this method of identifying the B hadron flavor as "B flavor tagging". The figure of merit to compare different tagging methods or algorithms is the so-called effective tagging power $\varepsilon\mathcal{D}^2 = \varepsilon(1-2\,p_W)^2$, where the efficiency ε represents the

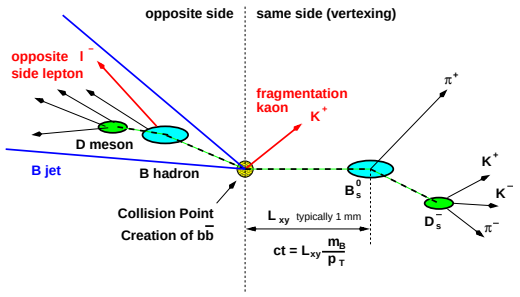

Fig. 5. Sketch of typical $b\bar{b}$ event indicating several B flavor tagging techniques.

fraction of events for which a flavor tag exists and p_W is the mistag probability indicating the fraction of events with a wrong flavor tag. The mistag probability is related to the dilution: $\mathcal{D} = 1 - 2\,p_W$. The experimentally observed mixing or CP asymmetries are, in fact, proportional to the dilution $\mathcal{D}$. A flavor tag which always returns the correct tag has a dilution of 1, while a random tag yielding the correct flavor 50% of the time has a dilution of zero.

Several methods to tag the initial b quark flavor have been used both at B-factories and hadron collider experiments. The flavor tagging methods can be divided into two groups, those that identify the flavor of the other b-hadron produced in the same event (opposite side tag - OST), and those that tag the initial flavor of the B candidates itself (same side tag - SST). The latter, being based on charge correlation between initial b quark and fragmentation particles is only possible at hadron colliders or Z-pole experiments.

Fig. 5 is a sketch of a $b\bar{b}$ event showing the B and $\bar{B}$ mesons originating from the primary $p\bar{p}$ interaction vertex and decaying at a secondary vertex indicating possible flavor tags on the decay vertex side (SST) as well as opposite side tags.

In the following the main aspects of the opposite side taggers used at both Tevatron and B-Factories and of the SST used for the B_s^0-$\overline{B}_s^0$ oscillation observation and in the first ϕ_s determination at Tevatron will be briefly discussed.

Opposite Side Tags

Both experiments at hadron colliders and B-Factories exploit three feature of B decays to estimate the flavour of the opposite B meson.

The "lepton tagging" looks for an electron or muon from the semileptonic decay of the opposite side B hadron in the event. The charge of this lepton is correlated with the flavor of the B hadron: an ℓ^- comes from a $b \to c\,\ell^-\bar{\nu}X$ transition, while an ℓ^+ originates from a $\bar{b}$ quark. Since the semileptonic B branching fraction is small, $\mathcal{B}(B \to \ell X) \sim 20\%$, lepton tags are expected to have low efficiency but high dilution because of the high purity of lepton identification.

The strangeness of Kaons or Λ from the subsequent charm decay $c \to sX$ is also correlated with the B flavor, e.g. a K^- results from the decay chain $b \to c \to s$ while a K^+ signals a $\bar{b}$ flavor. Searching for a charged Kaon from the opposite side B hadron decay is referred to as "Kaon tagging". This method is expected to have high efficiency but low dilution at hadron colliders since the challenge is to first identify Kaons among a vast background of pions through particle-id techniques, and then to discriminate the B decay Kaon candidates from all prompt Kaons produced in the collision by relying on Kaon impact parameter and reconstruction of secondary vertexes in the opposite

side [222].

Finally all other information carried by the tracks among the decays of the B mesons constitutes the third large tagging category. On average in fact the most energetic charged decay product carries the charge of the original b quark. At Tevatron the "jet charge tagging" exploits the fact that the sign of the momentum weighted sum of the particle charges of the opposite side secondary vertex from b (D0 [223]) or b jet (CDF [224]) is correlated to the charge of the b quark. Jet charge tags can reach very high efficiency but with low dilution. Furthermore, more than 20% of B decays contain charged D^* mesons which decay 66% of the times into a soft pion with the same charge. Soft pions can therefore also have a high charge correlation with the original b quark. The Belle and BaBar experiments input to multivariate tagging algorithms the charge of all tracks, with special treatment for the softest in the event to take into account this effect.

The algorithms to combine all the information use multivariate technique either exploiting directly the available output of the various tagging algorithms or starting by assigning each track candidate of coming from the "tagging" B meson into one category between lepton, kaon, soft pion (only for B-Factories) or generic track. Each experiment then has a different approach to exploit the information.

The BaBar experiment uses one Neural Network (NN) per category with different quantities in input depending on the category (see Ref. [225] for details): for instance the "Lepton" category would contain lepton identification quantities and the momentum. The output of these NNs based on single-particle information are themselves combined into several event-by-event NNs, that assess the likelihood of the flavor assignment. The tagging categories are mutually exclusive and for each event only one NN is evaluated. The algorithm of the Belle experiment is similar but exploits likelihood instead of NNs and has a single output (called r). In both cases the algorithms are tuned on MC, but the mistag probability is estimated on data control samples.

The experimental sensitivity is maximized upon using the expected dilution on an event by event basis, employing parameterizations derived by a combination of simulation and real data. As an example, the dilution of the lepton tagging is parameterized as a function of the lepton identification quality and of the $p_T^{\rm rel}$ of the tagging lepton (CDF [226, 227]) or of the lepton jet-charge (D0 [223]). The quantity $p_T^{\rm rel}$ is defined as the magnitude of the component of the tagging-lepton momentum that is perpendicular to the axis of the jet associated with the lepton tag. Variation of the dilution as a function of $p_T^{\rm rel}$ is shown left side of Fig. 6 for electron tags in CDF. The dilution is lower for low $p_T^{\rm rel}$ because fake leptons and leptons from sequential semileptonic decay ($b \to c \to \ell^+$) tend to have relatively low $p_T^{\rm rel}$ values. Also, to maximize the tagging power the dilution of the jet charge tags can be calculated separately for different quality of the opposite side secondary vertex information and parametrized as a linear function in the quantity $|Q_{jet}| \cdot \mathcal{P}_{\rm nn}$, where $\mathcal{P}_{\rm nn}$ expresses a probability for the jet to be a b jet, as displayed in Fig. 6 for jets containing a well separated secondary vertex in the CDF case. Flavor misidentification can occur because the jet charge does not reflect perfectly the true charge of the original b quark, due e.g. to mixing. In addition, the selected tagging jet may contain only a few or no tracks from the actual opposite side B hadron decay.

At Tevatron, the typical flavor tagging power of a single tagging algorithm is $\mathcal{O}(1\%)$. Limitations in opposite side tagging algorithms arise because the second bottom hadron is inside the detector acceptance in less than 40% of the time or it is possible that the second B hadron is a neutral B meson that mixed into its antiparticle. For example, the

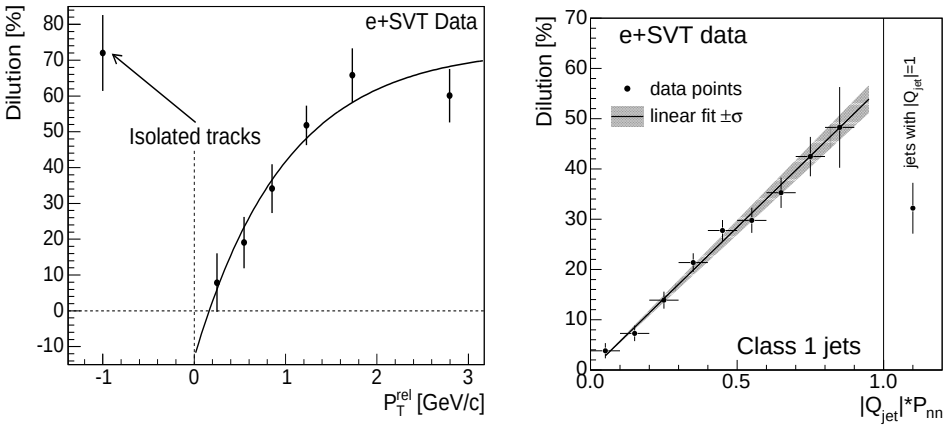

Fig. 6. Variation of dilution of the electron tags with $p_T^{\rm rel}$(left). Dilution as a function of $|Q_{jet}| \cdot \mathcal{P}_{\rm nn}$ for "jet-charge" tagging algorithm (right).

low efficiency of an opposite side lepton tag of $\sim 20\%$ from the semileptonic B hadron branching fraction together with a dilution of $\sim 30\%$ results in an estimated $\varepsilon\mathcal{D}^2 \sim 0.4 \times 0.2 \times 0.3^2 \sim 0.01$. At B-factories, better hermeticity of detectors, enhanced particle identification capability, and the absence of incoherent mixing as a source of dilution makes it possible to reach combining all the information together en effective tagging power $\varepsilon\mathcal{D}^2 \sim 0.30$ in both Belle and Babar. As an example of tagging performances for each experiment considered here, the obtained efficiencies ε, effective dilutions $\langle\mathcal{D}\rangle$, and effective tagging powers $\varepsilon\mathcal{D}^2$ are shown in Table 7.

In the case of opposite side flavor tags, the dilution is expected to be independent of the type of B meson (B^0,B^+,B_s) under study, hence can be studied on large inclusive semileptonic samples (CDF) or on B^0 or B^+ samples (D0) and then applied in B_s related measurement. The final calibration of the opposite side tagging methods come from a measurement of the B^0 oscillation frequency Δm_d in hadronic and semileptonic samples of B mesons at both B-factories and Tevatron experiments. A perfectly calibrated tagging method applied to a large sample of $\overline{B}^0$ mesons should result in a precise measurement of Δm_d. In turn one can use the well known world average value of Δm_d to check and re-calibrate the predicted dilutions of the opposite side tagging algorithms.

Same Side Flavor Tagging

The initial flavor of a B meson can additionally be tagged by exploiting correlations of the B flavor with the charge of particles produced in association with it (SST). Such correlations arise from b quark hadronization and from B^{**} decays. In the case of a B^- or $\overline{B}^0$ mesons, the fragmentation particles are mainly pions while $\overline{B}_s$ meson are primarily accompanied by fragmentation Kaons. In the $\overline{B}_s$ meson case we thus refer to this method as "same side Kaon tagging" (SSKT). In the simplest picture, where only pseudo-scalar mesons are produced directly by the fragmentation process, the following charged stable mesons are expected: a $\overline{B}^0$ will be produced along with π^-, a B^- will be produced with a π^+ or a K^+, and a $\overline{B}_s$ will be produced with a K^-. Corresponding relations are true for the charge conjugated B mesons. The idea of the same side tagging algorithm is to

Table 7
Tagging performances of the opposite side tagging algorithms at BaBar [228], Belle [229], D0 [223], and CDF [230]. Note that the individual tagger performance in the latter case are determined in non-exclusive sample so their sum is greater than the neural network (NN) based combined opposite side tagging for CDF. All errors given are statistical.

Category		Efficiency ε [%]		Effect. dilution $\langle\mathcal{D}\rangle$ [%]		Tagging Power $\varepsilon\mathcal{D}^2$ [%]	
BaBar	Belle ($r \in$)	BaBar	Belle	BaBar	Belle	BaBar	Belle
Lepton	0.875-1	8.96±0.07	14.4±0.9	99.4±0.3	97.0±0.5	7.98±0.11	13.5±0.9
Kaon I	0.75-0.875	10.82±0.07	9.8±0.7	89.4±0.3	78.2±0.9	8.65±0.3	6.0±0.5
Kaon II	0.625-0.75	17.19±0.09	10.7±0.8	71.0±0.4	68.4±1.0	8.68±0.17	5.0±0.5
Kaon-Pion	0.5-0.625	13.67±0.08	10.8±0.8	53.4±0.4	55.0±1.1	3.91±0.12	3.3±0.4
Pion	0.25-0.5	14.18±0.08	14.6±0.9	35.0±0.4	36.0±0.8	1.73±0.09	1.9±0.2
Other	0-0.25	9.54±0.07	39.7±1.5	17.0± 0.5	7.2±0.7	0.27 ±0.04	0.2±0.1
Total Tagging Power						31.2± 0.3	29.9±1.2
		CDF	D0	CDF	D0	CDF	D0
Muon		5.5 ± 0.1	6.6 ± 0.1	35.3 ± 1.1	47.3 ± 2.7	0.68 ± 0.05	1.48 ± 0.17
Electron		3.1 ± 0.1	1.8 ± 0.1	30.7 ± 1.1	34.1 ± 5.8	0.29 ± 0.01	0.21 ± 0.07
Jet Charge		90.5 ± 0.1	2.8 ± 0.1	9.5 ± 0.5	42.4 ± 4.8	0.80 ± 0.05	0.50 ± 0.11
Kaon		18.1 ± 0.1	N/A	11.1 ± 0.9	N/A	0.23 ± 0.02	N/A
Total Tagging Power						1.81± 0.10	2.19± 0.22

identify the leading fragmentation track charge and to determine the B initial flavor accordingly.

Several advantages compared to the opposite side tagging algorithms are worth mentioning. The SST shows a high efficiency since the leading fragmentation track is in the same detector region as the signal B hadron, thus, within the detector acceptance, and there are also no limitations due to branching ratios. The search region for same side tagging tracks is limited near the signal B direction. Due to this geometrical restriction, the SST is robust against background from the underlying event or multiple interactions. Finally neutral meson mixing does not dilute the useful charge correlation. These advantages are reflected in an higher flavor tagging dilution.

Unlike the opposite side flavor tagging algorithms, the performance of the same side algorithm cannot easily be quantified using data. Since SST is based on information from the signal B fragmentation process, its performance depends on the signal B species. Therefore, B^+ and B^0 modes can not be used to calibrate the same side tagging performance for B_s mesons. Instead, prior to the actual observation of B_s mixing, the experiments had to rely upon Monte Carlo simulation to quantify the performance of same side tagging for B_s mesons. High statistics B^+ and B^0 modes have been used to verify that specifically tuned Monte Carlo program accurately model the fragmentation process.

The CDF algorithm [231] starts selecting charged tracks with $p_T \geq 450\,\mathrm{MeV}/c$, good momentum and impact parameter resolution as potential tagging tracks. Fragmentation tracks originate from the primary vertex, therefore an impact parameter significance less than 4 is required. To reject background from multiple interactions, the tracks are

required to be close to the B_s candidates both along the beam direction and in $\Delta R = \sqrt{\Delta\eta^2 + \Delta\phi^2} \leq 0.7$.

About 60% of the tagged events have one and only one tagging track. Of the remaining events approximately one-third have all tagging tracks with the same charge. Therefore, the subsequent tagging algorithm makes a choice between multiple, oppositely charged tracks in about one-fourth of all tagged events. Several variables have been employed. The most sensitive was found to be the maximum longitudinal component of the tagging tracks with respect to the B momentum, and after that the largest likelihood to be a Kaon based on TOF and dE/dx measurements. A neural network is finally used to combine the available information. Examples of the dependence of the dilution on the variables discussed above are given in Fig. 7 for the subsample with only one tagging track.

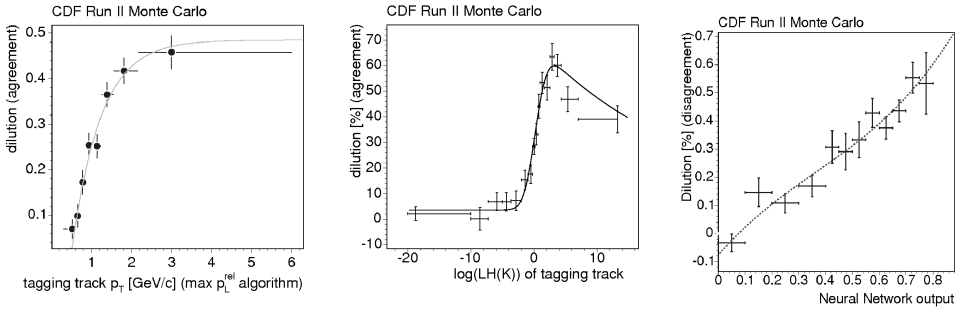

Fig. 7. (Left panel) Dilution of the maximum p_L^{rel} algorithm as a function of tagging track p_T. (Middle panel) Dilution for the Kaon identification based algorithm as function of Kaon likelihood. (Right panel) Dilution of the NN algorithm as a function of NN variable. The dots represent Monte Carlo data, the line is the parametrization, which has been used to determine the event-by-event dilution. Events with only one tagging track candidate around the B_s meson are displayed.

The performance of the SSKT algorithm has been evaluated for B^+, B^0 and B_s modes on several decay channels (see Table 8). The agreement between simulation and data in B^+ and B^0 modes suggests that the simulation can predict the tagger performance across all B species. The measured differences are used to evaluate a systematic uncertainty on SSKT for B_s mesons. Since the algorithm rely on the number of Kaons produced in the fragmentation process leading to the production of B_s mesons an additional important uncertainty is derived by the difference in data and simulation of the number of Kaons around the B_s direction of flight. Smaller systematic uncertainties arise considering b-quark production mechanism, fragmentation models, B^{**} rate and event pile-up.

Table 8
Performance of the NN based algorithm in data and Monte Carlo. Only statistical uncertainties are quoted.

[%]		$B^- \to D^0\pi^-$	$\overline{B}^0 \to D^+\pi^-$	$\overline{B}_s \to D_s^+\pi^-$
MC	ϵ	55.9 ± 0.1	56.6 ± 0.1	52.1 ± 0.3
	$\langle\mathcal{D}\rangle$	26.8 ± 0.2	16.1 ± 0.6	29.2 ± 0.7
data (1 fb^{-1})	ϵ	58.2 ± 0.3	57.2 ± 0.3	49.3 ± 1.3
	$\langle\mathcal{D}\rangle$	26.4 ± 0.8	15.2 ± 1.7	—

The tagging dilution evaluated for the $\overline{B}_s \to D_s^+\pi^-$ sample using the event-by-event predicted dilution derived from Monte Carlo yields $\langle\mathcal{D}\rangle = 24.9 - 29.3^{+3.3}_{-4.3}\%$ (for comparison using the maximum p_L^{rel} only gives $\langle\mathcal{D}\rangle = 23.7^{+2.6}_{-4.5}$ %). The overall SSKT tagging figure of merit is $\varepsilon\,\langle\mathcal{D}\rangle^2 = 3.1 - 4.3^{+1.0}_{-1.4}$, including statistical and systematic uncertainties (the given range reflect the performance of the CDF TOF system in different data taking periods). This result can be compared to the overall OST $\varepsilon\mathcal{D}^2 = 1.8 \pm 0.1\%$ for opposite side tagging on the same channel (note the significant channel dependence of the measured $\varepsilon\mathcal{D}^2$, mostly related to the B meson p_T spectrum of the reconstructed decays).

Also the D0 experiment recently introduced a same side tagger [232]. The track with $p_T > 500\,\mathrm{MeV}/c$ closest in ΔR to the B_s candidate flight direction is selected for tagging. Dilution is studied as a function of the product of the tagging track charge and ΔR, as well as forming a same side jet charge from the transverse momentum weighted sum of all tracks within a narrow cone around the B_s flight direction. The combined $\varepsilon\mathcal{D}^2$ from OST and SST quoted by the D0 collaboration is $4.68 \pm 0.54\%$ to be compared to $2.48 \pm 0.22\%$ from the OST alone.

3.2.3. *Vertexing*

For time dependent measurements determining the elapsed times (Δt in Sec. 3.2.1) is crucial. This is obtained by first measuring a length L and then computing $\Delta t = L/(c\,\beta\,\gamma)$. The vertexing techniques utilized to measure L are significantly different at B-Factories and hadron colliders because of the different boost and because time dependent measurements have two different needs: measure the difference in time between the two B mesons in an event at the B-Factories and measure the time of flight since the production of the B meson of insterest at the hadron colliders. The two approaches are therefore described separatetly in the following.

Vertex reconstruction at B-Factories

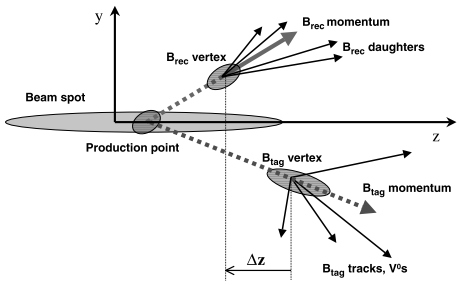

Fig. 8. Schematic view of the vertexing algorithm at B-Factories.

The B_{reco} vertex is reconstructed from charged tracks and photon candidates that are combined to make up intermediate mesons (e.g., J/ψ, D, K_S^0) and then treated as virtual particles. The trajectory of these virtual particles is computed from those of their decay particles, and, when appropriate, mass constraints are imposed to improve the knowledge of the kinematics. In the case of charmonium states such as $J/\psi K_S^0$, Belle uses only the dileptons from the J/ψ decay. In Belle, the vertex of the signal candidate is constrained to come from the beam-spot in the x-y plane and convolved with the finite B-meson lifetime. BABAR uses the beam-spot information only in the tag vertex

reconstruction. The resulting spatial resolution depends on the final state; it is typically 65 μm in BABAR and 75μm in Belle.

BABAR determines the Btag vertex by exploiting the knowledge of the center-of-mass four-momentum and an estimate of the interaction point or beam-spot position. This information, along with the measured three-momentum of the fully reconstructed Breco candidate, its decay vertex, and its error matrix, permits calculation of the Btag production point and three-momentum, with its associated error matrix (see Fig. 8). All tracks that are not associated with the Breco reconstruction are considered; K^0_S and Λ candidates are used as input to the fit in place of their daughters, but tracks consistent with photon conversions are excluded. To reduce the bias from charm decay products, the track with the largest χ^2 vertex contribution if greater than 6 is removed and the fit is iterated until no track fails this requirement.

Belle reconstructs the Btag vertex from well-reconstructed tracks that have hits in the silicon vertex detector and are not assigned to the Breco vertex. Tracks from K0S candidates and tracks farther than 1.8 mm in z or 500 μm in r from the Breco vertex are excluded. An iterative fit to these tracks is performed with the constraint that the vertex position be consistent with the beam spot. If the overall χ^2 is poor, the track with the worst χ^2 contribution is removed, unless it is identified as a high-momentum lepton. In this case, the lepton is retained and the track with the second-largest χ^2 is removed.

The resolution on Δz is dominated by the Btag vertex reconstruction and therefore is nearly independent of the reconstructed CP decay mode. Based on Monte Carlo simulation, it is estimated to be 190 μm. The Δz measurement is converted to a Δt measurement, and the corresponding resolution is 1.1 ps in BABAR and 1.43 ps in Belle because of the different center-of-mass boosts.

Decay Length Measurements at Tevatron In the Tevatron detectors, with a central geometry, the decay length is best measured in the transverse plane, the proper time t is computed from the flight distance in the transverse plane, L_{xy}. Thus, the expression for t and its resolution are:

$$t = \frac{L}{c\beta\gamma} = L_{xy}\frac{m_B}{c\ p_T} \qquad ; \qquad \sigma_t = \sigma_{L_{xy}}\frac{m_B}{c\ p_T} \oplus \frac{\sigma_{p_T}}{p_T}t \tag{99}$$

For fully reconstructed decays, the only significant uncertainty is from the decay distance measurement. Partially reconstructed decays have an additional term from p_T uncertainty which grows linearly with t.

The transverse flight distance of the B-meson, L_{xy}, is given by the transverse distance between the location of $p\bar{p}$ interaction, the Primary Vertex (PV), and the Secondary Vertex (SV), i.e. the decay point of the B-meson. The position of the PV is determined for each event by fitting the tracks in the underlying event to a common origin, exluding the tracks belonging to the B candidate.

The secondary vertex is determined by fitting to a common vertex the B dauther charged tracks, considering tertiary vertex from charm decay, and mass constraints on intermediate resonances where applicable. The error estimate on L_{xy} is obtained by combining the PV uncertainty with that provided by the SV fit. A gaussian resolution function is normally a good approximation but the error estimate from the vertex fit needs to be multiplied by a scale factor for a correct measurement. This rescaling is typically calculated from the lifetime distribution of prompt background (e.g. from prompt J/ψ and underlying event tracks for decays involving J/ψ, or from prompt charm production

and fake leptons for semileptonic decays). A peculiar situation arise when data biased in lifetime, due e.g. to trigger requirements, are used. In this case special samples can be manufactured combining a prompt charm meson with a randomly selected charged track, consistent with coming from the PV. The pseudo-decay length of this events is expected to peak at 0 and can be used to measure the decay length resolution scale factor.

The proper decay time resolution for fully reconstructed $\overline{B}_s \to D_s^+\pi^-$ and $\overline{B}_s \to D_s^+\pi^+\pi^-\pi^+$ decays with the CDF detector is shown in Fig. 9 (left). The mean proper decay time uncertainty corresponds to 86 fs, which has to be compared with the oscillation period for B_s mesons ≈ 350 fs, and shows the ability of the current Tevatron experiment vertex detectors to resolve the fast B_s oscillations.

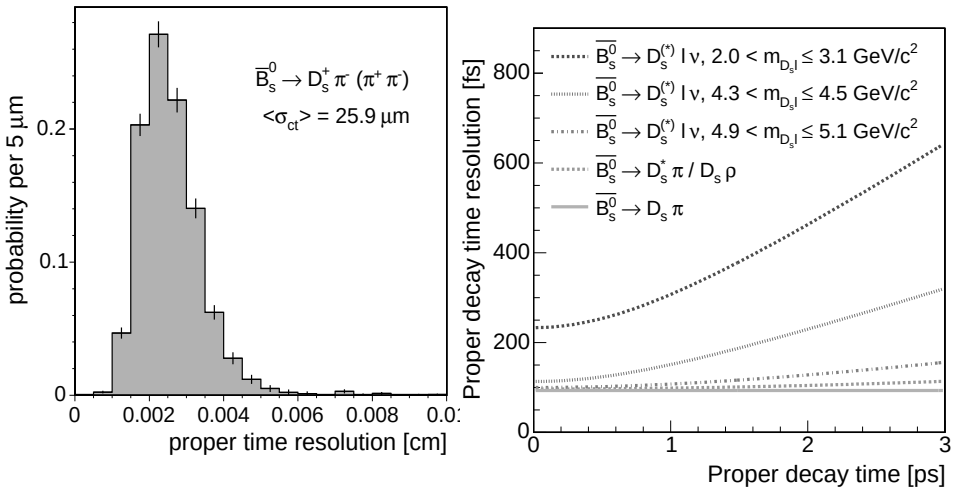

Fig. 9. The decay time resolution for fully reconstructed B_s decays in CDF (left) and the effective resolution for different values of missing (unreconstructed) semileptonic mass, as a function of the proper decay time (right).

For partially reconstructed decays, like semileptonic decays, there is an important additional uncertainty in the decay time due to the incompletely measured p_T of the B meson (Eq. 99). The distribution $F(k)$ of the fractional missing momentum $k = p_T^{\rm obs}/p_T(B)$ is extracted from Monte Carlo simulations and is rather wide with a typical RMS of 10 to 20%. The gaussian resolution function has to be convoluted with the distribution of this k factor in any time dependent measurement involving partially reconstructed or semi-leptonic decays. In semileptonic decays the missing neutrino momentum is correlated with the visible mass $D + \ell$, $M_{D\ell}$, hence it is useful to divide the data in bins of $M_{D\ell}$ taking advantage of the narrower width of $F(k)$ for higher $M_{D\ell}$ as shown in Fig. 9 (right).

An important complication in time dependent measurement is introduced by reconstruction or trigger bias on proper time (see e.g. section 3.1.4). To take in to account this effect a function $\xi(t)$, that describes the acceptance as a function of proper decay time and is derived from simulations, multiply proper time related terms in the likelihood fits. To derive it CDF assumes that for each accepted event i, the expected ct distribution without any bias is an exponential smeared by the experimental resolution function,

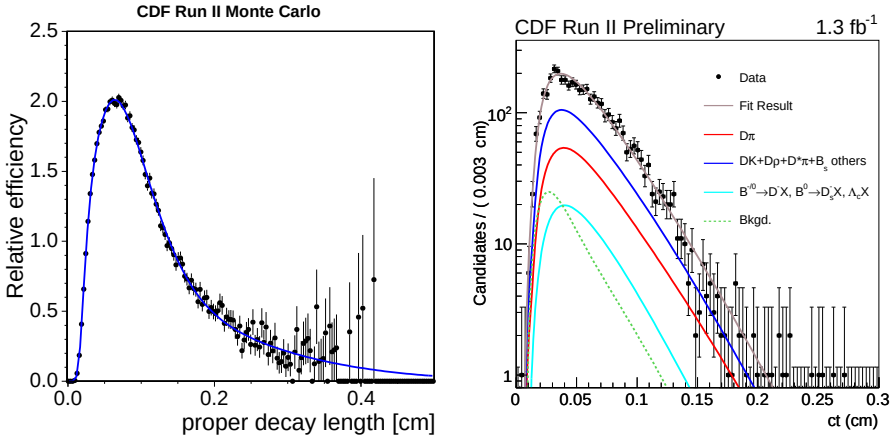

Fig. 10. A representative example of the dependence of trigger and selection efficiency on proper decay time from the displaced track trigger in CDF, vertical scale in arbitrary units (left). Lifetime fit to $\overline{B}_s \to D_s^+\pi^-$ sample from CDF (right)

where the width is the ct error (σ_{ct_i}) of that event. The denominator is the sum of the N expected distributions without any bias,

$$\xi(ct) \equiv \frac{\text{reconstructed } ct \text{ after trigger + selection}}{\sum_{i=1}^{N} \frac{1}{\tau} \exp\left(-\frac{ct}{c\tau}\right) \otimes G(ct;\sigma_{ct_i}) \otimes_k \mathcal{F}(k)}\,, \tag{100}$$

where the smearing with the k-factor distribution $\mathcal{F}(k)$ has to be included for incompletely reconstructed decays. The shape of the proper decay length efficiency curve is parametrized using analytically integrable functions and used to multiply proper time related terms in the likelihood fits. Fig. 10 shows a representative example of the proper time efficiency from the CDF experiment. The rapid turn-on of the curve is due to minimum impact parameter and L_{xy} significance requirements at the trigger and reconstruction level, while the turn-off at larger proper decay length is due to upper cut on impact parameter at the trigger level. Because each B decay mode has its own kinematic characteristics and selection requirements, an efficiency curve has to be derived separately for each channel.

The method has been extensively validated with Tevatron data, measuring B^0, B^+ and B_s and Λ_b lifetime a variety of fully adronic modes. As an example, a recent preliminary determination of the B_s lifetime in the $\overline{B}_s \to D_s^+\pi^-$ channel is shown in Fig. 10 right [233], giving $c\tau(B_s) = 455.0 \pm 12.2_{\rm st} \pm 8.2_{\rm sy}\,\mu$m, in good agreement with PDG averages.

3.2.4. *Charged Particle Identification*

Identification (ID) of charged particles (e, μ, π, K, p) plays a crucial role in flavor physics, in many cases π/K separation being both the most important and experimentally

challenging. Some of the most important PID techniques are sensitive to the particle's velocity; working in tandem with tracking, which provides a measurement of the particle's momentum, they separate the particles by mass. Other techniques exploit the unique interaction properties of specific particles.

The purpose of this primer is to describe conceptually the PID techniques employed in the detector experiments that provided the results included in this report. For a more general discussion, please see Chapters "Passage of particles through matter" and "Particle Detectors" in Ref. [4].

At the track momenta relevant to flavor physics, the rate of **ionization energy loss**, usually denoted $\mathrm{d}E/\mathrm{d}x$, to a good approximation is a constant for $e^{\pm}$ and a function only of the particle's velocity (but not its type) for the others. Measurements of $\mathrm{d}E/\mathrm{d}x$ are naturally provided by nearly all types of tracking detectors. The type of information provided is either the collected charge or time-over-threshold for each of the detector elements crossed by the track (which typically number from 8–10 to a few dozen). The truncated-mean algorithm, which discards a fixed fraction (typically $\sim 30\%$) of the samples with the highest $\mathrm{d}E/\mathrm{d}x$ values, is usually used to mitigate the effect of the long tail of the Landau–Vavilov distribution of the individual $\mathrm{d}E/\mathrm{d}x$ samples.

As a function of particle's velocity, the $\mathrm{d}E/\mathrm{d}x$ truncated mean reaches a minimum at $\beta\gamma = p/m \approx 3.5$–$4.5$ and rises rapidly as the particle's velocity decreases ($\mathrm{d}E/\mathrm{d}x \propto 1/\beta^2$ for $\beta\gamma \lesssim 1$). For this reason, $\mathrm{d}E/\mathrm{d}x$ is the most useful for $\mu/\pi/K/p$ separation at the momenta where for at least one of the particle types being separated $p/m \lesssim 1.4$ (e.g., at $p \lesssim 0.7$ GeV/c for K/π separation). At $\beta\gamma \gtrsim 6$, the $\mathrm{d}E/\mathrm{d}x$ truncated mean experiences a "relativistic rise", which is mild in gases, allowing weak (1-2 σ) π/K separation at $p \gtrsim 1.4$ GeV/c, but nearly non-existent in liquids and solids. Depending on the detector and the environment, measurements of $\mathrm{d}E/\mathrm{d}x$ can be affected by a large variety of sizable systematic effects, including aging, and thus development of a $\mathrm{d}E/\mathrm{d}x$ calibration technique that can reliably predict the $\mathrm{d}E/\mathrm{d}x$ mean value and resolution for a particle of a given type anywhere in the detector can be a great challenge, particularly when one wishes to exploit for PID the $\mathrm{d}E/\mathrm{d}x$ "relativistic rise" in a gaseous tracking system.

Examples of $\mathrm{d}E/\mathrm{d}x$ use in PID include the drift chambers in *BABAR* [207,234], Belle [235], BESII [211], CDF [236], CLEO-II [203], CLEO-III and CLEO-c [205], and KLOE [237]. In *BABAR* and Belle, $\mathrm{d}E/\mathrm{d}x$ K/π separation at low momenta is very important to B flavor tagging, and in CDF the $\mathrm{d}E/\mathrm{d}x$ "relativistic rise" is critically important to the study of B^0, B_s, $\Lambda_b \to h^+h'^-$ ($h = \pi, K, p$) decays. The *BABAR* silicon vertex tracker [207], with its 5 double-sided Si layers, is unique among Si vertex detectors at e^+e^- machines in its ability to provide useful $\mathrm{d}E/\mathrm{d}x$ information, which is particularly valuable for π/e separation at $p \lesssim 0.2$ GeV/c (e.g., in charm physics).

Time-of-flight (TOF) PID systems combine knowledge of the particle's creation time and trajectory with a high-precision measurement of its arrival time at the TOF detector, thus proving a measurement of its velocity. Given the time resolution of the currently deployed TOF detectors ($\sim$ 100-200 ps), they are limited in π/K separation of at least 2σ to $p \lesssim 1.5$ GeV/c. Examples include the TOF systems at Belle [238], BESII [211], CDF [219], and KLOE [237]. Complementarity of TOF and $\mathrm{d}E/\mathrm{d}x$ measurements is evident from the fact that $\mathrm{d}E/\mathrm{d}x$ separation in gas vanishes for π/K at 1.1 GeV/c, for e/π at 0.16 GeV/c, for e/K at 0.63 GeV/c, and for e/p at 1.2 GeV/c.

Detectors that exploit the **Cherenkov–Vavilov** radiation by charged particles moving faster than $v_{\mathrm{crit}} = c/n$, where n is the refraction coefficient of a solid, liquid or gaseous

radiator, tend to provide the best velocity-based PID at $p \gtrsim 1\,\mathrm{GeV}/c$. The cheapest and most simple are Cherenkov threshold detectors, where the refraction index of the radiator is chosen in such a way that in the kinematic range of interest the lighter of the two particle types being distinguished would be superluminal while the other one would not; additional information may be provided by comparing the observed number of Cherenkov photons with the one expected for each of the particle types. Belle employs silica aerogel with refraction indices varying from 1.01 to 1.03 [239].

Since Cherenkov radiation is emitted in a cone with an opening angle $\theta_\mathrm{C} = \cos^{-1}\frac{1}{n\beta}$, the particle's velocity can be determined by measuring the cone's opening angle. The most common, moderately expensive such technology is RICH (Ring-Imaging CHerenkov), where the cone is produced in a transparent solid, liquid or gaseous radiator (LiF in CLEO-III and CLEO-*c*, [206]) and projected onto a planar photon detector a certain distance away. Another, more expensive but space-saving ring-imaging technology is DIRC, used in *BABAR* [240], where the cone of Cherenkov light is produced and captured within a bar of synthetic fused silica running the length of the *BABAR* detector. The π/K separation achieved in $B \to Xh^\pm$ decays in *BABAR* by the DIRC (DCH $\mathrm{d}E/\mathrm{d}x$) varies from 13σ (1.0σ) at 1.5 GeV/c to 2.5σ (1.9σ) at 4.5 GeV/c [241]. However, due to the DIRC's mechanical complexity about 18% of reconstructed high-momentum tracks in *BABAR* miss the DIRC; similar coverage limitations are usually suffered by RICH and TOF systems as well.

For dedicated $e^\pm$ ID, the most distinctive and frequently used feature of their interactions with matter is the development of electromagnetic (EM) showers in thick absorbers. **EM calorimeters** seek to contain and measure the total shower energy E_cal. For $e^\pm$, the ratio E_cal/p is close to 1, while for the other charged particles the E_cal/p ratio will be either much smaller than 1 ("minimum-ionizing"), have a broad distribution mostly below 1 for those that shower hadronically, or have a poorly defined broad distribution for the antiprotons that annihilate in the calorimeter. Since the shapes of the EM showers produced by high-energy $e^\pm$ and photons are quite similar, the matching of calorimeter clusters to tracks extrapolated from the tracking system is of critical importance. The materials used in EM calorimeters the most frequently are blocks of heavy inorganic scintillators with no longitudinal segmentation. Thallium-doped CsI is used in *BABAR* [207], Belle [208, 242], CLEO [243], and BESIII. Even in the absence of longitudinal segmentation, limited information on the longitudinal shower shape (which is different for $e/\mu/\pi/K/p$) can be obtained for particles of sufficiently low momenta (which enter the calorimeter at an angle sufficiently different from 90°) by combining tracking and lateral cluster-shape information with a technique recently introduced in *BABAR* [244]. KLOE has a lead–scintillating fiber sampling EM calorimeter [245], which, thanks to its longitudinal segmentation, also provides good muon-hadron separation.

Unlike the other long-lived charged particles, muons do not shower. Hence, dedicated **muon ID** relies on muons' long path length in absorber thick enough to stop hadronic showers (5-8 hadronic interaction lengths is common). Instrumentation of the magnet's iron flux return with several layers of charged-particle detectors is a good approach since it allows monitoring of hadron-shower development (which also enables K^0_L ID) and precise matching of tracks with hits in the muon system. This approach is used in *BABAR* [207], Belle [246], BESII [211], and CLEO [203, 247].

Response of the detector as a whole, and each of the subdetectors individually, to the passage of charged particles of a given type can be studied with high-purity, high-

statistics calibration samples selected on the basis of the physics and kinematics of certain decays, with PID applied to the other particles in the decay to further enhance purity. In calibrating the PID response of a given subdetector, PID information from the rest of the detector can be used as well. Examples of calibration samples used in e^+e^- B factories include protons from $\Lambda \to p\pi^-$, pions and Kaons from $D^{*+} \to D^0\pi^+ (D^0 \to K^-\pi^+)$, pions from $K^0_S \to \pi^+\pi^-$, electrons and muons from $e^+e^- \to \ell^+\ell^-\gamma$.

The best PID performance is achieved by combining information from all subdetectors. The TOF, $\mathrm{d}E/\mathrm{d}x$ and ring-imaging Cherenkov measurements can be conveniently represented in the form of probability-distribution functions (PDFs), which makes likelihood-based hadron ID quite close to optimal. On the other hand, the calorimeter and muon-system quantities, which are more numerous and can be highly correlated, are either very difficult or impossible to adequately describe with PDFs. For this reason, the best PID performance can be achieved by advanced multivariate techniques such as neural nets and bagged decision trees.

3.2.5. *Background suppression*

The isolation of signal events in the presence of significant sources of backgrounds is critical for almost all measurements. This usually is achieved by an optimization of the event selection process designed to maximize the experimental sensitivity by suppressing the backgrounds effectively while retaining a sizable fraction of the signal. The choice of the method depends on both the nature of the signal and background events, and critically on the signal over background ratio which may vary from more than 100 to 10^{-6} or less.

The separation of signal and background processes relies both on the detector performance as well as kinematics of the final state produced. Large acceptance and the high resolution and efficiencies for the reconstruction of charged and neutral particles and the identification of leptons and hadrons over a wide range of energies are very important. A low rate of the misidentification of charged hadrons as leptons is critical, in particular for rare processes involving leptons.

Though the cross sections for heavy flavor particle production in hadronic interactions exceed the cross sections at e^+e^- colliders by several orders of magnitude, their fraction of the total interaction rate is small. Furthermore, the multiplicity of the final states is very large, and thus the combinatorial background to charm and beauty particles is extremely large for experiments at hadron colliders and for fixed-target experiments in high momentum hadron beams. Typical event triggers rely on the detection of charged hadrons and leptons of large transverse momentum and in some cases also on the isolation of decay vertices that are displaced from the primary interaction point. The analyses often focus on decays involving two- or three-body decays to intermediate states of narrow width, for instance J/ψ, D or D^* mesons. Because of the very large momenta of these intermediate states, the identification of particles that do not originate form the primary interaction point is a very powerful tool to suppress backgrounds.

Background conditions for the detection of charm and beauty particles at e^+e^- colliders are markedly different. There are two dominant sources of background, the so-called continuum background and combinatorial background from other particles in the final states from decays of resonances under study, for instance $J/\psi\,, \psi(3770)$, or $\Upsilon(nS)$ mesons. Two types of processes contribute to continuum background, QED processes, $e^+e^- \to$

$\ell^+\ell^-(\gamma)$ with $\ell = e, \mu$, or τ, and quark-pair production, $e^+e^- \to q\overline{q}$ with $q = u, d, s, (c)$. Both of these processes are impacted by energy losses due to initial state radiation.

At e^+e^- colliders operating near kinematic thresholds for pair production of charm or beauty particles, for instance the B Factories at $\Upsilon(4S)$ and the Charm Factories at the $\psi(3770)$ or above, the primary particles pairs are produced at very low momenta, leading to event topologies that are spherical, not jet-like.

Continuum background is characterized by lower multiplicities and higher momenta of charged and neutral particles. To suppress QED background, selected events are usually required to have at least three reconstructed charged particles. At sufficiently high c.m. energies, the fragmentation of the light quarks leads to a two-jet topology. Such events are characterized by variables that measure the alignment of particles within an event along a common axis. Among the variables that show sharply peaked distributions for jet-like events are:

- thrust, the maximum sum of the longitudinal momenta of all particles relative to a chosen axis; the trust distribution peaks at or just below 1.0 for two-body final states and two-jet events;
- $\cos\Delta\theta_{thrust}$, where $\Delta\theta_{thrust}$ is the angle between the thrust axis of one or the sum of all particles associated with the signal candidate and the thrust axis of the rest of the event; this distribution is flat for signal events and peaked near 1.0 for continuum background;
- the energy flow in conical shells centered on the thrust axis, typically nine double cones of 10 degrees; for continuum events most of the energy is contained in the inner cones, while for the more spherical signal events the energy is shared more uniformly among all cones;
- normalized Legendre moments can be viewed as continuous generalizations of the energy cones, typically the first and second of these moments are used, $L_j = \sum_i p_i |\cos\theta_i|^j$ with $j = 0$ or $j = 2$, where p_i and θ_i are the momentum and angle of any particles, except those related to the signal decay, relative to the thrust axis of the signal decay. In many cases these moments provide better discrimination of continuum events than the energy cones.
- $R_2 = H_2/H_0$, the ratio of second to zeroth Fox-Wolfram movements, with $H_2 = \sum_{i,j} |p_i||p_j| L_2(\cos\theta_{ij})$, calculated for all particles in the event, charged and neutral. The nth Fox-Wolfram moment is the momentum-weighted sum of Legendre polynomial of the nth order, computed for the cosine of the angles between all pairs of particles; the ratio R_2 peaks close to 1.0 for jet-like continuum events.

In practice the suppression of the continuum background is achieved by imposing restriction on many of these variables, either as sequential individual cuts, or by constructing a multivariable discriminant, a decision tree, or employing a neural network.

Fig. 11 shows examples of distributions for two of these variables for selected $B\overline{B}$ events.

For the isolation of exclusive decays of B or D mesons that are pair-produced at Beauty or Charm Factories two kinematic variables are commonly used to separate signal from background events. These variables make optimum use of the measured beam energies and are largely uncorrelated. The difference of the reconstructed and expected energy for the decay of a meson M is defined as $\Delta E = (q_M q_0 - s/2)/\sqrt{s}$, where $\sqrt{s} = 2E^*_{beam}$ is the total energy of the colliding beams in the c.m. frame, and q_M and q_0 are the Lorentz vectors representing the momentum of the candidate M and of the e^+e^- system, $q_0 =$

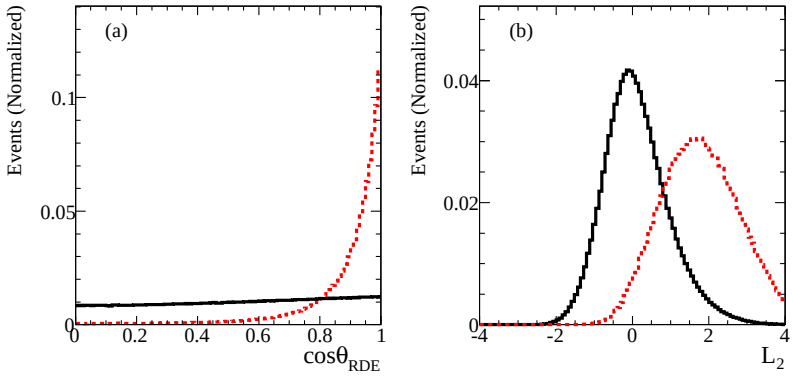

Fig. 11. *Distribution of variables used to suppress continuum background in selected candidates for* $B^0 \to K^-\pi^+\pi^0$ *decays [248] a)* $\cos\Delta\theta_{thrust}$*, b) the normalized Legendre moments* L_2*. The solid lines show the expectation for continuum background, the dotted lines represent the background distributions.*

$q_{e^-} + q_{e^+}$. In the c.m. system,

$$\Delta E = E^*_M - E^*_{beam}, \tag{101}$$

where E^*_M is the energy of the reconstructed meson M.

The second variable is often referred to as the energy-substituted mass, m_{ES}. In the laboratory frame, it can be determined from the measured three-momentum, $\boldsymbol{p}_M$, of the candidate M, without explicit knowledge of the masses of the decay products, $m_{ES} = \sqrt{(s/2 + \boldsymbol{p}_M \cdot \boldsymbol{p}_0)^2/E_0^2 - \boldsymbol{p}_M^2}$. In the c.m. frame ($\boldsymbol{p}_0 = 0$), this variable takes the familiar form,

$$m_{ES} = \sqrt{E^{*2}_{beam} - \boldsymbol{p}^{*2}_M}, \tag{102}$$

where $\boldsymbol{p}^*_M$ is the c.m. momentum of the meson M, derived from the momenta of its decay products, and its energy is substituted by E^*_{beam}.

An example of ΔE and m_{ES} distributions is given in Fig. 12 for a selected sample of rare B decays. ΔE is centered on zero and the m_{ES} distribution peaks at the B-meson mass. While resolution in ΔE is dominated by detector resolution, the resolution in m_{ES} is determined by the spread in the energy of the colliding beams, typically a few MeV. The flat background is composed of both continuum and $B\overline{B}$ events, its size depends on the decay mode under study and the overall event selection. There is a small component of peaking background due to backgrounds with kinematics very similar to the true decays.

For decays that cannot be fully reconstructed because of an undetected neutrino or K^0_L, the separation of signal and backgrounds is more challenging. The energy and momentum of the missing particle can be inferred from the measurement of all other particles in the event and the total energy and momentum of the colliding beams,

$$(E_{miss}, \boldsymbol{p}_{miss}) = (E_0, \boldsymbol{p}_0) - (\sum_i E_i, \sum_i \boldsymbol{p}_i). \tag{103}$$

If the only missing particle in the event is a neutrino or K^0_L, the missing mass should be close to zero or the Kaon mass and the missing momentum should be non-zero. Fig. 13a shows an example of a missing mass squared distribution, $E^2_{miss} - |\boldsymbol{p}_{miss}|^2$ for $B^- \to D^0\ell^-\overline{\nu}$ decays, selected in $B\overline{B}$ events tagged by a hadronic decay of the second B meson

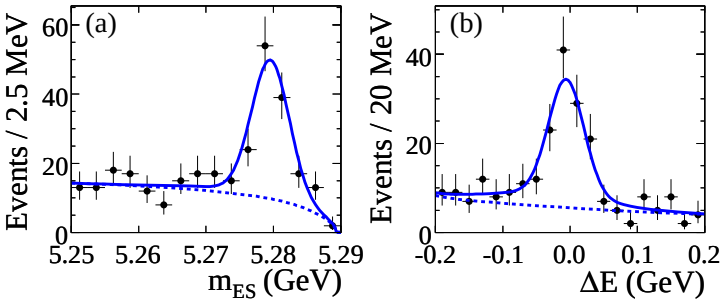

Fig. 12. *Distributions of a) ΔE and b) m_{ES} for a sample of $B^0 \to \omega K^0_S$ candidates [249]. The solid line represents the result of the fit to the data, the dotted line marks the background contributions.*

in the event. There is a narrow peak at zero for events in which the only missing particle is the neutrino, and a broad enhancement due to $B^- \to D^{*0}\ell^-\overline{\nu}$ decays, in which the low energy pion or photon from the decay $D^{*0} \to D^0\pi^0$ or $D^{*0} \to D^0\gamma$ escaped detection. Since the second B is fully reconstructed, there is very little combinatorial background.

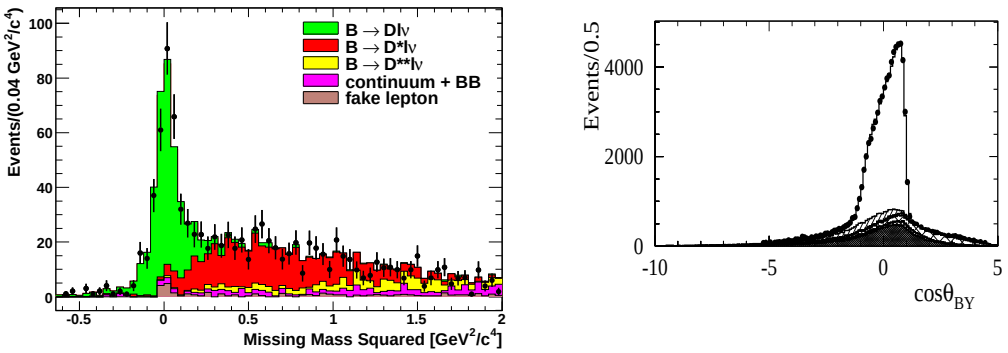

Fig. 13. *Distributions of the a) the missing mass squared for selected $B \to D\ell\nu$ candidates, in $B\overline{B}$ events tagged by a hadronic decay of the second B meson in the event [250], b) $\cos\theta_{BY}$, for a sample of $\overline{B}^0 \to D^{*+}\ell^-\overline{\nu}$ candidates [251] Her the unshaded histrogram indicates the signal distribution, on top of background contributions, mostly from other semileptonic B decays.*

For semileptonic B or D decays, $M \to H\ell\nu$, a variable first introduced by the CLEO Collaboration is used to suppress background,

$$\cos\theta_{BY} = \frac{(2E_BE_Y - M_M^2 - M_Y^2)}{2|\boldsymbol{p_M}||\boldsymbol{p}_Y|}. \tag{104}$$

For a true semileptonic decay in which the only missing particle is the neutrino, θ_{BY} is the angle between the momentum vectors $\boldsymbol{p_M}$ and $\boldsymbol{p}_Y = \boldsymbol{p}_H + \boldsymbol{p}_\ell$, and the condition $|\cos\theta_{BY}| \leq 1.0$ should be fulfilled, while for background events or incompletely reconstructed semileptonic decays the distribution extends to much larger values, thus enabling a clear separation from the signal decays (see Fig. 13b).

3.2.6. *Recoil Tagging Technique*

At e^+e^- colliders charged leptons and heavy flavor particles are produced in pairs, thus the detection of one member of the pair can be used to tag the presence of the other. In particular at Charm and B at B-Factories, operating at or near the threshold for charm or beauty particles tagging techniques not only identify the second member of the pair, they also can be used to measure their momentum and energy and uniquely determine their charge and flavor quantum numbers. Furthermore, near threshold, there are no other particle produced, and therefore the combinatorial background is significantly reduced. In addition, the kinematics of the final state are constrained such that given a fully reconstructed tag of one decays, the presence of a missing or undetectable particle like ν or K^0_L meson can be identified from the missing momentum and missing energy of the whole event (see for example [252]).

The tagging technique for $\psi(3770) \to D\overline{D}$ events was first developed by the Mark III collaboration [253] at SLAC, and has since been exploited in many analyses based on data from by $CLEO_c, BES, KLOE$, and the B Factories. For $\psi(3770) \to D^0\overline{D}^0$ events there are several tag modes, which can be divided into three categories: pure flavor tags such as $D^0 \to K^-e^+\nu_e$ and $D^0 \to \pi^-\mu^+\nu_\mu$; quasi-flavor tags for neutral mesons, such as $D^0 \to K^-\pi^+$, $D^0 \to K^-\pi^+\pi^0$ and $D^0 \to K^-\pi^+\pi^+\pi^-$, for which there is a small doubly-Cabibbo-suppressed contribution, and tags for CP-eigenstates such as $D^0 \to K^+K^-$ and $K^0_L\pi^0$. The quasi-flavor tags can be used to make precision measurements of branching fractions [254] and partial rates [255]. The three decays listed correspond to 25% of the total branching fraction. Since the $\psi(3770)$ is a $C = -1$ state, the detection of a tag with definite CP means that the other D meson in the event must be of opposite CP. Studies combined flavor and CP-tagged samples of $K\pi$ events [256] and $K^0_S\pi^+\pi^-$ [257] have resulted in the determination of the strong-phase parameters in D decay. Using low-multiplicity decays, such as $D^+ \to K^-\pi^+\pi^+$ and $D^+ \to K^0_S\pi^+$ has resulted in extremely clean samples, even for rare signal decays, and thus precise branching fraction and partial rate measurements.

Single-tag efficiencies and purities vary considerably depending on the number of tracks and neutrals in the decay. For example, $D^0 \to K^-\pi^+$ and $D^+ \to K^0_S\pi^+\pi^0$ tags have efficiencies of 65% and 22% and sample purities of $\sim 5\%$ and $\sim 50\%$, respectively. For fully reconstructed hadronic tags the discriminating variable (shown in Fig. 14) is the beam-constrained mass (see Sec. 3.2.5 and Eq. 102).

The recoil technique has also been used successfully in $e^+e^- \to D^+_sD^{*-}_s$ events at CLEO-c to measure branching fractions ([258]). Tag decays include $D^-_s \to K^+K^-\pi^-$, $D^-_s \to K^0_SK^-$, $D^-_s \to K^+K^-\pi^-\pi^0$ and $D^-_s \to \pi^+\pi^-\pi^-$ and correspond to approximately 20% of the total D^-_s branching fraction. The $D^{*-}_s \to D^-_s\gamma/\pi^0$ candidates are identified with or without the explicit reconstruction of the photon or π^0.

At the $\Upsilon(4S)$ resonance, the higher mass of the b mesons lead to much smaller individual branching fractions for individual decays, which means that the achievable tagging efficiencies are much lower. Nevertheless, both *BABAR* and *Belle* have developed and employed several tagging techniques. The cleanest samples are possible for tree-mediated hadronic decays of the form $B \to D^{(*)}X$, where X refers a hadronic state of one or more hadrons, up to five charged mesons (pions or Kaons), up to two neutral pions or a K^0_S, and the $D^{0,(*)}$, $D^{+,(*)}$or $D^{+,(*)}_s$ mesons are reconstructed in many different decays modes. The kinematic variables ΔE and $m_{\rm ES}$, introduced in Sec. 3.2.5, are used to iso-

late the true tag decays from combinatorial background and to estimate the purity of the tag samples. The purity of a given tag mode is used to separate the cleaner samples from those with high background, the actual choice usually depends on the signal mode under study. The tag efficiency is typically 0.3% and has a signal-to-noise ratio of 0.5 (see Fig. 14).

Significantly higher tag efficiencies can be obtained for semileptonic B decays, for instance $B \to D^{(*)}\ell\nu$ ($\ell = e, \mu$), with a branching fraction of more than 7% for each lepton. For D mesons the same decays listed above are used, are reconstructed and for the D^* mesons the decays are $D^{*+} \to D^0\pi^+, D^+\pi^0$ and $D^{*0} \to D^0\pi^0, D^0\gamma$. Due to the very small mass difference of the D^* and D mesons, the pions and photons from its decay are of low energy, and thus the mass difference $\Delta M = m(D\pi) - m(D)$ can be very well measured. The presence of a neutrino in the decay can be checked using the variable $cos\theta_{BY}$ defined in Eq. 104. As for hadronic tags, tag selection and its efficiency and purity are strongly dependent on the signal decay recoiling against the tag. Typical efficiencies are of order 0.5-1%.

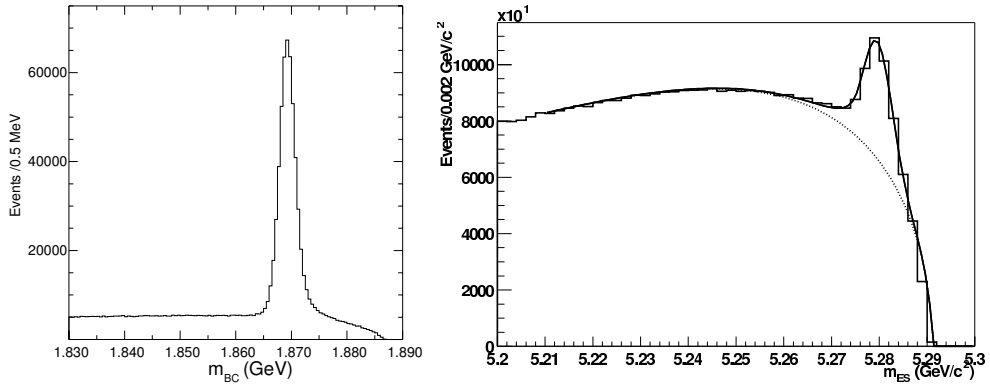

Fig. 14. *Distribution of the energy substituted mass for selected hadronic tag decays a) for D mesons in $\psi(3770)$ events at CLEO, and b) for B mesons in $\Upsilon(4S)$ decays at BABAR.*

The biggest advantage of the hadronic B tags over the semileptonic B tags is the better measurement of the reconstructed B momentum. This permits constraints on the signal decays in the recoil and precise reconstruction of the kinematic variables even in decays with a neutrino or missing neutral Kaon. Otherwise the two tags have similar performance. They are completely orthogonal samples and thus can be combined .

3.2.7. *Dalitz Plot Analysis*

The partial decay rate of a particle into a multi-body final state depends on the square of a Lorentz invariant matrix element $\mathcal{M}$. Such matrix element can be independent of the specific kinematic configuration of the final state or otherwise reveal a non-trivial structure in the dynamics of the decay. In the case, for instance, of a three-body decay $P \to 123$, invariant masses of pair of particles can be defined as $m_{ij}^2 = |p_i + p_j|^2$ where p_j (j=1,2,3) are the four-momenta of the final states particle. A plot of m_{ij}^2 versus m_{ik}^2 is commonly referred as Dalitz plot [259].

Dalitz plots distributions have been used since several decades to study the strong interaction dynamics in particle decays or in scattering experiment. In a three body

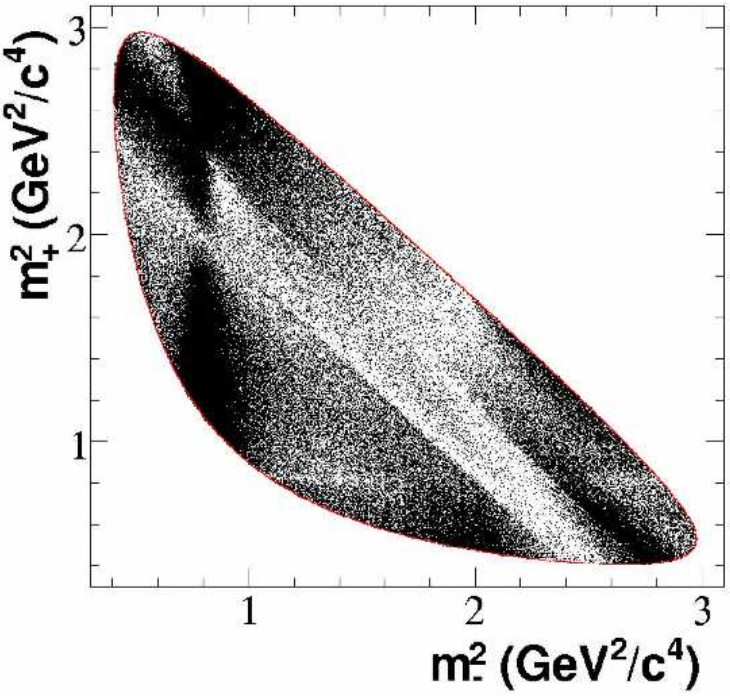

Fig. 15. Dalitz plot distribution of a high purity sample of $D^0 \to K_S\pi^+\pi^-$, with $m^2_- = |p_{K_S} + p_{\pi^-}|^2$ and $m^2_+ = |p_{K_S} + p_{\pi^+}|^2$ from [260]. The most visible features are described by a $K^{*-}(892)$ resonance (vertical band with two lobes) and a $\rho(770)$ resonance (diagonal band with two lobes). Interferences between resonances are distorting the distribution. The contours (solid red line) represent the kinematic limits of the decay.

decay of a meson, the underlying dynamics can be therefore represented by intermediate *resonances*. As an example in Fig.15 a Dalitz plot for the decay $D^0 \to K_S\pi^+\pi^-$ is shown: there are several visible structures due to competing and interfering resonances.

It is therefore a common practice to parameterize the matrix element as a coherent sum of two-body amplitudes (subscript r) [261],

$$\mathcal{M} \equiv \sum_r a_r e^{i\phi_r} \mathcal{A}_r(m^2_{13}, m^2_{23}) \tag{105}$$

An additional constant "non-resonant" term $a_{\rm NR}e^{i\phi_{\rm NR}}$ is sometimes included.

The parameters a_r and ϕ_r are the magnitude and phase of the amplitude for the component r. In the case of a D^0 decay the function $\mathcal{A}_r = F_D \times F_r \times T_r \times W_r$ is a Lorentz-invariant expression where F_D (F_r) is the Blatt-Weisskopf centrifugal barrier factor for the D (resonance) decay vertex [262] T_r is the resonance propagator, and W_r describes the angular distribution in the decay.

For T_r a relativistic Breit-Wigner (BW) parameterization with mass-dependent width is commonly used (for definitions see review in [261]). BW mass and width values are usually taken from scattering experiment or world averages provided by Particle Data Group.

The angular dependence W_r reflects the spin of the resonance and is described using either Zemach tensors [263–265] where transversality is enforced or the helicity formalism [266,267] when a longitudinal component in the resonance propagator is allowed (see Ref. [261] for a comprehensive summary).

Alternative parameterizations have been used especially to represent spin zero (S-wave) resonances. For this component the presence of several broad and overlapping resonances makes a simple BW model not adequate.For instance, K-matrix formalism with the P-vector approximation [268, 269] was used for $\pi\pi$ S-wave components.

In the context of flavor physics Dalitz model have been used as effective parameterizations to derive strong phase dependence. The knowledge of strong phases is relevant for analysis where the extraction of weak phases can be obtained through interferences between different resonances. Moreover, in the case of neutral meson decays the interference between flavor mixing and decay leads to time-dependent analyses (either for CP or flavor mixing measurements). For this reason Dalitz models have been included in such analyses (that are frequently referred for short as *time-dependent* Dalitz analyses).

4. Determination of $|V_{ud}|$ and $|V_{us}|$.

Unitarity of the bare (unrenormalized) CKM [1, 2] 3×3 quark mixing matrix V^0_{ij}, $i = u, c, t$ $j = d, s, b$ implies the orthonormal tree level relations

$$\sum_i V^{0*}_{ij} V^0_{ik} = \sum_i V^{0*}_{ji} V^0_{ki} = \delta_{jk} \tag{106}$$

Standard Model quantum loop effects are important and corrected for such that Eq. (106) continues to hold at the renormalized level [270]. That prescription generally involves normalization of all charged current semileptonic amplitudes relative to the Fermi constant

$$G_\mu = 1.166371(6) \times 10^{-5} \mathrm{GeV}^{-2} \tag{107}$$

obtained from the precisely measured (recently improved) muon lifetime [271]

$$\tau_\mu = \Gamma^{-1}(\mu^+ \to e^+ \nu_e \bar{\nu}_\mu(\gamma)) = 2.197019(21) \times 10^{-6} \mathrm{sec} \tag{108}$$

In all processes, Standard Model $\mathrm{SU}(3)_C \times \mathrm{SU}(2)_L \times \mathrm{U}(1)_Y$ radiative corrections are explicitly accounted for [272].

Of particular interest here is the first row constraint

$$|V_{ud}|^2 + |V_{us}|^2 + |V_{ub}|^2 = 1 \tag{109}$$

An experimental deviation from that prediction would be evidence for "new physics" beyond Standard Model expectations in the form of tree or loop level contributions to muon decay and/or the semileptonic processes from which the V_{ij} are extracted. Of course, if Eq. (109) is respected at a high level of certainty, it implies useful constraints on various "new physics" scenarios.

4.1. V_{ud} *from nuclear decays*

Nuclear beta decays between 0^+ states sample only the vector component of the hadronic weak interaction. This is important because the conserved vector current (CVC) hypothesis protects the vector coupling constant G_V from renormalization by background strong interactions. Thus, the G_V that occurs in nuclei should be the same as the one that operates between free up and down quarks. In that case, one can write $G_V = G_F V_{ud}$, which means that a measurement of G_V in nuclei, when combined with a measurement of the Fermi constant G_F in muon decay, yields the value of the CKM matrix element V_{ud}. To date, precise measurements of the beta decay between isospin analog states of spin, $J^\pi = 0^+$, and isospin, $T = 1$, provide the most precise value of V_{ud}.

A survey of the relevant experimental data has recently been completed by Hardy and Towner [273]. Compared to the previous survey [274] in 2005 there are 27 new publications, many with unprecedented precision. In some cases they have improved the average results by tightening their error assignments and in others by changing their central values. Penning-trap measurements of decay energies have been especially effective in this regard.

For each transition, three experimental quantities have to be determined: the decay energy, $Q_{\rm ec}$; the half-life of the decaying state, $t_{1/2}$; and the branching ratio, R, for the particular transition under study. The decay energy is used to calculate the phase space integral, f, where it enters as the fifth power. Thus, if f is required to have 0.1% precision then the decay energy must be known to 0.02% – a demand that is currently being surpassed by Penning-trap devices. The partial half-life is defined as $t = t_{1/2}/R$ and the product ft is

$$ft = \frac{K}{G_F^2 V_{ud}^2 \, \langle \tau_+ \rangle^2}, \tag{110}$$

where $K/(\hbar c)^6 = 2\pi^3 \hbar \ln 2/(m_e c^2)^5 = 8120.2787(11) \times 10^{-10}$ GeV^{-4} s. When isospin is an exact symmetry the initial and final states, being isospin analogs, are identical except that a proton has switched to a neutron. Since the operator describing the transition is simply the isospin ladder operator, τ_+, its matrix element, $\langle \tau_+ \rangle$, is independent of nuclear structure and is given by an isospin Clebsch-Gordan coefficient, which for isospin $T = 1$ states has the value $\sqrt{2}$. Hence,

$$ft = \frac{K}{2\, G_F^2 V_{ud}^2}, \tag{111}$$

and according to CVC the ft value is a constant independent of the nucleus under study. In practice, however, isospin is always a broken symmetry in nuclei, and beta decay occurs in the presence of radiative corrections, so a 'corrected' ft value is defined by

$$\mathcal{F}t \equiv ft(1 + \delta_R')\,(1 - (\delta_C - \delta_{NS})) = \frac{K}{2\, G_F^2 V_{ud}^2\,(1 + \Delta_{\rm R}^{\rm V})}; \tag{112}$$

so it is this corrected $\mathcal{F}t$ that is a constant. Here the radiative correction has been separated into three components: (i) $\Delta_{\rm R}^{\rm V}$ is a nucleus-independent part that includes the universal short-distance component S_{EW} affecting all semi-leptonic decays, defined later in Eq. (128). Being a constant, $\Delta_{\rm R}^{\rm V}$ is placed on the right-hand-side of Eq. (112); (ii) δ_R' is transition dependent, but only in a trivial way, since it just depends on the nuclear charge, Z, and the electron energy, E_e; while δ_{NS} is a small nuclear-structure

Table 9
Experimental ft values for $0^+ \rightarrow 0^+$ superallowed Fermi beta decays, the trivial nucleus-dependent component of the radiative correction, δ'_R, the nuclear-structure dependent isospin-symmetry-breaking and radiative correction taken together, $\delta_C - \delta_{NS}$, and the corrected $\mathcal{F}t$ values. The last line gives the average $\mathcal{F}t$ value and the χ^2 of the fit.

Parent	$ft(s)$	$\delta'_R(\%)$	$\delta_C - \delta_{NS}(\%)$	$\mathcal{F}t(s)$
^{10}C	3041.7 ± 4.3	1.679 ± 0.004	0.520 ± 0.039	3076.7 ± 4.6
^{14}O	3042.3 ± 2.7	1.543 ± 0.008	0.575 ± 0.056	3071.5 ± 3.3
^{22}Mg	3052.0 ± 7.2	1.466 ± 0.017	0.605 ± 0.030	3078.0 ± 7.4
^{26}Al^m	3036.9 ± 0.9	1.478 ± 0.020	0.305 ± 0.027	3072.4 ± 1.4
^{34}Cl	3049.4 ± 1.2	1.443 ± 0.032	0.735 ± 0.048	3070.6 ± 2.1
^{34}Ar	3052.7 ± 8.2	1.412 ± 0.035	0.845 ± 0.058	3069.6 ± 8.5
^{38}K^m	3051.9 ± 1.0	1.440 ± 0.039	0.755 ± 0.060	3072.5 ± 2.4
^{42}Sc	3047.6 ± 1.4	1.453 ± 0.047	0.630 ± 0.059	3072.4 ± 2.7
^{46}V	3050.3 ± 1.0	1.445 ± 0.054	0.655 ± 0.063	3074.1 ± 2.7
^{50}Mn	3048.4 ± 1.2	1.444 ± 0.062	0.695 ± 0.055	3070.9 ± 2.8
^{54}Co	3050.8 ± 1.3	1.443 ± 0.071	0.805 ± 0.068	3069.9 ± 3.3
^{62}Ga	3074.1 ± 1.5	1.459 ± 0.087	1.52 ± 0.21	3071.5 ± 7.2
^{74}Rb	3084.9 ± 7.8	1.50 ± 0.12	1.71 ± 0.31	3078 ± 13
			Average $\overline{\mathcal{F}t}$	3072.14 ± 0.79
			χ^2/ν	0.31

dependent term that requires a shell-model calculation for its evaluation. (iii) Lastly, δ_C is an isospin-symmetry breaking correction, typically of order 0.5%, that also requires a shell-model calculation for its evaluation.

In Tab. 9 are listed the experimental ft values from the survey of Hardy and Towner [273] for 13 transitions, of which 10 have an accuracy at the 0.1% level, and three at up to the 0.4% level. Also listed are the theoretical corrections, δ'_R and $\delta_C - \delta_{NS}$, taken from Ref. [275], and the corrected $\mathcal{F}t$ values. This data set is sufficient to provide a very demanding test of the CVC assertion that the $\mathcal{F}t$ values should be constant for all nuclear superallowed transitions of this type. In Fig. 16 the uncorrected ft values in the upper panel show considerable scatter, the lowest and highest points differing by 50 parts in 3000. This scatter is completely absent in the corrected $\mathcal{F}t$ values shown in the lower panel of Fig. 16, an outcome principally due to the nuclear-structure-dependent corrections, $\delta_C - \delta_{NS}$, thus validating the theoretical calculations at the level of current experimental precision. The data in Tab. 9 and Fig. 16 are clearly satisfying the CVC test. The weighted average of the 13 data is

$$\overline{\mathcal{F}t} = 3072.14 \pm 0.79 \text{ s}, \tag{113}$$

with a corresponding chi-square per degree of freedom of $\chi^2/\nu = 0.31$. Eq. (113) confirms the constancy of G_V – the CVC hypothesis – at the level of 1.3×10^{-4}.

Before proceeding to a determination of V_{ud} it has to be noted that the isospin-symmetry-breaking correction, δ_C, is taken from Towner and Hardy [275] who calculated proton and neutron radial functions as eigenfunctions of a Saxon-Woods potential. An alternative procedure used in the past by Ormand and Brown [276–278] takes the radial functions as eigenfunctions of a Hartree-Fock mean-field potential. The corrections obtained by Ormand and Brown were consistently smaller than the Saxon-Woods values and this difference was treated as a systematic error in previous surveys. In their most recent survey, though, Hardy and Towner [273] repeated the Hartree-Fock calculations, but with a change in the calculational procedure, and obtained results that were closer to the Saxon-Woods values. Even so, when these Hartree-Fock δ_C values are used in Eq. (112) the χ^2 of the fit to $\mathcal{F}t$ = constant becomes a factor of three larger. This in itself might be sufficient reason to reject the Hartree-Fock values, but to be safe an average of the Hartree-Fock and Saxon-Woods $\overline{\mathcal{F}t}$ values was adopted and a systematic error assigned that is half the spread between the two values. This leads to

$$\begin{aligned}\overline{\mathcal{F}t} &= 3071.83 \pm 0.79_{\rm stat} \pm 0.32_{\rm syst}\ {\rm s} \\ &= 3071.83 \pm 0.85\ {\rm s}. \end{aligned} \tag{114}$$

In the second line the two errors have been combined in quadrature.

Recently, Miller and Schwenk [279] have explored the formally complete approach to isospin-symmetry breaking, but produced no numerical results. The Towner-Hardy [273] values quoted here are based on a model whose approximations can be tested for $A = 10$ by comparing with the large no-core shell-model calculation of Caurier *et al* [280], which is as close to an exact calculation as is currently possible. The agreement between the two suggests that any further systematic error in the isospin-breaking correction is likely to be small.

The CKM matrix element V_{ud} is then obtained from

$$V_{ud}^2 = \frac{K}{2G_F^2(1+\Delta_{\rm R}^{\rm V})\overline{\mathcal{F}t}}, \tag{115}$$

where $\Delta_{\rm R}^{\rm V}$ is the nucleus-independent radiative correction taken from Marciano and Sirlin [281]: *viz.*

$$\Delta_{\rm R}^{\rm V} = (2.631 \pm 0.038)\%. \tag{116}$$

With $\overline{\mathcal{F}t}$ obtained from Eq. (114), the value of V_{ud} becomes

$$V_{ud} = 0.97425 \pm 0.00022. \tag{117}$$

Compared to the Hardy-Towner survey [274] of 2005, which obtained $V_{ud} = 0.97380(40)$, the central value has shifted by about one standard deviation primarily as a result of Penning-trap decay-energy measurements and a reevaluation of the isospin-symmetry breaking correction in 2007 [275]. The error is dominated by theoretical uncertainties; experiment only contributes 0.00008 to the error budget. Currently the largest contribution to the error budget comes from the nucleus-independent radiative correction $\Delta_{\rm R}^{\rm V}$ – recently reduced by a factor of two by Marciano and Sirlin [281]. Further improvements here will need some theoretical breakthroughs. Second in order of significance are the nuclear-structure-dependent corrections δ_C and δ_{NS}. So long as $0^+ \to 0^+$ nuclear decays provide the best access to V_{ud}, these corrections will need to be tested and honed. Here is where nuclear experiments will continue to play a critical role.

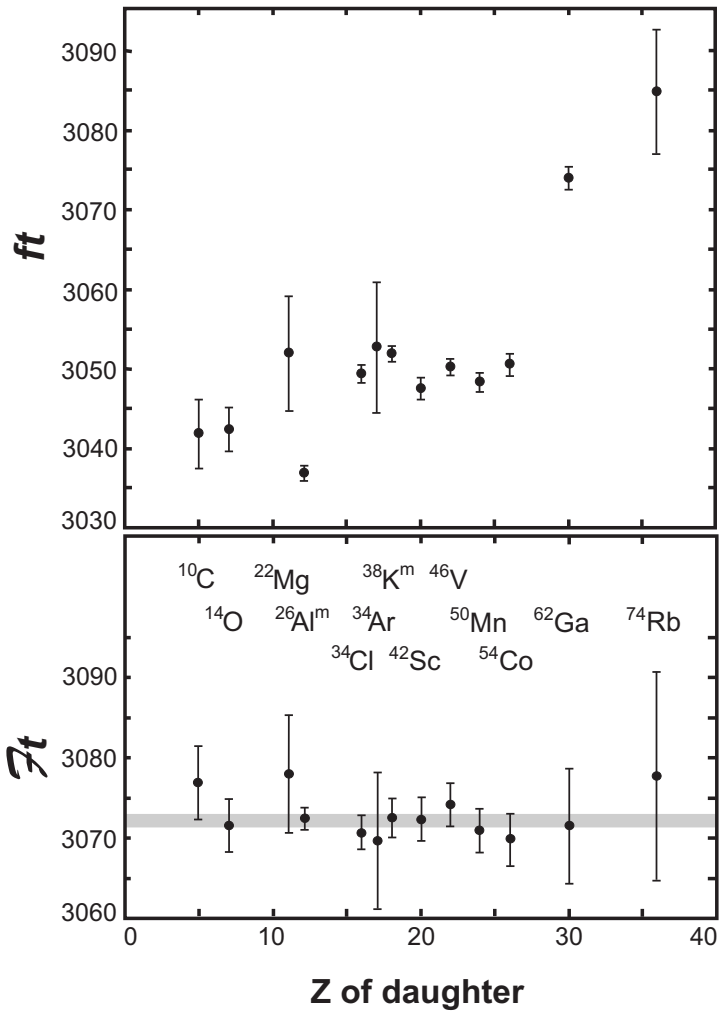

Fig. 16. In the top panel are plotted the uncorrected experimental ft values as a function of the charge on the daughter nucleus. In the bottom panel, the corresponding $\mathcal{F}t$ values as defined in Eq. (112) are given. The horizontal grey band in the bottom panel gives one standard deviation around the average $\overline{\mathcal{F}t}$.

4.2. V_{ud} *from neutron decay*

Although the result is not yet competitive, to extract V_{ud} from neutron β-decay is appealing because it does not require the application of corrections for isospin-symmetry breaking effects, δ_C, or nuclear-structure effects, δ_{NS}, as defined in the previous section on nuclear β-decay. However, it should be noted that the transition-dependent radiative correction, δ'_R, and the nucleus-independent radiative correction, $\Delta_{\rm R}^{\rm V}$, must still be applied to neutron β-decay observables; and the latter is, in fact, the largest contributor to the uncertainty in the nuclear value for V_{ud}.

In contrast to nuclear β-decays between 0^+ states, which sample only the weak vector

interaction, neutron β-decay proceeds via a mixture of the weak vector and axial-vector interactions. Consequently, three parameters are required for a description of neutron β-decay: G_F, the fundamental weak interaction constant; $\lambda \equiv g_A/g_V$, the ratio of the weak axial-vector and vector coupling constants; and the parameter of interest, V_{ud}. Thus, measurements of at least two observables (treating G_F as an input parameter) are required for a determination of V_{ud}.

A value for λ can be extracted from measurements of correlation coefficients in polarized neutron β-decay. Assuming time-reversal invariance, the differential decay rate distribution of the electron and neutrino momenta and the electron energy for polarized β-decay is of the form [282]

$$\frac{dW}{dE_e d\Omega_e d\Omega_\nu} \propto p_e E_e (E_0 - E_e)^2 \left[1 + a\frac{\boldsymbol{p}_e \cdot \boldsymbol{p}_\nu}{E_e E_\nu} + \langle \boldsymbol{\sigma}_n \rangle \cdot \left(A\frac{\boldsymbol{p}_e}{E_e} + B\frac{\boldsymbol{p}_\nu}{E_\nu} \right) \right], \qquad (118)$$

where E_e (E_ν) and $\boldsymbol{p}_e$ ($\boldsymbol{p}_\nu$) denote, respectively, the electron (neutrino) energy and momentum; E_0 (= 782 keV + m_e) denotes the β-decay endpoint energy, with m_e the electron mass; and $\langle \boldsymbol{\sigma}_n \rangle$ denotes the neutron polarization. Neglecting recoil-order corrections, the correlation coefficients a (the e-$\overline{\nu}_e$-asymmetry), A (the β-asymmetry), and B (the $\overline{\nu}_e$-asymmetry) can be expressed in terms of λ as [283, 284]

$$a = \frac{1-\lambda^2}{1+3\lambda^2}, \qquad A = -2\frac{\lambda^2+\lambda}{1+3\lambda^2}, \qquad B = 2\frac{\lambda^2-\lambda}{1+3\lambda^2}. \qquad (119)$$

At present, these correlation parameters have values $a = -0.103 \pm 0.004$, $A = -0.1173 \pm 0.0013$, and $B = 0.983 \pm 0.004$ [285]. Although B has been measured to the highest precision (0.41%), the sensitivity of B to λ is a factor ~ 10 less than that of a and A. Thus, the neutron β-asymmetry A yields the most precise result for λ.

A second observable is the neutron lifetime, τ_n, which can be written in terms of the above parameters as [281, 286, 287]

$$\frac{1}{\tau_n} = \frac{G_F^2 m_e^5}{2\pi^3} |V_{ud}|^2 (1+3\lambda^2) f (1 + \mathrm{RC}). \qquad (120)$$

Here, $f = 1.6887 \pm 0.00015$ is a phase space factor, which includes the Fermi function contribution [283], and $(1 + \mathrm{RC}) = 1.03886 \pm 0.00039$ denotes the total effect of all electroweak radiative corrections [281, 286]. After insertion of the numerical factors in Eq. (120), a value for V_{ud} can be determined from τ_n and λ according to [281, 286]

$$|V_{ud}|^2 = \frac{4908.7 \pm 1.9 \text{ s}}{\tau_n (1+3\lambda^2)}. \qquad (121)$$

The current status of a neutron-sector result for V_{ud} is summarized in Fig. 17, where $|\lambda|$ is plotted on the horizontal axis, and V_{ud} on the vertical axis. At present, the Particle Data Group [285] averages the four most recent measurements of the neutron β-asymmetry, A, performed with beams of polarized cold neutrons [288–291], and one combined measurement of A and B [292], to obtain their recommended value of $\lambda = -1.2695 \pm 0.0029$ (shown as the vertical error band). It should be noted that the error on the PDG average for λ (0.23%) is greater than that of the most precise individual result (0.15%) [291], because the error on the average has been increased by a $\sqrt{\chi^2/(N-1)}$ scale factor of 2.0 to account for the spread among the individual data points. Constraints between the values for V_{ud} and λ, computed according to Eq. (121) for two different values for the neutron lifetime, are shown as the angled error bands. The band labeled "PDG 2008"

represents the PDG's recommended value for $\tau_n = 885.7 \pm 0.8$ s, whereas the other band relies solely on the most recent result reported for τ_n of $878.5 \pm 0.7 \pm 0.3$ s [293], which disagrees by 6σ with the PDG average. Note that the PDG deliberately chose not to include this discrepant result in their most recent averaging procedure.

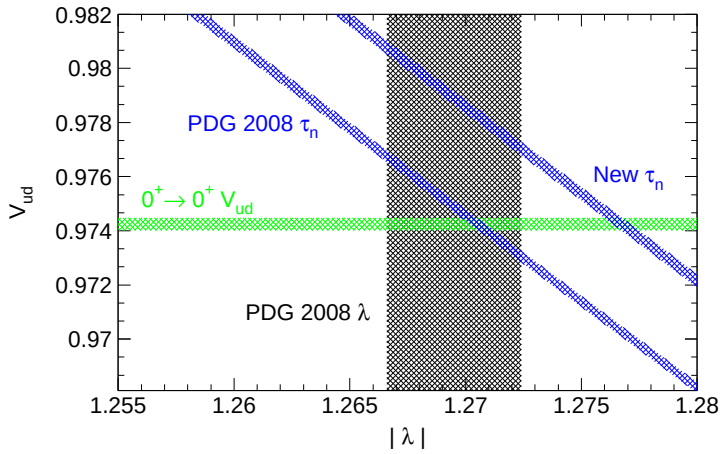

Fig. 17. Current status of V_{ud} from neutron β-decay. The vertical error band indicates the current PDG error on λ. The angled error bands show the constraints between V_{ud} and λ for two values of the neutron lifetime: the PDG recommended value, and that from a recent 6σ-discrepant result. For comparison, the horizontal error band denotes the value of V_{ud} from 0^+ nuclear β-decays discussed in the previous section.

The intersection of the error band for λ with the error band defined by the neutron lifetime determines the value for V_{ud}. Assuming the PDG value of $\tau_n = 885.7 \pm 0.8$ s yields [285]

$$V_{ud} = 0.9746 \pm 0.0004_{\tau_n} \pm 0.0018_{\lambda} \pm 0.0002_{\rm RC}, \tag{122}$$

where the subscripts denote the error sources. If the discrepant neutron lifetime result of $878.5 \pm 0.7 \pm 0.3$ s were employed instead, it would suggest a considerably larger value, $V_{ud} = 0.9786 \pm 0.0004_{\tau_n} \pm 0.0018_{\lambda} \pm 0.0002_{\rm RC}$. For comparison, the value for V_{ud} from nuclear β-decay discussed in the previous section is shown as the horizontal band. The neutron β-decay result derived from the PDG's recommended values for τ_n and λ is seen to be in excellent agreement with that from nuclear β-decay, albeit with an error bar that is a factor $\sim$ 7–8 larger.

An ongoing series of precision measurements of neutron β-decay observables aims to reduce the error on λ and resolve the lifetime discrepancy. The goal of two currently running experiments, the PERKEO III experiment at the Institut Laue-Langevin [287] (using a beam of cold neutrons) and the UCNA experiment at Los Alamos National Laboratory [294] (using stored ultracold neutrons), are sub-0.5% measurements of the neutron β-asymmetry, A. Since these two experiments employ different experimental approaches, they are sensitive to different systematic uncertainties. The combination of their results will reduce the λ-induced uncertainty for V_{ud} by up to a factor of ~ 3.

Finally, although the error on τ_n is not the dominant uncertainty, the 6σ discrepancy between the PDG average and the most recent result is clearly unsatisfactory. Indeed, multiple groups are now attempting to measure τ_n to a level of precision ranging between

1 s and 0.1 s. Hence, the next round of experiments should reach sufficient precision to definitively discriminate between the PDG average and the recent discrepant result.

4.3. V_{ud} *from pionic beta decay*

V_{ud} can also be obtained from the pion beta decay, $\pi^+ \to \pi^0 e^+ \nu_e[\gamma]$, which is a pure vector transition between two spin-zero members of an isospin triplet and is therefore analogous to the superallowed nuclear decays. Like neutron decay, it has the advantage that there are no nuclear-structure dependent corrections to be applied. Its major disadvantage, however, is that it is a very weak branch, $\mathcal{O}(10^{-8})$, in the decay of the pion. The corresponding decay width can be decomposed as

$$\Gamma_{\pi_{e3}} = \frac{G_F^2 M_{\pi^\pm}^5}{64\pi^3} S_{\rm EW} \left| V_{ud} f_+(0) \right|^2 I_0^{\pi\pi} \ (1 + \delta_{\rm EM}) \ . \tag{123}$$

In the above equation S_{EW} represents the universal short-distance electroweak correction (Eq. 128), $f_+(0)$ is the vector form-factor at zero momentum transfer, $I_0^{\pi\pi}$ the phase space factor, and $\delta_{\rm EM}$ the long-distance electromagnetic correction. As far as the strong interaction is concerned, the Ademollo-Gatto theorem [295] requires the deviation of $f_+(0)$ from its value 1 in the isospin limit to be quadratic in the quark mass difference $m_d - m_u$. This results in a very tiny correction $f_+(0) - 1 = -7 \times 10^{-6}$ at one-loop [296] and leads to the expectation that higher order strong interaction corrections will not disturb this nice picture. The corrections in (123) are therefore dominated by electromagnetic contributions. The long-distance electromagnetic corrections can be separated into a shift to the phase space integral $\delta I^{\pi\pi}/I_0^{\pi\pi} = 1.09 \times 10^{-3}$ as well as a structure dependent term [296]

$$\begin{aligned} \frac{1}{2} \cdot \delta_{\rm EM}\big|_{\rm str.dep.} &= -4\pi\alpha \left\{ \frac{2}{3} X_1 + \frac{1}{2} X_6^{\rm phys}(\mu) + \frac{1}{32\pi^2} \left(3 + \log \frac{m_e^2}{M_{\pi^\pm}^2} + 3 \log \frac{M_{\pi^\pm}^2}{\mu^2} \right) \right\} \\ &= (5.11 \pm 0.25) \times 10^{-3} \ , \end{aligned} \tag{124}$$

where we have used the recent results of [297] for the electromagnetic coupling constants $X_{1,6}$ entering in (124) (with a fractional uncertainty of 100%) to update the numerical result of Ref. [296]. Higher order corrections are expected to be strongly suppressed by $\sim (M_\pi/4\pi f_\pi)^2$. Combining the updated theory with the branching fraction $BR(\pi^+ \to \pi^0 e^+ \nu_e[\gamma]) = (1.040 \pm 0.004({\rm stat} \pm 0.004({\rm syst})) \times 10^{-8}$ from the PIBETA experiment [298], we find:

$$V_{ud} = 0.9741(2)_{\rm th}(26)_{\rm exp}. \tag{125}$$

V_{ud} from pion beta decay is in agreement with the more precise result, Eq. (117), from nuclear decays. A tenfold improvement on the experimental measurement would be needed to make this extraction competitive with nuclear decays.

4.4. *Determination of* $|V_{us}|$ *from* $K_{\ell 2}$ *and* $K_{\ell 3}$

Here we discuss the determination of $|V_{us}|$ from the combination of leptonic pion and Kaon decay and from semileptonic Kaon decay. We start with the status of the theoretical description of leptonic pion and Kaon decays and of semileptonic Kaon decays within

the SM, and the report on the status of the experimental results, particularly for the semileptonic decay.

4.4.1. *$P_{\ell 2}$ ($P = \pi, K$) rates within the SM*

Including all known short- and long-distance electroweak corrections, and parameterizing the hadronic effects in terms of a few dimensionless coefficients, the inclusive $P \to \ell\bar{\nu}_\ell(\gamma)$ decay rate can be written as [299, 300]

$$\Gamma_{P_{\ell 2(\gamma)}} = \Gamma^{(0)}_{P_{\ell 2}} S_{\rm EW} \left\{1 + \frac{\alpha}{\pi} F(m_\ell^2/M_P^2)\right\} \left\{1 - \frac{\alpha}{\pi}\left[\frac{3}{2}\log\frac{M_\rho}{M_P} + c_1^{(P)} + \frac{m_\ell^2}{M_\rho^2}\left(c_2^{(P)}\,\log\frac{M_\rho^2}{m_\ell^2} + c_3^{(P)} + c_4^{(P)}(m_\ell/M_P)\right) - \frac{M_P^2}{M_\rho^2}\,\tilde{c}_2^{(P)}\,\log\frac{M_\rho^2}{m_\ell^2}\right]\right\}, \tag{126}$$

where the decay rate in the absence of radiative corrections is given by

$$\Gamma^{(0)}_{P_{\ell 2}} = \frac{G_F^2 |V_P|^2 f_P^2}{4\pi}\, M_P\, m_\ell^2 \left(1 - \frac{m_\ell^2}{M_P^2}\right)^2, \qquad V_\pi = V_{ud}, \quad V_K = V_{us}\ . \tag{127}$$

The factor $S_{\rm EW}$ describes the short-distance electromagnetic correction [301, 302] which is universal for all semileptonic processes. To leading order it is given by

$$S_{\rm EW} = 1 + \frac{2\alpha}{\pi}\log\frac{M_Z}{M_\rho}\ . \tag{128}$$

Including also the leading QCD corrections [299], it assumes the numerical value $S_{\rm EW} = 1.0232$. The first term in curly brackets is the universal long-distance correction for a point-like meson. The explicit form of the one-loop function $F(x)$ can be found in [299]. The structure dependent coefficients $c_1^{(P)}$ are independent of the lepton mass m_ℓ and start at order e^2p^2 in chiral perturbation theory. The other coefficients appear only at higher orders in the chiral expansion. The one-loop result (order e^2p^2) for $c_1^{(P)}$ is given by [134],

$$c_1^{(\pi)} = -4\pi^2 E^r(M_\rho) - \frac{1}{2} + \frac{Z}{4}\left(3 + 2\log\frac{M_\pi^2}{M_\rho^2} + \log\frac{M_K^2}{M_\rho^2}\right), \tag{129}$$

$$c_1^{(K)} = -4\pi^2 E^r(M_\rho) - \frac{1}{2} + \frac{Z}{4}\left(3 + 2\log\frac{M_K^2}{M_\rho^2} + \log\frac{M_\pi^2}{M_\rho^2}\right), \tag{130}$$

where the electromagnetic low-energy coupling Z arising at order e^2p^0 can be expressed through the pion mass difference by the relation

$$M_{\pi^\pm}^2 - M_{\pi^0}^2 = 8\pi\alpha Z f_\pi^2 + \dots\ . \tag{131}$$

The quantity $E^r(M_\rho)$, being a certain linear combination of e^2p^2 low-energy couplings [134], cancels in the ratio $\Gamma_{K_{\ell 2(\gamma)}}/\Gamma_{\pi_{\ell 2(\gamma)}}$. As suggested by Marciano [303], a determination of $|V_{us}/V_{ud}|$ can be obtained by combining the experimental values for the decay rates with the lattice determination of f_K/f_π via

$$\frac{|V_{us}|f_K}{|V_{ud}|f_\pi} = 0.23872(30)\left(\frac{\Gamma_{K_{\ell 2(\gamma)}}}{\Gamma_{\pi_{\ell 2(\gamma)}}}\right)^{1/2} . \tag{132}$$

The small error is an estimate of unknown electromagnetic contributions arising at order e^2p^4.

In the standard model, the ratios $R^{(P)}_{e/\mu} = \Gamma_{P\to e\bar\nu_e(\gamma)}/\Gamma_{P\to\mu\bar\nu_\mu(\gamma)}$ are helicity suppressed as a consequence of the $V-A$ structure of the charged currents, constituting sensitive probes of new physics. In a first systematic calculation to order e^2p^4, the radiative corrections to $R^{(P)}_{e/\mu}$ have been obtained with an unprecedented theoretical accuracy [300, 304]. The two-loop effective theory results were complemented with a matching calculation of an associated counterterm, giving

$$R^{(\pi)}_{e/\mu} = (1.2352 \pm 0.0001)\times 10^{-4} , \qquad R^{(K)}_{e/\mu} = (2.477 \pm 0.001)\times 10^{-5} . \tag{133}$$

The central value of $R^{(\pi)}_{e/\mu}$ agrees with the results of a previous calculations [299, 305], pushing the theoretical uncertainty below the 0.1 per mille level. The discrepancy with a previous determination of $R^{(K)}_{e/\mu}$ can be traced back to inconsistencies in the analysis of [305].

4.4.2. *$K_{\ell 3}$ rates within the SM*

The photon-inclusive $K_{\ell 3}$ decay rates are conveniently decomposed as [285]

$$\Gamma_{K_{\ell 3(\gamma)}} = \frac{G_F^2 M_K^5}{192\pi^3} C_K^2 S_{\rm EW} \left|V_{us} f_+^{K^0\pi^-}(0)\right|^2 I_K^\ell(\lambda_{+,0}) \left(1 + \delta^{K\ell}_{\rm EM} + \delta^{K\pi}_{\rm SU(2)}\right) , \tag{134}$$

where $C_K^2 = 1$ (1/2) for the neutral (charged) Kaon decays, S_{EW} is the short distance electroweak correction, $f_+^{K^0\pi^-}(0)$ is the $K\to\pi$ vector form factor at zero momentum transfer, and $I_K^\ell(\lambda_{+,0})$ is the phase space integral which depends on the (experimentally accessible) slopes of the form factors (generically denoted by $\lambda_{+,0}$). Finally, $\delta^{K\ell}_{\rm EM}$ represent channel-dependent long distance radiative corrections and $\delta^{K\pi}_{\rm SU(2)}$ is a correction induced by strong isospin breaking.

Electromagnetic effects in $K_{\ell 3}$ decays

The results of the most recent calculation [306] of the four channel-dependent long-distance electromagnetic corrections $\delta^{K\ell}_{\rm EM}$ are shown in Tab. 10. The values given here were obtained to leading nontrivial order in chiral effective theory, working with a fully inclusive prescription of real photon emission. For the electromagnetic low-energy couplings appearing in the structure dependent contributions, the recent determinations of [297, 307] were employed. The errors in Tab. 10 are estimates of (only partially known) higher order contributions. The associated correlation matrix was found [306]

$$\begin{pmatrix} 1.0 & 0.081 & 0.685 & -0.147 \\ & 1.0 & -0.147 & 0.764 \\ & & 1.0 & 0.081 \\ & & & 1.0 \end{pmatrix} . \tag{135}$$

Table 10
Summary of the electromagnetic corrections to the fully-inclusive $K_{\ell 3(\gamma)}$ rate [306].

	$\delta_{\rm EM}^{K\ell}(\%)$
K^0_{e3}	0.99 ± 0.22
$K^\pm_{e3}$	0.10 ± 0.25
$K^0_{\mu 3}$	1.40 ± 0.22
$K^\pm_{\mu 3}$	0.016 ± 0.25

It is also useful to record the uncertainties on the linear combinations of $\delta_{\rm EM}^{K\ell}$ that are relevant for lepton universality and strong isospin-breaking tests [306]:

$$\delta_{\rm EM}^{K^0 e} - \delta_{\rm EM}^{K^0 \mu} = (-0.41 \pm 0.17)\% \tag{136}$$

$$\delta_{\rm EM}^{K^\pm e} - \delta_{\rm EM}^{K^\pm \mu} = (0.08 \pm 0.17)\% \tag{137}$$

$$\delta_{\rm EM}^{K^\pm e} - \delta_{\rm EM}^{K^0 e} = (-0.89 \pm 0.32)\% \tag{138}$$

$$\delta_{\rm EM}^{K^\pm \mu} - \delta_{\rm EM}^{K^0 \mu} = (-1.38 \pm 0.32)\% \ . \tag{139}$$

The corresponding electromagnetic corrections to the Dalitz plot densities can also be found in [306]. It is important to notice that the corrections to the Dalitz distributions can be locally large (up to $\sim 10\%$) with considerable cancellations in the integrated electromagnetic corrections.

Isospin breaking correction in $K_{\ell 3}$ decays

In (134), the same form factor $f_+^{K^0\pi^-}(0)$ (at zero-momentum transfer) is pulled out for all decay channels, where

$$\delta_{\rm SU(2)}^{K^0\pi^-} = 0 \ , \quad \delta_{\rm SU(2)}^{K^\pm\pi^0} = \left(\frac{f_+^{K^\pm\pi^0}(0)}{f_+^{K^0\pi^-}(0)} \right)^2 - 1 \ . \tag{140}$$

Note that the form factors denote the pure QCD quantities plus the electromagnetic contributions to the meson masses and to π^0-η mixing. The isospin breaking parameter $\delta_{\rm SU(2)}^{K^\pm\pi^0}$ is related to the π^0-η mixing angle via [308]

$$\delta_{\rm SU(2)}^{K^\pm\pi^0} = 2\sqrt{3}\Big(\varepsilon^{(2)} + \varepsilon_{\rm S}^{(4)} + \varepsilon_{\rm EM}^{(4)} + \dots\Big) \tag{141}$$

The dominant lowest-order contribution can be expressed in terms of quark masses [309]:

$$\varepsilon^{(2)} = \frac{\sqrt{3}}{4} \frac{m_d - m_u}{m_s - \widehat{m}} \ , \qquad \widehat{m} = \frac{m_u + m_d}{2} \ . \tag{142}$$

The explicit form of the strong and electromagnetic higher-order corrections in Eq. (141) can be found in [308]. The required determination of the quark mass ratio

$$R = \frac{m_s - \widehat{m}}{m_d - m_u} \tag{143}$$

uses the fact that the double ratio

$$Q^2 = \frac{m_s^2 - \widehat{m}^2}{m_d^2 - m_u^2} = R\,\frac{m_s/\widehat{m} + 1}{2} \tag{144}$$

can be expressed in terms of pseudoscalar masses and a purely electromagnetic contribution [309]:

$$Q^2 = \frac{\Delta_{K\pi} M_K^2 \big(1 + \mathcal{O}(m_q^2)\big)}{M_\pi^2 \big[\Delta_{K^0K^+} + \Delta_{\pi^+\pi^0} - (\Delta_{K^0K^+} + \Delta_{\pi^+\pi^0})_{\rm EM}\big]} \ , \quad \Delta_{PQ} = M_P^2 - M_Q^2 \ . \tag{145}$$

Due to Dashen's theorem [310], the electromagnetic term vanishes to lowest order $e^2 p^0$. At next-to-leading order it is given by [133, 311]

$$(\Delta_{K^0K^+} + \Delta_{\pi^+\pi^0})_{\rm EM} = e^2 M_K^2 \left[\frac{1}{4\pi^2} \left(3 \ln \frac{M_K^2}{\mu^2} - 4 + 2 \ln \frac{M_K^2}{\mu^2} \right) + \frac{4}{3} (K_5 + K_6)^r(\mu) \right.$$
$$\left. - 8 (K_{10} + K_{11})^r(\mu) + 16 Z L_5^r(\mu) \right] + \mathcal{O}(e^2 M_\pi^2) \ . \tag{146}$$

Based on their estimates for the electromagnetic low-energy couplings entering in (146), Ananthanarayan and Moussallam [307] found a rather large deviation from Dashen's limit, $(\Delta_{K^0K^+} + \Delta_{\pi^+\pi^0})_{\rm EM} = -1.5\, \Delta_{\pi^+\pi^0}$, which corresponds to [312] $Q = 20.7 \pm 1.2$ (the error accounts for the uncertainty due to higher order corrections). Such a small value for Q (compared to $Q_{\rm Dashen} = 24.2$) is also supported [313–315] by previous studies [11] . Together with [312] $m_s/\widehat{m} = 24.7 \pm 1.1$ (see also [317]) one finds $R = 33.5 \pm 4.3$ and finally, together with a determination of $\varepsilon_{\rm S}^{(4)}$ and $\varepsilon_{\rm EM}^{(4)}$, the result [312]

$$\delta_{\rm SU(2)}^{K^\pm \pi^0} = 0.058(8) \ . \tag{147}$$

4.4.3. *$K_{\ell 3}$ form factors*

The hadronic $K \to \pi$ matrix element of the vector current is described by two form factors (FFs), $f_+(t)$ and $f_-(t)$

$$\langle \pi^-(p_\pi) | \bar{s} \gamma^\mu u | K^0(p_K) \rangle = (p_K + p_\pi)^\mu f_+(t) + (p_K - p_\pi)^\mu f_-(t) \tag{148}$$

where $t = (p_K - p_\pi)^2 = (p_\ell + p_\nu)^2$. The vector form factor $f_+(t)$ represents the P-wave projection of the crossed channel matrix element $\langle 0 | \bar{s} \gamma^\mu u | K\pi \rangle$ whereas the S-wave projection is described by the scalar form factor defined as

$$f_0(t) = f_+(t) + \frac{t}{m_K^2 - m_\pi^2} f_-(t) \ . \tag{149}$$

By construction, $f_0(0) = f_+(0)$.

In order to compute the phase space integrals appearing in Eq. (134) we need experimental or theoretical inputs about the t-dependence of $f_{+,0}(t)$. In principle, chiral perturbation theory (ChPT) and lattice QCD are useful tools to set theoretical constraints. However, in practice the t-dependence of the FFs at present is better determined by measurements and by combining measurements and dispersion relations. To that aim, we introduce the normalized FFs

$$\tilde{f}_+(t) = \frac{f_+(t)}{f_+(0)} \ , \ \tilde{f}_0(t) = \frac{f_0(t)}{f_0(0)} \ , \ \tilde{f}_+(0) = \tilde{f}_0(0) = 1 \ . \tag{150}$$

[11] Note however that a recent analysis of $\eta \to 3\pi$ at the two-loop level [316] favors the value $Q = 23.2$.

Whereas $\tilde{f}_+(t)$ is accessible in the K_{e3} and $K_{\mu 3}$ decays, $\tilde{f}_0(t)$ is more difficult to measure since it is only accessible in $K_{\mu 3}$ decays, being kinematically suppressed in K_{e3} decays, and is strongly correlated with $\tilde{f}_+(t)$.

Moreover, measuring the scalar form factor is of special interest due to the existence of the Callan-Treiman (CT) theorem [318] which predicts the value of the scalar form factor at the so-called CT point, namely $t \equiv \Delta_{K\pi} = m_K^2 - m_\pi^2$,

$$C \equiv \tilde{f}_0(\Delta_{K\pi}) = \frac{f_K}{f_\pi}\frac{1}{f_+(0)} + \Delta_{CT}, \tag{151}$$

where $\Delta_{CT} \sim \mathcal{O}(m_{u,d}/4\pi F_\pi)$ is a small correction. ChPT at NLO in the isospin limit [309] gives

$$\Delta_{CT} = (-3.5 \pm 8) \times 10^{-3}\ , \tag{152}$$

where the error is a conservative estimate of the higher order corrections [319]. A complete two-loop calculation of Δ_{CT} [320], as well as a computation at $\mathcal{O}(p^4, e^2p^2, (m_d - m_u))$ [312], consistent with this estimate, have been recently presented.

The measurement of C provide a powerful consistency check of the lattice QCD calculations of f_K/f_π and $f_+(0)$, as will be discussed in Sec. 4.6.2.

Another motivation to measure the shape of the scalar form factor very accurately is that knowing the slope and the curvature of the scalar form factor allows one to perform a matching with the 2-loop ChPT calculations [321] and then determine fundamental constants of QCD such as $f_+(0)$ or the low-energy constants (LECs) C_{12}, C_{34} which appear in many ChPT calculations.

Parametrization of the form factors and dispersive approach

To determine the FF shapes, different experimental analyses of $K_{\ell 3}$ data have been performed in the last few years, by KTeV, NA48, and KLOE for the neutral mode and by ISTRA+ for the charged mode.

Among the different parameterizations available, one can distinguish two classes [322]. The class called class II in this reference contains parameterizations based on mathematical rigorous expansions where the slope, the curvature and all the higher order terms of the expansion are free parameters of the fit. In this class, one finds the Taylor expansion

$$\tilde{f}_{+,0}^{Tayl}(t) = 1 + \lambda'_{+,0}\frac{t}{M_\pi^2} + \frac{1}{2}\lambda''_{+,0}\left(\frac{t}{m_\pi^2}\right)^2 + \frac{1}{6}\lambda'''_{+,0}\left(\frac{t}{m_\pi^2}\right)^3 + \dots\ , \tag{153}$$

where $\lambda'_{+,0}$ and $\lambda''_{+,0}$ are the slope and the curvature of the FFs respectively, but also the so-called z-parametrization [323].

As for parameterizations belonging to class I, they correspond to parameterizations for which by using physical inputs, specific relations between the slope, the curvature and all the higher order terms of the Taylor expansion, Eq. (153) are imposed. This allows to reduce the correlations between the fit parameters since only one parameter is fitted for each FF. In this class, one finds the pole parametrization

$$\tilde{f}_{+,0}^{Pole}(t) = \frac{M_{V,S}^2}{M_{V,S}^2 - t}\ , \tag{154}$$

in which dominance of a single resonance is assumed and its mass $M_{V,S}$ is the fit parameter. Whereas for the vector FF a pole parametrization with the dominance of the

$K^*(892)$ ($M_V \sim 892$ MeV) is in good agreement with the data, for the scalar FF there is no such obvious dominance. One has thus to rely, at least for $\tilde{f}_0(t)$, on a dispersive parametrization. In such a construction, in addition to guarantee the good properties of analyticity and unitarity of the FFs, physical inputs such as the low energy $K\pi$ data and, in the case of the vector form factor, the dominance of K*(892) resonance are used.

The vector and scalar form factors are analytic functions in the complex t-plane, except for a cut along the positive real axis, starting at the first physical threshold where they develop discontinuities. They are real for $t < t_{\rm th} = (m_K + m_\pi)^2$. Cauchy's theorem implies that $\tilde{f}_{+,0}(t)$ can be written as a dispersive integral along the physical cut

$$\tilde{f}_{+,0}(t) \;=\; \frac{1}{\pi}\int_{t_{\rm th}}^{\infty} ds' \,\frac{{\rm Im}\tilde{f}_{+,0}(s')}{(s'-t-i0)} + \text{subtractions}\,, \tag{155}$$

where all the possible on-shell states contribute to its imaginary part ${\rm Im}\tilde{f}_{+,0}(s')$. A number of subtractions is needed to make the integral convergent.

A particularly appealing dispersive parametrization for the scalar form factor is the one proposed in Ref. [324]. Two subtractions are performed, one at $t = 0$ where by definition $\tilde{f}_0(0) = 1$, see Eq. (150), and the other one at the CT point. This leads to

$$\tilde{f}_0^{Disp}(t) = \exp\Big[\frac{t}{\Delta_{K\pi}}({\rm ln}C - G(t))\Big]\,, \tag{156}$$

with

$$G(t) = \frac{\Delta_{K\pi}(\Delta_{K\pi}-t)}{\pi}\int_{(m_K+m_\pi)^2}^{\infty}\frac{ds}{s}\frac{\phi_0(s)}{(s-\Delta_{K\pi})(s-t-i\epsilon)}\,, \tag{157}$$

assuming that the scalar FF has no zero. In this case the only free parameter to be determined from a fit to the data is C. $\phi_0(s)$ represents the phase of the form factor. According to Watson's theorem [325], this phase can be identified in the elastic region with the S-wave, $I = 1/2$ $K\pi$ scattering phase. The fact that two subtractions have been made in writing Eq. (156) allows to minimize the contributions from the unknown high-energy phase in the dispersive integral. The resulting function $G(t)$, Eq. (157), does not exceed 20% of the expected value of ln$C$ limiting the theoretical uncertainties which represent at most 10% of the value of $G(t)$ [324].

A dispersive representation for the vector FF has been built in a similar way [326]. Since there is no analog of the CT theorem, in this case, the two subtractions are performed at $t = 0$. Assuming that the vector FF has no zero, one gets

$$\tilde{f}_+^{Disp}(t) = \exp\Big[\frac{t}{m_\pi^2}\,(\Lambda_+ + H(t))\Big]\,,\; H(t) = \frac{m_\pi^2 t}{\pi}\int_{(m_K+m_\pi)^2}^{\infty}\frac{ds}{s^2}\frac{\phi_+(s)}{(s-t-i\epsilon)}\,. \tag{158}$$

with $\Lambda_+ \equiv m_\pi^2 d\tilde{f}_+(t)/dt|_{t=0}$ is the fit parameter and $\phi_+(s)$ the phase of the vector form factor. Here, in the elastic region, $\phi_+(t)$ equals the $I = 1/2$, P-wave Kπ scattering phase according to Watson's theorem [325]. Similarly to what happens for G, the two subtractions minimize the contribution coming from the unknown high energy phase resulting in a relatively small uncertainty on $H(t)$. Since the dispersive integral $H(t)$ represents at most 20% of the expected value of Λ_+, the latter can then be determined with a high precision knowing $H(t)$ much less precisely. For more details on the dispersive representations and a detailed discussion of the different sources of theoretical uncertainties entering the dispersive parametrization via the function G and H, see [324] and [326].

Using a class II parametrization for the FFs in a fit to $K_{\ell 3}$ decay distribution, only two parameters (λ'_+ and λ''_+ for a Taylor expansion, Eq. (153)) can be determined for $\tilde{f}_+(t)$ and only one parameter (λ'_0 for a Taylor expansion) for $\tilde{f}_0(t)$. Moreover these parameters are strongly correlated. It has also been shown in Ref. [324] that in order to describe the FF shapes accurately in the physical region, one has to go at least up to the second order in the Taylor expansion. Neglecting the curvature in the parametrization of $\tilde{f}_0(t)$ generates a bias in the extraction of λ'_0 which is then overestimated [324]. Hence, using a class II parametrization for $\tilde{f}_0(t)$ doesn't allow it to be extrapolated from the physical region ($m_\ell^2 < t < t_0 = (m_K - m_\pi)^2$) up to the CT point with a reliable precision. To measure the FF shapes from $K_{\ell 3}$ decays with the precision demanded in the extraction of $|V_{us}|$, it is preferable to use a parametrization in class I.

4.4.4. *Lattice determinations of $f_+(0)$ and f_K/f_π*

In this section we summarize the status of results of lattice QCD simulations for the semileptonic Kaon decay form factor $f_+(0)$ and for the ratio of Kaon and pion leptonic decay constants, f_K/f_π. For a brief introduction to lattice QCD we refer the reader to section 2.3.

Theoretical estimates of $f_+(0)$

The vector form factor at zero-momentum transfer, $f_+(0)$, is the key hadronic quantity required for the extraction of the CKM matrix element $|V_{us}|$ from semileptonic $K_{\ell 3}$ decays (cf. equation (134)). Within SU(3) ChPT one can perform a systematic expansion of $f_+(0)$ of the type

$$f_+(0) = 1 + f_2 + f_4 + ... \ , \tag{159}$$

where $f_n = \mathcal{O}[M_{K,\pi}^n/(4\pi f_\pi)^n]$ and the first term is equal to unity due to the vector current conservation in the SU(3) limit. Because of the Ademollo-Gatto (AG) theorem [295], the first non-trivial term f_2 does not receive contributions from the local operators of the effective theory and can be computed unambiguously in terms of the Kaon and pion masses (M_K and M_π) and the pion decay constant f_π. It takes the value $f_2 = -0.023$ at the physical point [327]. The task is thus reduced to the problem of finding a prediction for the quantity Δf, defined as

$$\Delta f \equiv f_4 + f_6 + ... = f_+(0) - (1 + f_2) \ , \tag{160}$$

which depends on the low-energy constants (LECs) of the effective theory and cannot be deduced from other processes.

The original estimate made by Leutwyler and Roos [327] was based on the quark model yielding $\Delta f = -0.016(8)$. More recently other analytical approaches have tried to determine the next-to-next-to-leading order (NNLO) term f_4 by writing it as

$$f_4 = L_4(\mu) + f_4^{loc}(\mu) \ , \tag{161}$$

where μ is the renormalization scale, $L_4(\mu)$ is the loop contribution computed in Ref. [328] and $f_4^{loc}(\mu)$ is the $\mathcal{O}(p^6)$ local contribution. For the latter various models have been adopted, namely the quark model in Ref. [328], the dispersion relations in Ref. [329] and the $1/N_c$ expansion in Ref. [330], obtaining $\Delta f = 0.001(10), \ -0.003(11), \ 0.007(12)$, respectively. These values are compatible with zero within the uncertainties and are

significantly larger than the LR estimate, leading to smaller SU(3)-breaking effects on $f_+(0)$.

Notice that in principle the next-to-next-to-leading order (NNLO) term f_4 may be obtained from the slope and the curvature of the scalar form factor $f_0(q^2)$, but present data from $K \to \pi\mu\bar{\nu}_\mu$ decays are not precise enough for an accurate determination.

A precise evaluation of $f_+(0)$, or equivalently Δf, requires the use of non-perturbative methods based on the fundamental theory of the strong interaction, such us lattice QCD simulations. Such determinations started recently with the quenched simulations of Ref. [331], where it was shown that $f_+(0)$ can be determined at the physical point with a $\simeq 1\%$ accuracy. The findings of Ref. [331] triggered various unquenched calculations of $f_+(0)$, namely those of Refs. [332–334] with $N_f = 2$ with pion masses above $\simeq 500$ MeV and two very recent ones from Ref. [335] with $N_f = 2 + 1$ and Ref. [336] with $N_f = 2$. In the former the simulated pion masses start from 330 MeV, while in the latter, they start from 260 MeV. In both cases the error associated with the chiral extrapolation was significantly reduced with respect to previous works thanks to the lighter pion masses.

In Ref. [336] the chiral extrapolation was performed using both SU(3) and SU(2) ChPT for f_2 (see Ref. [337]). In the latter case the Kaon field is integrated out and the effects of the strange quark are absorbed into the LECs of the new effective theory. The results obtained using SU(2) and SU(3) ChPT are found to be consistent within the uncertainties, giving support to the applicability of chiral perturbation theory at this order. We note that since no predictions in chiral perturbation theory for Δf as a function of the quark masses exists in a closed form, the lattice data for Δf is currently extrapolated to the physical point using phenomenologically motivated ansätze.

The results for $f_+(0)$ and Δf are summarized in Tab. 11, together with some relevant details concerning the various lattice set-ups, and those of $f_+(0)$ are shown in Fig. 18. It can be seen that:

i) all lattice results suggest a negative, sizable value for Δf in agreement with the LR estimate, but at variance with the results of the analytical approaches of Refs. [328–330], and

ii) the two recent lattice calculations of Refs. [335, 336] have reached an encouraging precision of $\simeq 0.5\%$ on the determination of $f_+(0)$.

Since simulations of lattice QCD are carried out in a finite volume, the momentum transfer q^2 for the conventionally used periodic fermion boundary conditions takes values corresponding to the Fourier modes of the Kaon or pion. Using a phenomenological ansatz for the q^2-dependence of the form factor one interpolates to $q^2 = 0$ where $f_+(0)$ is extracted, thereby introducing a major systematic uncertainty. A new method based on the use of partially twisted boundary conditions (cf. section 2.3) has been developed [338] which allows this uncertainty to be entirely removed by simulating directly at the desired kinematic point $q^2 = 0$.

Although the impact of discretization effects is expected to be small [12] , we emphasize that all available lattice calculations have been carried out at a single lattice spacing.

A systematic study of the scaling behavior of $f_+(0)$, using partially twisted boundary conditions and the extension of the simulations to lighter pion masses in order to improve

[12] The analysis from ETM [336], with fixed simulated quark mass, confirms that discretization effects are small with respect to present uncertainty.

Table 11
Summary of model and lattice results for $f_+(0)$ and Δf. The lattice errors include both statistical and systematic uncertainties.

Ref.	*Model/Lattice*	$f_+(0)$	Δf	M_π (MeV)	$M_\pi L$	a (fm)	N_f
[327]	LR	0.961 (8)	−0.016 (8)				
[328]	$ChPT + LR$	0.978 (10)	+0.001 (10)				
[329]	$ChPT + disp.$	0.974 (11)	−0.003 (11)				
[330]	$ChPT + 1/N_c$	0.984 (12)	+0.007 (12)				
[331]	$SPQ_{cd}R$	0.960 (9)	−0.017 (9)	$\gtrsim 500$	$\gtrsim 5$	$\simeq 0.07$	0
[332]	$JLQCD$	0.967 (6)	−0.010 (6)	$\gtrsim 550$	$\gtrsim 5$	$\simeq 0.09$	2
[333]	RBC	0.968 (12)	−0.009 (12)	$\gtrsim 490$	$\gtrsim 6$	$\simeq 0.12$	2
[334]	$QCDSF$	0.965 (?)	−0.012 (?)	$\gtrsim 590$	$\gtrsim 6$	$\simeq 0.08$	2
[336]	$ETMC$	0.956 (8)	−0.021 (8)	$\gtrsim 260$	$\gtrsim 4$	$\simeq 0.07$	2
[335]	$RBC + UKQCD$	0.964 (5)	−0.013 (5)	$\gtrsim 330$	$\gtrsim 4$	$\simeq 0.11$	$2+1$

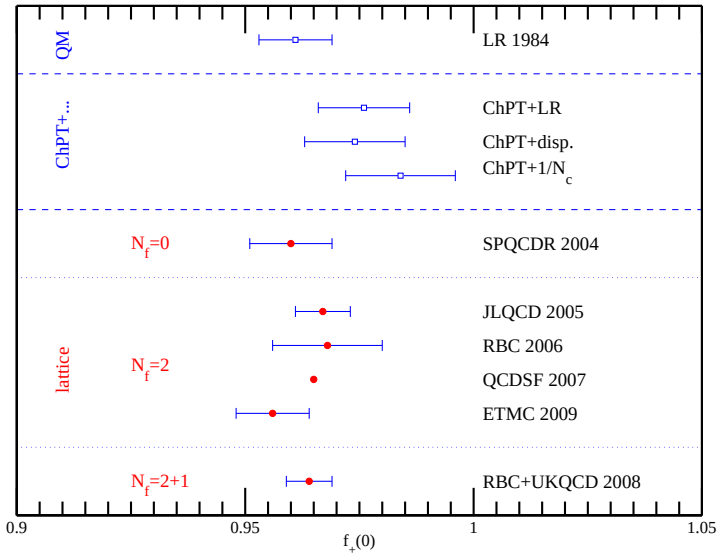

Fig. 18. Results of model (squares) and lattice (dots) calculations of $f_+(0)$.

the chiral extrapolation will be the priorities for the upcoming lattice studies of $K_{\ell 3}$ decays.

Theoretical estimates of f_K/f_π

As was pointed out in Ref. [303], an alternative to $K_{\ell 3}$ decays for obtaining a precise determination of $|V_{us}|$ is provided by the Kaon(pion) leptonic decays $K(\pi) \to \mu\bar{\nu}_\mu(\gamma)$. In this case, the key hadronic quantity is the ratio of the Kaon and pion decay constants, f_K/f_π.

In contrast to $f_+(0)$, the pseudoscalar decay constants are not protected by the AG

theorem [295] against corrections linear in the SU(3) breaking. Moreover the first non-trivial term (of order $\mathcal{O}(p^4)$) in the chiral expansion of f_K/f_π depends on the LECs and therefore it cannot be predicted unambiguously within ChPT. This is the reason why the most precise determinations of f_K/f_π come from lattice QCD simulations.

During the recent years various collaborations have provided new results for f_K/f_π using unquenched gauge configurations with both 2 and 2+1 dynamical flavors. They are summarized in Tab. 12, together with some relevant details concerning the various lattice set-ups. They are shown graphically in Fig. 19.

Table 12
Summary of lattice results for f_K/f_π. The errors include both statistical and systematic uncertainties.

Ref.	*Collaboration*	f_K/f_π	M_π (MeV)	$M_\pi L$	a (fm)	N_f
[106, 339]	*MILC*	$1.197\ ^{+\ 7}_{-13}$	$\gtrsim 240$	$\gtrsim 4$	$\to 0$	$2+1$
[340]	*HPQCD*	1.189 (7)	$\gtrsim 250$	$\gtrsim 4$	$\to 0$	$2+1$
[341]	*BMW*	1.185 (15)	$\gtrsim 190$	$\gtrsim 5$	$\to 0$	$2+1$
[342]	*Aubin et al.*	1.191(23)	$\gtrsim 240$	$\gtrsim 3.8$	$\to 0$	$2+1$
[343]	*ETMC*	1.210 (18)	$\gtrsim 260$	$\gtrsim 4$	$\to 0$	2
[344]	*NPLQCD*	$1.218\ ^{+11}_{-24}$	$\gtrsim 290$	$\gtrsim 4$	$\simeq 0.13$	$2+1$
[110]	*RBC/UKQCD*	1.205 (65)	$\gtrsim 330$	$\gtrsim 4$	$\simeq 0.11$	$2+1$
[107]	*PACS − CS*	1.189 (20)	$\gtrsim 160$	$\gtrsim 2$	$\simeq 0.09$	$2+1$

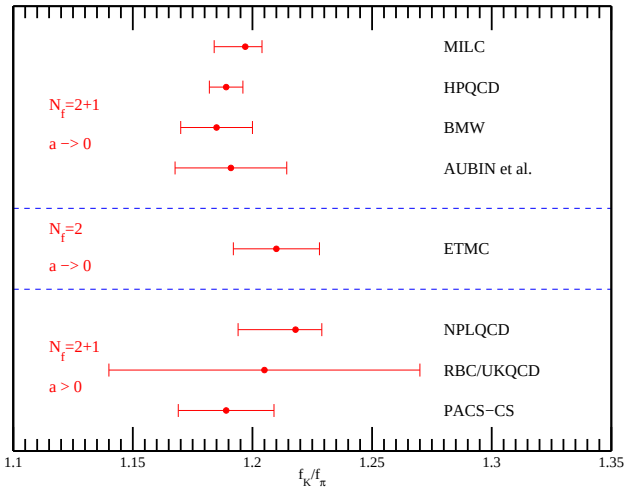

Fig. 19. Results of lattice calculations of f_K/f_π.

A few comments are in order:

i) finite size effects are kept under good control by the constraint $M_\pi L \gtrsim 4$, which is adopted by all collaborations except Ref. [107];

ii) the continuum extrapolation, which allows discretization effects to be safely removed, has been performed by several collaborations;

iii) the convergence of the SU(3) chiral expansion for f_K/f_π appears to be questionable, mainly because large NLO corrections are already required to account for the large difference between the experimental value of f_π and the value of the decay constant in the massless SU(3) limit;

iv) the convergence of the SU(2) chiral expansion is much better and thanks to the light pion masses reached in the recent lattice calculations, the uncertainty related to the chiral extrapolation to the physical point is kept to the percent level [110];

v) little is known about the details of the chiral and continuum extrapolation in Ref. [340] (HPQCD) which is currently the most precise lattice prediction for f_K/f_π; in particular about the priors on many parameters that have been introduced;

vi) It is worth repeating (cf. section 2.3) that there exist conceptional concerns about the staggered fermion formulation - the results by MILC, HPQCD, Aubin *et al.* and NPLQCD use staggered fermions and need to be confirmed by conceptually clean fermion formulations.

Summary of lattice results

We note that the Flavia Net Lattice Averaging Group (FLAG) has just started to periodically compile and publish (web and journal) lattice QCD results for SM observables and parameters. In addition, averages will be computed where feasible and a classification of the quality of lattice results by means of a simple color coding will be provided in order to facilitate understanding of lattice results for non-experts. For a first status report see [345].

Hence, no average over lattice results will be provided here. We merely identify those results that have a good control over systematic uncertainties and have been published in journals and refer the reader to the forthcoming FLAG document for averages.

For $f_+(0)$ the 2+1 flavor result by the RBC+UKQCD [335] collaboration is the most advanced calculation,

$$f_+(0) = 0.964(5) \quad N_f = 2+1\,. \tag{162}$$

while for 2 flavors it is the result by ETM [336],

$$f_+(0) = 0.956(8) \quad N_f = 2\,. \tag{163}$$

For f_K/f_π with $N_f = 2+1$ dynamical quarks, the currently most precise predictions are by MILC [106]

$$f_K/f_\pi = 1.197(^{+7}_{-13}) \quad N_f = 2+1\,, \tag{164}$$

and HPQCD [340]

$$f_K/f_\pi = 1.189(7) \quad N_f = 2+1\,, \tag{165}$$

both using the same set of staggered sea quark configurations.

For illustrative purposes the latter result will be used later in section 4.6. We also emphasize the currently most precise result with $N_f = 2$ dynamical quarks by the ETM collaboration [343]:

$$f_K/f_\pi = 1.210(18)\ (N_f = 2)\,. \tag{166}$$

At the current level of precision the comparison of the $N_f = 2$ and $N_f = 2 + 1$ result indicates a rather small contribution of the strange sea quarks to the ratio of decay constants.

4.4.5. *Data Analysis*

We perform fits to world data on the BRs and lifetimes for the K_L and $K^{\pm}$, with the constraint that BRs add to unity. This is the correct way of using the new measurements. A detailed description of the fit is given in Ref [346]. The present version of our fits uses only published measurements.

K_L leading branching ratios and τ_L

Numerous measurements of the principal K_L BRs, or of various ratios of these BRs, have been published recently. For the purposes of evaluating $|V_{us}|f_+(0)$, these data can be used in a PDG-like fit to the K_L BRs and lifetime, so all such measurements are interesting.

KTeV has measured five ratios of the six main K_L BRs [347]. The six channels involved account for more than 99.9% of the K_L width and KTeV combines the five measured ratios to extract the six BRs. We use the five measured ratios in our analysis: $\mathcal{B}(K_{\mu 3})/\mathcal{B}(K_{e3}) = 0.6640(26)$, $\mathcal{B}(\pi^+\pi^-\pi^0)/\mathcal{B}(K_{e3}) = 0.3078(18)$, $\mathcal{B}(\pi^+\pi^-)/\mathcal{B}(K_{e3}) = 0.004856(28)$, $\mathcal{B}(3\pi^0)/\mathcal{B}(K_{e3}) = 0.4782(55)$, and $\mathcal{B}(2\pi^0)/\mathcal{B}(3\pi^0) = 0.004446(25)$. The errors on these measurements are correlated; this is taken into account in our fit.

NA48 has measured the ratio of the BR for K_{e3} decays to the sum of BRs for all decays to two tracks, giving $\mathcal{B}(K_{e3})/(1 - \mathcal{B}(3\pi^0)) = 0.4978(35)$ [348].

Using $\phi \to K_L K_S$ decays in which the K_S decays to $\pi^+\pi^-$, providing normalization, KLOE has directly measured the BRs for the four main K_L decay channels [349]. The errors on the KLOE BR values are dominated by the uncertainty on the K_L lifetime τ_L; since the dependence of the geometrical efficiency on τ_L is known, KLOE can solve for τ_L by imposing $\sum_x \mathcal{B}(K_L \to x) = 1$ (using previous averages for the minor BRs), thereby greatly reducing the uncertainties on the BR values obtained. Our fit makes use of the KLOE BR values before application of this constraint: $\mathcal{B}(K_{e3}) = 0.4049(21)$, $\mathcal{B}(K_{\mu 3}) = 0.2726(16)$, $\mathcal{B}(3\pi^0) = 0.2018(24)$, and $\mathcal{B}(\pi^+\pi^-\pi^0) = 0.1276(15)$. The dependence of these values on τ_L and the correlations between the errors are taken into account. KLOE has also measured τ_L directly, by fitting the proper decay time distribution for $K_L \to 3\pi^0$ events, for which the reconstruction efficiency is high and uniform over a fiducial volume of $\sim 0.4\lambda_L$. They obtain $\tau_L = 50.92(30)$ ns [350].

There are also two recent measurements of $\mathcal{B}(\pi^+\pi^-)/\mathcal{B}(K_{\ell 3})$, in addition to the KTeV measurement of $\mathcal{B}(\pi^+\pi^-)/\mathcal{B}(K_{e3})$ discussed above. The KLOE collaboration obtains $\mathcal{B}(\pi^+\pi^-)/\mathcal{B}(K_{\mu 3}) = 7.275(68) \times 10^{-3}$ [351], while NA48 obtains $\mathcal{B}(\pi^+\pi^-)/\mathcal{B}(K_{e3}) = 4.826(27) \times 10^{-3}$ [352]. All measurements are fully inclusive of inner bremsstrahlung. The KLOE measurement is fully inclusive of the direct-emission (DE) component, DE contributes negligibly to the KTeV measurement, and a residual DE contribution of 0.19% has been subtracted from the NA48 value to obtain the number quoted above.

We fit the 13 recent measurements listed above, together with eight additional ratios of the BRs for subdominant decays. The complete list of 21 inputs is given in Table 14. As free parameters, our fit has the seven largest K_L BRs (those to K_{e3}, $K_{\mu 3}$, $3\pi^0$, $\pi^+\pi^-\pi^0$, $\pi^+\pi^-$, π^0 and $\gamma\gamma$) and the K_L lifetime, as well as two additional parameters necessary for

Table 13
Results of fit to K_L BRs and lifetime.

Parameter	Value	S
$\mathcal{B}(K_{e3})$	0.4056(9)	1.3
$\mathcal{B}(K_{\mu 3})$	0.2704(10)	1.5
$\mathcal{B}(3\pi^0)$	0.1952(9)	1.2
$\mathcal{B}(\pi^+\pi^-\pi^0)$	0.1254(6)	1.1
$\mathcal{B}(\pi^+\pi^-)$	$1.967(7) \times 10^{-3}$	1.1
$\mathcal{B}(\pi^+\pi^-\gamma)$	$4.15(9) \times 10^{-5}$	1.6
$\mathcal{B}(\pi^+\pi^-\gamma)$ DE	$2.84(8) \times 10^{-5}$	1.3
$\mathcal{B}(2\pi^0)$	$8.65(4) \times 10^{-4}$	1.4
$\mathcal{B}(\gamma\gamma)$	$5.47(4) \times 10^{-4}$	1.1
τ_L	51.16(21) ns	1.1

the treatment of the direct emission (DE) component in the radiation-inclusive $\pi^+\pi^-$ decay width. Our definition of $\mathcal{B}(\pi^+\pi^-)$ is now fully inclusive of inner bremsstrahlung (IB), but exclusive of the DE component. The fit also includes $\mathcal{B}(\pi^+\pi^-\gamma)$ and $\mathcal{B}(\pi^+\pi^-\gamma_{\rm DE})$, the branching ratios for decays to states with a photon with $E^*_\gamma > 20$ MeV, and with a photon from DE with $E^*_\gamma > 20$ MeV, respectively. Other parameterizations are possible, but this one most closely represents the input data set and conforms to recent PDG usage. With 21 input measurements, 10 free parameters, and the constraint that the sum of the BRs (except for $\mathcal{B}(\pi^+\pi^-\gamma)$, which is entirely included in the sum of $\mathcal{B}(\pi^+\pi^-)$ and $\mathcal{B}(\pi^+\pi^-\gamma_{\rm DE})$) equal unity, we have 12 degrees of freedom. The fit gives $\chi^2 = 19.8$ ($P = 7.1\%$).

The evolution of the average values of the BRs for $K_{L\ell 3}$ decays and for the important normalization channels is shown in Fig. 21.

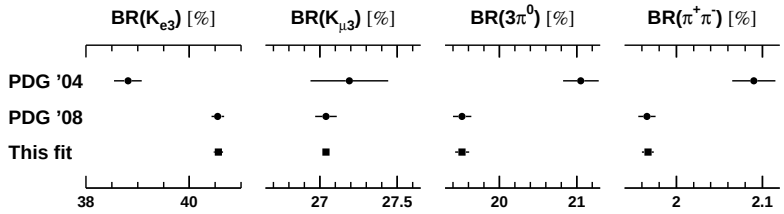

Fig. 20. Evolution of average values for main K_L BRs.

K_S leading branching ratios and τ_S

KLOE has measured the ratio $\mathrm{BR}(K_S \to \pi e\nu)/\mathrm{BR}(K_S \to \pi^+\pi^-)$ with 1.3% precision [353], making possible an independent determination of $|V_{us}|\, f_+(0)$ to better than 0.7%. In [354], KLOE combines the above measurement with their measurement $rm\mathcal{B}(K_S \to \pi^+\pi^-)/rm\mathcal{B}(K_S \to \pi^0\pi^0) = 2.2459(54)$. Using the constraint that the K_S BRs sum to

Table 14
Input data used for the fit to K_L BRs and lifetime (all the references refer to PDG08 [285]).

Parameter	Value	Source
τ_{K_L}	50.92(30) ns	Ambrosino 05C
τ_{K_L}	51.54(44) ns	Vosburgh 72
$\mathcal{B}K_{e3}$	0.4049(21)	Ambrosino 06
$\mathcal{B}K_{\mu 3}$	0.2726(16)	Ambrosino 06
$\mathcal{B}K_{\mu 3}/\mathcal{B}K_{e3}$	0.6640(26)	Alexopoulos 04
$\mathcal{B}3\pi^0$	0.2018(24)	Ambrosino 06
$\mathcal{B}3\pi^0/\mathcal{B}K_{e3}$	0.4782(55)	Alexopoulos 04
$\mathcal{B}\pi^+\pi^-\pi^0$	0.1276(15)	Ambrosino 06
$\mathcal{B}\pi^+\pi^-\pi^0/\mathcal{B}K_{e3}$	0.3078(18)	Alexopoulos 04
$\mathcal{B}\pi^+\pi^-/\mathcal{B}K_{e3}$	0.004856(29)	Alexopoulos 04
$\mathcal{B}\pi^+\pi^-/\mathcal{B}K_{e3}$	0.004826(27)	Lai 07
$\mathcal{B}\pi^+\pi^-/\mathcal{B}K_{\mu 3}$	0.007275(68)	Ambrosino 06F
$\mathcal{B}K_{e3}/\mathcal{B}2$ tracks	0.4978(35)	Lai 04B
$\mathcal{B}\pi^0\pi^0/\mathcal{B}3\pi^0$	0.004446(25)	Alexopoulos 04
$\mathcal{B}\pi^0\pi^0/\mathcal{B}\pi^+\pi^-$	0.4391(13)	PDG etafit [285]
$\mathcal{B}\gamma\gamma/\mathcal{B}3\pi^0$	0.00279(3)	Adinolfi 03
$\mathcal{B}\gamma\gamma/\mathcal{B}3\pi^0$	0.00281(2)	Lai 03
$\mathcal{B}\pi^+\pi^-/\mathcal{B}\pi^+\pi^-(\gamma)$	0.0208(3)	Alavi-Harati 01B
$\mathcal{B}\pi^+\pi^-\gamma_{DE}/\mathcal{B}\pi^+\pi^-\gamma$	0.689(21)	Abouzaid 06A
$\mathcal{B}\pi^+\pi^-\gamma_{DE}/\mathcal{B}\pi^+\pi^-\gamma$	0.683(11)	Alavi-Harati 01B
$\mathcal{B}\pi^+\pi^-\gamma_{DE}/\mathcal{B}\pi^+\pi^-\gamma$	0.685(41)	Ramberg 93

unity and assuming the universality of lepton couplings, they determine the BRs for $\pi^+\pi^-$, $\pi^0\pi^0$, K_{e3}, and $K_{\mu 3}$ decays.

Our fit is an extension of the analysis in [354]. We perform a fit to the data on the K_S BRs to $\pi^+\pi^-$, $\pi^0\pi^0$, and K_{e3} that uses, in addition to the above two measurements:
- the measurement from NA48, $\Gamma K_S \to \pi e\nu/\Gamma K_L \to \pi e\nu$ [355], where the denominator is obtained from the results of our K_L fit;
- the measurement of τ_S (not assuming CPT) from NA48 [285], 89.589(70) ps;
- the measurement of τ_S (not assuming CPT) from KTeV [285], 89.58(13) ps;
- the result $\mathrm{BR}K_{\mu 3}/\mathrm{BR}K_{e\,3} = 0.66100(214)$, obtained from the assumption of universal lepton couplings, the values of the quadratic (vector) and linear (scalar) form-factor parameters from our fit to form-factor data, and the long-distance electromagnetic corrections discussed in Sec. 4.4.2.

The free parameters are the four BRs listed above plus τ_S. With six inputs and one constraint (on the sum of the BRs), the fit has one degree of freedom and gives $\chi^2 = 0.0038$ ($P = 95\%$). The results of the fit are listed in Table 15.

Table 15
Results of fit to K_S BRs and lifetime

Parameter	Value	S
$\mathcal{B}\pi^+\pi^-$	0.6920(5)	1.0
$\mathcal{B}\pi^0\pi^0$	0.3069(5)	1.0
$\mathcal{B}K_{e3}$	$7.05(8) \times 10^{-4}$	1.0
$\mathcal{B}K_{\mu 3}$	$4.66(6) \times 10^{-4}$	1.0
τ_S	$4.66(6) \times 10^{-4}$	1.0

$K^\pm$ leading branching ratios and $\tau^\pm$

There are several new results providing information on $K^\pm_{\ell 3}$ rates. The NA48/2 collaboration has published measurements of the three ratios $\mathcal{B}(K_{e3}/\pi\pi^0)$, $\mathcal{B}(K_{\mu 3}/\pi\pi^0)$, and $\mathcal{B}(K_{\mu 3}/K_{e3})$ [356]. These measurements are not independent; in our fit, we use the values $\mathcal{B}(K_{e3}/\pi\pi^0) = 0.2470(10)$ and $\mathcal{B}(K_{\mu 3}/\pi\pi^0) = 0.1637(7)$ and take their correlation into account.

KLOE has measured the absolute BRs for the K_{e3} and $K_{\mu 3}$ decays [357]. In $\phi \to K^+K^-$ events, K^+ decays into $\mu\nu$ or $\pi\pi^0$ are used to tag a K^- beam, and vice versa. KLOE performs four separate measurements for each $K_{\ell 3}$ BR, corresponding to the different combinations of Kaon charge and tagging decay. The final averages are $\mathcal{B}(K_{e3}) = 4.965(53)(38)\%$ and $\mathcal{B}(K_{\mu 3}) = 3.233(29)(26)\%$. KLOE has also measured the absolute branching ratio for the $\pi\pi^0$ [358] and $\mu\nu$ decay [359].

Our fit takes into account the correlation between these values, as well as their dependence on the $K^\pm$ lifetime. The world average value for $\tau_\pm$ is nominally quite precise. However, the PDG error is scaled by 2.1; the confidence level for the average is 0.17%. It is important to confirm the value of $\tau_\pm$. The new measurement from KLOE, $\tau_\pm = 12.347(30)$ ns, agrees with the PDG average.

Our fit for the six largest $K^\pm$ branching ratios and lifetime uses the measurements in Table 17, including the six measurements noted above. We have recently carried out a comprehensive survey of the $K^\pm$ data set, which led to the elimination of 11 measurements currently in the 2008 PDG fit. Finally, we note that after the elimination of the 1970 measurement of $\Gamma(\pi^\pm\pi^\pm\pi^\mp)$ from Ford et al.(Ford70 in Ref. [285]), the input data set provides no strong constraint on the $\pi^\pm\pi^\pm\pi^\mp$ branching ratio, which increases the uncertainties on the resulting BR values. The fit uses 17 input measurements, seven free parameters, and one constraint, giving 11 degrees of freedom. We obtain the results in Table 16. The fit gives $\chi^2 = 25.8$ ($P = 0.69\%$). The comparatively low P-value reflects some tension between the KLOE and NA48/2 measurements of the $K_{\ell 3}$ branching ratios.

Both the significant evolution of the average values of the $K_{\ell 3}$ BRs and the effect of the correlations with $\mathcal{B}(\pi\pi^0)$ are evident in Fig. 21.

Measurement of BR(K_{e2})/BR($K_{\mu 2}$)

Experimental knowledge of $K_{e2}/K_{\mu 2}$ was poor until recently. The current world average $R_K = \mathcal{B}(K_{e2})/\mathcal{B}(K_{\mu 2}) = (2.45 \pm 0.11) \times 10^{-5}$ dates back to three experiments of the 1970s [285] and has a precision of about 5%. Two new measurements were reported recently by NA62 and KLOE (see Tab. 18). A preliminary result based on about 14,000 K_{e2} events, was presented at the 2009 winter conferences by the KLOE collaboration [360].

Table 16
Results of fit to $K^{\pm}$ BRs and lifetime.

Parameter	Value	S
$\mathcal{B}(K_{\mu 2})$	63.47(18)%	1.3
$\mathcal{B}(\pi\pi^0)$	20.61(8)%	1.1
$\mathcal{B}(\pi\pi\pi)$	5.573(16)%	1.2
$\mathcal{B}(K_{e3})$	5.078(31)%	1.3
$\mathcal{B}(K_{\mu 3})$	3.359(32)%	1.9
$\mathcal{B}(\pi\pi^0\pi^0)$	1.757(24)%	1.0
$\tau_{\pm}$	12.384(15) ns	1.2

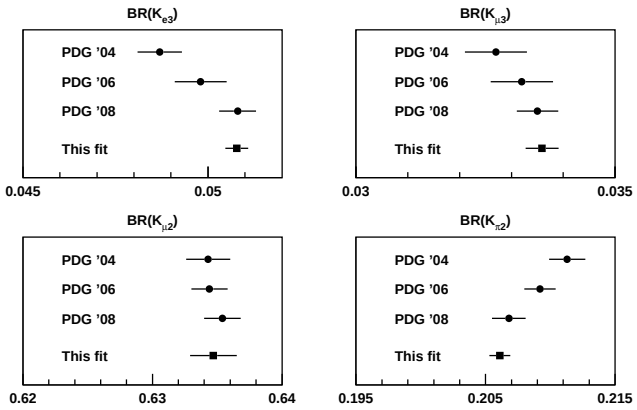

Fig. 21. Evolution of average values for main $K^{\pm}$ BRs.

Preliminary result from NA62, based on about 50,000 K_{e2} events from the 2008 data set was presented in at KAON 2009 [361]. Both the KLOE and the NA62 measurements are inclusive with respect to final state radiation contribution due to bremsstrahlung. The small contribution of $K_{l2\gamma}$ events from direct photon emission from the decay vertex was subtracted by each of the experiments. Combining these new results with the current PDG value yields a current world average of

$$R_K = (2.498 \pm 0.014) \times 10^{-5}, \tag{167}$$

in good agreement with the SM expectation [300] and, with a relative error of 0.56%, an order of magnitude more precise than the previous world average.

Measurements of $\boldsymbol{K_{\ell 3}}$ slopes

For K_{e3} decays, recent measurements of the quadratic slope parameters of the vector form factor $(\lambda'_+, \lambda''_+)$, see Eq. 153 are available from KTeV [362], KLOE [363], ISTRA+ [364], and NA48 [365].

We show the results of a fit to the K_L and K^- data in the first column of Tab. 19, and to only the K_L data in the second column. With correlations correctly taken into

Table 17
Input data used for the fit to $K^\pm$ BRs and lifetime (all the references refer to PDG08 [285]). The two 1995 values of the $K^\pm$ lifetime from Koptev et al. are averaged with $S = 1.6$ before being included in the fit as a single value.

Parameter	Value	Source
$\tau_{K^\pm}$	12.368(41) ns	Koptev 95 (*)
$\tau_{K^\pm}$	12.380(16) ns	Ott 71
$\tau_{K^\pm}$	12.443(38) ns	Fitch 65B
$\tau_{K^\pm}$	12.347(30) ns	Ambrosino 08
$\mathcal{B}K_{\mu 2}$	0.6366(17)	Ambrosino 06A
$\mathcal{B}\pi\pi^0$	0.2066(11)	[358]
$\mathcal{B}\pi\pi^0/\mathcal{B}K_{\mu 2}$	0.3329(48)	Usher 92
$\mathcal{B}\pi\pi^0/\mathcal{B}K_{\mu 2}$	0.3355(57)	Weissenberg 76
$\mathcal{B}\pi\pi^0/\mathcal{B}K_{\mu 2}$	0.3277(65)	Auerbach 67
$\mathcal{B}K_{e3}$	0.04965(53)	Ambrosino 08A
$\mathcal{B}K_{e3}/\mathcal{B}\pi\pi^0 + K_{\mu 3} + \pi 2\pi^0$	0.1962(36)	Sher 03
$\mathcal{B}K_{e3}/\mathcal{B}\pi\pi^0$	0.2470(10)	Batley 07A
$\mathcal{B}K_{\mu 3}$	0.03233(39)	Ambrosino 08A
$\mathcal{B}K_{\mu 3}/\mathcal{B}\pi\pi^0$	0.1636(7)	Batley 07A
$\mathcal{B}K_{\mu 3}/\mathcal{B}K_{e3}$	0.671(11)	Horie 01
$\mathcal{B}\pi\pi^0\pi^0$	0.01763(26)	Aloisio 04A
$\mathcal{B}\pi\pi^0\pi^0/\mathcal{B}\pi\pi\pi$	0.303(9)	Bisi 65

Table 18
Results and prediction for $R_K = \mathcal{B}(K_{e2})/\mathcal{B}(K_{\mu 2})$.

	R_K $[10^{-5}]$
PDG	2.45 ± 0.11
NA48/2	2.500 ± 0.016
KLOE	2.493 ± 0.031
SM prediction	2.477 ± 0.001

account, both fits give good values of χ^2/ndf. The significance of the quadratic term is 4.2σ from the fit to all data, and 3.5σ from the fit to K_L data only.

Including or excluding the K^- slopes has little impact on the values of λ'_+ and λ''_+; in particular, the values of the phase-space integrals change by just 0.07%. The errors on the phase-space integrals are significantly smaller when the K^- data are included in the average.

KLOE, KTeV, and NA48 also quote the values shown in Tab. 20 for M_V from pole (see Eq. 154) fits to $K_{L\,e3}$ data. The average value of M_V from all three experiments is $M_V = 875 \pm 5$ MeV with χ^2/ndf $= 1.8/2$. The three values are quite compatible with each other and reasonably close to the known value of the $K^{\pm *}(892)$ mass (891.66 ± 0.26 MeV).

Table 19
Average of quadratic fit results for K_{e3} slopes.

	K_L and K^- data	K_L data only
	4 measurements	3 measurements
	χ^2/ndf = 5.3/6 (51%)	χ^2/ndf = 4.7/4 (32%)
$\lambda'_+ \times 10^3$	25.2 ± 0.9	24.9 ± 1.1
$\lambda''_+ \times 10^3$	1.6 ± 0.4	1.6 ± 0.5
$\rho(\lambda'_+, \lambda+'')$	-0.94	-0.95
$I(K^0_{e3})$	0.15463(21)	0.15454(29)
$I(K^\pm_{e3})$	0.15900(22)	0.15890(30)

Table 20
Pole fit results for K^0_{e3} slopes.

Experiment	M_V (MeV)	$\langle M_V \rangle = 875 \pm 5$ MeV
KLOE	$870 \pm 6 \pm 7$	χ^2/ndf = 1.8/2
KTeV	881.03 ± 7.11	$\lambda'_+ \times 10^3 = 25.42(31)$
NA48	859 ± 18	$\lambda''_+ = 2 \times \lambda'^2_+$
		$I(K^0_{e3}) = 0.15470(19)$

The values for λ'_+ and λ''_+ from expansion of the pole parametrization are qualitatively in agreement with the average of the quadratic fit results. More importantly, for the evaluation of the phase-space integrals, using the average of quadratic or pole fit results gives values of $I(K^0_{e3})$ that differ by just 0.03%.

For $K_{\mu 3}$ decays, recent measurements of the slope parameters $(\lambda'_+, \lambda''_+, \lambda_0)$ are available from KTeV [362], KLOE [366], ISTRA+ [367], and NA48 [368]. We will not use the ISTRA+ result for the average because systematic errors have not been provided. We use the $K_{e3} - K_{\mu 3}$ averages provided by the experiments for KTeV and KLOE. NA48 does not provide such an average, so we calculate it for inclusion in the fit.

We have studied the statistical sensitivity of the form-factor slope measurements using Monte Carlo techniques. The conclusions of this study are a) that neglecting a quadratic term in the parametrization of the scalar form factor when fitting results leads to a shift of the value of the linear term by about 3.5 times the value of the quadratic term; and b) that because of correlations, it is impossible to measure the quadratic slope parameter from quadratic fits to the data at any plausible level of statistics. The use of the linear representation of the scalar form factor is thus inherently unsatisfactory. The effect is relevant when testing the CT theorem Eq. (151) discussed in section 4.6.2.

The results of the combination are listed in Tab. 21.

The value of χ^2/ndf for all measurements is terrible; we quote the results with scaled errors. This leads to errors on the phase-space integrals that are ∼60% larger after inclusion of the new $K_{\mu 3}$ NA48 data.

The evaluations of the phase-space integrals for all four modes are listed in each case. Correlations are fully accounted for, both in the fits and in the evaluation of the integrals. The correlation matrices for the integrals are of the form

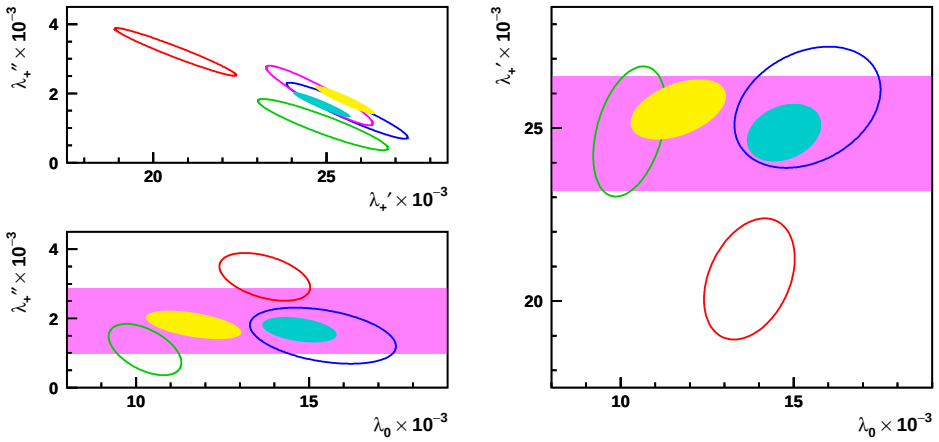

Fig. 22. 1-σ contours for λ'_+, λ''_+, λ_0 determinations from KLOE(blue ellipse), KTeV(red ellipse), NA48(green ellipse), and world average with(filled yellow ellipse) and without(filled cyan ellipse) the NA48 $K_{\mu 3}$ result.

Table 21
Averages of quadratic fit results for K_{e3} and $K_{\mu 3}$ slopes.

χ^2/ndf	$29/8$ (3×10^{-4})
$\lambda'_+ \times 10^3$	24.5 ± 0.9 $(S = 1.1)$
$\lambda''_+ \times 10^3$	1.8 ± 0.4 $(S = 1.3)$
$\lambda_0 \times 10^3$	11.7 ± 1.4 $(S = 1.9)$
$\rho(\lambda'_+, \lambda''_+)$	-0.94
$\rho(\lambda'_+, \lambda_0)$	$+0.44$
$\rho(\lambda''_+, \lambda_0)$	-0.52
$I(K^0_{e3})$	0.15449(20)
$I(K^\pm_{e3})$	0.15885(21)
$I(K^0_{\mu 3})$	0.10171(32)
$I(K^\pm_{\mu 3})$	0.10467(33)
$\rho(I_{e3}, I_{\mu 3})$	$+0.53$

$$\begin{array}{cccc} +1 & +1 & \rho & \rho \\ +1 & +1 & \rho & \rho \\ \rho & \rho & +1 & +1 \\ \rho & \rho & +1 & +1 \end{array}$$

where the order of the rows and columns is K^0_{e3}, $K^\pm_{e3}$, $K^0_{\mu 3}$, $K^\pm_{\mu 3}$, and $\rho = \rho(I_{e3}, I_{\mu 3})$ as listed in the table.

Adding the $K_{\mu 3}$ data to the fit does not cause drastic changes to the values of the

phase-space integrals for the K_{e3} modes: the values for $I(K^0_{e3})$ and $I(K^\pm_{e3})$ in Tab. 21 are qualitatively in agreement with those in Tab. 19. As in the case of the fits to the K_{e3} data only, the significance of the quadratic term in the vector form factor is strong (3.6σ from the fit to all data).

4.5. $|V_{us}|$ *determination from tau decays*

A very precise determination of V_{us} can be obtained from the semi-inclusive hadronic decay width of the τ lepton into final states with strangeness [369, 370]. The ratio of the Cabibbo-suppressed and Cabibbo-allowed τ decay widths directly measures $(V_{us}/V_{ud})^2$, up to very small SU(3)-breaking corrections which can be theoretically estimated with the needed accuracy.

The inclusive character of the total τ hadronic width renders possible an accurate calculation of the ratio [371–375]

$$R_\tau \;\equiv\; \frac{\Gamma[\tau^- \to \nu_\tau \,\text{hadrons}\,(\gamma)]}{\Gamma[\tau^- \to \nu_\tau e^- \bar{\nu}_e(\gamma)]} \;=\; R_{\tau,V} + R_{\tau,A} + R_{\tau,S}\,, \tag{168}$$

using analyticity constraints and the operator product expansion. One can separately compute the contributions associated with specific quark currents: $R_{\tau,V}$ and $R_{\tau,A}$ correspond to the Cabibbo-allowed decays through the vector and axial-vector currents, while $R_{\tau,S}$ contains the remaining Cabibbo-suppressed contributions.

To a first approximation the Cabibbo mixing can be directly obtained from experimental measurements, without any theoretical input. Neglecting the small SU(3)-breaking corrections from the $m_s - m_d$ quark-mass difference, one gets:

$$|V_{us}|^{\text{SU(3)}} = \;|V_{ud}|\,\left(\frac{R_{\tau,S}}{R_{\tau,V+A}}\right)^{1/2} \;=\; 0.210 \pm 0.003\,. \tag{169}$$

We have used $|V_{ud}| = 0.97425 \pm 0.00022$ (cf. Eq. (117)), $R_\tau = 3.640 \pm 0.010$ and the value $R_{\tau,S} = 0.1617 \pm 0.0040$ [370], which results from the recent BaBar [376] and Belle [377] measurements of Cabibbo-suppressed tau decays [378]. The new branching ratios measured by BaBar and Belle are all smaller than the previous world averages, which translates into a smaller value of $R_{\tau,S}$ and $|V_{us}|$. For comparison, the previous value $R_{\tau,S} = 0.1686 \pm 0.0047$ [379] resulted in $|V_{us}|^{\text{SU(3)}} = 0.215 \pm 0.003$.

This rather remarkable determination is only slightly shifted by the small SU(3)-breaking contributions induced by the strange quark mass. These corrections can be theoretically estimated through a QCD analysis of the difference [369, 370, 380–387]

$$\delta R_\tau \;\equiv\; \frac{R_{\tau,V+A}}{|V_{ud}|^2} - \frac{R_{\tau,S}}{|V_{us}|^2}\,. \tag{170}$$

Since the strong interactions are flavor blind, this quantity vanishes in the SU(3) limit. The only non-zero contributions are proportional to the mass-squared difference $m_s^2 - m_d^2$ or to vacuum expectation values of SU(3)-breaking operators such as $\delta O_4 \equiv \langle 0|m_s \bar{s} s - m_d \bar{d} d|0\rangle = (-1.4 \pm 0.4) \cdot 10^{-3}$ GeV^4 [369, 380]. The dimensions of these operators are compensated by corresponding powers of m_τ^2, which implies a strong suppression of δR_τ [380]:

$$\delta R_\tau \;\approx\; 24\, S_{\text{EW}} \,\left\{ \frac{m_s^2(m_\tau^2)}{m_\tau^2}\,\left(1 - \epsilon_d^2\right)\,\Delta(\alpha_s) - 2\pi^2\,\frac{\delta O_4}{m_\tau^4}\,Q(\alpha_s) \right\}\,, \tag{171}$$

where $\epsilon_d \equiv m_d/m_s = 0.053 \pm 0.002$ [317]. The perturbative QCD corrections $\Delta(\alpha_s)$ and $Q(\alpha_s)$ are known to $O(\alpha_s^3)$ and $O(\alpha_s^2)$, respectively [380, 387].

The theoretical analysis of δR_τ involves the two-point vector and axial-vector correlators, which have transverse ($J = 1$) and longitudinal ($J = 0$) components. The $J = 0$ contribution to $\Delta(\alpha_s)$ shows a rather pathological behavior, with clear signs of being a non-convergent perturbative series. Fortunately, the corresponding longitudinal contribution to δR_τ can be estimated phenomenologically with a much better accuracy, $\delta R_\tau|^L = 0.1544 \pm 0.0037$ [369, 388], because it is dominated by far by the well-known $\tau \to \nu_\tau \pi$ and $\tau \to \nu_\tau K$ contributions [389]. To estimate the remaining $L + T$ component, one needs an input value for the strange quark mass. Taking the range $m_s(m_\tau) = (100 \pm 10)$ MeV [$m_s(2\,\text{GeV}) = (96 \pm 10)$ MeV], which includes the most recent determinations of m_s from QCD sum rules and lattice QCD [388], one gets finally $\delta R_{\tau,th} = \delta R_\tau|^L + \delta R_\tau|^{L+T} = 0.216 \pm 0.016$, which implies [370]

$$|V_{us}| \,=\, \left(\frac{R_{\tau,S}}{\frac{R_{\tau,V+A}}{|V_{ud}|^2} - \delta R_{\tau,\text{th}}} \right)^{1/2} \,=\, 0.2165 \pm 0.0026_{\,\text{exp}} \pm 0.0005_{\,\text{th}}\,. \qquad (172)$$

A larger central value, $|V_{us}| = 0.2212 \pm 0.0031$, is obtained with the old world average for $R_{\tau,S}$.

Notice that the theoretical input only appears through the quantity $\delta R_{\tau,th}$, which is one order of magnitude smaller than the ratio $R_{\tau,V+A}/|V_{ud}|^2 = 3.665 \pm 0.012$. Theoretical uncertainties are thus very suppressed, although a number of issues deserve further investigation. These include (i) an assessment of the uncertainty due to different prescriptions (Contour Improved Perturbation Theory versus Fixed Order Perturbation Theory) for the slow-converging $D = 2$, L+T correlator series, which could shift $|V_{us}|$ by up to ~ 0.0020 [390]; (ii) addressing the stability of the extracted $|V_{us}|$ by using alternate sum rules that involve different weights, $w(s)$, and/or spectral integral endpoints $s_0 < m_\tau 2$ [384, 391]. With theory errors at the level of Eq. (172), experimental errors would dominate, in contrast to the situation encountered in $K_{\ell 3}$ decays.

The phenomenological determination of $\delta R_\tau|^L$ contains a hidden dependence on V_{us} through the input value of the Kaon decay constant f_K. Although the numerical impact of this dependence is negligible, it can be taken explicitly into account. Using the measured $K^-/\pi^- \to \bar{\nu}_\mu \mu^-$ decay widths and the τ lifetime [285], one can determine the Kaon and pion contributions to R_τ with better accuracy than the direct τ decay measurements, with the results $R_\tau|^{\tau^- \to \nu_\tau K^-} = (0.04014 \pm 0.00021)$ and $R_\tau|^{\tau^- \to \nu_\tau \pi^-} = (0.6123 \pm 0.0025)$. The corresponding longitudinal contributions are just given by $R_\tau|_L^{\tau^- \to \nu_\tau P^-} \equiv R_\tau|^{\tau^- \to \nu_\tau P^-} - R_\tau|_{L+T}^{\tau^- \to \nu_\tau P^-} = -2(m_P^2/m_\tau^2) R_\tau|^{\tau^- \to \nu_\tau P^-}$ $(P = K, \pi)$.

Subtracting the longitudinal contributions from Eq. (172), one gets an improved formula to determine V_{us} with the best possible accuracy [370]:

$$|V_{us}|^2 \,=\, \frac{\tilde{R}_{\tau,S}}{\frac{\tilde{R}_{\tau,V+A}}{|V_{ud}|^2} - \delta\tilde{R}_{\tau,\text{th}}} \,\equiv\, \frac{R_{\tau,S} - R_\tau|_L^{\tau^- \to \nu_\tau K^-}}{\frac{R_{\tau,V+A} - R_\tau|_L^{\tau^- \to \nu_\tau \pi^-}}{|V_{ud}|^2} - \delta\tilde{R}_{\tau,\text{th}}}\,, \qquad (173)$$

where $\delta\tilde{R}_{\tau,\text{th}} \equiv \delta\tilde{R}_\tau|^L + \delta R_{\tau,\text{th}}|^{L+T} = (0.033 \pm 0.003) + (0.062 \pm 0.015) = 0.095 \pm 0.015$. The subtracted longitudinal correction $\delta\tilde{R}_\tau|^L$ is now much smaller because it does not contain any pion or Kaon contribution. Using the same input values for $R_{\tau,S}$ and $R_{\tau,V+A}$, one recovers the V_{us} determination obtained before in Eq. (172), with an error of ± 0.0030.

Table 22
Summary of $|V_{us}| \times f_+(0)$ determination from all channels.

mode	$\|V_{us}\| \times f_+(0)$	% err	BR	τ	Δ	Int
$K_L \to \pi e\nu$	0.2165(5)	0.26	0.09	0.20	0.11	0.06
$K_L \to \pi\mu\nu$	0.2175(6)	0.32	0.15	0.18	0.15	0.16
$K_S \to \pi e\nu$	0.2157(13)	0.61	0.60	0.03	0.11	0.06
$K^\pm \to \pi e\nu$	0.2162(11)	0.52	0.31	0.09	0.41	0.06
$K^\pm \to \pi\mu\nu$	0.2168(14)	0.65	0.47	0.08	0.42	0.16
average	0.2166(5)					

Sizable changes on the experimental determination of $R_{\tau,S}$ are to be expected from the full analysis of the huge BaBar and Belle data samples. In particular, the high-multiplicity decay modes are not well known at present and their effect has been just roughly estimated or simply ignored. Thus, the result (172) could easily fluctuate in the near future. However, it is important to realize that the final error of the V_{us} determination from τ decay is likely to remain dominated by the experimental uncertainties. If $R_{\tau,S}$ is measured with a 1% precision, the resulting V_{us} uncertainty will get reduced to around 0.6%, i.e. ± 0.0013, making τ decay the competitive source of information about V_{us}.

An accurate measurement of the invariant-mass distribution of the final hadrons in Cabibbo-suppressed τ decays could make possible a simultaneous determination of V_{us} and the strange quark mass, through a correlated analysis of several SU(3)-breaking observables constructed with weighted moments of the hadronic distribution [369, 380, 381]. However, the extraction of m_s suffers from theoretical uncertainties related to the convergence of the associated perturbative QCD series. A better understanding of these QCD corrections is needed in order to improve the present determination of m_s [369, 380, 384–387].

4.6. *Physics Results*

In this section we summarize the results for $|V_{us}|$ discussed in the previous sections and based on these results we give constraints on physics beyond the SM. Instead of averages for lattice results for f_K/f_π we use $f_K/f_\pi = 1.189(7)$ by HPQCD [340] for illustrative purposes (cf. the discussion at the end of section 4.4.4).

4.6.1. *Determination of* $|V_{us}| \times f_+(0)$ *and* $|V_{us}|/|V_{ud}| \times f_K/f_\pi$

This section describes the results that are independent of the theoretical parameters $f_+(0)$ and f_K/f_π.

Determination of $|V_{us}| \times f_+(0)$

The value of $|V_{us}| \times f_+(0)$ has been determined from (134) using the world average values reported in section 4.4.5 for lifetimes, branching ratios and phase space integrals, and the radiative and $SU(2)$ breaking corrections discussed in section 4.4.2.

The results are given in Tab. 22, and are shown in Fig. 23 for $K_L \to \pi e\nu$, $K_L \to \pi\mu\nu$, $K_S \to \pi e\nu$, $K^\pm \to \pi e\nu$, $K^\pm \to \pi\mu\nu$, and for the combination. The average,

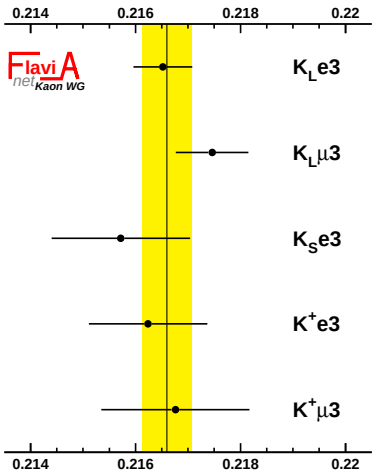

Fig. 23. Display of $|V_{us}| \times f_+(0)$ for all channels.

$$|V_{us}| \times f_+(0) = 0.2166(5), \tag{174}$$

has an uncertainty of about of 0.2%. The results from the five modes are in good agreement, the fit probability is 55%. In particular, comparing the values of $|V_{us}| \times f_+(0)$ obtained from $K^0_{\ell 3}$ and $K^\pm_{\ell 3}$ we obtain a value of the SU(2) breaking correction

$$\delta^K_{SU(2)_{exp.}} = 5.4(8)\%$$

in agreement with the CHPT calculation reported in Eq. 147: $\delta^K_{SU(2)} = 5.8(8)\%$.

4.6.2. *A test of lattice calculation: the Callan-Treiman relation*

As described in Sec. 4.4.3 the Callan-Treiman relation fixes the value of scalar form factor at $t = m_K^2 - m_\pi^2$ (the so-called Callan-Treiman point) to the ratio $(f_K/f_\pi)/f_+(0)$. The dispersive parametrization for the scalar form factor proposed in [324] and discussed in Sec. 4.4.3 allows the available measurements of the scalar form factor to be transformed into a precise information on $(f_K/f_\pi)/f_+(0)$, completely independent of the lattice estimates.

Very recently KLOE [392], KTeV [393], ISTRA+ [394], and NA48 [368] have produced results on the scalar FF behavior using the dispersive parametrization. The results are given in Tab. 23 for all four experiments.

Fig. 24 shows the values for $f_+(0)$ determined from the scalar form factor slope measurements obtained using the Callan-Treiman relation and $f_K/f_\pi = 1.189(7)$. The value of $f_+(0) = 0.964(5)$ from UKQCD/RBC is also shown. As already noted in Sec. 4.4.5, the NA48 result is difficult to accommodate. Here one can see that this results is also inconsistent with the theoretical estimates of $f_+(0)$. In particular, it violates the Fubini-Furlan bound $f_+(0) < 1$ [395]. For this reason, the NA48 result will be excluded when using the Callan-Treiman constraint.

Table 23
Experimental results for log(C).

Experiment	$\log(C)$	mode
KTeV	0.195(14)	$K_{L\mu 3}$
KLOE	0.217(16)	$K_{L\mu 3}$ and K_{Le3}
NA48	0.144(14)	$K_{L\mu 3}$
ISTRA+	0.211(13)	$K^-_{\mu 3}$

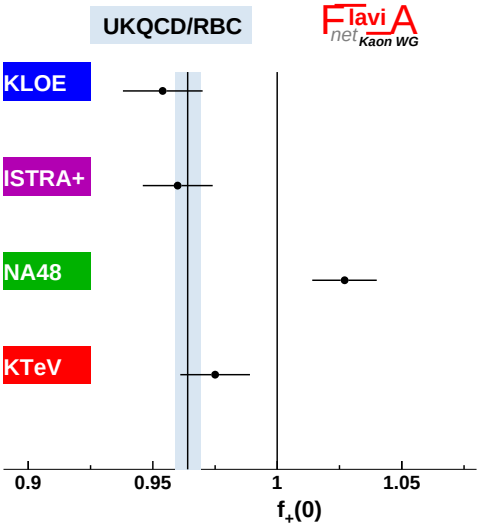

Fig. 24. Values for $f_+(0)$ determined from the scalar form factor slope using the Callan-Treiman relation and $f_K/f_\pi = 1.189(7)$. The UKQCD/RBC result $f_+(0) = 0.964(5)$ is also shown.

We combine the average of the above results, $\log C = 0.207 \pm 0.008$, with the lattice determinations of $f_K/f_\pi = 1.189(7)$ and $f_+(0) = 0.964(5)$ using the constraint given by the Callan-Treiman relation. The results of the combination are given in Tab. 24. The fit

Table 24
Results from the form factor fit.

$\log C$	$f_+(0)$	f_K/f_π
0.204(6)	0.964(4)	1.187(6)
correlation matrix		
1.	-0.44	0.52
	1.	0.28
		1.

probability is 99%, confirming the agreement between experimental measurements and lattice determinations. The accuracies of f_K/f_π and $f_+(0)$ are also slightly improved,

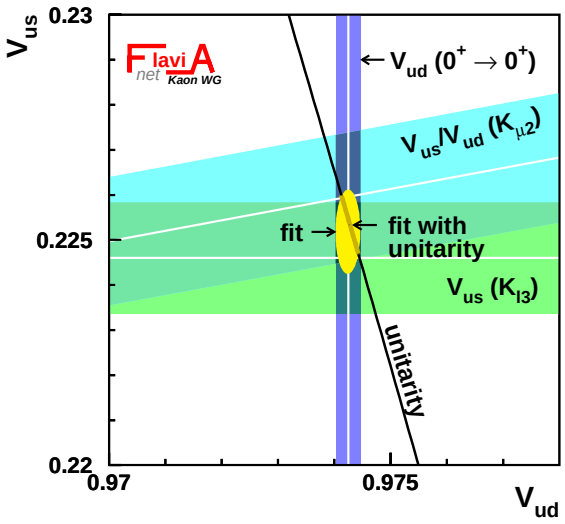

Fig. 25. Results of fits to $|V_{ud}|$, $|V_{us}|$, and $|V_{us}|/|V_{ud}|$.

and this effect can be better seen in the ratio $f_+(0)/(f_K/f_\pi)$, which is directly related to the Callan-Treiman constraint.

Determination of $|V_{us}|/|V_{ud}| \times f_K/f_\pi$

An independent determination of $|V_{us}|$ is obtained from $K_{\ell 2}$ decays. The most important mode is $K^+ \to \mu^+\nu$, which has been measured by KLOE with a relative uncertainty of about 0.3%. Hadronic uncertainties are minimized by making use of the ratio $\Gamma(K^+ \to \mu^+\nu)/\Gamma(\pi^+ \to \mu^+\nu)$.

Using the world average values of $\mathrm{BR}(K^\pm \to \mu^\pm\nu)$ and of $\tau^\pm$ given in Sec. 4.4.5 and the value of $\Gamma(\pi^\pm \to \mu^\pm\nu) = 38.408(7)\ \mu s^{-1}$ from [285] we obtain:

$$|V_{us}|/|V_{ud}| \times f_K/f_\pi = 0.2758 \pm 0.0007\ . \tag{175}$$

4.6.3. *Test of Cabibbo Universality or CKM unitarity*

To determine $|V_{us}|$ and $|V_{ud}|$ we use the value $|V_{us}| \times f_+(0) = 0.2166(5)$ reported in Tab. 22, the result $|V_{us}|/|V_{ud}| f_K/f_\pi = 0.2758(7)$ discussed in Sec. 4.6.2, $f_+(0) = 0.964(5)$, and $f_K/f_\pi = 1.189(7)$. From the above we find:

$$|V_{us}| = 0.2246 \pm 0.0012 \qquad [K_{\ell 3}\ \text{only}]\ , \tag{176}$$

$$|V_{us}|/|V_{ud}| = 0.2319 \pm 0.0015 \qquad [K_{\ell 2}\ \text{only}]\ . \tag{177}$$

A slightly less precise determination of $|V_{us}|/|V_{ud}| = 0.2304(^{+0.0026}_{-0.0015})$ is obtained using the value of f_K/f_π from MILC [106]. These determinations can be used in a fit together with the the evaluation of $|V_{ud}|$ from $0^+ \to 0^+$ nuclear beta decays quoted in section 4.1: $|V_{ud}|$=0.97425 ± 0.00022. The global fit gives

$$|V_{ud}| = 0.97425(22) \qquad |V_{us}| = 0.2252(9) \qquad [K_{\ell 3,\ell 2}\ +\ 0^+ \to 0^+]\ , \tag{178}$$

with $\chi^2/\text{ndf} = 0.52/1$ (47%). This result does not make use of CKM unitarity. If the unitarity constraint is included, the fit gives

$$|V_{us}| = \sin\theta_C = \lambda = 0.2253(6) \qquad \text{[with unitarity]} \tag{179}$$

Both results are illustrated in Fig. 25.

Using the (rather negligible) $|V_{ub}|^2 \simeq 1.5 \times 10^{-5}$ in conjunction with the above results leads to

$$|V_{ud}|^2 + |V_{us}|^2 + |V_{ub}|^2 = 0.9999(4)_{V_{ud}}(4)_{V_{us}} = 0.9999(6) \tag{180}$$

The outstanding agreement with unitarity provides an impressive confirmation of Standard Model radiative corrections [281, 286](at about the 60 sigma level!). It can be used to constrain "new physics" effects which, if present, would manifest themselves as a deviation from 1, *i.e.* what would appear to be a breakdown of unitarity.

We will give several examples of the utility Eq. (180) provides for constraining "new physics". Each case is considered in isolation, *i.e.* it is assumed that there are no accidental cancellations.

Exotic Muon Decays

If the muon can undergo decay modes beyond the Standard Model $\mu^+ \to e^+\nu_e\bar{\nu}_\mu$ and its radiative extensions, those exotic decays will contribute to the muon lifetime. That would mean that the "real" Fermi constant, G_F, is actually smaller than the value in Eq. (107) and we should be finding

$$|V_{ud}|^2 + |V_{us}|^2 + |V_{ub}|^2 = 1 - BR(\text{exotic muon decays}) \tag{181}$$

A unitarity sum below 1 could be interpreted as possible evidence for such decays. Alternatively, Eq. (180) provides at (one-sided) 95% CL

$$BR(\text{exotic muon decays}) < 0.001 \tag{182}$$

That is, of course, not competitive with, for example, the direct bound $BR(\mu^+ \to e^+\gamma) < 1 \times 10^{-11}$ [285]. However, for decays such as $\mu^+ \to e^+\bar{\nu}_e\nu_\mu$ (wrong neutrinos), Eq. (182) is about a factor of 10 better than the direct constraint [285] $BR(\mu^+ \to e^+\bar{\nu}_e\nu_\mu) < 0.012$. That constraint is useful for possible future neutrino factories where the neutrino beams originate from muon decays. If such a decay were to exist, it would provide a background to neutrino oscillations.

Another way to illustrate the above constraint is to extract the Fermi constant from nuclear, K and B decays assuming the validity of CKM unitarity without employing muon decay. Values in Eq. 178 give

$$G_F^{\text{CKM}} = 1.166279(261) \times 10^{-5}\text{GeV}^{-2} \quad \text{CKM Unitarity} \tag{183}$$

which is in fact the second best determination of G_F, after Eq. (107). The comparison between G_μ in Eq. (107) and G_F^{CKM} in Eq. (183) is providing the constraints on "new physics", if it affects them differently. So far, they are equal to within errors.

Heavy Quarks and Leptons

As a second example, consider the case of new heavy quarks or leptons that couple to the ordinary 3 generations of fermions via mixing [270]. For a generic heavy charge $-1/3$

D quark from a 4th generation, mirror fermions, $\mathrm{SU}(2)_L$ singlets etc., one finds at the one-sided 95% CL

$$|V_{uD}| \leq 0.03 \tag{184}$$

Considering that $|V_{ub}| \simeq 0.004$, such an indirect constraint appears not to be very stringent but it can be useful in some models to rule out large loop induced effects from mixing. In the case of heavy neutrinos with $m_N > m_\mu$, one finds similarly

$$|V_{\ell N}| < 0.03 \quad , \quad \ell = e, \mu \tag{185}$$

Four Fermion Operators

If there are induced dim. 6 four fermion operators of the form

$$\mp i \frac{2\pi}{\Lambda^2} \bar{u} \gamma_\mu d \bar{e}_L \gamma^\mu \nu_e \tag{186}$$

where Λ is a high effective mass scale due to compositeness, leptoquarks, excited W^* bosons (*e.g.* extra dimensions) or even heavy loop effects, they will interfere with the Standard Model beta decay amplitudes and give $G_F^{\mathrm{CKM}} = G_\mu \left(1 \pm \frac{\sqrt{2}\pi}{G_\mu \Lambda^2}\right)$. One finds at 90%CL

$$\Lambda > 30 \text{ TeV} \tag{187}$$

Similar constraints apply to new 4 fermion lepton operators that contribute to $\mu^+ \to e^+ \nu_e \bar{\nu}_\mu$. Of course, in some cases there can be a cancellation between semileptonic and purely leptonic effects and no bound results.

The high scale bounds in Eq. (187) apply most directly to compositeness because no coupling suppression was assumed. For leptoquarks, W^* bosons etc. the bounds should be about an order of magnitude smaller due to weak couplings. A m_{W^*} bound of about 4∼6 TeV results if we assume it affects leptonic and semileptonic decays very differently; but that assumption may not be valid and may need to be relaxed (see below). In the case of new loop effects, those bounds should be further reduced by another order of magnitude. For example, we next consider the effect of heavy Z' bosons in loops that enter muon and charged current semileptonic decays differently where a bound of about 400 GeV is obtained.

Additional Z' Gauge Bosons

As next example, we consider the existence of additional Z' bosons that influence unitarity at the loop level by affecting muon and semi-leptonic beta decays differently [396]. In general, we found that the unitarity sum was predicted to be greater than one in most scenarios. In fact, one expects

$$\begin{aligned} |V_{ud}|^2 + |V_{us}|^2 + |V_{ub}|^2 &= 1 + 0.01 \lambda \ell n \; X/(X-1) \\ X &= m_{Z'}^2/m_W^2 \end{aligned} \tag{188}$$

where λ is a model dependent quantity of $O(1)$. It can have either sign, but generally $\lambda > 0$.

In the case of SO(10) grand unification $Z' = Z_\chi$ with $\lambda \simeq 0.5$, one finds at one-sided 90% CL

$$m_{Z_\chi} > 400\text{GeV} \tag{189}$$

That bound is somewhat smaller than tree level bounds on Z' bosons from atomic parity violation and polarized Moller scattering [397, 398] as well as the direct collider search bounds [285] $m_{Z_\chi} > 720$ GeV.

Charged Higgs Bosons

A particularly interesting test is the comparison of the $|V_{us}|$ value extracted from the helicity-suppressed $K_{\ell 2}$ decays with respect to the value extracted from the helicity-allowed $K_{\ell 3}$ modes. To reduce theoretical uncertainties from f_K and electromagnetic corrections in $K_{\ell 2}$, we exploit the ratio $Br(K_{\ell 2})/Br(\pi_{\ell 2})$ and we study the quantity

$$R_{l23} = \left| \frac{V_{us}(K_{\ell 2})}{V_{us}(K_{\ell 3})} \times \frac{V_{ud}(0^+ \to 0^+)}{V_{ud}(\pi_{\ell 2})} \right| . \tag{190}$$

Within the SM, $R_{l23} = 1$, while deviation from 1 can be induced by non-vanishing scalar- or right-handed currents. Notice that in R_{l23} the hadronic uncertainties enter through $(f_K/f_\pi)/f_+(0)$.

Effects of scalar currents due to a charged Higgs give [346]

$$R_{l23} = \left| 1 - \frac{m_{K^+}^2}{M_{H^+}^2} \left(1 - \frac{m_d}{m_s} \right) \frac{\tan^2 \beta}{1 + \epsilon_0 \tan \beta} \right| , \tag{191}$$

whereas for right-handed currents we have

$$R_{l23} = 1 - 2 \, (\epsilon_s - \epsilon_{ns}) \ . \tag{192}$$

In the case of scalar densities (MSSM), the unitarity relation between $|V_{ud}|$ extracted from $0^+ \to 0^+$ nuclear beta decays and $|V_{us}|$ extracted from $K_{\ell 3}$ remains valid as soon as form factors are experimentally determined. This constrain together with the experimental information of $\log C^{MSSM}$ can be used in the global fit to improve the accuracy of the determination of R_{l23}, which in this scenario turns to be

$$R_{l23}|^{\text{exp}}_{\text{scalar}} = 1.004 \pm 0.007 \ . \tag{193}$$

Here $(f_K/f_\pi)/f_+(0)$ has been fixed from lattice. This ratio is the key quantity to be improved in order to reduce present uncertainty on R_{l23}.

The measurement of R_{l23} above can be used to set bounds on the charged Higgs mass and $\tan\beta$. Fig. 26 shows the excluded region at 95% CL in the M_H–$\tan\beta$ plane (setting $\epsilon_0 = 0.01$). The measurement of $\text{BR}(B \to \tau\nu)$ [145, 146, 399] can be also used to set a similar bound in the M_H–$\tan\beta$ plane. While $B \to \tau\nu$ can exclude quite an extensive region of this plane, there is an uncovered region in the exclusion corresponding to a destructive interference between the charged-Higgs and the SM amplitude. This region is fully covered by the $K \to \mu\nu$ result.

In the case of right-handed currents [324], R_{l23} can be obtained from a global fit to the values of eqs. (174) and (175). Here $\log C^{\text{exp}}$ is free of new physics effects and can be also used to constrain $(f_K/f_\pi)/f_+(0)$ together with lattice results (namely the values in Tab. 24). The result is

$$R_{l23}|^{\text{exp}}_{\text{RHcurr.}} = 1.004 \pm 0.006 \ . \tag{194}$$

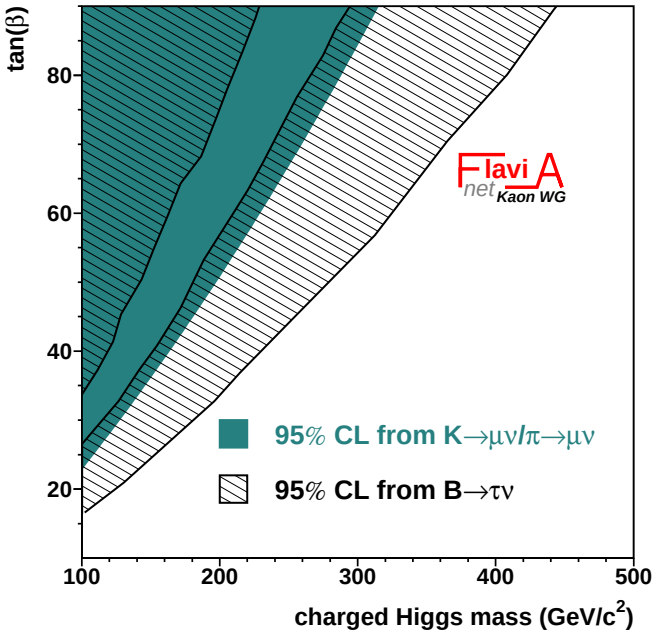

Fig. 26. Excluded region in the charged Higgs mass-tan β plane. The region excluded by $B \to \tau\nu$ is also indicated.

In addition, interesting unitarity constraints can be placed on supersymmetry [400–402] where SUSY loops affect muon and semileptonic decays differently. Again, one expects constraints up to mass scales of $O(500$ GeV), depending on the degree of cancellation between squark and slepton effects.

In the future, the unitarity constraint could improve from ± 0.0006 to ± 0.0004 if $f_+(0)$ and f_K/f_π errors as well as uncertainties from radiative corrections can be reduced. Such an improvement will be difficult, but particularly well motivated if an apparent violation starts to emerge or the LHC makes a relevant "new physics" discovery.

As an added comment, we again mention that eqs. (107) and (183) represent our two best measurements of the Fermi constant. Their agreement reinforces the validity of using G_μ to normalize electroweak charged and neutral current amplitudes in other precision searches for "new physics". In fact, either G_μ or $G_F^{\rm CKM}$ could be used without much loss of sensitivity, since all other experiments are currently less precise than both. For example, one of the next best determinations of the Fermi constant (which is insensitive to m_t) comes from [286]

$$G_F^{(2)} = \frac{\pi\alpha}{\sqrt{2} m_W^2 \sin^2\theta_W(m_Z)_{\overline{MS}}(1-\Delta r(m_Z)_{\overline{MS}})} \tag{195}$$

where

$$\alpha^{-1} = 137.035999084(51) \tag{196a}$$

$$m_W = 80.398(25)\ \text{GeV} \tag{196b}$$

$$\sin^2\theta_W(m_Z)_{\overline{MS}} = 0.23125(16) \tag{196c}$$

$$\Delta r(m_Z)_{\overline{MS}} = 0.0696(2) \tag{196d}$$

One finds

$$G_F^{(2)} = 1.165629(1100) \times 10^{-5}\ \text{GeV}^{-2} \tag{197}$$

with an uncertainty about 180 times larger than G_μ and about 4 times larger than $G_F^{\rm CKM}$. The value in Eq. (197) is, nevertheless, very useful for constraining "new physics" that affects it differently than G_μ or $G_F^{\rm CKM}$. Perhaps the two best examples are the S parameter [403, 404]

$$S \simeq \frac{1}{6\pi} N_D \tag{198}$$

which depends on the number of new heavy $\mathrm{SU}(2)_L$ doublets (e.g. $N_D = 4$ in the case of a 4th generation) and a generic W^* Kaluza-Klein excitation associated with extra dimensions [286] that has the same quark and lepton couplings. Either would contribute to G_μ or $G_F^{\rm CKM}$ but not to $G_F^{(2)}$. Therefore, one has the relation

$$G_\mu \simeq G_F^{\rm CKM} \simeq G_F^{(2)}(1 + 0.0085S + \mathcal{O}(1)\frac{m_W^2}{m_{W^*}^2}) \tag{199}$$

The good agreement among all three Fermi constants then suggests $m_{W^*} > 2 \sim 3$ TeV and $S \simeq 0.1 \pm 0.1$ (consistent with zero). Those constraints are similar to what is obtained from global fits to all electroweak data. Taken at face value they suggest any "new physics" near the TeV scale that we hope to unveil at the LHC is hiding itself quite well from us in precision low energy data. It will be interesting to see what the LHC finds.

4.6.4. *Tests of Lepton Flavor Universality in $K_{\ell 2}$ decays*

The ratio $R_K = \Gamma(K_{\mu 2})/\Gamma(K_{e2})$ can be precisely calculated within the Standard Model. Neglecting radiative corrections, it is given by

$$R_K^{(0)} = \frac{m_e^2}{m_\mu^2}\,\frac{(m_K^2 - m_e^2)^2}{(m_K^2 - m_\mu^2)^2} = 2.569 \times 10^{-5}, \tag{200}$$

and reflects the strong helicity suppression of the electron channel. Radiative corrections have been computed with effective theories [300], yielding the final SM prediction

$$\begin{aligned} R_K^{\rm SM} &= R_K^{(0)}(1 + \delta R_K^{\rm rad.corr.}) \\ &= 2.569 \times 10^{-5} \times (0.9622 \pm 0.0004) = (2.477 \pm 0.001) \times 10^{-5}\ . \end{aligned} \tag{201}$$

Because of the helicity suppression within then SM, the K_{e2} amplitude is a prominent candidate for possible sizable contributions from physics beyond the SM. Moreover, when normalizing to the $K_{\mu 2}$ rate, we obtain an extremely precise prediction of the K_{e2} width within the SM. In order to be visible in the $K_{e2}/K_{\mu 2}$ ratio, the new physics must violate lepton flavor universality.

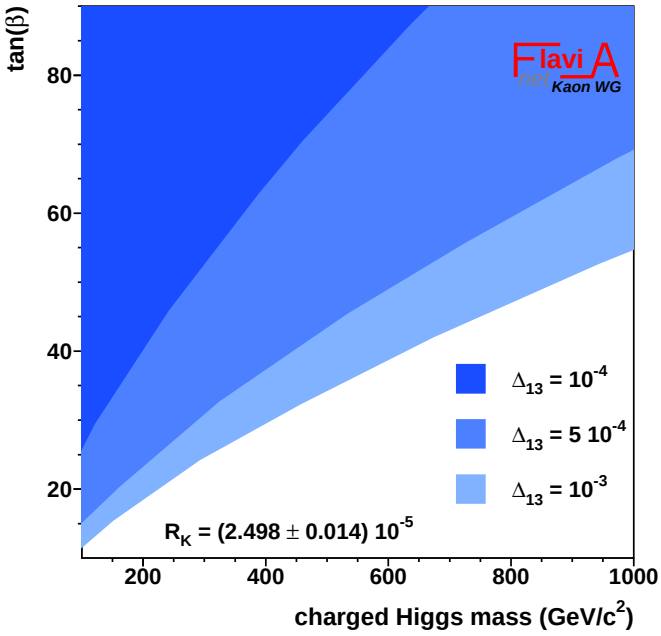

Fig. 27. Exclusion limits at 95% CL on $\tan\beta$ and the charged Higgs mass $M_{H^\pm}$ from R_K for different values of Δ_{13}.

Recently it has been pointed out that in a supersymmetric framework sizable violations of lepton universality can be expected in K_{l2} decays [405]. At the tree level, lepton flavor violating terms are forbidden in the MSSM. However, these appear at the one-loop level, where an effective $H^+ l\nu_\tau$ Yukawa interaction is generated. Following the notation of Ref. [405], the non-SM contribution to R_K can be written as

$$R_K^{\mathrm{LFV}} \approx R_K^{\mathrm{SM}} \left[1 + \left(\frac{m_K^4}{M_{H^\pm}^4}\right)\left(\frac{m_\tau^2}{m_e^2}\right)|\Delta_{13}|^2 \tan^6\beta\right] \ . \tag{202}$$

The lepton flavor violating coupling Δ_{13}, being generated at the loop level, could reach values of $\mathcal{O}(10^{-3})$. For moderately large $\tan\beta$ values, this contribution may therefore enhance R_K by up to a few percent. Since the additional term in Eq. 202 goes with the fourth power of the meson mass, no similar effect is expected in π_{l2} decays.

The world average result for R_K presented in Sec. 4.4.5 gives strong constraints for $\tan\beta$ and $M_{H^\pm}$, as shown in Fig. 27. For values of $\Delta_{13} \approx 10^{-3}$ and $\tan\beta > 50$ the charged Higgs masses is pushed above 1000 GeV/c^2 at 95% CL.

5. Semileptonic B and D decays: $|V_{cx}|$ and $|V_{ub}|$

In this section, we address semileptonic decays that proceed at the tree level of the weak interaction. We focus on decays of the lightest pseudoscalar mesons, D for charm and B for bottom, because higher excitations decay hadronically (or, in case of the B^*,

radiatively) to the D and B and thus have negligibly small semileptonic partial widths. The amplitude for quark flavor change in these processes is proportional to a CKM matrix element, providing a direct way to "measure" the CKM matrix.

Purely leptonic decays of pseudoscalars are, of course, also directly sensitive to the CKM matrix, but they require a spin flip. Their rate is, hence, helicity suppressed by a factor $(m_\ell/m_P)^2$, where m_P is the pseudoscalar meson mass and m_ℓ the mass of the daughter lepton. This suppression makes purely leptonic decays more sensitive to non-Standard processes, and therefore less reliable channels for the determination of CKM matrix elements than semileptonic decays.

As with the determination of $|V_{us}|$ in the semileptonic decay $K \to \pi\ell\nu$, discussed in Sec. 4, one can determine $|V_{cs}|$ from $D \to K\ell\nu$, $|V_{cd}|$ from $D \to \pi\ell\nu$, $|V_{ub}|$ from $B \to \pi\ell\nu$, and $|V_{cb}|$ from $B \to D^{(*)}\ell\nu$, by combining measurements of the differential decay rate with lattice-QCD calculations for the hadronic part of the transition, commonly described with form factors. This section starts with the three heavy-to-light decays, and then proceeds to heavy-to-heavy decays for which heavy-quark symmetry plays a crucial role. $|V_{cb}|$ and $|V_{ub}|$ can also be determined from *inclusive* semileptonic B decays, because the large energy scale m_b and the inclusion of all final-state hadrons makes these processes amenable to the operator-product expansion (OPE). Within the OPE the short-distance QCD can be calculated in perturbation theory, and the long-distance QCD can be measured from kinematic distributions. While this is rather straightforward for $|V_{cb}|$ it is more subtle $|V_{ub}|$ so these two topics are treated in separate subsections.

5.1. *Exclusive semileptonic B and D decays to light mesons π and K*

5.1.1. *Theoretical Background*

Heavy-to-light semileptonic decays, in which a B or D meson decays into a light pseudoscalar or vector meson (such as a pion or ρ meson), are sensitive probes of quark flavor-changing interactions. The decay rate for $H \to P\ell\nu$ semileptonic decay is given by

$$\frac{d\Gamma}{dq^2} = \frac{G_F^2|V_{qQ}|^2}{24\pi^3}\frac{(q^2-m_\ell^2)^2\sqrt{E_P^2-m_P^2}}{q^4 m_H^2}\left\{\left(1+\frac{m_\ell^2}{2q^2}\right)m_H^2(E_P^2-m_P^2)\left[f_+(q^2)\right]^2 + \frac{3m_\ell^2}{8q^2}(m_H^2-m_P^2)^2\left[f_0(q^2)\right]^2\right\}, \quad (203)$$

where $q \equiv p_H - p_P$ is the momentum transferred to the lepton pair and $|V_{qQ}|$ is the relevant CKM matrix element. The form factors, $f_+(q^2)$ and $f_0(q^2)$, parametrize the hadronic matrix element of the heavy-to-light vector current, $V^\mu \equiv i\bar{q}\gamma^\mu Q$:

$$\langle P|V^\mu|H\rangle = f_+(q^2)\left(p_H^\mu + p_P^\mu - \frac{m_H^2-m_P^2}{q^2}\,q^\mu\right) + f_0(q^2)\frac{m_H^2-m_P^2}{q^2}\,q^\mu, \quad (204)$$

where $E_P = (m_H^2+m_P^2-q^2)/2m_H$ is the energy of the light meson in the heavy meson's rest frame. The kinematics of semileptonic decay require that the form factors are equal at zero momentum-transfer, $f_+(0) = f_0(0)$. In the limit $m_\ell \to 0$, which is a good approximation for $\ell = e$, μ, the form factor $f_0(q^2)$ drops out and the expression for the decay rate simplifies to

$$\frac{d\Gamma}{dq^2} = \frac{G_F^2|V_{qQ}|^2}{192\pi^3 m_H^3}\left[(m_H^2+m_P^2-q^2)^2 - 4m_H^2m_P^2\right]^{3/2}|f_+(q^2)|^2. \quad (205)$$

Using the above expression, a precise experimental measurement of the decay rate, in combination with a controlled theoretical calculation of the form factor, allows for a clean determination of the CKM matrix element $|V_{qQ}|$.

Analyticity and unitarity

It is well-established that the general properties of analyticity and unitarity largely constrain the shapes of heavy-to-light semileptonic form factors [406–410]. All form factors are analytic in q^2 except at physical poles and threshold branch points. Because analytic functions can always be expressed as convergent power series, this allows the form factors to be written in a particularly useful manner.

Consider a change of variables that maps q^2 in the semileptonic region onto a unit circle:

$$z(q^2, t_0) = \frac{\sqrt{1 - q^2/t_+} - \sqrt{1 - t_0/t_+}}{\sqrt{1 - q^2/t_+} + \sqrt{1 - t_0/t_+}}, \tag{206}$$

where $t_+ \equiv (m_H + m_P)^2$, $t_- \equiv (m_H - m_P)^2$, and t_0 is a constant to be discussed later. In terms of this new variable, z, the form factors have a simple form:

$$P(q^2)\phi(q^2, t_0)f(q^2) = \sum_{k=0}^{\infty} a_k(t_0) z(q^2, t_0)^k. \tag{207}$$

In order to preserve the analytic structure of $f(q^2)$, the function $P(q^2)$ vanishes at poles below the H-P pair-production threshold that contribute to H-P pair-production as virtual intermediate states. For example, in the case of $B \to \pi\ell\nu$ decay, $P(q^2)$ incorporates the location of the B^* pole:

$$P_+^{B\to\pi\ell\nu}(q^2) = z(q^2, m_{B^*}). \tag{208}$$

For the case of D meson semileptonic decays, the mass of the D^* meson is above the D-π production threshold, but the D_s^* is below D-K production threshold. Hence

$$P_+^{D\to\pi\ell\nu}(q^2) = 1, \tag{209}$$

$$P_+^{D\to K\ell\nu}(q^2) = z(q^2, m_{D_s^*}). \tag{210}$$

In the expression for $f(q^2)$, Eq. (207), $\phi(q^2, t_0)$ is any analytic function. It can be chosen, however, to make the unitarity constraint on the series coefficients have a simple form. The standard choice for $\phi_+(q^2, t_0)$, which enters the expression for $f_+(q^2)$, is [410]:

$$\begin{aligned}\phi_+(q^2, t_0) = &\sqrt{\frac{3}{96\pi\chi_J^{(0)}}} \left(\sqrt{t_+ - q^2} + \sqrt{t_+ - t_0}\right) \left(\sqrt{t_+ - q^2} + \sqrt{t_+ - t_-}\right)^{3/2} \\ &\times \left(\sqrt{t_+ - q^2} + \sqrt{t_+}\right)^{-5} \frac{(t_+ - q^2)}{(t_+ - t_0)^{1/4}},\end{aligned} \tag{211}$$

where $\chi_J^{(0)}$ is a numerical factor that can be calculated using perturbation theory and the operator product expansion. A similar function can be derived for the irrelevant form factor $f_0(q^2)$.

Given the above choices for $P(q^2)$ and $\phi(q^2, t_0)$, unitarity constrains the size of the series coefficients:

$$\sum_{k=0}^{N} a_k^2 \lesssim 1, \tag{212}$$

Table 25
Physical region in terms of the variable z for various semileptonic decays given the choice $t_0 = 0.65t_-$.

$B \to \pi l\nu$	$-0.34 < z < 0.22$
$D \to \pi l\nu$	$-0.17 < z < 0.16$
$D \to Kl\nu$	$-0.04 < z < 0.06$

where this holds for any value of N. In the case of the $B \to \pi\ell\nu$ form factor, the sizes of the series coefficients (a_ks) turn out to be much less than 1 [411]. Becher and Hill recently pointed out that this is due to the fact that the b-quark mass is so large, and used heavy-quark power-counting to derive a tighter constraint on the a_ks:

$$\sum_{k=0}^{N} a_k^2 \leq \left(\frac{\Lambda}{m_Q}\right)^3, \tag{213}$$

where Λ is a typical hadronic scale [412]. The above expression suggests that the series coefficients should be larger for D-meson form factors than for B-meson form factors. This, however, has not been tested.

In order to accelerate the convergence of the power-series in z, the free parameter t_0 in Eq. (206) can be chosen to make the range of $|z|$ as small as possible. For the value $t_0 = 0.65t_-$ used in Ref. [410], the ranges of $|z|$ for some typical heavy-to-light semileptonic decays are given in Tab. 25. The tight heavy-quark constraint on the size of the coefficients in the z-expansion, in conjunction with the small value of $|z|$, ensures that only the first few terms in the series are needed to describe heavy-to-light semileptonic form factors to a high accuracy.

Other model-independent parameterizations of heavy-to-light semileptonic form factors base on analyticity and unitarity have been proposed and applied to the case of $B \to \pi\ell\nu$ decay by Bourrely, Caprini, and Lellouch [413] and by Flynn and Nieves [414, 415]. Bourrely *et al.* use the series expansion in z described above, but choose simpler outer function, $\phi(q^2, t_0) = 1$. This leads, however, to a more complicated constraint on the series coefficients, which is no longer diagonal in the series index k. Flynn and Nieves use multiply-subtracted Omnès dispersion relations to parametrize the form factor shape in terms of the elastic B-π scattering phase shift and the value of $f_+(q^2)$ at a few subtraction points below the B-π production threshold.

Lattice QCD

In lattice-QCD calculations and in heavy-quark effective theory (HQET), it is easier to work with a different linear combination of the form factors:

$$\langle P|V^\mu|H\rangle = \sqrt{2m_H}\left[v^\mu f_\parallel(E_P) + p_\perp^\mu f_\perp(E_P)\right], \tag{214}$$

where $v^\mu = p_H^\mu/m_H$ is the velocity of the heavy meson, $p_\perp^\mu = p_P^\mu - (p_P \cdot v)v^\mu$ is the component of the light meson momentum perpendicular to v, and $E_P = p_P \cdot v = (m_H^2 + m_P^2 - q^2)/(2m_H)$ is the energy of the light meson in the heavy meson's rest frame. In the heavy meson's rest frame, the form factors $f_\parallel(E_P)$ and $f_\perp(E_P)$ are directly proportional to the hadronic matrix elements of the temporal and spatial vector current:

$$f_\parallel(E_P) = \frac{\langle P|V^0|H\rangle}{\sqrt{2m_H}} \tag{215}$$

$$f_\perp(E_P) = \frac{\langle P|V^i|H\rangle}{\sqrt{2m_H}} \frac{1}{p_P^i}. \tag{216}$$

Lattice QCD simulations therefore typically determine $f_\parallel(E_P)$ and $f_\perp(E_P)$, and then calculate the form factors that appear in the heavy-to-light decay width using the following equations:

$$f_0(q^2) = \frac{\sqrt{2m_H}}{m_H^2 - m_P^2} \left[(m_H - E_P) f_\parallel(E_P) + (E_P^2 - m_P^2) f_\perp(E_P)\right], \tag{217}$$

$$f_+(q^2) = \frac{1}{\sqrt{2m_H}} \left[f_\parallel(E_P) + (m_H - E_P) f_\perp(E_P)\right]. \tag{218}$$

These expressions automatically satisfy the kinematic constraint $f_+(0) = f_0(0)$.

The goal is to evaluate the hadronic matrix elements on the right-hand side of Eqs.(215) and (216) via numerical simulations in lattice QCD. Such simulations are carried out with operators, V_μ^L, written in terms of the lattice heavy and light quark fields appearing in the lattice actions. Hence, an important step in any lattice determination of hadronic matrix elements is the matching between continuum operators such as V_μ and their lattice counterparts. The matching takes the form

$$\langle P|V_\mu|H\rangle = Z_{V_\mu}^{Qq} \langle P|V_\mu^L|H\rangle. \tag{219}$$

For heavy-light currents with dynamical (as opposed to static) heavy quarks, the matching factors $Z_{V_\mu}^{Qq}$ have been obtained to date either through a combination of perturbative and nonperturbative methods or via straight one-loop perturbation theory. Uncertainties in $Z_{V_\mu}^{Qq}$ can be a major source of systematic error in semileptonic form factor calculations and methods are being developed for complete nonperturbative determinations in order to reduce such errors in the future.

Another important feature of lattice simulations is that calculations are carried out at nonzero lattice spacings and with *up*- and *down*-quark masses m_q that are larger than in the real world. Results are obtained for several lattice spacings and for a sequence of m_q values and one must then extrapolate to both the continuum and the physical quark mass limits. These two limits are intimately connected to each other, and it is now standard to use chiral perturbation theory (χPT) that has been adapted to include discretization effects [416–421].

The initial pioneering work on B and D meson semileptonic decays on the lattice were all carried out in the quenched approximation [422–426]. This approximation which ignores effects of sea quark-antiquark pairs has now been overcome and most recent lattice calculations include vacuum polarization from $N_f = 2 + 1$ or $N_f = 2$ dynamical light quark flavors. Unquenched calculations of $B \to \pi\ell\nu$ semileptonic decays have been carried out by the Fermilab/MILC and the HPQCD collaborations using the MILC collaboration $N_f = 2 + 1$ configurations [411, 427, 428]. Both collaborations use improved staggered (AsqTad) quarks for light valence and sea quarks. They differ, however, in their treatment of the heavy b quark. Fermilab/MILC employs the heavy clover action and HPQCD the nonrelativistic NRQCD action. The dominant errors in both calculations are due to statistics and the chiral extrapolation. The next most important error stems from

discretization corrections for the Fermilab/MILC and operator matching for the HPQCD collaborations, respectively. It is important that simulations based on other light quark lattice actions be pursued in the future as a cross check.

In the case of $D \to K$ and $D \to \pi$ semileptonic decays, there exists to-date only one $N_f = 2 + 1$ calculation, again based on AsqTad light and clover heavy quarks, by the Fermilab Lattice and MILC collaborations [427]. Recently two groups have initiated $N_f = 2$ calculations, and their results are still at a preliminary stage. The ETM collaboration uses "twisted mass" light and charm quarks at maximal twist [429], whereas Bećirević, Haas and Mescia use improved Wilson quarks and configurations created by the QCDSF collaboration [430, 431]. The latter group employs double ratio methods and twisted boundary conditions to allow more flexibility in picking out many values of q^2. There has also been a recent exploratory study with improved Wilson quark action which, although still quenched, is at a very small lattice spacing of around 0.04 fm [432]. These authors have considered both B and D decays.

Light-cone QCD Sum Rules

Light-cone sum rules (LCSR) [433–435] combine the idea of the original QCD sum rules [436, 437] with the elements of the theory of hard exclusive processes. LCSR are used in a wide array of applications (for a review, see [438]), in particular, for calculating $B \to \pi, K, \eta, \rho, K^*$ and $D \to \pi, K$ form factors [439–449]. The starting point is a specially designed correlation function where the product of two currents is sandwiched between the vacuum and an on-shell state. In the case of $\bar{B}^0 \to \pi^+$ form factor

$$\begin{aligned} F_\mu(p,q) &= i \int d^4x e^{iqx} \langle \pi^+(p) \mid T\{\bar{u}\gamma_\mu b(x), m_b \bar{b} i\gamma_5 d(0)\} \mid 0\rangle \\ &= \left(\frac{2 f_B f^+_{B\pi}(q^2) m_B^2}{m_B^2 - (p+q)^2} + \sum_{B_h} \frac{2 f_{B_h} f^+_{B_h\pi}(q^2) m_{B_h}^2}{m_{B_h}^2 - (p+q)^2} \right) p_\mu + O(q_\mu)\,, \end{aligned} \tag{220}$$

where the factor proportional to p_μ is transformed into a hadronic sum by inserting a complete set of hadronic states between the currents. This sum also represents, schematically, a dispersion integral over the hadronic spectral density. The lowest-lying B-state contribution contains the desired $B \to \pi$ form factor multiplied by the B decay constant.

At spacelike $(p+q)^2 \ll m_b^2$ and at small and intermediate $q^2 \ll m_b^2$, the time ordered product in Eq. (220) may also be expanded near the light-cone $x^2 \sim 0$, thereby resumming local operators into distribution amplitudes:

$$F((p+q)^2, q^2) = \sum_{t=2,3,4} \int Du_i \sum_{k=0,1} \left(\frac{\alpha_s}{\pi}\right)^k \; T_k^{(t)}((p+q)^2, q^2, u_i, m_b, \mu) \varphi_\pi^{(t)}(u_i, \mu)\,. \tag{221}$$

This generic expression is a convolution (at the factorization scale μ) of calculable short-distance coefficient functions $T_k^{(t)}$ and universal pion light-cone distribution amplitudes (DA's) $\varphi_\pi^{(t)}(u_i, \mu)$ of twist $t \geq 2$. The integration goes over the pion momentum fractions $u_i = u_1, u_2, ...$ distributed among quarks and gluons. Importantly, the contributions to Eq. (221) corresponding to higher twist and/or higher multiplicity pion DA's are suppressed by inverse powers of the b-quark virtuality $((p+q)^2 - m_b^2)$, allowing one to retain a few low twist contributions in this expansion. Currently, analyses of Eq. (220) can include all LO contributions of twist 2,3,4 quark-antiquark and quark-antiquark-gluon DA's of the pion and the $O(\alpha_s)$ NLO corrections to the twist 2 and 3 two-particle coefficient functions.

Furthermore, one uses quark-hadron duality to approximate the sum over excited B_h states in Eq. (220) by the result from the perturbative QCD calculation introducing the effective threshold parameter s_0^B. The final step involves a Borel transformation $(p+q)^2 \to M^2$, where the scale of the Borel parameter M^2 reflects the characteristic virtuality at which the correlation function is calculated. The resulting LCSR for the $B \to \pi$ form factor has the following form

$$f_{B\pi}^+(q^2) \;=\; \frac{e^{m_B^2/M^2}}{2m_B^2 f_B}\frac{1}{\pi}\int_{m_b^2}^{s_0^B} ds\,\mathrm{Im}\,F^{(OPE)}(s,q^2)e^{-s/M^2}, \tag{222}$$

where $\mathrm{Im}F^{(OPE)}$ is directly calculated from the double expansion (221). The intrinsic uncertainty introduced by the quark-hadron duality approximation is minimized by calculating the B meson mass using the derivative of the same sum rule. The main input parameters, apart from α_s and b quark mass (taken in the $\overline{\rm MS}$ scheme), include the nonperturbative normalization constants and nonasymptotic coefficients for each given twist component, e.g., for the twist-2 pion DA φ_π these are f_π and the Gegenbauer moments a_i. For twist-3,4 the recent analysis can be found in Ref. [450]. For the B-meson decay constant entering LCSR (222) one usually employs the conventional QCD sum rule for the two-point correlator of $\bar b i\gamma_5 q$ currents with $O(\alpha_s)$ accuracy (the most complete sum rule in $\overline{\rm MS}$-scheme is presented in [451]). More details on the numerical results, sources of uncertainties and their estimates can be found in the recent update [448]. Further improvement of the LCSR calculation of heavy-to-light form factors is possible, if one gets a better understanding of the quark-hadron duality approximation in B channel, and a more accurate estimation of nonperturbative parameters of pion DA's.

Despite their intrinsically approximate nature, LCSRs represent a useful analytic method providing a unique possibility to calculate both hard and soft contributions to the transition form factors. Different versions of LCSR employing B-meson distribution amplitudes [452] as well as the framework of SCET [453, 454] have also been introduced.

5.1.2. *Measurements of D Branching Fractions and q^2 Dependence*

In the last few years, a new level of precision has been achieved in measurements of branching fractions and hadronic form factors for exclusive semileptonic D decays by the Belle, BaBar, and CLEO collaborations. In this section, we focus on semileptonic decays, $D \to P\ell\nu_\ell$, where D represents a D^0 or D^+, P a pseudoscalar meson, charged or neutral, either π or K, and ℓ a muon or electron. In addition, we also present a BaBar analysis of $D_s^+ \to K^+K^-\ell^+\nu_\ell$, which provided first evidence of an S-wave contribution.

The results from the B-Factories (Babar and Belle) are based on very large samples of D mesons produced via the process $e^+e^- \to c\bar c$ recorded at about 10.58 GeV c.m. energy. CLEO-c experiment relies on a sample of $\psi(3770) \to D\overline{D}$ events, which is smaller, but allows for very clean tags and excellent q^2 resolution. Two of the four recent analyses tag events by reconstructing a hadronic decay of one of the D mesons in the event, in addition to the semileptonic decay of the other. The total number of tagged events serves as a measure of the total sample of D mesons and thus provides the absolute normalization for the determination of the semileptonic branching fractions. Untagged analyses typically rely on the relative normalization to a sample of D decays with a well measured branching fraction. The analyses use sophisticated techniques for background suppression (Fisher discriminants) and resolution enhancement (kinematic fits). The neutrino momentum

and energy is equated with the reconstructed missing momentum and energy relying on energy-momentum conservation. The detailed implementation and resolution varies significantly among the measurements and cannot be presented here in detail.

The BaBar Collaboration reports a study of $D^0 \to K^- e^+ \nu_e$ based on a luminosity of 75 fb^{-1} [455]. They analyze $D^{*+} \to D^0 \pi^+$ decays, with $D^0 \to K^- e^+ \nu_e$. The analysis exploits the two-jet topology of $e^+e^- \to c\bar{c}$ events. The events are divided by the plane perpendicular to the event thrust axis into two halves, each equivalent to a jet produced by c- or $\overline{c}$-quark fragmentation. The energy of each jet is estimated from its measured mass and the total c.m. energy. To determine the momentum of the D and the energy of the neutrino a kinematic fit is performed to the total event, constraining the invariant mass of the $K^- e^+ \nu_e$ candidate to the D^0 mass. The D direction is approximated by the direction opposite the vector sum of the momenta of all other particles in the event, except the Kaon and lepton associated with the signal candidate. The neutrino energy is estimated as the difference between the total energy of the jet containing the Kaon and charged lepton and the sum of the particle energies in that jet. To suppress combinatorial background each D^0 candidate is combined with a π^+ of the same charge as the lepton and the mass difference is required to be small, $\delta M = M(D^0\pi^+) - M(D^0) < 0.160$ GeV. The background-subtracted q^2 distribution is corrected for efficiency and detector resolution effects.

For BaBar's analysis [455], the normalization of the form factor at $q^2 = 0$ is $f_+^K(0) = 0.727 \pm 0.007 \pm 0.005 \pm 0.007$, where the first error is statistical, the second systematic, and the third due to uncertainties of external input parameters. In addition to the traditional parametrization of the form factors as a function of q^2 using pole approximations, BaBar also performed a fit in terms of the expansion in the parameter z. The results are presented in Fig. 28. A fit to a polynomial shows that data are compatible with a linear dependence, which is fully consistent with the modified pole ansatz for $f_+(q^2)$.

BaBar also reports the branching fraction for $D^0 \to K^- e^+ \nu_e$. To obtain the normalization for the signal sample, they perform a largely identical analysis to isolate a sample of $D^0 \to K^-\pi^+$ decays, and combine it with the world average $\mathcal{B}(D^0 \to K^-\pi^+) = (3.80 \pm 0.07)\%$. The result, the ratio of branching fractions, $R_D = \mathcal{B}(D^0 \to K^- e^+ \nu_e)/\mathcal{B}(D^0 \to K^-\pi^+) = 0.927 \pm 0.007 \pm 0.012$, translates to $\mathcal{B}(D^0 \to K^- e^+ \nu_e) = (3.522 \pm 0.027 \pm 0.045 \pm 0.065)\%$, where the last error represents the uncertainty of $\mathcal{B}(D^0 \to K^-\pi^+)$.

The Belle Collaboration has analyzed a sample of 282 fb^{-1}, recorded at or just below the $\Upsilon(4S)$ resonance [456]. They search for the process, $e^+e^- \to c\bar{c} \to D_{\rm tag}^{(*)} D_{\rm sig}^{*+} X$, with $D_{\rm sig}^{*+} \to D^0 \pi_{\rm soft}^+$ [456]. Here X represents additional particles from c-quark fragmentation. The $D_{\rm tag}$ is reconstructed as a D^0 or D^+, in decay modes $D \to K(n\pi)$ with $n = 1, 2, 3$. In events that contain a $D_{\rm sig}^{*+}$, the recoil of the $D_{\rm tag}^{(*)} X \pi_{\rm soft}^+$ provides an estimate of the signal D^0-meson energy and momentum vector. Figure 29 shows the invariant mass spectrum as derived from the $D_{\rm tag}^{(*)} X \pi_{\rm soft}^+$ system. This distribution determines the number of D^0's in the candidate sample and provides an absolute normalization. In this sample a search for semileptonic decays $D^0 \to \pi^- \ell^+ \nu_\ell$ or $D^0 \to K^- \ell^+ \nu_\ell$ is performed; here the charged lepton is either an electron or muon. Pairs of a hadron and a lepton of opposite sign are identified and the neutrino four-momentum is obtained from energy-momentum conservation. Fig. 30 shows the distribution for the missing mass squared, M_ν^2, which for signal events is required to be consistent with zero, < 0.05 GeV$^2/c^4$.

The resulting branching fractions are $\mathcal{B}(D^0 \to K^-\ell^+\nu_\ell) = (3.45 \pm 0.07 \pm 0.20)\%$ and $\mathcal{B}(D^0 \to \pi^-\ell^+\nu_\ell) = (0.255 \pm 0.019 \pm 0.016)\%$. The measured form factors as a function of q^2 are also included in Fig. 33 for both decay modes. The normalization of the form factors at $q^2 = 0$ are $f_+^K(0) = 0.695 \pm 0.007 \pm 0.022$ and $f_+^\pi(0) = 0.624 \pm 0.020 \pm 0.030$.

The CLEO Collaboration analyzed data recorded at the mass at the $\psi(3770)$ resonance, which decays exclusively to $D\bar{D}$ pairs. They report measurements of semileptonic decays of both D^0 and D^+, for both untagged and tagged events. For the untagged analysis [458] the normalization of $D\bar{D}$ pairs is based on a separate analysis [254]. Individual hadrons, π^-, π^0, K^-, or K_S, are paired with an electron and the missing momentum and energy of the entire event are used to estimate the neutrino four-momentum. The missing mass

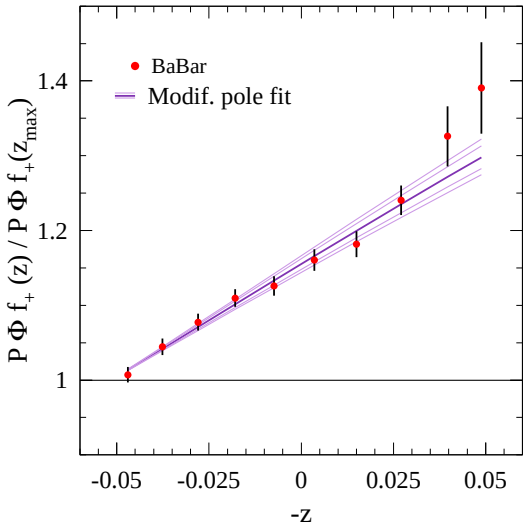

Fig. 28. Babar analysis of $D^0 \to K^-e^+\nu_e$ [455]: Measured values for $P \times \Phi \times f_+$ versus $-z$, normalized to 1.0 at $z = z_{max}$. The straight lines represent the expectation from the fit to the modified pole ansatz, the result in the center, as well as the statistical and total uncertainties on either side.

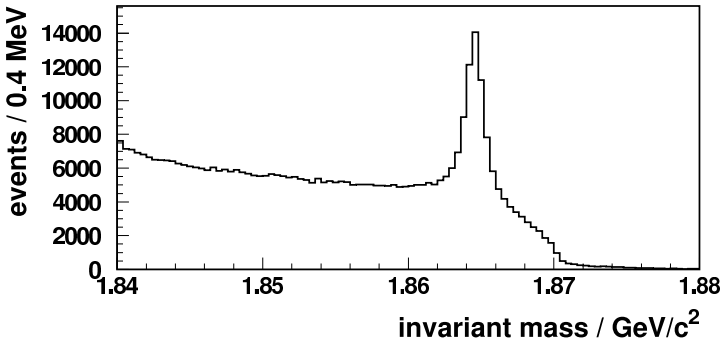

Fig. 29. Belle experiment [456]: Invariant mass distribution for $D^0_{\rm sig}$ candidates.

squared is required to be consistent with zero. Additionally, the four-momentum of the signal candidates, i.e., the sum of the hadron, lepton and neutrino energies must be consistent with the known energy and mass of the D meson. The yield of D mesons is extracted in five q^2 bins. The CLEO Collaboration reports the branching fractions, $\mathcal{B}(D^0 \to K^- \, e^+ \, \nu_e) = (3.56 \pm 0.03 \pm 0.09)\%$, $\mathcal{B}(D^0 \to \pi^- \, e^+ \, \nu_e) = (0.299 \pm 0.011 \pm 0.09)\%$, $\mathcal{B}(D^+ \to \bar{K}^0 \, e^+ \, \nu_e) = (8.53 \pm 0.13 \pm 0.23)\%$, and $\mathcal{B}(D^+ \to \pi^0 \, e^+ \, \nu_e) = (0.373 \pm 0.022 \pm 0.013)\%$. Figure 33 includes the CLEO-c untagged results for $f_+(q^2)$ versus q^2.

Recent results of the CLEO-c tagged analysis [255] were reported for the first time at this workshop. This analysis is based on a luminosity of 281 pb^{-1}. To tag events, all events are required to have a hadronic D decay, fully reconstructed in one of eight channels for D^0 and one of six channels for D^+. Since the $D\bar{D}$ system is produced nearly at rest, the D candidate should have an energy consistent with the beam energy. The beam-energy substituted mass, m_{ES}, is required to be consistent with the known D mass. For this sample of events, an electron is paired with a hadron, π^-, π^0, K^-, or K_S. In $D\bar{D}$ events with a signal semileptonic decay, the only unidentified particle is the neutrino. Its energy and momentum are derived from the missing energy and momentum. The measured difference of these two quantities, $U = E_\nu - P_\nu$, is used to discriminate signal from background. Fig. 31 shows the U distribution for the four semileptonic decay modes. The requirement of a hadronic tag results in extremely pure samples. For the decay $D^0 \to K^- \, e^+ \, \nu_e$ the signal-to-noise ratio is about 300. Based on these selected samples CLEO-c reports the branching fractions, $\mathcal{B}(D^0 \to K^- \, e^+ \, \nu_e) = (3.61 \pm 0.05 \pm 0.05)\%$, $\mathcal{B}(D^0 \to \pi^- \, e^+ \, \nu_e) = (0.314 \pm 0.013 \pm 0.004)\%$, $\mathcal{B}(D^+ \to \bar{K}^0 \, e^+ \, \nu_e) = (8.90 \pm 0.17 \pm 0.21)\%$, and $\mathcal{B}(D^+ \to \pi^0 \, e^+ \, \nu_e) = (0.384 \pm 0.027 \pm 0.023)\%$. Figure 33 shows the CLEO-c results for $f_+(q^2)$ versus q^2.

The CLEO Collaboration has computed the average of the untagged and tagged results, taking into account all correlations. The results for the branching fractions are shown in Tab. 26. The untagged analysis contains about 2.5 times more events but has larger backgrounds and different systematic uncertainties. The product of the form factor $f_+(0)$ and the CKM matrix element is extracted from the combined measurements, $f_+^K(0)|V_{cs}| = 0.744 \pm 0.007 \pm 0.005$ and $f_+^\pi(0)|V_{cd}| = 0.143 \pm 0.005 \pm 0.002$.

Since the time that the above results were reported at CKM2008, CLEO collaboration has completed a new tagged analysis which is based on the entire 818 pb^{-1} of data recorded at the $\psi(3770)$ resonance [459]. The results for the most recent branching fraction measurements are, $\mathcal{B}(D^0 \to K^- \, e^+ \, \nu_e) = (3.50 \pm 0.03 \pm 0.04)\%$, $\mathcal{B}(D^0 \to$

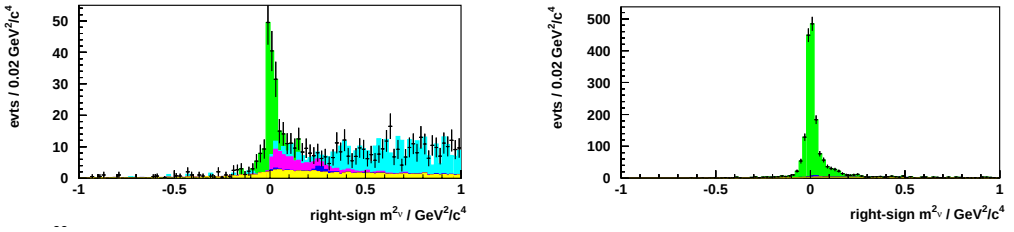

Fig. 30. Belle experiment [456, 457]: Missing mass squared distribution for $D^0_{\rm sig}$ candidates. Left: $D^0 \to \pi^- \ell^+ \nu_\ell$; right: $D^0 \to K^- \ell^+ \nu_\ell$. The $D^0 \to K^- \ell^+ \nu_\ell$ and fake D^0 backgrounds are derived from data and are shown in magenta and yellow respectively. The cyan histogram shows the contribution from $D^0 \to K^*/\rho \ell^+ \nu_\ell$ as determined from simulation.

Table 26
CLEO-c: Absolute branching fractions for tagged, untagged and averaged results.

	Tagged	Untagged	Average
$\pi^- e^+ \nu_e$	$0.308 \pm 0.013 \pm 0.004$	$0.299 \pm 0.011 \pm 0.008$	$0.304 \pm 0.011 \pm 0.005$
$\pi^0 e^+ \nu_e$	$0.379 \pm 0.027 \pm 0.002$	$0.373 \pm 0.022 \pm 0.013$	$0.378 \pm 0.020 \pm 0.012$
$K^- e^+ \nu_e$	$3.60 \pm 0.05 \pm 0.05$	$3.56 \pm 0.03 \pm 0.09$	$3.60 \pm 0.03 \pm 0.06$
$\bar{K}^0 e^+ \nu_e$	$8.87 \pm 0.17 \pm 0.21$	$8.53 \pm 0.13 \pm 0.23$	$8.69 \pm 0.12 \pm 0.19$

$\pi^-\,\mathrm{e}^+\,\nu_e) = (0.288 \pm 0.008 \pm 0.003)\%$, $\mathcal{B}(D^+ \to \bar{K}^0\,\mathrm{e}^+\,\nu_e) = (8.83 \pm 0.10 \pm 0.20)\%$, and $\mathcal{B}(D^+ \to \pi^0\,\mathrm{e}^+\,\nu_e) = (0.405 \pm 0.016 \pm 0.009)\%$. The measured form factors as a function of q^2 for this analysis are shown at the bottom of Fig. 33. The product of the form factor $f_+(0)$ and the CKM matrix element is extracted from an isospin-combined fit which yields $f_+^K(0)|V_{cs}| = 0.719 \pm 0.006 \pm 0.005$ and $f_+^\pi(0)|V_{cd}| = 0.150 \pm 0.004 \pm 0.001$. The new CLEO-c results are consistent with the previous CLEO-c measurements and supersede those measurements.

At this conference BaBar reported a measurement of $D_s^+ \to K^+K^-\ell^+\nu_\ell$ decays [460]. Events with a K^+K^- mass in the range $1.01 - 1.03\,\mathrm{GeV}/c^2$ are selected, corresponding to $\phi \to K^+K^-$ decays, except for a small S-wave contribution which is observed for the first time. Since the final state meson is a vector, the decay rate depends on five variables, the mass squared of the K^+K^- pair, q^2 and three decay angles, and on three form factors, A_1, A_2 and V, for which the q^2 dependence is assumed to be dominated by a single pole,

$$V(q^2) = \frac{V(0)}{1 - q^2/m_V^2}, \quad A_{1,2}(q^2) = \frac{A_{1,2}(0)}{1 - q^2/m_A^2}, \tag{223}$$

with a total of five parameters, the normalizations $V(0), A_1(0), A2(0)$ and the pole masses m_V and m_A. In a data sample of $214\,\mathrm{fb}^{-1}$, the BaBar Collaboration selects about 25,000 signal decays, about 50 times more than the earlier analysis by FOCUS [461]. The signal yield and the form factor ratios are extracted from a binned maximum likelihood fit to the

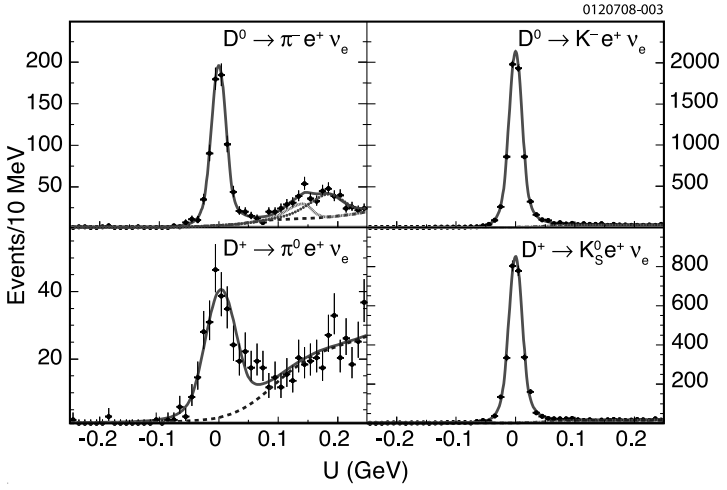

Fig. 31. CLEO-c tagged analysis [255]: Signal distributions ($U = E_\nu - P_\nu$) for the four semileptonic D decay channels.

four-dimensional decay distribution, $r_2 = A_2(0)/A_1(0) = 0.763 \pm 0.071 \pm 0.065$ and $r_V = V(0)/A_1(0) = 1.849 \pm 0.060 \pm 0.095$, as well as the pole mass $m_A = 2.28^{+0.23}_{-0.18} \pm 0.18\,\mathrm{GeV}/c^2$. The sensitivity to m_V is weak and therefore this parameter is fixed to $2.1\,\mathrm{GeV}/c^2$. The result of the fit is shown in Fig. 32. The small S-wave contribution, which can be associated with $f_0 \to K^+K^-$ decays, corresponds to $(0.22^{+0.12}_{-0.08} \pm 0.03)\%$ of the $K^+K^-e^+\nu_e$ decay rate. The $D_s^+ \to K^+K^-e^+\nu_e$ branching fraction is measured relative to the decay $D_s^+ \to K^+K^-\pi^+$, resulting in $\mathcal{B}(D_s^+ \to K^+K^-e^+\nu_e)/\mathcal{B}(D_s^+ \to K^+K^-\pi^+) = 0.558 \pm 0.007 \pm 0.016$, from which the absolute total branching fraction $\mathcal{B}(D_s^+ \to \phi e^+\nu_e) = (2.61 \pm 0.03 \pm 0.08 \pm 0.15)\%$ is obtained. By comparing this quantity with the predicted decay rate, using the fitted parameters for the form factors, the absolute normalization $A_1(0) = 0.607 \pm 0.011 \pm 0.019 \pm 0.018$ was determined for the first time. The third error stated here refers to the combined uncertainties from various external inputs, namely branching fractions for D_s^+, and ϕ, the D_s^+ lifetime and $|V_{cs}|$. Lattice QCD calculations for this decay have been performed only in the quenched approximation. They agree with the experimental results for $A_1(0)$, r_2 and m_A, but are lower than the measured value of r_V. It would be interesting to see if unquenched calculations are in better agreement with experimental results.

In summary, BaBar, Belle and CLEO-c have measured D meson semileptonic branching fractions and hadronic form factors in a variety of decay modes, using complementary experimental approaches. The results from the experiments are highly consistent. With lattice QCD prediction for the form factors, these results will allow a precise determination of V_{cs} and V_{cd}. Fig. 33 shows a compilation of all form factor measurements, $f_+(q^2)$ versus q^2. All analyses presented here have performed studies of the q^2 parameterizations

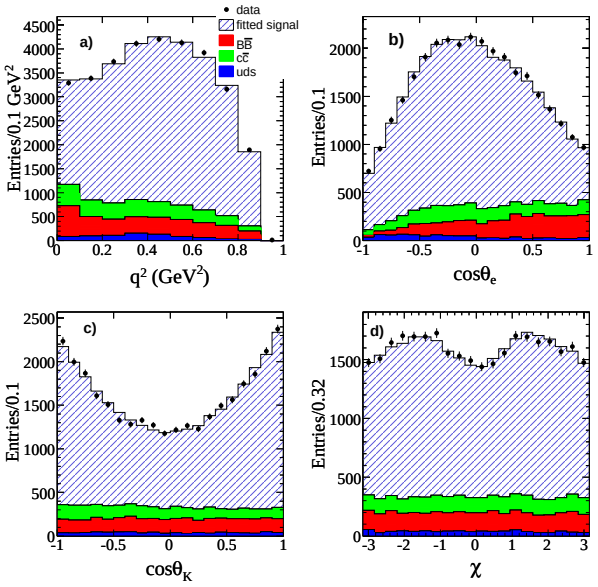

Fig. 32. BaBar [460]: Projected distributions of the four kinematic variables. The data (points with statistical errors) are compared to the sum of four contributions: the fitted signal (hatched histograms) and the estimated background contributions (different colored histograms) from $B\overline{B}$, $c\overline{c}$, and the sum of $u\overline{u}$, $d\overline{d}$, and $s\overline{s}$ events.

Table 27
Summary of the form factors parameters obtained by the different experiments for $D \to K$ semileptonic decays. The first column gives the simple pole mass, the second the parameter α used in the modified pole model, and the third the normalization.

	$M_{\rm pole}[\,{\rm GeV}/c^2]$	α	$f_+(0)$
Belle [456]	$1.82 \pm 0.04 \pm 0.03$	$0.52 \pm 0.08 \pm 0.06$	$0.695 \pm 0.007 \pm 0.022$
BaBar [455]	$1.884 \pm 0.012 \pm 0.015$	$0.38 \pm 0.02 \pm 0.03$	$0.727 \pm 0.007 \pm 0.005 \pm 0.007$
CLEO-c [459]	$1.93 \pm 0.02 \pm 0.01$	$0.30 \pm 0.03 \pm 0.01$	$0.739 \pm 0.007 \pm 0.005$
LQCD [463]		$0.50 \pm 0.04 \pm 0.07$	$0.73 \pm 0.03 \pm 0.07$

and extractions of the associated parameters. A summary of these measurements is given in Tabs. 27 and 28, as well as the values obtained by lattice QCD computation [463]. The reader is referred to the references for more details.

Measurements of $D \to \pi\ell\nu_\ell$ and $D \to V\ell\nu_\ell$ will benefit from the increased data samples expected in the near future. Of particular interest is the anticipated $\psi(3770)$ running of BES-III. The BES-III Collaboration began data accumulation in July of 2008. The experiment is comparable to CLEO-c in detector design but has superior muon identification performance, but worse performance for hadron identification, and is expected to

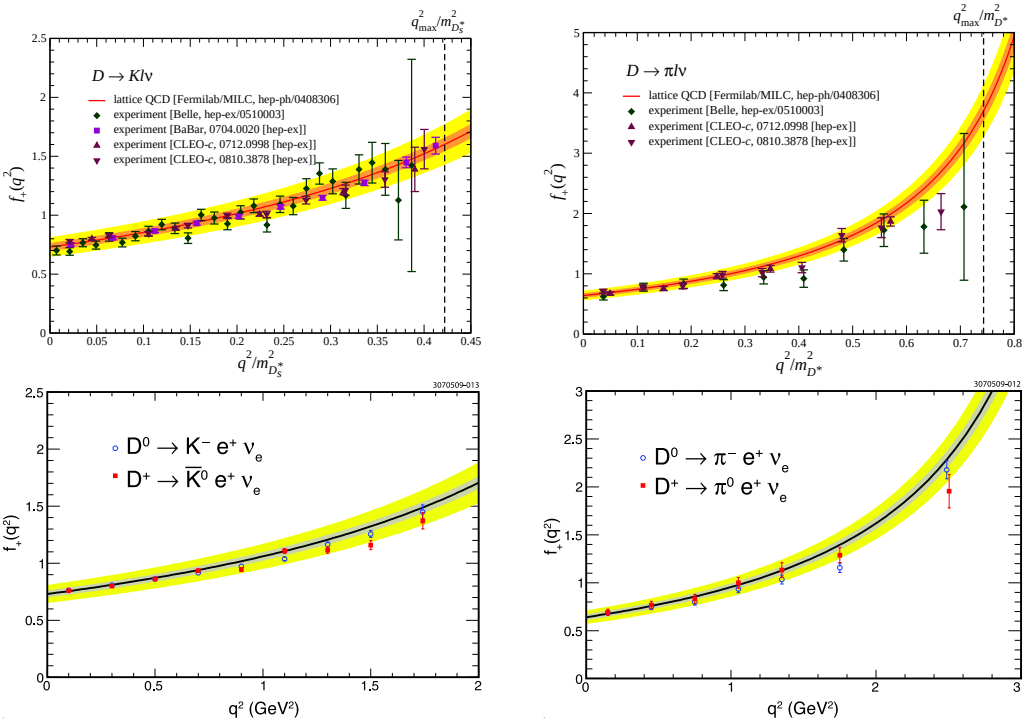

Fig. 33. Compilation of the form factor $f_+(q^2)$ versus q^2 for the semileptonic D decays with a Kaon (left) and pion (right). Top plots, adapted from Ref. [462], include measurements through the end of 2008. Bottom plots show results of a recent CLEO-c analysis [459]. In all plots the lines are the LQCD results of Ref. [463]; the inner band represents statistical uncertainty and the outer band includes the systematic uncertainty.

Table 28
Summary of the form factors parameters obtained by the different experiments for $D \to \pi$ semileptonic decays. The first column gives the simple pole mass, the second the parameter α used in the modified pole model, and the third the normalization.

	$M_{\rm pole}[\,{\rm GeV}/c^2]$	α	$f_+(0)$
Belle [456]	$1.97 \pm 0.08 \pm 0.04$	$0.10 \pm 0.21 \pm 0.10$	$0.624 \pm 0.020 \pm 0.030$
CLEO-c [459]	$1.91 \pm 0.02 \pm 0.01$	$0.21 \pm 0.07 \pm 0.02$	$0.666 \pm 0.019 \pm 0.004 \pm 0.003$
LQCD [463]		$0.44 \pm 0.04 \pm 0.07$	$0.64 \pm 0.03 \pm 0.06$

accumulate at least an order of magnitude more data. The muon identification will allow access to all the semileptonic modes covered in this section from a single experiment.

5.1.3. *Measurements of B branching fractions and q^2 dependence*

Exclusive semileptonic decays $B \to X_u \ell\nu$, where X_u denotes a charmless hadronic final state, have been reported by the CLEO, BaBar, and Belle collaborations [464–473]. The specification of the final state provides good kinematic constraints and an effective background rejection, but results in lower signal yields compared with inclusive measurements. Three experimental techniques that differ in the way the second B meson in the $B\overline{B}$ event is treated have been employed in these measurements. The second B meson is either fully reconstructed in a hadronic decay mode ("hadronic tags"), partially reconstructed in a semileptonic decay mode ("semileptonic tags") or not reconstructed at all ("untagged"). The tagged and untagged methods differ greatly in terms of signal efficiency and purity.

$B \to \pi\ell\nu$

The $B \to \pi\ell\nu$ decay is the most promising decay mode for a precise determination of $|V_{ub}|$, both for experiment and for theory. A number of measurements with different tagging techniques exist, but at present the untagged analyses, which were first performed by the CLEO collaboration [465], still provide the most precise results. In untagged analyses, the momentum of the neutrino is inferred from the missing energy and momentum in the whole event. The neutrino is combined with a charged lepton and a pion to form a $B \to \pi\ell\nu$ candidate. The biggest experimental challenge is the suppression of the $B \to X_c\ell\nu$ background. Additional background sources are $e^+e^- \to q\overline{q}$ ($q = u, d, s, c$) continuum events, which dominate at low q^2, and feed-down from other $B \to X_u\ell\nu$ decays, which dominate at high q^2.

The BaBar experiment has measured the $B \to \pi\ell\nu$ branching fraction and q^2 spectrum with a good accuracy [466]. In this analysis, the signal yields are extracted from a maximum-likelihood fit to the two-dimensional ΔE vs. $m_{\rm ES}$ distribution of the signal B meson in twelve bins of q^2 (see Fig. 34). This fit allows for an extraction of the q^2 dependence of the form factor $f_+(q^2)$. The shape of the measured spectrum is compatible with the ones predicted from LQCD [427,428] and LCSR [444] calculations, but incompatible with the ISGW2 quark model [474]. A fit to the q^2 spectrum using the Becirevic-Kaidalov (BK) parametrization yields a shape parameter $\alpha = 0.52 \pm 0.05 \pm 0.03$ with a goodness-of-fit of $P(\chi^2) = 0.65$. Other parameterizations, e.g. the z-expansion, have been used in a simultaneous fit of the BaBar data and LQCD calculations [411]. The measured partial branching fractions are extrapolated to the full decay rate and, in combination with recent form-factor calculations, used to determine $|V_{ub}|$

The leading experimental systematic uncertainties are associated with the reconstruction of charged and neutral particles, which impact the modeling of the missing momentum reconstruction, and with backgrounds from continuum events at low q^2 and from $B \to X_u \ell\nu$ decays at high q^2. Due to the feed-down from $B \to \rho\ell\nu$ decays, the uncertainties on the branching fraction and form factors for this decay mode contribute to the systematic uncertainty. A simultaneous measurement of $B \to \pi\ell\nu$ and $B \to \rho\ell\nu$ decays can reduce this uncertainty.

Recently several tagged measurements have appeared [467, 468, 471, 472]. They have led to a simpler and more precise reconstruction of the neutrino momentum and have low backgrounds and a uniform acceptance in q^2. This is achieved, however, at the expense of much smaller signal samples which limit the statistical precision of the form-factor measurement. Semileptonic-tag measurements have a signal-to-background ratio of around 1–2 and yield ~ 0.5 signal decays per fb^{-1}. The signal is extracted from the distribution of events in $\cos^2\phi_B$, where ϕ_B is the angle between the direction of either B meson and the plane containing the momentum vectors of the tag-side $D^*\ell$ system and the signal-side $\pi\ell$ system [467]. Hadronic-tag measurements reach signal-to-background ratios of up to ~ 10 and yield ~ 0.1 signal decays per fb^{-1}. Here the signal is extracted from the missing-mass squared distribution (see Fig. 35).

Tab. 29 summarizes all $B \to \pi\ell\nu$ branching-fraction measurements; shown are the total branching fraction as well as the partial branching fractions for $q^2 < 16$ GeV^2 and $q^2 > 16$ GeV^2 with statistical and systematic uncertainties. The measurements agree well among each other. A combination of all measurements results in an average branching fraction of 1.34×10^{-4} with a precision of 6% (4% statistical and 4% systematic).

$B \to \eta/\eta'/\rho/\omega\ell\nu$

In addition to $B \to \pi\ell\nu$, the experiments have measured other semileptonic final states with a pseudoscalar meson, η [465, 467, 469, 475] or η' [464, 467, 475], or a vector meson, ρ [464, 465, 470–472] or ω [469, 473]. They are important ingredients to the determination

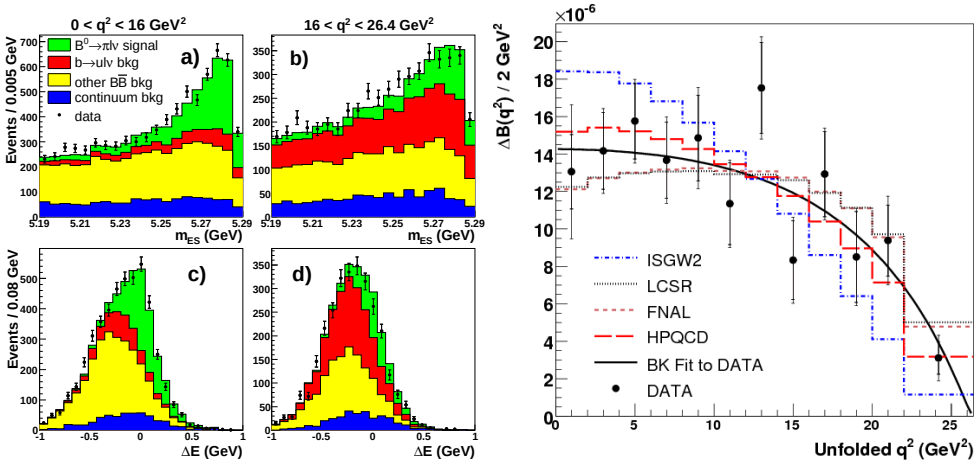

Fig. 34. Untagged $B \to \pi\ell\nu$ measurement from BaBar [466]. Left: ΔE and $m_{\rm ES}$ projections for $q^2 < 16$ GeV^2 and $q^2 > 16$ GeV^2. Right: Measured q^2 spectrum compared with a fit of the BK parametrization and with theory predictions from LQCD [427, 428], LCSR [444] and the ISGW2 quark model [474].

Table 29
Total and partial branching fractions for $B^0 \to \pi^- \ell^+ \nu$ with statistical and systematic uncertainties. Measurements of $\mathcal{B}(B^+ \to \pi^0 \ell^+ \nu)$ have been multiplied by a factor $2\tau_{B^0}/\tau_{B^+}$.

	$\mathcal{L}(\text{fb}^{-1})$	$\mathcal{B} \times 10^4$	$\Delta\mathcal{B}(q^2 < 16) \times 10^4$	$\Delta\mathcal{B}(q^2 > 16) \times 10^4$
BaBar no tag (π^-) [466]	206	$1.45 \pm 0.07 \pm 0.11$	$1.08 \pm 0.06 \pm 0.09$	$0.38 \pm 0.04 \pm 0.05$
CLEO no tag (π^-,π^0) [464]	16	$1.38 \pm 0.15 \pm 0.11$	$0.97 \pm 0.13 \pm 0.09$	$0.41 \pm 0.08 \pm 0.04$
BaBar sl. tag (π^-) [467]	348	$1.39 \pm 0.21 \pm 0.08$	$0.92 \pm 0.16 \pm 0.05$	$0.46 \pm 0.13 \pm 0.03$
Belle sl. tag (π^-) [471]	253	$1.38 \pm 0.19 \pm 0.15$	$1.02 \pm 0.16 \pm 0.11$	$0.36 \pm 0.10 \pm 0.04$
BaBar sl. tag (π^0) [467]	348	$1.80 \pm 0.28 \pm 0.15$	$1.38 \pm 0.23 \pm 0.11$	$0.45 \pm 0.17 \pm 0.06$
Belle sl. tag (π^0) [471]	253	$1.43 \pm 0.26 \pm 0.15$	$1.05 \pm 0.23 \pm 0.12$	$0.37 \pm 0.15 \pm 0.04$
BaBar had. tag (π^-) [468]	211	$1.07 \pm 0.27 \pm 0.19$	$0.42 \pm 0.18 \pm 0.06$	$0.65 \pm 0.20 \pm 0.13$
Belle had. tag (π^-) [472]	605	$1.12 \pm 0.18 \pm 0.05$	$0.85 \pm 0.16 \pm 0.04$	$0.26 \pm 0.08 \pm 0.01$
BaBar had. tag (π^0) [468]	211	$1.54 \pm 0.41 \pm 0.30$	$1.05 \pm 0.36 \pm 0.19$	$0.49 \pm 0.23 \pm 0.12$
Belle had. tag (π^0) [472]	605	$1.24 \pm 0.23 \pm 0.05$	$0.85 \pm 0.16 \pm 0.04$	$0.41 \pm 0.11 \pm 0.02$
Average		$1.36 \pm 0.05 \pm 0.05$	$0.94 \pm 0.05 \pm 0.04$	$0.37 \pm 0.03 \pm 0.02$

Table 30
Total branching fractions for exclusive $B \to X_u \ell \nu$ decays with $X_u = \eta, \eta', \rho,$ or ω. †The BaBar collaboration reports an upper limit of $\mathcal{B}(B^+ \to \eta' \ell^+ \nu) < 0.47$ at 90% CL [467].

Decay mode	$\mathcal{B} \times 10^4$	$\sigma_{stat} \times 10^4$	$\sigma_{syst} \times 10^4$
$B^+ \to \eta \ell^+ \nu$ (BaBar average) [469]	0.37	0.06	0.07
$B^+ \to \eta' \ell^+ \nu$ (CLEO no tag) [464]†	2.66	0.80	0.56
$B^0 \to \rho^- \ell^+ \nu$ (average)	2.80	0.18	0.16
$B^+ \to \omega \ell^+ \nu$ (BaBar no tag) [469]	1.14	0.16	0.08

of the composition of the inclusive $B \to X_u \ell \nu$ rate. They may also help to further constrain theoretical form-factor calculations and provide valuable cross-checks for the determination of $|V_{ub}|$ from $B \to \pi \ell \nu$. The LQCD calculations for these final states are challenging. For the flavor-neutral final-state mesons, η, η' and ω, the matrix element contains contributions from quark-disconnected diagrams. For the ρ final state, the large width of the ρ resonance complicates the calculations.

The η and η' modes have been measured by the CLEO and BaBar collaboration. The limit on $\mathcal{B}(B \to \eta' \ell \nu)$ published by BaBar [467] agrees only marginally with the CLEO result [464] (at the 2.6σ level). Further measurements are needed to resolve this discrepancy. In the future, a measurement of the ratio $R_{\eta'\eta} = \mathcal{B}(B \to \eta' \ell \nu)/\mathcal{B}(B \to \eta \ell \nu)$ would be interesting to constrain the gluonic singlet contribution to the $B \to \eta^{(\prime)}$ form factor, as proposed in [447].

The $B \to \rho \ell \nu$ decay has a larger rate than charmless semileptonic decays into pseudoscalar mesons, but one must deal with the non-resonant $\pi\pi$ contribution, which leads to a sizable systematic uncertainty. The kinematics of decays with vector mesons are described by three form factors. The statistical precision in current analyses is still too low to measure these form factors. As an example, Fig. 35 shows the missing-mass and q^2 spectra of $B \to \rho \ell \nu$ and $B \to \omega \ell \nu$ decays measured by the Belle collaboration in a hadronic-tag analysis [472]. Tab. 30 summarizes the most precise branching fraction results for semileptonic B decays to low-mass charmless hadrons heavier than the pion.

Prospects for exclusive charmless decays

The outlook for further improvements in these measurements for the full B-factory

datasets and for a Super B factory is good. It can be expected that for $B \to \pi\ell\nu$ the untagged measurements will remain the most precise up to integrated luminosities of several ab^{-1}. To reduce the systematic uncertainties of untagged measurements, a better knowledge of inclusive $B \to X_u\ell\nu$ decays is important, since they are the biggest limitation in the high-q^2 region where LQCD calculations exist. In addition, a significant fraction of the $B\overline{B}$ background comes from events, where the signal B meson has been wrongly reconstructed by assigning one or more particles from the decay of the other B meson to the signal decay. To reduce this uncertainty, much effort is needed to improve the simulation of generic B-meson decays. With the full B-factory dataset, a precision of about 4-5% should be achievable for the total $B \to \pi\ell\nu$ branching fraction.

The tagged measurements in particular will improve with larger data samples. The systematic uncertainties in these measurements have a significant statistical component and thus the total experimental error is expected to fall as $1/\sqrt{N}$. For the higher-mass states, the tagged measurements should soon give the most precise branching-fraction results. However, the larger data samples from untagged analyses will be needed to extract information on the three form factors involved in decays with a vector meson. For an integrated luminosity of 1–2 ab^{-1}, several thousand $B \to \rho\ell\nu$ and $B \to \omega\ell\nu$ decays can be expected. These signal samples will allow us to obtain some information on the form factors or ratios of form-factors through a simultaneous fit of the q^2 spectrum and decay-angle distributions, similar to the study of $B \to D^*\ell\nu$ decays. A measurement of all three form factors will most likely not be feasible with the current B-factory data samples.

5.1.4. *Determination of* $|V_{cs}|$, $|V_{cd}|$, $|V_{ub}|$

Once both the form factor $|f_+(q^2)|^2$ and the experimental decay width $\Gamma(q_{\mathrm{min}})$ are known, the CKM matrix element $|V_{qQ}|$ can be determined in several ways. We briefly describe the two most common methods below.

Until recently the standard procedure used to extract CKM matrix elements from

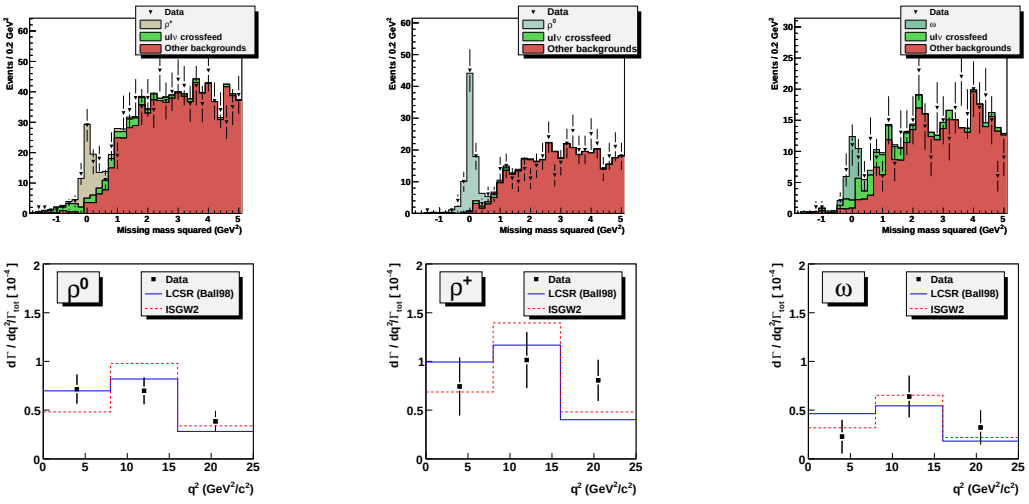

Fig. 35. Belle hadronic-tag measurements [472]: Missing-mass squared distributions and q^2 spectra for $B \to \rho\ell\nu$ and $B \to \omega\ell\nu$ decays.

exclusive semileptonic decays has been to integrate the theoretically determined form factor over a region of q^2 and then combine it with the experimentally measured decay rate in this region:

$$\frac{\Gamma(q_{\rm min})}{|V_{qQ}|^2} = \frac{G_F^2}{192\pi^3 m_H^3} \int_{q^2_{\rm min}}^{q^2_{\rm max}} dq^2 \left[(m_H^2 + m_P^2 - q^2)^2 - 4m_H^2 m_P^2\right]^{3/2} |f_+(q^2)|^2. \quad (224)$$

The integration requires a continuous parametrization of the form factor between $q^2_{\rm min}$ and $q^2_{\rm max}$ that is typically obtained by fitting the theoretical form factor result to a model function such as the Bećirević-Kaidalov (BK) [476] or Ball-Zwicky (BZ) parametrization [444]. The three-parameter BK Ansatz,

$$f_+(q^2) = \frac{f_+(0)}{(1 - q^2/m^2_{B^*})\,(1 - \alpha\, q^2/m^2_{B^*})}, \quad (225)$$

$$f_0(q^2) = \frac{f_+(0)}{(1 - q^2/\beta m^2_{B^*})}, \quad (226)$$

incorporates many essential features of the form factor shape such as the kinematic constraint at $q^2 = 0$, heavy-quark scaling, and the location of the B^* pole. The four-parameter BZ Ansatz extends the BK expression for $f_+(q^2)$ by including an additional pole to capture the effects of multiparticle states.

In general, the use of a model function to parametrize the form factor introduces assumptions that make it difficult to quantify the agreement between theory and experiment and gives rise to a systematic uncertainty in the CKM matrix element $|V_{qQ}|$ that is hard to estimate. It is likely that this error can be safely neglected when interpolating between data points. Thus the choice of fit function should have only a slight impact on the exclusive determinations of $|V_{cs}|$ and $|V_{cd}|$ because lattice-QCD calculations and experimental measurements possess a large region of overlap in q^2. It is less clear, however, how well the BK and BZ Ansätze can be trusted to extrapolate the form factor shape beyond the reach of the numerical lattice-QCD data or the experimental data. Thus one should be cautious in using them for the exclusive determination of $|V_{ub}|$ via Eq. (224), since an extrapolation in q^2 is necessary both for lattice QCD, which is most accurate at high q^2, and for experimental measurements, which are most precise at low values of q^2. In particular, comparisons of lattice and experimental determinations of BK or BZ fit parameters are potentially misleading, because apparent inconsistencies could simply be due to the inadequacy of the parametrization.

Recently, several groups have begun to use model-independent parameterizations for the exclusive determination of $|V_{ub}|$ [410–415, 477]. This avoids the concerns about the BK and BZ Ansätze outlined above, and should become the standard method for determining $|V_{ub}|$ and other CKM matrix elements from semileptonic decays in the near future. For concreteness, here we focus on the z-expansion given in Eq. (207), but the procedure for determining $|V_{ub}|$ outlined here should apply to other model-independent parameterizations. Because the z-expansion relies only on analyticity and unitarity, it can be trusted to extrapolate the form factor shape in q^2 beyond the reach of the data. One can easily check for consistency between theory and experiment using this parametrization by fitting the data separately and comparing the slope (a_1/a_0), curvature (a_2/a_0), and so forth. Finally, because as many terms can be added to the convergent series as are

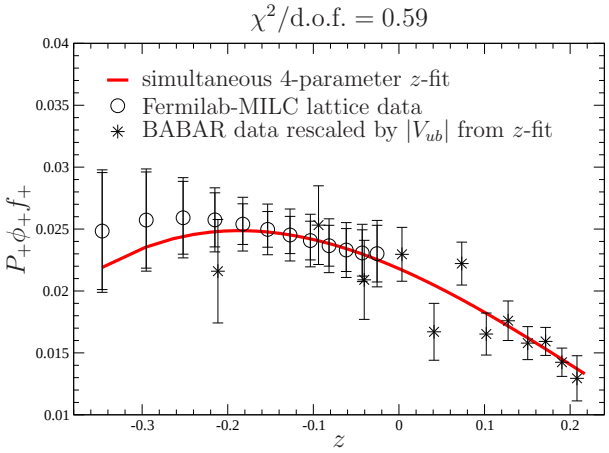

Fig. 36. Model-independent determination of $|V_{ub}|$ from a simultaneous fit of lattice and experimental $B \to \pi\ell\nu$ semileptonic form factor data to the z-parametrization [411]. Inclusion of terms in the power-series through z^3 yields the maximum uncertainty in $|V_{ub}|$; the corresponding 4-parameter z-fit is given by the red curve in both plots. The circles denote the Fermilab-MILC lattice-QCD calculation [411], while the stars indicate the 12-bin Babar data [466], rescaled by the value of $|V_{ub}|$ determined in the simultaneous z-fit.

needed to describe the $B \to \pi\ell\nu$ form factor to the desired accuracy, the parametrization can be systematically improved as theoretical and experimental data get better.

Once the shapes of the theoretical and experimental form factor data are determined to be consistent, the CKM matrix element $|V_{ub}|$ is given simply by the ratio of the normalizations, $|V_{ub}| = a_0^{\text{exp.}}/a_0^{\text{theo.}}$. The total uncertainty in $|V_{ub}|$ can be reduced, however, by fitting the theoretical and experimental data simultaneously, leaving the relative normalization as a free parameter to be determined [411]. The combined fit incorporates all of the available data, thereby allowing the numerical lattice QCD data primarily to dictate the shape at high q^2 and the experimental data largely to determine the shape at low q^2. Although the theoretical and experimental data are uncorrelated, it is important to include the correlations between experiments or between theoretical calculations, despite the fact that they can be difficult to ascertain. Fig. 36 shows an example combined fit to the model-independent z-parametrization that uses 2+1 flavor lattice QCD results from Fermilab/MILC [411] and experimental data from BABAR [466].

Combining the most recent experimental measurements of $D \to K\ell\nu$ and $D \to \pi\ell\nu$ form factors with the 2+1 flavor lattice QCD calculations from the Fermilab/MILC collaboration [285, 463], CLEO finds [459]

$$|V_{cd}| = 0.234 \pm 0.007 \pm 0.025, \tag{227}$$

$$|V_{cs}| = 0.985 \pm 0.012 \pm 0.103, \tag{228}$$

where the errors are experimental and theoretical, respectively. These determinations rely upon the BK parametrization, both to parametrize the theoretical $D \to \pi\ell\nu$ and $D \to K\ell\nu$ form factor shapes for use in Eq. (224) and within the lattice QCD calculation itself. Although this is unlikely to introduce a significant systematic error, use of one of the many model-independent functional forms available would be preferable. The largest uncertainties in both $|V_{cs}|$ and $|V_{cd}|$ are from discretization errors in the lattice QCD

calculation, and can be reduced by simulating at a finer lattice spacing. Because the lattice calculations of the $D \to \pi\ell\nu$ and $D \to K\ell\nu$ form factors can improved in a straightforward manner, without requiring new techniques, we expect the errors in both $|V_{cd}|$ and $|V_{cs}|$ to decrease significantly in the near future.

Most recent exclusive determinations of $|V_{ub}|$ rely upon the 2+1 flavor lattice QCD calculations of the $B \to \pi\ell\nu$ form factor of the HPQCD and Fermilab/MILC collaborations [285, 427, 428]. Those which use model-independent parameterizations of the form factor shape often incorporate additional theoretical points from light cone sum rules, soft collinear effective theory, and chiral perturbation theory [410, 412, 413, 415]. All of the results for $|V_{ub}|$ are consistent within uncertainties. We show a representative sample of these results, along with two model-dependent determinations that rely on the BK and BZ parameterizations for comparison, in Fig. 37. Below we quote the most recent calculation by Fermilab/MILC because this is the only one to use a model-independent parametrization along with the full correlation matrices, derived directly from the data, for both theory and experiment [411]:

$$|V_{ub}| = (3.38 \pm 36) \times 10^{-3}, \tag{229}$$

where the total uncertainty is the sum of statistical, systematic, and experimental errors added in quadrature. The dominant theoretical uncertainty in $|V_{ub}|$ comes from statistics and the extrapolation to the physical up and down quark masses and to the continuum. The sub-dominant uncertainties, which are of comparable size, are due to the perturbative renormalization of the heavy-light vector current and heavy-quark discretization errors in the action and current. All of these errors can be reduced by increasing statistics and simulating at a finer lattice spacing. We therefore expect the total uncertainty in $|V_{ub}|$ determined from $B \to \pi\ell\nu$ semileptonic decay to decrease in the next few years.

5.2. $B \to D^{(*)}\ell\nu$ *decays for* $|V_{cb}|$

5.2.1. *Theoretical background: HQS and HQET*

The matrix elements of semileptonic decays can be related to a set of form factors. In the conventions of refs. [478–480], the matrix elements relevant for $B \to D^{(*)}\ell\nu$ decays are

$$\frac{\langle D|\mathcal{V}^\mu|B\rangle}{\sqrt{m_B m_D}} = (v_B + v_D)^\mu h_+ + (v_B - v_D)^\mu h_-, \tag{230}$$

$$\frac{\langle D^*_\alpha|\mathcal{V}^\mu|B\rangle}{\sqrt{m_B m_{D^*}}} = \varepsilon^{\mu\nu\rho\sigma} v_B^\nu v_{D^*}^\rho \epsilon_\alpha^{*\sigma} h_V, \tag{231}$$

$$\frac{\langle D^*_\alpha|\mathcal{A}^\mu|B\rangle}{\sqrt{m_B m_{D^*}}} = i\epsilon_\alpha^{*\nu}[h_{A_1}(1+w)g^{\mu\nu} - (h_{A_2} v_B^\mu + h_{A_3} v_{D^*}^\mu) v_B^\nu], \tag{232}$$

where m_B and $m_{D^{(*)}}$ are the masses of the B and $D^{(*)}$ mesons, respectively, $v_{B,D^{(*)}} = p_{B,D^{(*)}}/m_{B,D^{(*)}}$ is the 4-velocity of the mesons, $\varepsilon^{\mu\nu\rho\sigma}$ is the totally antisymmetric tensor in 4 dimensions, and ϵ_α^μ is the polarization vector of D^*_α, with

$$\sum_{\alpha=1}^{3} \epsilon_\alpha^{*\mu} \epsilon_\alpha^\nu = -g^{\mu\nu} + v_{D^*}^\mu v_{D^*}^\nu. \tag{233}$$

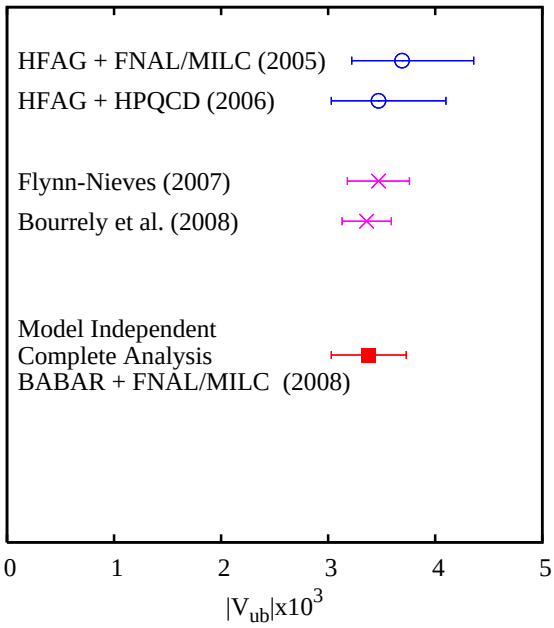

Fig. 37. Determinations of $|V_{ub}|$ that rely upon 2+1 flavor lattice QCD calculations. The upper two results use the BK and BZ parameterizations, respectively, to describe the the $B \to \pi\ell\nu$ form factor, while the lower three results use different model-independent parameterizations.

The form factors depend on the heavy-light meson masses, and on the velocity transfer from initial to final state $w = v_B \cdot v_{D^{(*)}}$. The values of w are constrained by kinematics to fall in the range

$$1 \leq w \leq \frac{m_B^2 + m_{D^{(*)}}^2}{2 m_B m_{D^{(*)}}}, \tag{234}$$

with the largest value of w around 1.5. The usual invariant $q^2 = m_B^2 + m_{D^{(*)}}^2 - 2 w m_B m_{D^{(*)}}$.

The differential rate for the decay $B \to D\ell\nu$ is

$$\frac{d\Gamma(B \to D\ell\nu)}{dw} = \frac{G_F^2}{48\pi^3} m_D^3 (m_B + m_D)^2 (w^2 - 1)^{3/2} |V_{cb}|^2 |\mathcal{G}(w)|^2, \tag{235}$$

with

$$\mathcal{G}(w) = h_+^{B\to D}(w) - \frac{m_B - m_D}{m_B + m_D} h_-^{B\to D}(w). \tag{236}$$

The differential rate for the semileptonic decay $\overline{B} \to D^* \ell \overline{\nu}_\ell$ is

$$\frac{d\Gamma(B \to D^*\ell\nu)}{dw} = \frac{G_F^2}{4\pi^3} m_{D^*}^3 (m_B - m_{D^*})^2 \sqrt{w^2 - 1} |V_{cb}|^2 \chi(w) |\mathcal{F}(w)|^2, \tag{237}$$

where $\chi(w)|\mathcal{F}_{B\to D^*}(w)|^2$ contains a combination of four form factors that must be calculated nonperturbatively. At zero recoil $\chi(1) = 1$, and $\mathcal{F}(1)$ reduces to a single form factor, $h_{A_1}(1)$. At non-zero recoil, all four form factors contribute, yielding

$$\chi(w) = \frac{w+1}{12}\left(5w + 1 - \frac{8w(w-1)m_B m_{D^*}}{(m_B - m_{D^*})^2}\right), \tag{238}$$

$$\mathcal{F}(w) = h_{A_1}(w)\frac{1+w}{2}\sqrt{\frac{H_0^2(w) + H_+^2(w) + H_-^2(w)}{3\chi(w)}}, \tag{239}$$

with

$$H_0(w) = \frac{w - m_{D^*}/m_B - (w-1)R_2(w)}{1 - m_{D^*}/m_B}, \tag{240}$$

$$H_\pm(w) = t(w)\left[1 \mp \sqrt{\frac{w-1}{w+1}}R_1(w)\right], \tag{241}$$

$$t^2(w) = \frac{m_B^2 - 2w m_B m_{D^*} + m_{D^*}^2}{(m_B - m_{D^*})^2}, \tag{242}$$

$$R_1(w) = \frac{h_V(w)}{h_{A_1}(w)}, \tag{243}$$

$$R_2(w) = \frac{h_{A_3}(w) + (m_{D^*}/m_B)h_{A_2}(w)}{h_{A_1}(w)}. \tag{244}$$

Eqs. (235) and (237) hold for vanishing lepton mass, and there are corrections analogous to those in Eq. (203). For semimuonic decays, these effects are included in recent experimental analyses.

In the limit of infinite heavy-quark mass, all heavy quarks interact in the same way in heavy light mesons. This phenomenon is known as heavy quark symmetry (HQS). For example, given that a heavy quark has spin quantum number 1/2, the quark has a chromomagnetic moment $g/(2m_Q)$, which vanishes as the heavy quark m_Q goes to infinity. Thus, in a meson, the interaction between the spin of the heavy quark and the light degrees of freedom is suppressed. The heavy-light meson is then symmetric under a change in the z-component of the heavy-quark spin, and this is known as heavy-quark spin symmetry.

In the heavy-quark limit we have that the velocity of the heavy quark is conserved in soft processes. Thus, the mass-dependent piece of the momentum operator can be removed by a field redefinition,

$$h_Q(v,x) = \frac{1+\not{v}}{2}e^{im_Q v\cdot x}Q(x), \tag{245}$$

where $(1+\not{v})/2$ is a projection operator, and $Q(x)$ is the conventional quark field in QCD. If the quark has a total momentum P^α, the new field carries a residual momentum $k^\alpha = P^\alpha - m_Q v^\alpha$. In the limit $m_Q \to \infty$, the effective Lagrangian for heavy quarks interacting via QCD becomes

$$\mathcal{L}_{\rm HQET} = \overline{h}_Q iv\cdot D h_Q, \tag{246}$$

where $D^\alpha = \partial^\alpha - ig_s t_a A_a^\alpha$ is the covariant derivative. For large but finite m_Q, this Lagrangian receives corrections from terms of higher-dimension proportional to inverse powers of m_Q. These corrections break the HQS of the leading order Lagrangian, but are well-defined at each order of the expansion, and can be included in a systematic way.

The resulting Lagrangian is known as the Heavy-Quark Effective Theory (HQET). The higher-dimension operators in the HQET come with coefficients that are determined by matching to the underlying, fundamental theory, namely QCD.

In lattice simulations, it is not possible to treat quarks where the mass in lattice units am_Q is large compared to 1 using conventional light-quark methods. All lattice heavy-quark methods make use of HQET in order to avoid the large discretization effects that would result from such a naive treatment. For lattices currently in use, $am_c \sim 0.5 - 1.0$ and $am_b \sim 2-3$, so HQET methods are essential for precision calculations. For a technical review of these methods, see Ref. [86].

One approach consists in simulating a discrete version of the HQET action, introduced in Ref. [481], by treating the sub-leading operators as insertions in correlation functions. The matching procedure is particularly complicated on the lattice because of the presence of power divergences that arise as a consequence of the mixing of operators of lower dimensions with the observable of interest, but it can be carried out with non-perturbative accuracy [482] by means of a finite volume technique (see also [483] for a review of the subject).

The Fermilab approach makes use of the fact that the Wilson fermion action reproduces the static quark action in the infinite mass limit. Higher dimension operators can then be adjusted in a systematic way. Each higher dimension operator has a counterpart in HQET, and once the coefficients of the new operators are tuned to the appropriate values, the lattice action gives the continuum result, to a given order in HQET. To order $\Lambda_{\rm QCD}/2m_Q$, the only new operator is a single dimension 5 term, and this is the same term that is added to the Wilson fermion action to improve it in the light quark sector. (The power of 2 is a combinatoric factor appropriate to the HQET expansion.) This improved action is known as the Sheikholeslami- Wohlert action [484], and the tunings of the parameters in this action appropriate to heavy quarks is the Fermilab method now in common use [83, 485]. Higher order improvement to the Fermilab method, including operators of even higher dimension, has been proposed in Ref. [486].

Another approach to handle with heavy quarks on the lattice is the so-called "step-scaling method" [487]. Within the step-scaling method the dynamics of the heavy quarks is resolved by making simulations on small volumes ($L \simeq 0.5$ fm) without recurring to any approximation but introducing, at intermediate stages, finite volume effects. These are subsequently accounted for by performing simulations on progressively larger volumes and by relying on the observation that sub-leading operators enter the HQET expansion of finite volume effects multiplied by inverse powers of Lm_Q. The success of this approach depends on the possibility of computing the finite volume observable, finite volume effects and their product with smaller errors and systematics with respect to the ones that would be obtained by a direct calculation. The strength of the method is a great freedom in the definition of the observable on finite volumes provided that its physical value is recovered at the end of the procedure.

The Fermilab Lattice Collaboration introduced a double ratio in order to compute h_+ at zero-recoil [488]

$$\frac{\langle D|\overline{c}\gamma_4 b|\overline{B}\rangle\langle\overline{B}|\overline{b}\gamma_4 c|D\rangle}{\langle D|\overline{c}\gamma_4 c|D\rangle\langle\overline{B}|\overline{b}\gamma_4 b|\overline{B}\rangle} = |h_+(1)|^2 \,. \tag{247}$$

This double ratio has the advantage that the statistical errors and many of the systematic errors cancel. The discretization errors are suppressed by inverse powers of heavy-quark

mass as $\alpha_s(\Lambda_{\rm QCD}/2m_Q)^2$ and $(\Lambda_{\rm QCD}/2m_Q)^3$ [83], and much of the current renormalization cancels, leaving only a small correction that can be computed perturbatively [85]. The extra suppression of discretization errors by a factor of $\Lambda_{\rm QCD}/2m_Q$ occurs at zero-recoil for heavy-to-heavy transitions, and is a consequence of Luke's Theorem [489].

In order to obtain h_-, it is necessary to consider non-zero recoil momenta. In this case, Luke's theorem does not apply, and the HQET power counting leads to larger heavy-quark discretization errors. However, this is mitigated by the small contribution of h_- to the branching fraction. The form factor h_- can be determined from the double ratio [488]

$$\frac{\langle D|\overline{c}\gamma_j b|\overline{B}\rangle\langle D|\overline{c}\gamma_4 c|D\rangle}{\langle D|\overline{c}\gamma_4 b|\overline{B}\rangle\langle D|\overline{c}\gamma_j b|D\rangle} = \left[1-\frac{h_-(w)}{h_+(w)}\right]\left[1+\frac{h_-(w)}{2h_+(w)}(w-1)\right], \tag{248}$$

which can be extrapolated to the zero-recoil point $w=1$. Using the double ratios of Eqs. (247) and (248) the latest (preliminary) unquenched determinations of $h_+(1)$ and $h_-(1)$ from the Fermilab Lattice and MILC Collaborations combine to give [490]

$$\mathcal{G}(1) = 1.074(18)(16), \tag{249}$$

where the first error is statistical and the second is the sum of all systematic errors in quadrature.

The form factor at zero-recoil needed for $B\to D^*\ell\nu$ has been computed by the Fermilab Lattice and MILC Collaborations using the double ratio [491]

$$\frac{\langle D^*|\overline{c}\gamma_j\gamma_5 b|\overline{B}\rangle\langle\overline{B}|\overline{b}\gamma_j\gamma_5 c|D^*\rangle}{\langle D^*|\overline{c}\gamma_4 c|D^*\rangle\langle\overline{B}|\overline{b}\gamma_4 b|\overline{B}\rangle} = |h_{A_1}(1)|^2, \tag{250}$$

where again, the discretization errors are suppressed by inverse powers of heavy-quark mass as $\alpha_s(\Lambda_{\rm QCD}/2m_Q)^2$ and $(\Lambda_{\rm QCD}/2m_Q)^3$, and much of the current renormalization cancels, leaving only a small correction that can be computed perturbatively [85]. They extrapolate to physical light quark masses using the appropriate rooted staggered chiral perturbation theory [492]. Including a QED correction of 0.7% [302], they obtain [491]

$$\mathcal{F}(1) = 0.927(13)(20), \tag{251}$$

where the first error is statistical and the second is the sum of systematic errors in quadrature.

Because of the kinematic suppression factors $(w^2-1)^{3/2}$ and $(w^2-1)^{1/2}$ appearing in Eqs. (235) and (237), respectively, the experimental decay rates at zero recoil must be obtained by extrapolation. The extrapolation is guided by theory, where Ref. [493] have used dispersive constraints on the form factor shapes, together with heavy-quark symmetry to provide simple, few parameter, extrapolation formulas expanded about the zero-recoil point,

$$h_{A_1}(w) = h_{A_1}(1)\left[1-8\rho^2_{D^*}z+(53\rho^2_{D^*}-15)z^2-(231\rho^2_{D^*}-91)z^3\right], \tag{252}$$

$$R_1(w) = R_1(1)-0.12(w-1)+0.05(w-1)^2, \tag{253}$$

$$R_2(w) = R_2(1)+0.11(w-1)-0.06(w-1)^2, \tag{254}$$

$$\mathcal{G}(w) = \mathcal{G}(1)\left[1-8\rho^2_{D}z+(51\rho^2_{D}-10)z^2-(252\rho^2_{D}-84)z^3\right], \tag{255}$$

with

$$z = \frac{\sqrt{w+1}-\sqrt{2}}{\sqrt{w+1}+\sqrt{2}}. \tag{256}$$

Table 31
Quenched results for $\mathcal{G}(w)$ and $\Delta(w)$ at non zero recoil [478, 479]. The notation "(q)" stays for the unknown systematics coming from the quenching approximation. QED corrections not included.

w	$\mathcal{G}(w)$	$\Delta(w)$
1.000	1.026(17)(q)	0.466(26)(q)
1.030	1.001(19)(q)	0.465(25)(q)
1.050	0.987(15)(q)	0.464(24)(q)
1.100	0.943(11)(q)	0.463(24)(q)
1.200	0.853(21)(q)	0.463(23)(q)

Table 32
Quenched results for $\mathcal{F}(w)$ and $\mathcal{F}(w)/\mathcal{G}(w)$ at non zero recoil [480]. The notation "(q)" stands for the unknown systematics coming from the quenching approximation. QED corrections not included.

w	$\mathcal{F}(w)$	$\mathcal{F}(w)/\mathcal{G}(w)$
1.000	0.917(08)(05)(q)	0.878(10)(04)(q)
1.010	0.913(09)(05)(q)	0.883(09)(04)(q)
1.025	0.905(10)(05)(q)	0.891(09)(04)(q)
1.050	0.892(13)(04)(q)	0.905(10)(04)(q)
1.070	0.880(17)(04)(q)	0.914(12)(05)(q)
1.075	0.877(18)(04)(q)	0.916(12)(05)(q)
1.100	0.861(23)(04)(q)	0.923(16)(05)(q)

This approach is employed below to determine $\mathcal{G}(1)|V_{cb}|$ and $\mathcal{F}(1)|V_{cb}|$.

These extrapolations introduce a systematic error into the extraction of $|V_{cb}|$ that, although mild for $B \to D^*\ell\nu$, can be eliminated by calculating the form factors at non zero recoil. A first step on this route has been done by applying the step scaling method to calculate, in the *quenched* approximation, $\mathcal{G}(w)$ and $\mathcal{F}(w)$ for values of w where experimental data are directly available. The form factors have been defined on the lattice entirely in terms of ratios of three-point correlation functions, analogously to the double ratios discussed above, obtaining in such a way a remarkable statistical and (a part from quenching) systematic accuracy. All the details of the calculations, including chiral and continuum extrapolations and discussions on the sensitiveness of finite volume effects on the heavy quark masses, can be found in refs. [478–480]. The results are shown in Tab. 31 and Tab. 32. The quantity $\Delta(w)$ appearing in Tab. 31 is required to parametrize the decay rate $B \to D\tau\nu_\tau$ and its knowledge with non perturbative accuracy opens the possibility to perform lepton-flavor universality checks on the extraction of $|V_{cb}|$ from this channel. On the one hand, the phenomenological relevance of the results of Tab. 31 and Tab. 32 is limited by the quenching uncertainty that cannot be reliably quantified. On the other hand, these results shed light on the systematics on $|V_{cb}|$ coming from the extrapolation of the experimental decay rates at zero recoil. The agreement at zero recoil with the full QCD results, Eqs. (249) and (251), suggests that the unestimated quenching error may be comparable to the present statistical error.

5.2.2. *Measurements and Tests*

Measurements of the partial decay widths $d\Gamma/dw$ for the decays $B \to D^{(*)}\ell\nu$ have been performed for more than fifteen years on data recorded at the $\Upsilon(4S)$ resonance (CLEO, Babar, Belle), and at LEP. Though this review will cover only the most recent measurements, it will offer an almost complete overview of the analysis techniques employed so

far.

A semileptonic decay is reconstructed by combining a charged lepton, ℓ, either an electron or a muon, and a charm meson of the appropriate charge and flavor. To reject non-$B\overline{B}$ background, only leptons with momentum $p_\ell < 2.3$ GeV/c are accepted. To suppress fake leptons and leptons from secondary decays, a lower bound p_ℓ is usually applied, in the range from 0.6 to 1.2 GeV/c, depending on the analysis. D mesons are fully reconstructed in several hadronic decay channels. Charged and neutral D^* are identified by their decays to $D\pi$. In $\Upsilon(4S)$ decays, the energy and momentum of the B mesons, E_B and $|\boldsymbol{p}_B|$, are well known [13]. Since the neutrino escapes detection, the B decay usually is not completely reconstructed. However, kinematic constraints can be applied to reject background. In particular, if the massless neutrino is the only unobserved particle, the B-meson direction is constrained to lie on a cone centered along the $D^{(*)}\ell$ momentum vector, $\boldsymbol{p}_{D^{(*)}\ell}$, with an opening angle θ_{BY} bounded by the condition $|\cos\theta_{BY}| \leq 1$ (see Eq. 104 for the exact definition). Background events from random $D^{(*)}\ell$ combinations are spread over a much larger range in $\cos\theta_{BY}$ and decays of the type $B \to D^{(*)}\pi\pi\ell\nu$, where the additional pions are not reconstructed, accumulate mainly below $\cos\theta_{BY} = -1$.

The differential decay rate $d^4\Gamma/dw d\cos\theta_\ell d\cos\theta_V d\chi$ depends on four variables: $w = v_B \cdot v_{D^{(*)}}$, θ_ℓ, the angle between the lepton direction in the virtual W rest frame and the W direction in the B rest frame, θ_V, the angle between the D-meson direction in the D^* rest frame and the D^* direction in the B rest frame, and χ, the angle between the plane determined from the D^* decay products and the plane defined by the two leptons. In HQET, the decay rate is parametrized in term of four quantities: the normalization $\mathcal{F}(1)|V_{cb}|$, the slope $\rho^2_{D^*}$, and the form-factor ratios $R_1(1)$ and $R_2(1)$. Many measurements of $\mathcal{F}(1)|V_{cb}|$ and $\rho^2_{D^*}$ rely on the differential decay rates, integrated over the three angles, $d\Gamma(B \to D^*\ell\nu)/dw$ and thus require external knowledge of $R_1(1)$ and $R_2(1)$.

Following the first measurement by CLEO [494], the Babar [251], and Belle [495] Collaborations have employed much larger samples of reconstructed neutral B mesons to determine $R_1(1)$ and $R_2(1)$ from a fit to the four-dimensional differential decay rate. Figure 38 shows a comparison of the data and the fit results from the recent Belle analysis, for the projections of the four kinematic variables. Tab. 33 lists the results of the fully-differential measurements from Babar and Belle.

In a recent Babar analysis [496] a sample of about 23,500 $B^- \to D^{*0}\ell^-\bar{\nu}$ decays has been selected from about 2×10^7 $\Upsilon(4S) \to B\bar{B}$ events. The signal yield is determined in ten bins in w to measure $d\Gamma(B^- \to D^{*0}\ell^-\bar{\nu})/dw$ with minimal model dependence. The fitted values of $\mathcal{F}(1)|V_{cb}|$ and $\rho^2_{D^*}$ are given in Tab. 33.

The large integrated luminosities and the deeper understanding of B mesons properties accumulated in recent years have allowed B-factories to perform new measurements of semileptonic decays based on innovative approaches. Babar has recently published results on $\mathcal{G}(w)|V_{cb}|$ and $\mathcal{F}(w)|V_{cb}|$, based on an inclusive selection of $B \to D\ell\nu X$ decays, where only the D meson and the charged lepton are reconstructed [497]. To reduce background from $D^{**}\ell\nu$ decays and other background sources, the lepton momentum is restricted

[13] In LEP experiments the direction of the B meson is obtained from the vector joining the primary vertex to the B decay vertex, the neutrino energy is computed from the missing energy in the event. A missing energy technique is also applied by $\Upsilon(4S)$ experiments to improve background rejection in $B \to D\ell\nu$ measurements.

Table 33
Summary of the B-factories results on form factors and $|V_{cb}|$ from semileptonic B decays.

Mode	Ref.	$\mathcal{F}(1)\|V_{cb}\| \cdot 10^3$	$\rho^2_{D^*}$	R_1	R_2
$B^- \to D^{*0}\ell^-\bar{\nu}$	[496]	$35.9 \pm 0.6 \pm 1.4$	$1.16 \pm 0.06 \pm 0.08$	-	-
$\bar{B}^0 \to D^{*+}\ell^-\bar{\nu}$	[495]	$34.4 \pm 0.2 \pm 1.0$	$1.29 \pm 0.05 \pm 0.03$	$1.50 \pm 0.05 \pm 0.06$	$0.84 \pm 0.03 \pm 0.03$
$\bar{B}^0 \to D^{*+}\ell^-\bar{\nu}$	[251]	$34.4 \pm 0.3 \pm 1.1$	$1.19 \pm 0.05 \pm 0.03$	$1.43 \pm 0.06 \pm 0.04$	$0.83 \pm 0.04 \pm 0.02$
$B \to D^{(*)}\ell^-\bar{\nu}$	[497]	$35.9 \pm 0.2 \pm 1.2$	$1.22 \pm 0.02 \pm 0.07$	-	-

Mode	Ref.	$\mathcal{G}(1)\|V_{cb}\| \cdot 10^3$	ρ^2_D
$B \to D\ell^-\bar{\nu}$	[497]	$43.1 \pm 0.8 \pm 2.3$	$1.20 \pm 0.04 \pm 0.07$
$B \to D\ell^-\bar{\nu}$	[250]	$43.0 \pm 1.9 \pm 1.4$	$1.20 \pm 0.09 \pm 0.04$

$p_\ell > 1.2\,\mathrm{GeV}/c$, and the D mesons are reconstructed only in the two simplest and cleanest decay modes, $D^0 \to K^-\pi^+$ and $D^+ \to K^-\pi^+\pi^+$.

Signal decays with D and D^* mesons in the final states are separated from background processes (mainly semileptonic decays involving higher mass charm mesons, D^{**}) on a statistical basis. The $V-A$ structure of the weak decays favors larger values of p_ℓ for the vector meson D^* than for the scalar D. using the three-dimensional distributions of the lepton momentum p_ℓ, the D momentum p_D, and $\cos\theta_{BY}$.

The signal and background yields, the values of ρ^2_D, $\rho^2_{D^*}$, $\mathcal{G}(1)|V_{cb}|$ and $\mathcal{F}(1)|V_{cb}|$ are obtained from a binned χ^2 fit to the three-dimensional distributions of the lepton momentum p_ℓ, the D momentum p_D, and $\cos\theta_{BY}$, separately for the $D^0\ell$ and $D^+\ell$

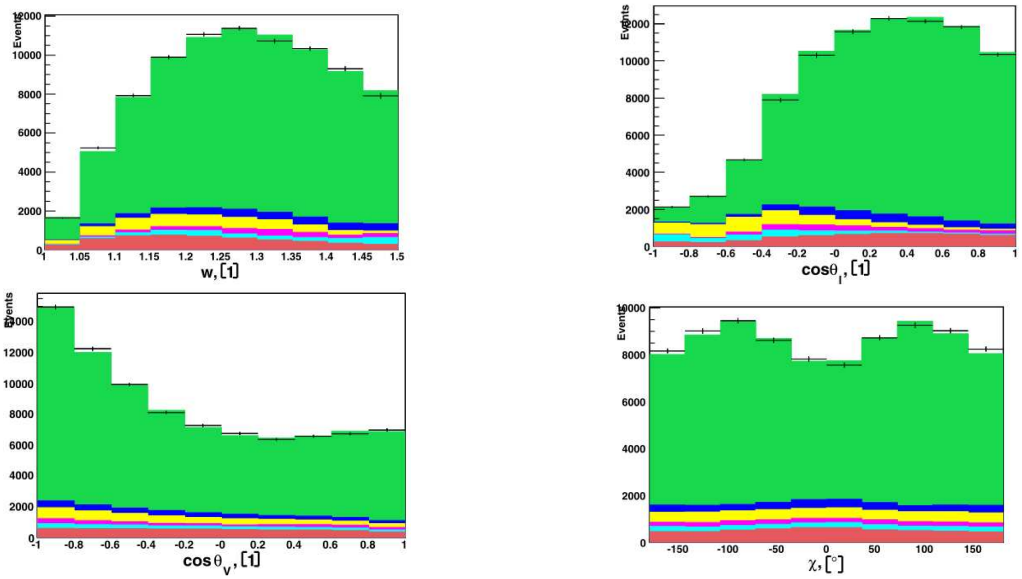

Fig. 38. Belle [495]: Results of the four-dimensional fit to the $B^0 \to D^{*+}\ell\nu$ decay rate in terms one one-dimensional projections: w (top-left), $\cos\theta_\ell$ (top-right), $\cos\theta_V$ (bottom left) and χ (bottom right). The data (points) are compared to the sum of the fitted contribution, signal (green) and several background sources (in different colors).

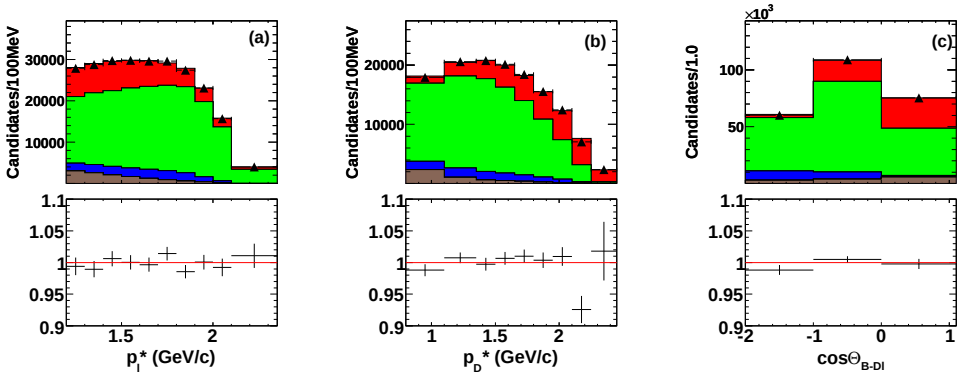

Fig. 39. BaBar [497]: Projected distributions for selected $B \to D^0 e^- \bar{\nu}_e X$ events a) p_ℓ, (b) p_D, and (c) $\cos\theta_{BY}$. The data (points) are compared to the fit result, showing contributions from $D\ell\nu$ (red), $D^*\ell\nu$ (green), $D^{**}\ell\nu$ (blue) decays, and residual background (taupe).

samples. The contribution from neutral and charged B decays in each sample are obtained from the ratio of measured branching fractions of $\Upsilon(4S) \to B^+B^-$, $\Upsilon(4S) \to B^0\bar{B}^0$, the branching fractions for charged and neutral D^* mesons to D mesons, and by imposing equal semileptonic decay rates for charged and neutral B mesons. As an example, Fig. 39 shows the results of the fit in one-dimensional projections for the $D^0 e^- \bar{\nu}_e X$ sample. An alternative fit with $\mathrm{R}_1(1)$ and $\mathrm{R}_2(1)$ as free parameters gives results consistent with the fully differential measurements cited above, albeit with larger statistical and systematic errors.

Since the $D\ell\nu$ and $D^*\ell\nu$ decays are measured simultaneously, the comparison of their form factors to validate the QCD predictions is straightforward. The measured form factor ratio at zero recoil $\mathcal{G}(1)/\mathcal{F}(1) = 1.23 \pm 0.09$ confirms the lattice QCD prediction of 1.16 ± 0.04. The difference of the slope parameters $\rho^2_D - \rho^2_{D^*} = 0.01 \pm 0.04$ is consistent with zero, as predicted [498].

The large luminosity accumulated in the B-factories permits the use of tagged event samples, for which one of the two B mesons is fully reconstructed in an hadronic final state (more than 1000 modes are considered) and a semileptonic decay of the other B is reconstructed from the remaining particles in the event. Since the momentum of the tagged B is measured, the kinematic properties of the semileptonic B are fully determined. This technique results in a sizable background reduction and thus a much lower bound on the lepton momentum ($p_\ell > 0.6$ GeV/c), a much more precise determination of w, and therefore a remarkable reduction of the systematic error, at the cost of an increase in the statistical error (the tagging efficiency does not exceed 0.5%). While several measurements of semileptonic branching fractions exist to date, only BaBar has presented a form factor determination, $\mathcal{G}(1)|V_{cb}|$ and ρ^2_D, with a tagged sample of $B \to D\ell\nu$ decays [250].

The yield of signal events in ten equal size w bins is obtained from a fit to the distribution of the missing mass squared, $\mathcal{M}^2_\nu = (P_B - P_D - P_\ell)^2$. An example is shown in Fig. 40. A fit to the background-subtracted and efficiency-corrected signal yield, summed over charged and neutral B decays, is used to extract the form-factor parameters, the normalization $\mathcal{G}|V_{cb}|$, and the slope, ρ^2_D. The signal yield and the fitted form factor as a

function of w are shown in Fig. 40. The results of this measurement, and of all the others discussed so far, are reported in Tab. 33. There is very good consistency among all of the most recent measurements.

By integrating the differential decays rates the branching fractions for $B \to D^{\ell}\nu$ and $B \to D^*\ell\nu$ decays can be determined with good precision. However, there has been a long standing problem with the measured semileptonic branching fractions. The sums of the branching fractions for $B \to D\ell^-\bar{\nu}$, $B \to D^*\ell^-\bar{\nu}$ and $B \to D^{(*)}\pi\ell^-\bar{\nu}$ decays [499, 500], $9.5 \pm 0.3\%$ for B^+ and $8.9 \pm 0.2)\%$ for B^0, are significantly smaller than the measured inclusive $B \to X_c\ell\nu$ branching fractions of $10.89 \pm 0.16\%$ and $10.15 \pm 0.16\%$ for B^+ and B^0, respectively. Branching fractions for $B \to D^{**}\ell\nu$ decay are still not well known, and furthermore, the assumption that the four D^{**} mesons decay exclusively to $D\pi$ and $D^*\pi$ final states is largely untested experimentally. And even among the measured values for the single largest B branching fraction, $\mathcal{B}(B \to D^*\ell\nu)$, there is a spread that exceeds the stated errors significantly.

5.2.3. *Determination of Form Factors and* $|V_{cb}|$

Fig. 41 shows the one sigma contour plots for all the measurements of $\mathcal{G}(w)|V_{cb}|$ and $\mathcal{F}(w)|V_{cb}|$ performed so far. While there is a good agreement among the five measurements of $B \to D\ell\nu$ decays, there is less consistency among the ten D* results, specifically two of the older measurements differ significantly from the recent, more precise measurements. Tab. 34 shows the averages of form factor measurements. Using the values of $\mathcal{G}(1)$ and $\mathcal{F}(1)$ reported in Eqs. (249) and (251) we obtain

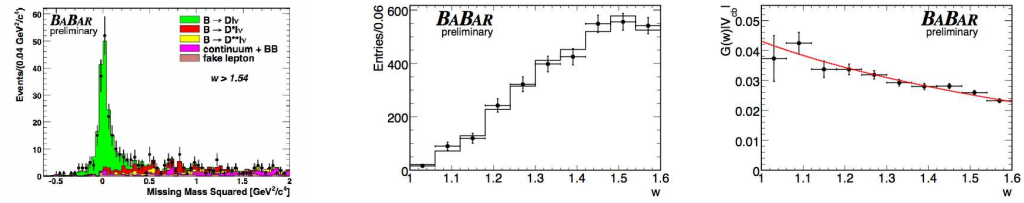

Fig. 40. BaBar analysis of tagged $B \to D\ell\mu$ decays [250] Data (points) compared to fit results, left: $\mathcal{M}_\nu^2$ for $w > 1.54$, center: signal event yield for the sum of charged and neutral B decays, right: $\mathcal{G}(w)$ vs w, as obtained from efficiency-corrected yields (data points) and the result of the form factor fit (solid line).

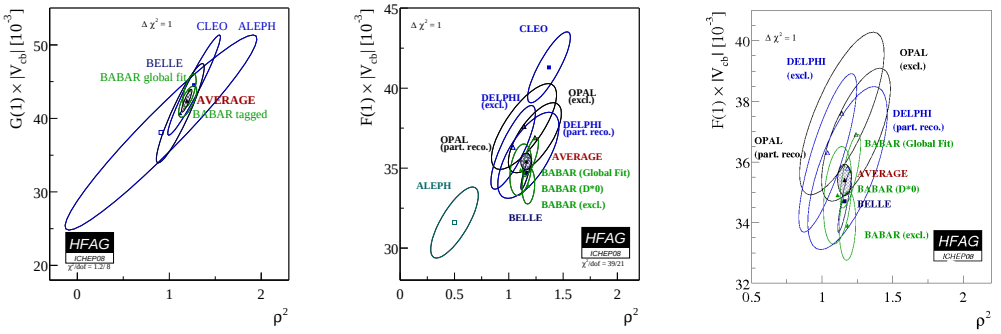

Fig. 41. HFAG: One sigma contour plots for all measurements of $\mathcal{G}(1)|V_{cb}|$ (left), $\mathcal{F}(1)|V_{cb}|$ (center), and $\mathcal{F}(1)|V_{cb}|$ with the two measurements that are least consistent with the average removed (right).

Table 34
Averages for form factors extrapolations and slopes.

Process	$\mathcal{G}(1)\lvert V_{cb}\rvert$, $\mathcal{F}(1)\lvert V_{cb}\rvert$	$\rho^2_{D^{(*)}}$
$B \to D\ell\nu$	42.4 ± 1.6	1.19 ± 0.05
$B \to D^*\ell\nu$	35.41 ± 0.52	1.16 ± 0.05

$$|V_{cb}| = (39.4 \pm 1.4 \pm 0.9) \times 10^{-3} \text{ from } B \to D\ell\nu, \tag{257}$$

$$|V_{cb}| = (38.28 \pm 0.71 \pm 0.99) \times 10^{-3} \text{ from } B \to D^*\ell\nu, \tag{258}$$

where the first error is from experiment and the second from unquenched lattice QCD. The two results agree well. It is not straightforward for combine these two results, because the correlations between the two sets of measurements and two calculations have not been analyzed. Assuming a correlation of 50% for both, we obtain the average value from exclusive decays

$$|V_{cb}| = (38.6 \pm 1.1) \times 10^{-3}, \tag{259}$$

where experimental and lattice-QCD errors have been added in quadrature.

5.3. *Inclusive CKM-favored B decays*

5.3.1. *Theoretical Background*

The inclusive $\bar{B} \to X_c\ell\bar{\nu}$ decay rate can be calculated using the operator product expansion (OPE). Applied to heavy quark decays, the OPE amounts to an expansion in inverse powers of the heavy quark mass and is often referred to as heavy-quark expansion (HQE). Using this technique, the non-perturbative input needed to predict the rate is reduced to a few matrix elements of local operators in HQET. Together with $|V_{cb}|$, m_b, and m_c, these heavy-quark parameters can be extracted from a moment analysis, i.e. by fitting the theoretical predictions for the decay rate and moments of decay spectra to the available experimental results.

The application of the OPE to semileptonic heavy hadron decays was developed quite some time ago [501–504]. A detailed discussion of the technique can, for example, be found in the textbook [505]. For a review focusing on the extraction of $|V_{cb}|$ and the heavy quark parameters, see [506] and the PDG review [285]. In the following, we briefly recall some of the basic concepts, review recent progress in evaluating higher-order perturbative corrections, and briefly discuss possible limitations of the approach. After this, we review the available experimental data and the results of the moment analysis.

The $\bar{B} \to X_c\ell\bar{\nu}$ decay is mediated by the effective Hamiltonian

$$\mathcal{H}_{\text{eff}} = \frac{G_F}{\sqrt{2}} V_{cb}\; J^\mu\, J^\ell_\mu = \frac{G_F}{\sqrt{2}} V_{cb}\, \bar{c}\,\gamma^\mu\,(1-\gamma_5)\,b\;\bar{\ell}\,\gamma_\mu\,(1-\gamma_5)\,\nu\,. \tag{260}$$

Neglecting electromagnetic corrections, the decay rate factors into a product of a leptonic tensor $L_{\mu\nu}$ and a hadronic tensor $W_{\mu\nu}$, which are given by the matrix elements of two leptonic and two hadronic currents. Using the optical theorem, the hadronic tensor can be obtained from the imaginary part of the forward matrix element of the product $\mathbf{T}_{\mu\nu}$ of two weak currents, $2M_B\, W_{\mu\nu} = -2\,\text{Im}\langle B(p_B)|\,\mathbf{T}_{\mu\nu}\,|B(p_B)\rangle$. The OPE expands the time-ordered product $\mathbf{T}_{\mu\nu}$ into a sum of local HQET operators O_i of increasing dimension

$$\mathbf{T}_{\mu\nu} = -i \int d^4x e^{-iqx} \mathbf{T}\left[J_\mu^\dagger(x)\, J_\nu(0)\right] = \sum_i C^i_{\mu\nu}(v\cdot q, q^2, m_b, m_c)\, O_i(0)\,. \tag{261}$$

In order to perform the expansion, a velocity vector v^μ, with $v^2 = 1$, is introduced to split the b-quark momentum into $p_b^\mu = m_b v^\mu + r^\mu$, where the components of the residual momentum r^μ are independent of the b-quark mass. It is usually chosen to be the meson velocity, $v^\mu = p_B^\mu/M_B$. Because Eq. (261) is an operator relation, it holds for arbitrary matrix elements. To determine the Wilson coefficients $C^i_{\mu\nu}$ one considers partonic matrix elements of Eq. (261) in perturbation theory.

The OPE separates the physics associated with large scales such as m_b, which enter the Wilson coefficients $C^i_{\mu\nu}$, from the non-perturbative dynamics entering the matrix elements of the operators O_i. In this context, it is important that the operators on the right-hand side of Eq. (261) are defined in HQET so that their matrix elements are independent of m_b up to power corrections and are governed by non-perturbative dynamics associated with the scale $\Lambda_{\rm QCD}$. Since the Wilson coefficients of higher dimensional operators in Eq. (261) contain inverse powers of m_b, their contributions to the rate are suppressed by powers of $\Lambda_{\rm QCD}/m_b$. The leading operator in Eq. (261) has dimension three and is given by a product of two HQET heavy quark fields $O_3 = \bar h_v\, h_v$. Up to power corrections, its B-meson matrix element is one. Dimension four operators can be eliminated using the equation of motion and the leading power corrections arise from two dimension five operators: the kinetic operator $O_{\rm kin}$ and the chromomagnetic operator $O_{\rm mag}$, whose B-meson matrix elements are denoted by λ_1 and λ_2 [507] or μ_π^2 and μ_G^2 [503]. Different schemes are used to define these parameters, but to leading order and leading power they are given by

$$\begin{aligned}
\langle O_{\rm kin}\rangle &\equiv \frac{1}{2M_B}\langle \bar B(p_B)|\, \bar h_v (iD)^2 h_v\, |\bar B(p_B)\rangle = -\mu_\pi^2 = \lambda_1\,, \\
\langle O_{\rm mag}\rangle &\equiv \frac{1}{2M_B}\langle \bar B(p_B)|\, \frac{g}{2}\, \bar h_v \sigma_{\mu\nu} G^{\mu\nu} h_v\, |\bar B(p_B)\rangle = \mu_G^2 = 3\lambda_2\,.
\end{aligned} \tag{262}$$

In order for the OPE to converge, it is necessary that the scales entering the Wilson coefficients are all larger than $\Lambda_{\rm QCD}$. This condition is violated in certain regions of phase-space. In order to get reliable predictions, one needs to consider sufficiently inclusive quantities such as the total rate, which takes the form [501–504]

$$\Gamma(\bar B \to X_c \ell \bar\nu) = \frac{G_F^2 |V_{cb}|^2 m_b^5}{192\pi^3}\left\{ f(\rho) + k(\rho)\frac{\mu_\pi^2}{2m_b^2} + g(\rho)\frac{\mu_G^2}{2m_b^2}\right\}, \tag{263}$$

up to corrections suppressed by $(\Lambda_{\rm QCD}/m_b)^3$, and with $\rho = m_c^2/m_b^2$. The Wilson coefficients $f(\rho)$, $k(\rho)$ and $g(\rho)$ can be calculated in perturbation theory. They are obtained by taking the imaginary part of $C^i_{\mu\nu}$, contracting with the lepton tensor $L^{\mu\nu}$ and integrating over the leptonic phase space. We have written the expansion in inverse powers of m_b, but it is the energy release $\Delta E \sim m_b - m_c$ which dictates the size of higher order corrections. Other suitable inclusive observables include the spectral moments

$$\left\langle E_\ell^n\, E_X^m (M_X^2)^l \right\rangle = \frac{1}{\Gamma_0}\int_{E_0}^{E_{\rm max}} dE_\ell \int dE_X \int dM_X^2 \frac{d\Gamma}{dE_X\, dM_X^2\, dE_\ell} E_\ell^n\, E_X^m (M_X^2)^l, \tag{264}$$

with $\Gamma_0 = \Gamma(E_\ell > E_0)$ for low values of n, m, and l, with a moderate lepton energy cut E_0. The OPE for the moments Eq. (264) depends on the *same* operator matrix elements

as the rate Eq. (263), but the calculable Wilson coefficients $f(\rho)$, $g(\rho)$, and $k(\rho)$ will be different for each moment. Note that the coefficient $k(\rho)$ of the kinetic operator is linked to the leading power coefficient $f(\rho)$, for example $k(\rho) = -f(\rho)$ for the total rate. The corresponding relations for the moments are given in [508].

By measuring the rate and several spectral moments Eq. (264), and fitting the theoretical expressions to the data, one can simultaneously extract $|V_{cb}|$, the quark masses m_b and m_c, as well as the heavy quark parameters such as μ_π and μ_G. Two independent implementations of this moment analysis are currently used [509, 510] and [511] (based on [506, 512]). Both groups include terms up to third order in $\Lambda_{\rm QCD}/m_b$ [513] and evaluate leading order Wilson coefficients to one-loop accuracy [514–520]. In addition, they also include the part of the two-loop corrections which is proportional β_0 [512, 521–526]. However, the two fits use different schemes for the masses and heavy quark parameters. The analysis of [511] is performed in the kinetic scheme [527], while [509, 510] adopt the $1S$-scheme [528] as their default choice. Both schemes, as well as others, such as the potential-subtracted [529] and the shape-function scheme [530], are designed to improve the perturbative behavior by reducing the large infrared sensitivity inherent in the pole scheme. Two-loop formulae for the conversion among the different schemes can be found in [531].

It has been noticed that the two-loop terms appearing in the conversion of m_b among schemes were in some cases larger than the uncertainties quoted after fitting in a given scheme [532]. This indicates that higher-order corrections to the Wilson coefficients can no longer be neglected. Recently, a number of new perturbative results for the Wilson coefficients have become available, however, they have not yet been implemented into the moment analysis. The Wilson coefficient of the leading order operator O_3 has been evaluated to two-loop accuracy [533, 534]. The numerical technique used in [533] allows for the calculation of arbitrary moments and its results are confirmed by an independent analytical calculation of the rate and the first few E_ℓ and E_X moments [534]. An earlier estimate of the two-loop corrections [535] needed to be revised in view of the new results [536]. At the same accuracy, one should also include the one-loop corrections to the coefficients of the kinetic and chromomagnetic operators. So far, only the corrections for the kinetic operator are available [508]. Furthermore, the tree-level OPE has been extended to fourth order in $\Lambda_{\rm QCD}/m_b$ [537].

In addition to perturbative and non-perturbative corrections, the hadronic decay rates will contain terms which are not captured by the OPE. While such terms are exponentially suppressed in completely Euclidean situations, they are not guaranteed to be negligible for the semileptonic rate and its moments [538]. These violations of quark-hadron duality are difficult to quantify. Model estimates seem to indicate that the effects on the rate are safely below the 1% level for the total rate [539, 540], but they could be larger for the spectral moments. Other issues studied in the recent literature concern the role of the charm quarks [541, 542] and potential new physics effects [543, 544].

5.3.2. *Measurements of Moments*

Measurements of the semileptonic B branching fraction and inclusive observables in $B \to X_c \ell \nu$ decays relevant to the determination of the heavy quark parameters in the OPE have been obtained by the BaBar [545–547], Belle [548,549], CDF [550], CLEO [551] and DELPHI [552] Collaborations. The photon-energy spectrum in $B \to X_s \gamma$ decays,

which is particularly sensitive to the b-quark mass, m_b, has been studied by BaBar [553, 554], Belle [555, 556] and CLEO [557]. In this section, we briefly review new or updated measurements of $B \to X_c \ell \nu$ decays.

BaBar has updated their previous measurement of the hadronic mass moments $\langle M_X^{2n} \rangle$ [546] and obtained preliminary results based on a dataset of 210 fb^{-1} taken at the $\Upsilon(4S)$ resonance [547]. In this analysis, the hadronic decay of one B meson in $\Upsilon(4S) \to B\overline{B}$ is fully reconstructed ($B_{\rm tag}$) and the semileptonic decay of the second B is inferred from the presence of an identified lepton (e or μ) among the remaining particles in the event ($B_{\rm sig}$). This fully reconstructed tag provides a significant reduction in combinatorial backgrounds and results in a sample of semileptonic decays with a purity of about 80%. Particles that are not used in the reconstruction of $B_{\rm tag}$ and are not identified as the charged lepton are assigned to the X_c system, and its mass M_X is calculated using some kinematic constraints for the whole event.

From the M_X spectrum, BaBar calculates the hadronic mass moments $\langle M_X^n \rangle$, $n = 1, \ldots, 6$ as a function of a lower limit on the lepton momenta in the center-of-mass (c.m.) frame ranging from 0.8 to 1.9 GeV/c. These moments are distorted by acceptance and finite resolution effects and an event-by-event correction is derived from Monte Carlo (MC) simulated events. These corrections are approximated as linear functions of the observed mass with coefficients that depend on the lepton momentum, the multiplicity of the X_c system and $E_{\rm miss} - c|\boldsymbol{p}_{\rm miss}|$, where $E_{\rm miss}$ and $\boldsymbol{p}_{\rm miss}$ are the missing energy and 3-momentum in the event, respectively. Note that in this analysis mixed mass and c.m. energy moments $\langle N_X^{2n} \rangle$, $n = 1, 2, 3$, with $N_X = M_X^2 c^4 - 2\tilde{\Lambda} E_X + \tilde{\Lambda}^2$ and $\tilde{\Lambda} = 0.65$ GeV are measured in addition to ordinary hadronic mass moments. These mixed moments are expected to better constrain some heavy quark parameters, though they are not yet used in global fit analyses.

Belle has recently measured the c.m. electron energy [548] and the hadronic mass [549] spectra in $B \to X_c \ell \nu$ decays, based on 140 fb^{-1} of $\Upsilon(4S)$ data. The experimental procedure is very similar to the BaBar analysis, *i.e.*, the hadronic decay of one B meson in the event is fully reconstructed. The main difference to the BaBar analysis is that detector effects in the spectra are removed by unfolding using the Singular Value Decomposition (SVD) algorithm [558] with a detector response matrix determined by MC simulation. The moments are calculated from the unfolded spectra. Belle measures the partial semileptonic branching fraction and the c.m. electron energy moments $\langle E_e^n \rangle$, $n = 1, \ldots, 4$, for minimum c.m. electron energies ranging from 0.4 to 2.0 GeV. In the hadronic mass analysis [549] the first and second moments of M_X^2 are measured for minimum c.m. lepton energies between 0.7 and 1.9 GeV.

Another interesting analysis of inclusive $B \to X_c \ell \nu$ decays comes from the DELPHI experiment [552] operating at LEP. In this study, the b-frame lepton energy $\langle E_l^n \rangle$, $n = 1, 2, 3$, and the hadronic mass M_X^{2n}, $n = 1, \ldots, 5$, moments are measured without applying any selection on the lepton energy in the b-frame. This is possible because DELPHI measures decays of b-hadrons in $Z^0 \to b\overline{b}$ events. b-hadrons are produced with significant kinetic energy in the laboratory frame, so that charged leptons produced at rest in the b-frame can be observed in the detector.

Table 35
Results of the global fit analyses by BaBar and Belle in terms of $|V_{cb}|$ and the b-quark mass m_b, including the χ^2 of the fit over the number of degrees of freedom. Note that the fit results for m_b in the kinetic and 1S schemes can be compared only after scheme translation.

	$\lvert V_{cb}\rvert$ (10^{-3})	m_b (GeV)	χ^2/ndf.
BaBar kinetic [547]	41.88 ± 0.81	4.552 ± 0.055	$8/(27-7)$
Belle kinetic [555]	41.58 ± 0.90	4.543 ± 0.075	$4.7/(25-7)$
Belle 1S [555]	41.56 ± 0.68	4.723 ± 0.055	$7.3/(25-7)$

Table 36
Measurements of the lepton energy $\langle E_\ell^n \rangle$ and hadronic mass moments $\langle M_X^{2n} \rangle$ in $B \to X_c \ell \nu$ and the photon energy moments $\langle E_\gamma^n \rangle$ in $B \to X_s \gamma$ used in the combined HFAG fit.

Experiment	$\langle E_\ell^n \rangle$	$\langle M_X^{2n} \rangle$	$\langle E_\gamma^n \rangle$
BaBar	$n = 0,1,2,3$ [545]	$n = 1,2$ [547]	$n = 1,2$ [553, 554]
Belle	$n = 0,1,2,3$ [548]	$n = 1,2$ [549]	$n = 1,2$ [556]
CDF		$n = 1,2$ [550]	
CLEO		$n = 1,2$ [551]	$n = 1$ [557]
DELPHI	$n = 1,2,3$ [552]	$n = 1,2$ [552]	

5.3.3. *Global Fits for $|V_{cb}|$ and m_b*

The OPE calculation of the $B \to X_c \ell \nu$ weak decay rate depends on a set of heavy quark parameters that contain the soft QCD contributions. These parameters can be determined from other inclusive observables in B decays, namely the lepton energy $\langle E_\ell^n \rangle$ and hadronic mass moments $\langle M_X^{2n} \rangle$ in $B \to X_c \ell \nu$ and the photon energy moments $\langle E_\gamma^n \rangle$ in $B \to X_s \gamma$. Once these parameters are known, $|V_{cb}|$ can be determined from measurements of the semileptonic B branching fraction. This is the principle of the global fit analyses for $|V_{cb}|$. On the theory side, these analyses require OPE predictions of the aforementioned inclusive observables, in addition to a calculation of the semileptonic width. At present, two independent sets of theoretical formulae have been derived including non-perturbative corrections up to $\mathcal{O}(1/m_b^3)$, referred to as the kinetic [506,512,559] and the 1S scheme [510], according to the definition of the b-quark mass used.

Tab. 35 summarizes the results of the global fit analyses performed by BaBar [547] and Belle [555] in terms of $|V_{cb}|$ and the b-quark mass m_b. BaBar uses 27 and Belle 25 measurements of the partial $B \to X_c \ell \nu$ branching fraction and the moments in $B \to X_c \ell \nu$ and $B \to X_s \gamma$ decays. Measurements at different thresholds in the lepton or photon energy are highly correlated. Correlations between measurements and between their theoretical predictions must therefore be accounted for in the definition of the χ^2 of the fit. The BaBar analysis performs a fit in the kinetic mass scheme only. In this framework, the free parameters are: $|V_{cb}|$, $m_b(\mu)$, $m_c(\mu)$, $\mu_\pi^2(\mu)$, $\mu_G^2(\mu)$, $\rho_D^3(\mu)$ and $\rho_{LS}^3(\mu)$, where μ is the scale taken to be 1 GeV. In addition, Belle fits their data also in the 1S scheme. Here, the free parameters are: $|V_{cb}|$, m_b, λ_1, ρ_1, τ_1, τ_2 and τ_3. The only external input in these analyses is the average B lifetime $\tau_B = (1.585 \pm 0.006)$ ps [560].

HFAG has combined the available $B \to X_c \ell \nu$ and $B \to X_s \gamma$ data from different experiments to extract $|V_{cb}|$ and m_b. Using 64 measurements in total (Tab. 36), the analysis is carried out in the kinetic scheme. The procedure is very similar to the analyses

Table 37
Combined HFAG fit to all experimental data (Tab. 36). In the last column we quote the χ^2 of the fit over the number of degrees of freedom.

Dataset	$\lvert V_{cb}\rvert$ (10^{-3})	m_b (GeV)	μ_π^2 (GeV^2)	χ^2/ndf.
$X_c\ell\nu$ and $X_s\gamma$	41.54 ± 0.73	4.620 ± 0.035	0.424 ± 0.042	$26.4/(64-7)$
$X_c\ell\nu$ only	41.31 ± 0.76	4.678 ± 0.051	0.410 ± 0.046	$20.3/(53-7)$

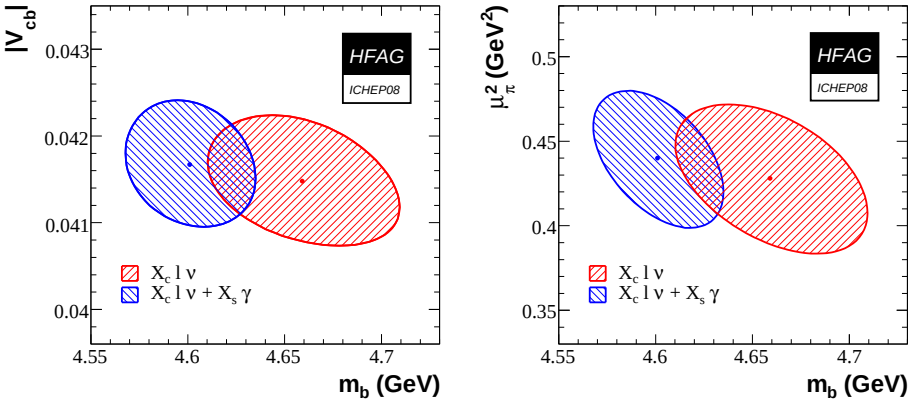

Fig. 42. $\Delta\chi^2 = 1$ contours for the HFAG fit for $|V_{cb}|$ and m_b in the $(m_b, |V_{cb}|)$ and (m_b, μ_π^2) planes, with and without $B \to X_s\gamma$ data.

of the B-factory datasets described above. The results for $|V_{cb}|$, m_b and μ_π^2 are quoted in Tab. 37 and Fig. 42. Recently, concerns have been raised about the inclusion of $B \to X_s\gamma$ moments, because their prediction is not based on pure OPE but involves modeling of non-OPE contributions using a shape function. We therefore also quote the results of a fit without the $B \to X_s\gamma$ data (53 measurements).

The current result for $|V_{cb}|$ based on fits to lepton-energy, hadronic-mass, and photon-energy moments by HFAG is

$$|V_{cb}| = (41.54 \pm 0.73) \times 10^{-3}, \tag{265}$$

where theoretical and experimental uncertainties have been combined. This value differs from the exclusive determination of $|V_{cb}|$, Eq. (259), at the 2σ level. Note that the inclusive fits lead to values χ^2 that are substantially smaller than should be expected, which may point to a problem with the input errors or correlations. The determination of m_b and m_c will be further discussed in Sec. 5.4.2.

5.4. *Inclusive CKM-suppressed B decays*

5.4.1. *Theoretical Overview*

The inclusive semileptonic B decays into charmless final states are described by the same local OPE we have considered above for the CKM favored ones. The relevant non-perturbative matrix elements are those measured in the fit to the moments discussed in Sec. 5.3. In the total width there is one additional contribution from a four-quark operator related to the Weak Annihilation (WA) between the b quark and a spectator [561],

whose analogue in the CKM favored decay is suppressed by the large charm mass. In an arbitrary, properly defined scheme the total semileptonic width is through $O(1/m_b^3, \alpha_s^2)$

$$\Gamma[\bar{B} \to X_u e \bar{\nu}] = \frac{G_F^2 \, m_b^5}{192\pi^3} |V_{ub}|^2 \left[1 + \frac{\alpha_s}{\pi} p_u^{(1)} + \frac{\alpha_s^2}{\pi^2} p_u^{(2)} - \frac{\mu_\pi^2}{2m_b^2} - \frac{3\mu_G^2}{2m_b^2} + \left(\frac{77}{6} + 8 \ln \frac{\mu_{\rm WA}^2}{m_b^2} \right) \frac{\rho_D^3}{m_b^3} + \frac{3\rho_{LS}^3}{2m_b^3} + \frac{32\pi^2}{m_b^3} B_{\rm WA}(\mu_{\rm WA}) \right], \quad (266)$$

where $B_{\rm WA}$ is the B meson matrix element of the WA operator evaluated at the scale $\mu_{\rm WA}$. Since $B_{\rm WA}$ vanishes in the factorization approximation, WA is phenomenologically important only to the extent factorization is violated at $\mu_{\rm WA}$. We therefore expect it to contribute less than 2-3% to the difference between B^0 and B^+ widths and, due to its isosinglet component, to the total width of both neutral and charged B [562, 563]. The latter and the $\ln \mu_{\rm WA}$ in the coefficient of ρ_D^3 originate in the mixing between WA and Darwin operators [564]. The dominant parametric uncertainty on the total width currently comes from m_b, due to the m_b^5 dependence. The theoretical uncertainty from missing higher order corrections has been estimated to be at most 2% in the kinetic scheme [562]. Assuming 35 MeV precision on m_b, $|V_{ub}|$ could presently be extracted from the total decay rate with a theoretical error smaller than 2.5%.

Unfortunately, most experimental analyses apply severe cuts to avoid the charm background. The cuts limit the invariant mass of the hadronic final state, X, and destroy the convergence of the local OPE introducing a sensitivity to the effects of Fermi motion of the heavy quark inside the B meson. These effects are not suppressed by powers of $1/m_b$ in the restricted kinematic regions. The Fermi motion is inherently non-perturbative; within the OPE it can be described by a nonlocal distribution function, called the shape function (SF) [565, 566], whose lowest integer moments are given by the same expectation values of local operators appearing in Eq.(266). In terms of light-cone momenta $P^\pm = E_X \mp p_X$, a typical event in the SF region has $P^+ \ll P^- = O(m_b)$, with P^+ not far above the QCD scale. The emergence of the SF is also evident in perturbation theory: soft-gluon resummation gives rise to a *b quark* SF when supplemented by an internal resummation of running coupling corrections, see e.g. [567–570]. This SF has the required support properties, namely it extends the kinematic ranges by energies of $O(\Lambda_{QCD})$, and it is stable under higher order corrections. The *quark* SF can therefore be predicted under a few assumptions, as we will see below. The inclusion of power corrections related to the difference between b quark and B meson SFs and the proper matching to the OPE are important issues in this context. An alternative possibility is to give up predicting the SF. Since the OPE fixes the first few moments of the SF, one can parametrize it in terms of the known non-perturbative quantities employing an ansatz for its functional form. The uncertainty due to the functional form can be evaluated by varying it, a process that has been recently systematized [571]. Finally, one can exploit the universality of the SF, up to $1/m_b$ corrections, and extract it from the photon spectrum of $B \to X_s\gamma$, which is governed by the same dynamics as inclusive semileptonic decays [565, 566, 572, 573]. Notice that rates in restricted phase space regions always show increased sensitivity to m_b, up to twice that in Eq.(266).

Subleading contributions in $1/m_b$ are an important issue, and acquire a different character depending on the framework in which they are discussed. For instance, if one expands in powers of the heavy quark mass the non-local OPE that gives rise to the

SF, the first subleading order sees the emergence of many largely unconstrained *subleading SFs* [574–576] that break the universality noted above. An alternative procedure has been developed in [577], where the only expansion in $1/m_b$ is at the level of local OPE. A single *finite* m_b distribution function has been introduced for each of the three relevant structure functions at fixed q^2. All power-suppressed terms are taken into account in the OPE relations for the integer moments of the SFs, which are computed, like Eq.(266) through $O(\Lambda^3)$. Finally, in the context of resummed perturbation theory, power corrections appear in moment space and can be parametrized.

Perturbative corrections also modify the physical spectra: the complete $O(\alpha_s)$ and $O(\beta_0\alpha_s^2)$ corrections to the triple differential spectrum [578, 579] are available, while the $O(\alpha_s^2)$ have been recently computed in the SF region only [580–583]. There is a clear interplay between perturbative corrections and the proper definition of the SF beyond lowest order, a problem that has been addressed in different ways, see below.

The experimental cuts can aggravate the uncertainty due to WA. Indeed, WA effects are expected to manifest themselves only at maximal q^2 and lead to an uncertainty that depends strongly on the cuts employed. In the experimental analyses the high-q^2 region could therefore either be excluded or used to put additional constraints on the WA matrix element [564, 584, 585]. Moreover, the high-q^2 spectrum is not properly described by the OPE (see [577] and references therein) and should be modeled, while its contribution to the integrated rate can be parametrized by the WA matrix element $B_{\rm WA}$. In particular, at $\mu_{\rm WA} = 1$GeV, the positivity of the q^2 spectrum implies a positive value of $B_{\rm WA}(1{\rm GeV})$, leading to a decrease in the extracted $|V_{ub}|$ [577].

All the problems outlined above have been extensively discussed in the literature. We will now consider four practical implementations, briefly discussing their basic features.

DGE The approach of Refs. [567–570] uses resummed perturbation theory in moment–space to compute the on-shell decay spectrum in the entire phase space; non-perturbative effects are taken into account as power corrections in moment space. Resummation is applied to both the 'jet' and the 'soft' (quark distribution or SF) subprocesses at NNLL [14], dealing directly with the double hierarchy of scales ($\Lambda \ll \sqrt{\Lambda m_b} \ll m_b$) characterizing the decay process. Consequently, the shape of the spectrum in the kinematic region where the final state is jet-like is largely determined by a calculation, and less by parametrization. The resummation method employed, Dressed Gluon Exponentiation (DGE), is a general resummation formalism for inclusive distributions near a threshold [587]. It goes beyond the standard Sudakov resummation by incorporating an internal resummation of running–coupling corrections (renormalons) in the exponent and has proved effective in a range of applications [587]. DGE adopts the Principal Value procedure to regularize the Sudakov exponent and thus *define* the non-perturbative parameters. In particular, this definition applies to the would-be $1/m_b$ ambiguity of the 'soft' Sudakov factor, which cancels exactly [588] against the pole–mass renormalon when considering the spectrum in physical hadronic variables. The same regularization used in the Sudakov exponent must be applied in the computation of the regularized b pole mass from the input $m_b^{\overline{\rm MS}}$. This makes DGE calculation consistent with the local OPE up to $\mathcal{O}(\Lambda^2/m_b^2)$.

ADFR In this model based on perturbative resummation [589] the integral in the Sudakov exponent is regulated by the use of the *analytic coupling* [590], which is finite in

[14] The 'jet' logarithms are similar to those resummed in the approach of Ref. [586]; there however 'soft' logarithms are not resummed.

the infrared and is meant to account for all non-perturbative effects. The resummation is performed at NNLL, while the non-logarithmic part of the spectra is computed at $O(\alpha_s)$ in the on-shell scheme, setting the pole b mass numerically equal to M_B. In contrast with DGE, this procedure does not enforce the cancellation of the renormalon ambiguity associated with m_b, and thus it violates the local OPE at $O(\Lambda/m_b)$, resulting in an uncontrolled $O(\Lambda)$ shift of the P^+ spectrum. The model reproduces b fragmentation data and the photon spectrum in $B \to X_s\gamma$, but does not account for $O(\Lambda/m_b)$ power corrections relating different processes. The normalization (total rate) is fixed by the total width of $B \to X_c\ell\nu$, avoiding the m_b^5 dependence, but introducing a dependence on m_c.

BLNP The SF approach of Ref. [586] employs a modified expansion in inverse powers of m_b, where at each order the dynamical effects associated with soft gluons, $k^+ \sim P^+ \sim \Lambda$ are summed into non-perturbative shape functions. As mentioned above, at leading power there is one such function; beyond this order there are several different functions. To extend the calculation beyond this particular region, the expansion is designed to match the local OPE when integrated over a significant part of the phase space. In this way two systematic expansions in inverse powers of the mass are used together. In this *multiscale* OPE, developed following SCET methodology (cf. Sec. 2.2), the differential width is given by

$$\frac{d\Gamma}{dP^+\,dP^-\,dE_l} = HJ \otimes S + \frac{1}{m_b} H_i' J_i \otimes S_i' + \dots \tag{267}$$

where soft (S), jet (J), and hard (H) functions depend on momenta $\sim \Lambda, \sqrt{\Lambda m_b}, m_b$, respectively. The jet and hard functions are computed perturbatively at $O(\alpha_s)$ in the *shape function scheme*, resumming Sudakov logs at NNLL, while the soft functions are parametrized at an intermediate scale, $\mu \sim 1.5\,\text{GeV}$, using the local OPE constraints on their first moments computed at $O(1/m_b^2)$ and a set of functional forms. Although the subleading SFs are largely unconstrained, BLNP find that the experimentally-relevant partial branching fractions remain under good control: the largest uncertainty in the determination of $|V_{ub}|$ is due to m_b.

GGOU The kinetic scheme used in Sec. 5.3 to define the OPE parameters, is employed in [577] to introduce the distribution functions through a factorization formula for the structure functions W_i,

$$W_i(q_0, q^2) \propto \int dk_+ \; F_i(k_+, q^2, \mu) W_i^{\text{pert}} \left[q_0 - \frac{k_+}{2}\left(1 - \frac{q^2}{m_b M_B}\right), q^2, \mu \right], \tag{268}$$

where the distribution functions $F_i(k_+, q^2, \mu)$ depend on the light-cone momentum k_+, on q^2 (through subleading effects) and on the infrared cutoff μ [577]. As the latter inhibits soft gluon emission, the spectrum has only collinear singularities whose resummation is numerically irrelevant. The perturbative corrections in W_i^{pert} include $O(\alpha_s^2\beta_0)$ contributions, which alone decrease the value of $|V_{ub}|$ by about 5%. The functions $F_i(k_+, q^2, \mu)$ are constrained by the local OPE expressions for their first moments at fixed q^2 and $\mu = 1\,\text{GeV}$, computed including all $1/m_b^3$ corrections. A vast range of functional forms is explored, leading to a 1-2% uncertainty on $|V_{ub}|$ [577].

Although conceptually quite different, the above approaches generally lead to roughly consistent results when the same inputs are used and the theoretical errors are taken into account. In Fig. 43(a) we show the normalized electron energy spectrum computed in the

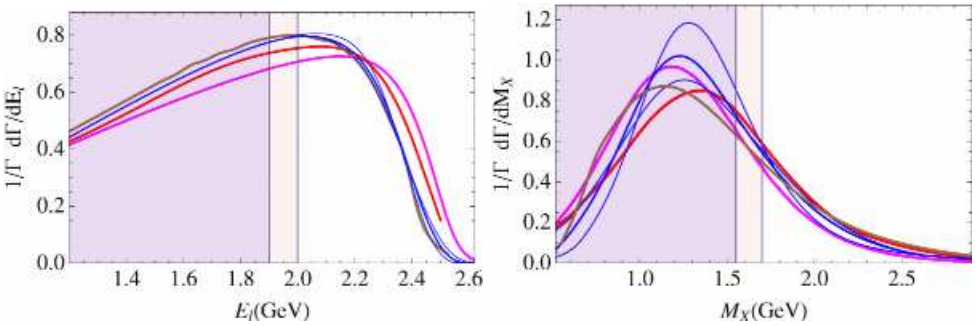

Fig. 43. Comparison of different theoretical treatments of inclusive $b \to u$ transitions: (a) E_l spectrum; (b) M_X spectrum. Red, magenta, brown and blue lines refer, respectively, to DGE, ADFR, BLNP, GGOU with a sample of three different functional forms. The actual experimental cuts at $E_l = 1.9, 2.0\,\text{GeV}$ and $M_X = 1.55, 1.7\,\text{GeV}$ are also indicated.

latest implementations of the four approaches. Except in ADFR, the spectrum depends sensitively on m_b. An accurate measurement of the electron spectrum can discriminate between at least some of the methods. The same applies to the M_X spectrum, which is shown in Fig. 43(b) for $E_l > 1\,\text{GeV}$.

5.4.2. *Review of m_b determinations*

As we have just seen, theoretical predictions of inclusive B decays can depend strongly on m_b. Thus, uncertainties in the knowledge of m_b can affect the determination of other parameters. To achieve the high precision in the theoretical predictions required by experimental data it is important to avoid the $\mathrm{O}(\Lambda_{\mathrm{QCD}})$ renormalon ambiguities related to the pole mass parameter and to consider the quark masses as renormalization scheme dependent couplings of the Standard Model Lagrangian that have to be determined from processes that depend on them. Thus having precise control over the scheme-dependence of the bottom quark mass parameters is as important as reducing their numerical uncertainty.

Predictions for B meson decays also suffer from renormalon ambiguities of order $\Lambda^2_{\mathrm{QCD}}/m_b$ or smaller. These ambiguities cannot in general be removed solely by a particular choice of a bottom mass scheme. Additional subtractions in connection with fixing specific schemes for higher order non-perturbative matrix element in the framework of the OPE are required to remove these ambiguities. Some short-distance bottom mass schemes have been proposed together with additional subtractions concerning the kinetic operator λ_1 or μ_π^2. In the following we briefly review the prevalent perturbative bottom mass definitions which were employed in recent analyses of inclusive B decays. A more detailed review on quark mass definitions including analytic formulae has been given in the CKM 2003 Report [591].

$\overline{\mathrm{MS}}$ **mass**: The most common short-distance mass parameter it the $\overline{\mathrm{MS}}$ mass $\overline{m}_b(\mu)$, which is defined by regularizing QCD with dimensional regularization and subtracting the UV divergences in the $\overline{\mathrm{MS}}$ scheme. As a consequence the $\overline{\mathrm{MS}}$ mass depends on the renormalization scale μ. Since the UV subtractions do not contain any infrared sensitive terms, the $\overline{\mathrm{MS}}$ mass is only sensitive to scales of order or larger than m_b. The $\overline{\mathrm{MS}}$ mass is therefore disfavored for direct use in the theoretical description of inclusive B decays. However, it is still useful as a reference mass. The relation between the pole mass and the

$\overline{\rm MS}$ mass is known to $\mathrm{O}(\alpha_s^3)$ [592–594], see Sec. 2.1 of the 2003 report [591] for analytic formulae.

Threshold masses The shortcomings of the $\overline{\rm MS}$ masses in describing inclusive B decays can be resolved by so-called threshold masses [595]. The prevalent threshold mass definitions are the kinetic, the shape function and the 1S mass schemes. They are free of an ambiguity of order $\Lambda_{\rm QCD}$ through in general scale-dependent subtractions.

The *kinetic mass* is defined as [596, 597]

$$m_{b,\rm kin}(\mu_{\rm kin}) = m_{b,\rm pole} - \left[\bar\Lambda(\mu_{\rm kin})\right]_{\rm pert} - \left[\frac{\mu_\pi^2(\mu_{\rm kin})}{2m_{b,\rm pole}}\right]_{\rm pert}, \tag{269}$$

where $\left[\bar\Lambda(\mu_{\rm kin})\right]_{\rm pert}$ and $\left[\mu_\pi^2(\mu_{\rm kin})\right]_{\rm pert}$ are perturbative evaluations of HQET matrix elements that describe the difference between the pole and the B meson mass. The term $\mu_{\rm kin}$ is the subtraction scale. To avoid the appearance of large logarithmic terms it should be chosen somewhat close to the typical momentum fluctuations within the B meson. The relation between the kinetic mass and the pole mass is known to $\mathrm{O}(\alpha_s^2)$ and $\mathrm{O}(\alpha_s^3\beta_0^2)$ [598, 599], see the 2002 report [591] for analytic formulae.

The *shape function mass* [530, 531] is defined from the condition that the OPE for the first moment of the leading order shape function for the $B \to X_u \ell\nu$ and $B \to X_s\gamma$ decays in the endpoint regions vanishes identically. The relation between the shape function mass and the pole mass is known at $\mathcal{O}(\alpha_s^2)$ and reads

$$\begin{aligned} m_b^{\rm SF}(\mu_{\rm SF},\mu) = m_{b,\rm pole} &- \mu_{\rm SF}\,\frac{C_F\alpha_s(\mu)}{\pi}\left[1 - 2\ln\frac{\mu_{\rm SF}}{\mu} + \frac{\alpha_s(\mu)}{\pi}\,k_1(\mu_{\rm SF},\mu)\right] \\ &- \frac{\mu_\pi^2(\mu_{\rm SF},\mu)}{3\mu_{\rm SF}}\,\frac{C_F\alpha_s(\mu)}{\pi}\left[2\ln\frac{\mu_{\rm SF}}{\mu} + \frac{\alpha_s(\mu)}{\pi}\,k_2(\mu_{\rm SF},\mu)\right], \end{aligned} \tag{270}$$

where

$$\begin{aligned} k_1(\mu_{\rm SF},\mu) = {}& \frac{47}{36}\,\beta_0 + \left(\frac{10}{9} - \frac{\pi^2}{12} - \frac{9}{4}\,\zeta_3 + \frac{\kappa}{8}\right) C_A + \left(-8 + \frac{\pi^2}{3} + 4\zeta_3\right) C_F \\ &+ \left[-\frac{4}{3}\,\beta_0 + \left(-\frac{2}{3} + \frac{\pi^2}{6}\right) C_A + \left(8 - \frac{2\pi^2}{3}\right) C_F\right] \ln\frac{\mu_{\rm SF}}{\mu} \\ &+ \left(\frac{1}{2}\,\beta_0 + 2C_F\right) \ln^2\frac{\mu_{\rm SF}}{\mu}, \end{aligned} \tag{271}$$

$$\begin{aligned} k_2(\mu_{\rm SF},\mu) = {}& -k_1(\mu_{\rm SF},\mu) + \frac{7}{6}\,\beta_0 + \left(\frac{1}{3} - \frac{\pi^2}{12}\right) C_A + \left(-5 + \frac{\pi^2}{3}\right) C_F \\ &+ \left(-\frac{1}{2}\,\beta_0 - C_F\right) \ln\frac{\mu_{\rm SF}}{\mu}. \end{aligned} \tag{272}$$

The relation depends on the momentum cutoff $\mu_{\rm SF}$ which enters the definition of the first moment and on the (non-perturbative and infrared subtracted) kinetic energy matrix element μ_π^2 defined from the ratio of the second and zeroth moment of the shape function. Since the shape function is renormalization scale dependent, the shape function mass depends on also on the renormalization scale μ. In practical applications the SF mass has been considered for $\mu = \mu_{\rm SF}$, $m_b^{\rm SF}(\mu_{\rm SF}) \equiv m_b^{\rm SF}(\mu_{\rm SF},\mu_{\rm SF})$.

The *1S mass* [528,600,601] is defined as one half of the perturbative series for the mass of the $n = 1$, ${}^3S_1$ bottomonium bound state in the limit $m_b \gg m_b v \gg m_b v^2 \gg \Lambda_{\rm QCD}$. In contrast to the kinetic and shape-function masses, the subtraction scale involved in the 1S mass is tied dynamically to the inverse Bohr radius $\sim m_b\alpha_s$ of the bottomonium ground state and therefore does not appear as an explicit parameter. The 1S mass scheme is known completely to $\mathrm{O}(\alpha_s^3)$, see the 2003 report [591] for analytic formulae.

In Tab. 38 the numerical values of the bottom quark kinetic, shape function and 1S masses are provided for different values for the strong coupling taking the $\overline{\rm MS}$ mass $\overline{m}_b(\overline{m}_b)$ as a the reference input. Each entry corresponds to the mass using the respective 1-loop/2-loop/3-loop relations as far as they are available and employing a common renormalization scale for the strong coupling when the pole mass is eliminated. As the renormalization scale we employed $\mu = \overline{m}_b(\overline{m}_b)$ to minimize the impact of logarithmic terms involving the cutoff scales $\mu_{\rm kin,SF}$ and the scale $\overline{m}_b(\overline{m}_b)$ [602]. Numerical approximations for the conversion formulae at the respective highest available order accounting in particular for the dependence on $\alpha_s^{(n_f=5)}(M_Z)$ and the renormalization scale μ read:

$$m_b^{\rm 1S} = 1.032\, m_b^{\rm kin}(1\ {\rm GeV}) \,+\, 1.9\,\Delta\alpha_s \,-\, 0.003\,\Delta\mu\,, \tag{273}$$

$$m_b^{\rm SF}(1.5\ {\rm GeV}) = 1.005\, m_b^{\rm kin}(1\ {\rm GeV}) \,+\, 0.9\,\Delta\alpha_s \,-\, 0.006\,\Delta\mu \,-\, 0.003\,\Delta\mu_\pi^2\,, \tag{274}$$

$$m_b^{\rm SF}(1.5\ {\rm GeV}) = 0.976\, m_b^{\rm 1S} \,-\, 0.9\,\Delta\alpha_s \,+\, 0.001\,\Delta\mu \,-\, 0.003\,\Delta\mu_\pi^2\,, \tag{275}$$

$$\overline{m}_b(\overline{m}_b) = 0.917\, m_b^{\rm kin}(1\ {\rm GeV}) \,-\, 8.2\,\Delta\alpha_s \,+\, 0.005\,\Delta\mu\,, \tag{276}$$

$$\overline{m}_b(\overline{m}_b) = 0.888\, m_b^{\rm 1S} \,-\, 9.9\,\Delta\alpha_s \,+\, 0.006\,\Delta\mu\,, \tag{277}$$

$$\overline{m}_b(\overline{m}_b) = 0.916\, m_b^{\rm SF}(1.5\ {\rm GeV}) \,-\, 8.0\,\Delta\alpha_s \,+\, 0.017\,\Delta\mu \,+\, 0.003\,\Delta\mu_\pi^2\,, \tag{278}$$

where $\Delta\alpha_s = [\alpha_s^{(5)}(M_Z) - 0.118]$ GeV, $\Delta\mu = (\mu - 4.2\ {\rm GeV})$, $\Delta\mu_\pi^2 = [\mu_\pi^2(1.5\ {\rm GeV}) - 0.15\ {\rm GeV}^2]\ {\rm GeV}^{-1}$. The formulae agree with the respective exact relations to better than 10 MeV (for 3.7 GeV $< \mu <$ 4.7 GeV). The theoretical uncertainties from missing higher order terms are reflected in the renormalization scale dependence of the conversion formulae.

Bottom quark mass determinations

There are two major methods to determine the bottom mass with high precision: spectral sum rules using data for the bottom production rate in e^+e^- collisions, and fits to moments obtained from distributions of semileptonic $B \to X_c\ell\nu$ and radiative $B \to X_s\gamma$ decays. Both rely on the validity of the operator product expansion and the input of higher order perturbative corrections. The results obtained from both methods are compatible. Lattice determinations still have larger uncertainties and suffer from systematic effects, which need to be better understood to be competitive to the previous two methods. A summary of recent bottom mass determinations is given in Tab. 39.

Spectral e^+e^- sum rules

The spectral sum rules start from the correlator $\Pi(q^2)$ of two electromagnetic bottom quark currents and are based on the fact that derivatives of Π at $q^2 = 0$ are related to moments of the total cross section $\sigma(e^+e^- \to b\bar{b})$,

Table 38
Numerical values of the bottom quark kinetic, 1S and shape function masses in units of GeV for a given $\overline{\rm MS}$ value $\overline{m}_b(\overline{m}_b)$ using $\mu = \overline{m}_b(\overline{m}_b)$, $n_l = 4$ and three values of $\alpha_s^{(5)}(m_Z)$. Flavor matching was carried out at $\mu = \overline{m}_b(\overline{m}_b)$. For the shape function mass $\mu_\pi^2(1.5\ {\rm GeV}) = 0.15\ {\rm GeV}^2$ was adopted. Numbers with an asterisk are given in the large-β_0 approximation.

$\overline{m}_b(\overline{m}_b)$	$m_{b,\rm kin}(1\,{\rm GeV})$	$m_{b,\rm 1S}$	$m_{b,\rm SF}(1.5\,{\rm GeV})$
$\alpha_s^{(5)}(m_Z) = 0.116$			
4.10	4.36/4.42/4.45*	4.44/4.56/4.60	4.34/4.44/-
4.15	4.41/4.48/4.50*	4.49/4.61/4.65	4.39/4.50/-
4.20	4.46/4.53/4.56*	4.54/4.66/4.71	4.45/4.55/-
4.25	4.52/4.59/4.61*	4.60/4.72/4.76	4.50/4.61/-
4.30	4.57/4.64/4.67*	4.65/4.77/4.81	4.56/4.66/-
$\alpha_s^{(5)}(m_Z) = 0.118$			
4.10	4.37/4.44/4.46*	4.45/4.57/4.62	4.35/4.46/-
4.15	4.42/4.49/4.52*	4.50/4.63/4.67	4.40/4.51/-
4.20	4.47/4.55/4.57*	4.55/4.68/4.73	4.46/4.57/-
4.25	4.52/4.60/4.63*	4.61/4.73/4.78	4.51/4.62/-
4.30	4.58/4.66/4.69*	4.66/4.79/4.84	4.56/4.68/-
$\alpha_s^{(5)}(m_Z) = 0.120$			
4.10	4.37/4.45/4.48*	4.46/4.59/4.64	4.36/4.48/-
4.15	4.43/4.51/4.54*	4.51/4.64/4.70	4.41/4.53/-
4.20	4.48/4.56/4.59*	4.56/4.70/4.75	4.47/4.59/-
4.25	4.54/4.62/4.65*	4.62/4.75/4.80	4.52/4.64/-
4.30	4.59/4.67/4.71*	4.67/4.81/4.86	4.57/4.70/-

$$\mathcal{M}_n \;=\; \frac{12\,\pi^2\,Q_b^2}{n!}\left(\frac{d}{dq^2}\right)^n \Pi(q^2)\bigg|_{q^2=0} \;=\; \int \frac{ds}{s^{n+1}}\,R(s)\,, \tag{279}$$

where $R = \sigma(e^+e^- \to b\bar{b})/\sigma(e^+e^- \to \mu^+\mu^-)$. From Eq. (279) it is possible to determine the bottom quark mass using an operator product expansion [603,604]. One has to restrict the moments to $n \lesssim 10$ such that the momentum range contributing to the moment is sufficient larger than $\Lambda_{\rm QCD}$ and the perturbative contributions dominate. Here the most important non-perturbative matrix element is the gluon condensate, but its contribution is very small.

Nonrelativistic e^+e^- sum rules: For the large n, $4 \lesssim n \lesssim 10$, the moments are dominated by the bottomonium bound states region and the experimentally unknown parts of the $b\bar{b}$ continuum cross section are suppressed. Depending on the moment the overall experimental uncertainties in the b quark mass are between 15 and 20 MeV. Sum rule analyses using threshold masses and based on NNLO fixed order computations in the framework of NRQCD [599, 605–607] yield consistent results but suffer from relatively large NNLO corrections to the normalization of the moments $\mathcal{M}_n$. Uncertainties in the bottom mass at the level of below 50 to 100 MeV were achieved by making assumptions on the behavior of higher order corrections. The use of renormalization group improved

Table 39
Collection in historical order in units of GeV of recent bottom quark mass determinations from spectral sum rules and the $\Upsilon(1S)$ mass. Only results where α_s was taken as an input are shown. The uncertainties quoted in the respective references have been added quadratically. All numbers have been taken from the respective publications.

author	$\overline{m}_b(\overline{m}_b)$	other mass	comments, Ref.
nonrelativistic spectral sum rules			
Melnikov	98 4.20 ± 0.10	$M_{\rm kin}^{\rm 1GeV} = 4.56 \pm 0.06$	NNLO, $m_c = 0$ [599]
Hoang	99 4.20 ± 0.06	$M_{\rm 1S} = 4.71 \pm 0.03$	NNLO, $m_c = 0$ [605]
Beneke	99 4.26 ± 0.09	$M_{\rm PS}^{\rm 2GeV} = 4.60 \pm 0.11$	NNLO, $m_c = 0$ [606]
Hoang	00 4.17 ± 0.05	$M_{\rm 1S} = 4.69 \pm 0.03$	NNLO, $m_c \neq 0$ [607]
Eidemüller	02 4.24 ± 0.10	$M_{\rm PS}^{\rm 2GeV} = 4.56 \pm 0.11$	NNLO + $O(\alpha_s^2)$, $m_c = 0$ [608]
Pineda	06 4.19 ± 0.06	$M_{\rm PS}^{\rm 2GeV} = 4.52 \pm 0.06$	NNLL partial, $m_c = 0$ [609]
relativistic spectral sum rules			
Kühn	01 4.19 ± 0.05		$O(\alpha_s^2)$ [610]
Bordes	02 4.19 ± 0.05		$O(\alpha_s^2)$, finite energ. s.r. [611]
Corcella	02 4.20 ± 0.09		$O(\alpha_s^2)$, continuum err.incl. [612]
Hoang	04 4.22 ± 0.11		$O(\alpha_s^2)$, contour improved [613]
Boughezal	06 4.21 ± 0.06		$O(\alpha_s^3)$ [614]
Kühn	07 4.16 ± 0.03		$O(\alpha_s^3)$ [615]
moments from $B \to X_c \ell \nu$ and $B \to X_s \gamma$ distributions			
HFAG (ICHEP 08)	08 4.28 ± 0.07	$M_{\rm kin}^{\rm 1GeV} = 4.66 \pm 0.05$	$B \to X_c \ell \nu$, $O(\alpha_s^2 \beta_0)$ [560]
	4.23 ± 0.05	$M_{\rm kin}^{\rm 1GeV} = 4.60 \pm 0.03$	$B \to X_c \ell \nu$, $B \to X_s \gamma$, $O(\alpha_s^2 \beta_0)$ [560]
	4.17 ± 0.04	$M_{\rm 1S} = 4.70 \pm 0.03$	$B \to X_c \ell \nu$ & $B \to X_s \gamma$, $O(\alpha_s^2 \beta_0)$ [560]
	4.22 ± 0.07	$M_{\rm 1S} = 4.75 \pm 0.06$	$B \to X_c \ell \nu$, $O(\alpha_s^2 \beta_0)$ [560]

NRQCD computations in Ref. [609] yields an uncertainty of 60 MeV without making such assumptions. However, the analysis of Ref. [609] neglects known large NNLL order contributions to the anomalous dimension of the quark pair production currents [616].

Relativistic sum rules: For small n, $1 \leq n \lesssim 4$, the experimentally unmeasured parts of the $b\bar{b}$ continuum cross section above the Υ resonance region constitute a substantial contribution to the spectral moments and uncertainties below the 100 MeV level are only possible using theory to predict the continuum contributions [612]. For the theoretical determination of the moments usual fixed order perturbation theory can be employed. The most recent bottom quark mass determinations [614, 615] use perturbation theory at $O(\alpha_s^3)$ and obtain $\overline{m}_b(\overline{m}_b)$ with an uncertainty between 25 and 58 MeV.

Inclusive B decay moments

As already discussed in Sec. 5.3 the analysis of moments of lepton energy and hadron invariant mass moments obtained from spectra in the semileptonic decay $B \to X_c \ell \nu$ and of radiative photon energy moments from $B \to X_s \gamma$ allows to determine the bottom quark threshold masses. Currently the theoretical input for the moment computations

includes $O(\alpha_s)$ and $\mathcal{O}(\alpha_s^2\beta_0)$ corrections for the partonic contribution and tree-level Wilson coefficients for the power corrections [510, 512, 526]; it would be desirable to include the known full $O(\alpha_s^2)$ corrections into the analysis. For what concerns the determination of m_b, the results based on combined $B \to X_c\ell\nu$ and $B \to X_s\gamma$ data are in agreement with the e^+e^- sum rule determinations, while using only $B \to X_c\ell\nu$ data leads to slightly larger m_b with larger error, which are, however, still compatible with the other determinations. In fact, the semileptonic moments are mostly sensitive to a combination of m_b and m_c, as apparent from Fig.44, where various determinations of m_c and m_b are compared.

Lattice QCD

In principle, lattice QCD should provide sound ways of determining the quark masses: each bare mass is adjusted until one particular hadron mass agrees with experiment. In practice, there are several approaches. One is to convert the bare mass of the lattice action to a more familiar renormalization scheme. Another is to define the mass via ratios of matrix elements derived from the CVC or PCAC relations. Finally, one can compute short-distance objects that are sensitive to the (heavy) quark masses, for which continuum perturbation theory can be used [618]. For the first two methods, a matching procedure is needed to relate the bare lattice mass, or currents, to a continuum scheme, such as $\overline{\rm MS}$. The matching can be done in perturbation theory—the state of the art for light quarks is two-loop [619]—or via nonperturbative matching [483]. When con-

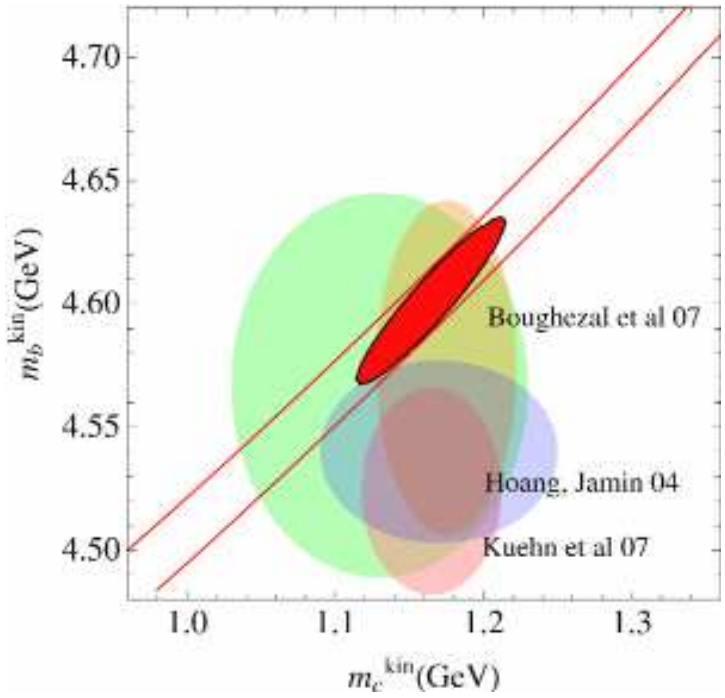

Fig. 44. Comparison of different determinations of m_c and m_b in the kinetic scheme. The red ellipse refers to the semileptonic fit discussed in Sec. 5.3, the large green ellipse to the 2007 PDG values, and the others to various e^+e^- sum rule determinations listed in Table 39, taking into account the sizable theoretical error in the change of scheme. Figure updated from [617].

sidering nonperturbatively matched results from lattice QCD, one should bear in mind that the match is to an RI-MOM scheme or to the renormalization-group independent (RGI) mass. Final conversion to the $\overline{\rm MS}$ scheme always entails perturbation theory, because dimensional regulators, and hence their minimal subtractions, are defined only in perturbation theory.

For bottom quarks, light-quark methods do not carry over straightforwardly [86]. Consequently, unquenched determinations of m_b have been limited to one-loop accuracy [620] while nonperturbatively matched determinations remain quenched [621]. They are, thus, not competitive with the other determinations of m_b discussed here. For charm the situation is almost the same, except on the finest lattices with the most-improved actions. Then, as discussed below, it is possible to use moments of the charmonium correlator and continuum $\mathrm{O}(\alpha_s^3)$ perturbation theory [622], or to employ two-loop matching, which is still in progress [623].

Charm mass determinations

Due to the increased precision in the data and in the theoretical description the charm quark mass is also an important input parameter in the analysis of inclusive B decays. Due to its low mass the use of threshold masses is not imperative for the charm quark, and the most common scheme is the $\overline{\rm MS}$ mass. The most precise measurements are obtained from e^+e^- sum rules. More recently, charm mass measurements with small uncertainties are also obtained from inclusive B decays. In the e^+e^- sum rule analyses of Refs. [614, 615] based on fixed order perturbation theory at $\mathrm{O}(\alpha_s^3)$ the results $\overline{m}_c(\overline{m}_c) = 1.295 \pm 0.015$ GeV and 1.286 ± 0.013 GeV, respectively, were obtained. In was, however, pointed out in Ref. [613] based on an $\mathrm{O}(\alpha_s^2)$ analysis that carrying out the analysis in fixed-order perturbation theory might underestimate the theory error due to a discrepancy of the predictions in fixed-order and in contour-improved perturbation theory. In the analysis of Ref. [622] lattice calculations of moments of different current-current correlators, defined in analogy to Eq. (279), and $\mathrm{O}(\alpha_s^3)$ fixed-order computations of these moments were combined and the result $\overline{m}_c(\overline{m}_c) = 1.268 \pm 0.009$ GeV was obtained. This analysis avoids the usually large conversion uncertainties when lattice masses are converted to the $\overline{\rm MS}$ continuum mass, however, it might also suffer from the theory issue pointed out in Ref. [613]. Thus this issue certainly deserves further investigation. More recently, measurement of the charm mass with small uncertainties were also obtained from fits to inclusive B decay spectra. In Refs. [624] and [511] the results $\overline{m}_c(\overline{m}_c) = 1.22 \pm 0.06$ GeV and 1.24 ± 0.09 GeV, respectively, were obtained. These results are compatible with the e^+e^- sum rule analyses.

5.4.3. *Measurements and tests*

The experimental measurements of inclusive charmless semileptonic B decays are dominated by measurements at the $\Upsilon(4S)$ resonance. They fall into two broad categories: so-called "tagged" measurements, in which the companion B meson is fully reconstructed in a hadronic decay mode (see Sec. 3.2.6), which allows an unambiguous association of particles with the semileptonic B decay and the determination of the B decay rest frame; and untagged measurements, in which only a charged lepton and, in some cases, the missing momentum vector for the event are measured.

The untagged measurements tend to have high efficiency but poor signal to noise, and are sensitive to $e^+e^- \to q\overline{q}$ continuum background. The main source of background is

from $b \to c\ell\overline{\nu}$ decays. Existing measurements all require the lepton momentum to exceed 1.9 GeV in the $\Upsilon(4S)$ rest frame. Those analyses that utilize the missing momentum vector generally have improved background rejection, but also have additional uncertainties due to the modeling of sources of missing momentum, such as imperfect track and cluster reconstruction, the response to neutral hadrons and the presence of additional neutrinos. The partial branching fraction in a specified kinematic region is determined in some analyses by a cut-and-count method, and in others by a fit of the measured spectrum to the predicted shapes of the signal and background components. In all cases the fits use coarse binning in regions where the differential distributions are highly sensitive to details of the shape function.

The tagged measurements require the presence of an electron or muon with $E_\ell > 1.0$ GeV amongst the particles not used in the reconstruction of the hadronic B decay. These analyses provide measurements of the kinematic variables of the hadronic system associated with the semileptonic decay, such as m_X and P_+, as well as of q^2. They also provide additional handles for suppressing background, which comes predominantly from the Cabibbo-favored decays $b \to c\ell\overline{\nu}$; these include charge correlations between the fully-reconstructed B meson and the lepton, the veto of Kaons from the semileptonically-decaying $\overline{B}$, and constraints on the charge sum of reconstructed tracks and on the reconstructed missing mass-squared in the event. This power has a cost; the net selection efficiency is $< 1\%$ relative to an untagged analysis, and is not well understood in absolute terms due to incomplete knowledge of the decay modes that contribute to the fully-reconstructed B meson sample. As a result, these analyses measure ratios of branching fractions, usually relative to the inclusive semileptonic partial branching fraction for $E_e > 1.0$ GeV. Examples of measurements from these two categories are shown in Figs. 45 and 46.

The large $b \to c\ell\overline{\nu}$ background is reduced in most analyses by making restrictive kinematic cuts. The measured quantity is then a (sometimes small) fraction of the full $b \to u\ell\overline{\nu}$ rate. As discussed in section 5.4.1, these restrictions introduce sensitivity to the nonperturbative shape function, and significantly increase the sensitivity to m_b. The choice of kinematic cuts is a balance between statistical and systematic uncertainties, which increase as kinematic cuts are relaxed, and theoretical and parametric uncertainties, which decrease under these conditions.

The best determinations to date of various $b \to u\ell\overline{\nu}$ partial rates are given in Tab. 40. The experimental systematic uncertainties affecting all analyses are due to track reconstruction and electron identification. Untagged analyses are relatively more sensitive to bremsstrahlung and radiative corrections. The tagged analyses have additional uncertainties due to the determination of event yields via fits to the invariant mass spectra of fully-reconstructed B candidates. Uncertainties due to the modeling of $b \to c\ell\overline{\nu}$ decays are correlated between measurements, but their magnitude varies depending on the cuts applied and the analysis strategy; most analyses include some data-based evaluation of the level of this background. The leading sources of uncertainty arise from uncertainties in the form factors for $\overline{B} \to D^*\ell\overline{\nu}$ decays and limited knowledge of semileptonic decays to higher mass charm states. The modeling of $b \to u\ell\overline{\nu}$ decays is relevant to all analyses to the extent that the precise mix of exclusive states, which is not well measured, affects the acceptance and reconstruction efficiency. In some analyses an additional sensitivity arises due to the use of a $b \to u\ell\overline{\nu}$ component in a fit to the measured kinematic observable; the shape of this component then affects the result. The sensitivity of each analysis to

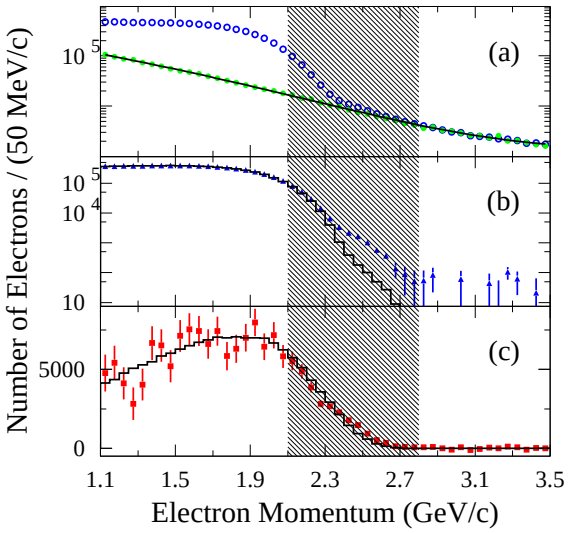

Fig. 45. The inclusive electron energy spectrum [625] from BaBar is shown for (a) on-peak data and q^2 continuum (histogram); (b) data subtracted for non-$B\overline{B}$ contributions (points) and the simulated contribution from B decays other than $b \to u\ell\nu$ (histogram); and (c) background-subtracted data (points) with a model of the $b \to u\ell\nu$ spectrum (histogram).

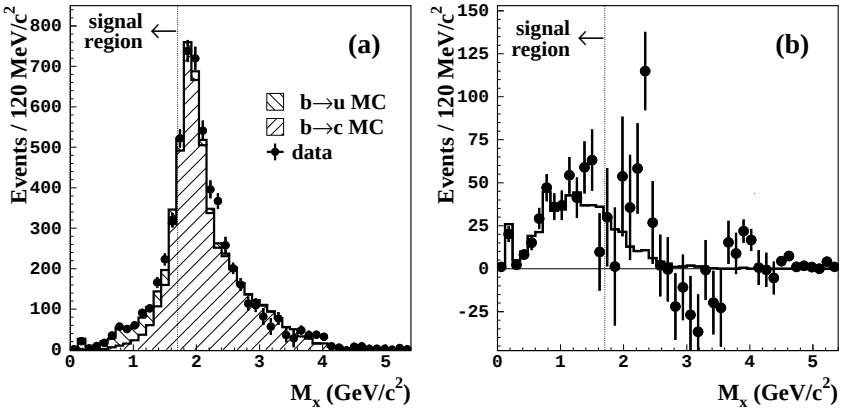

Fig. 46. The hadronic invariant mass spectrum [626] in Belle data (points) is shown in (a) with histograms corresponding to the fitted contributions from $b \to c\ell\nu$ and $b \to u\ell\nu$. After subtracting the expected contribution from $b \to c\ell\nu$, the data (points) are compared to a model $b \to u\ell\nu$ spectrum (histogram) in (b).

weak annihilation varies as a function of the acceptance cuts used.

The larger data sets now available allow less restrictive kinematic cuts that encompass up to 90% or more of the total $b \to u\ell\overline{\nu}$ rate, which significantly reduces the impact of theoretical uncertainties. A preliminary result from Belle [627] uses a multivariate analysis on a tagged sample to measure the full $b \to u\ell\overline{\nu}$ rate for $E_\ell > 1.0$ GeV, and

quotes an experimental uncertainty of 6% on $|V_{ub}|$ and smaller theoretical uncertainties than measurements made in more restrictive kinematic regions. Given the challenging nature of the measurements that include large regions dominated by $b \to c\ell\overline{\nu}$ decays, it is valuable to have results based on complementary techniques. Untagged measurements of the fully inclusive electron spectrum can also be pushed further into the region dominated by $b \to c\ell\overline{\nu}$ decays; there are prospects for pushing down to $E_e > 1.6$ GeV while maintaining experimental errors at the $< 5\%$ level on $|V_{ub}|$.

The availability of measured partial rates in different kinematic regions allows a test of the theoretical predictions, as ratios of partial rates are independent of $|V_{ub}|$. One gauge of the consistency of the measured and predicted partial rates is the χ^2 of the $|V_{ub}|$ average within each theoretical framework. These are given in Tab. 40 In each case a reasonable χ^2 probability is obtained. One can also probe directly the ratios of particular partial rates.

5.4.4. *Determination of* $|V_{ub}|$

As described in the previous section, the large background from the $b \to c\ell\nu$ decays is the chief experimental limitation in the determination of the total branching fraction for $b \to u\ell\nu$ decays.The different analyses are characterized by kinematic cuts applied on: the lepton energy (E_ℓ), the invariant mass of the hadron final state (M_X), the light-cone component of the hadronic final state momentum along the jet direction (P^+), the two dimensional distributions M_X-q^2 and E_ℓ-$s^{\max}$, where q^2 is the squared transferred momentum to the lepton pair and $s^{\max}$ is the maximal ${M_X}^2$ at fixed q^2 and E_ℓ. Given the large variety of analyses performed, and the differences in background rejection cuts used in the different experimental techniques, each analysis measures a partial rate in a different phase-space region. The differential rates needed from the theory to extract $|V_{ub}|$ from the experimental results have been calculated using each theoretical approach. The challenge of averaging the $|V_{ub}|$ measurements from the different analyses is due mainly to the complexity of combining measurements performed with different systematic assumptions and with potentially-correlated systematic uncertainties. Different analyses often use a different decomposition of their systematic uncertainties, so achieving consistent definitions for any potentially correlated contributions requires close coordination with the experiments. Also, some tagged analyses produce partial rates in several kinematic variables, like M_X, M_X-q^2 and P^+, based on the same data sample, so the statistical correlation among the analyses needs to be accounted for. As a result, only those analyses for which the statistical correlation is provided are included in the average. Systematic uncertainties that are uncorrelated with any other sources of uncertainty appearing in an average are lumped with the statistical error. Those systematic errors correlated with at least one other measurement are treated explicitly. Examples of correlated systematic errors include uncertainties in the branching fractions for exclusive $b \to c\ell\nu$ and $b \to u\ell\nu$ decay modes, the tracking, particle identification and luminosity uncertainties for analyses performed in the same experiment, etc.

The theoretical errors for a given calculation are considered completely correlated among all the analyses. No uncertainty is assigned for possible duality violations.

For BLNP, we have considered theoretical errors due to the HQE parameters m_b and μ_π^2, the functional form of the shape function, the subleading shape functions, the variation of the matching scales, and weak annihilation.

Table 40
Partial branching fraction and $|V_{ub}|$ from inclusive $b \to u\ell\overline{\nu}$ measurements. The values determined using different theoretical calculations are given along with the corresponding theory uncertainty; the experimental error on $|V_{ub}|$ is quoted separately. The f_u values are from BLNP. The ADFR values for the endpoint analyses refer to $E_e > 2.3\,\text{GeV}$.

Method	$\Delta\text{BF}\times 10^5$	f_u^{BLNP}	$(\lvert V_{ub}\rvert \times 10^5)$			
(GeV)			BLNP	GGOU	DGE	ADFR
$E_e > 2.1$ [628]	$33 \pm 2 \pm 7$	0.20	$383 \pm 45^{+32}_{-33}$	$368 \pm 43^{+24}_{-38}$	$358 \pm 42^{+28}_{-25}$	$349 \pm 20^{+24}_{-24}$
E_e-q^2 [629]	$44 \pm 4 \pm 4$	0.20	$428 \pm 29^{+36}_{-37}$	not avail.	$404 \pm 27^{+28}_{-30}$	$390 \pm 26^{+23}_{-24}$
m_X-q^2 [630]	$74 \pm 9 \pm 13$	0.35	$423 \pm 45^{+29}_{-30}$	$414 \pm 44^{+33}_{-34}$	$420 \pm 44^{+23}_{-18}$	$397 \pm 42^{+23}_{-23}$
$E_e > 1.9$ [631]	$85 \pm 4 \pm 15$	0.36	$464 \pm 43^{+29}_{-31}$	$453 \pm 42^{+22}_{-30}$	$456 \pm 42^{+28}_{-24}$	$326 \pm 17^{+22}_{-22}$
$E_e > 2.0$ [625]	$57 \pm 4 \pm 5$	0.28	$418 \pm 24^{+29}_{-31}$	$405 \pm 23^{+22}_{-32}$	$406 \pm 27^{+27}_{-26}$	$346 \pm 14^{+24}_{-23}$
$m_X < 1.7$ [626]	$123 \pm 11 \pm 12$	0.69	$390 \pm 26^{+24}_{-26}$	$386 \pm 26^{+18}_{-21}$	$403 \pm 27^{+26}_{-20}$	$393 \pm 26^{+24}_{-24}$
$m_X < 1.55$ [632]	$117 \pm 9 \pm 7$	0.61	$402 \pm 19^{+27}_{-29}$	$398 \pm 19^{+26}_{-28}$	$423 \pm 20^{+21}_{-16}$	$404 \pm 19^{+25}_{-26}$
m_X-q^2 [632]	$77 \pm 8 \pm 7$	0.35	$432 \pm 28^{+29}_{-31}$	$422 \pm 28^{+33}_{-35}$	$426 \pm 28^{+23}_{-19}$	$415 \pm 27^{+24}_{-24}$
$P^+ < 0.66$ [632]	$94 \pm 9 \pm 8$	0.60	$365 \pm 24^{+25}_{-27}$	$343 \pm 22^{+28}_{-27}$	$370 \pm 24^{+31}_{-24}$	$356 \pm 23^{+23}_{-23}$
Average			$406 \pm 15^{+25}_{-27}$	$403 \pm 15^{+20}_{-25}$	$425 \pm 15^{+21}_{-17}$	$384 \pm 13^{+23}_{-20}$
χ^2/d.f.			13.9/8	9.4/7	7.1/8	16.1/8

For DGE, the theoretical errors are due to the effect of the α_s and m_b uncertainties on the prediction of the event fraction and the total rate, weak annihilation and the change and variation of the scale of the matching scheme.

The theoretical errors for GGOU are from the value of α_s, m_b and non-perturbative parameters, higher order perturbative and non-perturbative corrections, the modeling of the q^2 tail, the weak annihilation matrix element and the functional form of the distribution functions at fixed q^2 and $\mu = 1\,\text{GeV}$.

Finally, the theoretical errors considered for ADFR are related to the uncertainties on α_s, $|V_{cb}|$, m_c, and the semileptonic branching fraction. In addition, a different method to extract $|V_{ub}|$ from the semileptonic rate is used, which does not depend on the inclusive semileptonic charm rate, and pole quark masses are employed instead of the $\overline{\text{MS}}$ ones.

The theoretical errors are all characterized by uncertainties whose size and derivative as a function of the rate are different, affecting in different ways the $|V_{ub}|$ averages.

The methodology and the results provided by the Heavy Flavor Averaging Group (HFAG) are presented in this section. To meaningfully combine the different analyses, the central values and errors are rescaled to a common set of input parameters. Specifically for the $b \to u\ell\nu$ analyses, the average B lifetime used for the measurements is (1.573 ± 0.009) ps. Moreover, a rescaling factor to account for final state radiation is applied to the partial branching fractions used for the CLEO and Belle endpoint measurements.

The fit performed to obtain the value of the b quark mass is described in Sec. 5.3. The value of m_b from the global fit in the kinetic scheme is used for all the four frameworks for consistency, translated to the different mass schemes as needed. Note that the models depend strongly on the b quark mass, except for ADFR, so it is very important to use a precise determination of the b quark mass. The results obtained by these methods and the corresponding averages are shown in Tab. 40.

All the methods are consistent with the current data. Fig. 47 compares $|V_{ub}|$ extracted in each experimental analysis using different frameworks. The results of DGE, BLNP, GGOU agree in all cases within theoretical non-parametric errors. We take as our evaluation of $|V_{ub}|$ from inclusive semileptonic decays the arithmetic average of the values and errors of these three determinations to find

$$|V_{ub}| = (411^{+27}_{-28}) \times 10^{-5}. \tag{280}$$

Although in these three cases the χ^2/d.f. reported in Tab. 40 is good, a small WA contribution can marginally improve it. Differences among these theory approaches can be uncovered by additional experimental information on the physical spectra. For instance, the endpoint analyses of *BABAR* and Belle already allow us to extract $|V_{ub}|$ at values of $E_{\rm cut}$ ranging from 1.9 to 2.3 GeV. The two plots in Fig 48 compare $|V_{ub}|$ extracted in the four theory frameworks at various $E_{\rm cut}$. *BABAR*'s more precise results lead to stable values of $|V_{ub}|$ for $E_{\rm cut} \leq 2.2\,{\rm GeV}$ in BLNP and GGOU, but it must be stressed that the shape of the spectrum strongly depends on m_b and no conclusion can presently be drawn.

As mentioned above, the leading shape function can also be measured in $b \to s\gamma$ de-

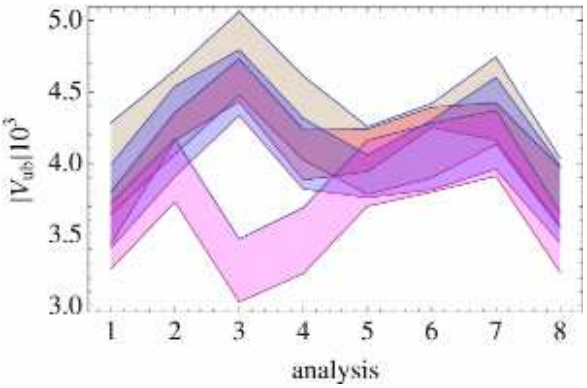

Fig. 47. Comparison of $|V_{ub}|$ extracted from experiment as in Tab. 40 (with the exception of the second line) using the color code introduced in Fig. 43 for the four frameworks. The bands correspond to theory errors depurated of common parametric errors.

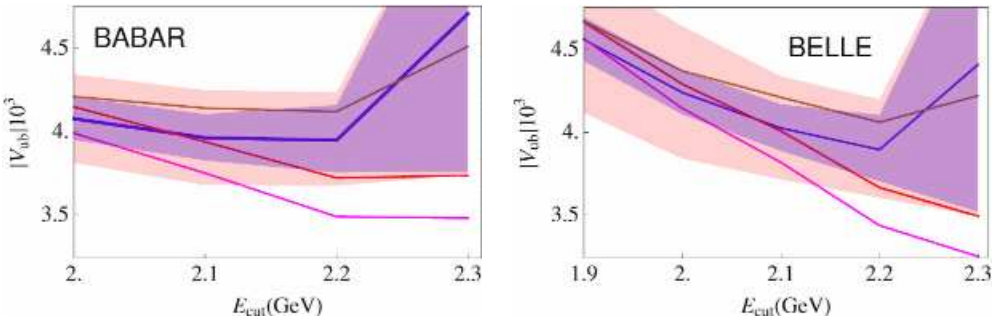

Fig. 48. $|V_{ub}|$ extracted from the lepton endpoint by *BABAR* and Belle as a function of the cut on the lepton energy. The bands correspond to GGOU theory errors depurated of the parametric and WA error and to the latter combined with the experimental one.

cays, and there are prescriptions that relate directly the partial rates for $b \to s\gamma$ and $b \to u\ell\nu$ decays [572, 573, 633, 634], thus avoiding any parametrization of the shape function. However, uncertainties due to the sub-leading shape function remain. The *BABAR* measurement in Ref. [625] has been analyzed by in Ref. [635] to obtain $|V_{ub}| = (4.28 \pm 0.29 \pm 0.29 \pm 0.26 \pm 0.28) \times 10^{-3}$ and $|V_{ub}| = (4.40 \pm 0.30 \pm 0.41 \pm 0.23) \times 10^{-3}$ using calculations from Refs. [634] and [572,573], respectively. These results are consistent with the inclusive $|V_{ub}|$ average.

Another approach is to measure $b \to u\ell\nu$ transitions over the full phase space, thereby reducing theoretical uncertainties. In the first measurement of this type, *BABAR* [636] found $|V_{ub}| = (4.43 \pm 0.45 \pm 0.29) \times 10^{-3}$. A preliminary BELLE measurement of 90% of the full $b \to u\ell\overline{\nu}$ rate quotes $|V_{ub}| \times 10^5$ as follows: [627] $437 \pm 26^{+23}_{-21}$ (BLNP), $446 \pm 26^{+15}_{-16}$ (DGE), $441 \pm 26^{+12}_{-22}$ (GGOU). The last error in each case combines uncertainties from theory and m_b, and is smaller than in less-inclusive measurements.

The inclusive determinations of $|V_{ub}|$ are about $\sim 2\sigma$ larger than those obtained from exclusive $B \to \pi\ell\nu$. The estimated uncertainty on $|V_{ub}|$ from inclusive decays is presently smaller than from exclusive decays. The value of $|V_{ub}|$ predicted from the measured $\sin 2\beta$ value is closer to the exclusive result [637].

The experimental results and theoretical computations presented in this chapter represent an enormous effort, and their distillation into determinations of $|V_{ub}|$ and $|V_{cb}|$ have required close communication among the participants.

6. Rare decays and measurements of $|V_{td}/V_{ts}|$

6.1. *Introduction*

In this chapter we will discuss a particular subclass of B, K, and D meson decays, so-called rare decays. These transitions have been the subject of a considerable number of experimental and theoretical investigations. Being rare processes mediated by loop diagrams in the SM, they all test the flavor structure of the underlying theory at the level of quantum corrections and provide information on the couplings and masses of heavy virtual particles appearing as intermediate states. The resulting sensitivity to non-standard contributions, such as charged Higgs bosons, SUSY particles, Kaluza-Klein (KK) excitations or other exotics arising in extensions of the SM, allows for an indirect observation of NP, a strategy complementary to the direct production of new particles. Whereas the latter option is reserved to the Tevatron and the LHC, the indirect searches performed by CLEO, *BABAR*, Belle, and other low-energy experiments already impose severe restrictions on the parameter space of a plethora of NP scenarios, while they do not exclude the possibility that CDF, D0, or LHC*b* may find significant deviations from the SM expectations in certain rare processes, and thus evidence for NP, prior to a direct discovery of the associated new states by the high-p_T experiments ATLAS and CMS.

Among the rare decays, the radiative $b \to (s, d)\gamma$ transitions play a special role. Proceeding at rates of order $G_F^2\alpha$, they are parametrically enhanced over all other loop-induced, non-radiative rare decays that are proportional to $G_F^2\alpha^2$. The helicity violating $b \to (s, d)\gamma$ amplitudes are dominated by perturbative QCD effects which replace the quadratic GIM suppression present in the electroweak vertex by a logarithmic one. This mild suppression of the QCD corrected amplitudes reduces the sensitivity of these

processes to high-scale physics, but makes them wonderful laboratories to study both perturbative and non-perturbative strong-interaction phenomena. Since the $b \to (s,d)\gamma$ transitions receive sizable contributions from top-quark loops involving the couplings $|V_{ts}|$ or $|V_{td}|$, radiative B-meson decays may be in addition used to test the unitarity of the CKM matrix and to over-constrain the Wolfenstein parameters $\bar{\rho}$ and $\bar{\eta}$. The theoretical and experimental status of both the inclusive $B \to X_{s,d}\gamma$ and exclusive $B \to (K^*, \rho, \omega)\gamma$ modes is reviewed in Sec.s 6.2 and 6.3.

Useful complementary information on the chiral nature of the flavor structure of possible non-standard interactions can be obtained from the studies of purely leptonic and semileptonic rare decays. Tree-level processes like $B \to \tau\nu$ or $B \to D\tau\nu$ provide a unique window on scalar interactions induced by charged Higgs bosons exchange, while loop-induced decays such as $B_{s,d} \to \mu^+\mu^-$ and $B \to (X_s, K, K^*)\ell^+\ell^-$ also probe the magnitude and phase of $SU(2)$ breaking effects arising from Z-penguin and electroweak box amplitudes. The latter contributions lead to a quadratic GIM mechanism in the corresponding decay amplitudes and therefore to an enhanced sensitivity to the scale of possible non-standard interactions. In contrast to the two-body decay modes $B \to \tau\nu$ and $B_{s,d} \to \mu^+\mu^-$, the three-body decays $B \to D\tau\nu$ and $B \to (X_s, K, K^*)\ell^+\ell^-$ allow one to study non-trivial observables beyond the branching fraction by kinematic measurements of the decay products. In the presence of large statistics, expected from the LHC and a future super flavor factor, angular analyses of the $b \to c\tau\nu$ and $b \to s\ell^+\ell^-$ channels will admit model-independent extractions of the coupling constants multiplying the effective interaction vertices. The recent progress achieved in the field of purely leptonic and semileptonic rare decays is summarized in Sec.s 6.4 to 6.6.

Our survey is rounded off in Sec.s 6.7 and 6.8 with concise discussions of various rare K and D meson decays. In the former case, the special role of the $K \to \pi\nu\bar{\nu}$ and $K_L \to \pi^0\ell^+\ell^-$ modes is emphasized, which due to their theoretical cleanness and their enhanced sensitivity to both non-standard flavor and CP violation, are unique tools to discover or, if no deviation is found, to set severe constraints on non-MFV physics where the hard GIM cancellation present in the SM and MFV is not active.

6.2. *Inclusive* $B \to X_{s,d}\gamma$

6.2.1. *Theory of inclusive* $B \to X_{s,d}\gamma$

The inclusive decay $B \to X_s\gamma$ is mediated by a FCNC and is loop suppressed within the SM. Comparing the experimentally measured branching fraction with that obtained in the SM puts constraints on all NP models which alter the strength of FCNCs. These constraints are quite stringent, because theory and experiment show good agreement within errors that amount to roughly 10% on each side. To reach this accuracy on the theory prediction requires to include QCD corrections to NNLO in perturbation theory. In this section we describe the SM calculation of the branching fraction to this order, elaborate on some theoretical subtleties related to experimental cuts on the photon energy, and give examples of the implications for NP models. We also summarize the status of $B \to X_d\gamma$ decays, for which experimental results have recently become available.

The calculation of QCD corrections to the $B \to X_s\gamma$ branching fraction is complicated by the presence of widely separated mass scales, ranging from the mass of the top quark and the electroweak gauge bosons to those of the bottom and charm quarks. A

straightforward expansion in powers of α_s leads to terms of the form $\alpha_s \ln(M_W/m_b) \sim 1$ at each order in perturbation theory, so fixed-order perturbation theory is inappropriate. One uses instead the EFT techniques discussed in Sec. 2.1, to set up an expansion in RG improved perturbation theory. After integrating out the top quark and the electroweak gauge bosons, the leading-power effective Lagrangian reads

$$\mathcal{L}_{\rm eff} = \mathcal{L}_{\rm QCD\times QED} + \frac{G_F}{\sqrt{2}} \sum_{q=u,c} V_{qs}^* V_{qb} \left[C_1(\mu) Q_1^q + C_2(\mu) Q_2^q + \sum_{i=3}^{8} C_i(\mu) Q_i \right] . \quad (281)$$

The Wilson coefficients C_i are obtained at a high scale $\mu_0 \sim M_W$ as a series in α_s by matching Green's functions in the SM with those in the EFT. They are then evolved down to a low scale $\mu \sim m_b$ by means of the RG. Solving the RG equations requires the knowledge of the anomalous dimensions of the operators, and the counting in RG-improved perturbation theory is such that the anomalous dimensions must be known to one order higher in α_s than the matching coefficients themselves. The Wilson coefficients and anomalous dimensions to the accuracy needed for the NNLO calculation were obtained in [27, 28] and [24, 29, 30], respectively.

The final step in the calculation consists in the evaluation of the decay rate $\Gamma(B \to X_s\gamma)_{E_\gamma > E_0}$ using the effective Lagrangian (281). The cut on the photon energy is required to suppress background in the experimental measurements. The rate is calculated in the heavy-quark expansion, which uses that $\Lambda_{\rm QCD} \ll m_b, m_c$. The leading-order result can be written as

$$\Gamma(B \to X_s\gamma)_{E_\gamma > E_0} = \frac{G_F^2 \alpha m_b^5}{32\pi^4} |V_{ts}^* V_{tb}|^2 \sum_{i,j=1}^{8} C_i(\mu) C_j(\mu) G_{ij}(E_0) \,, \quad (282)$$

where we have neglected contributions from $Q_{1,2}^u$, which are CKM suppressed. The functions G_{ij} can be calculated in fixed-order perturbation theory as long as $\Lambda_{\rm QCD} \ll m_b - 2E_0 = \Delta$. In that case, they are obtained from the partonic matrix elements of the $b \to X_s\gamma$ decay. Results at NLO in α_s are known completely [638]. At NNLO, exact results are available only for G_{77} [639–641]. Concerning the NNLO corrections to the other elements G_{ij}, it is reasonable to focus on terms where $i, j \in \{1, 2, 7, 8\}$, since the Wilson coefficients C_{3-6} are small. For those terms, the set of NNLO diagrams generated by inserting a bottom, charm, or light-quark loop into the gluon lines of the NLO diagrams are also known [642–645], with the exception of G_{18} and G_{28}. An estimate of the remaining NNLO corrections was performed in [646], by calculating the full corrections to the elements G_{ij} in the asymptotic limit $m_c \gg m_b/2$, and then interpolating them to three different boundary conditions at $m_c = 0$ to find results at the physical value $m_c \approx m_b/4$.

The results of the various NNLO corrections discussed above lead to the numerical analysis of [647], which found

$$\mathcal{B}(B \to X_s\gamma)_{E_\gamma > 1.6\,\rm GeV} = (3.15 \pm 0.23) \times 10^{-4} \,. \quad (283)$$

The total error was obtained by adding in quadrature the uncertainties from hadronic power corrections (5%), parametric dependences (3%), and the interpolation in the charm quark mass (3%). The most significant unknown stems from hadronic power corrections scaling as $\alpha_s \Lambda_{\rm QCD}/m_b$ [648]. For the (Q_7, Q_8) interference, this involve hadronic matrix elements of four-quark operators with trilocal light-cone structure, which were estimated in the vacuum insertion approximation to change the branching fraction by about

$-[0.3, 3.0]\%$. Corrections of similar or larger size may arise from non-local $\alpha_s \Lambda_{\rm QCD}/m_b$ corrections due to the $(Q_{1,2}, Q_7)$ interference, but these have not yet been estimated.

The fixed-order calculation relies on the parametric counting $\Delta \sim m_b$. However, measurements of the branching fractions are limited to values above a photon energy cut $E_0 = 1.6\,\text{GeV}$, corresponding to $\Delta \sim 1.4\,\text{GeV}$, so it can be argued the counting $\Lambda_{\rm QCD} \ll \Delta \ll m_b$ is more appropriate. In that case, to properly account for the photon energy cut requires to separate contributions from a hard scale $\mu_h \sim m_b$, the soft scale $\mu_s \sim \Delta$, and an intermediate scale $\mu_i \sim \sqrt{m_b \Delta}$. An EFT approach able to separate these scales and to resum large logarithms of their ratios was developed in [649], and extended to NNLO in RG-improved perturbation theory in [650–652]. An approach which used the same factorization of scales, but a different approach to resummation, called dressed gluon exponentiation (DGE), was pursued in [567,569]. Compared to [652], the DGE approach includes additional effects arising from the resummation of running-coupling corrections in the power-suppressed Δ/m_b contributions.

The consistency between the SM prediction (283) and the experimental world average as given in Tab. 41, provides strong constraints on many extensions of the SM. The prime example is the bound on the mass of the charged Higgs boson in the 2HDM of type II (2HDM-II) [653–655] that amounts to $M_{H^+} > 295\,\text{GeV}$ at 95% CL [647], essentially independent of $\tan\beta$. This is much stronger than other available direct and indirect constraints on M_{H^+}.

The inclusive $b \to s\gamma$ transition has also received a lot of attention in SUSY extensions of the SM [147,148,655–657]. In the limit of $M_{\rm SUSY} \gg M_W$, SUSY effects can be absorbed into the coupling constants of local operators in an EFT [135]. The Higgs sector of the MSSM is modified by these non-decoupling corrections and can differ notably from the native 2HDM-II model. Some of the corrections to $B \to X_s\gamma$ in the EFT are enhanced by $\tan\beta$, as $\alpha_s \tan\beta \sim 1$ for $\tan\beta \gg 1$, and need to be resummed if applicable. In the large $\tan\beta$ regime the relative sign of the chargino contribution is given by $-\text{sgn}(A_t\mu)$. For $\text{sgn}(A_t\mu) > 0$, the chargino and charged Higgs boson contributions interfere constructively with the SM amplitude and this tends to rule out large positive values of the product of the trilinear soft SUSY breaking coupling A_t and the Higgsino parameter μ. In the MSSM with generic sources of flavor violation, $B \to X_s\gamma$ implies stringent bounds on the flavor-violating entries in the down-squark mass matrix. In particular, for small and moderate values of $\tan\beta$ all four mass insertions $(\delta^d_{23})_{AB}$ with $A, B = L, R$ except for $(\delta^d_{23})_{RR}$ are determined entirely by $B \to X_s\gamma$ 2.5.2.3. The bounds on $|(\delta^d_{23})_{AB}|$ amount to 4×10^{-1}, 6×10^{-2}, and 2×10^{-2} for the LL, LR, and RL insertion.

In the portion of the SUSY parameter space with inverted scalar mass hierarchy, realized in the class of SUSY GUT scenarios, chargino contributions to $b \to s\gamma$ are strongly enhanced. As a result, SUSY GUT models with third generation Yukawa unification and universal squark and gaugino masses at the GUT scale are unable to accommodate the value of the bottom-quark mass without violating either the constraint from $B \to X_s\gamma$ or $B_s \to \mu^+\mu^-$, unless the scalar masses are pushed into the few TeV range [658]. A potential remedy consists in relaxing Yukawa to b–τ unification, but even then the predictions for $\mathcal{B}(B \to X_s\gamma)$ tend to be at the lower end of the range favored by experiment [659].

In non-SUSY extensions of the SM, contributions due to Kaluza-Klein (KK) excitations in models with universal extra dimensions (UEDs) interfere destructively with the SM amplitude, $B \to X_s\gamma$ leads to powerful bounds on the inverse compactification radius $1/R$ [660,661]. Exclusion limits have been obtained in the five- and six-dimensional case

and amount to $1/R > 600\,\text{GeV}$ [662] and $1/R > 650\,\text{GeV}$ [663] at 95% CL. These bounds exceed the limits that can be derived from any other direct measurement.

The discussion so far dealt with $B \to X_s\gamma$. Recently, a first measurement of the $B \to X_d\gamma$ branching fraction has been presented [664]. Compared to $B \to X_s\gamma$, the nominal theoretical difference is to replace $s \to d$ in the effective Lagrangian (281), in which case the terms proportional to $Q^u_{1,2}$ are no longer CKM suppressed. The implications of this have been studied in [665], where it was pointed out that the ratio $\mathcal{B}(B \to X_s\gamma)/\mathcal{B}(B \to X_d\gamma)$ can be calculated with reduced theoretical uncertainty. This was used along with the experimental results to determine $|V_{td}/V_{ts}|$ in [664]. A possible subtlety is that in [665] the total branching fraction has been calculated, whereas the experimental measurements are limited to the region $M_{X_s} < 1.8\,\text{GeV}$ of hadronic invariant masses, where "shape-function" effects are expected to be important.

6.2.2. *Experimental methods and status of $B \to X_{s,d}\gamma$*

The analysis of the inclusive $B \to X_s\gamma$ decay at the B factories is rather complicated. The quantities to be measured are the differential decay rate, i.e., the photon energy spectrum as well as the total branching fraction. There are three methods for the inclusive analyses: fully inclusive, semi-inclusive, and B recoil.

The idea of the fully inclusive method is to subtract the photon energy spectrum of the on-resonant $e^+e^- \to \Upsilon(4S) \to B\overline{B}$ events by that of the continuum $e^+e^- \to q\overline{q}$ events. This method is free from the uncertainty of the final state, and can exploit the whole available statistics. However, the signal purity is very low, and the background suppression is a key issue. The photon energy is obtained in the $\Upsilon(4S)$ rest frame and not in the B rest frame, since the momentum of the B is unknown.

Panel (a) of Fig. 49 shows the photon energy spectrum after suppressing the continuum background, using event topology, and vetoing high energy photons from π^0 or η using the invariant mass of the candidate high energy photon, and of any other photons in the event. The largest background is from the continuum events, and is subtracted using the continuum data. This subtraction requires correction due to small center-of-mass energy difference for the event selection efficiency, photon energy, and photon multiplicity between the on-resonant and continuum sample. As shown in panel (b) of Fig. 49, the subtracted spectrum still suffers from huge backgrounds from B decays, which are subtracted using the MC sample. Here, the MC sample needs to be calibrated with data using control samples to reproduce the yields of π^0, η, etc. The final photon spectrum, obtained with the prescribed procedure, for $b \to s\gamma$ events, is shown in panel (c) of Fig. 49. It can be seen that the errors increase rapidly for photon energies below 2 GeV due to the very large continuum background in that region. For this reason all measurements of the branching ratio introduce a cutoff E_γ^{min} and then extrapolate to get $\mathcal{B}(E_\gamma > 1.6\,\text{GeV})$ which is compared to the theory prediction. Measurements by CLEO, BABAR, and Belle using the fully inclusive method are listed in Tab. 41. The results are consistent with the SM expectation (283).

In the semi-inclusive method, also called "sum-of-exclusive" method, the reconstruction of the $B \to X_s\gamma$ signal is performed by the sum of certain hadronic final states X_s that are exclusively reconstructed. Typically, X_s is reconstructed from one Kaon plus up to four pions including up to one or two neutral pions, but also modes with three Kaons or an η are used. The advantage of this method is a better signal purity compared

Fig. 49. (a) On-resonant data (open circle), scaled continuum data (open square) and continuum background subtracted (filled circle) photon energy spectrum. (b) The spectra of photons from B decays (MC). (c) The extracted photon spectrum for $B \to X_s\gamma$. The plots are taken from [666].

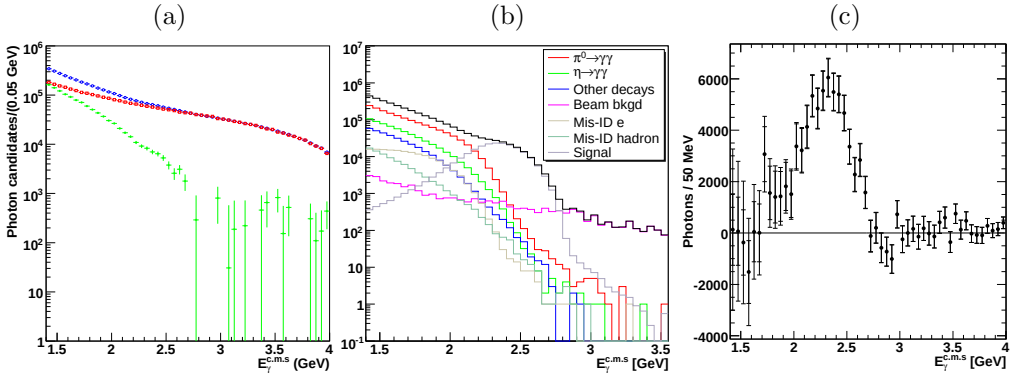

to the fully inclusive method. The background suppression is still important, but the detailed correction of the MC samples and the precise determination of the luminosity of the off-resonance sample, used in the fully inclusive method, are not necessary. Another advantage is that the photon energy in the B rest frame can be measured from the mass of the X_s system. However, this method can reconstruct only a part of the X_s system, and suffers from the large uncertainty in the fraction of the total width present in the exclusive modes that are reconstructed. The measurements from *BABAR* and Belle are listed in Tab. 41.

It is also possible to measure the CP asymmetry, $A_{\rm CP}$, of $B \to X_s\gamma$ with the semi-inclusive method, since most of the final states provide flavor information. In the SM, $A_{\rm CP}$ is predicted to be less than 1% [667,668], but some models beyond the SM predict much larger values of $A_{\rm CP}$ [667–670]. The measurement of *BABAR* leads to $A_{\rm CP} = -0.010 \pm 0.030_{\rm stat} \pm 0.014_{\rm syst}$ for $M_{X_s} < 2.8\,{\rm GeV}$ [671] while Belle finds $A_{\rm CP} = 0.002 \pm 0.050_{\rm stat} \pm 0.030_{\rm syst}$ for $M_{X_s} < 2.1\,{\rm GeV}$ [672].

BABAR recently reported a first measurement of $B \to X_d\gamma$ using the semi-inclusive approach [664]. In this analysis, seven exclusive final states in the range $0.6\,{\rm GeV} < M_{X_d} < 1.8\,{\rm GeV}$ are reconstructed. Although the analysis suffers from a large background from continuum events, mis-reconstructed $B \to X_s\gamma$ events, and an large uncertainty in missing modes, *BABAR* obtained the branching fraction in this mass range to be $(7.2 \pm 2.7_{\rm stat} \pm 2.3_{\rm syst}) \times 10^{-6}$.

In the B recoil method, one of the two produced B mesons is fully reconstructed in a hadronic mode, and an isolated photon is identified in the rest of the event. This method provides a very clean signal, and one obtains simultaneously the flavor, charge, and momentum of the B meson. The drawback is a very low efficiency. In the analysis with 210 fb^{-1} by *BABAR* [673], 6.8×10^5 B mesons are tagged and 119 ± 27 signal events are found. The result is limited by statistics and is not competitive with the other methods listed in Tab. 41. However, this method is promising for a future super flavor factory.

Table 41
Inclusive branching fractions of radiative B decays. $E_\gamma^{\rm min}$ and $\mathcal{B}(E_\gamma > E_\gamma^{\rm min})$ are the minimum energy and branching fraction reported in the paper, while $\mathcal{B}(E_\gamma > 1.6\,{\rm GeV})$ is the rescaled branching fraction. The size of the data sets is given in units of fb^{-1} and the branching fractions are in units of 10^{-6}.

Method	Data set	$E_\gamma^{\rm min}$	$\mathcal{B}(E_\gamma > E_\gamma^{\rm min})$	$\mathcal{B}(E_\gamma > 1.6\,{\rm GeV})$	Ref.
CLEO fully inclusive	9	2.0	$305 \pm 41 \pm 26$	329 ± 53	[557]
BABAR fully inclusive	82	1.9	$367 \pm 29 \pm 34 \pm 29$	392 ± 56	[553]
BABAR semi-inclusive	82	1.9	$327 \pm 18\,^{+55}_{-40}\,^{+4}_{-9}$	349 ± 57	[554]
BABAR B-recoil	210	1.9	$366 \pm 85 \pm 60$	391 ± 111	[673]
Belle semi-inclusive	6	2.24	—	369 ± 94	[674]
Belle fully inclusive	605	1.7	$332 \pm 16 \pm 37 \pm 1$	337 ± 43	[666]
Average	–	–	–	$352 \pm 23 \pm 9$	
Theory prediction	–	–	–	315 ± 23	[647]

6.2.3. *Theory of photon energy spectrum and moments*

The basic motivation to study the photon energy spectrum in $B \to X_s\gamma$ is the fact that backgrounds prohibit a measurement of the branching fraction for non-hard photons. Despite significant progress, the current measurements still have sizable errors below $E_\gamma \sim 2\,{\rm GeV}$. Raising the photon energy cut $E_\gamma > E_0$ significantly increases the accuracy of the measurements, but requires an larger extrapolation to the "total" width, thereby introducing some model dependence.

In contrast to the branching ratio, the photon energy spectrum is largely insensitive to NP [675]. It can thus be used for precision studies of perturbative and non-perturbative strong-interaction effects. In particular, the measured spectrum allows to extract the value of the mass of the bottom quark from its first moment $\langle E_\gamma \rangle \sim m_b/2$, its average kinetic energy μ_π^2 from its second moment, and gives direct information on the importance of the B meson "shape function" for different values of E_0. The measurements of m_b and μ_π^2 using $B \to X_s\gamma$ are complementary to the determinations using the inclusive moments of $B \to X_c\ell\bar{\nu}$. Fits to the measured moments [511, 555] based on the 1S [510] and the kinetic scheme [512,566] have been very useful, and constitute today an important input to the determination of $|V_{ub}|$ [560].

The calculation of the $B \to X_s\gamma$ photon spectrum is a complex theoretical problem. First of all, there is no unique way to define the total $B \to X_s\gamma$ width owing to both the soft divergence of the (Q_7, Q_8) interference term and the possibility of secondary photon emission in non-radiative $b \to s$ decays. Furthermore, the local OPE in $B \to X_s\gamma$ does not apply to contributions from operators other than Q_7, in which the photon couples to light quarks [676, 677]. In the case of the (Q_7, Q_8) interference, the resulting $\mathcal{O}(\alpha_s\Lambda_{\rm QCD}/m_b)$ corrections to the total rate have been estimated in [648]. A detailed study of the impact of these and similar enhanced non-local power-corrections on the photon energy spectrum is in progress [].

Even in the case of the Q_7 self-interference, where an local OPE for the total width exists, the calculation of the spectrum is highly non-trivial. The main difficulty arises due to the jet-like structure of the decay process, where an energetic hadronic system, $E_{X_s} \sim E_\gamma \sim \mathcal{O}(m_b/2)$, with a relatively small mass, $\mathcal{O}(\sqrt{m_b\Lambda_{\rm QCD}})$, recoils against the photon.

In the endpoint region, the $B \to X_s\gamma$ spectrum can be computed as a convolution between a perturbatively calculable coefficient function and the quark distribution function $S(l^+)$. While the non-perturbative content of $S(l^+)$ is in principle clear, a calculation by existing non-perturbative methods is not possible, so that in practice one must model the function $S(l^+)$ using a suitable parametrization. Information on the corresponding model parameters can be obtained from the experimental measurements of the first few moments of inclusive decay spectra, which in turn determine the moments of the "shape function".

Significant progress has been made since the first dedicated calculation of the spectrum [675]. The state-of-the-art calculations are based on the factorization picture of inclusive decays near the endpoint [678]. Consider for example the measurement of the partial $B \to X_s\gamma$ width with $E_\gamma > E_0$. The key observation is that near the endpoint, i.e., for $\Delta \ll m_b$, and to leading order in $\Lambda_{\rm QCD}/m_b$ there are three separate dynamical processes which are quantum mechanically incoherent. A soft subprocess, S, which is characterized by soft gluons with momenta of order $\Delta = m_b - 2E_\gamma$, a jet subprocess, J, summing up collinear hard radiation with virtualities of order of $\sqrt{m_b\Delta}$, and a hard function, H, associated with virtual gluons with momenta of order m_b. The factorized decay width takes the form

$$\Gamma(\Delta) = H(m_b)J(\sqrt{m_b\Delta}) \otimes S(\Delta) \,+\, \mathcal{O}(\Lambda_{\rm QCD}/m_b)\,. \tag{284}$$

This factorization formula, originally proposed in [678], was rederived in the framework of SCET [41, 530]. It serves as a basis for a range of approaches, facilitating the resummation of large Sudakov logarithms associated with the double hierarchy of scales $m_b \gg \sqrt{m_b\Delta} \gg \Delta$. This includes DGE [567–569, 588, 679] and a multi-scale OPE (MSOPE) [650–652, 680].

Using SCET, it is possible to systematically define additional non-local operators that contribute to the decay spectra at subleading powers of $\Lambda_{\rm QCD}/m_b$ [681–683]. Unfortunately, the corresponding subleading "shape functions" are not well constrained since starting at $\mathcal{O}(\Lambda_{\rm QCD}/m_b)$ the number of functions exceeds the number of observables. Thus, estimating non-perturbative corrections to (284) remains a notoriously difficult task.

While (284) only holds for $\Delta \ll m_b$, its use may vary depending on the extent at which effects on the lowest scale are described by perturbation theory. If $\Delta \gg \Lambda_{\rm QCD}$ it is useful to compute the quark distribution function perturbatively [588,650] rather than to parametrize it. In contrast, when $\Delta \sim \Lambda_{\rm QCD}$ this function becomes non-perturbative. Two different approaches based on SCET have been developed to deal with these two regimes, MSOPE for the former and a formalism based on parametrization of the shape functions for the latter [530]. In contrast, DGE, which is at the outset derived in the regime $\Delta \gg \Lambda_{\rm QCD}$, has been extended to the regime $\Delta \sim \Lambda_{\rm QCD}$ by constraining the Borel transform of $S(l^+)$ and then parametrizing non-perturbative corrections depending on the soft scale in moment space.

Beyond the conceptual issues discussed so far, much progress has been made on the calculation side. In particular, the Q_7 self-interference part of the spectrum has been computed to NNLO accuracy [639, 684]. In addition, all the necessary ingredients for Sudakov resummation at NNLO of both the soft and the jet function are in place [588,650, 651,685,686]. Some additional higher-order corrections are known, in particular, running-coupling corrections [569,642,679], but unfortunately complete NNLO calculations of the

$(Q_7, Q_{1,2})$ and $(Q_{1,2}, Q_{1,2})$ interference terms are not available at present.

Systematic NNLO analysis of the $B \to X_s\gamma$ branching fraction and spectrum have been performed by three groups [569, 647, 652]. While the first analysis works at fixed-order in perturbation theory, the latter two articles are based on Sudakov resummation utilizing (284). The MSOPE result has been combined with the fixed-order predictions by computing the fraction of events $1-T$ that lies in the range $E_0 = [1.0, 1.6]\,\text{GeV}$. The analysis [652] finds $1-T = 0.07^{+0.03}_{-0.05\,\text{pert}} \pm 0.02_{\text{hard}} \pm 0.02_{\text{pars}}$, where the individual errors are perturbative, hadronic, and parametric. The quoted value is almost twice as large as the estimate $1-T = 0.04 \pm 0.01_{\text{pert}}$ obtained in fixed-order perturbation theory [647]. In contrast, in the DGE approach [569] one finds a much thinner tail of the photon energy spectrum at NNLO, $1-T = 0.016 \pm 0.003_{\text{pert}}$, which is consistent with the result obtained in fixed order perturbation theory.

Given the common theoretical basis for the resummation, the opposite conclusions drawn in [652] and [569] may look surprising. The main qualitative differences between the two calculations are as follows. First, the result [652] is plagued by a significant additional theoretical error related to low-scale, $\mu \sim \Delta$, perturbative corrections, indicating the presence of large subleading logarithmic corrections to the soft function. In contrast, the DGE approach [569] supplements Sudakov resummation with internal resummation of running-coupling corrections, which is necessary to cure the endpoint divergence of the fixed-logarithmic-accuracy expansion. Second, the MSOPE approach [652] identified a high sensitivity to the matching procedure, dealing with terms that are suppressed by powers of Δ/m_b for $E_\gamma \sim m_b/2$, but are not small away from the endpoint [569, 687]. The analysis [569], on the other hand, has used additional information on the small E_γ behavior of the different interference terms, which is known to all orders in perturbation theory, to extend the range of applicability of resummation to the tail region.

In conclusion, progress on the theory front, in particular in factorization and resummation of perturbation theory, and in explicit higher order calculations, significantly improved our knowledge of the photon energy spectrum in $B \to X_s\gamma$. Nevertheless, uncertainties of both perturbative and non-perturbative origin remain, which deserve further theoretical investigations.

6.2.4. *Experimental results of photon energy spectrum and moments*

In the case of the semi-inclusive and B recoil methods, the photon energy spectrum can be measured directly in the B meson rest frame. The semi-inclusive method suffers from large uncertainty from the hadronic system, while the B recoil method requires much more statistics. Presently, precise measurements of the photon energy spectrum are therefore provided only with the fully inclusive method.

In the fully inclusive method, it is not possible to know the momentum of the B meson for each photon, so only the photon energy distribution in the $\Upsilon(4S)$ rest frame is directly measurable. As a result the raw photon energy spectrum has to be corrected not only for the photon detection efficiency of the calorimeter and other selection efficiency, but also for the smearing effect between the B meson and the $\Upsilon(4S)$ frame. The energy spectrum is also smeared by the response of the calorimeter. The correction due to smearing, which is also referred to as "unfolding", depends on the signal models and its parameters. CLEO [557] uses a signal model by Ali and Greub [688], while a model by Kagan and Neubert [675] is used by both *BABAR* [553] and Belle [666]. The latter collaboration also

considers other models [559, 569, 572, 586].

The photon energy spectrum is often represented in terms of the first two moments, i.e., mean and variance, above a certain energy threshold. For example, *BABAR* [553] obtains $\langle E_\gamma \rangle = (2.346 \pm 0.032_{\rm stat} \pm 0.011_{\rm syst})\,{\rm GeV}$ and $\langle E_\gamma^2 \rangle - \langle E_\gamma \rangle^2 = (0.0226 \pm 0.0066_{\rm stat} \pm 0.0020_{\rm syst})\,{\rm GeV}^2$ for $E_\gamma > 2.0\,{\rm GeV}$, while Belle [666] $\langle E_\gamma \rangle = (2.281 \pm 0.032_{\rm stat} \pm 0.053_{\rm syst} \pm 0.002_{\rm boos})\,{\rm GeV}$ and $\langle E_\gamma^2 \rangle - \langle E_\gamma \rangle^2 = (0.0396 \pm 0.0156_{\rm stat} \pm 0.0214_{\rm syst} \pm 0.0012_{\rm boos})\,{\rm GeV}^2$ for $E_\gamma > 1.7\,{\rm GeV}$, where the last errors in the Belle measurements are from the boost correction. In these measurements, branching fractions and moments with different photon energy thresholds are also obtained. Parameters useful for the $|V_{cb}|$ and $|V_{ub}|$ determinations such as the bottom-quark mass m_b or its mean momentum squared μ_π^2 can be obtained by fitting the theoretical predictions to the measured moments. This is discussed in detail in Sec. 5.3.

One of the challenges in the measurement is to lower the energy threshold of the photon. The contamination of the background from B decays becomes more severe rapidly, as the threshold is lowered, especially in the region below 2 GeV. So far, with growing data sets, measurements with lower photon energy threshold have been performed. However, the results with lower cut on the photon energy tend to give larger systematic, and model errors. This raises the question which threshold value is optimal to determine $|V_{cb}|$ and $|V_{ub}|$. Another issue is that the uncertainty of m_b is included in the signal model error for the measurements of the moments, but the measured moments themselves are used to determined m_b. The latter issue could probably be avoided by performing a simultaneous determination of the parameters in question from the raw photon energy spectrum.

6.3. *Exclusive $B \to V\gamma$ decays*

6.3.1. *Theory of exclusive $B \to V\gamma$ decays*

The exclusive decays $B_{(s)} \to V\gamma$, with $V \in \{K^*, \rho, \omega, \phi\}$, are mediated by FCNCs and thus test the flavor sector in and beyond the SM. After matching onto the effective Lagrangian (281), the main theoretical challenge is to evaluate the hadronic matrix elements of the operators Q_{1-8}. QCDF is a model-independent approach based on the heavy-quark expansion [689–691], and the bulk of this section is devoted to describing this formalism. At the end of the section we briefly mention the "perturbative QCD" (pQCD) approach [692–694]. Although the hadronic uncertainties inherent to the exclusive decay modes are a barrier to precise predictions, we shall see that the exclusive decays nonetheless provide valuable information on the CKM elements $|V_{td}/V_{ts}|$ and allow to put constraints on the chiral structure of possible non-standard interactions.

QCDF is the statement that in the heavy-quark limit the hadronic matrix element of each operator in the effective Lagrangian can be written in the form

$$\langle V\gamma\,|Q_i|\,\bar{B}\rangle = T_i^{\rm I}\,F^{B\to V_\perp} + \int_0^\infty \frac{d\omega}{\omega}\phi_+^B(\omega)\int_0^1 du\,\phi_\perp^V(u)T_i^{\rm II}(\omega,u) + \mathcal{O}\left(\frac{\Lambda_{\rm QCD}}{m_b}\right). \quad (285)$$

The form factor $F^{B\to V_\perp}$ and the light-cone distribution amplitudes (LCDAs) ϕ_+^B, $\phi_\perp^V$ are non-perturbative, universal objects. The hard-scattering kernels $T_i^{\rm I,II}$ can be calculated as a perturbative series in α_s. The elements $T_i^{\rm I}$ ($T_i^{\rm II}$) are referred to as "vertex corrections" ("spectator corrections"). The hard-scattering kernels have been known completely at

order α_s (NLO) for some time [689–691], and recently some of the α_s^2 (NNLO) corrections have also been calculated [695].

An all orders proof of the QCDF formula (285) was performed in [696], using the technology of SCET. The EFT approach also allows to separate physics from the two perturbative scales m_b and $\sqrt{m_b \Lambda_{\rm QCD}}$, and to resum perturbative logarithms of their ratio using the RG. The numerical impact of this resummation has been investigated in [695, 696].

The predictive power of QCDF is limited by hadronic uncertainties related to the LCDAs and QCD form factors, as well as by power corrections in $\Lambda_{\rm QCD}/m_b$. For instance, the form factors $F^{B\to V_\perp}$ can be calculated with QCD sum rules to an accuracy of about 15%, which implies an uncertainty of roughly 30% on the $B \to V\gamma$ branching fractions. More troublesome is the issue of power corrections. A naive dimensional estimate indicates that these should be on the order of 10%, but this statement is hard to quantify. Since SCET is an effective theory which sets up a systematic expansion in α_s and $\Lambda_{\rm QCD}/m_b$, it has the potential to extend the QCDF formalism to subleading order in $\Lambda_{\rm QCD}/m_b$. However, in cases where power corrections have been calculated, the convolution integrals over momentum fractions do not always converge [697]. These "endpoint divergences" are at present a principle limitation on the entire formalism.

Although a comprehensive theory of power corrections is lacking, it is nonetheless possible to estimate some of the corrections which are believed to be large, or which play an important role in phenomenological applications. One such correction stems from the annihilation topology, which has been shown to factorize at leading order in α_s [690]. Annihilation gives the leading contribution to isospin asymmetries, and is also important for $B^\pm \to \rho^\pm\gamma$ branching fractions, where it is enhanced by a factor of $C_{1,2}/C_7$. The $\Lambda_{\rm QCD}/m_b$ corrections from annihilation have been included in all recent numerical studies [446, 698–700], and part of the $\Lambda_{\rm QCD}^2/m_b^2$ correction, so-called "long-distance photon emission", has been calculated in [446]. Some additional $\alpha_s\Lambda_{\rm QCD}/m_b$ corrections from annihilation and spectator scattering needed to calculate isospin asymmetries were dealt with in [697]. Corrections from three-particle Fock states in the B and V mesons, most significant for indirect CP asymmetries, were estimated in [446].

We now give numerical results for some key observables in $B \to V\gamma$ decays, and compare them with experiment. The ratio of $B \to K^*\gamma$ and $B \to \rho\gamma$ branching fractions is useful for the determination of $|V_{td}/V_{ts}|$. To understand why this is the case, consider the expression

$$\frac{\mathcal{B}(B^0 \to \rho^0\gamma)}{\mathcal{B}(B^0 \to K^{*0}\gamma)} = \frac{1}{2\xi^2}\left|\frac{V_{td}}{V_{ts}}\right|^2 \left[1 - 2R_{ut}\epsilon_0 \cos\alpha \cos\theta_0 + R_{ut}^2\epsilon_0^2\right]. \tag{286}$$

Analogous expressions hold for charged decays and $B \to \omega\gamma$. The quantities ϵ_0 and $\cos\theta_0$ can be calculated in QCDF, and vanish at leading order in $\Lambda_{\rm QCD}/m_b$ and α_s. Beyond leading order they are approximately 10%, but the factor inside the brackets remains close to unity, due to a additional suppression from the CKM factors $\cos\alpha \sim 0.1$ and $R_{ut} = |(V_{ud}V_{ub})/(V_{td}V_{tb})| \sim 0.5$. Therefore, by far, the dominant theoretical uncertainty is related to the form factor ratio $\xi = F^{B\to K^*}/F^{B\to\rho}$. The ratio of form factors can be calculated with better accuracy than the form factors themselves and has been estimated using light-cone sum rules to be 1.17 ± 0.09 [446]. Extracting $|V_{td}/V_{ts}|$ from (286) and averaging with determinations from the charged mode and the $B \to \omega\gamma$ decay yields the results given in Sec. 6.3.3.

Direct and isospin CP asymmetries, $A_{\rm CP}$ and $A_{\rm I}$, provide useful tests of the SM and the QCDF approach. In QCDF, direct CP asymmetries in $B \to V\gamma$ decays are suppressed by at least one power of α_s and isospin asymmetries by at least one power of $\Lambda_{\rm QCD}/m_b$, so both of these are predicted to be small. We first consider $B \to \rho\gamma$ decays. In that case the QCDF prediction for the direct CP asymmetry is about -10% [699, 700] and agrees well with the recent experimental results quoted in Sec. 6.3.2. The QCDF result for $A_{\rm I}$ depends strongly on $\cos\alpha$, but in the preferred range of α near 90° is roughly between zero and -10% [699,700]. Values closer to the central experimental value can be generated if one assumes a large contribution from non-perturbative charming penguins [701], which would be in contradiction with the power counting of QCDF. Given the large experimental errors it is not yet possible to draw a definite conclusion. For $B \to K^*\gamma$ decays, the direct CP asymmetries are strongly suppressed due to the CKM structure of the decay amplitude. The isospin asymmetry comes out to be $(3 \pm 4)\%$ [560], which is compatible with predictions from QCDF [446, 697–699]. This isospin asymmetry is very sensitive to the magnitude and sign of the ratio C_6/C_7.

Finally, we consider indirect CP asymmetries. In the SM, these are suppressed by powers of $m_{s,d}/m_b$ or arise from the presence of three-particle Fock states in the B and V mesons, which are $\Lambda_{\rm QCD}/m_b$ corrections to the leading order factorization formula [702]. A calculation performed in [446] indicates that the corrections from three-particle Fock states are much smaller than the generic size of a $\Lambda_{\rm QCD}/m_b$ power correction, so that the indirect CP asymmetries are estimated to be below the 3% level for all decay modes. The asymmetries could be much larger in extensions of the SM with altered chiral structure such as left-right symmetric models [446]. The current experimental results are within their large errors consistent with zero [703, 704].

A modified implementation of the heavy-quark expansion is provided by the pQCD approach [692–694]. The main difference compared to QCDF is that pQCD attempts to calculate the QCD form factors perturbatively. The assumptions required for such a treatment have been questioned in [705]. However, numerical results for most observables are in rough agreement with those from QCDF. A recent comparison between the branching fractions, isospin and CP asymmetries obtained within the two theoretical setups can be found in [446].

6.3.2. *Experimental results for exclusive $B \to V\gamma$ decays*

The exclusive reconstruction of radiative $B \to V\gamma$ decays or other multi-body decays such as $B \to K\pi\gamma$ is usually straightforward. The dominant background originates from the continuum process $e^+e^- \to q\overline{q}$, which is experimentally suppressed by means of event shape variables.

Vetoing high energetic photons from π^0 or η is also useful. The background from B decays is small in the low hadronic mass region, but becomes larger for higher hadronic mass, i.e., lower photon energy. Therefore, in the analysis of the exclusive final states with more than two particles, it is necessary to apply a cut on the hadronic mass, which is typically around 2 to 2.5 GeV. The contribution of the cross-feed from radiative B decays to other final states also becomes a significant background in some modes.

The first observation of radiative B decays has been established in 1993 by CLEO [706] by a measurement of the $B \to K^*\gamma$ mode. They found 13 events in the signal region in a data sample of 1.4 fb^{-1}, and measured the branching fraction $\mathcal{B}(B \to K^*\gamma) =$

Table 42
Measured branching fractions of radiative B decays. Only modes with evidence are listed. The size of the data sets is given in the units of fb^{-1}.

	Belle			*BABAR*		
Mode	$\mathcal{B}$ (10^{-6})	Data set	Ref.	$\mathcal{B}$ (10^{-6})	Data set	Ref.
$B^0 \to K^{*0}\gamma$	$40.1 \pm 2.1 \pm 1.7$	78	[707]	$45.8 \pm 1.0 \pm 1.6$	347	[708]
$B^0 \to K^{*+}\gamma$	$42.5 \pm 3.1 \pm 2.4$	78	[707]	$47.3 \pm 1.5 \pm 1.7$	347	[708]
$B^+ \to K_1(1270)^+\gamma$	$43 \pm 9 \pm 9$	140	[709]	–	–	–
$B^0 \to K_2^*(1430)^0\gamma$	$13 \pm 5 \pm 1$	29	[710]	$12.2 \pm 2.5 \pm 1.0$	81	[711]
$B^+ \to K_2^*(1430)^+\gamma$	–	–	–	$14.5 \pm 4.0 \pm 1.5$	81	[711]
$B^+ \to K^+\eta\gamma$	$8.4 \pm 1.5\,^{+1.2}_{-0.9}$	253	[712]	$7.7 \pm 1.0 \pm 0.4$	423	[713]
$B^0 \to K^0\eta\gamma$	$8.7\,^{+3.1\,+1.9}_{-2.7\,-1.6}$	253	[712]	$7.1\,^{+2.1}_{-2.0} \pm 0.4$	423	[713]
$B^+ \to K^+\eta'\gamma$	$3.2\,^{+1.2}_{-1.1} \pm 0.3$	605	[714]	–	–	–
$B^+ \to K^+\phi\gamma$	$3.4 \pm 0.9 \pm 0.4$	90	[715]	$3.5 \pm 0.6 \pm 0.4$	211	[716]
$B^+ \to p\overline{\Lambda}\gamma$	$2.45\,^{+0.44}_{-0.38} \pm 0.22$	414	[717]	–	–	–
$B^+ \to K^+\pi^-\pi^+\gamma$	$25.0 \pm 1.8 \pm 2.2$	140	[709]	$29.5 \pm 1.3 \pm 2.0$	211	[718]
$B^+ \to K^0\pi^+\pi^0\gamma$	–	–	–	$45.6 \pm 4.2 \pm 3.1$	211	[718]
$B^0 \to K^0\pi^+\pi^-\gamma$	$24.0 \pm 4.0 \pm 3.0$	140	[709]	$18.5 \pm 2.1 \pm 1.2$	211	[718]
$B^0 \to K^+\pi^-\pi^0\gamma$	–	–	–	$40.7 \pm 2.2 \pm 3.1$	211	[718]
$B_s^0 \to \phi\gamma$	$57\,^{+18\,+12}_{-15\,-11}$	24	[719]	–	–	–
$B^+ \to \rho^+\gamma$	$0.87\,^{+0.29\,+0.09}_{-0.27\,-0.11}$	605	[720]	$1.20\,^{+0.42}_{-0.37} \pm 0.20$	423	[721]
$B^0 \to \rho^0\gamma$	$0.78\,^{+0.17\,+0.09}_{-0.16\,-0.10}$	605	[720]	$0.97\,^{+0.24}_{-0.22} \pm 0.06$	423	[721]
$B^0 \to \omega\gamma$	$0.40\,^{+0.19}_{-0.17} \pm 0.13$	605	[720]	$0.50\,^{+0.27}_{-0.23} \pm 0.09$	423	[721]

$(45 \pm 15_{\text{stat}} \pm 3_{\text{syst}}) \times 10^{-6}$. Now, the measurements by *BABAR* and Belle are based on data set that are more than 100 times larger and start to be dominated by systematics, as can be seen from Tab. 42. Unfortunately, it is not easy to predict the branching fractions of exclusive modes precisely, and hence it is difficult to compare the results with theory.

What can be predicted more precisely are the direct CP or charge asymmetry A_{CP} and the isospin asymmetry A_{I}. They are defined as

$$\begin{aligned} A_{\text{CP}} &= \frac{\Gamma(\overline{B} \to \overline{K}^*\gamma) - \Gamma(B \to K^*\gamma)}{\Gamma(\overline{B} \to \overline{K}^*\gamma) + \Gamma(B \to K^*\gamma)}\,, \\ A_{\text{I}} &= \frac{\Gamma(B^0 \to K^{*0}\gamma) - \Gamma(B^+ \to K^{*+}\gamma)}{\Gamma(B^0 \to K^{*0}\gamma) + \Gamma(B^+ \to K^{*+}\gamma)}\,, \end{aligned} \tag{287}$$

and similarly for the other decay modes. In the case of $B \to K^*\gamma$, *BABAR* obtained $A_{\text{CP}} = -0.009 \pm 0.017_{\text{stat}} \pm 0.011_{\text{syst}}$ and $A_{\text{I}} = 0.029 \pm 0.019_{\text{stat}} \pm 0.016_{\text{syst}} \pm 0.018_{\text{prod}}$ [708] while the results of Belle read $A_{\text{CP}} = -0.015 \pm 0.044_{\text{stat}} \pm 0.012_{\text{syst}}$ and $A_{\text{I}} = 0.034 \pm 0.044_{\text{stat}} \pm 0.026_{\text{syst}} \pm 0.025_{\text{prod}}$ [707]. The last errors in A_{I} arise from the production ratio of B^0 and B^+ for which *BABAR* and Belle assume the values 1.044 ± 0.050 and 1.020 ± 0.034, respectively. The direct CP asymmetry has also been measured in the $B \to \rho\gamma$ system by Belle which finds $A_{\text{CP}} = -0.11 \pm 0.32_{\text{stat}} \pm 0.09_{\text{syst}}$ [720]. The corresponding experimental

Table 43
Measurements of tCPV of radiative B decays. Only the S terms are shown. The size of the data sets is given in units of fb^{-1}.

	Belle			*BABAR*		
Mode	S	Data set	Ref.	S	Data set	Ref.
$B^0 \to K^{*0}\gamma$	$-0.32\,^{+0.36}_{-0.33} \pm 0.05$	492	[703]	$-0.03 \pm 0.29 \pm 0.03$	423	[704]
$B^0 \to K^0_S\pi^0\gamma^\dagger$	$-0.10 \pm 0.31 \pm 0.07$	492	[703]	–	–	–
$B^0 \to K^0_S\pi^0\gamma^\ddagger$	–	–	–	$-0.78 \pm 0.59 \pm 0.09$	423	[704]
$B^0 \to K^0_S\eta\gamma$	–	–	–	$-0.18\,^{+0.49}_{-0.46} \pm 0.12$	423	[713]
$B^0 \to K^0_S\rho^0\gamma$	$0.11 \pm 0.33\,^{+0.05}_{-0.09}$	605	[723]	–	–	–

† $M_{K\pi} < 1.8\,\text{GeV}$ ‡ $1.1\,\text{GeV} < M_{K\pi} < 1.8\,\text{GeV}$

results for the isospin asymmetry read $A_\text{I} = -0.43^{+0.25}_{-0.22_\text{stat}} \pm 0.10_\text{syst}$ from *BABAR* [721] and $A_\text{I} = -0.48^{+0.21}_{-0.19_\text{stat}}\,^{+0.08}_{-0.09_\text{syst}}$ from Belle [720]. Within errors, the measured values of A_CP and A_I are consistent with the SM predictions discussed in Sec. 6.3.1.

Another important variable is the time-dependent CP asymmetry. In the SM, the photon from the $b \to s\gamma$ process is almost polarized. Photons from B^0 are right-handed, while photons from $\overline{B}^0$ are left-handed. So if the photon is completely polarized, B^0 and $\overline{B}^0$ cannot decay into a common final state, and mixing-induced CP violation does not happen. Indeed, the time-dependent CP violation (tCPV) in radiative B decays $B \to f_\text{CP}\gamma$, where f_CP denotes a CP eigenstate, is expected to be within a few percent even when we consider the possible enhancement due to the strong interaction. Therefore, the measurement of tCPV for $b \to s\gamma$ is a probe of the photon polarization, and large values of tCPV would be a signal of the presence of non-standard right-handed interactions.

The final state in $K^{*0} \to K^0_S\pi^0$ is a CP eigenstate, but it is not essential whether the decay goes through K^{*0} or not. Actually, final states can be any of the type $P_1P_2\gamma$, where P_1 and P_2 are pseudoscalar mesons [722]. In consequence, the measurements have been performed not only for $B \to K^{*0}\gamma \to K^0_S\pi^0\gamma$ but also for the non-resonant mode $B \to K^0_S\pi^0\gamma$. In Tab. 43 we list the measured S terms of the various tCPV. Since the final state $K^0_S\pi^0\gamma$ does not include charged tracks that come from the B vertex, the B decay vertex has to be calculated using the K^0_S trajectory, which causes lower efficiency. Although the error is still large, the result is consistent with vanishing CP asymmetry.

Many other exclusive final states have also been found by *BABAR* and Belle. Tab. 42 shows the decays with experimental evidence and their branching fractions. Radiative decays through kaonic resonances are observed for $B \to K^*_2(1430)\gamma$ and $B \to K_1(1270)\gamma$, in addition to $B \to K^*\gamma$. The other listed modes are three- or four-body decays. Measurements of these branching ratios provide a better understanding of the composition of $b \to s\gamma$ final states, and potentially reduce the systematic errors due to hadronization in the inclusive analysis with the sum of exclusive method. Some exclusive modes can also be used to study the tCPV. As shown in Tab. 43, *BABAR* has performed the first measurement of tCPV for $B^0 \to K^0_S\eta\gamma$, while Belle has reported the first evidence of $B^+ \to K^+\eta'\gamma$, whose neutral mode is also usable for an tCPV analysis.

Belle has recently reported the measurement of tCPV in $B^0 \to K^0_S\rho^0\gamma \to K^0_S\pi^+\pi^-\gamma$ [723]. The advantage of this mode is that the B decay vertex can be determined from two charged pions. On the other hand, there exists a contamination from other decays with

the same final state such as $B^0 \to K^{*+}\pi^-\gamma$. Since $K_1(1270)$ and $K^*(1680)$ have significant branching fractions to $K\rho$, it is necessary to estimate the fraction of $B \to K_1(1270)\gamma$ and $B \to K^*(1680)\gamma$ in the entire $B \to K\pi\pi\gamma$ decay. Belle uses the charged mode $B^+ \to K^+\pi^+\pi^-\gamma$ in order to disentangle the composition, and, assuming the isospin relation, estimates the dilution factor to the effective S in the ρ^0 mass window. The result listed in Tab. 43 shows that the size of the error is competitive to those for $B^0 \to K^{*0}\gamma$.

Radiative decays of the B_s meson have been studied by Belle using the data taken at the $\Upsilon(5S)$ center-of-mass energy, and the decay $B_s \to \phi\gamma$ has been observed as shown in Tab. 42. LHCb is expected to perform the study of the time-dependent asymmetry of this mode [724]. With respect to the B_d system, there is an additional observable A^Δ in the formula of the asymmetry:

$$A_{\rm CP}(t) = \frac{S\sin(\Delta m_s t) - C\cos(\Delta m_s t)}{\cosh(\Delta\Gamma_s t/2) - A^\Delta \sinh(\Delta\Gamma_s/2)}\,. \tag{288}$$

The extra contribution A^Δ parametrizes the fraction of wrongly polarized photons, and is sensitive to NP as well as the S term. According to the MC simulation, LHCb is expected to reach sensitivities of $\sigma(A^\Delta) \sim 0.22$ and $\sigma(S) \sim 0.11$ for 2 fb^{-1}, which demonstrates that the prospects for a measurement of the photon polarization at LHCb are promising.

6.3.3. *Determinations of $|V_{td}/V_{ts}|$ from $b \to (s,d)\gamma$*

Since the $b \to d\gamma$ process is suppressed by a factor of $|V_{td}/V_{ts}|$ compared to $b \to s\gamma$, its branching fraction is useful to extract the ratio $|V_{td}/V_{ts}|$ by means of (286). The exclusive modes to be studied in the case of $b \to d\gamma$ are $B \to (\rho,\omega)\gamma$. Due to their small branching fractions, the continuum background suppression is a key issue in the analysis. In addition, the good particle identification of the *BABAR* and Belle detectors is essential to separate $B \to \rho\gamma$ from $B \to K^*\gamma$. Both *BABAR* and Belle have observed clear signals of these modes. The current values of the branching fractions are given in Tab. 42.

The input value for the extraction of $|V_{td}/V_{ts}|$ is the branching ratio of $B \to (\rho,\omega)\gamma$ and $B \to K^*\gamma$. One can perform a simultaneous fit to $B \to (\rho,\omega)\gamma$ and $B \to K^*\gamma$ or calculate the ratio from the individual fits to $B \to (\rho,\omega)\gamma$ and $B \to K^*\gamma$, so as to cancel common systematic errors. In order to obtain the combined branching fraction of $B \to (\rho,\omega)\gamma$, one assumes the isospin relation $\mathcal{B}(B \to (\rho,\omega)\gamma) = \mathcal{B}(B^+ \to \rho^+\gamma) = 2\,(\tau_{B^+}/\tau_{B^0})\,\mathcal{B}(B^0 \to \rho^0\gamma) = 2\,(\tau_{B^+}/\tau_{B^0})\,\mathcal{B}(B^0 \to \omega\gamma)$. From the combined branching fraction of $B \to \rho^+\gamma$, $B \to \rho^0\gamma$, and $B \to \omega\gamma$, *BABAR* and Belle have extracted the values 0.039 ± 0.008 and $0.0284 \pm 0.0050_{\rm stat}\,^{+0.0027}_{-0.0029_{\rm syst}}$ for $\mathcal{B}(B \to (\rho,\omega)\gamma)/\mathcal{B}(B \to K^*\gamma)$, respectively. These measurements translate into $|V_{td}/V_{ts}| = 0.233\,^{+0.025}_{-0.024_{\rm expr}} \pm 0.021_{\rm theo}$ for *BABAR* [721] and $0.195\,^{+0.020}_{-0.019_{\rm expr}} \pm 0.015_{\rm theo}$ for Belle [720], where the first (second) error in $|V_{td}/V_{ts}|$ is of experimental (theoretical) nature. The values extracted from the individual decay modes can also be found in the latter references.

Future precise measurements of $B \to X_d\gamma$ also provide a promising way to determine the ratio $|V_{td}/V_{ts}|$. Using the value of $\mathcal{B}(B \to X_d\gamma)$ as given in Sec. 6.2.2 leads to $|V_{td}/V_{ts}| = 0.177 \pm 0.043_{\rm expr} \pm 0.001_{\rm theo}$ [664]. Although the given theory error is likely to be underestimated, as it does not take into account an uncertainty due to the experimental cut on M_{X_d}, the quoted numbers make clear that determinations of $|V_{td}/V_{ts}|$ from $B \to X_d\gamma$ are at the moment essentially only limited by experiment.

So far, the central values of $|V_{td}/V_{ts}|$ extracted from $b \to (s,d)\gamma$ are compatible with the ones following from $B_{d,s}$ mixing [220], although both the experimental and theoretical uncertainties are significantly larger in the former case. While thus not suitable for a precise determination of $|V_{td}/V_{ts}|$, the $b \to (s,d)\gamma$ results are complementary to those from neutral meson mixing, since they could be affected differently by NP. It is therefore worthwhile to try to improve the measurements of $b \to (s,d)\gamma$ with one order of magnitude larger luminosities.

6.4. *Purely leptonic rare decays*

6.4.1. *Theory of purely leptonic rare decays*

The charged-current processes $P \to \ell\nu$ are the simplest flavor-violating helicity suppressed observables. Both in the SM and models of NP with a extended Higgs sector these modes appear already at the tree level. The charged Higgs contribution is proportional to the Yukawa couplings of quarks and leptons, but it can compete with the contribution arising form $W^{\pm}$-boson exchange due to the helicity suppression of $P \to \ell\nu$ [145]. Taking into account the resummation of the leading $\tan\beta = v_u/v_d$ corrections to all orders, the $H^{\pm}$ contributions to the $P \to \ell\nu$ amplitude within a MFV supersymmetric framework leads to the following ratio [146, 399]

$$R_{P\ell\nu} = \frac{\mathcal{B}^{\rm SM}(P \to \ell\nu)}{\mathcal{B}^{\rm SUSY}(P \to \ell\nu)} = \left[1 - \left(\frac{m_P^2}{m_{H^\pm}^2}\right)\frac{\tan^2\beta}{1+\epsilon_0\tan\beta}\right]^2 , \tag{289}$$

where ϵ_0 denotes the effective coupling which parametrizes the non-holomorphic corrections to the down-type Yukawa interaction. One typically has $\epsilon_0 \sim 10^{-2}$. For a natural choice of the MSSM parameters, the relation (289) implies a suppression with respect to the SM in the $B \to \tau\nu$ decay of $\mathcal{O}(10\%)$, but an enhancement is also possible for very light $M_{H^\pm}$.

Performing a global t of the unitarity triangle, one obtains the following SM prediction $\mathcal{B}(B \to \tau\nu)_{\rm SM} = (0.87 \pm 0.19) \times 104]$. The major part of the total error stems from the uncertainty due to the B-meson decay constant f_B. The latter prediction is 1.7σ below the current world average $\mathcal{B}(B \to \tau\nu)_{\rm exp} = (1.51 \pm 0.33) \times 10^4$. However, systematic errors in the lattice determinations of f_B in conjunction with the limited experimental statistics do not allow to draw a clear-cut conclusion about the presence of beyond the SM physics in $B \to \tau\nu$ at the moment.

The expression for $R_{K\mu\nu}$ is obtained from (289) by replacing m_B^2 with m_K^2. Although the charged Higgs contributions are now suppressed by a factor $m_K^2/m_B^2 \sim 1/100$, $K \to \ell\nu$ is competitive with $B \to \tau\nu$ due to the excellent experimental resolution [346] and the good theoretical control of the former. The best strategy to fully exploit the NP sensitivity of the K_{l2} system is to consider the observable $R_{K\mu\nu}/R_{\pi\mu\nu}$ [146, 346] that is proportional to $(f_K/f_\pi)^2$. Once a well established unquenched lattice calculations of f_K/f_π will be available, $R_{K\mu\nu}/R_{\pi\mu\nu}$ will play a relevant role in both constraining and probing scenarios with a extended Higgs sector.

The SM prediction for the $B_s \to \mu^+\mu^-$ branching fraction is $\mathcal{B}(B_s \to \mu^+\mu^-)_{\rm SM} = (3.37 \pm 0.31) \times 10^{-9}$ [725] while the current 95% CL upper bound from CDF reads $\mathcal{B}(B_s \to \mu^+\mu^-)_{\rm exp} < 5.8 \times 10^{-8}$ [726], which still leaves room for enhancements of the branching fraction relative to the SM of more than factor of 10. In particular, the

MSSM with large $\tan\beta$ provides a natural framework where large departures from the SM expectations of $\mathcal{B}(B_s \to \mu^+\mu^-)$ are allowed [153].

The important role of $\mathcal{B}(B_{s,d} \to \ell^+\ell^-)$ in the large $\tan\beta$ regime of the MSSM has been widely discussed in the literature. The leading non-SM contribution to $B \to \ell^+\ell^-$ decays is generated by a single tree-level amplitude, i.e., the neutral Higgs exchange $B \to A^0, H^0 \to \ell^+\ell^-$. Since the effective FCNC coupling of the neutral Higgs bosons appears only at the quantum level, in this case the amplitude has a strong dependence on other MSSM parameters of the soft sector in addition to $M_{A^0} \sim M_{H^0}$ and $\tan\beta$. In particular, a key role is played by the μ term and the up-type trilinear soft-breaking term, A_U, which control the strength of the non-holomorphic terms. The leading parametric dependence of the scalar FCNC amplitude from these parameters is given by

$$\mathcal{A}(B_s \to \mu^+\mu^-) \propto \frac{m_b m_\mu}{M_{A^0}^2} \frac{\mu A_U}{M_{\tilde{q}}^2} \tan^3\beta \; m_b(\bar{b}_R s_L)(\bar{\mu}_L \mu_R)\,. \tag{290}$$

More quantitatively, the pure SUSY contributions can be summarized by the approximate formula

$$\mathcal{B}(B_s \to \mu^+\mu^-) \simeq \frac{5\times 10^{-8}}{\left(1+0.5\,\dfrac{\tan\beta}{50}\right)^4} \left(\frac{\tan\beta}{50}\right)^6 \left(\frac{500\text{GeV}}{M_{A^0}}\right)^4 \left(\frac{\epsilon_Y}{3\times 10^{-3}}\right)^2 , \tag{291}$$

where $\epsilon_Y \sim 3\times 10^{-3}$ holds in the limit of all the SUSY masses and A_U equal. The approximation (291) shows that $\mathcal{B}(B_s \to \mu^+\mu^-)$ already poses interesting constraints on the MSSM parameter space, especially for light M_{A^0} and large values of $\tan\beta$. However, given the specific dependence on μ and A_U, the present $\mathcal{B}(B_s \to \mu^+\mu^-)$ bound does not exclude the large $\tan\beta$ effects in $P \to \ell\nu$ already discussed.

6.4.2. *Experimental results on purely leptonic rare decays*

To measure the branching fraction for $B \to \tau\nu$ is a big challenge as there are at least three neutrinos in the final state. To get a sufficiently pure signal sample the recoil technique discussed in Sec. 3.2.6 is used. On the tagging side a semi-leptonic or a fully reconstructed hadronic state is required, and on the signal side the visible particles from the τ decay. On top of this the most powerful discriminating variable is excess energy in the calorimeter.

The first Belle analysis used fully hadronic tag decays and had a $3.5\,\sigma$ signal with 449×10^6 $B\overline{B}$ pairs [727]. *BABAR* used both hadronic and semileptonic tag decays and had a $2.6\,\sigma$ signal with 383×10^6 $B\overline{B}$ pairs [728, 729]. The latest Belle analysis uses semileptonic tag decays with one prong τ decays and 657×10^6 $B\overline{B}$ pairs. In this sample they find 154 signal events with a significance of $3.8\,\sigma$. This results in a branching fraction of $(1.65^{+0.38}_{-0.37_{\rm stat}}{}^{+0.35}_{-0.37_{\rm syst}})\times 10^{-4}$. All the results are summarized in Tab. 44. Searches have also been made for the decay $B^+ \to \mu^+\nu_\mu$ where *BABAR* has set a 90% CL upper limit of 1.3×10^{-6} [730] and Belle at 1.7×10^{-6} [731].

Searches for $B_s \to \mu^+\mu^-$ are only carried out at hadron machines, whereas $B_d \to \mu^+\mu^-$ is being searched for at the B-factories as well, even if the measurements are no longer competitive with the Tevatron results. CDF and D0 build multivariate discriminants that combine muon identification with kinematics and lifetime information. This keeps signal efficiency high while rejecting $\mathcal{O}(10^6)$ larger backgrounds including Drell-Yan continuum,

Table 44
Summary of the $B \to \tau\nu_\tau$ measurements.

Experiment	Tagging method	Data set	Significance	$\mathcal{B}(10^{-4})$	Ref.
Belle	Hadronic	449M	$3.5\,\sigma$	$1.79^{+0.56\,+0.46}_{-0.49\,-0.51}$	[727]
BABAR	Semileptonic	383M	-	$0.9 \pm 0.6 \pm 0.1$	[728]
BABAR	Hadronic	383M	$2.2\,\sigma$	$1.8^{+0.9}_{-0.8} \pm 0.4$	[729]
Belle	Semileptonic	657M	$3.8\,\sigma$	$1.65^{+0.38\,+0.35}_{-0.37\,-0.37}$	[732]
Average				1.51 ± 0.33	

Table 45
An overview of the limits set on the decays of the type $B \to \ell^+\ell^-$.

Experiment	Decay	Data set	90% CL Limit ($\times 10^8$)	Ref.
D0	$B_s \to \mu^+\mu^-$	$1.3\,\text{fb}^{-1}$	9.4	[735]
CDF	$B_s \to \mu^+\mu^-$	$2.0\,\text{fb}^{-1}$	4.7	[726]
CDF	$B_s \to e^\pm\mu^\mp$	$2.0\,\text{fb}^{-1}$	20	[736]
CDF	$B_s \to e^+e^-$	$2.0\,\text{fb}^{-1}$	28	[736]
CDF	$B_d \to \mu^+\mu^-$	$2.0\,\text{fb}^{-1}$	1.5	[726]
CDF	$B_d \to e^\pm\mu^\mp$	$2.0\,\text{fb}^{-1}$	6.4	[736]
CDF	$B_d \to e^+e^-$	$2.0\,\text{fb}^{-1}$	8.3	[736]
BABAR	$B_d \to \mu^+\mu^-$	384M	11.3	[737]
BABAR	$B_d \to e^+e^-$	384M	5.2	[737]
BABAR	$B_d \to e^\pm\mu^\mp$	384M	9.2	[737]
Belle	$B_d \to \mu^+\mu^-$	85M	16	[738]
Belle	$B_d \to e^+e^-$	85M	19	[738]
Belle	$B_d \to e^\pm\mu^\mp$	85M	17	[738]

sequential $b \to c \to s$ decays, $b\bar{b} \to \mu^+\mu^- + X$ decays, and hadrons faking muons. Background estimates are checked in multiple control regions, and then the signal-like region of the discriminant output is inspected for excess of events clustering at the B mass. The overlap between B_s and B_d search regions, due to limited mass resolution, is smaller at CDF allowing independent results on each mode. There is no evidence of a signal and the best limit at 90% CL is $\mathcal{B}(B_s \to \mu^+\mu^-) < 4.7 \times 10^{-8}$ [726].

In the near future it is expected that both CDF and D0 will reach a limit of $\mathcal{B}(B_s \to \mu^+\mu^-)$ at 2×10^{-8} with $8\,\text{fb}^{-1}$ of data. This is just a factor six above the SM expectation and will set serious constraints on NP as outlined in the previous section. Assuming no signal, LHCb will be able to exclude $\mathcal{B}(B_s \to \mu^+\mu^-)$ to be above the SM level with just $2\,\text{fb}^{-1}$ of data corresponding to one nominal year of data taking. A $5\,\sigma$ discovery at the SM level will require several years of data taking and all three LHC experiments are competitive for this [733, 734].

Other rare leptonic decay modes have been searched for including rare D^0 decays and the LFV decay $B \to e\mu$. All of these results are summarized in Tab. 45.

6.5. *Semileptonic modes*

6.5.1. $B \to D\tau\nu$ *modes*

In the framework of the 2HDM-II, charged Higgs boson exchange contributes significantly not only to $B \to \tau\nu$ but also to $B \to D\tau\nu$ decays already at tree level, if $\tan\beta = \mathcal{O}(50)$. Due to the recent data accumulated at the B factories, these channels become a standard tool to constrain the effective coupling g_S of a charged Higgs boson to right-handed down-type fermions [739–741].

While $\mathcal{B}(B \to \tau\nu)$ is more sensitive to charged-Higgs effects than $\mathcal{B}(B \to D\tau\nu)$, the latter branching fraction has a much smaller theoretical uncertainty. The prediction for $\mathcal{B}(B \to \tau\nu)$ involves the B-meson decay constant f_B, which is obtained from lattice calculations, and the CKM element $|V_{ub}|$, both suffering from large errors, $\delta(|V_{ub}|f_B) \sim 20\%$. In contrast, the vector and scalar form factors F_V and F_S in $B \to D\tau\nu$ are well under control, $\delta(|V_{cb}|F_V) < 4\%$ and $\delta(|V_{cb}|F_S) < 7\%$. First, $|V_{cb}|F_V(q^2)$ is extracted from the measured q^2 spectrum in $B \to D\ell\nu$ [560]. Second, $F_S(q^2)$ is constrained by F_V at $q^2 = (p_B - p_D)^2 = 0$ and by heavy-quark symmetry at maximal q^2. Since two parameters are sufficient to describe the $B \to D$ form factors, $F_S(q^2)$ is thus fixed [739,742]. Thanks to this good precision, present data on $\mathcal{B}(B \to D\tau\nu)$ can almost completely exclude the window around $g_S = 2$ left by $\mathcal{B}(B \to \tau\nu)$ at 95% CL [742].

Since charged-Higgs effects exhibit a q^2 dependence distinct from longitudinal $W^\pm$-boson exchange, the differential distribution $d\Gamma(B \to D\tau\nu)/dq^2$ is more sensitive than the branching ratio $\mathcal{B}(B \to D\tau\nu)$ [743]. Notice that in the differential distribution charged-Higgs effects can be detected not only from the normalization of the decay mode, but also from the shape of the spectrum.

To further increase the sensitivity to charged Higgs boson exchange, one can include information on the polarization of the τ lepton. Though the latter is not directly accessible at the B factories, in the decay chain $B \to D\nu[\tau \to \pi\nu]$ the τ spin is directly correlated with the direction of the pion in the final state. To combine this correlation with the sensitivity from the q^2 distribution, an unbinned fit to the triple-differential distribution $d\Gamma(B \to D\bar{\nu}[\tau^- \to \pi^-\bar{\nu}])/(dE_D\, dE_\pi\, d\cos\theta_{D\pi})$ should be performed [739]. Here $E_D,\ E_\pi$, denote the energies of the mesons and $\theta_{D\pi}$ is the angle between D and π^- in the B rest frame. The exploration of both differential distributions in a comprehensive experimental analysis makes the $B \to D\tau\nu$ mode particularly well-suited to detect charged-Higgs effects and to distinguish them from other possible NP contributions.

6.6. *Semileptonic neutral currents decays*

6.6.1. *Theory of inclusive* $B \to X_s\ell^+\ell^-$

The study of $b \to s\ell^+\ell^-$ transitions can yield useful complementary information, when confronted with the less rare $b \to s\gamma$ decays, in testing the flavor sector of the SM. In particular, a precise measurement of the inclusive $B \to X_s\ell^+\ell^-$ decay distributions would be welcome in view of NP searches, because they are amenable to clean theoretical descriptions for dilepton invariant masses in the ranges $q^2 \in [1,6]\,\mathrm{GeV}^2$ and $q^2 > 14.4\,\mathrm{GeV}^2$. The inclusive $B \to X_s\ell^+\ell^-$ rate can be written as follows

$$\frac{d^2\Gamma}{dq^2\, d\cos\theta_l} = \frac{3}{8}\left[(1+\cos^2\theta_l)\, H_T(q^2) + 2\,\cos\theta_l\, H_A(q^2) + 2\,(1-\cos^2\theta_l)\, H_L(q^2)\right] , \tag{292}$$

where $q^2 = (p_\ell^+ + p_\ell^-)^2$ and θ_l is the angle between the negatively charged lepton and the $\overline{B}$ meson in the center-of-mass frame of the lepton pair. At leading order and up to an overall $(m_b^2 - q^2)^2$ factor one has

$$\begin{aligned}
H_T(q^2) &\propto 2q^2 \left[\left(C_9 + 2C_7\,\frac{m_b^2}{q^2}\right)^2 + C_{10}^2\right] , \\
H_A(q^2) &\propto -4q^2 C_{10}\left(C_9 + 2C_7\,\frac{m_b^2}{q^2}\right) , \\
H_L(q^2) &\propto \left[(C_9 + 2C_7)^2 + C_{10}^2\right] .
\end{aligned}$$

The coefficients $H_i(q^2)$ are three independent functions of the Wilson coefficients of the effective Hamiltonian (281). Hence separate measurements of these three quantities lead to better constraints on the coefficients C_7, C_9, and C_{10}. In terms of the functions $H_i(q^2)$ the total rate and the forward-backward asymmetry (FBA) are given by $d\Gamma/dq^2 = H_T(q^2)+H_L(q^2)$ and $dA_{\rm FB}/dq^2 = 3/4\, H_A(q^2)$. The double differential rate (292) is known at NNLO in QCD [24, 27, 744–751] and at NLO in QED [750, 752, 753]. In addition non-perturbative corrections scaling as $\Lambda^2_{\rm QCD}/m_b^2$, $\Lambda^3_{\rm QCD}/m_b^3$, or $\Lambda^2_{\rm QCD}/m_c^2$ [754–760] have been calculated.

A comment on QED corrections is necessary. After inclusion of the NLO QED matrix elements, the electron and muon channels receive contributions proportional to $\ln(m_b^2/m_\ell^2)$. These results correspond to the process $B \to X_s\ell^+\ell^-$ in which QED radiation is included in the X_s system and the dilepton invariant mass does not contain any photon. In the *BABAR* and Belle experiments the inclusive decay is measured as a sum over exclusive states. As a consequence the log-enhanced QED corrections are not directly applicable to the present experimental results and have to be modified [761]. We also add that potentially large corrections to $R_K = \Gamma(B \to X_s\mu^+\mu^-)_{q^2\in[q_0^2,q_1^2]}/\Gamma(B \to X_s e^+e^-)_{q^2\in[q_0^2,q_1^2]}$, which in the SM is to an excellent approximation equal to 1, can arise from collinear photon emission. Since the actual net effect of these corrections depends on the experimental cuts, an good understanding of this issue is crucial to put reliable bounds on possible NP effects from a measurement of R_K.

Cuts on the dilepton and hadronic invariant masses are necessary to reject backgrounds from resonant charmonium production, $B \to X_s\psi(c\bar{c}) \to X_s\ell^+\ell^-$, and double semileptonic decays, $B \to X_c\ell^-\bar{\nu} \to X_s\ell^+\ell^-\nu\bar{\nu}$, respectively. The first cut, in particular, forces us to consider separately the low- and high-q^2 regions corresponding to dilepton invariant masses of $q^2 \in [1, 6]$ GeV^2 and $q^2 > 14.4$ GeV^2, respectively. In the low-q^2 region the OPE is well behaved and power corrections are small, but the effect of the M_{X_s} cut is quite important. The present experimental analyses correct for this effect utilizing a Fermi motion model [762]. In the high-q^2 region M_{X_s} cuts are irrelevant but the OPE itself breaks down, resulting in large $\Lambda_{\rm QCD}/m_b$ power corrections. Both these problems can be addressed as discussed at the very end of this subsection.

The most up-to-date SM predictions in the case of muons in the final state read

$$
\begin{aligned}
&\mathcal{B}_{q^2\in[1,6]\,\mathrm{GeV}^2} = (1.59 \pm 0.11) \times 10^{-6}\,,\\
&\mathcal{B}_{q^2>14\ \mathrm{GeV}^2} = (2.42 \pm 0.66) \times 10^{-7}\,,\\
&q_0^2 = (3.50 \pm 0.12)\,\mathrm{GeV}^2\,,\\
&\bar{\mathcal{A}}_{q^2\in[1,3.5]\,\mathrm{GeV}^2} = (-9.09 \pm 0.91)\%\,,\\
&\bar{\mathcal{A}}_{q^2\in[3.5,6]\,\mathrm{GeV}^2} = (7.80 \pm 0.76)\%\,,
\end{aligned}
\tag{293}
$$

where q_0^2 denotes the location of the zero in the FBA spectrum and $\bar{\mathcal{A}}_{\rm bin}$ are the integrated FBA in the $q^2 \in [1, 3.5]\,\mathrm{GeV}^2$ and $q^2 \in [3.5, 6]\,\mathrm{GeV}^2$ bins. We emphasize that the quoted errors do not take into account uncertainties related to the presence of enhanced local power corrections scaling as $\alpha_s \Lambda_{\rm QCD}/m_b$. Based on simple dimensional reasons these unknown corrections can be estimated to induce errors at the order of 5%.

Finally, let us mention three possible improvements in the experimental analyses. First, a measurement of the low-q^2 rate normalized to the semileptonic $B \to X_u \ell\nu$ rate with the same M_{X_s} cut would have a much reduced sensitivity to the actual M_{X_s} cut employed [763]. Second, the convergence of the OPE is greatly enhanced for the high-q^2 rate normalized to the semileptonic $B \to X_u \ell\nu$ rate with the same q^2 cut [760], as can be seen by comparing the relative error in (293) with the SM prediction for this new ratio which reads $\mathcal{R}_{q^2>14\ \mathrm{GeV}^2} = (2.29 \pm 0.30) \times 10^{-3}$ [753]. Third, the angular decomposition of the rate and the separate extraction of $H_T(q^2)$ and $H_A(q^2)$ would result in much stronger constraints on the Wilson coefficients [764].

6.6.2. *Experimental results on inclusive $B \to X_s \ell^+\ell^-$*

In a fully inclusive analysis of the rare electroweak penguin decay $B \to X_s \ell^+\ell^-$, where $\ell^+\ell^-$ is either e^+e^- or $\mu^+\mu^-$, some difficulties arise, since an abundant source of leptons is produced in semileptonic B and D decays. For example, the branching fraction for two semileptonic B decays, $\mathcal{B}(B \to X_c \ell\nu) = (10.64 \pm 0.11)\%$ [560], is about four orders of magnitude larger than that of the signal. Since standard kinematic constraints like the the beam-energy-substituted mass, $m_{\rm ES}$, or the difference between the reconstructed B meson energy in the center-of-mass frame and its known value, ΔE, cannot be used here, one needs to develop other analysis strategies. So far two alternative methods were developed that allows one to reduce these backgrounds. The first so-called recoil method is based on kinematic constraints of the $\Upsilon(4S) \to B\bar{B}$ decays. By performing a complete reconstruction of the other B meson in a hadronic final state plus requiring a lepton pair the residual background consists of two consecutive semileptonic decays of the signal B candidate. This is reduced by requirements on missing energy in the whole events, event shapes, and vertex information. Since the B reconstruction efficiency is of the order of 0.1%, the present $B\bar{B}$ sample are not sufficiently large to use this method. The second so-called semi-inclusive method consists of summing up exclusive final states.

Both *BABAR* and Belle focused on the second method. Using 89 (152) million $B\bar{B}$ events *BABAR* (Belle) reconstructed final states from a K^+ or a K_S^0 and up to two (four) pions recoiling against the lepton pair, where at most one π^0 was accepted [765, 766]. In both analyses, event shape variables, kinematic variables, and vertex information are combined into likelihood functions for signal, $B\bar{B}$ backgrounds, and $e^+e^- \to q\bar{q}$ continuum backgrounds. The likelihood ratios are optimized to enhance signal-like events. The signal is extracted from an extended maximum likelihood fit to the $m_{\rm ES}$ distribution

Table 46
BABAR and Belle measurements of the partial branching fractions for the $B \to X_s \ell^+ \ell^-$ decay in different bins of q^2. The J/ψ and $\psi(2S)$ veto regions differ for the e^+e^- and $\mu^+\mu^-$ modes. The latter are shown in parentheses.

Experiment	q^2 [GeV^2]	$\mathcal{B}\,[10^{-7}]$
BaBar [765]	0.04–1.0	$0.8 \pm 3.6^{+0.7}_{-0.4}$
	1.0–4.0	$16 \pm 6 \pm 5$
	4.0–7.29 (7.84)	$18 \pm 8 \pm 4$
	10.56 (10.24)–11.90 (12.60)	$10 \pm 8 \pm 2$
	14.44–25.0	$6.4 \pm 3.2^{+1.2}_{-0.9}$
Belle [766]	0.04–1.0	$11.34 \pm 4.83^{+4.60}_{-2.71}$
	1.0–6.0	$14.93 \pm 5.04^{+4.11}_{-3.21}$
	6.0–7.27 (7.55) & 10.54 (10.22)– 11.81 (12.50) & 14.33 (14.33)–14.4	$7.32 \pm 6.14^{+1.84}_{-1.91}$
	14.4–25.0	$4.18 \pm 1.17^{+0.61}_{-0.68}$

after selecting a signal-like region in ΔE. Both analyses found significant event yields, measuring branching fractions of

$$\begin{aligned} \mathcal{B}(B \to X_s \ell^+ \ell^-) &= (5.6 \pm 1.5_{\rm stat} \pm 0.6_{\rm syst} \pm 1.1_{\rm mode}) \times 10^{-6}\,, \\ \mathcal{B}(B \to X_s \ell^+ \ell^-) &= \left(4.11 \pm 0.83_{\rm stat}{}^{+0.85}_{-0.81\,{\rm syst}}\right) \times 10^{-6}\,, \end{aligned} \tag{294}$$

where the J/ψ and $\psi(2S)$ veto regions have been excluded and the third error of the *BABAR* number corresponds to the uncertainty induced by the Fermi motion model [762]. The partial branching fractions in bins of q^2 as measured by *BABAR* and Belle are summarized in Tab. 46. *BABAR* also measured the direct CP asymmetry $(N_{\bar{B}} - N_B)/(N_{\bar{B}} + N_B) = -0.22 \pm 0.26 \pm 0.02$, where $N_{B(\bar{B})}$ are the signal yields for $B(\bar{B}) \to X_s \ell^+ \ell^-$. All results are consistent with the SM predictions discussed in Sec. 6.6.1.

6.6.3. *Theory of exclusive $b \to s\ell^+\ell^-$ modes*

The theoretical calculation of exclusive $b \to s\ell^+\ell^-$ amplitudes is complicated by the fact that one encounters non-factorizable QCD dynamics. Some of these effects can be estimated using perturbative methods based on the heavy-quark expansion. To be concrete, we focus on the decays $B \to K^* \ell^+ \ell^-$ and comment on other decay modes at the end of this section.

Assuming the K^* to be on the mass shell, the decay $\bar{B}^0 \to \bar{K}^{*0}(\to K^- \pi^+)\ell^+\ell^-$ is completely described by four independent kinematic variables; namely, the lepton-pair invariant mass, q^2, and the three angles θ_l, θ_{K^*}, ϕ. The sign of the angles for the $\overline{B}$ decay show great variation in the literature. Therefore we present here an explicit definition. $\boldsymbol{p}$ denote three momentum vectors in the $\overline{B}$ rest frame, $\boldsymbol{q}$ the same in the di-muon rest frame, and $\boldsymbol{r}$ in the $\overline{K}^{*0}$ rest frame, the z-axis is defined as as the direction of the $\overline{K}^{*0}$ in the $\overline{B}$ rest frame. Three unit vectors are given in the following way: the first one is in the direction of the z-axis where the θ angles are measured with respect to, and the other two are perpendicular to the di-muon and $\overline{K}^{*0}$ decay planes.

$$\boldsymbol{e}_z = \frac{\boldsymbol{p}_{K^-} + \boldsymbol{p}_{\pi^+}}{|\boldsymbol{p}_{K^-} + \boldsymbol{p}_{\pi^+}|}\,, \qquad \boldsymbol{e}_l = \frac{\boldsymbol{p}_{\mu^-} \times \boldsymbol{p}_{\mu^+}}{|\boldsymbol{p}_{\mu^-} \times \boldsymbol{p}_{\mu^+}|}\,, \qquad \boldsymbol{e}_K = \frac{\boldsymbol{p}_{K^-} \times \boldsymbol{p}_{\pi^+}}{|\boldsymbol{p}_{K^-} \times \boldsymbol{p}_{\pi^+}|}\,. \tag{295}$$

It follows for the $\overline{B}$

$$\cos\theta_l = \frac{\boldsymbol{q}_{\mu^+}\cdot\boldsymbol{e}_z}{|\boldsymbol{q}_{\mu^+}|}\,, \qquad \cos\theta_K = \frac{\boldsymbol{r}_{K^-}\cdot\boldsymbol{e}_z}{|\boldsymbol{r}_{K^-}|} \tag{296}$$

and

$$\sin\phi = (\boldsymbol{e}_l\times\boldsymbol{e}_K)\cdot\boldsymbol{e}_z\,, \qquad \cos\phi = \boldsymbol{e}_K\cdot\boldsymbol{e}_l\,. \tag{297}$$

The angles are defined in the intervals

$$-1\leqslant\cos\theta_l\leqslant 1\,, \qquad -1\leqslant\cos\theta_K\leqslant 1\,, \qquad -\pi\leqslant\phi<\pi\,, \tag{298}$$

where in particular it should be noted that the ϕ angle is signed.

In words, for the $\overline{B}$ the angle θ_l is measured as the angle between the ℓ^+ and the z-axis in the dimuon rest frame. As the $\overline{B}$ flies in the direction of the z-axis in the dimuon rest frame this is equivalent to measuring θ_l as the angle between the ℓ^+ and the $\overline{B}$ in the di-lepton rest frame. The angle θ_K is measured as the angle between the Kaon and the z-axis measured in the $\overline{K}^{*0}$ rest frame. Finally ϕ is the angle between the normals to the planes defined by the $K\pi$ system and the $\mu^+\mu^-$ system in the rest frame of the $\overline{B}$ meson.

For the B the definition is such that the angular distributions will stay the same as for the $\overline{B}$ in the absence of CP violation. This means that for all the definitions above, ℓ^- is interchanged with ℓ^+, K^+ with K^- and and π^+ with π^-.

Following [764], the doubly differential decay rate for $\overline{B}\to\bar{K}^*\ell^+\ell^-$ can be decomposed as in the inclusive case (292). Here the helicity amplitude $H_T(q^2)$ determines the rate for transversely polarized K^* mesons, $H_L(q^2)$ the longitudinal rate, and $H_A(q^2)$ is responsible for the lepton FBA. In terms of transversity amplitudes, which are relevant for the angular analysis of $B\to K^*(K\pi)\ell^+\ell^-$, these functions read [767]

$$\begin{aligned} H_T(q^2) &= |A_{\perp\,L}|^2 + |A_{\perp\,R}|^2 + |A_{\parallel\,L}|^2 + |A_{\parallel\,R}|^2\,,\\ H_L(q^2) &= |A_{0\,L}|^2 + |A_{0\,R}|^2\,,\\ H_A(q^2) &= 2\,\mathrm{Re}\left[A_{\parallel\,R}\,A^*_{\perp\,R} - A_{\parallel\,L}\,A^*_{\perp\,L}\right]\,. \end{aligned} \tag{299}$$

The transversity amplitudes themselves can be written as [689, 699, 767]

$$\begin{aligned} A_{\perp\,L,R} &\propto \left[(C_9\mp C_{10})\,\frac{V(q^2)}{m_B+m_{K^*}} + \frac{2m_b}{q^2}\,\mathcal{T}_1(q^2)\right]\,,\\ A_{\parallel\,L,R} &\propto \left[(C_9\mp C_{10})\,\frac{A_1(q^2)}{m_B-m_{K^*}} + \frac{2m_b}{q^2}\,\mathcal{T}_2(q^2)\right]\,,\\ A_{0\,L,R} &\propto \left[(C_9\mp C_{10})\left\{\frac{A_1(q^2)}{m_B-m_{K^*}} - \frac{m_B^2-q^2}{m_B^2}\,\frac{A_2(q^2)}{m_B+m_{K^*}}\right\}\right.\\ &\quad \left. + \frac{2m_b}{m_B^2}\left\{\mathcal{T}_2(q^2) - \frac{m_B^2-q^2}{m_B^2}\,\mathcal{T}_3(q^2)\right\}\right]\,. \end{aligned} \tag{300}$$

Here we neglected some terms of order $m^2_{K^*}/m^2_B$, and did not show the kinematic normalization factors which can be found in [767]. The ingredients in (300) are: first, the SM short-distance Wilson coefficients $C_{9,10}$ of the $b\to s\ell^+\ell^-$ operators in the weak effective Lagrangian (281), which are to be tested against NP. [15] Second, the vector- and

[15] NP contributions to the operators Q'_{7-10}, that are obtained from Q_{7-10} by exchanging left- by right-handed fields everywhere, can easily be included [767].

axial-vector $B \to K^*$ transition form factors $V, A_{1,2}$ which have to be estimated by non-perturbative methods. Third, the q^2-dependent functions $\mathcal{T}_i(q^2)$ that contain factorizable and non-factorizable effects from virtual photons via the operators Q_{1-8} in (281). In the "naive factorization approximation", the functions $\mathcal{T}_i(q^2)$ are again expressed in terms of short-distance Wilson coefficients, $B \to K^*$ transition form factors, and quark-loop functions, which are perturbative if q^2 lies outside the vector-resonance region. Corrections to "naive factorization" can and should be systematically computed in the $m_b \to \infty$ limit, if we restrict ourselves [16] to the window $q^2 \in [1,6]\,\text{GeV}^2$. The QCDF theorem [689, 699] which can be further justified in SCET, takes the schematic form

$$\begin{aligned} \mathcal{T}_1(q^2) &\simeq \frac{m_B^2}{m_B^2 - q^2}\,\mathcal{T}_2(q^2) \\ \mathcal{T}_3(q^2) &- \frac{m_B^2}{m_B^2 - q^2}\,\mathcal{T}_2(q^2) \end{aligned} \;\simeq\; \begin{cases} \xi_\perp(q^2)\, C_\perp(q^2) + \phi_B^\pm(\omega) \otimes \phi_{K^*}^\perp(u) \otimes T_\perp(\omega, u)\,, \\ \xi_\parallel(q^2)\, C_\parallel(q^2) + \phi_B^\pm(\omega) \otimes \phi_{K^*}^\parallel(u) \otimes T_\parallel(\omega, u)\,, \end{cases} \tag{301}$$

where $\xi_{\perp,\parallel}$ are universal form factors arising in the combined heavy-quark-mass and large-recoil-energy limit [769, 770], $C_{\perp,\parallel}$ and $T_{\perp,\parallel}$ are perturbative coefficient functions including vertex corrections and spectator effects, respectively, and ϕ_B and ϕ_{K^*} denote hadronic LCDAs which again have to be estimated from non-perturbative methods. On the one hand, the reduction of form factors in the symmetry limit is a crucial ingredient to obtain a precise estimate of the FBA [770–772]. On the other hand, observables like the isospin asymmetry between charged and neutral decays are sensitive to Λ_{QCD}/m_b corrections to (301), which generally are small but difficult to estimate very precisely [699, 773, 774].

To be concrete, let us quote some theoretical predictions for individual SM rates and asymmetries in the low-q^2 region, following the numerical analysis in [699] but using updated values for the B lifetimes. We first note that the hadronic uncertainties for the partial rates in that region are dominated by the form factor uncertainties, and therefore should be considered as less useful for precision tests of the SM. These uncertainties drop out to a large extent in the prediction for the FBA in particular in the vicinity of the zero of the FBA [17]. This is illustrated in panel (a) of Fig. 50. For the zero of the FBA one obtains

$$\begin{aligned} q_0^2(B^0 \to K^{*0}\ell^+\ell^-) &= \left(4.36^{+0.33}_{-0.31}\right)\,\text{GeV}^2\,, \\ q_0^2(B^\pm \to K^{*\pm}\ell^+\ell^-) &= \left(4.15^{+0.27}_{-0.27}\right)\,\text{GeV}^2\,. \end{aligned} \tag{302}$$

Considering the FBA for the partially integrated rates

$$A_{\text{FB}} = \frac{\int_0^1 \frac{d\Gamma}{d\cos\theta_l} d\theta_l - \int_{-1}^0 \frac{d\Gamma}{d\cos\theta_l} d\theta_l}{\int_0^1 \frac{d\Gamma}{d\cos\theta_l} d\theta_l + \int_{-1}^0 \frac{d\Gamma}{d\cos\theta_l} d\theta_l} \tag{303}$$

one obtains

$$A_{\text{FB}}^{\text{low-}q^2} = \begin{cases} -0.033^{+0.014}_{-0.016}\,, & \text{for } B^0 \to K^{*0}\ell^+\ell^-\,, \\ -0.062^{+0.018}_{-0.023}\,, & \text{for } B^\pm \to K^{*\pm}\ell^+\ell^-\,. \end{cases} \tag{304}$$

[16] In principle, the region $4m_c^2 \ll q^2 \le m_b^2$ can be treated in heavy hadron chiral perturbation theory [768].

[17] The form factor dependence could be further reduced by normalizing the FBA to the transverse rate, instead of the full rate.

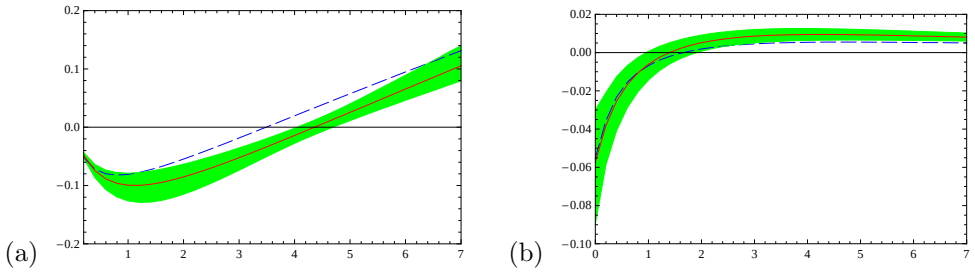

Fig. 50. (a) Theoretical estimate for differential FBA in $B^0 \to K^{*0}\ell^+\ell^-$. (b) Estimate for differential isospin asymmetry. The dashed line denotes the LO result. The solid line with the error band the NLO prediction with parametric uncertainties.

The corresponding predictions for the isospin asymmetry are shown in panel (a) of Fig. 50, and the partially integrated isospin asymmetry is estimated as

$$A_{\rm I}^{\text{low-}q^2} = \frac{\int d\Gamma^0 - \int d\Gamma^\pm}{\int d\Gamma^0 + \int d\Gamma^\pm} = 0.007^{+0.003}_{-0.003}\,. \tag{305}$$

Notice that the perturbative errors can be reduced by resummation of large logarithms in SCET [775] or the computation of higher-order corrections, but irreducible systematic uncertainties from both higher-order $\Lambda_{\rm QCD}/m_b$ corrections, and the restricted precision of the form factor estimates from LCSR or LQCD remain.

Let us finally consider further exclusive decay modes that can be used to test the $b \to s\ell^+\ell^-$ transition. The decay into a pseudoscalar Kaon, $B \to K\ell^+\ell^-$, is similar to the decay into a longitudinal vector meson [689, 776]. An interesting observable for the identification of NP is the ratio R_K already mentioned in Sec. 6.6.1. One should also mention the decay $B_s \to \phi\ell^+\ell^-$, where a recent model-independent analysis of NP effects based on "naive" factorization has been given [777]. A SM analysis including NLO effects is straightforward and will be discussed elsewhere [778].

A related process is $B \to \rho\ell^+\ell^-$ which probes the $b \to d\ell^+\ell^-$ transition in and beyond the SM. Due to the different CKM hierarchy it may show potentially larger isospin and *CP*-violating effects than its counterparts in $b \to s\ell^+\ell^-$ [689]. It is also useful as a cross-check for the factorization approach.

6.6.4. *Angular observables in* $B \to K^*\ell^+\ell^-$

Besides the branching fractions, the FBA and CP-violating observables, the exclusive decay $\overline{B}^0 \to \overline{K}^{*0}\ell^+\ell^-$ with an angular analysis of the subsequent $\overline{K}^{*0} \to K^-\pi^+$ decay offers the possibility to further constrain NP [767, 774, 779–782]. The decay is described by 4 independent kinematic variables: the lepton-pair invariant mass squared, q^2, and the three angles θ_l, θ_K, ϕ. Summing over final-state spins, the differential decay distribution can be expressed in terms of 9 independent functions [783–787], which are related to the transversity amplitudes [18] discussed around (299) and (300), and which are invariant under the following symmetry transformations [782]

[18] Another transversity amplitude A_t does not contribute for massless leptons.

$$
\begin{aligned}
A_{i\,L} &\to \cos\theta\, e^{+i\phi_L}\, A_{i\,L} - \sin\theta\, e^{-i\phi_R}\, A^*_{i\,R}\,, \\
A_{i\,R} &\to \sin\theta\, e^{-i\phi_L}\, A^*_{i\,L} + \cos\theta\, e^{+i\phi_R}\, A_{i\,R}\,, \\
A_{\perp L} &\to +\cos\theta\, e^{+i\phi_L}\, A_{\perp L} + \sin\theta\, e^{-i\phi_R}\, A^*_{\perp R}\,, \\
A_{\perp R} &\to -\sin\theta\, e^{-i\phi_L}\, A^*_{\perp L} + \cos\theta\, e^{+i\phi_R}\, A_{\perp R}\,.
\end{aligned}
\tag{306}
$$

Here $i = \|, 0$. Any experimental observable constructed from the transversity amplitudes thus has to be invariant under these symmetries or would require to measure the helicity of the decay products which is not possible at LHCb or a super flavor factory. For instance, this excludes the asymmetry $A_T^{(1)}$ defined in [784], despite its very attractive NP sensitivity [767, 780].

As it has been emphasized in [782], one can construct angular observables which simultaneously fulfill a number of requirements, namely: i) small theoretical uncertainties due to cancellations of form-factor dependencies, ii) good experimental resolution at LHCb and/or super flavor factory, iii) high sensitivity to NP effects, including contributions from new operators in the weak effective Hamiltonian. Focusing on the sensitivity to right-handed operator Q_7', where one would encounter the combination of Wilson coefficients $(C_7 + C_7')$ in $A_{\perp L,R}$ and $(C_7 - C_7')$ in $A_{\| L,R}$ and $A_{0L,R}$, the authors of [782] identify the following three observables to satisfy the above criteria

$$
A_T^{(2)} = \frac{|A_\perp|^2 - |A_\||^2}{|A_\perp|^2 + |A_\||^2}\,, \quad A_T^{(3)} = \frac{|A_0 A_\|^*|}{|A_0|\,|A_\perp|}\,, \quad A_T^{(4)} = \frac{|A_{0L} A_{\perp L}^* - A_{0R}^* A_{\perp R}|}{|A_0 A_\|^*|}\,, \tag{307}
$$

where $A_i A_j^* = A_{iL} A_{jL}^* + A_{iR} A_{jR}^*$. In particular, the dependence on the form factors $\xi_{\perp,\|}$ drops out to first approximation if one neglects α_s and $\Lambda_{\rm QCD}/m_b$ corrections.

In Fig. 51, the theoretical estimates and experimental sensitivity for $A_T^{(2)}$, $A_T^{(3)}$, and $A_T^{(4)}$ are plotted as a function of q^2. In each theoretical plot on the left-hand side the thin dark line is the central NLO result for the SM and the narrow inner dark (orange) band corresponds to the related uncertainties due to both input parameters and perturbative scale dependence. Light gray (green) bands refer to $\Lambda_{\rm QCD}/m_b = \pm 5\%$ corrections considered for each spin amplitude, while for the darker gray (green) one considers $\Lambda_{\rm QCD}/m_b = \pm 10\%$ corrections. The curves labeled (a) to (d) correspond to four different benchmark points in the MSSM. For more details we refer to [782]. The experimental sensitivity for a data set corresponding to 10 fb^{-1} of integrated luminosity at LHCb is given in each figure on the right, assuming SM rates. Here the solid (red) line shows the median extracted from the fit to the ensemble of data, and the dashed (black) line shows the theoretical input distribution. The inner and outer bands correspond to 1σ and 2σ experimental errors.

The observables $A_T^{(3)}$ and $A_T^{(4)}$ offer sensitivity to the longitudinal spin amplitude $A_{0L,R}$ in a controlled way, i.e., the theoretical uncertainties from NLO corrections turn out to be very small. Concerning the sensitivity to right-handed currents, one observes sizable deviations from the SM for $A_T^{(2)}$, $A_T^{(3)}$, and $A_T^{(4)}$ in the 4 SUSY benchmark scenarios studied in [782]. For a recent discussion of other NP scenarios we refer to [774]. Comparing the theoretical and experimental figures, it can be seen that in particular $A_T^{(3)}$ offers great promise to distinguish between such NP models.

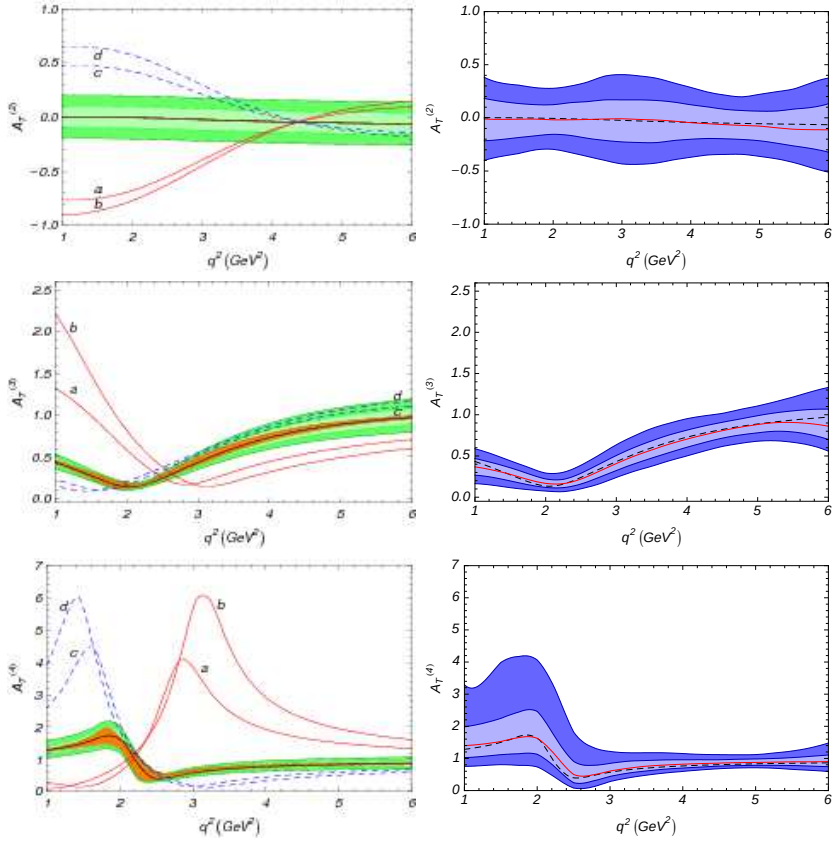

Fig. 51. The asymmetries $A_T^{(2)}$, $A_T^{(3)}$, and $A_T^{(4)}$ as a function of q^2, with theoretical errors (left panels), and experimental errors (right panels). See text for details. Fig.s taken from [782].

6.6.5. *Experimental results on exclusive* $b \to (s,d)\ell^+\ell^-$

The exclusive electroweak decay $B \to K\ell^+\ell^-$ is a $b \to s$ transition that was first observed by Belle [788] in a sample of 31 million $B\bar{B}$ events. Using 123 million $B\bar{B}$ events *BABAR* confirmed the observation and reported first evidence for $B \to K^*\ell^+\ell^-$ [789] which was confirmed later by Belle [790]. In the most recent studies *BABAR* and Belle have reconstructed ten final states consisting of $K^\mp$, $K^0_S(\to \pi^+\pi^-)$, $K^\mp\pi^\pm$, $K^\mp\pi^0$ or $K^0_S(\to \pi^+\pi^-)\pi^\mp$ besides the lepton pair using 384 million and 657 million $B\bar{B}$ events, respectively [791–793]. The signal yields in individual final states are extracted from the $m_{\rm ES}$ and ΔE distributions. The main background arises from random combinations of leptons from B and D decays. As in the semi-inclusive analysis this combinatorial background is suppressed by using event shape variables, kinematic variables, and vertex information that are combined into a neural network (*BABAR*) or a likelihood ratio (Belle). The multivariate observables are optimized separately for each mode, for each type of background, $B\bar{B}$ or $e^+e^- \to q\bar{q}$, and each q^2 region.

Total branching fractions measured by *BABAR*, Belle, and CDF are in agreement with each other and the SM predictions [772,794]. The interest, however, has shifted towards rate asymmetries, since many uncertainties in both predictions and measurements cancel

as explained in Sec. 6.6.3. *BABAR* and Belle so far studied isospin asymmetries, $A_{\rm I}^{K^{(*)}}$, direct CP asymmetries, $A_{\rm CP}^{K^{(*)}}$, and lepton forward-backward asymmetries, $A_{\rm FB}$, as well as the K^* longitudinal polarization, F_L, and the ratio of rates to $\mu^+\mu^-$ and e^+e^- final states, $R_{K^{(*)}}$. With increased statistics both experiments started to explore the q^2 dependence of these observables.

The CP-averaged isospin asymmetry and direct CP asymmetry are defined by

$$\begin{aligned} A_{\rm I}^{K^{(*)}} &= \frac{\mathcal{B}(B^0 \to K^{(*)0}\ell^+\ell^-) - (\tau_0/\tau_+)\mathcal{B}(B^\pm \to K^{(*)\pm}\ell^+\ell^-)}{\mathcal{B}(B^0 \to K^{(*)0}\ell^+\ell^-) + (\tau_0/\tau_+)\mathcal{B}(B^\pm \to K^{(*)\pm}\ell^+\ell^-)}, \\ A_{\rm CP}^{K^{(*)}} &= \frac{\mathcal{B}(\overline{B} \to \overline{K}^{(*)}\ell^+\ell^-) - \mathcal{B}(B \to K^{(*)}\ell^+\ell^-)}{\mathcal{B}(\overline{B} \to \overline{K}^{(*)}\ell^+\ell^-) + \mathcal{B}(B \to K^{(*)}\ell^+\ell^-)}, \end{aligned} \tag{308}$$

where τ_0 and τ_+ are the B^0 and B^+ lifetimes, respectively. $A_{\rm CP}$ is predicted to be $\mathcal{O}(10^{-3})$ in the SM. NP at the electroweak scale, however, could produce a significant enhancement [781]. The ratios $R_{K^{(*)}}$ are sensitive to the presence of a neutral SUSY Higgs boson [795]. In the SM, R_K is expected to be unity modulo a small correction accounting for differences in phase space [796] and possibly QED radiation. For $m_{\ell^+\ell^-} \geq 2m_\mu$, R_{K^*} should be also close to unity. Due to the $1/q^2$ dependence of the photon penguin contribution, however, there is a significant rate enhancement in the $B \to K^* e^+e^-$ mode for $m_{e^+e^-} < 2m_\mu$ decreasing the SM expectation of R_{K^*} to 0.75. New scalar and pseudoscalar contributions may modify this prediction. The possible size of these effects is however already bounded severely by the Tevatron limits on $B_s \to \mu^+\mu^-$.

Present results of branching fractions, rate-based asymmetries, and lepton-flavor ratios are summarized in Tab.s 47 and 48. At the present level of precision branching fractions, $R_{K^{(*)}}$, and $A_{\rm CP}$ are in good agreement with the SM. While $A_{\rm I}$ agrees with the SM for large values of q^2, the *BABAR* measurement of $A_{\rm I}$ in the low-q^2 region deviates from the SM expectation [773] by almost 4 σ for the combination of the $B \to K\ell^+\ell^-$ and $B \to K^*\ell^+\ell^-$ modes. Though consistent with the SM expectation the Belle results support the *BABAR* observations at low q^2.

The angular distribution of $B \to K^*\ell^+\ell^-$ depends on the three angles defined in eqs. 296 and 297. The one-dimensional angular distributions in $\cos\theta_K$ and $\cos\theta_\ell$ simply are

$$\begin{aligned} W(\theta_K) &= \frac{3}{2}F_L\cos^2\theta_K + \frac{3}{4}(1-F_L)(1-\cos^2\theta_K)\,, \\ W(\theta_\ell) &= \frac{3}{4}F_L(1-\cos^2\theta_\ell) + \frac{3}{8}(1-F_L)(1+\cos^2\theta_\ell) + A_{\rm FB}\cos\theta_\ell\,. \end{aligned} \tag{309}$$

While $W(\theta_K)$ depends only on F_L, $W(\theta_\ell)$ depends both on F_L and $A_{\rm FB}$. The FBA is proportional to the difference of two interference terms that include products of the Wilson coefficients C_9C_{10} and C_7C_{10}. In the first term the main q^2 dependence originates from the q^2 dependence of C_9 while in the second term it results from the $1/q^2$ dependence of the photon penguin contribution.

BABAR and Belle measured F_L and $A_{\rm FB}$ in different bins of q^2. After extracting the event yield from the m_{ES} distribution, F_L is determined first from a fit to $W(\theta_K)$. Then $A_{\rm FB}$ is determined from a fit to $W(\theta_\ell)$ for fixed signal yields and fixed F_L. The results are summarized in Tab. 49. The *BABAR* and Belle results for F_L and $A_{\rm FB}$ in comparison to their SM predictions and three scenarios, that result from changing the sign of the Wilson coefficients C_7, or C_9C_{10}, or both combinations with respect to the SM values are shown

Table 47
Measurements of the partial branching fractions and isospin asymmetries for the $B \to K\ell^+\ell^-$ and $B \to K^*\ell^+\ell^-$ decays in different bins of q^2.

Experiment	Mode	q^2 [GeV^2]	$\mathcal{B}\,[10^{-7}]$	$A_{\rm I}$
BABAR [792]	$B \to K\ell^+\ell^-$	0.1–7.02	$0.181^{+0.39}_{-0.36} \pm 0.008$	$-1.43^{+0.56}_{-0.85} \pm 0.05$
		10.24–12.96 or >14.06	$0.135^{+0.040}_{-0.037} \pm 0.007$	$0.28^{+0.24}_{-0.30} \pm 0.03$
	$B \to K^*\ell^+\ell^-$	0.1–7.02	$0.43^{+0.11}_{-0.10} \pm 0.03$	$-0.56^{+0.17}_{-0.15} \pm 0.03$
		10.24–12.96 or >14.06	$0.42^{+0.10}_{-0.10} \pm 0.03$	$0.18^{+0.36}_{-0.28} \pm 0.04$
Belle [793]	$B \to K\ell^+\ell^-$	0.0–2.0	$0.81^{+0.18}_{-0.16} \pm 0.05$	$-0.33^{+0.33}_{-0.25} \pm 0.05$
		2.0–5.0	$0.58^{+0.16}_{-0.14} \pm 0.04$	$-0.49^{+0.45}_{-0.34} \pm 0.04$
		5.0–8.86	$0.86^{+0.18}_{-0.16} \pm 0.05$	$-0.19^{+0.26}_{-0.22} \pm 0.05$
		10.09–12.86	$0.55^{+0.16}_{-0.14} \pm 0.03$	$-0.29^{+0.37}_{-0.29} \pm 0.05$
		14.18–16.0	$0.38^{+0.19}_{-0.12} \pm 0.02$	$-0.40^{+0.61}_{-0.69} \pm 0.04$
		> 16.0	$0.98^{+0.20}_{-0.18} \pm 0.06$	$0.11^{+0.24}_{-0.21} \pm 0.05$
		1.0–6.0	$1.36^{+0.23}_{-0.21} \pm 0.08$	$-0.41^{+0.25}_{-0.20} \pm 0.04$
	$B \to K^*\ell^+\ell^-$	0.0–2.0	$1.46^{+0.40}_{-0.35} \pm 0.12$	$-0.67^{+0.18}_{-0.16} \pm 0.03$
		2.0–5.0	$1.29^{+0.38}_{-0.34} \pm 0.10$	$1.17^{+0.72}_{-0.82} \pm 0.02$
		5.0–8.86	$0.99^{+0.41}_{-0.36} \pm 0.08$	$-0.47^{+0.31}_{-0.29} \pm 0.04$
		10.09–12.86	$2.24^{+0.44}_{-0.40} \pm 0.18$	$0.00^{+0.20}_{-0.21} \pm 0.05$
		14.18–16.0	$1.05^{+0.29}_{-0.26} \pm 0.08$	$0.16^{+0.30}_{-0.35} \pm 0.05$
		> 16.0	$2.04^{+0.27}_{-0.24} \pm 0.16$	$-0.02^{+0.20}_{-0.21} \pm 0.05$
		1.0–6.0	$1.49^{+0.45}_{-0.40} \pm 0.12$	
CDF [797]	$B^+ \to K^+\ell^+\ell^-$	<8.4 or 10.2–13.0 or >14.1	$5.9 \pm 1.5 \pm 0.4$	$-0.33^{+0.33}_{-0.25} \pm 0.05$
CDF [797]	$B^0 \to K^{*+}\ell^+\ell^-$	<8.4 or 10.2–13.0 or >14.1	$8.1 \pm 3.0 \pm 1.0$	

Table 48
BABAR and Belle measurements of total branching fractions, CP asymmetries, and lepton flavor ratios for the $B \to K\ell^+\ell^-$ and $B \to K^*\ell^+\ell^-$ decays. For $B \to K^*\ell^+\ell^-$ the pole region, $q^2 < m_\mu^2$, is included in R_{K^*}. The CP asymmetries are given for $B \to K^+\ell^+\ell^-$ and the combined $B \to K^*\ell^+\ell^-$ modes.

Experiment	Mode	$\mathcal{B}\,[10^{-7}]$	$A_{\rm CP}$	$R_{K^{(*)}}$
BABAR [792]	$B \to K\ell^+\ell^-$	$3.9^{+0.7}_{-0.7} \pm 0.2$	$-0.18^{+0.18}_{-0.18} \pm 0.01$	$0.96^{+0.44}_{-0.34} \pm 0.05$
	$B \to K^*\ell^+\ell^-$	$11.1^{+1.9}_{-1.8} \pm 0.7$	$0.01^{+0.16}_{-0.15} \pm 0.01$	$1.1^{+0.42}_{-0.32} \pm 0.07$
Belle [793]	$B \to K\ell^+\ell^-$	$4.8^{+0.5}_{-0.4} \pm 0.3$	$-0.04^{+0.1}_{-0.1} \pm 0.02$	$1.03^{+0.19}_{-0.19} \pm 0.06$
	$B \to K^*\ell^+\ell^-$	$10.8^{+1.1}_{-1.0} \pm 0.9$	$-0.10^{+0.10}_{-0.10} \pm 0.01$	$0.83^{+0.17}_{-0.17} \pm 0.08$

in Fig. 52. At the present level of precision both F_L and $A_{\rm FB}$ are consistent with the SM expectations. For $B \to K\ell^+\ell^-$, the measurement of $A_{\rm FB}$ is consistent with zero as expected in the SM. It is important to emphasize, that models in which the sign of C_7 is reversed while $C_{9,10}$ receive only small non-standard corrections are disfavored at the 3σ level by the combination of the $\mathcal{B}(B \to X_s\gamma)$ and $\mathcal{B}(B \to X_s\ell^+\ell^-)$ measurements [798]. The hypothetical NP scenario corresponding to the green dashed curves in Fig. 52 is

Table 49
BABAR and Belle measurements of the K^* longitudinal polarizations and the lepton FBAs for the $B \to K^*\ell^+\ell^-$ decays in different bins of q^2.

Experiment	q^2 [GeV^2]	F_L	$A_{\rm FB}$
BABAR [791]	0.1–6.25	$0.35^{+0.16}_{-0.16} \pm 0.04$	$0.24^{+0.18}_{-0.23} \pm 0.05$
	10.24–12.96 or >14.06	$0.71^{+0.20}_{-0.22} \pm 0.04$	$0.76^{+0.52}_{-0.32} \pm 0.07$
Belle [793]	0.0–2.0	$0.29^{+0.21}_{-0.18} \pm 0.02$	$0.47^{+0.26}_{-0.32} \pm 0.03$
	2.0–5.0	$0.75^{+0.21}_{-0.22} \pm 0.05$	$0.14^{+0.20}_{-0.26} \pm 0.07$
	5.0–8.86	$0.65^{+0.26}_{-0.27} \pm 0.06$	$0.47^{+0.16}_{-0.25} \pm 0.14$
	10.09–12.86	$0.17^{+0.17}_{-0.15} \pm 0.03$	$0.43^{+0.18}_{-0.20} \pm 0.03$
	14.18–16.0	$-0.15^{+0.27}_{-0.23} \pm 0.07$	$0.70^{+0.16}_{-0.22} \pm 0.10$
	> 16.0	$0.12^{+0.15}_{-0.13} \pm 0.02$	$0.66^{+0.11}_{-0.16} \pm 0.04$
	1.0–6.0	$0.67^{+0.23}_{-0.23} \pm 0.05$	$0.26^{+0.27}_{-0.30} \pm 0.07$

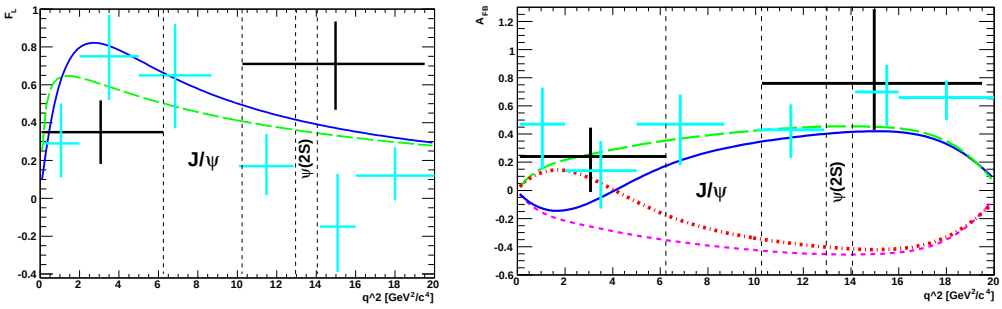

Fig. 52. Measurements of F_L (left) and of $A_{\rm FB}$ (right) as a function of q^2 for $B \to K^*\ell^+\ell^-$ from *BABAR* (black points) and Belle (cyan points). The curves show predictions for four cases, the SM (blue solid curve), the flipped-sign C_7 case (green dashed curve), the case of flipped-sign C_9C_{10} (magenta dotted curve), and the case with both flipped-sign C_7 and C_9C_{10} (red dash-dotted curve).

thus in variance with the available data on the inclusive $b \to s\gamma, \ell^+\ell^-$ transitions. This observation makes clear that to bound the values of the various Wilson coefficients one should exploit all the experimental information in the $b \to s\gamma$ and $b \to s\ell^+\ell^-$ sector combining both inclusive and exclusive channels.

The exclusive decays $B \to \pi(\rho)\ell^+\ell^-$ are the corresponding $b \to d$ transitions that are suppressed with respect to the $b \to s$ transitions by $|V_{td}/V_{ts}|^2$. *BABAR* [799] searched for $B \to \pi\ell^+\ell^-$ events using 230 million $B\bar{B}$ events while Belle [800] searched for $B \to (\pi, \rho, \omega)\ell^+\ell^-$ modes using 657 million $B\bar{B}$ events. The lowest branching fraction upper limit is set for the $B \to \pi\ell^+\ell^-$ mode by Belle yielding $\mathcal{B}(B \to \pi\ell^+\ell^-) < 4.9 \times 10^{-8}$ at 90% CL which just lies a factor of around 1.5 above the central value of the SM prediction which reads $\mathcal{B}(B \to \pi\ell^+\ell^-) = (3.3 \pm 1.0) \times 10^{-8}$ [801].

The LHCb experiment will collect $\sim 7 \times 10^3$ fully reconstructed $B^0 \to K^{*0}\mu^+\mu^-$ events per $2\,\text{fb}^{-1}$ integrated luminosity [802]. At the LHC design luminosity, such an data-set will be acquired in a single year of data-taking. Before such conditions are achieved, with even the data from the LHC pilot run, a $0.1\,\text{fb}^{-1}$ integrated luminosity would therefore give a comparable number of events to the final dataset expected from

the B-factory experiments [791, 793] and CDF [797]. The branching ratio for this decay is already measured with a precision comparable to the level of theoretical uncertainties. LHCb's experimental exploration will therefore focus on angular observables such as the forward-backward asymmetry $A_{\rm FB}$.

Given the background expected from simulation studies [802], LHCb will be able to determine the zero-crossing point of this asymmetry by counting forward- and backward-events with a statistical precision of $0.5\,\text{GeV}^2$ with $2\,\text{fb}^{-1}$ integrated luminosity [803]. Additional systematic contributions to this precision from e.g. the determination of acceptance and trigger efficiencies are under study. A measurement with a statistical uncertainty at the level of present theoretical uncertainties on the zero-crossing point (see Sec. 6.6.3) will therefore require a $10\,\text{fb}^{-1}$ integrated luminosity. However, using information from the θ_K angular distribution, in particular, by making a simultaneous fit for both the $A_{\rm FB}$ and F_L observables, a factor ~ 2 increase in the statistical precision can be obtained [804]. Adding the information from the angle ϕ, a full angular fit will give a further $\sim 30\%$ increase in the precision [805]. More significantly, such a full angular fit will give access to the underlying amplitudes, from which any observable can then be formed. As detailed in Sec. 6.6.4, LHCb will be able to measure, with good precision, other theoretically well controlled observables such as $A_T^{(2,3,4)}$ (see Eq 307), which will give very different new physics sensitivity to $A_{\rm FB}$. Studies indicate that full angular fits can be made to converge with data-sets in excess of the expectation from $2\,\text{fb}^{-1}$ integrated luminosity. In practise, performing such a fit will require excellent understanding of the trigger and detector efficiencies and will be a later LHCb measurement.

6.6.6. *Rare $K \to \pi\nu\bar{\nu}, \ell^+\ell^-$ decays in and beyond the SM*

The rare decays $K_L \to \pi^0\nu\bar{\nu}$, $K^+ \to \pi^+\nu\bar{\nu}$, and $K_L \to \pi^0\ell^+\ell^-$ proceed dominantly through heavy-quark induced FCNC. Since their rates in the SM are predicted with high precision, they offer the cleanest and clearest window into the sector of $s \to d$ transitions. Their study is thus complementary to B physics in searching for NP, and constraining the possible models.

6.6.6.1. *Prediction within the SM.* The electroweak processes inducing the rare K decays are of three types: Z penguin and $W^\pm$ boxes, single- and double-photon penguin. The former as well as the CP-violating single-photon penguin, are always dominated by short-distance physics, i.e., the top- and charm-quark contribution. On the other hand, the CP-conserving photon penguins are fully dominated by the long-distance up-quark contribution, in which case they get further enhanced by the $\Delta I = 1/2$ rule. These contributions are to be evaluated in χPT, by relating them to other, well-measured observables.

For $K_L \to \pi^0\nu\bar{\nu}$ and $K^+ \to \pi^+\nu\bar{\nu}$, short-distance physics dominates because of the absence of photon penguins and the quadratic GIM breaking exhibited in the Z penguin. The calculation of the branching ratios can be split into several pieces. First, the top quark contribution X_t is known including NLO QCD effects [806, 807]. While NLO electroweak effects have been estimated in the large top-quark mass limit [808]. In the charm-quark sector, the NNLO QCD [809, 810] and electroweak [811] corrections have been computed, significantly reducing the scheme and scale ambiguities in the corresponding quantity P_c. For both these contributions, the matrix elements of the resulting

dimension-six operator, encoded in κ_L and κ_+, are obtained from the full set of $K_{\ell 3}$ data, including isospin-breaking and long-distance QED corrections [812]. Higher-dimensional contributions for the charm quark, which are negligible in the case of the top quark since they are suppressed by m_K^2/m_t^2, as well as the residual up-quark contributions are parametrized by $\delta P_{u,c}$, which has been estimated using χPT [813]. The error on $\delta P_{u,c}$ may be reduced through LQCD studies [814]. Finally, the rate for $K_1 \approx K_S$ and $K_2 \approx K_L$ are similar, and thus indirect CP-violation, $K_L \to \varepsilon K_2 \to \pi^0\nu\bar{\nu}$, is below the percent level since the smallness of $\varepsilon_K \sim 10^{-3}$ cannot be compensated [815]. Putting all these pieces together, the $K \to \pi\nu\bar{\nu}$ rates are predicted with a high level of accuracy in the SM

$$\begin{aligned} \mathcal{B}\left(K_L \to \pi^0\nu\bar{\nu}\right) &= (2.54 \pm 0.35) \times 10^{-11}\,, \\ \mathcal{B}\left(K^+ \to \pi^+\nu\bar{\nu}\right) &= (8.51 \pm 0.73) \times 10^{-11}\,. \end{aligned} \tag{310}$$

The composition of the quoted errors is as follows $69\%_{\rm CKM}$, $12\%_{\rm para}$, $15\%_{X_t}$, $4\%_{\kappa_L}$ and $52\%_{\rm CKM}$, $17\%_{\rm para}$, $12\%_{X_t}$, $12\%_{\delta P_{u,c}}$, $5\%_{P_c}$, $2\%_{\kappa_+}$, where the parametric uncertainty combines the errors on m_t, m_c, and α_s.

For the $K \to \pi\ell^+\ell^-$ modes, besides the short-distance top- and charm-quark contributions, some long-distance effects arise due to the photon penguins. For the CP-odd K_2, the single-photon penguin is CP-violating, hence still short-distance dominated, and is known precisely [816]. On the other hand, the double-photon penguin is a purely long-distance CP-conserving contribution. It has been evaluated from $K_L \to \pi^0\gamma\gamma$ data, and turns out to be competitive in the muon case [817, 818]. For the K^+ and the CP-even K_1, the CP-conserving single-photon penguin completely dominates, hence these modes do not give us access to the short-distance physics. Further, this photon penguin is large enough to compensate for $\varepsilon_K \sim 10^{-3}$ in the indirect CP-violating $K_L \to \varepsilon K_1 \to \pi^0\gamma^* \to \pi^0\ell^+\ell^-$ contribution [819]. This piece can be brought under control thanks to the $\mathcal{B}(K_S \to \pi^0\ell^+\ell^-)$ measurements, up to its interference sign [817,820–822]. Nevertheless, the current experimental accuracy for $\mathcal{B}(K_S \to \pi^0\ell^+\ell^-)$ still represents the largest source of uncertainty in the $\mathcal{B}(K_L \to \pi^0\ell^+\ell^-)$ predictions, which are

$$\begin{aligned} \mathcal{B}(K_L \to \pi^0 e^+ e^-) &= 3.54^{+0.98}_{-0.85}\ \left(1.56^{+0.62}_{-0.49}\right) \times 10^{-11}\,, \\ \mathcal{B}(K_L \to \pi^0 \mu^+ \mu^-) &= 1.41^{+0.28}_{-0.26}\ \left(0.95^{+0.22}_{-0.21}\right) \times 10^{-11}\,, \end{aligned} \tag{311}$$

for constructive (destructive) interference.

For the $K_L \to \ell^+\ell^-$ modes, though the short-distance top- and charm-quark contributions are predicted with excellent accuracy [823], it is the long-distance two-photon penguin which dominates. Its theoretical estimation is problematic because, contrary to $K_L \to \pi^0\gamma\gamma \to \pi^0\ell^+\ell^-$, it i) diverges in χPT [824] and ii) produces the final lepton pair in the same state as the short-distance processes, and hence interferes with them with an unknown sign. Better measurements of $K_S \to \pi^0\gamma\gamma$ and $K^+ \to \pi^+\gamma\gamma$ could settle this issue [825]. These two problems have, up to now, upset attempts to extract the subleading short-distance top- and charm-quark components from the well-measured $\mathcal{B}(K_L \to \mu^+\mu^-)$.

6.6.6.2. *Sensitivity to NP effects.* Rare K decays are ideally suited to search for NP effects. Indeed, besides the loop suppression of the underlying FCNC processes, they are

significantly CKM suppressed. Compared to $\mathcal{A}(b \to s, d)$, the amplitudes in the $s \to d$ sector scale as

$$\begin{aligned} \mathcal{A}(s \to d) &\sim |V_{td}^* V_{ts}| \sim \lambda^5 \,, \\ \mathcal{A}(b \to d) &\sim |V_{td}^* V_{tb}| \sim \lambda^3 \,, \\ \mathcal{A}(b \to s) &\sim |V_{ts}^* V_{tb}| \sim \lambda^2 \,, \end{aligned} \tag{312}$$

with $\lambda \sim 0.22$. If NP is generic, i.e., it does not follow the CKM scaling (312), it is clear that the constraints from rare K decays are typically the most stringent. Stated differently, a measurement of $K_L \to \pi^0 \nu\bar{\nu}$ close to its SM prediction is the most difficult to reconcile with the existence of generic NP at a reasonably low scale around a TeV.

NP models in which the CKM scalings (312) are preserved are referred to as of MFV type [135]. When this is the case, NP can show up at a low scale without violating experimental bounds, including those from rare K decays. In addition, when MFV is enforced within a particular model like the MSSM, the effects are expected to be rather small, often beyond the experimental sensitivity. This has been analyzed at moderate [826] or large $\tan\beta$ [144, 827, 828], without R-parity [829], or with MFV imposed at the GUT scale [157, 158]. Turning this around, the rare K decays emerge as one of the best places to look for deviations of the MFV hypothesis [137, 830, 831]. If the flavor-breaking transitions induced by the NP particles are not precisely aligned with those of the SM, large effects can show up. This is true even given the current measurement of the $K^+ \to \pi^+ \nu\bar{\nu}$ mode. The model-independent bound it implies on the $K_L \to \pi^0 \nu\bar{\nu}$ mode is still about 30 times higher that the SM prediction [832].

Each NP model affects the basic electroweak FCNC differently. If it enters into the Z penguin, the two $K \to \pi\nu\bar{\nu}$ modes exhibit the best sensitivity. This happens for example in the MSSM from chargino-squark loops at moderate $\tan\beta$ [833–837] or charged-Higgs-quark loops at large $\tan\beta$ [828], with R-parity violation [838–840], in little Higgs models without [170] and with [171–173, 841] T-parity, and in the presence of extra-dimensions [181, 663, 842]. In most of these models, correlated changes to the short-distance photon penguin are induced [843,844], and these could then be probed and disentangled using the $K_L \to \pi^0 \ell^+ \ell^-$ modes. Combined measurements of all the rare K decay modes can serve as a powerful discriminator among models [818,822]. Further, purely electromagnetic effects could also be present, as in the electromagnetic operators, for which the $K_L \to \pi^0 \ell^+ \ell^-$ modes are clean probes while ε' is problematic [845].

In addition, NP could occur with helicity-suppressed couplings proportional to the fermion mass. Typical examples are the neutral Higgs-induced FCNC, as generated in the MSSM at large $\tan\beta$ [142, 144, 153, 827]. Obviously, the $K_L \to \pi^0 \mu^+ \mu^-$ and $K_L \to \mu^+ \mu^-$ modes are the only available windows for such helicity-suppressed effects in the $s \to d$ sector. Therefore, these effects can in principle be disentangled from NP in the Z or photon penguins by a combined analysis of all the rare K decay modes [822].

In conclusion, the $K \to \pi\nu\bar{\nu}$ modes offer one of the best opportunities to find a irrefutable signal of NP in the field of flavor physics. Furthermore, combining information on the different $K \to \pi\nu\bar{\nu}$ and $K_L \to \pi^0 \ell^+ \ell^-$ channels allows one to probe and disentangle NP effects in most of the different types of FCNC interactions. Being either free of hadronic uncertainties, or these being under sufficiently good theoretical control, the stage is set for a complete and detailed study of $s \to d$ transitions.

6.6.7. *Experimental status of $K \to \pi\nu\bar{\nu}$ and $K_L \to \pi\ell^+\ell^-$*

The E787 and E949 experiments have established the feasibility of observing the $K^+ \to \pi^+\nu\bar{\nu}$ decay using a stopped Kaon beam [197]. Observation of seven candidate events by E787 and E949 yields $\mathcal{B}(K^+ \to \pi^+\nu\bar{\nu}) = \left(1.73^{+1.15}_{-1.05}\right) \times 10^{-10}$ when the relative acceptance and measured background are taken into account with a likelihood method [846]. It has been estimated that, assuming the SM decay rate, a stopped K^+ experiment could accumulate hundreds of $K^+ \to \pi^+\nu\bar{\nu}$ events, using a copious proton source such as Project-X at FNAL [847]. The NA62 experiment at CERN seeks to observe on the order of a hundred $K^+ \to \pi^+\nu\bar{\nu}$ decays using a decay-in-flight technique in an unseparated 75 GeV beam.

The experiment E391a has set a limit of $\mathcal{B}(K_L \to \pi^0\nu\bar{\nu}) < 670 \times 10^{-10}$ at 90% CL in a sample of 5.1×10^9 K_L decays [848]. The experimental result is still larger than the model-independent limit [832] of $\mathcal{B}(K_L \to \pi^0\nu\bar{\nu}) < 14.6 \times 10^{-10}$ at 90% CL implied by the $K^+ \to \pi^+\nu\bar{\nu}$ results. E391a is currently analyzing an additional 3.6×10^9 K_L decays and plans to implement an upgraded detector in the experiment E14 at JPARC that would have a sensitivity comparable to the expected SM $K_L \to \pi^0\nu\bar{\nu}$ decay rate.

The experimental limits on $K_L \to \pi^0 e^+ e^-$ and $K_L \to \pi^0\mu^+\mu^-$ are 2.8×10^{-10} and 3.8×10^{-10} at 90% CL by the KTeV collaboration [4]. The $K_L \to \pi^0 e^+ e^-$ mode suffers from an irreducible background from $K_L \to \gamma\gamma e^+ e^-$ decays, $\mathcal{B}(K_L \to \gamma\gamma e^+ e^-) = (5.95 \pm 0.33) \times 10^{-7}$, that can be suppressed by a precise diphoton mass resolution. There are currently no experiments planned to continue the search for these decays.

6.7. *Rare D meson decays*

6.7.1. *Rare leptonic decays*

In the Standard Model (SM) flavor-changing neutral current (FCNC) decays of charm hadrons are highly suppressed by the GIM mechanism [849]. In the process $D^0 \to X_u\ell^+\ell^-$ this leads to branching fractions of $\mathcal{O}(10^{-8})$ [850]. However, this process can be enhanced by the presence of long-distance contributions, increasing the branching fractions by several orders of magnitude [850]. The effect of these long distance contributions from intermediate resonances can be separated by examining the invariant mass of the lepton pair (e.g. $\phi \to \ell^+\ell^-$). In radiative charm decays (e.g. $c \to u\gamma$), the long distance contributions are not so easily determined, making it increasingly difficult to study the short-distance effects. The branching fractions of the $D^0 \to \ell^+\ell^-$ final state are predicted to be $\mathcal{O}(10^{-13})$ [850], including contributions from long distance processes.

Lepton family-number violating (LFV), and lepton-number violating (LV) decays are strictly forbidden in the SM. The processes are allowed in extensions to the SM with non-zero neutrino mass but at a very low level [850]. A large impact is expected to come from R-parity violating super-symmetry. Depending on the size of the R-parity violating couplings, branching fractions for these processes can be enhanced up to the $\mathcal{O}(10^{-6})$ level for differing $c \to u\ell^+\ell^-$ processes.

The search for FCNC processes in charm decays has not received the attention that the K and B meson sectors have attracted. The current measurements of these decays (Tab. 50-52) agree with SM predictions, and there are ongoing efforts to improve both theoretical predictions and experimental limits. There is also ongoing effort to measure new effects such as *CP* violation in these processes.

Table 50
90% confidence limits on Flavor-changing neutral current, (FCNC), lepton family-number (LFV) violating, or lepton-number (LV) violating decay modes of the D^+ (left) and the D_s^+ (right) [285].

Process	Decay type	Upper limit	Reference
$\pi^+ e^+e^-$	FCNC	$< 7.4 \times 10^{-6}$	[851]
$\pi^+ \mu^+\mu^-$	FCNC	$< 3.9 \times 10^{-6}$	[852]
$\rho^+\mu^+\mu^-$	FCNC	$< 5.6 \times 10^{-4}$	[853]
$K^+ e^+e^-$	N/A [a]	$< 6.2 \times 10^{-6}$	[851]
$K^+ \mu^+\mu^-$	N/A[a]	$< 9.2 \times 10^{-6}$	[854]
$\pi^+ e^\pm \mu^\mp$	LFV	$< 3.4 \times 10^{-5}$	[855]
$K^+ e^\pm \mu^\mp$	LFV	$< 6.8 \times 10^{-5}$	[855]
$\pi^- e^+ e^+$	LV	$< 3.6 \times 10^{-6}$	[851]
$\pi^- \mu^+ \mu^+$	LV	$< 4.8 \times 10^{-6}$	[854]
$\pi^- e^+ \mu^+$	LV	$< 5.0 \times 10^{-5}$	[855]
$\rho^-\mu^+ \mu^+$	LV	$< 5.6 \times 10^{-4}$	[853]
$K^- e^+ e^+$	LV	$< 4.5 \times 10^{-6}$	[851]
$K^- \mu^+ \mu^+$	LV	$< 1.3 \times 10^{-5}$	[854]
$K^- e^+ \mu^+$	LV	$< 1.3 \times 10^{-4}$	[856]
$K^{*-} \mu^+ \mu^+$	LV	$< 8.5 \times 10^{-4}$	[853]

Process	Decay type	Upper limit	Reference
$\pi^+ e^+e^-$	N/A[a]	$< 2.7 \times 10^{-4}$	[855]
$\pi^+ \mu^+\mu^-$	N/A[a]	$< 2.6 \times 10^{-5}$	[854]
$K^+ e^+e^-$	FCNC	$< 1.6 \times 10^{-3}$	[855]
$K^+ \mu^+\mu^-$	FCNC	$< 3.6 \times 10^{-5}$	[854]
$K^{*-} \mu^+\mu^-$	FCNC	$< 1.4 \times 10^{-3}$	[853]
$\pi^+ e^\pm \mu^\mp$	LFV	$< 6.1 \times 10^{-4}$	[855]
$K^+ e^\pm \mu^\mp$	LFV	$< 6.3 \times 10^{-4}$	[855]
$\pi^- e^+ e^+$	LV	$< 6.9 \times 10^{-4}$	[855]
$\pi^- \mu^+ \mu^+$	LV	$< 2.9 \times 10^{-5}$	[854]
$\pi^- e^+ \mu^+$	LV	$< 7.3 \times 10^{-4}$	[855]
$K^- e^+ e^+$	LV	$< 6.3 \times 10^{-4}$	[855]
$K^- \mu^+ \mu^+$	LV	$< 1.3 \times 10^{-5}$	[854]
$K^- e^+ \mu^+$	LV	$< 6.8 \times 10^{-4}$	[855]
$K^{*-} \mu^+ \mu^+$	LV	$< 1.4 \times 10^{-3}$	[853]

[a] These modes are not a useful test for FCNC, because both quarks must change flavor.

Table 51
90% confidence limits on flavor-changing neutral current (FCNC), or lepton-number (LV) violating decay modes of the Λ_c [285].

Process	Decay type	Upper limit	Reference
$p\mu^+\mu^-$	FCNC	$< 3.4 \times 10^{-4}$	[853]
$\Sigma^-\mu^+ \mu^+$	LV	$< 7.0 \times 10^{-4}$	[853]

Therefore, searching for FCNC, LFV, or LV modes in the charm sector is a relatively inviting place to investigate new physics in the SM. Similar arguments hold for rare decays in the K and B sector. However, the charm system is unique in that it couples an up-type quark to new physics.

It is clear that due to the relatively little experimental progress in this area within the last decade and the large data sets from the flavor factories, that there is a several orders of magnitude in precision to be gained from re-reanalyzing these measurements with meaningful limits to be derived which may have the potential to constrain parameter space for many new physics models. At present the upper limits for branching fractions for those modes more recently measured [851,852,858] are starting to confine the allowed parameter space of R-parity violating super-symmetric models.

Table 52
90% confidence limits on flavor-changing neutral current (FCNC), lepton family-number (LFV) violating, or lepton-number (LV) violating decay modes of the D^0 [285].

Process	Decay type	Upper limit	Reference	Process	Decay type	Upper limit	Reference
$\gamma\gamma$	FCNC	$< 2.7 \times 10^{-5}$	[857]	$\overline{K}^{*0}\ \mu^+\mu^-$	N/A[a]	$< 2.4 \times 10^{-5}$	[860]
e^+e^-	FCNC	$< 1.2 \times 10^{-6}$	[858]	$\pi^+\pi^-\ \pi^0\ \mu^+\mu^-$	FCNC	$< 8.1 \times 10^{-4}$	[853]
$\mu^+\mu^-$	FCNC	$< 1.3 \times 10^{-6}$	[858]	$e^\pm\ \mu^\mp$	LFV	$< 8.1 \times 10^{-7}$	[858]
$\pi^0\ e^+e^-$	FCNC	$< 4.5 \times 10^{-5}$	[859]	$\pi^0\ e^\pm\ \mu^\mp$	LFV	$< 8.6 \times 10^{-5}$	[859]
$\pi^0\ \mu^+\mu^-$	FCNC	$< 1.8 \times 10^{-4}$	[853]	$\eta e^\pm\ \mu^\mp$	LFV	$< 1.0 \times 10^{-4}$	[859]
ηe^+e^-	FCNC	$< 1.1 \times 10^{-4}$	[859]	$\pi^+\pi^-\ e^\pm\ \mu^\mp$	LFV	$< 1.5 \times 10^{-5}$	[860]
$\eta\mu^+\mu^-$	FCNC	$< 5.3 \times 10^{-4}$	[859]	$\rho^0 e^\pm\ \mu^\mp$	LFV	$< 4.9 \times 10^{-5}$	[859]
$\pi^+\pi^-\ e^+e^-$	FCNC	$< 3.73 \times 10^{-4}$	[860]	$\omega e^\pm\ \mu^\mp$	LFV	$< 1.2 \times 10^{-4}$	[859]
$\rho^0 e^+e^-$	FCNC	$< 1.0 \times 10^{-4}$	[859]	$K^-K^+\ e^\pm\ \mu^\mp$	LFV	$< 1.8 \times 10^{-4}$	[860]
$\pi^+\pi^-\ \mu^+\mu^-$	FCNC	$< 3.0 \times 10^{-5}$	[860]	$\phi e^\pm\ \mu^\mp$	LFV	$< 3.4 \times 10^{-5}$	[859]
$\rho^0\mu^+\mu^-$	FCNC	$< 2.2 \times 10^{-5}$	[860]	$\overline{K}^0\ e^\pm\ \mu^\mp$	LFV	$< 1.0 \times 10^{-4}$	[859]
ωe^+e^-	FCNC	$< 1.8 \times 10^{-4}$	[859]	$K^-\ \pi^+\ e^\pm\ \mu^\mp$	LFV	$< 5.53 \times 10^{-4}$	[859]
$\omega\mu^+\mu^-$	FCNC	$< 8.3 \times 10^{-4}$	[859]	$\overline{K}^{*0}\ e^\pm\ \mu^\mp$	LFV	$< 8.3 \times 10^{-5}$	[860]
$K^+K^-\ e^+e^-$	FCNC	$< 3.15 \times 10^{-4}$	[860]	$\pi^-\ \pi^-\ e^+\ e^+$ + c.c	LV	$< 1.12 \times 10^{-4}$	[860]
ϕe^+e^-	FCNC	$< 5.2 \times 10^{-5}$	[859]	$\pi^-\ \pi^-\ \mu^+\ \mu^+$ + c.c	LV	$< 2.9 \times 10^{-5}$	[860]
$K^+K^-\ \mu^+\mu^-$	FCNC	$< 3.3 \times 10^{-5}$	[860]	$K^-\ \pi^-\ e^+\ e^+$ + c.c	LV	$< 2.06 \times 10^{-4}$	[860]
$\phi\mu^+\mu^-$	FCNC	$< 3.1 \times 10^{-5}$	[860]	$K^-\ \pi^-\ \mu^+\ \mu^+$ + c.c	LV	$< 3.9 \times 10^{-4}$	[860]
$\overline{K}^0\ e^+e^-$	N/A[a]	$< 1.1 \times 10^{-4}$	[859]	$K^-\ K^-\ e^+\ e^+$ + c.c	LV	$< 1.52 \times 10^{-4}$	[860]
$\overline{K}^0\ \mu^+\mu^-$	N/A[a]	$< 2.6 \times 10^{-4}$	[853]	$K^-\ K^-\ \mu^+\ \mu^+$ + c.c	LV	$< 9.4 \times 10^{-5}$	[860]
$K^-\ \pi^+\ e^+e^-$	FCNC	$< 3.85 \times 10^{-4}$	[860]	$\pi^-\ \pi^-\ e^+\ \mu^+$ + c.c	LV	$< 7.9 \times 10^{-5}$	[860]
$\overline{K}^{*0}\ e^+e^-$	N/A[a]	$< 4.7 \times 10^{-5}$	[860]	$K^-\ \pi^-\ e^+\ \mu^+$ + c.c	LV	$< 2.18 \times 10^{-4}$	[860]
$K^+\ \pi^+\ \mu^+\mu^-$	FCNC	$< 3.59 \times 10^{-4}$	[860]	$K^-\ K^-\ e^+\ \mu^+$ + c.c	LV	$< 5.7 \times 10^{-5}$	[860]

[a] These modes are not a useful test for FCNC, because both quarks must change flavor.

6.7.2. *D and D_s decay constants from lattice QCD*

Quark confinement inside hadrons makes the direct experimental determination of how quarks change from one flavor to another via the weak interactions impossible. Instead we must study experimentally the decay of a hadron, calculate the effect of the strong force on the quarks in the hadron and then correct for this to expose the quark interaction with the W boson. The simplest such hadron decay is annihilation of a charged pseudoscalar into a W and thence into a lepton and an antineutrino. The leptonic width of such a pseudoscalar meson, P, of quark content $a\overline{b}$ (or $\overline{a}b$) is given by:

$$\Gamma(P \to l\nu_l(\gamma)) = \frac{G_F^2 |V_{ab}|^2}{8\pi} f_P^2 m_l^2 m_P \left(1 - \frac{m_l^2}{m_P^2}\right)^2 . \qquad (313)$$

V_{ab} is from the Cabibbo-Kobayashi-Maskawa (CKM) matrix element which encapsulates the Standard Model description of quark coupling to the W. f_P, the decay constant, parametrizes the amplitude for the meson annihilation to a W and is basically the probability for the quark and antiquark to be in the same place. It is defined by:

$$f_P m_P =< 0|\overline{\psi}(x)\gamma_0\gamma_5\psi(x)|P(\boldsymbol{p}=0) > \tag{314}$$

Note that f_P is a property of the meson in pure QCD. In the real world there is also electromagnetism and so the experimental rate must be corrected for this. It is a small (1-2%) effect, except for very heavy mesons (Bs) decaying to very light leptons (electrons) [261]. If V_{ab} is known from elsewhere an experimental value for Γ gives f_P, to be compared to theory. If not, an accurate theoretical value for f_P, combined with experiment, can yield a value of V_{ab}.

Accuracy in both experiment and theory is important for useful tests of the Standard Model. Here the numerical techniques of lattice QCD come to the fore for the theoretical calculation because it is now possible to do such calculations accurately [91] and the pseudoscalar decay constant is one of the simplest quantities to calculate in lattice QCD.

A lattice QCD calculation proceeds by splitting space-time up into a lattice of points (with spacing a) and generating sets of gluon fields on the lattice that are 'typical snapshots of the vacuum'. For accurate calculations these snapshots need to include the effect of quark-antiquark pairs, known as 'sea' quarks, generated by energy fluctuations in the vacuum. The important sea quarks are those which cost little energy to make i.e. the light u, d and s. Unfortunately in lattice QCD it is numerically expensive to work with sea u and d masses that are close to their physical values and we have to extrapolate to the physical point from heavier values using chiral perturbation theory. Valence quarks that make up a hadron are propagated through these gluon fields, allowing any number of interactions. We tie together appropriate valence quark and antiquark propagators to make, for example, a meson correlator which is then printed out as a function of lattice time, t (we sum on spatial lattice sites to project on to zero spatial momentum). We fit as a function of t to a multi-exponential form:

$$< 0|H^\dagger(0)H(t)|0 >= \sum_i A_i(e^{-E_i t} + e^{-E_i(T-t)}) \tag{315}$$

where T is the time extent of the lattice. The smallest value of E_i (corresponding to the state that survives to large t) is the ground state mass in that channel, and A_i is the square of the matrix element between the vacuum and P of the operator H used to create and destroy the hadron. If H is the local temporal axial current of equation 314 (and this is the operator used if the valence quark and antiquark are simply tied together at the same start and end points matching colors and spins) then A_0 will be directly related to the decay constant of the ground state pseudoscalar.

For K and π mesons several very accurate decay constant determinations have been done now in lattice QCD including the full effect of u, d and s quarks in the sea, and at several values of the lattice spacing. Extrapolations to the physical point in the u/d mass and $a = 0$ have been done with a full error budget. The lattice value of f_K/f_π can be used to determine V_{us} to 1% accuracy. (* This is presumably described in the subsection on strange physics, so you only need a reference to that here *).

For the charged charmed mesons D_d and D_s the lattice determination of the decay constant can be compared to an experimental one derived from the leptonic decay rate if

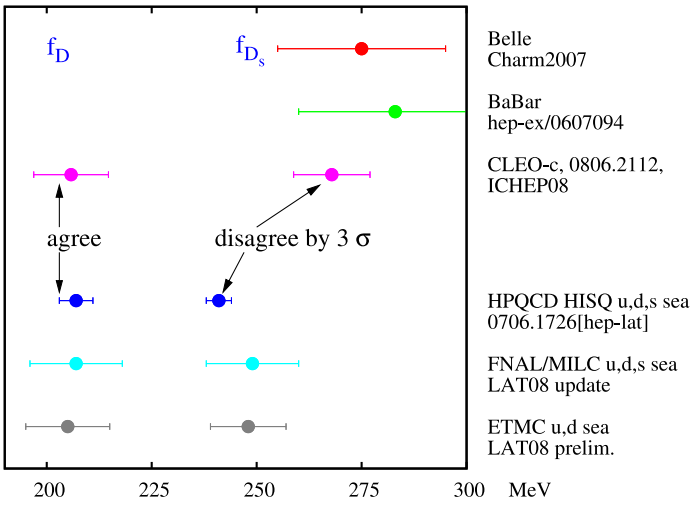

Fig. 53. A comparison of lattice results for the D and D_s decay constant [340,429,861] and experimental results obtained from the leptonic decay rate using CKM elements V_{cs} and V_{cd} from elsewhere [457,862–865]. There is agreement between lattice and experiment for f_D, but not for f_{D_s}.

values of V_{cd} and V_{cs} are assumed (usually $V_{us} = V_{cd}$ and $V_{ud} = V_{cs}$). This is an important test of modern lattice techniques, that can be used to calibrate lattice errors. The errors expected in the D/D_s case are similar to those for K/π. The statistical errors on the raw lattice numbers are similar, and the extrapolations that must be done in the u/d mass are less of an issue than for π. Indeed for the D_s, which has no valence u/d quark, there is very little dependence on the (sea) u/d mass and so very little extrapolation.

The extrapolations to $a = 0$ are worse for D/D_s than for K/π and the reason is that the charm quark mass in lattice units, $m_c a$, is relatively large. Typically a lattice result at non-zero lattice spacing will have a power series dependence on the lattice spacing with the scale of the a-dependent terms set by a typical momentum inside the bound state. Extrapolations to $a = 0$ can then be done using this functional form, and the resulting error will depend on the size of the extrapolation. For charm physics the scale of the a-dependent terms is set by m_c and we expect

$$m = m_{a=0}(1 + A(m_c a)^2 + B(m_c a)^4 + \ldots). \tag{316}$$

The extrapolation can then be quite severe, and will determine the final error, if we do not take steps to control or eliminate terms in this series by improving the action.

The Highly Improved Staggered Quark (HISQ) action for charm quarks [866] eliminates the $(m_c a)^2$ term and results at three values of the lattice spacing then give an accurate extrapolation to $a = 0$ with a 2% final error [340]. Alternatives to this are the 'Fermilab interpretation' of improved Wilson quarks [861] and the twisted mass formalism [429]. Both have larger errors than for HISQ at present. Improved Wilson quarks have discretization errors at $\alpha_s(m_c a)$ in principle but the Fermilab interpretation removes the leading errors that come from the kinetic energy, and experience has shown that a-dependence is small in this formalism. However, relativity is given up and this means, for example, that the masses of mesons cannot be as accurately tuned and a renormalisation factor is needed to relate the decay constant on the lattice to a result appropriate to the real world (at $a = 0$). The twisted mass formalism uses a relativistic

framework with errors appearing first at $m_c a)^2$. It has so far been applied at two values of the lattice spacing for gluon field configurations that do not include s sea quarks, so are not completely realistic.

Fig. 53 shows a comparison of these lattice calculations to new experimental results from CLEO-c for both f_D and f_{D_s} (which appeared after [340,861]) and older results for f_{D_s} from BaBar [865]. The good agreement between lattice and experiment for f_D (and f_K and f_π) contrasts with the 3σ disagreement for f_{D_s} and it has been suggested that this is a harbinger of new physics [867]. Improved experimental errors for f_{D_s} will shed light on this. Meanwhile, lattice calculations and their systematic errors are also being tested against other quantities in charm physics [868].

6.7.3. *Experimental results on f_D*

Fully leptonic decays of $D^+_{(s)}$ mesons depend upon both the weak and strong interactions. The weak part is straightforward to describe in terms of the annihilation of the quark antiquark pair to a W^+ boson. The strong interaction is required to describe the gluon exchange between the quark and antiquark. The strong interaction effects are parametrized by the decay constant, $f_{D^+_{(s)}}$, such that the total decay rate is given by

$$\Gamma(D^+_{(s)} \to l^+\nu) = \frac{G_F^2}{8\pi} f^2_{D^+_{(s)}} m_l^2 M_{D^+_{(s)}} [1 - \frac{m_l^2}{M^2_{D^+_{(s)}}}]^2 |V_{cd(s)}|^2 \ ,$$

where G_F is the Fermi coupling constant, $M_{D^+_{(s)}}$ and m_l are the $D^+_{(s)}$ meson and final state lepton masses, respectively, and $V_{cd(s)}$ is a Cabibbo-Kobayashi-Maskawa (CKM) matrix element. The values of V_{cd} and V_{cs} can be equated V_{us} and V_{ud}, which are well known. Therefore, within the standard model, measurements of the fully leptonic decay rates allow a determination of $f_{D^+_{(s)}}$.

Measurements of $f_{D^+_{(s)}}$ can be compared to calculations from theories of QCD, the most precise of which use unquenched lattice techniques (see for example Ref. [340].) Similar calculations of strong parameters in B meson decay are relied upon to extract CKM matrix elements, such as $|V_{td}|/|V_{ts}|$ from the rates of B mixing. Therefore, comparing predictions for $f_{D^+_{(s)}}$ to measurements is important for validating the QCD calculation techniques. Deviations of experimental measurements from theoretical predictions may be a consequence of non-SM physics (see for example Ref. [867]).

CLEO-c provides the most precise experimental determinations of f_{D^+} [863] and $f_{D_s^+}$ [258,869] to date. All measurements at CLEO-c exploit the recoil technique described in Sec. 3.2.6.

The determination of f_{D^+} uses six hadronic decays of the D^- as tags: $K^+\pi^-\pi^-$, $K^+\pi^-\pi^-\pi^0$, $K^0_S\pi^-$, $K^0_S\pi^-\pi^-\pi^+$, $K^0_S\pi^-\pi^0$ and $K^+K^-\pi^-$. The analysis is performed on 818 pb^{-1} of $e^+e^- \to \psi(3770) \to D\bar{D}$ data. 460,000 tagged events are reconstructed. The fully leptonic decay reconstructed is $D^+ \to \mu^+\nu_\mu$, Events are considered as signal if they contain a single additional charged track of opposite charge to the fully reconstructed tag decay. Events with additional neutral energy deposits in the calorimeter are vetoed. The beam-energy constrained missing-mass squared, MM^2 is computed:

$$MM^2 = (E_{beam} - E_{\mu^+})^2 - (-\mathbf{p}_{D^-} - \mathbf{p}_{\mu^+})^2 \ ,$$

where E_{beam} is the beam energy, $\mathbf{p}_{D^-}$ is the three-momentum of the fully reconstructed D^- decay and E_{μ^+} ($\mathbf{p}_{\mu^+}$) is the energy (three-momentum) of the μ^+ candidate. For signal events the measured MM^2 will be close to zero (the ν mass).

The sample of events is then divided depending upon whether the energy the μ^+ candidate deposits in the electromagnetic calorimeter is more or less than 300 MeV; 98.8% of μ^+ deposit less than 300 MeV. The yield of $D^+ \to \mu^+\nu$ events is extracted by a fit to the MM^2 distribution of μ candidates depositing less than 300 MeV.

The fit to data produces the following results:

$$\mathcal{B}(D^+ \to \mu^+\nu) = (3.82 \pm 0.32 \pm 0.09) \times 10^{-4} \,,$$

and

$$f_{D^+} = (205.8 \pm 8.5 \pm 2.5)\text{MeV} \,,$$

where first uncertainty is statistical and the second uncertainty is systematic. Furthermore, the ratio between $\mu\nu$ and the small $D^+ \to \tau^+(\pi^+\nu)\nu$ contribution has been fixed to the SM expectation. The systematic uncertainty contains significant contributions from radiative corrections, particle identification efficiency and background assumptions. The measurement is in good agreement with the theoretical prediction of Follana *et al.* [340] of $f_{D^+} = (207 \pm 4)$ MeV.

The CLEO-c measurements of $f_{D_s^+}$ are made with a data set corresponding to 600 pb^{-1} of integrated luminosity collected at a center-of-mass energy of 4.170 GeV, which is close to the maximum of the $D_s^+ D_s^{*-}$ production cross-section. One analysis reconstructs $D_s^+ \to \mu^+\nu$ and $D_s^+ \to \tau^+(\pi^+\bar{\nu})\nu$ events [258] and the other reconstructs $D_s^+ \to \tau^+(e^+\nu\bar{\nu})\nu$ events [869]. These are briefly reviewed in turn.

The analysis of $D_s^+ \to \mu^+\nu$ and $D_s^+ \to \tau^+(\pi^+\bar{\nu})\nu$ reconstructs $D_s^{-*} \to D_s^-\gamma$ tags in nine hadronic D_s^+ decay modes. The number of tags reconstructed is approximately 44,000. Signal candidates are reconstructed in an almost identical fashion to the measurements of f_{D^+} and the resulting MM^2 distribution and fit are shown in Fig. 54 (a). The principal results from this analysis are:

$$\mathcal{B}(D_s^+ \to \mu^+\nu) = (0.591 \pm 0.037 \pm 0.018)\% \,,$$
$$\mathcal{B}(D_s^+ \to \tau^+\nu) = (6.42 \pm 0.81 \pm 0.18)\% \,,$$

and

$$f_{D_s^+} = (263.3 \pm 8.2 \pm 3.9) \text{ MeV}.$$

The main systematic uncertainty is from the D_s^{*+} tag yields.

The selection of $D_s^+ \to \tau^+(e^+\nu\bar{\nu})\nu$ only uses three of the purest D_s^- tags: $\phi\pi^-$, $K^{*0}K^-$ and $K^-K_S^0$. There are 26,300 tagged events reconstructed. Events with a single charged track of opposite sign, which is compatible with being an electron, are selected as signal candidates. The distribution of extra energy, E_{extra}, in these events, with the background evaluated in the tag D_s^- mass sidebands subtracted, is shown in Fig. 54 (a). The signal peaks close to 150 MeV, which is the energy of the photon in $D_s^{*+} \to D_s^+\gamma$ decays. A binned fit to this distribution gives the following results:

$$\mathcal{B}(D_s^+ \to \tau^+\nu) = (0.530 \pm 0.47 \pm 0.22)\%$$

and

$$f_{D_s^+} = (252.5 \pm 11.1 \pm 5.2) \text{ MeV}.$$

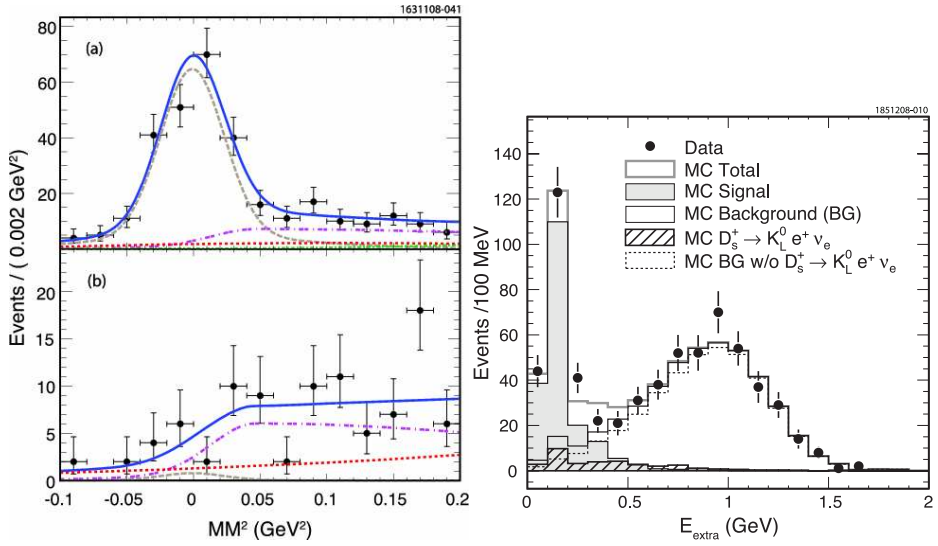

(a) (b)

Fig. 54. Fits to the (a) MM^2 and (b) $E_{\rm extra}$ distributions used to extract the $D_s^+ \to l\nu$ yields at CLEO-c. In (a) the solid line is the total fit result, the dashed line is the $\mu\nu$ component, the dot-dashed line is the $\tau\nu$ component and the dotted line is background.

The main systematic uncertainty is from the estimation of the $D_s^+ \to K_L^0 e^+\nu$ peaking backgrounds.

The two results for $f_{D_s^+}$ give an average value of

$$f_{D_s^+} = (259.5 \pm 6.6 \pm 3.1)\ \text{MeV}\ ,$$

which is 2.3σ larger than the recent lattice calculation $f_{D_s^+} = (241 \pm 3)$ MeV [340].

BABAR [865] and Belle [456] have also measured $f_{D_s^+}$, but the results are much less precise than those from CLEO-c. However, these results were made with a fraction of their data sets and will be updated. be

7. Measurements of Γ, $\Delta\Gamma$, Δm and mixing-phases in K, B, and D meson decays

The phenomenon of meson-antimeson oscillation, being a flavor changing neutral current (FCNC) process, is very sensitive to heavy degrees of freedom propagating in the mixing amplitude and, therefore, it represents one of the most powerful probes of New Physics (NP). In K and $B_{d,s}$ systems the comparison of observed meson mixing with the Standard Model (SM) prediction has achieved a good accuracy and plays a fundamental role in constraining not only the Unitarity Triangle (UT) but also possible extensions of the SM. Very recently the evidence for flavor oscillation in the D system has been also revealed, providing complementary information with respect to the K and $B_{d,s}$ systems, since it involves mesons with up-type quarks.

We recall here the basic formalism of meson-antimeson mixing, starting from the K system. In principle, one could describe neutral meson mixing with a unique formalism.

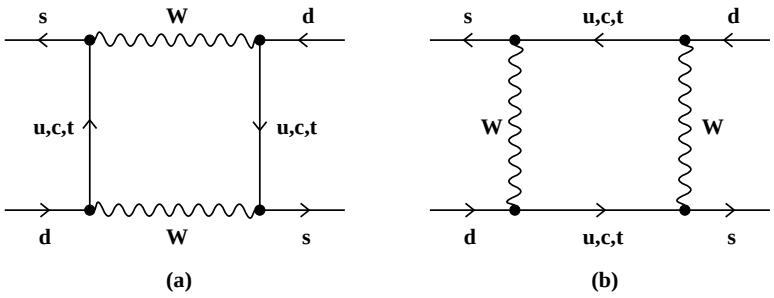

Fig. 55. *Box diagrams contributing to $K^0 - \bar{K}^0$ mixing in the SM.*

However, we present different formalisms for K, B, and D mixing to make contact with previous literature, considering also that different approximations are used.

The neutral Kaons $K^0 = (\bar{s}d)$ and $\bar{K}^0 = (s\bar{d})$ are flavor eigenstates which in the SM can mix via weak interactions through the box diagrams shown in Fig. 55. In the presence of flavor mixing the time evolution of the K^0-$\bar{K}^0$ system is described by

$$i\frac{d}{dt}\begin{pmatrix} K^0(t) \\ \bar{K}^0(t) \end{pmatrix} = \hat{H}\begin{pmatrix} K^0(t) \\ \bar{K}^0(t) \end{pmatrix}, \tag{317}$$

where the the Hamiltonian $\hat{H}$ is a 2×2 non-hermitian matrix which can be decomposed as $\hat{H} = \hat{M} - i\hat{\Gamma}/2$. The matrices $\hat{M}$ and $\hat{\Gamma}$ are hermitian and their elements respectively describe the dispersive and absorptive part of the time evolution of the Kaon states.

We note that, in terms of K^0 and $\bar{K}^0$, the CP eigenstates are given by [19]

$$K_\pm = \frac{1}{\sqrt{2}}(K^0 \pm \bar{K}^0)\,, \qquad CP|K_\pm\rangle = \pm|K_\pm\rangle\,. \tag{318}$$

The Hamiltonian eigenstates, called *short* and *long* due to the significant difference between their decay time, can be written as

$$K_S = \frac{K_+ + \bar{\epsilon}\,K_-}{\sqrt{(1+|\bar{\epsilon}|^2)}}\,, \qquad K_L = \frac{K_- + \bar{\epsilon}\,K_+}{\sqrt{(1+|\bar{\epsilon}|^2)}}\,. \tag{319}$$

They coincide with CP eigenstates but for a small admixture governed by a small complex parameter $\bar{\epsilon}$, defined as

$$\frac{1-\bar{\epsilon}}{1+\bar{\epsilon}} = -\sqrt{\frac{M_{12}^* - i\Gamma_{12}^*/2}{M_{12} - i\Gamma_{12}/2}}\,. \tag{320}$$

In the K system, the smallness of $\bar{\epsilon} \simeq \mathcal{O}(10^{-3})$ implies $\mathrm{Im}M_{12} \ll \mathrm{Re}M_{12}$ and $\mathrm{Im}\Gamma_{12} \ll \mathrm{Re}\Gamma_{12}$. Consequently, the mass difference between the mass eigenstates K_L and K_S can be well approximated by the simple expression:

$$\Delta M_K \equiv M_{K_L} - M_{K_S} = -2ReM_{12}\,, \tag{321}$$

where the off-diagonal element M_{12} is given by

$$M_{12} = \langle K^0|\mathcal{H}_{eff}^{\Delta S=2}|\bar{K}^0\rangle\,, \tag{322}$$

[19] The phase convention is chosen so that $CP|K^0\rangle = |\bar{K}^0\rangle$ and $CP|\bar{K}^0\rangle = |K^0\rangle$.

with $\mathcal{H}_{eff}^{\Delta S=2}$ being the effective Hamiltonian that describes $\Delta S = 2$ transitions, defined in Sec. 2.1. Notice that Eq. (321) only gives the short-distance part of ΔM_K. Long-distance contributions, however, are present due to the exchange of light meson states and are difficult to estimate. On the other hand, the imaginary part of the amplitudes discussed below are not affected by these contributions, which have Cabibbo-suppressed imaginary part.

We now discuss the parameters ε_K and $\varepsilon'_K/\varepsilon_K$. which are used to measure indirect and direct CP violatons in the K system. Since a two pion final state is CP even while a three pion final state is CP odd, $K_{\rm S}$ and $K_{\rm L}$ preferably decay to 2π and 3π respectively, via the following CP conserving decay modes: $K_{\rm L} \to 3\pi$ (via K_2), $K_{\rm S} \to 2\pi$ (via K_1). Given how $K_{\rm L}$ and $K_{\rm S}$ are not CP eigenstates, they can also decay, with small branching fractions, as follows: $K_{\rm L} \to 2\pi$ (via K_1), $K_{\rm S} \to 3\pi$ (via K_2). This CP violation is called indirect as it does not proceed via explicit breaking of the CP symmetry in the decay itself, but via the mixing of the CP state with opposite CP parity to the dominant one. We note that $\bar{\epsilon}$ depends on the phase convention of the K meson states and hence it is not measurable by itself. A phase-independent parameter which provides a measure of the indirect CP violation is

$$\varepsilon_K = \frac{A(K_{\rm L} \to (\pi\pi)_{I=0})}{A(K_{\rm S} \to (\pi\pi)_{I=0})}, \tag{323}$$

which, using the already-mentioned approximations as well as $\Delta M \simeq -\Delta\Gamma$ and $\Gamma_{12} \simeq (A_0^*)^2$, is related to $\bar{\epsilon}$ by

$$\varepsilon_K = \bar{\epsilon} + i\xi = \left(\frac{{\rm Im}M_{12}}{2{\rm Re}M_{12}} + \xi\right) \exp({\rm i}\phi_\epsilon) \sin\phi_\epsilon\,, \quad \text{with} \quad \xi = \frac{{\rm Im}A_0}{{\rm Re}A_0}\,, \tag{324}$$

where the phase ϕ_ϵ is measured to be $(43.51 \pm 0.05)^\circ$ [4]. The amplitude A_0 appearing in Eq. (324) is defined through

$$\begin{aligned} A(K^0 \to \pi^+\pi^-) &= \sqrt{\frac{2}{3}} A_0 e^{i\delta_0} + \sqrt{\frac{1}{3}} A_2 e^{i\delta_2}\,, \\ A(K^0 \to \pi^0\pi^0) &= \sqrt{\frac{2}{3}} A_0 e^{i\delta_0} - 2\sqrt{\frac{1}{3}} A_2 e^{i\delta_2}\,, \end{aligned} \tag{325}$$

where the subscript $I = 0, 2$ denotes states with isospin $0, 2$. Hence, $\delta_{0,2}$ are the corresponding strong phases, and the weak CKM phases are contained in A_0 and A_2. Indirect CP violation reflects the fact that the mass eigenstates are not CP eigenstates. Direct CP violation, on the other hand, is realized via a direct transition of a CP odd to a CP even state or vice-versa. A measure of the direct CP violation in $K_L \to \pi\pi$ is characterized by a complex parameter ε'_K defined as [20]

$$\varepsilon'_K = \frac{1}{\sqrt{2}} {\rm Im}\left(\frac{A_2}{A_0}\right) e^{i\Phi}, \qquad \Phi = \pi/2 + \delta_2 - \delta_0, \tag{326}$$

with amplitudes $A_{0,2}$ defined in Eq. (325). Extracting the strong phases $\delta_{0,2}$ from $\pi\pi$ scattering yields $\Phi \approx \pi/4$. Experimentally, the ratio $\varepsilon'_K/\varepsilon_K$ can be determined by measuring the ratios

$$\eta_{00} = \frac{A(K_{\rm L} \to \pi^0\pi^0)}{A(K_{\rm S} \to \pi^0\pi^0)}, \qquad \eta_{+-} = \frac{A(K_{\rm L} \to \pi^+\pi^-)}{A(K_{\rm S} \to \pi^+\pi^-)}. \tag{327}$$

[20] Actually direct CP violation is accounted for by ${\rm Re}(\varepsilon'_K)$.

In fact, from Eqs. (327) and (325), one finds

$$\eta_{00} \simeq \varepsilon_K - 2\varepsilon'_K, \quad \eta_{+-} \simeq \varepsilon_K + \varepsilon'_K\,, \tag{328}$$

by exploiting the smallness of ε_K and ε'_K, using $\mathrm{Im}A_i \ll \mathrm{Re}A_i$ and $\omega = \mathrm{Re}A_2/ReA_0 = 0.045 \ll 1$, which corresponds to the $\Delta I = 1/2$ rule. The ratio $\varepsilon'_K/\varepsilon_K$ can then be measured from

$$\left|\frac{\eta_{00}}{\eta_{+-}}\right|^2 \simeq 1 - 6\ \mathrm{Re}\left(\frac{\varepsilon'_K}{\varepsilon_K}\right)\,. \tag{329}$$

The formalism recalled in the case of the K system is basically the same for the B_d and B_s systems. There is however a notation difference for the neutral mass eigenstates, which are denoted *heavy* and *light* and are expressed in terms of the flavor eigenstates as

$$B_q^{L,H} = \frac{1}{\sqrt{(1+|(q/p)_q|^2)}}(B_q \pm (q/p)_q \bar{B}_q)\,, \qquad (q = d, s) \tag{330}$$

with $(q/p)_q$ parameterizing indirect CP violation. This parameter is similar to $\bar{\epsilon}$ for Kaons. Comparing Eqs. (319) and (330), one finds $q/p = (1-\bar{\epsilon})/(1+\bar{\epsilon})$.

Similar to the Kaon case, the phase of $(q/p)_q$ depends on the phase convention of the B meson states, but the absolute value $|(q/p)_q|$ can be measured. Further interesting experimental observables in the B_d and B_s systems are the mass and width differences: $\Delta M_{B_q} \equiv M_{B_H} - M_{B_L}$ and $\Delta\Gamma_{B_q} \equiv \Gamma_{B_L} - \Gamma_{B_H}$. They can be written in terms of the dispersive, M_{12}^q, and absorptive, Γ_{12}^q, matrix elements as

$$\begin{aligned}
(\Delta M_{B_q})^2 - \frac{1}{4}(\Delta\Gamma_{B_q})^2 &= 4|M_{12}^q|^2 - |\Gamma_{12}^q|^2\,,\\
\Delta M_{B_q}\Delta\Gamma_{B_q} = -4Re(M_{12}^q\Gamma_{12}^{q*})\,, \quad |(q/p)_q| &= \left|\sqrt{\frac{2M_{12}^{q*} - i\Gamma_{12}^{q*}}{2M_{12}^q - i\Gamma_{12}^q}}\right|\,.
\end{aligned} \tag{331}$$

The dispersive element M_{12}^q is related to the matrix element of the effective $\Delta B = 2$ Hamiltonian, defined in Sec. 2.1, as it can be straightforwardly derived from Eq. (322). The absorptive matrix element Γ_{12}^q can be written as

$$\Gamma_{12}^q = \frac{1}{2M_{B_q}}\,\mathrm{Disc}\langle B_q|i\int d^4x \mathcal{T}\left(\mathcal{H}_{eff}^{\Delta B=1}(x)\,\mathcal{H}_{eff}^{\Delta B=1}(0)\right)|\bar{B}_q\rangle\,, \tag{332}$$

where "Disc" picks up the discontinuities across the physical cut in the time-ordered product of the $\Delta B = 1$ Hamiltonians, defined in Sec. 2.1. The relations in Eq. (331) can be simplified by exploiting the smallness of the ratio $\Gamma_{12}^q/M_{12}^q \sim \mathcal{O}(m_b^2/m_t^2) \sim 10^{-3}$, which allows neglecting $\mathcal{O}(m_b^4/m_t^4)$ terms, so that one can write

$$\Delta M_{B_q} = 2|M_{12}^q|\,, \quad \Delta\Gamma_{B_q} = -\Delta M_{B_q} Re\left(\frac{\Gamma_{12}^q}{M_{12}^q}\right)\,, \quad |(q/p)_q| = 1 - \frac{1}{2}Im\left(\frac{\Gamma_{12}^q}{M_{12}^q}\right)\,. \tag{333}$$

Other important CP-violating observables, associated in the CKM phase convention to the phases of the B_q mixing amplitudes, are the CKM angles

$$\beta = \arg\left(-\frac{V_{cb}^* V_{cd}}{V_{tb}^* V_{td}}\right)\,, \quad \beta_s = \arg\left(-\frac{V_{tb}^* V_{ts}}{V_{cb}^* V_{cs}}\right)\,. \tag{334}$$

Note that $V_{cb}^* V_{cd}$ and $V_{cb}^* V_{cs}$ are approximately real in the CKM phase convention so that $M_{12}^d \simeq |M_{12}^d| e^{2\mathrm{i}\beta}$ and $M_{12}^s \simeq |M_{12}^s| e^{-2\mathrm{i}\beta_s}$. Moreover, the two angles have different size: $\beta \sim 1$ and $\beta_s \sim \lambda^2 \sim \mathcal{O}(10^{-2})$.

The angle β can be measured, for instance, in the time-dependent CP asymmetry of $b \to c\bar{c}s$ transitions. In particular, for the golden channel $B_d \to J/\psi K_S$ and neglecting doubly Cabibbo-suppressed contributions to the decay amplitudes, one obtains

$$a_{CP}^{B\to J/\psi\, K_S}(t) = \sin(2\beta)\sin(\Delta M_{B_d} t)\,. \tag{335}$$

We refer the reader to Sec. 7.2.3 for more details. The extraction of the angle β_s is more problematic. In analogy to the previous case, the decay $B_s \to J/\psi\,\phi$ is sensitive to the phase of the B_s mixing amplitude. In this case, a time-dependent angular analysis is required to separate CP-odd and CP-even contributions. This analysis provides a joint measurement of Γ_s, $\Delta\Gamma_s$ and ϕ_s, where $\phi_s = \arg(\lambda_{J/\psi\,\phi})$ with $\lambda_{J/\psi\,\phi} = (q/p)_s A(\bar{B}_s \to (J/\psi\,\phi)_f)/A(B_s \to (J/\psi\,\phi)_f)$ with $f = \{0, \|, \perp\}$ (details on the experimental measurements can be found in Sec. 7.2.4). Discarding doubly Cabibbo-suppressed terms, the ratios $\bar{A}/A$ are real, so that ϕ_s could give access to the mixing phase. In the same approximation, the SM mixing phase β_s vanishes. Therefore, a measurement of the B_s mixing phase as small as the SM one requires controlling the Cabibbo-suppressed terms in the decay amplitudes. For an attempt see Ref. [870]. On the other hand, an unsuppressed B_s mixing phase generated by NP can be measured using $B_s \to J/\psi\,\phi$ with good accuracy. Another angle related to the B_s mixing phase is $\phi_s' = \arg(-M_{12}^s/\Gamma_{12}^s)$, from which one can write

$$\Delta\Gamma_{B_s} = 2|\Gamma_{12}^s|\cos\phi_s', \quad a_{\rm fs}^s = \frac{|\Gamma_{12}^s|}{|M_{12}^s|}\sin\phi_s'\,. \tag{336}$$

Similar to ϕ_s, ϕ_s' coincides with the phase of the B_s mixing amplitude up to doubly Cabibbo-suppressed terms. Therefore, $\phi_s' \simeq \phi_s$ is a sensitive probe of large NP contributions to the B_s mixing phase, but cannot be used to determine β_s. Indeed, ϕ_s' turns out to be very small in the SM, as the leading term in Γ_{12}^s has the same phase of M_{12}^s while the corrections are both Cabibbo and GIM suppressed.

Finally, the study of mixing and CP violation in the D system is based on the same formalism as for B mesons. A peculiarity of D mesons is that CP violation in mixing is strongly suppressed within the SM by the CKM combination $V_{cb}V_{ub}^*$, so that the matrix elements M_{12}^D and Γ_{12}^D of the $\Delta C = 2$ effective Hamiltonian (see Sec. 2.1) are real to a good approximation. Long-distance contributions which cannot be accounted for by the effective Hamiltonian plague computations of D-$\bar{D}$ mixing observables, even more than in the case of ΔM_K. The short-distance (SD) part of the mass and width differences can be computed. They are given by:

$$\begin{aligned}
\Delta M_D^{\rm SD} &= M_{D_H} - M_{D_L} = 2{\rm Re}\sqrt{(M_{12}^D - \frac{i}{2}\Gamma_{12}^D)(M_{12}^{D*} - \frac{i}{2}\Gamma_{12}^{D*})}\,,\\
\Delta\Gamma_D^{\rm SD} &= \Gamma_{D_H} - \Gamma_{D_L} = -4{\rm Im}\sqrt{(M_{12}^D - \frac{i}{2}\Gamma_{12}^D)(M_{12}^{D*} - \frac{i}{2}\Gamma_{12}^{D*})}\,.
\end{aligned} \tag{337}$$

For the D system, the experimental information on the mass and width differences is provided by the time-integrated observables

$$x_D = \frac{\Delta M_D}{\Gamma_D}\,, \qquad y_D = \frac{\Delta\Gamma_D}{2\Gamma_D}\,. \tag{338}$$

7.1.1. *Theoretical prediction for ΔM_K, ε_K, and $\varepsilon'_K/\varepsilon_K$*

The expression for the mass difference Δm_K has been given in Eq. (321). The short-distance contributions, which are represented by the real parts of the box diagrams (see Fig. 55) with charm quark and top quark exchanges, are known at NLO in QCD [34]. The dominant contribution is represented by charm exchanges, due to the smallness of the real parts of the CKM top quark couplings, which is not compensated by the effect of having heavier quarks running in the loop. Non-negligible contribution comes from the box diagrams with simultaneous charm and top exchanges. In spite of the accuracy achieved in the short-distance part, a reliable theoretical prediction of Δm_K is prevented by relevant long-distance contributions which are difficult to estimate. The calculated short-distance part leads in fact to a value of $\sim 80\%$ [871] of the experimentally observed mass difference between the neutral Kaon states of $\Delta m_K = (3.483 \pm 0.006) \cdot 10^{-12}\,\mathrm{MeV}$ [4].

Theoretical predictions for the parameter of indirect CP violation ε_K have been sofar obtained from the expression (324) by neglecting the term ξ, which constitutes a small contribution, and approximating the phase ϕ_ϵ to $\pi/4$, so that $|\varepsilon_K|$ can be written as:

$$|\varepsilon_K| = C_\varepsilon \hat{B}_K A^2 \lambda^6 \overline{\eta} \{ -\eta_1 S_0(x_c)(1 - \frac{\lambda^2}{2}) + \eta_3 S_0(x_c, x_t) + \eta_2 S_0(x_t) A^2 \lambda^4 (1 - \overline{\rho}) \}\,, \quad (339)$$

where $C_\varepsilon = \frac{G_F^2 f_K^2 M_K M_W^2}{6\sqrt{2}\pi^2 \Delta m_K}$. However, it has been recently pointed out [872] that the adopted approximations might no longer be justified, due to the improved theoretical accuracy in both perturbative and non-perturbative contributions. In Eq. (339) the Inami-Lim functions $S_0(x_{c,t})$ and $S_0(x_c, x_t)$ [873] contain the box-contributions from the charm and top-quark exchange with $x_i = m_i^2/M_W^2$, while η_i $(i = 1, 2, 3)$ describe (perturbative) short-distance QCD-corrections [33–35]. The Kaon bag parameter $\hat{B}_K$ measures the deviation of the $\Delta S = 2$ hadronic matrix element from its value in the vacuum saturation approach:

$$\hat{B}_K \;=\; \frac{\langle \overline{K}^0 | \hat{Q}^{\Delta S=2} | K^0 \rangle}{\frac{8}{3} f_K^2 m_K^2}\,. \quad (340)$$

Therefore, $\hat{B}_K$ contains all the non-perturbative QCD contributions for ε_K. Currently the best determination of this parameter is available from lattice simulations of QCD with either 2+1 or 2 dynamical quark flavors, which avoid the systematic uncertainty due to "quenching" in earlier lattice studies done without dynamical quarks (cf. Sec. 2.3). At this time, the most accurate results (obtained independently with 2+1 dynamical quark flavors) by RBC/UKQCD [874] and Aubin et al. [875] quote a combined statistical and systematic uncertainty of 5.4 and 4.0 per cent for $\hat{B}_K$, respectively. That means that the contribution from $\hat{B}_K$ to the total uncertainty in ε_K is now comparable to the second biggest contribution, which originates from $|V_{cb}|$. This CKM-matrix element is nowadays known with 2.3 per cent accuracy [4] but enters ε_K in the fourth power.

In most current lattice calculations, due to algorithmic and computational limitations, the simulated up- and down-quark masses are heavier than their physical values, thus requiring an extrapolation for $\hat{B}_K$ to those light quark masses guided by chiral perturbation theory (ChPT, see Sec. 2.4). Fig. 56 summarizes the currently available lattice results with either $N_f = 2 + 1$ or 2 dynamical quarks. The RBC/UKQCD [110, 874] and the HPQCD [876] results both were obtained with $N_f = 2 + 1$, where the former used

the domain-wall and the latter the staggered fermion formulation. The work by Aubin et al. [875] used a mixed action approach, where domain-wall valence fermions have been calculated on a 2+1 flavor background of dynamical staggered quarks. In case of the RBC/UKQCD result, crucial ingredients for obtaining a small uncertainty in the final number were the use of Kaon SU(2)-ChPT to extrapolate to light physical quark masses and the use of a non-perturbative renormalization technique. The HPQCD result was obtained using degenerate Kaons (made of two quarks of mass $m_s/2$) and used a perturbative renormalization technique. Results with $N_f = 2$ are available from JLQCD [877] using dynamical overlap fermions and from ETMC [878] using twisted mass fermions [21], both with non-perturbative renormalization. While ETMC also used Kaon SU(2)-ChPT, the JLQCD result was extrapolated using NLO SU(3)-ChPT with analytic NNLO-terms added. All these dynamical results except the one from Aubin et al. were obtained at a single value for the finite lattice spacing a (values indicated in Fig. 56), meaning that a continuum extrapolation is still missing. But the RBC/UKQCD and the HPQCD results account for this fact in the systematic error estimate. For the near future, one should expect updates to these results, containing, e.g. simulations at finer lattice spacings and lighter dynamical quark masses and therefore further increasing the accuracy of the value $\hat{B}_K$ obtained from lattice calculations.

Estimates of the Kaon bag parameter in the chiral limit ($m_u, m_d, m_s \to 0$) are available from lattice simulations [110], large N_C approximation [879–881] or the QCD-hadronic duality [882].

As far as indirect CP violation is concerned, the parameter $\varepsilon'_K/\varepsilon_K$ can be written by using the operator-product expansion (OPE) as an expression involving the hadronic $K \to (\pi\pi)$ operators Q_6 and Q_8 given in Eq. (44) of Sec. 2.1, see e.g. [889]. Here ε'_K can be expressed in terms of isospin amplitudes and is an experimentally measurable (complex) parameter. The hadronic matrix elements Q_6, Q_8 contribute most to the uncertainties in the theoretical prediction for $\varepsilon'_K/\varepsilon_K$. On the lattice, usually an indirect approach [890] is pursued, which measures $K \to \pi$ and $K \to$ vacuum operators instead and relates those via chiral perturbation to the wanted $K \to (\pi\pi)$ operators. For quenched studies see [891,892], for recent work using dynamical domain-wall fermions see [893]. The latter work raises some doubts about the applicability of this approach, which is based on SU(3)-ChPT to be valid around the strange quark mass. A different technique, based on the calculation of finite volume correlation functions, is described in [77], which might turn out to be more successful in the future. See also [894] for an alternative approach, i.e. to study $\varepsilon'_K/\varepsilon_K$ in the small box approach (ϵ-regime).

7.1.2. *Experimental methods and results*

The Kaon system was the first playground for the understanding of the violation of the CP symmetry. In the years before the B system was investigated, all forms of CP violation had been observed in the Kaon system. These are CP violation in the Kaon mixing, with the measurement of $\mathrm{Re}(\varepsilon_K)$, in the direct decay, providing a non-null result on $Re(\varepsilon'_K/\varepsilon_K)$ and in the interference between mixing and decay, through the determination of the η_{+-} phase, ϕ_{+-}. CP violation has been observed in the K_L decay to the CP-even eigenstate of two pions, in the time-integrated charge asymmetry of the K_L semileptonic decay rates,

[21] The ETMC result is still preliminary. No systematic errors are included yet.

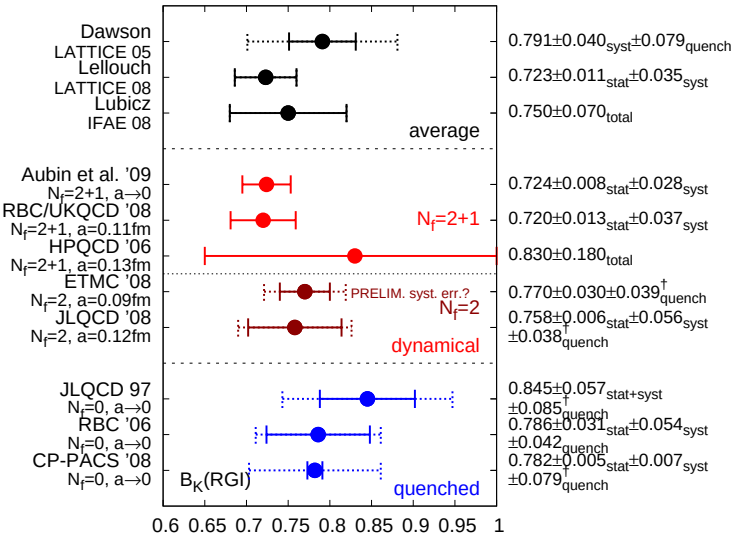

Fig. 56. Summary of lattice results for $\hat{B}_K$: included are recent results from dynamical $N_f = 2 + 1$ [110, 874–876] and $N_f = 2$ [877, 878] simulations. Also shown are quenched ($N_f = 0$) results from JLQCD [883], RBC [884], and CP-PACS [885]. For comparison, the figure includes the old lattice average from the Lattice 2005 conference [886] and two recently published averages [887,888], too. *Solid errorbars* do not include the error due to quenching, which is added in the *dashed errorbars*.
† A (conservative) quenching error of 5% or 10% has been assigned to $N_f = 2$ or quenched results, respectively, where no estimate for this systematic error has been provided (see Sec. 2.3).

in the $K_L \to \pi^+\pi^-\gamma$ channel, and in the angular asymmetry of the $K_L \to e^+e^-\pi^+\pi^-$ decays.

Direct CP violation through $\Delta S = 1$ processes has been measured as a tiny difference in the ratios of the branching ratios of the K_L to the CP-even eigenstates, $K_L \to \pi^+\pi^-$ and $K_L \to \pi^0\pi^0$, normalized to the K_S branching ratio for the same final state (Eq. 329). Precise measurements in the Kaon sector have been obtained with different techniques by the present generation of experiments (KTeV, NA48 and KLOE). Results on all of the major branching ratios, lifetimes and the K_L mass are summarized in Sec. 4.4.5, where analyses of interest for the $|V_{us}|$ determination are discussed. Several of these new measurements are not in good agreement with the average of older data. This is the case of the CP-violating decays, $K_L \to \pi^+\pi^-$, $K_L \to \pi^0\pi^0$, whose branching ratios as measured by KTeV [347] in year 2004 are 5% and 8% lower, respectively, than previous world averages. KLOE and NA48 recently confirmed [351, 352] the KTeV result on the BR($K_L \to \pi^+\pi^-$).

KTeV has measured the BR($K_L \to \pi^+\pi^-$) and the BR($K_L \to \pi^0\pi^0$) [347] from the analysis of all of the main K_L decay channels, as described in Sec. 4.4.5. The CP-violating charged channel was selected among events not satisfying the criteria for semileptonic

and $\pi^+\pi^-\pi^0$ decays, by imposing cuts on the $m_{\pi\pi}$ invariant mass and on the two-track transverse momentum-squared. The $K_L \to \pi^0\pi^0$ events are identified by the reconstruction of exactly four clusters in the calorimeter. The photons are paired to have two pions pointing to a single decay vertex and the pion invariant mass is required to be consistent with the Kaon mass. Major systematic uncertainties come from the precision on the knowledge of the efficiency reconstruction and to a less extent from radiative corrections to charged modes, Monte Carlo statistics and background subtraction.

The KLOE measurement [351] has been obtained from the relative ratio of $K_L \to \pi^+\pi^-$ and $K_L \to \pi\mu\nu$ decays, the absolute semileptonic branching ratio BR($K_L \to \pi\mu\nu$) being previously determined [349] from the measurement of all the major decay modes, using the tagging technique to obtain the absolute branching fractions and imposing the constraint on the sum of the branching fractions to solve the dependence on the K_L lifetime. The K_L sample at KLOE, operating at the Frascati ϕ factory, is tagged by the reconstruction of the $K_S \to \pi^+\pi^-$ decays, giving a precise determination of the K_L momentum. In order to minimize the difference on trigger efficiency between the two selected channels, the pions from K_S decay are requested to release in the calorimeter energy enough to trigger the data acquisition system.

The CP-violating channel was selected by a fit with a linear combination of Monte Carlo shapes for signal and background to the $\sqrt{E^2_{miss} + |p^2_{miss}|}$ distribution, where E_{miss} is the missing energy in the hypothesis of the two charged pion decay. The precision is dominated by the accuracy on tagging and tracking efficiency, which depend on corrections applied to the Monte Carlo sample, necessary to resolve small discrepancies between the Monte Carlo-predicted distributions and those obtained from data control samples.

NA48 measured the relative decay widths $\Gamma(K_L \to \pi^+\pi^-)/\Gamma(K_L \to \pi e\nu)$ [352] from a sample of two-track events selected for the analysis, which results in the semileptonic Ke3 branching ratio normalized to all of the two-track modes [348]. The CP-violating channel was selected by analysis requirements on the $m_{\pi\pi}$ invariant mass, the Kaon transverse momentum-squared, the ratio of the reconstructed energy and the particle momentum, E/P (which is very effective in separating electrons from μ and π), and finally using the muon veto system for Kμ3 rejection. Systematic uncertainties are due to the knowledge of Kaon spectrum, background contamination from Kμ3 decays, and to a less extent radiative corrections, trigger efficiencies and Monte Carlo statistics. The obtained branching fractions are summarized in Tab. 53, together with the CP-violation parameter $|\eta_{+-}|$, defined in Eq. 327, and Re(ε_K).

Table 53
$K_L \to \pi^+\pi^-$ branching ratios as measured by KTeV [347], KLOE [351] and NA48 [352]. compared with previous world average [895]. For Re(ε_K), the average value of $\phi_{+-} = (43.4 \pm 0.7)^\circ$ and $Re(\varepsilon'_K/\varepsilon_K) = (16.5 \pm 2.6) \times 10^{-4}$ have been used.

Source	BR($K_L \to \pi^+\pi^-$)	$\lvert\eta_{+-}\rvert$	Re(ε_K)
PDG 04	$(20.90 \pm 0.25)10^{-4}$ [895]	$(22.88 \pm 0.14)10^{-4}$	$(16.6 \pm 0.2)10^{-4}$
KTeV 04	$(19.75 \pm 0.12)10^{-4}$ [347]	$(22.28 \pm 0.10)10^{-4}$	$(16.1 \pm 0.2)10^{-4}$
KLOE 06	$(19.63 \pm 0.21)10^{-4}$ [351]	$(22.19 \pm 0.13)10^{-4}$	$(16.1 \pm 0.2)10^{-4}$
NA48 07	$(19.69 \pm 0.19)10^{-4}$ [352]	$(22.23 \pm 0.12)10^{-4}$	$(16.1 \pm 0.2)10^{-4}$

Direct CP violation has been established by precision measurements from NA48 [896] and KTeV [187], giving $Re(\varepsilon'_K/\varepsilon_K) = (14.7 \pm 2.2) \times 10^{-4}$ and $Re(\varepsilon'_K/\varepsilon_K) = (20.7 \pm 2.8) \times 10^{-4}$, respectively. The measurements hitherto summarized are used in the fit procedure described in the "CP violation in Klong decays" Review [285], which obtains the value of

$$|\epsilon_K| = (2 \cdot |\eta_{+-}| + |\eta_{00}|)/3 = (2.229 \pm 0.012) \times 10^{-3} \tag{341}$$

The KTeV collaboration recently announced the final result on $Re(\varepsilon'_K/\varepsilon_K)$, obtained with an improved analysis of the entire data set [897, 898]. The systematic error was reduced from 2.4 $\times 10^{-4}$ to 1.8 $\times 10^{-4}$ and the statistical uncertainty from 1.5 $\times 10^{-4}$ to 1.1 $\times 10^{-4}$, giving $Re(\varepsilon'_K/\varepsilon_K) = (19.2 \pm 1.1_{stat} \pm 1.8_{syst}) \times 10^{-4}$. The results from the two experiments are consistent within 1.7 σ. The new average, after scaling uncertainties to take into account the consistency level of the measurements, and including contributions from ΔI=3/2 amplitudes [899], not present in Eq.323, is $Re(\varepsilon'_K/\varepsilon_K) = (16.4 \pm 1.9) \times 10^{-4}$.

The KTeV experiment also measured the phase of the CP-violating decays. They used simultaneous measurements of events from two nearly parallel Kaon beams, with one of the beams passing through a thick regenerator, for precise determination of acceptances and contamination for both the charged ($\pi^+\pi^-$) and neutral ($\pi^0\pi^0$) modes. To reduce systematic uncertainties, the regenerator positions were alternated between the two beams once per minute. $Re(\varepsilon'_K/\varepsilon_K)$ has been obtained by a fit to the vacuum-to-regenerator ratio for charged and neutral modes, taking into account the K_L-K_S interference pattern in the regenerator sample [187]. Together with $Re(\varepsilon'_K/\varepsilon_K)$, the fit provides the best results on $\phi_{00} - \phi_{+-} = (0.29 \pm 0.31)^\circ$, $\Delta M_K = M_{K_L} - M_{K_S} = 3.465(7) 10^{-12}$ MeV and the K_S lifetime, $\tau_S = 89.62(5) 10^{-12}$ s.

The unitarity relation applied to time evolution of the neutral Kaon state leads to the Bell-Steinberger relation expressing CP and CPT violation parameters in terms of Kaon decay widths.

$$\begin{aligned} &\left[\frac{\Gamma_S + \Gamma_L}{\Gamma_S - \Gamma_L} + i \tan\phi_{\rm SW}\right] \times \left[\frac{{\rm Re}(\epsilon)}{1 + |\epsilon|^2} - i{\rm Im}(\delta)\right] \\ &= \frac{1}{\Gamma_S - \Gamma_L} \sum_f \mathcal{A}_L(f) \mathcal{A}_S^*(f), \end{aligned} \tag{342}$$

where

$$\phi_{\rm SW} = \arctan\left(\frac{2\Delta M_K}{\Gamma_S - \Gamma_L}\right) . \tag{343}$$

Besides testing CPT symmetry, the unitarity constraint for the neutral Kaon system, which receives relevant contributions only from few final states, really improves the precision on the Re(ε_K) parameter. The measurements of the K_L , K_S branching fractions and lifetimes, together with the KLOE upper limits on the $K_S \to \pi^0\pi^0\pi^0$ mode [900], on the time-integrated charge asymmetry of the K_S semileptonic decay [353], and the new result on ϕ_{+-} announced by KTeV [897, 898], have improved the accuracy on both CP- and CPT-violation parameters, Re(ε_K) and $Im(\delta)$. The results published in Ref. [901] were mostly based on the KLOE measurements. These have been revised for the "CPT invariance tests in neutral Kaon decay" Review [285] using the entire set of published data from KTeV and NA48, and then updated by the FlaviaNet Kaon Working Group to include the preliminary results on the $\eta_{\pi\pi}$ phases from the KTeV experiment [897, 898]. The results are summarized in Tab. 54.

Table 54
CP and CPT violation parameters from the unitarity constraint (Bell-Steinberger relation).

Source	Re(ε_K)	$Im(\delta)$	Ref.
KLOE 06	$(15.96 \pm 0.13)10^{-4}$	$(0.04 \pm 0.21)10^{-4}$	[901]
PDG 08	$(16.12 \pm 0.06)10^{-4}$	$(-0.06 \pm 0.19)10^{-4}$	[285]
FlaviaNet 08	$(16.12 \pm 0.06)10^{-4}$	$(-0.01 \pm 0.14)10^{-4}$	

Overall, the measurements in the Kaon sector to date constitute a precise data set consistent with CPT symmetry and unitarity. The comparison with CP-violation parameters in the B sector confirms that the CKM mechanism is the major source of CP-violation in meson decays. Still, Kaon physics has to meet the challenging experimental program on CP violation in very rare, and especially $K_L \to \pi\nu\nu$, decays which is extremely promising for constraining the CKM parameters and the physics beyond the SM as discussed in Sec. 6.6.6.

7.2. *The B-meson system*

7.2.1. *Lifetimes,* $\Delta\Gamma_{B_q}$, A^q_{SL} *and* ΔM_{B_q}

Heavy meson mixing plays a particularly important role in placing constraints on NP, since this loop process can be computed quite reliably using the heavy-quark expansion (HQE). Similarly, the hierarchy of lifetimes of heavy hadrons can be understood in the HQE, which makes use of the disparity of scales present in the decays of hadrons containing b-quarks. HQE predicts the ratios of lifetimes of beauty mesons [902–905], which now agree with the experimental observations within experimental and theoretical uncertainties. The most recent theoretical predictions show evidence of excellent agreement of theoretical and experimental results [906–911]. This agreement also provides us with some confidence that quark-hadron duality, which states that smeared partonic amplitudes can be replaced by the hadronic ones, is expected to hold in inclusive decays of heavy flavors. It should be pointed out that the low experimental value of the ratio $\tau(\Lambda_b)/\tau(B_d)$ has long been a puzzle for the theory. Only recent next-to-leading order (NLO) calculations of perturbative QCD [906–908] and $1/m_b$ corrections [909–911] to spectator effects as well as recent Tevatron measurements practically eliminated this discrepancy.

The inclusive decay rate of a heavy hadron H_b and B-meson mixing parameters can be most conveniently computed by employing the optical theorem to relate the decay width to the imaginary part of the forward matrix element of the transition operator:

$$\Gamma(H_b) = \frac{1}{2M_{H_b}}\, Disc\langle H_b|i\int d^4x \mathcal{T}\left(\mathcal{H}_{eff}^{\Delta B=1}(x)\,\mathcal{H}_{eff}^{\Delta B=1}(0)\right)|H_b\rangle\,, \tag{344}$$

where $H_{\rm eff}^{\Delta B=1}$ represents the effective $\Delta B = 1$ Hamiltonian, given in Sec. 2.1.

In the heavy-quark limit, the energy release is large, so that the correlator in Eq. (344) is dominated by short-distance physics. The OPE can be applied as explained in Sec. 2.1, leading to a prediction for the decay widths of Eq. (344) as a series of local operators of increasing dimension suppressed by powers of $1/m_b$:

$$\Gamma(H_b) = \frac{1}{2M_{H_b}}\sum_k \langle H_b|\mathcal{T}_k|H_b\rangle = \sum_k \frac{C_k(\mu)}{m_b^k}\langle H_b|\mathcal{O}_k^{\Delta B=0}(\mu)|H_b\rangle, \tag{345}$$

with the scale dependence of the Wilson coefficients compensated by the scale dependence of the matrix elements.

It is customary to make predictions for the ratios of lifetimes (widths), as many theoretical uncertainties cancel out in the ratio. Since the differences of lifetimes should come from the differences in the light sectors of heavy hadrons, at the leading order in HQE all beauty hadrons with light spectators have the same lifetime. The difference between meson and baryon lifetimes first occurs at order $1/m_b^2$ and is essentially due to the different structure of mesons and baryons, amounting to at most $1-2\%$ [904].

The main effect appears at the $1/m_b^3$ level and comes from dimension-six four-quark operators, whose contribution is enhanced due to the phase-space factor $16\pi^2$. They are thus capable of inducing corrections of order $16\pi^2(\Lambda_{QCD}/m_b)^3 = \mathcal{O}(5-10\%)$. These operators introduce through the so-called Weak Annihilation (WA) and Pauli Interference (PI) diagrams, a difference in lifetimes for both heavy mesons and baryons. Their effects have been computed [502, 904, 912–916] including NLO perturbative QCD corrections [906–908] and $1/m_b$ corrections [909–911]. The non-perturbative contribution is enclosed in the matrix elements of the mentioned operators, which are the following four

$$\begin{aligned} &O_1^q = \bar{b}_i\gamma^\mu(1-\gamma_5)b_i\bar{q}_j\gamma_\mu(1-\gamma_5)q_j,\ O_2^q = \bar{b}_i\gamma^\mu\gamma_5 b_i\bar{q}_j\gamma_\mu(1-\gamma_5)q_j, \\ &\widetilde{O}_1^q = \bar{b}_i\gamma^\mu(1-\gamma_5)b_j\bar{q}_i\gamma_\mu(1-\gamma_5)q_j,\ \widetilde{O}_2^q = \bar{b}_i\gamma^\mu\gamma_5 b_j\bar{q}_i\gamma_\mu(1-\gamma_5)q_j. \end{aligned} \tag{346}$$

The matrix elements of these operators are parameterized in a different way depending on whether or not the light quark q of the operator enters as a valence quark in the external hadronic state [906]. In this way one can distinguish the contribution of the contraction of the light quark in the operator with the light quark in the hadron, which is the only one calculated in lattice QCD [917–920]. Computing the contribution of the contraction of two light quarks in the operator, which vanishes in the vacuum saturation approximation, has been so far prevented by the difficult problem of subtracting power divergences. By combining the results for the perturbative and non-perturbative contributions discussed above, the theoretical predictions for the lifetime ratios read

$$\tau(B^+)/\tau(B^0) = 1.06 \pm 0.02\,,\ \tau(B_s)/\tau(B^0) = 1.00 \pm 0.01\,,\ \tau(\Lambda_b)/\tau(B^0) = 0.91 \pm 0.04\,. \tag{347}$$

Similar calculations yield B-mixing parameters presented in the form of expansion in $1/m_b^n$. The width difference is related the matrix elements M_{12}^q and Γ_{12}^q as in Eq. (333) and by using the HQE it can be written as

$$\begin{aligned} \Delta\Gamma_{B_q} = &\frac{G_F^2 m_b^2}{6\pi(2M_{B_q})}(V_{cb}^* V_{cq})^2 \cdot \\ &\left\{[F(z)+P(z)]\,\langle Q\rangle + [F_S(z)+P_S(z)]\,\langle Q_S\rangle + \delta_{1/m} + \delta_{1/m^2}\right\}, \end{aligned} \tag{348}$$

where $z = m_c^2/m_b^2$ and the two $\Delta B = 2$ operators are defined as

$$Q = (\bar{b}_i q_i)_{V-A}(\bar{b}_j q_j)_{V-A}, \qquad Q_S = (\bar{b}_i q_i)_{S-P}(\bar{b}_j q_j)_{S-P}\,. \tag{349}$$

The matrix elements for Q and Q_S are known to be

$$\langle Q \rangle \equiv \langle \overline{B}_q | Q | B_q \rangle = f_{B_q}^2 M_{B_q}^2 2 \left(1 + \frac{1}{N_c}\right) B_{B_q},$$

$$\langle Q_S \rangle \equiv \langle \overline{B}_q | Q_S | B_q \rangle = -f_{B_q}^2 M_{B_q}^2 \frac{M_{B_q}^2}{(m_b + m_s)^2} \left(2 - \frac{1}{N_c}\right) B_{B_q}^S,$$

A theoretical prediction for the $B_{d,s}$ width differences then requires to calculate non-perturbatively the decay constants $f_{B_{d,s}}$ and the bag parameters $B_{B_{d,s}}$ and $B^S_{B_{d,s}}$. Several unquenched lattice calculations of the decay constants have been performed with $N_f = 2$ or $N_f = 2 + 1$ dynamical fermions [921–928]. They have been obtained by treating the b quark on the lattice with two different approaches, either FNAL [485] or non-relativistic QCD. A collection of these results is provided in Ref. [887], where the following averages are estimated

$$f_{B_d} = (200 \pm 20)\,\text{MeV}\,, \qquad f_{B_s} = (245 \pm 25)\,\text{MeV}\,. \tag{350}$$

The average for f_{B_s} takes into account all the existing $N_f = 2$ and $N_f = 2 + 1$ results. For f_{B_d} the lattice determination is more delicate, because its value is enhanced by chiral logs effects relevant at low quark masses. In order to properly account for these effects, simulations at light values of the quark mass (typically $m_{ud} < m_s/2$) are required. For this reason, the f_{B_d} average provided in Ref. [887] and given in Eq. (350) is derived by taking into account only the results obtained by the HPQCD [926] and FNAL/MILC [928] collaborations, by using the MILC gauge field configurations generated at light quark masses as low as $m_s/8$. A more recent HPQCD calculation [927] of f_{B_d} and f_{B_s}, as well as of the bag parameters B_{B_d} and B_{B_s}, came out after the averages in Ref. [887] were performed. Since the new results are consistent with the old ones, the averages [887] can be considered up to date.

Also for the bag parameters, a collection of quenched [929–931] and unquenched ($N_f = 2$ and $N_f = 2+1$) [924,927,932,933] results can be found in Ref. [887]. A first observation is that the dependence on the light quark mass, that should allow to distinguish between B_d and B_s mesons, is practically invisible. For the $B_{B_{d,s}}$ bag parameters, the unquenched results tend to be slightly lower than the quenched determinations, though still well compatible within the errors, and lead to the averages [887]

$$B_{B_d}^{\overline{\text{MS}}}(m_b) = B_{B_s}^{\overline{\text{MS}}}(m_b) = 0.80 \pm 0.08\,, \tag{351}$$

in the $\overline{\text{MS}}$ scheme at the renormalization scale $\mu = m_b$, which correspond to the renormalization group invariant parameters

$$\hat{B}_{B_d} = \hat{B}_{B_s} = 1.22 \pm 0.12\,. \tag{352}$$

The bag parameters $B^S_{B_{d,s}}$ have been recently calculated without the unquenched approximation only by one lattice collaboration [932], finding no evidence of quenching effects. The averages given in Ref. [887], include also previous quenched lattice results, and in the $\overline{\text{MS}}$ scheme at the renormalization scale $\mu = m_b$ they read

$$B^S_{B_d} = B^S_{B_s} = 0.85 \pm 0.10\,. \tag{353}$$

The Wilson coefficients of these operators have been computed at NLO in QCD [934–936] and, together with $1/m_b$-suppressed effects [937], lead to the theoretical predictions [938]

$$\frac{\Delta\Gamma_{B_d}}{\Gamma_{B_d}} = (4.1 \pm 0.9 \pm 1.2) \cdot 10^{-3}\,, \qquad \frac{\Delta\Gamma_{B_s}}{\Gamma_{B_s}} = (13 \pm 2 \pm 4) \cdot 10^{-2}\,. \tag{354}$$

We observe that the theoretical predictions above are obtained by expressing the ratio $\Delta\Gamma/\Gamma$ as $(\Delta\Gamma/\Delta M)_{th.}/(\Delta M/\Gamma)_{exp.}$, i.e. by using the available accurate experimental measurements for the lifetimes and the mass differences. Moreover, they are obtained in a different operator basis $\{Q, \tilde{Q}_s\}$, with $\tilde{Q}_S = (\bar{b}_i q_j)_{S-P}(\bar{b}_j q_i)_{S-P}$, where there do not appear strong cancelations due to NLO and $1/m_b$-suppressed contributions [938]. The differences between the central values of $\Delta\Gamma_{B_q}/\Gamma_{B_q}$ computed in the "old" and "new" bases, which come from uncalculated α_s/m_b and α_s^2 corrections, turn out to be quite large. A conservative 30% uncertainty is taken into account by the second errors in Eq. (354).

The experimental observable $|(q/p)_q|$, whose deviation from unity describes CP violation due to mixing, is related to M_{12}^q and Γ_{12}^q, through Eq. (333). The theoretical prediction of $|(q/p)_q|$ is therefore based on the same perturbative and non-perturbative calculation discussed for the width differences, while the CKM contribution to $|(q/p)_q|$ is different from that in $\Delta\Gamma_{B_q}/\Gamma_{B_q}$. The updated theoretical predictions are [934–936]

$$|(q/p)_d| - 1 = (2.96 \pm 0.67) \cdot 10^{-4}\,, \quad |(q/p)_s| - 1 = (1.28 \pm 0.28) \cdot 10^{-5}\,. \tag{355}$$

Experimentally, information on the CP violation parameter $|(q/p)_q|$ is provided by the measurement of the semileptonic CP asymmetry, defined as

$$A_{SL}^q = \frac{\Gamma(B^0(t) \to l^- \bar{\nu} X) - \Gamma(\bar{B}^0(t) \to l^+ \nu X)}{\Gamma(B^0(t) \to l^- \bar{\nu} X) - \Gamma(\bar{B}^0(t) \to l^+ \nu X)} \tag{356}$$

which is related to $|(q/p)_q|$ through

$$A_{SL}^q = 2(1 - |(q/p)_q|)\,. \tag{357}$$

We conclude this section on B mesons by discussing the mass difference. In contrast to ΔM_K, in this case the long-distance contributions are estimated to be very small and $\Delta M_{B_{d,s}}$ is very well approximated by the relevant box diagrams, which are analogous to those shown in Fig. 55 for Kaons. Moreover, due to $m_{u,c} \ll m_t$, only the top sector can contribute significantly, whereas the charm sector and the mixed top-charm contributions are entirely negligible. Thus, the theoretical expression for M_{12}^q, to which the mass difference is related through Eq. (333), can be written as

$$M_{12}^q = \frac{G_F^2 M_{B_q} M_W^2}{12\pi^2} \left(V_{tb} V_{tq}^*\right)^2 \eta_B S_0(x_t) f_{B_q}^2 \hat{B}_{B_q}, \qquad (q = d, s)\,, \tag{358}$$

where $S_0(x_t)$ is the Inami-Lim function and $\hat{\eta}_B \approx 0.551$ represents the NLO QCD correction [33].

The mass differences in the B_d and B_s systems are proportional to $|V_{td}|^2$ and $|V_{ts}|^2$, respectively, thus representing important constraints on the UT, provided that the multiplied hadronic matrix elements are calculated. In order to involve reduced hadronic uncertainties, it is convenient to use as experimental constraints the ratio $\Delta M_{B_s}/\Delta M_{B_d}$ and ΔM_{B_s}, since the strange-bottom sector is not affected by the uncertainty due to the chiral extrapolation. On the other hand the UT analysis, being overconstrained, can be performed without using some inputs. In this way, the mass difference ΔM_{B_s} can be predicted with an accuracy of approximately 10%, as shown in Sec. 10 where the whole UT analysis is discussed.

Experiments have published measurements of all flavors of B hadrons. The B factories have produced precision measurements of the B^+ and B^0 lifetimes. In addition to the light

mesons, the Tevatron experiments have also measured B_s^0, Λ_b and B_c lifetimes. Selected measurements and the agreement of the world average fit with theoretical prediction are listed in Table 55.

A typical lifetime measurement consists of two steps: signal isolation and lifetime fitting. In the signal isolation step one tries to obtain the cleanest signal without cutting on lifetime-related variables (impact parameter, vertex displacement etc). Fitting the lifetime distribution is usually done with a log likelihood fit (binned or unbinned) in which the signal lifetime distribution is a convolution of an exponential and the detector lifetime resolution function, while the background lifetime distribution is typically an ad-hoc parametrization based on a sample in which the signal was anti-selected (e.g. mass sidebands).

The B factory experiments have measured B^+ and B^0 lifetimes in fully reconstructed hadronic decays as well as semileptonic $B^0 \to lD^*\nu$ and partially reconstructed hadronic $B^0 \to D^{*-}\pi^+$ and $B^0 \to D^{*-}\rho^+$ decays. The common element of all B factory measurements is the reconstruction of the lifetime exploiting the boost in the z direction from asymmetric colliding beams. As discussed in Section 3.2.3, the time measurement comes from correcting the displacement, L by the boost factor: $\Delta t = L/c\beta\gamma$. The decay time Δt is the decay time between two vertices in the z direction. The B mesons are always pair produced in the B factory environment, and the decays of each of the B mesons is a completely independent event from the other. Therefore, one can measure the lifetime of a B meson by starting the time interval Δt with the decay time of one of the B mesons and ending it with the decay of the other B meson. For measurements utilizing partially reconstructed (e.g. D^*+) decays, many handles specific to the B factory environment are used. In the particular example of semileptonic decays involving the, D^{*+}, the $D^{*+} \to \pi^+ D^0$ the D^0 decay is not explicitely reconstructed. Instead, the small phase space for the D^* decay is exploited to infer the direction and energy of the D^* from that of the soft pion. The momenta of the D^+, the lepton, and the center of mass energy are used to infer the momentum of the neutrino. The invariant mass of the neutrino computed from the same variables provides a powerful variable which eliminates a large fraction of the $B\overline{B}$ combinatorial background.

Tevatron experiments have access to B^0, B^+ as well as B_s^0, Λ_b and B_c decays and have reported lifetime measurements for all of them. The B^0 and B^+ lifetimes are measured both in semileptonic and fully reconstructed hadronic decays. The corrections for semileptonic decays are different than in B factory experiments. Samples are gathered by triggering on a lepton; CDF also requires a displaced track to further increase the B fraction of the sample. Lacking the initial energy of the B meson, inclusive reconstruction is not possible. The D/D^* meson has to be reconstructed explicitely, incurring a large branching ratio penalty. As discussed in more detail in Section 3.2.3, the energy of the neutrino is also unknown, so the computation of the decay proper time incurres a K-factor correction which has to be derived from Monte Carlo simulation of B meson decays. The $D0$ experiment directly measures the ratio of B^+ and B^0 lifetimes by fitting the ratio of observed B^+ and B^0 decay times (no K factor correction is applied) to a predicted distribution which depends on the lifetime ratio. B^0, B^+, B_s^0, and Λ_b lifetimes are also measured with fully reconstructed hadronic final states. For the B^0, B^+ and B_s^0 mesons the most common final state is $B \to D\pi$. Data samples for these analyses are gathered by triggering on displaced vertices, as described in Section 3.2.3. This trigger sculpts the lifetime distribution. This effect and the correction techniques used in the

analyses are discussed in detail in Section 3.2.3. The lifetime ratio of $\tau(\Lambda_b)/\tau(B^0)$ has been of considerable interest. There has been a long standing disagreement between theoretical predictions and experimental results. The Λ_b lifetime has been measured both in the $\Lambda_b \to J/\psi\Lambda$ and $\Lambda_b \to \Lambda_c\pi$ decays. Data for the first decay channel is gathered with dimuon triggers which are not lifetime biased. Data for the second channel is gathered through the displaced track trigger and requires similar corrections to those applied to fully hadronic B meson decays. The B_c meson occupies a special place amongst the B-hadrons as it can decay weakly via the b or c quark, making its lifetime considerably shorter than those of light B mesons. Due to its relatively large branching fraction, Tevatron experiments measure the B_c lifetime in semileptonic decays ($B_c \to J/\Psi l\nu$). The B_c mass is measured in hadronic decays, where lifetime cuts are used to reject background. Similar to semileptonic light B decays, the B_c momentum cannot be fully reconstructed; K-factor corrections based on Monte Carlo simulation are necessary.

Table 55 lists representative measurements from the different experiments and current world average results. Most of the B hadron lifetimes are now in good agreement with theoretical predictions [939] [940], except for the B_s^0 lifetime which is currently significantly lower than the predicted value.

As discussed in Section 7.2.1, additional information can be extracted from the measurement of lifetime differences between the heavy and light eigenstates. At the Tevatron the lifetime difference in the B_s system is accessible in the decay $B_s \to J/\psi\phi$ which gives rise to both CP-even and CP-odd final states. It is possible to separate the two CP components of the decay and measure the lifetime difference through a simultaneous fit to the time evolution and angular distributions of the decay products of the J/ψ and ϕ mesons. Fig. 57 shows the lifetime projections for the $\Delta\Gamma$ measurements at CDF and D0 with the CP even and CP odd components fitted separatly. Both experiments have so far analysed 2.8 fb^{-1} of data. The results [232, 941] are still compatible with a $\Delta\Gamma$ of zero. It should be noted that if $\Delta\Gamma$ is not zero, the flavor specific (equal mix of B_s^H and B_s^L at t=0) and CP specific B_s lifetimes will be distinct.

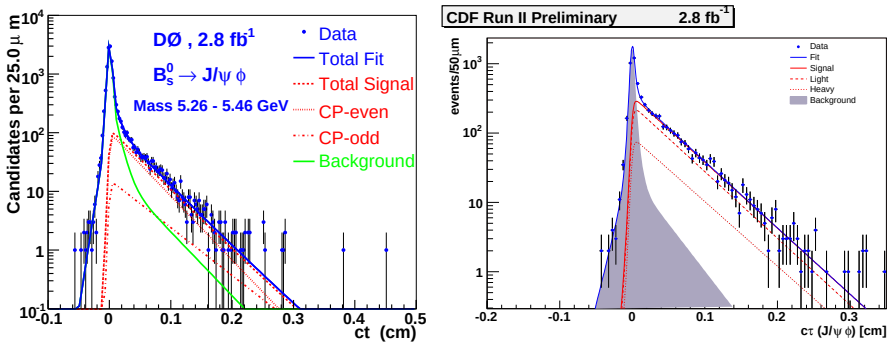

Fig. 57. Lifetime projection for $B_s^0 \to J/\psi\phi$ decay candiates in the signal region. In the left panel, the projection of the $D0$ fit. In the right panel, the corresponding projection by the CDF collaboration.

7.2.2. *B meson mixing*

Mixing measurements utilize lifetime and flavor tagging information, as described in Section 3.2.2. As discussed in Section 3.2.1, the time evolution of the probability density

Table 55
Representative measurements from different experiments and world average lifetimes. The ratios of world average hadron lifetimes to the B^0 lifetime are compared to theoretical predictions.

Hadron	Source	Result [ps]	Ratio $\tau(B_x)/\tau(B^0)$	Theory Pred. Ratio
B^0				
	BABAR	$1.504 \pm 0.013^{+0.018}_{-0.013}$		
	Belle	$1.534 \pm 0.008 \pm 0.010$		
	CDF	$1.524 \pm 0.030 \pm 0.016$		
	*D*0	$1.414 \pm 0.018 \pm 0.034$		
	PDG	1.525 ± 0.009		
B^+				$1.04 - 1.08$
	Belle	$1.635 \pm 0.011 \pm 0.011$		
	BABAR	$1.673 \pm 0.032 \pm 0.023$		
	CDF	$1.630 \pm 0.016 \pm 0.011$		
	*D*0	$- - -$	$1.080 + -0.016 + -0.014$	
	PDG	1.638 ± 0.011	1.07 ± 0.01	
B_s^0				$0.99 - 1.01$
	CDF	$1.36 \pm 0.09^{+0.06}_{-0.05}$		
	*D*0	$1.3980.044^{+0.028}_{-0.025}$		
	PDG	1.425 ± 0.041	0.934 ± 0.027	
Λ_b				$0.87 - 0.95$
	*D*0	$1.218^{+0.130}_{-0.115} \pm 0.0427$		
	CDF	$1.593^{+0.083}_{-0.078} \pm 0.0337$		
	PDG	$1.383^{+0.049}_{-0.048}$	0.91 ± 0.03	
B_c^+				$0.31 - 0.36$
	CDF	$0.475^{+0.053}_{-0.049} \pm 0.018$		
	*D*0	$0.448^{+0.038}_{-0.036} \pm 0.032$		
	PDG	0.453 ± 0.041	0.29 ± 0.03	

function for a B meson tagged with flavor η to decay with flavor f is given by Equation 98. The relevant experimental parameters that come into play are the effective tagging power (ϵD^2), proper time resolution and signal. These differ significantly between the B factory experiments and hadron colliders. Opposite side flavor tagger properties for the different experiments are compared in Table 7. The main difficulty with flavor tagging in hadron colliders is that the opposite side B meson is not in the detector acceptance most of the time. This is not the case with B factories due to the coherent production and controlled boost of the $B\overline{B}$ meson pair.

Mixing in the B_d meson sector was established 25 years ago by the Argus Collaboration [942] and precision measurements where available since the beginning of the asymmetric B-Factory program, since they can exploit both the large luminosity and the boost of the center-of-mass frame. A compilation of measurements from all contributing

experiments is shown in Figure Fig. 58. The most accurate measurements come from Belle and *BABAR*, where one of the two B mesons is fully via in their semileptonic decay and the other B tagged as B^0 or $\bar{B}^0$.

The most significant contribution of the Tevatron experiments to B mixing is the observation of B_s^0 oscillations. The analysis layout is very similar to that for B^0 mixing. Clean signal reconstruction, proper time resolution and flavor tagger dilution are essential. The probability density function for tagged decays also follows the formalism of Equation 98. The significant difference with respect to B^0 mixing is the high expected oscillation frequency (~ 18 ps^{-1}). The high frequency makes excellent proper time reconstruction essential; in order to resolve the oscillation frequency, the detector resolution has to be better than one oscillation period. The now-standard way of interpreting and combining results was first proposed by Moser and Roussarie [943] and is called an amplitude scan. Mathematically very similar to a Fourier transformation of the tagged lifetime distribution, this method involves re-fitting the data with different probe frequencies, while floating the oscillation amplitude. The amplitudes are then reported as a function of probe frequency. An amplitude significantly different from zero indicates the presence of an oscillation signal. Figure 59 shows the most recent results from CDF and D0. The CDF result [220] is consistent with oscillations at $\Delta M_{B_s} = 17.77 \pm 0.10$ (stat) $\pm$ 0.07 (syst) ps^{-1}. The signal significance is found to be 5.4σ. The $D0$ result [944] shows consistency with an oscillation signal at $\Delta M_{B_s} = 18.53 \pm 0.93$ (stat) $\pm$ 0.30 (sys) ps^{-1}. The significance of the signal corresponds to 2.9σ and supersedes the original two-sided bound $17 < \Delta M_{B_s} < 21$ps^{-1} at 90% CL [945].

7.2.3. *Measurements of the angle β in tree dominated processes*

The Standard Model (SM) of electroweak interactions describes charge conjugation-parity (*CP*) violation as a consequence of an irreducible complex phase in the three-generation Cabibbo-Kobayashi-Maskawa (CKM) quark-mixing matrix [1,2]. In this framework, neutral B decays to *CP* eigenstates containing a charmonium and K^0 meson provide a direct measurement of sin2β [946, 947]. The unitarity triangle angle β (or Φ_1) is $\arg\left[-V_{\rm cd}V_{\rm cb}^*/V_{\rm td}V_{\rm tb}^*\right]$ where the V_{ij} are CKM matrix elements.

$B^0 \to J/\psi\,\pi^0$ proceeds instead via a Cabibbo-suppressed $b \to c\bar{c}d$ transition: the tree amplitude has the same weak phase as the $b \to c\bar{c}s$ transition, therefore we expect the corresponding values of S and C to be $-\sin2\beta$ and 0 respectively, unless penguin amplitudes or other contributions are significant.

The current status of measurements of sin2β from charmonium decays are presented in what follows and cover $b \to c\bar{c}s$ and $b \to c\bar{c}d$ transitions. Additional results on determining the sign of β are also mentioned using the measurement of cos2β in $b \to c\bar{c}s$decays.

Most of the measurements presented here are based on data collected by the *BABAR* and the Belle experiments. The difference between the proper decay times of the signal B meson (B_{rec}) and of the other B meson (B_{tag}) is used to measure the time-dependent *CP*-asymmmetries, $\mathcal{A}_{CP}$. The initial flavor of B_{rec} is identified by using information from B_{tag}. $\mathcal{A}_{CP}$ is defined as

$$\mathcal{A}_{CP}(t) \equiv \frac{N(\overline{B}^0(t) \to f) - N(B^0(t) \to f)}{N(\overline{B}^0(t) \to f) + N(B^0(t) \to f)} = S\sin(\Delta m_d t) - C\cos(\Delta m_d t), \qquad (359)$$

where $N(\overline{B}^0(t) \to f)$ is the number of $\overline{B}^0$ that decay into the CP-eigenstate f after a

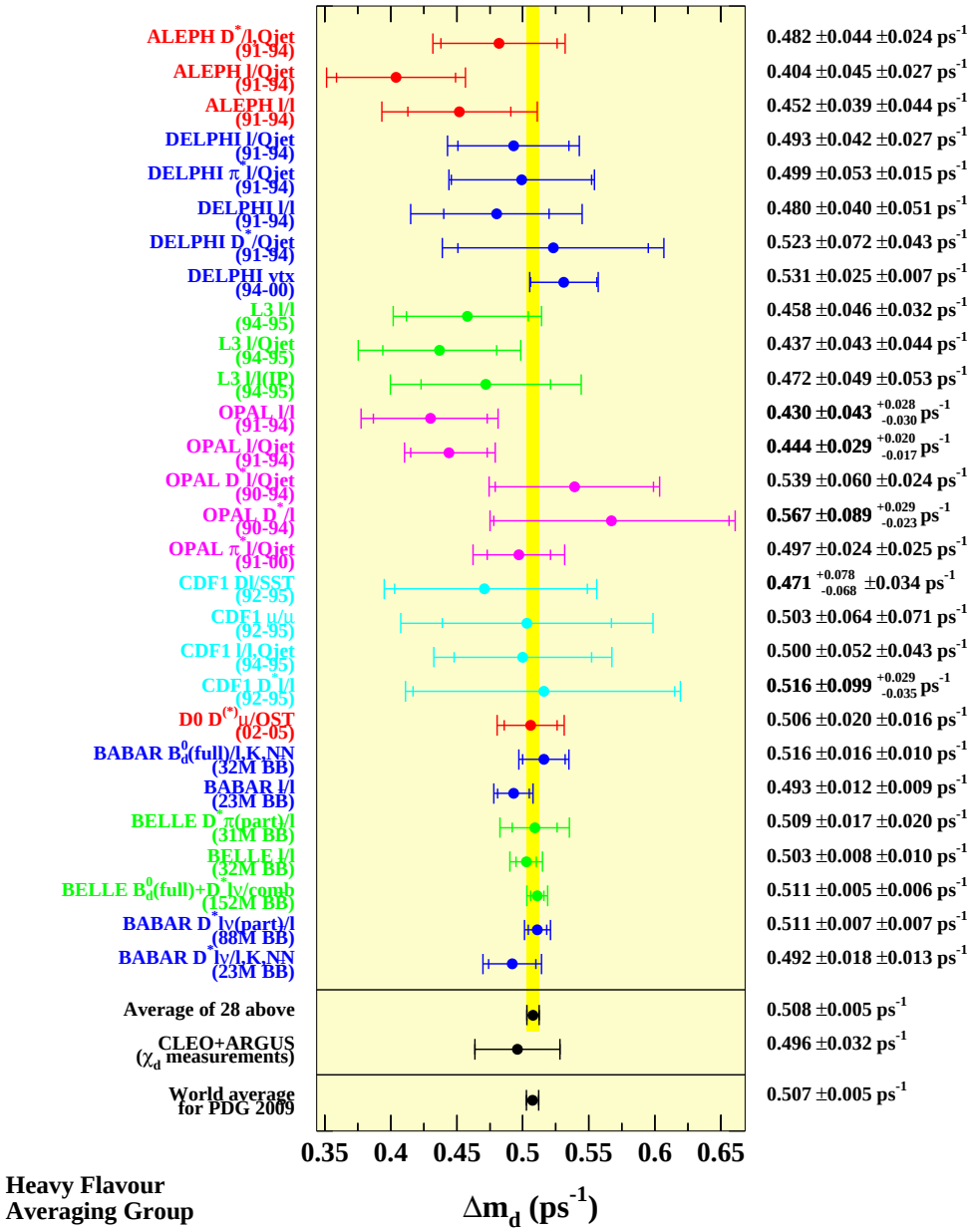

Fig. 58. Summary and average of ΔM_{B_d} measurements. See [560] for the full list of references.

time t and Δm_d is the difference between the B mass eigenstates. Belle reports results using the variable $A \equiv -C$.

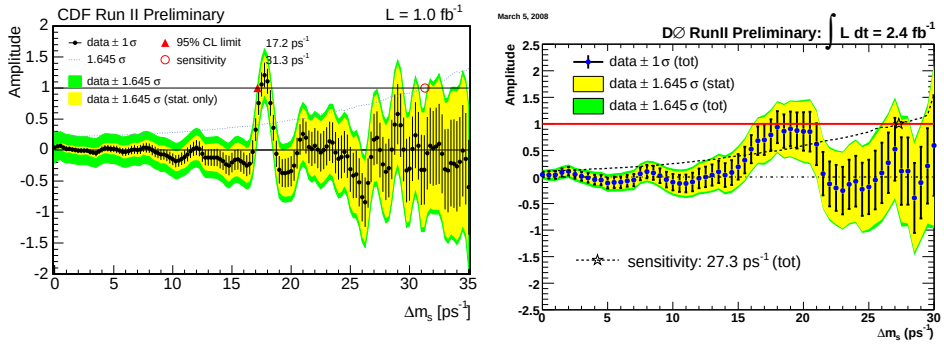

Fig. 59. Amplitude scans for the B_s oscillation fits. CDF and $D0$ results are shown in the left and right panel, respectively.

In the SM, direct CP violation in $b \to c\bar{c}s$ decays is negligible. Under this assumption, the CP violation parameters S and C are given by $S_{b\to c\bar{c}s} = -\eta_f \sin 2\beta$ and $C_{b\to c\bar{c}s} = 0$, where η_f is -1 for $(c\bar{c})K^0_S$ decays (e.g. $J/\psi K^0_S$, $\psi(2S)K^0_S$, $\chi_{c1}K^0_S$, $\eta_c K^0_S$ [22]) and η_f is $+1$ for the $(c\bar{c})K^0_L$ (e.g. $J/\psi K^0_L$) state. The $J/\psi K^{*0}(K^{*0} \to K^0_S\pi^0)$ final state is an admixture of CP even and CP odd amplitudes for which we use $\eta_f = 0.504 \pm 0.033$. To be consistent with other time-dependent CP measurements, we show the results in terms of $C_f = \eta_f C$ and $S_f = \eta_f S$. Using 425.7fb^{-1} of integrated luminosity, the *BABAR* experiment measured the time-dependent CP asymmetry parameters for the $J/\psi K^0_S$, $\psi(2S)K^0_S$, $\chi_{c1}K^0_S$, $\eta_c K^0_S$ and $J/\psi K^0_L$ modes combined [948] [23]:

$$C_f = 0.026 \pm 0.020(stat) \pm 0.016(syst), \quad S_f = 0.691 \pm 0.029(stat) \pm 0.014(syst).$$

C_f and S_f for each of the decay modes within the CP sample and of the $J/\psi K^0(K^0_S + K^0_L)$ sample were also measured [948]. These results are preliminary. The Belle experiment measured these parameters from $J/\psi K^0_S$ and $J/\psi K^0_L$ decays using a data sample of 492fb^{-1} and found [949]:

$$C_f = -0.018 \pm 0.021(stat) \pm 0.014(syst), \quad S_f = 0.642 \pm 0.031(stat) \pm 0.017(syst).$$

Belle also reported results from the $\psi(2S)K^0_S$ decay using 605fb^{-1} [950]:

$$C_f = -0.039 \pm 0.069(stat) \pm 0.049(syst), \quad S_f = 0.718 \pm 0.090(stat) \pm 0.033(syst).$$

The analysis of $b \to c\bar{c}s$ decay modes imposes a constraint on $\sin 2\beta$ only, but a four-fold ambiguity in the determination of the angle β remains. It is possible to reduce this ambiguity by measuring $\cos 2\beta$ using the angular and time-dependent asymmetry in $B^0 \to J/\psi K^{*0}(K^{*0} \to K^0_S\pi^0)$ decays. The results of the fit treating $\sin 2\beta$ and $\cos 2\beta$ as independent variables give $\cos 2\beta = +3.32^{+0.76}_{-0.96} \pm 0.27$ [951] for *BABAR*. Using the outcome of fits to simulated samples, the sign of $\cos 2\beta$ is determined to be positive at the 86% confidence level. Belle reported $\cos 2\beta = +0.56 \pm 0.11 \pm 0.27$ [952]. These results are

[22] Charge-conjugate reactions are included implicitly unless otherwise specified.
[23] Unless otherwise stated, all results are quoted with the first error being statistical and the second systematic.

compatible with the Standard Model expectations. Other measurements also contribute to reduce the ambiguity.

The time-dependent CP asymmetry parameters were measured in the $B^0 \to J/\psi\,\pi^0$ decay and are also consistent with the SM. Using a dataset of 425fb^{-1}, the *BABAR* experiment measured [953]:

$$C_f = -0.20 \pm 0.19(stat) \pm 0.03(syst), \quad S_f = -1.23 \pm 0.21(stat) \pm 0.04(syst).$$

This is evidence for CP violation as S and C are measured to have non-zero values at a 4σ confidence level. The results reported by the Belle experiment using 492fb^{-1} are [954]:

$$C_f = -0.08 \pm 0.16(stat) \pm 0.05(syst), \quad S_f = -0.65 \pm 0.21(stat) \pm 0.05(syst).$$

The measurements of sin2β in charmonium decays are in excellent agreement with the SM expectations [955]. The results presented above are summarized in Fig. 60. High precision measurements using larger datasets are anticipated in the next few years.

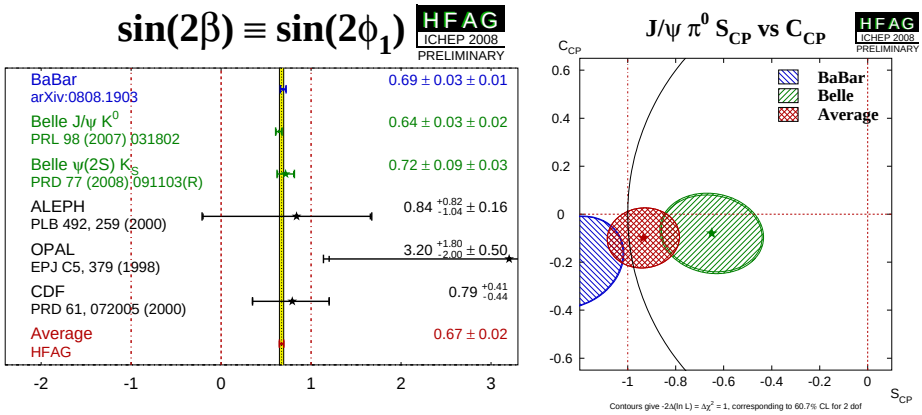

Fig. 60. HFAG averages. In the left panel, the average of sin2β from all experiments. In the right panel, the summary plot of S versus C for $B^0 \to J/\psi\,\pi^0$.

7.2.4. *Measurement of the B_s meson mixing phase*

The B_s mixing phase is accessible through the time-evolution of $B_s \to J/\psi\,\phi$ decays, which is sensitive to the relative phase between the mixing and the $\bar{b} \to \bar{c}c\bar{s}$ quark-level transition, $\beta_s^{J/\psi\phi} = \beta_s^{\rm SM} + \beta_s^{\rm NP}$. This phase is responsible for *CP*-violation. In the Standard Model it equals to $\beta_s^{\rm SM} = \arg(-V_{ts}V_{tb}^*/V_{cs}V_{cb}^*) \approx 0.02$ [637, 956]. Any sizeable deviation from this value would be unambiguous evidence of new physics [957]. If new physics contributes a phase ($\beta_s^{\rm NP}$), this would also enter $\phi_s^{J/\psi\phi} = \phi_s^{\rm SM} - 2\beta_s^{\rm NP}$, which is the phase difference between mixing and decay into final states common to B_s and $\overline{B}_s$, and is tiny in the SM: $\phi_s^{\rm SM} = \arg(-M_{12}/\Gamma_{12}) \approx 0.004$ [938]. The phase $\phi_s^{J/\psi\phi}$ enters the decay-width difference between light and heavy states, $\Delta\Gamma = \Gamma_L - \Gamma_H = 2|\Gamma_{12}|\cos(\phi_s^{J/\psi\phi})$ and equals $\Delta\Gamma^{\rm SM} \approx 2|\Gamma_{12}| = 0.096 \pm 0.036$ ps^{-1} in the Standard Model [938], thus playing a rôle in $B_s \to J/\psi\,\phi$ decays. Since the SM values for $\beta_s^{J/\psi\phi}$ and $\phi_s^{J/\psi\phi}$ cannot be

resolved with the resolution of current experiments, the following approximation is used: $\phi_s^{J/\psi\phi} \approx -2\beta_s^{\rm NP} \approx -2\beta_s^{J/\psi\phi}$, which holds in case of sizable NP contributions.

The measurement of $\beta_s^{J/\psi\phi}$ is analogous to the determination of the phase $\beta = \arg(-V_{cd}V_{cb}^*/V_{td}V_{tb}^*)$ in $B^0 \to J/\psi K_S^0$ decays, except for a few additional complications. The oscillation frequency in the B_s system is about 35 times higher than in B^0 mesons, requiring excellent decay-time resolution. The decay of a pseudoscalar meson (B_s) into two vector mesons (J/ψ and ϕ) produces two *CP*-even states (orbital angular momentum $L = 0, 2$), and one *CP*-odd state ($L = 1$), which need to be separated for maximum sensitivity. Finally, the value of the SM expectation for $\beta_s^{J/\psi\phi}$ is approximately 30 times smaller [946] than β.

Both Tevatron experiments have performed measurements of the time-evolution of flavor-tagged $B_s \to J/\psi(\to \mu^+\mu^-)\phi(\to K^+K^-)$ decays [958]. The CDF analysis is described in the following, a similar analysis is performed by D0. Events enriched in J/ψ decays are selected by a trigger that requires the spatial matching between a pair of two-dimensional, oppositely-curved, tracks in the multi-wire drift chamber (coverage $|\eta| < 1$) and their extrapolation outward to track-segments reconstructed in the muon detectors (drift chambers and scintillating fibers). In the offline analysis, a kinematic fit to a common space-point is applied between the candidate J/ψ and another pair of tracks consistent with being Kaons originated from a ϕ meson decay. An artificial neural network trained on simulated events (to identify signal, S) and B_s mass sidebands (for background, B) is used for an unbiased optimization of the selection. The quantity $S/\sqrt{S+B}$ is maximized using kinematic and particle identification (PID) information. Discriminating observables include Kaon-likelihood from the combination of $\mathrm{d}E/\mathrm{d}x$ and TOF information, transverse momenta of the B_s and ϕ mesons, the K^+K^- mass, and the quality of the vertex fit.

The sensitivity to the mixing phase is enhanced if the evolution of *CP*-even eigenstates, *CP*-odd eigenstates, and their interference is separated. This is done by using the angular distributions of final state particles to statistically determine the *CP*-composition of the signal. The angular distributions are studied in the transversity basis, which allows a convenient separation between *CP*-odd and *CP*-even terms in the equations of the time-evolution.Sensitivity to the phase increases if the evolution of bottom-strange mesons produced as B_s or $\overline{B}_s$ are studied independently. The time development of flavor-tagged decays contains terms proportional to $\sin(2\beta_s^{J/\psi\phi})$, reducing the ambiguity with respect to the untagged case ($\propto |\sin(2\beta_s^{J/\psi\phi})|$). Building on techniques used in the B_s mixing frequency measurement [220], the production flavor is inferred using flavor tagging techniques discussed in Sec. 3.2.2

The tagging power, $\epsilon D^2 \approx 4.5\%$, is the product of an efficiency ϵ, the fraction of candidates with a flavor tag, and the square of the dilution $D = 1 - 2w$, where w is the mistag probability. The proper time of the decay and its resolution are known on a per-candidate basis from the position of the decay vertex, which is determined with an average resolution of approximately 27 μm (90 fs^{-1}) in $B_s \to J/\psi\,\phi$ decays. Information on B_s candidate mass and its uncertainty, angles between final state particles' trajectories (to extract the *CP*-composition), production flavor, and decay length and its resolution are used as observables in a multivariate unbinned maximum likelihood fit of the time evolution. The fit accounts for direct decay amplitude, mixing followed by the decay, and their interference. Direct *CP*-violation is expected to be small and is not considered.

The outputs of the fit are the phase $\beta_s^{J/\psi\phi}$, the decay-width difference $\Delta\Gamma$, and 25 other "nuisance" parameters ($\boldsymbol{\nu}$). These include the mean B_s decay-width ($\Gamma = (\Gamma_L + \Gamma_H)/2$), the squared magnitudes of linear polarization amplitudes ($|A_0|^2$, $|A_\parallel|^2$, $|A_\perp^2|$), the *CP*-conserving ("strong") phases ($\delta_\parallel = \arg(A_\parallel A_0^*)$, $\delta_\perp = \arg(A_\perp A_0^*)$), and others.

The acceptance of the detector is calculated from a Monte Carlo simulation and found to be consistent with observed angular distributions of random combinations of four tracks in data. CDF also validated the angular-mass-lifetime model by measuring lifetime and polarization amplitudes in 7800 $B^0 \to J/\psi\ K^*$ decays, which show angular features similar to the B_s sample: $c\tau(B^0) = 456 \pm 6(stat) \pm 6(syst)\,\mu$m, $|A_0|^2 = 0.569 \pm 0.009(stat) \pm 0.009(syst)$, $|A_\parallel|^2 = 0.211 \pm 0.012(stat) \pm 0.006(syst)$, $\delta_\parallel = -2.96 \pm 0.08(stat) \pm 0.03(syst)$, and $\delta_\perp = 2.97 \pm 0.06(stat) \pm 0.01(syst)$. The results, consistent and competitive with most recent B–factories' results [959], support the reliability of the model. Additional confidence is provided by the precise measurement of lifetime and width-difference in untagged $B_s \to J/\psi\,\phi$ decays [960].

Tests of the fit on simulated samples show biased, non-Gaussian distributions of estimates and multiple maxima, because the likelihood is invariant under the transformation $\mathcal{T} = (2\beta_s^{J/\psi\phi} \to \pi - 2\beta_s^{J/\psi\phi}, \Delta\Gamma \to -\Delta\Gamma, \delta_\parallel \to 2\pi - \delta_\parallel, \delta_\perp \to \pi - \delta_\perp)$, and the resolution on $\beta_s^{J/\psi\phi}$ was found to depend crucially on the true values of $\beta_s^{J/\psi\phi}$ and $\Delta\Gamma$. CDF quotes therefore a frequentist confidence region in the $(\beta_s^{J/\psi\phi}, \Delta\Gamma)$ plane rather than point-estimates for these parameters. Obtaining a correct and meaningful region requires projecting the full 27-dimensional region into the $(\beta_s^{J/\psi\phi}, \Delta\Gamma)$ plane. A common approximate method is the profile likelihood approach. For every point in the $(\beta_s^{J/\psi\phi}, \Delta\Gamma)$ plane, $\hat{\boldsymbol{\nu}}$ are the values of nuisance parameters that maximize the likelihood. Then $-2\Delta\ln(L_p)$ is typically used as a χ^2 variable to derive confidence regions in the two-dimensional space $(\beta_s^{J/\psi\phi}, \Delta\Gamma)$. Simulations show that in the present case the approximation fails. The resulting regions contain the true values with lower probability than the nominal confidence level (C.L.) because the $-2\Delta\ln(L_p)$ distribution has longer tails than a χ^2. A full confidence region construction is therefore needed, using simulation of a large number of pseudo-experiments to derive the actual distribution of $-2\Delta\ln(L_p)$, with a potential for an excessive weakening of the results from systematic uncertainties. However, in a full confidence limit construction, the use of $-2\Delta\ln(L_p)$ as ordering function is close to optimal for limiting the impact of systematic uncertainties [961, 962]. With this method, it is possible to account for the effect of systematic uncertainties just by randomly sampling a limited number of points in the space of all nuisance parameters: a specific value $(\beta_s^{J/\psi\phi}, \Delta\Gamma)$ is excluded only if it can be excluded for any assumed value of the nuisance parameters within 5σ of their estimate on data. Fig. 61 shows the confidence regions obtained by the two experiments with 2.8 fb^{-1} of Tevatron data.

A separate handle on CP violation is available through semileptonic B_s decays and has been performed by the D0 collaboration on 2.8 fb^{-1} of Tevatron data. The flavor of the B_s meson in the final state is determined by the muon charge in the decay $B_s \to D_s^- \mu^+ \nu X$ with $D_s^- \to \phi\pi^-$ and $\phi \to K^+K^-$. A combined tagging method is then used to determine the initial state flavor. A time-dependent fit to B_s candidate distributions yields the CP violation parameter

$$A_{sl}^s = -0.0024 \pm 0.0117\ (\text{stat})^{+0.0015}_{-0.0024}\ (\text{syst}). \tag{360}$$

This is the first direct measurement [953] of the time integrated flavor untagged charge

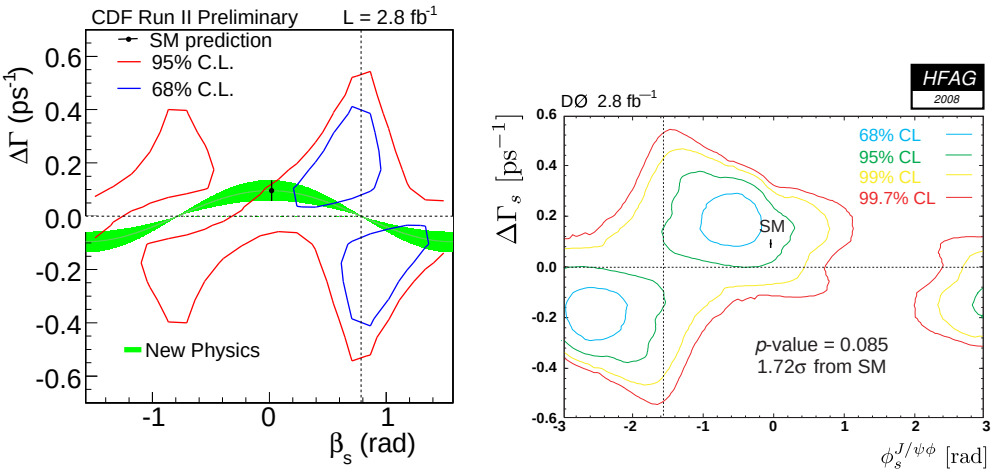

Fig. 61. Confidence region in the $(\beta_s^{J/\psi\phi}, \Delta\Gamma)$ plane obtained with 2.8 fb^{-1} of CDF (left panel) and D0(right panel) data. The green band is the region allowed by any NP contribution not entering $|\Gamma_{12}|$, and assuming $2|\Gamma_{12}| = 0.096 \pm 0.036$ ps^{-1} [938].

asymmetry in semileptonic B_s^0 decays. $A_{SL}^{s,\mathrm{unt.}}$ has also been obtained from a data sample corresponding to an integrated luminosity of 1.3 fb^{-1} in comparing the decay rate $B_s \to \mu^+ D_s^- \nu X$, $D_s^- \to \phi\pi^-$, $\phi \to K^+K^-$ with its charge conjugated decay rate. The asymmetry amounts to

$$A_{SL}^{s,\mathrm{unt.}} = [1.23 \pm 0.97\ (\mathrm{stat}) \pm 0.17\ (\mathrm{syst})] \times 10^{-2}, \tag{361}$$

assuming that $\Delta m_s / \overline{\Gamma_s} \gg 1$. The result can be further related to the CP-violating phase in B_s^0 mixing via

$$\frac{\Delta\Gamma_s}{\Delta m_s} \tan\phi_s = [2.45 \pm 1.93\ (\mathrm{stat}) \pm 0.35\ (\mathrm{syst})] \times 10^{-2}. \tag{362}$$

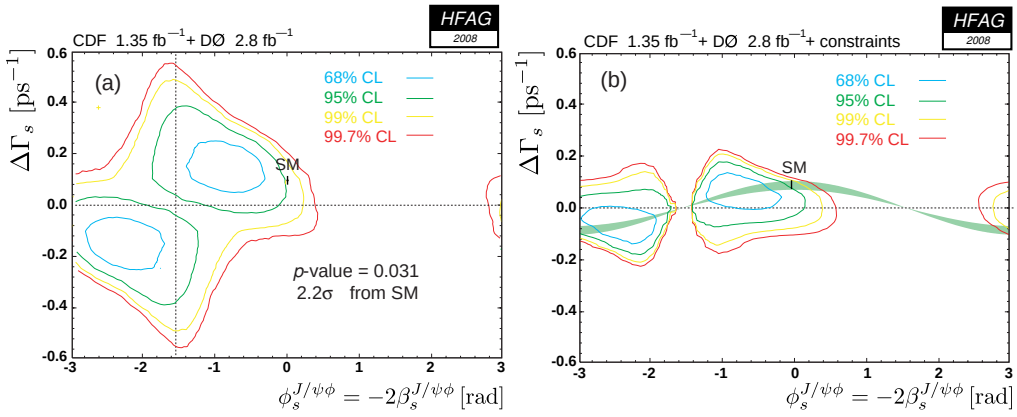

Fig. 62. Contour plots of D0and CDF combined results in the $(\Delta\Gamma_s, \phi_s)$ plane for different confidence levels. In the left panel, the combination of two results without constraints. In the right panel, constraints of the measured charge asymmetry A_{SL}^s and B_s^0 lifetime are taken into account.

The world best knowledge on the B_s mixing phase at this time comes from combining the two Tevatron results and applying all available constraints to the calculation. Fig. 62 shows the combination of the results from the two Tevatron experiments. The current combined result is based on the 1.35 fb^{-1} dataset from CDF and the 2.8 fb^{-1} dataset from D0. The unconstrained result is consistent with the Standard Model prediction within 2.2σ. Adding constraints from A^s_{SL} and the B_s flavor specific lifetime measurements, the discrepancy betwen the Standard Model prediction and the combined result increases to 2.3σ.

7.3. *The D-meson system*

7.3.1. *Theoretical prediction for ΔM_D and CP violation within the SM and beyond*

The SM calculation of ΔM_D is plagued by long-distance contributions, responsible for very large theoretical uncertainties. The short-distance contribution in ΔM_D [963, 964], indeed, is highly suppressed both by a factor $(m_s^2 - m_d^2)/M_W^2$ generated by the GIM mechanism and by a further factor $(m_s^2 - m_d^2)/m_c^2$ due to the fact that the external momentum, of the order of m_c, is communicated to the internal light quarks in box-diagrams. These factors explain why the box-diagrams are so small for D mesons relative to K and $B_{d,s}$ mesons where the GIM mechanism enters as m_c^2/M_W^2 and m_t^2/M_W^2 and external momenta can be neglected.

Theoretical estimates of charm mixing in the SM have been performed using either quarks or hadrons as basic degrees of freedom. The former method, like that used in $B_{d,s}$ mixing, consists in analyzing the mixing by using a sum of local operators ordered by dimension according to OPE [965]. Roughly speaking, the result at the leading order in the OPE (where operators of dimension $D = 6$ contribute) and in QCD from the $s\overline{s}$ intermediate state yields the result [966] $y_{\rm D} \sim F(z)(|V_{us}|/|V_{cs}|)^2 \sim 0.01$ where $F(z) = 1/2 + \mathcal{O}(z)$ with $z \equiv (m_s/m_c)^2 \simeq 0.006$. This seems to reproduce the correct magnitude. Such is, however, not the case, as severe flavor cancellations with the $d\bar{d}$, $s\bar{d}$, $d\bar{s}$ intermediate states occur (the leading terms in the z-expansion for $x_{\rm D}$ and $y_{\rm D}$ respectively become z^2 and z^3 at order α_s^0 and just z^2 at order α_s^1). The result through $\mathcal{O}(\alpha_s)$ is tiny, $x_{\rm D} \simeq y_{\rm D} \sim 10^{-6}$ [966]. Evidently the OPE for charm is slowly convergent, although higher orders of the OPE do contain terms in which the z-suppression is less severe [967, 968]. The problem is that the number of local operators increases sharply with the operator dimension D (e.g. $D = 6$ has two operators, $D = 9$ has fifteen, and so on). To make matters worse, the matrix elements of the various local operators are unknown and can be only roughly approximated in model calculations. QCD lattice determinations would be of great use, but are currently unavailable.

The other method, which considers hadronic degrees of freedom, is based on the following relation between the width difference and the absorptive matrix element given in Eq. (337), with

$$\Gamma_{12}^D = \frac{1}{2M_D}\, Disc\langle D^0|i\int d^4x \mathcal{T}\left(\mathcal{H}_{eff}^{\Delta C=1}(x)\,\mathcal{H}_{eff}^{\Delta C=1}(0)\right)|\bar{D}^0\rangle\,, \tag{363}$$

To get $y_{\rm D}$, defined in Eq. (338), one inserts intermediate states between the $\Delta C = 1$ effective Hamiltonians (see Sec. 2.1). This method yielded an early estimate for $y_{\rm B_s}$ (where the dominant contributions are few in number [969]), but for charm mixing many matrix elements contribute. The result of using a theoretical model [970] gives $y_{\rm D} \sim 10^{-3}$,

which is too small. This shows how delicate the sum over many contributions seems to be.

Another approach is to rely more on charm decay data and less on the underlying theory [971,972]. Given that SU(3) breaking occurs at second order in charm mixing [973], perhaps all two-particle and three-particle sectors contribute very little. However, this cannot happen for the four-particle intermediate states because the decay of D^0 into four-Kaon states is kinematically forbidden. In fact, Ref. [974] claims that these multiparticle sectors can generate $y_D \sim 10^{-2}$. The complicate picture is worsened by the fact that a dispersion relation calculation [974] using charm decay widths as input predicts a negative value for $x_{\rm D}$, i.e. of opposite sign with respect to the experimental measurement. The determination of $x_{\rm D}$ in the SM is certainly subtle enough to deserve further study and, at the same time, to strengthen the motivation for studying NP models of D^0 mixing.

NP contributions to charm mixing can affect $y_{\rm D}$ as well as $x_{\rm D}$. We do not consider the former here, instead refering the reader to refs. [975, 976]. The study of $x_{\rm D}$ in Ref. [977] considers 21 New Physics models, arranged in terms of extra gauge bosons (LR models, etc), extra scalars (multi-Higgs models, etc), extra fermions (little Higgs models, etc), extra dimensions (split fermion models, etc), and extra global symmetries (SUSY, etc). The strategy for calculating the effect of NP on D^0 mixing is, for the most part, straightforward. One considers a particular NP model and calculates the mixing amplitude as a function of the model parameters. If the mixing signal is sufficiently large, constraints on the parameters are obtained. Of these 21 NP models, only four (split SUSY, universal extra dimensions, left-right symmetric and flavor-changing two-higgs doublet) are ineffective in producing charm mixing at the observed level. This has several causes, e.g. the NP mass scale is too large, severe cancellations occur in the mixing signal, etc. This means that 17 of the NP models can produce charm mixing. We refer to Ref. [977] for details.

Finally, we observe that for a deeper understanding of $D^0 - \bar{D}^0$ mixing, there remain additional avenues to explore, among them correlating NP contributions between charm mixing and rare charm decays and providing a comprehensive account of CP violations (both SM and NP) in $D^0 - \bar{D}^0$ mixing.

7.3.2. *Experimental results*

Recent studies have shown evidence for mixing in the D^0-$\overline{D}^0$ system at the 1% level [978–981]. The measured values can be accommodated by the Standard Model (SM) [968,971–974] where the largest predictions for x_D and y_D are of $\mathcal{O}(10^{-2})$. These measurements provide strong constraints on new physics models [977, 982, 983]. An observation of *CP* violation in D^0-$\overline{D}^0$ mixing with the present experimental sensitivity would provide evidence for physics beyond the SM [984], and a search for this effect in the charm system is considered elsewhere [985]. Presented here is an overview of recent mixing measurements.

The first evidence analysis studies right-sign (RS), Cabibbo-favored (CF) decay $D^0 \to K^-\pi^+$ and the wrong-sign (WS) decay $D^0 \to K^+\pi^-$. The latter can be produced via the doubly Cabibbo-suppressed (DCS) decay $D^0 \to K^+\pi^-$ or via mixing followed by a CF decay $\overline{D}^0 \to K^+\pi^-$. The DCS decay has a small rate $R_{\rm D}$ of order $\tan^4\theta_C \approx 0.3\%$ relative to CF decay. D^0 and $\overline{D}^0$ are distinguished by their production in the decay $D^{*+} \to \pi_{\rm s}^+ D^0$ where the $\pi_{\rm s}^+$ is referred to as the "slow pion". In RS decays the $\pi_{\rm s}^+$ and Kaon have opposite charges, while in WS decays the charges are the same.

The time dependence of the WS decay rate is used to separate the contributions of DCS decays from D^0-$\overline{D}^0$ mixing. For the WS decay of a meson produced as a D^0 at time $t = 0$ in the limit of small mixing ($|x_D|$, $|y_D| \ll 1$) and *CP* conservation this is approximated as

$$\frac{T_{\rm WS}(t)}{e^{-\Gamma t}} \propto R_{\rm D} + \sqrt{R_{\rm D}} y'_f \, \Gamma t + \frac{x'^2_f + y'^2_f}{4} (\Gamma t)^2 \,, \tag{364}$$

where $x'_f = x_D \cos\delta_f + y_D \sin\delta_f$, $y'_f = -x_D \sin\delta_f + y_D \cos\delta_f$, where f is the final state accessible to both D^0 and $\overline{D}^0$ decays, and δ_f is the relative strong phase between the DCS and CF amplitudes. This makes it possible to measure the quantities x_D and y_D, if the strong phase difference δ_f is known. To search for *CP* violation, Eq. (364) is applied to D^0 and $\overline{D}^0$ samples separately.

Evidence for D^0-$\overline{D}^0$ mixing in $D^0 \to K^+\pi^-$ decays has been reported by the *BABAR* collaboration [978]. The mixing parameters were found to be $x'^2_{K\pi} = [-0.22 \pm 0.30$ (stat.) $\pm$ 0.21 (syst.)$] \times 10^{-3}$ and $y'_{K\pi} = [9.7 \pm 4.4$ (stat.) ± 3.1 (syst.)$] \times 10^{-3}$, and a correlation between them of -0.94. This result is inconsistent with the no-mixing hypothesis with a significance of 3.9 σ, with no evidence for *CP* violation.

The quantum coherence between pair-produced D^0 and $\overline{D}^0$ in $\psi(3770)$ decays can be used to study charm mixing and to make a determination of the relative strong phase $\delta_{K\pi}$ [988]. Using data collected with the CLEO-c detector at $E_{cm} =$ 3.77 GeV, as well as branching fraction input from other experiments a value of $\cos\delta_{K\pi} = 1.03^{+0.31}_{-0.17} \pm 0.06$ was found, where the uncertainties are statistical and systematic, respectively. In addition, by further including external measurements of charm mixing parameters, another measurement of $\cos\delta_{K\pi} = 1.10 \pm 0.35 \pm 0.07$, as well as $x_D \sin\delta_{K\pi} = (4.4^{+2.7}_{-1.8} \pm 2.9) \times 10^{-3}$ and $(\delta_{K\pi} = 22^{+11}_{-12}\ ^{+9}_{-11})\ ^\circ$, was made.

The initial evidence by the *BABAR* experiment was first confirmed by the CDF collaboration [986, 987]. The CDF analysis was performed on a signal sample of 12.7×10^3 $D^0 \to K^+\pi^-$ decays gathered with the displaced track trigger. This corresponds to an integrated luminosity of 1.5 fb^{-1}. The analysis considers D^0 decays with proper decay times between 0.75 and 10 mean D^0 lifetimes. The mixing parameters are measured to be $R_D = 3.04 \pm 0.55 (\times 10^{-3})$, $y' = 8.54 \pm 7.55 (\times 10^{-3})$, $x'^2 = -0.12 \pm 0.35 (\times 10^{-3})$. The data are inconsistent with the no mixing hypothesis ($y' = x'^2 = 0$) with a probability equivalent to 3.8 Gaussian standard deviations.

Further evidence for mixing was reported by the *BABAR* collaboration using a time-dependent Dalitz plot analysis of the WS $D^0 \to K^+\pi^-\pi^0$ decays [981]. The advantage of an amplitude analysis across the Dalitz plot is that the interference term in Eq. 364, produces a variation in average decay time as a function of position in the Dalitz plot that is sensitive to the complex amplitudes of the resonant isobars as well as the mixing parameters. In this study, the change in the average decay time and the interference between the $D^0 \to K^{*+}\pi^-$ and $D^0 \to \rho^- K^+$ amplitudes are the origin of the sensitivity to mixing. Assuming *CP* conservation, the mixing parameters $x'_{K\pi\pi^0} = [2.61\ ^{+0.57}_{-0.68}$ (stat.) $\pm$ 0.39 (syst.)]%, and $y'_{K\pi\pi^0} =$ [-0.06 $^{+0.55}_{-0.64}$ (stat.) $\pm$ 0.34 (syst.)]% were extracted. This result is inconsistent with the no-mixing hypothesis with a significance of 3.2 σ. No evidence of *CP* violation in mixing was observed.

The CLEO collaboration pioneered an analysis of $D^0 \to K^0_S\pi^+\pi^-$ decays using a time-dependent Dalitz plot analysis [989], allowing for a direct determination of x_D and

y_D. Due to the presence of CP-eigenstates in the final state, the amplitudes of D^0 and $\overline{D}^0$ are entangled, so that the analysis is free of unknown phases. The Belle collaboration has repeated this analysis [990], first assuming CP conservation and subsequently allowing for CP violation. Assuming negligible CP violation, the mixing parameters $x_D = (0.80 \pm 0.29^{+0.09+0.10}_{-0.07-0.14})\%$ and $y_D = (0.33 \pm 0.24^{+0.08+0.06}_{-0.12-0.08})\%$ were measured, where the errors are statistical, experimental systematic, and systematic due to the amplitude model uncertainties, respectively. This corresponds to a deviation of 2.4 σ significance from the no-mixing hypothesis. Allowing for CP violation, the CPV parameters $|q/p| = 0.86^{+0.30+0.06}_{-0.29-0.03} \pm 0.08$ and $\arg(q/p) = (-14^{+16+5+2}_{-18-3-4})^\circ$ have been obtained.

One consequence of D^0-$\overline{D}^0$ mixing is that the D^0 decay time distribution can be different for decays to different CP eigenstates [991]. Using the ratios of lifetimes extracted from a sample of D^0 mesons produced through the process $D^{*+} \to D^0\pi^+$, that decay to $K^-\pi^+$, K^-K^+, or $\pi^+\pi^-$, the lifetimes of the CP-even, Cabibbo-suppressed modes K^-K^+ and $\pi^+\pi^-$ are compared to that of the CP-mixed, Cabibbo-favored mode $K^-\pi^+$ to obtain a measurement of y_{CP}, which in the limit of CP conservation corresponds to the mixing parameter y_D. Both Belle [979] and *BABAR* [980] have produced measurements of D^0-$\overline{D}^0$ mixing parameters, at 3.2 and 3.0 σ from the no mixing expectation, respectively. All current results are shown in Fig. 63. No evidence for a CP asymmetry between D^0 and $\overline{D}^0$ decays has been found.

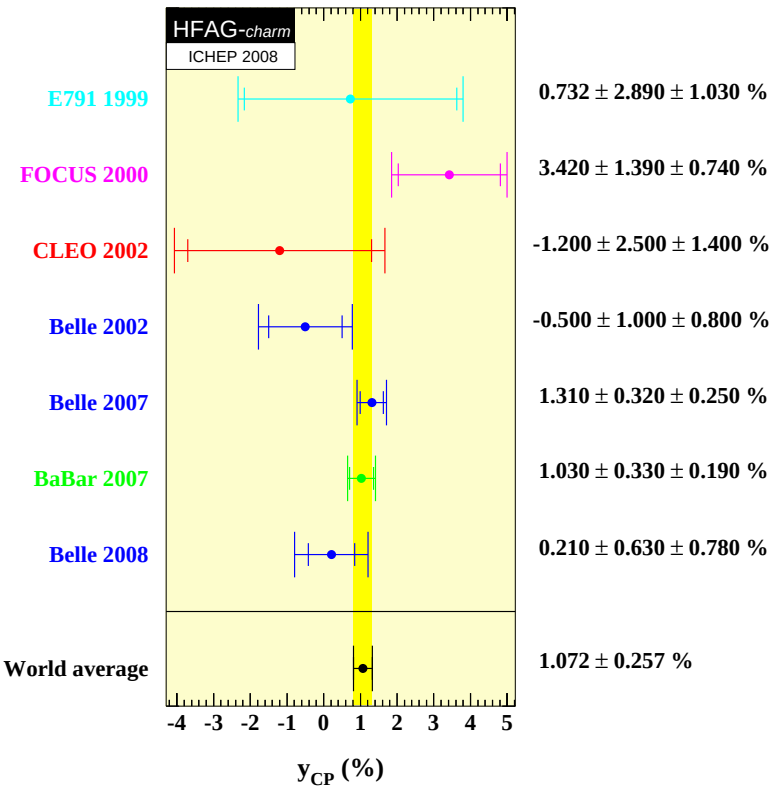

Fig. 63. Current measurements of y_{CP}. The mean $y_{CP} \approx 1$ % differs significantly from zero [560].

The mixing parameter y_{CP} has also been measured by the Belle Collaboration, using a flavor-untagged sample of $D^0 \to K^0_S K^+ K^-$ decays [992]. By measuring the difference in lifetimes between D^0 mesons decaying to $K^0_S\ K^+K^-$ in two different m(K^+K^-) regions with different contributions of CP even and odd eigenstates they determine $y_{CP} = (0.21 \pm 0.63 \pm 0.78 \pm 0.01(\text{model}))\%$. This result, is also included in Fig. 63.

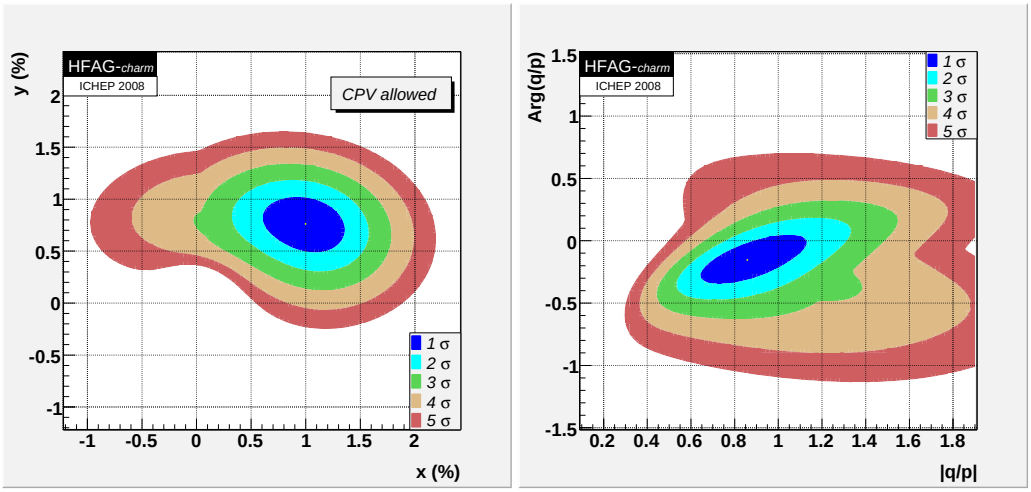

Fig. 64. World averages from the Heavy Flavor Averaging Group (HFAG): χ^2 contours for x_D vs. y_D, and $|q/p|$ vs. Arg(q/p).

A global average has been constructed from 28 mixing variables (including those mentioned above), by the Heavy Flavor Averaging Group (HFAG) [560], as shown in Fig. 64. The no-mixing point $x_D = y = 0$ is excluded at 9.8 σ, and the values $x_D \approx y \approx 1$ % are favored, but to date no single measurement exceeds 5 σ.

7.4. *Future Outlook*

With planned data taking coming to an end for some of the main experiments contributing to lifetime and mixing results, attention is now turning to the flavor program of the Large Hadron Collider. With a dedicated heavy flavor experiment (LHCb), two powerful multi-purpose detectors (ATLAS and CMS), and plans for tremendous integrated luminosity samples, expectations of precision results are very high. In this chapter we review expected performance for some of the most interesting results that are expected to come from the LHC.

7.4.1. *B meson mixing and lifetimes*

The first B meson lifetime measurements at LHC experiments will be used as calibration measurements to understand detector effects on time-dependant analyses. Very large samples of fully reconstructed B^+ and B^0 candidates will be available very early after the LHC starts, and will allow comparison with existing precise lifetime measurements. For example, at ATLAS, 1024 reconstructed $B^0 \to J/\psi K^{*0}$ are expected after 10 pb^{-1} of data, which will allow a lifetime measurement with 10% precision after approximatively

one month of data taking. Similarly, the LHCb experiment will reconstruct 1.735 million $B^+ \to J/\psi K^+$ candidates for 2 fb^{-1} of data, with a small background over signal ratio, allowing not to use any lifetime selection criteria and thus to determine lifetime resolution functions. Hadronic decay modes will also be reconstructed with large samples. The LHCb experiment will reconstruct 1.34 million $B^0 \to D^-(K^-\pi^+\pi^-)\pi^+$ decays in 2 fb^{-1} of data. The expected proper time resolution of 33.9 fs will allow LHCb to reach the current B^0 lifetime precision (0.009 ps) with 60000 events, considering only statistical errors.

Measurements of Λ_b lifetimes are expected to improve significantly with LHC results. LHCb expects to reconstruct 2.3×10^4 events for 2 fb^{-1} of data in the decay mode $\Lambda_b \to J\psi(\mu^+\mu^-)\Lambda(p\pi)$. The anticipated proper time resolution for these decays is 41.5 fs, yielding to a lifetime measurement with a statistical precision of 0.027 ps. The ATLAS experiment will reconstruct 4500 events in the same decay mode with 10 fb^{-1} of data.

LHC experiments plan on precisely measuring the B_c^+ lifetime. The B_c^+ production cross-section is roughly 20 times larger at the LHC than at the Tevatron. About 10^9 $B_c^\pm$ will be produced per year in LHCb. Measurement of the B_c^+ lifetime will be an interesting window on the proportions of its three decay mechanisms: b decay, c decay and anihilation. The most promising decay chanel that will be used for the analysis is $B_c^+ \to J/\psi\pi^+$. Assuming a B_c^+ production cross-section of 0.4 μb and a branching fraction for $B_c^+ \to J/\psi\pi^+$ equal to 1.3×10^{-3}, 700 events are expected for 2 fb^{-1} of data at LHCb, and 80 events for 10 fb^{-1} at CMS, leading to a statistical precision on the lifetime measurement of 0.026 ps at LHCb and 0.055 ps at CMS.

The reconstruction of the flavor specific decay mode $B_s^0 \to D_s^+\pi^-$ with $D_s^+ \to K^+K^-\pi^+$ will allow the measurement of the B_s^0 mixing frequency Δm_s together with the B_s^0 width difference, $\Delta\Gamma_s$. 155000 reconstructed candidates are expected at LHCb in 2 fb^{-1} of data, with a small background over signal ratio $\frac{B}{S} \in [0.06; 0.4]$ at 90% confidence level. The mass resolution is expected to be 17 MeV/c^2 and a proper time resolution of 33 fs is anticipated. This implies measurements of the B_s^0 lifetime to a precision of 0.013 ps. The expected uncertainty on Δm_s is 0.008 ps^{-1}. $\Delta\Gamma_s$ will be measured to 0.03 ps^{-1} precision, assuming a central value of $\Delta\Gamma_s$ equal to 0.068 ps^{-1}. A more precise $\Delta\Gamma_s$ determination is expected to be obtained from the time-dependant angular analysis of the decay mode $B_s^0 \to J/\psi\phi$. Preliminary studies show that a precision of 0.021 ps^{-1} can be reached at ATLAS with 10 fb^{-1} of data, 0.010 ps^{-1} at CMS with 10 fb^{-1} of data assuming perfect tagging, and 0.008 ps^{-1} at LHCb with 2 ps^{-1} of data.

In summary, very precise lifetime measurements of the B^0 and B^+ mesons will be available very soon after LHC starts and will be used to calibrate LHC detectors for further lifetime measurements. Parameters of the B_s^0 hadron (τ_s, Δm_s) will reach similar precisions to those currently available for B^0 and B^+. These measurements are expected to rapidly become limited by systematics uncertainties. Precision studies of other B hadrons, such as the lifetime of the B_c^+ and Λ_b, will be conducted at the CMS, ATLAS, and LHCb experiments.

7.4.2. *Measurements of the B_s meson mixing phase*

As discussed in Sec. 7.2.4 and [993], the most precise measurement of β_s can be obtained via a tagged time-dependent angular analysis of the $B_s \to J/\psi\,\phi$ decay mode. In order to disentangle the two CP eigenstates, the three amplitudes are statistically

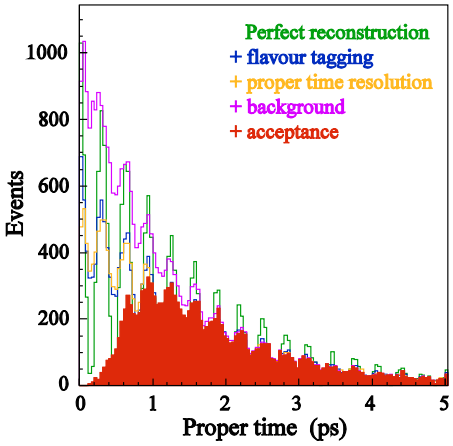

Fig. 65. LHCb toy Monte Carlo simulation of the proper time distribution of right-sign tagged $B_s^0 \to D_s^+\pi^-$ decays. The toy simulation is based on resolutions, efficiencies, and tagging power estimated from full detector simulation.

separated through an angular analysis. The oscillation amplitude of the time-dependent angular distributions is proportional to the CP-violation phase β_s. In the following text we compare the key performance parameters for this measurement between the three experiments.

Offline selections for the three experiments are based on basic quantities like particle identification, p_T of the decay products, vertex quality and, only for ATLAS and CMS, b-vertex displacement. The MuonID capability is similar for the three experiments (muon efficiency of $\sim$ 90 % for a misidentification rate of $\sim$ 1%, but dependent with p_T, η for central detectors). Hadron identification capability is higher for LHCb due to the powerful RICH system [994] which allows to Kaon identification with an efficiency of $\sim$ 88%. The pion misidentification rate of $\sim$ 3%.

The expected momentum resolution is $\sigma_p/p = (0.3 - 0.5)\%$ for LHCb and $\sigma_{p_T}/p_T = 1 - 2\%$ for ATLAS/CMS. This provides a B_s mass resolution of $\sim$ 17 MeV/c^2 for LHCb without use of a J/Ψ mass constraint in the fit. CMS and ATLAS predict B_s mass resolutions of $\sim 14 - 16$ MeV /c^2, using a J/Ψ mass constraint in the fit. LHCb does not make use of the J/Ψ mass constraint because this requirement modifies the proper time acceptance of the decaying B_s.

ATLAS/CMS use an offline selection with B_s lifetime selection cuts. This selection gets rid of most of the prompt combinatorial background but also modifies heavily the proper time acceptance that must be corrected afterwards. LHCb will optimize the B_s signal selection by minimizing the bias on the proper time and angular acceptances.

For the time being, LHCb and ATLAS are developing tagged analyses, while CMS is currently reporting an untagged one. ATLAS will use several taggers mainly based on leptons and vertex charge. The combined tag gives an effective tagging power of $\epsilon_{eff} = \epsilon_{tag}(1 - 2\omega)^2 = 4.6\%$. LHCb expects excellent hadron identification and therefore can profit also from both same side and opposite side Kaon taggers. The combined tag is expected to have an effective tagging power of $\epsilon_{eff} = 6.2\%$. Tagging calibration will be performed at LHCb using flavor specific decays, namely $B^0 \to J/\psi\ K^*$ and B^+ to J/ψ

K^+ for calibration of OS taggers, and $B_s \to D_s\pi$ for calibration of the same side tagger. The last key ingredient is the proper time resolution, σ_τ. Expected average proper time resolutions are 83 fs, 77 fs and 40 fs, for ATLAS, CMS and LHCb, respectively. At the time of this report, Monte Carlo samples with full simulation which were available for studies have limited statistics: ~ 7 pb^{-1} of inclusive $J/\Psi \to \mu^+ mu^-$ were available for the LHCb studies, and 20 - 50 pb^{-1} of $b \to J/\Psi(\mu\mu)X$ for ATLAS/CMS. The Monte Carlo with full detector simulation cannot be used to perform a full analysis evaluation. However, these samples can be used to estimate yield, background fractions, mass, proper time and angle distributions, resolutions, and acceptances. The extracted quantities are then used in toy Monte Carlo ensembles in order to estimate the sensitivity to $2\beta_s$ (and other parameters) via results of unbinned maximum likelihood fits.

Tab. 56 summarizes the expected precision for $2\beta_s$ and $\Delta\Gamma_s$ after 1/4 of a nominal year of running. The estimated event yield, background contamination, effective tagging efficiency ϵD^2 and proper time resolutions $\sigma(\tau)$ are also listed per experiment. These studies assumed values of $2\beta_s \sim 0.04$ for β_s and $\Delta\Gamma_s$ and $\Delta\Gamma_s/\overline{\Gamma}_s \sim 0.1$. ATLAS, CMS and LHCb have a strong potential to increase the precision of the measurements of the B_s CP violating phase well beyond the present CDF and $D0$ results. These precision measurements will open opportunities to probe for effects beyond the Standard Model.

Table 56
Summary table for ATLAS, CMS and LHCb. We show the untagged signal yield for a luminosity corresponding to a 1/4 year of running at nominal luminosity, the B/S ratio, the effective tagging efficienc y, the proper time resolution and the sensitivity on $2\beta_s$ and $\Delta\Gamma_s/\overline{\Gamma}_s$.

	ATLAS	CMS	LHCb
$\mathcal{L}$[fb^{-1}]	2.5	2.5	0.5
signal yield [untagged]	22.5 k	27 k	28.5 k
B/S	0.18	0.25	2
dominant background	long-lived	long-lived	prompt
ϵD^2	4.6 %	N/A	6.2 %
$\sigma(\tau)$	83 fs	77 fs	40 fs
$\sigma(2\beta_s)$	0.16	N/A	0.06
$\sigma(\Delta\Gamma_s/\overline{\Gamma}_s)/(\Delta\Gamma_s/\overline{\Gamma}_s)$	0.45	0.28	0.17

7.4.3. *D^0 mixing and CP violation*

As the dedicated flavor experiment at CERN's Large Hadron Collider (LHC), LHCb is the only LHC experiment currently planning measurements of D^0-$\overline{D^0}$ mixing and charm CP violation. The following studies document the expected performance of the LHCb experiment.

Many of the features that make LHCb an excellent B physics laboratory also make LHCb well-suited for many charm physics studies at unprecedented levels of precision [995]. The silicon Vertex Locator (VELO) will provide the excellent vertex resolutions necessary for time dependent measurements: an estimated 45 fs proper time resolution is expected for $D^0 \to K^-\pi^+$ decays where the D^0 mesons are produced in b-hadron decays. The LHCb tracking system will supply precise momentum measurements The projected mass resolution for two body decays of D^0 mesons is estimated to be 6 MeV/c^2 The

LHCb Ring Imaging Cherenkov (RICH) detectors will provide excellent K–π discrimination over a wide momentum range from 2 GeV/c to 100 GeV/c. Finally, the LHCb trigger system will have a high statistics charm stream, so that the large charm production in LHC collisions can be exploited for precision measurements.

LHCb will perform both time-dependent and time-integrated CP violation searches. Each time-dependent D^0-$\overline{D^0}$ mixing measurement will be analyzed in charge conjugate subsets to measure possible CP violating effects. Measurements with promptly produced charm mesons and with charm mesons produced in b-hadron decays will be pursued. Analysis methods for both sources are under development. Preliminary studies for measurements with secondary charm are currently more complete. Initial studies have focused on D^{*+}–tagged two-body $D^0 \to h^- h'^+$ decays. Multi-body decays to charged products and up to one K^0_S are suitable for precision measurements at LHCb and will be investigated. In four body hadronic decays, plans for CP violation searches include complete amplitude analyses and analyses of quantities that are odd under time reversal.

Simulated events from a full interaction and LHCb detector simulation have been used to estimate LHCb's potential performance in charm mixing analyses. Preliminary event selection studies on these simulated events indicate a yield of approximately 8 million D^{*+}–tagged $D^0 \to K^- K^+$ decays in 10fb^{-1} of collisions. The D^{*+} was produced in a b-hadron decay in these studies. [996]. This yield estimate includes the expected effects of both the L0 and the HLT triggers. This corresponds to a statistical precision of approximately 4×10^{-4} for the CP asymmetry search. The selection used in the study was optimized for the wrong sign (WS) $D^0 \to K\pi$ decays. Reoptimizing for $D^0 \to KK$ is expected to result in even higher yields. Similar studies predict approximately 1.2 billion D^{*+}–tagged $D^0 \to KK$ decays in 10 fb^{-1} after the L0 trigger, before the HLT trigger. Efficient strategies to select these events in the HLT are under investigation.

LHCb will measure D^0-$\overline{D^0}$ mixing in as many channels as it can efficiently reconstruct. Initial studies have focused on the two main mixing measurements possible with D^{*+}–tagged two-body $D^0 \to h^- h'^+$ decays—mixing from analysis of WS $K\pi$ decays, and the ratio of lifetimes of singly Cabibbo suppressed (SCS) and right sign (RS) decays.

Time-dependent analyses require precise measurements of the creation and decay vertices of the D^0 mesons. The scale of the required precision is set by the approximately 4 mm mean laboratory flight distance for a 60 GeV/c D^0 (the mean momentum of secondary D^{*+}–tagged D^0 decays). The decay vertex of a two-body D^0 decay can be determined precisely from its products with a resolution of ~ 260 μm along the beam axis. For promptly produced D^0 decays, the precisely measured primary interaction vertex (resolution ~ 60 μm along the beam axis [995]) is the creation vertex.

For secondary charm decays, the additional charged tracks must come from the b-hadron decay that produced the D^{*+}. LHCb has been developing techniques to partially reconstruct the parent b-hadron that produced the D^{*+} [996]. Initial results from these developments are promising. As shown in the $B_{\rm part}$ column of Tab. 57, using a partial reconstruction dramatically improves the precision of the estimated D^0 creation vertex and, consequently, the measured D^0 proper time. Fig. 66 shows that this process produces precisely measured proper times that closely reproduce the generated proper time distribution. The b-hadron partial reconstruction is approximately 60% efficient with respect to all selected secondary D^{*+}–tagged $D^0 \to h^- h'^+$ decays.

Toy Monte Carlo studies have been used to estimate LHCb's statistical sensitivities to the mixing parameters x'^2 and y' in a two-body WS mixing study and to the mixing

Table 57
Estimated resolutions of D^0, D^{*+}, and $B_{\rm part}$ vertices, and of D^0 proper time in simulated LHCb data. The D^0 proper time, τ_{D^0}, is estimated both using the D^{*+} vertex as the creation vertex in the first column, and using the $B_{\rm part}$ vertex as the creation vertex in the last column.

	D^0	D^{*+}	$B_{\rm part}$
x	22 μm	190 μm	18 μm
y	17 μm	140 μm	18 μm
z	260 μm	4200 μm	240 μm
τ_{D^0}	0.47 ps		0.045 ps

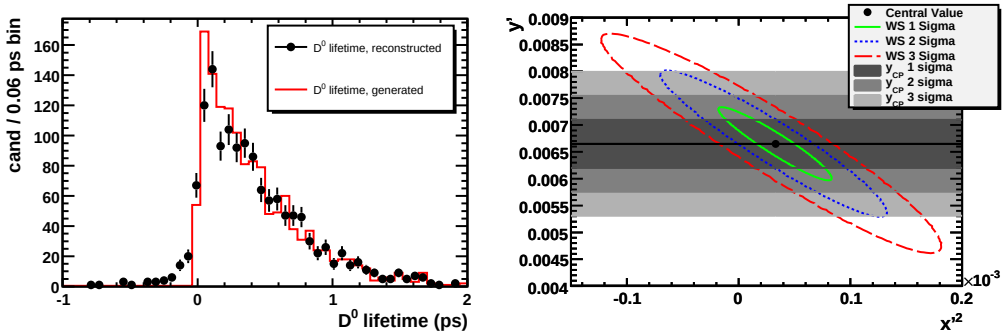

Fig. 66. In the left panel, the distribution of the proper times for simulated D^0 mesons from $B \to D^{*+}X$ decays. The solid lines are the generated proper times and the points are the estimated D^0 proper times using the estimated parent B decay vertex as the D^0 production vertex. In the right panel, the sensitivities in $10\,{\rm fb}^{-1}$ from the WS study and the $y_{\rm CP}$ study. Contours correspond to 1σ, 2σ, and 3σ confidence levels from the WS study. Horizontal bands correspond to 1σ, 2σ, and 3σ confidence levels from the $y_{\rm CP}$ study.

parameter $y_{\rm CP}$ in a two-body lifetime ratio study.

Selection studies in fully simulated LHCb events predict a yield of roughly 230,000 D^{*+}–tagged WS decays $10\,{\rm fb}^{-1}$ of LHCb data. Again, the D^{*+} mesons originate in the decays of b-hadrons in this study. The $10\,{\rm fb}^{-1}$ signal and background yields, proper time resolution, and proper time acceptance of this selection were used in a toy Monte Carlo study to estimate the LHCb statistical sensitivity to x'^2 and y':

$$\sigma_{\rm stat}(x'^2) = \pm 0.064 \times 10^{-3}; \quad \sigma_{\rm stat}(y') = \pm 0.87 \times 10^{-3} \quad [996].$$

The same selection studies referred to in Sec. 7.4.3 estimate that a lifetime ratio analysis on $10\,{\rm fb}^{-1}$ of LHCb data would incorporate approximately 8 million D^{*+}–tagged $D^0 \to K^-K^+$ decays from b-hadron decays. The $10\,{\rm fb}^{-1}$ signal and background yields, the proper time resolution, and the proper time acceptance of this selection were used in a toy Monte Carlo study to estimate the LHCb statistical sensitivity to $y_{\rm CP}$:

$$\sigma_{\rm stat}(y_{\rm CP}) = \pm 0.5 \times 10^{-3} \quad [996].$$

Strategies to reduce the systematic uncertainties to commensurate precision are in development. While systematic uncertainties are still under study, but LHCb will certainly

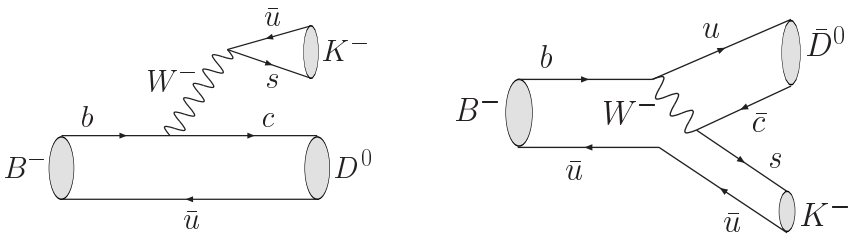

Fig. 67. Leading Feynman diagrams contributing to the $B^+ \to DK^+$ decay. From [260].

have the statistical power to make precision measurements in charm CP violation and D^0-$\overline{D^0}$ mixing.

8. Measurement of the angle γ in tree dominated processes

8.1. *Overview of Theoretically Pristine Approaches to Measure γ*

Among the fundamental parameters of the Standard Model of particle physics, the angle $\gamma = \arg\left(-V_{ud}V_{ub}^*/V_{cd}V_{cb}^*\right)$ of the Unitarity Triangle formed from elements of the Cabibbo-Kobayashi-Maskawa quark mixing matrix [1, 2] has a particular importance. It is the only CP violating parameter that can be measured using only tree-level decays, and thus it provides an essential benchmark in any effort to understand the baryon asymmetry of the Universe. Strategies to measure fundamental parameters of the Standard Model and to search for New Physics by overconstraining the Unitarity Triangle inevitably require a precise measurement of γ.

Fortunately, there is a theoretically pristine approach to measure γ using tree-dominated $B \to DK$ decays [997–999]. The approach exploits the interference between D^0 and $\bar{D}^0$ amplitudes that occurs when the neutral D meson is reconstructed in decay that is accessible to both flavor states. Feynman diagrams for the relevant B decays are shown in Fig. 67. The original approach uses D decays to CP eigenstates [998, 999], but variants using doubly-Cabibbo-suppressed decays [1000,1001], singly-Cabibbo-suppressed decays [1002] and multibody final states such as $K^0_S\pi^+\pi^-$ [257,1003,1004], and many others besides, have been proposed.

Considering D decays to CP eigenstates (CP even and odd denoted by D_1 and D_2 respectively), and defining

$$r_B e^{i\delta_B} = \frac{\mathcal{A}\left(B^+ \to D^0 K^+\right)}{\mathcal{A}\left(B^+ \to \overline{D}^0 K^+\right)}\,, \tag{365}$$

the dependence on γ of the decay rates is found to be as follows (as illustrated in Fig. 68).

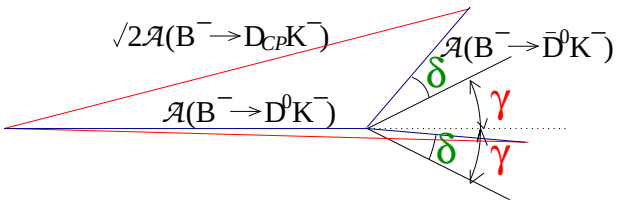

Fig. 68. Illustration of the sensitivity to γ that arises from the interference of $B^+ \to D^0 K^+$ and $B^+ \to \overline{D}^0 K^+$ decay amplitudes.

$$\mathcal{A}\left(B^- \to D_1 K^-\right) \propto \frac{1}{2}\left(1 + r_B e^{i(\delta_B - \gamma)}\right) \longrightarrow \tag{366}$$
$$\Gamma\left(B^- \to D_1 K^-\right) \propto 1 + r_B^2 + 2 r_B \cos\left(\delta_B - \gamma\right)$$
$$\mathcal{A}\left(B^- \to D_2 K^-\right) \propto \frac{1}{2}\left(1 - r_B e^{i(\delta_B - \gamma)}\right) \longrightarrow \tag{367}$$
$$\Gamma\left(B^- \to D_2 K^-\right) \propto 1 + r_B^2 - 2 r_B \cos\left(\delta_B - \gamma\right)$$
$$\mathcal{A}\left(B^+ \to D_1 K^+\right) \propto \frac{1}{2}\left(1 + r_B e^{i(\delta_B + \gamma)}\right) \longrightarrow \tag{368}$$
$$\Gamma\left(B^+ \to D_1 K^+\right) \propto 1 + r_B^2 + 2 r_B \cos\left(\delta_B + \gamma\right)$$
$$\mathcal{A}\left(B^+ \to D_2 K^+\right) \propto \frac{1}{2}\left(1 - r_B e^{i(\delta_B + \gamma)}\right) \longrightarrow \tag{369}$$
$$\Gamma\left(B^+ \to D_2 K^+\right) \propto 1 + r_B^2 - 2 r_B \cos\left(\delta_B + \gamma\right)$$

From the above expressions it is clear that CP violation effects will be enhanced for values of r_B close to unity. It can also be seen that measurements of rates (and rate asymmetries) alone yield information on $x_\pm = r_B \cos(\delta_B \pm \gamma)$. This leads to ambiguities in the extraction of γ. These can be resolved, and the overall precision improved, when information on $y_\pm = r_B \sin(\delta_B \pm \gamma)$ is obtained, as can be achieved from Dalitz plot analyses, for example.

To avoid relying on theoretical estimates of the hadronic parameters r_B and δ_B, these parameters must also be determined from the data. Once that is done, the underlying method has essentially zero theoretical uncertainty. The largest effects are due to charm mixing and possible CP violation effects in the D decays [1005]. However, once measured it is possible to take these effects into account in the analysis. Similarly, when decays of neutral B mesons are used, there is a potential systematic effect if the possible $B^0_{(s)}$–$\overline{B}^0_{(s)}$ width difference is neglected [1006, 1007].

As already mentioned above, many different decays in the "$B \to DK$" family can be used to gain sensitivity to γ. Not only charged but also neutral B decays can be used. Any decay of the neutral D meson that is accessible to both D^0 and $\overline{D}^0$ can be used. Furthermore decays with excited D and/or K states not only provide additional statistics. In the former case there is an effective strong phase difference of π between the cases that the D^* is reconstructed as $D\pi^0$ and $D\gamma$ that is particularly beneficial when D decays to doubly-Cabibbo-suppressed final states are analyzed [1008]. When K^* mesons are used, their natural width can be handled by the introduction of effective hadronic parameters [1009]; alternatively a Dalitz plot analysis of the $B \to DK\pi$ decay removes this problem and maximizes the sensitivity to γ [1010]. Ultimately it is clear that the

best sensitivity to γ will be obtained by combining as many statistically independent measurements as possible.

8.2. *Experimental results on γ from $B \to DK$ decays*

8.2.1. *GLW analyses*

The technique of measuring γ proposed by Gronau, London and Wyler (and called GLW) [998, 999] makes use of D^0 decays to *CP* eigenstates, such as K^+K^-, $\pi^+\pi^-$ (*CP*-even) or $K^0_S\pi^0$, $K^0_S\phi$ (*CP*-odd). Since both D^0 and $\bar{D}^0$ can decay into the same CP eigenstate (D_{CP}, or D_1 for a CP-even state and D_2 for a CP-odd state), the $b \to c$ and $b \to u$ processes shown in Fig. 67 interfere in the $B^\pm \to D_{CP}K^\pm$ decay channel. This interference may lead to direct CP violation. To measure D meson decays to CP eigenstates a large number of B meson decays is required since the branching fractions to these modes are of order 1%. To extract γ using the GLW method, the following observables sensitive to CP violation are used: the asymmetries

$$\begin{aligned} \mathcal{A}_{1,2} &\equiv \frac{\mathcal{B}(B^- \to D_{1,2}K^-) - \mathcal{B}(B^+ \to D_{1,2}K^+)}{\mathcal{B}(B^- \to D_{1,2}K^-) + \mathcal{B}(B^+ \to D_{1,2}K^+)} \\ &= \frac{2r_B \sin\delta' \sin\gamma}{1 + r_B^2 + 2r_B \cos\delta' \cos\gamma} \end{aligned} \tag{370}$$

and the double ratios

$$\begin{aligned} \mathcal{R}_{1,2} &\equiv \frac{\mathcal{B}(B^- \to D_{1,2}K^-) + \mathcal{B}(B^+ \to D_{1,2}K^+)}{\mathcal{B}(B^- \to D^0K^-) + \mathcal{B}(B^+ \to D^0K^+)} \\ &= 1 + r_B^2 + 2r_B \cos\delta' \cos\gamma, \end{aligned} \tag{371}$$

where

$$\delta' = \begin{cases} \delta_B & \text{for } D_1 \\ \delta_B + \pi & \text{for } D_2 \end{cases}, \tag{372}$$

and r_B and δ_B were defined in the previous section. The value of r_B is given by the ratio of the CKM matrix elements $|V^*_{ub}V_{cs}|/|V^*_{cb}V_{us}| \sim 0.38$ times a color suppression factor. Here we assume that mixing and CP violation in the neutral D meson system can be neglected.

Instead of four observables $\mathcal{R}_{1,2}$ and $\mathcal{A}_{1,2}$, only three of which are independent (since $\mathcal{A}_1\mathcal{R}_1 = -\mathcal{A}_2\mathcal{R}_2$), an alternative set of three parameters can be used:

$$x_\pm = r_B \cos(\delta_B \pm \gamma) = \frac{\mathcal{R}_1(1 \mp \mathcal{A}_1) - \mathcal{R}_2(1 \mp \mathcal{A}_2)}{4}, \tag{373}$$

and

$$r_B^2 = \frac{\mathcal{R}_1 + \mathcal{R}_2 - 2}{2}. \tag{374}$$

The use of these observables allows for a direct comparison with the methods involving analyses of the Dalitz plot distributions of multibody D^0 decays (see Sec. 8.2.3), where the same parameters $x_\pm$ are obtained.

Measurements of $B \to D_{\rm CP}K$ decays have been performed by both the BaBar [1011] and Belle [1012] collaborations, while CDF has recently made measurements using CP-even decays only [1013]. The most recent update is BaBar's analysis using a data sample

Table 58
Results of the GLW analysis by BaBar [1011].

$\mathcal{R}_1$	$1.06 \pm 0.10 \pm 0.05$
$\mathcal{R}_2$	$1.03 \pm 0.10 \pm 0.05$
$\mathcal{A}_1$	$+0.27 \pm 0.09 \pm 0.04$
$\mathcal{A}_2$	$-0.09 \pm 0.09 \pm 0.02$
x_+	$-0.09 \pm 0.05 \pm 0.02$
x_-	$+0.10 \pm 0.05 \pm 0.03$
r_B^2	$0.05 \pm 0.07 \pm 0.03$

of 382M $B\overline{B}$ pairs [1011]. The analysis uses D^0 decays to K^+K^- and $\pi^+\pi^-$ as CP-even modes, $K^0_S\pi^0$ and $K^0_S\omega$ as CP-odd modes.

The results of the analysis (both in terms of asymmetries and double ratios, and the alternative $x_\pm, r_B^2$ set of parameters) are shown in Tab. 58. As follows from (370) and (372), the signs of the $\mathcal{A}_1$ and $\mathcal{A}_2$ asymmetries should be opposite, which is confirmed by the experiment. The $x_\pm$ values are in good agreement with those obtained by the Dalitz plot analysis technique (see 8.2.3). Note that the measurement of $\mathcal{A}_1$ deviates from zero by 2.8 standard deviations.

A summary of measurements of observables with the GLW method is given in Fig. 69. As well as the results using $B \to D_{\rm CP}K$ decays, this compilation also includes measurements from the decay channels $B \to D^*_{\rm CP}K$ and $B \to D_{\rm CP}K^*$.

8.2.2. *ADS analyses*

The difficulties in the application of the GLW methods are primarily due to the small magnitude of the CP asymmetry of the $B^\pm \to D_{CP}K^\pm$ decay probabilities, which may lead to significant systematic uncertainties in the measurement of CP violation. An alternative approach was proposed by Atwood, Dunietz and Soni [1000, 1001]. Instead of using D^0 decays to CP eigenstates, the ADS method uses Cabibbo-favored and doubly Cabibbo-suppressed decays: $\overline{D}^0 \to K^-\pi^+$ and $D^0 \to K^-\pi^+$. In the decays $B^+ \to [K^-\pi^+]_D K^+$ and $B^- \to [K^+\pi^-]_D K^-$, the suppressed B decay corresponds to the Cabibbo-allowed D^0 decay, and vice versa. Therefore, the interfering amplitudes are of similar magnitudes, and one can expect significant CP asymmetry.

The observable that is measured in the ADS method is the fraction of the suppressed and allowed branching ratios:

$$\begin{aligned}\mathcal{R}_{ADS} &= \frac{\mathcal{B}(B^\pm \to [K^\mp\pi^\pm]_D K^\pm)}{\mathcal{B}(B^\pm \to [K^\pm\pi^\mp]_D K^\pm)} \\ &= r_B^2 + r_D^2 + 2r_B r_D \cos\gamma\cos\delta,\end{aligned} \tag{375}$$

where r_D is the ratio of the doubly Cabibbo-suppressed and Cabibbo-allowed D^0 decay amplitudes [560]:

$$r_D = \left|\frac{A(D^0 \to K^+\pi^-)}{A(D^0 \to K^-\pi^+)}\right| = 0.058 \pm 0.001, \tag{376}$$

and δ is the sum of strong phase differences in B and D decays: $\delta = \delta_B + \delta_D$. Once a significant signal is seen, the direct CP asymmetry must be measured,

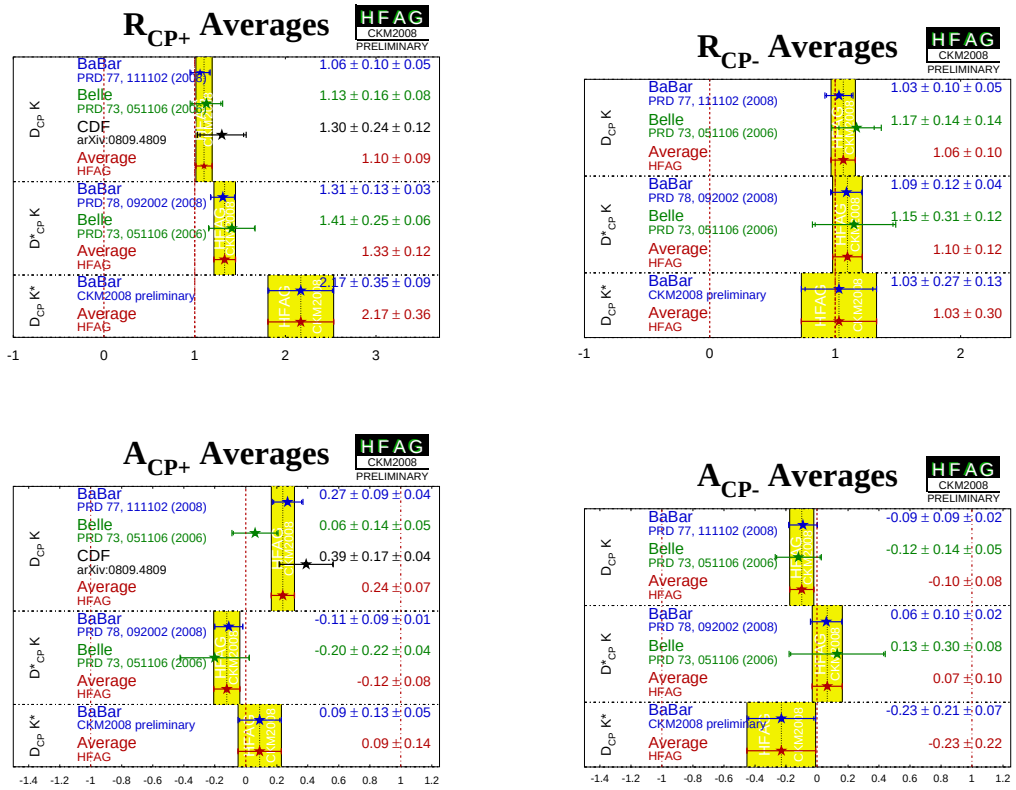

Fig. 69. Compilations and world averages of measurements of observables using the GLW method. Top left: $\mathcal{R}_1$; top right: $\mathcal{R}_2$; bottom left: $\mathcal{A}_1$; bottom right: $\mathcal{A}_2$.

$$\begin{aligned}\mathcal{A}_{ADS} &= \frac{\mathcal{B}(B^- \to [K^+\pi^-]_D K^-) - \mathcal{B}(B^+ \to [K^-\pi^+]_D K^+)}{\mathcal{B}(B^- \to [K^+\pi^-]_D K^-) + \mathcal{B}(B^+ \to [K^-\pi^+]_D K^+)} \\ &= \frac{2 r_B r_D \sin\gamma \sin\delta}{r_B^2 + r_D^2 + 2 r_B r_D \cos\gamma \cos\delta}.\end{aligned} \tag{377}$$

Studies of ADS channels have been performed by both BaBar [1014] and Belle [1015]. Unfortunately, the product branching ratios into the final states of interest are so small that they cannot be observed using the current experimental statistics. The most recent update of the ADS analysis is that from Belle using 657M $B\overline{B}$ pairs [1015]. The analysis uses $B^\pm \to DK^\pm$ decays with D^0 decaying to $K^+\pi^-$ and $K^-\pi^+$ modes (and their charge-conjugated partners). The ratio of suppressed and allowed modes is found to be

$$\mathcal{R}_{ADS} = (8.0^{+6.3+2.0}_{-5.7-2.8}) \times 10^{-3}. \tag{378}$$

Since the signal in the suppressed modes is not significant, the CP asymmetry is inevitably consistent with zero:

$$\mathcal{A}_{ADS} = -0.13^{+0.98}_{-0.88} \pm 0.26. \tag{379}$$

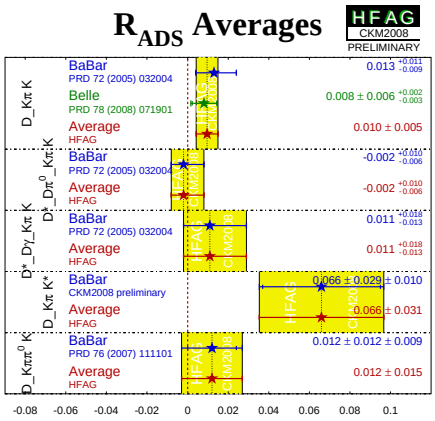

Fig. 70. Compilations and world averages of measurements of observables using the ADS method.

A summary of measurements of observables with the ADS method is given in Fig. 70. As well as the results using the decays $B \to DK$ with $D \to K\pi$, this compilation also includes measurements from the decay channels $B \to D^*K$ with $D \to K\pi$ and the decays $D^* \to D\pi^0$ and $D^* \to D\gamma$ treated distinctly [1008], $B \to DK^*$ with $D \to K\pi$ and $B \to DK$ with $D \to K\pi\pi^0$.

The ADS analysis currently does not give a significant constraint on γ, but it provides important information on the value of r_B. Using the conservative assumption $\cos\gamma\cos\delta = -1$ one obtains the upper limit $r_B < 0.19$ at 90% CL. A somewhat tighter constraint can be obtained by using the γ and δ_B measurements from the Dalitz plot analyses (see Sec. 8.2.3), and the recent CLEO-c measurement of the strong phase $\delta_D = (22^{+11+9}_{-12-11})^\circ$ [988, 1016].

8.2.3. *Dalitz plot analyses*

A Dalitz plot analysis of a three-body final state of the D meson allows one to obtain all the information required for determination of γ in a single decay mode. The use of a Dalitz plot analysis for the extraction of γ was first discussed in the context of the ADS method [1000,1001]. This technique uses the interference of Cabibbo-favored $D^0 \to K^-\pi^+\pi^0$ and doubly Cabibbo-suppressed $\overline{D}{}^0 \to K^-\pi^+\pi^0$ decays. However, the small rate for the doubly Cabibbo-suppressed decay limits the sensitivity of this technique.

Three body final states such as $K^0_S\pi^+\pi^-$ [257,1003] have been suggested as promising modes for the extraction of γ. Like in the GLW or ADS method, the two amplitudes interfere as the D^0 and $\overline{D}{}^0$ mesons decay into the same final state $K^0_S\pi^+\pi^-$; we denote the admixed state as $\tilde{D}_+$. Assuming no CP asymmetry in neutral D decays, the amplitude of the $\tilde{D}_+$ decay as a function of Dalitz plot variables $m^2_+ = m^2_{K^0_S\pi^+}$ and $m^2_- = m^2_{K^0_S\pi^-}$ is

$$f_{B^+} = f_D(m^2_+, m^2_-) + r_B e^{i(\delta_B+\gamma)} f_D(m^2_-, m^2_+)\,, \tag{380}$$

where $f_D(m^2_+, m^2_-)$ is the amplitude of the $\overline{D}{}^0 \to K^0_S\pi^+\pi^-$ decay.

Similarly, the amplitude of the $\tilde{D}_-$ decay from $B^- \to DK^-$ process is

$$f_{B^-} = f_D(m_-^2, m_+^2) + r_B e^{i(\delta_B - \gamma)} f_D(m_+^2, m_-^2)\,. \tag{381}$$

The $\overline{D}^0 \to K^0_S\pi^+\pi^-$ decay amplitude can be determined at the B factories from the large samples of flavor-tagged $\overline{D}^0 \to K^0_S\pi^+\pi^-$ decays produced in continuum e^+e^- annihilation. [In fact, only $|f_D|^2$ can be determined from flavor tagged data, but a model assumption can be made to describe the variation of the strong phase across the Dalitz plot. Approaches to avoid such model-dependence are discussed in more detail below.] Once f_D is known, a simultaneous fit of B^+ and B^- data allows the contributions of r_B, γ and δ_B to be separated. The method has only a two-fold ambiguity: the solutions at (γ, δ_B) and $(\gamma + 180^\circ, \delta_B + 180^\circ)$ cannot be distinguished. References [257] and [1017] give more detailed descriptions of the technique.

Both Belle and BaBar collaborations recently reported updates of their γ measurements using Dalitz plot analysis. The preliminary result from Belle [1018] uses a data sample of 657M $B\overline{B}$ pairs and two modes, $B^\pm \to DK^\pm$ and $B^\pm \to D^*K^\pm$ with $D^* \to D\pi^0$. The neutral D meson is reconstructed in the $K^0_S\pi^+\pi^-$ final state in both cases.

To determine the decay amplitude, $D^{*\pm}$ mesons produced via the $e^+e^- \to c\bar{c}$ continuum process are used, which then decay to a neutral D meson and a charged pion. The flavor of the neutral D meson is tagged by the charge of the pion in the decay $D^{*-} \to \overline{D}^0\pi^-$. B factories offer large sets of such charm data: 290.9×10^3 events are used in the Belle analysis with only 1.0% background.

The description of the $\overline{D}^0 \to K^0_S\pi^+\pi^-$ decay amplitude is based on the isobar model. The amplitude f_D is represented by a coherent sum of two-body decay amplitudes and one nonresonant decay amplitude. The model includes a set of 18 two-body amplitudes: five Cabibbo-allowed amplitudes: $K^*(892)^+\pi^-$, $K^*(1410)^+\pi^-$, $K^*_0(1430)^+\pi^-$, $K^*_2(1430)^+\pi^-$ and $K^*(1680)^+\pi^-$; their doubly Cabibbo-suppressed partners; eight amplitudes with K^0_S and a $\pi\pi$ resonance: $K^0_S\rho$, $K^0_S\omega$, $K^0_Sf_0(980)$, $K^0_Sf_2(1270)$, $K^0_Sf_0(1370)$, $K^0_S\rho(1450)$, $K^0_S\sigma_1$ and $K^0_S\sigma_2$; and a flat nonresonant term.

The selection of $B^\pm \to D^{(*)}K^\pm$ decays is based on the CM energy difference $\Delta E = \sum E_i - E_{\rm beam}$ and the beam-constrained B meson mass $M_{\rm bc} = \sqrt{E^2_{\rm beam} - (\sum \boldsymbol{p}_i)^2}$, where $E_{\rm beam}$ is the CM beam energy, and E_i and $\boldsymbol{p}_i$ are the CM energies and momenta of the B candidate decay products. To suppress background from $e^+e^- \to q\bar{q}$ ($q = u, d, s, c$) continuum events, variables that characterize the event shape are used. At the first stage of the analysis, when the $(M_{\rm bc}, \Delta E)$ distribution is fitted in order to obtain the fractions of the background components, a requirement on the event shape is imposed to suppress the continuum events. The number of such "clean" events is 756 for $B^\pm \to DK^\pm$ mode with 29% background, and 149 events for $B^\pm \to D^*K^\pm$ mode with 20% background. In the Dalitz plot fit, events are not rejected based on event shape variables, these are used in the likelihood function to better separate signal and background events.

The Dalitz distributions of the B^+ and B^- samples are fitted separately, using Cartesian parameters $x_\pm = r_\pm \cos(\delta_B \pm \gamma)$ and $y_\pm = r_\pm \sin(\delta_B \pm \gamma)$, where the indices "+" and "−" correspond to B^+ and B^- decays, respectively. In this approach the amplitude ratios (r_+ and r_-) are not constrained to be equal for the B^+ and B^- samples. Confidence intervals in r_B, γ and δ_B are then obtained from the $(x_\pm, y_\pm)$ using a frequentist technique.

The values of the parameters r_B, γ and δ_B obtained from the combination of $B^\pm \to DK^\pm$ and $B^\pm \to D^*K^\pm$ modes are presented in Tab. 59. Note that in addition to the detector-related systematic error which is caused by the uncertainties of the background

Table 59
Results of the combination of $B^+ \to DK^+$ and $B^+ \to D^*K^+$ modes by Belle [1018].

Parameter	1σ interval	2σ interval	Systematic error	Model uncertainty
ϕ_3	$76^\circ\ ^{+12^\circ}_{-13^\circ}$	$49^\circ < \phi_3 < 99^\circ$	4°	9°
r_{DK}	0.16 ± 0.04	$0.08 < r_{DK} < 0.24$	0.01	0.05
r_{D^*K}	0.21 ± 0.08	$0.05 < r_{D^*K} < 0.39$	0.02	0.05
δ_{DK}	$136^\circ\ ^{+14^\circ}_{-16^\circ}$	$100^\circ < \delta_{DK} < 163^\circ$	4°	23°
δ_{D^*K}	$343^\circ\ ^{+20^\circ}_{-22^\circ}$	$293^\circ < \delta_{DK} < 389^\circ$	4°	23°

Table 60
Signal yields of different modes used for Dalitz analysis by BaBar collaboration [260].

B decay	D decay	Yield
$B^\pm \to DK^\pm$	$\overline{D}^0 \to K^0_S\pi^+\pi^-$	600 ± 31
	$\overline{D}^0 \to K^0_S K^+K^-$	112 ± 13
$B^\pm \to [D\pi^0]_{D^*}K^\pm$	$\overline{D}^0 \to K^0_S\pi^+\pi^-$	133 ± 15
	$\overline{D}^0 \to K^0_S K^+K^-$	32 ± 7
$B^\pm \to [D\gamma]_{D^*}K^\pm$	$\overline{D}^0 \to K^0_S\pi^+\pi^-$	129 ± 16
	$\overline{D}^0 \to K^0_S K^+K^-$	21 ± 7
$B^\pm \to DK^{*\pm}$	$\overline{D}^0 \to K^0_S\pi^+\pi^-$	118 ± 18

description, imperfect simulation, *etc.*, the result suffers from the uncertainty of the D decay amplitude description. The statistical confidence level of CP violation for the combined result is $(1 - 5.5 \times 10^{-4})$, corresponding to 3.5 standard deviations.

In contrast to the Belle analysis, the BaBar analysis based on a data sample of 383M $B\overline{B}$ pairs [260] includes seven different decay modes: $B^\pm \to DK^\pm$, $B^\pm \to D^*K^\pm$ with $D^0 \to D\pi^0$ and $D\gamma$, and $B^\pm \to DK^{*\pm}$, where the neutral D meson is reconstructed in $K^0_S\pi^+\pi^-$ and $K^0_S K^+K^-$ (except for $B^\pm \to DK^{*\pm}$ mode) final states. The signal yields for these modes are shown in Tab. 60.

The differences from the Belle model of $\overline{D}^0 \to K^0_S\pi^+\pi^-$ decay are as follows: the K-matrix formalism [268,269,1019] is used to describe the $\pi\pi$ S-wave, while the $K\pi$ S-wave is parametrized using $K^*_0(1430)$ resonances and an effective range nonresonant component with a phase shift [1020]. The description of $\overline{D}^0 \to K^0_S K^+K^-$ decay amplitude uses an isobar model that includes eight two-body decays: $K^0_S a_0(980)^0$, $K^0_S\phi(1020)$, $K^0_S f_0(1370)$, $K^0_S f_2(1270)^0$, $K^0_S a_0(1450)^0$, $K^- a_0(980)^+$, $K^+ a_0(980)^-$, and $K^- a_0(1450)^+$.

The fit to signal samples is performed in a similar way to the Belle analysis, using an unbinned likelihood function that includes Dalitz plot variables and in addition B meson invariant mass and event-shape variables to better separate signal and background events. From the combination of all modes, BaBar obtains $\gamma = (76^{+23}_{-24} \pm 5 \pm 5)^\circ$ (mod 180°), where the first error is statistical, the second is experimental systematic, and the third is the D^0 model uncertainty. The values of the amplitude ratios are $r_B = 0.086 \pm 0.035 \pm 0.010 \pm 0.011$ for $B^\pm \to DK^\pm$, $r^*_B = 0.135 \pm 0.051 \pm 0.011 \pm 0.005$ for $B^\pm \to D^*K^\pm$, and $\kappa r_s = 0.163^{+0.088}_{-0.105} \pm 0.037 \pm 0.021$ for $B^\pm \to DK^{*\pm}$ (here κ accounts for possible nonresonant $B^\pm \to DK^0_S\pi^\pm$ contribution). The combined significance of direct CP violation is 99.7%, or 3.0 standard deviations.

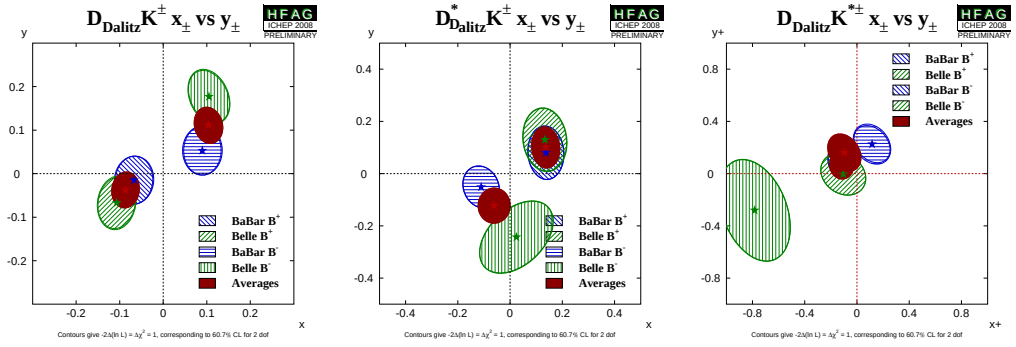

Fig. 71. World averages of measurements of observables in the Cartesian parametrization of the Dalitz method. Left: $(x_\pm, y_\pm)$ for $B \to DK$; (middle): $(x_\pm, y_\pm)$ for $B \to D^*K$ ($D^* \to D\pi^0$ and $D^* \to D\gamma$ combined); (right): $(x_\pm, y_\pm)$ for $B \to DK^*$. The Belle results use only $D \to K^0_S\pi^+\pi^-$, while the BaBar results include also $D \to K^0_S K^+K^-$. The averages do not include model uncertainities.

Summaries of measurements of observables with the Dalitz plot method are given in Figs. 71 and 72.

8.2.4. *Other techniques*

In decays of neutral B mesons to final states such as DK both amplitudes involving D^0 and $\overline{D}^0$ are color-suppressed. Consequently, the value of r_B is larger, with naïve estimates giving $r_B \sim 0.4$. In the decay $B^0 \to DK^*(892)^0$ the flavor of the B meson is tagged by the charge of the Kaon produced in the $K^*(892)^0$ decay ($K^+\pi^-$ or $K^-\pi^+$) [1021], so that a time-dependent analysis is not necessary.

Searches for doubly Cabibbo-suppressed decays have not yet yielded a significant signal, but allow limits to be put on r_B. The most recent results are from BaBar using a data sample of 465M $B\overline{B}$ pairs [1022]. BaBar has studied $D \to K\pi$, $D \to K\pi\pi^0$ and $D \to K\pi\pi\pi$, and has found $\mathcal{R}_{\rm ADS}(K\pi) < 0.244$ at the 95% confidence level. The results can be combined using external information from CLEO-c [988, 1016, 1023] to obtain $r_S \in [0.07, 0.41]$ at the 95% confidence level, where r_S is the equivalent of the parameter r_B modified due to the finite width of the K^{*0} resonance [1009].

BaBar have also performed a Dalitz plot analysis of the three-body decay $\overline{D}^0 \to K^0_S\pi^+\pi^-$ decay in $B^0 \to DK^*(892)^0$ [1024]. The technique, and the decay model are similar to that used for $B^\pm \to DK^{*\pm}$ decays (see Sec. 8.2.3). The analysis is based on 371M $B\overline{B}$ pairs, and yields the following constraints: $\gamma = (162 \pm 56)^\circ$, $r_B < 0.55$ with 90% CL.

It is also possible to measure γ by exploiting the interference between $b \to c$ and $\overline{b} \to \overline{u}$ decays that occurs due to B^0–$\overline{B}^0$ mixing using a time-dependent analysis. Since the interference occurs via oscillations, the mixing phase is also involved and the analysis is sensitive to the combination of angles $\sin(2\beta+\gamma)$. In this approach, the abundant decays such as $B \to D\pi$ and $B \to D^*\pi$ can be used; however the size of the CP violation effect depends on the magnitude of the ratio of the $b \to u$ over $b \to c$ amplitudes, usually denoted R, which is naïvely expected to take values $R \sim 0.02$ for these decays. Consequently these measurements are still statistics limited, as well as being potentially sensitive to systematics caused by any mismodelling of the large CP-conserving component. The sta-

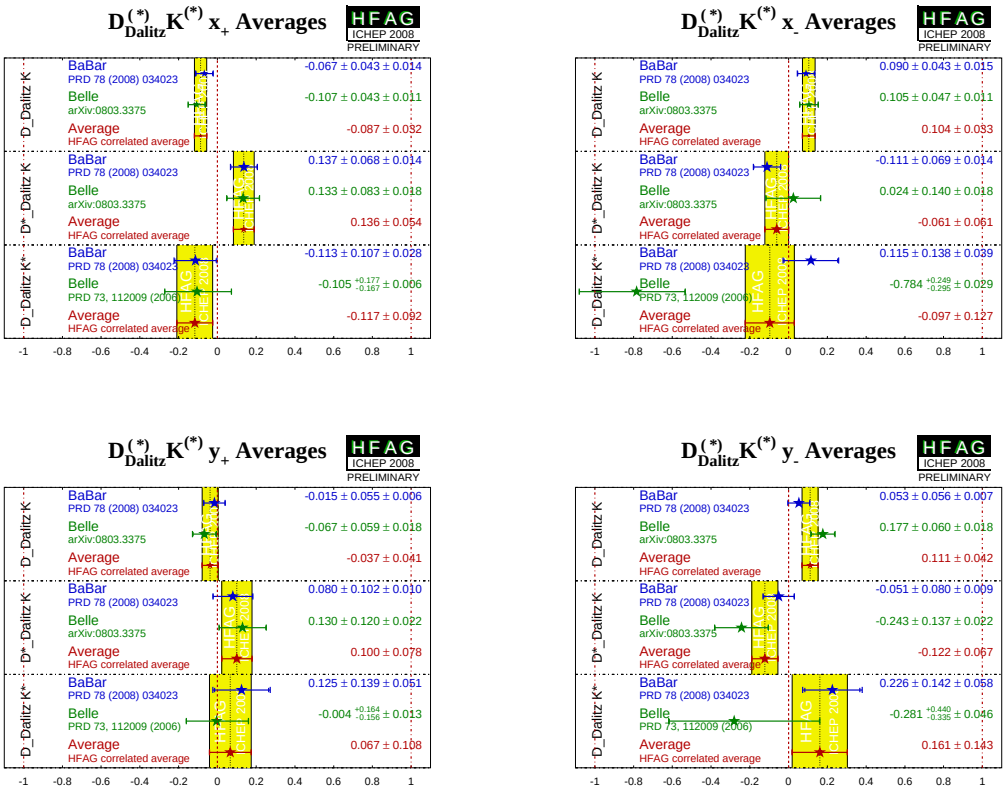

Fig. 72. World averages of measurements of observables in the Cartesian parametrization of the Dalitz method from HFAG [560]. Top left: x_+; top right: x_-; bottom left: y_+; bottom right: y_-. The data is described in the caption to Fig. 71.

tistical precision can be improved by using partial reconstruction for $B \to D^*\pi$ decays as well as the more conventional "full" reconstruction. A summary of measurements of these modes from BaBar [1025, 1026] and Belle [1027, 1028] is given in Fig. 73.

Another similar neutral B decay mode is $B^0 \to D^{\mp}K^0\pi^{\pm}$, where time-dependent Dalitz plot analysis is sensitive to $2\beta + \gamma$ [1029, 1030]. One advantage of this technique compared to the methods based on $B^0 \to D^{(*)}\pi$ decays is that, since both $b \to c$ and $b \to u$ diagrams involved in this decay are color-suppressed, the expected value of the ratio of their magnitudes R is larger. Secondly, $2\beta + \gamma$ is measured with only a two-fold ambiguity (compared to four-fold in $B^0 \to D^{(*)}\pi$ decays). In addition, all strong amplitudes and phases can be, in principle, measured in the same data sample.

The BaBar collaboration has performed the analysis based on 347M $B\overline{B}$ pairs data sample [1031]. The $B^0 \to D^{\mp}K^0\pi^{\pm}$ Dalitz plot is found to be dominated by $B^0 \to D^{**0}K^0_S$ (both $b \to u$ and $b \to c$ transitions) and $B^0 \to D^-K^{*+}$ ($b \to c$ only) states. From an unbinned maximum likelihood fit to the time-dependent Dalitz distribution, the value of $2\beta + \gamma$ as a function of R is obtained. The value of R cannot be determined with the current data sample, therefore, the value $R = 0.3$ is used, and its uncertainty is taken

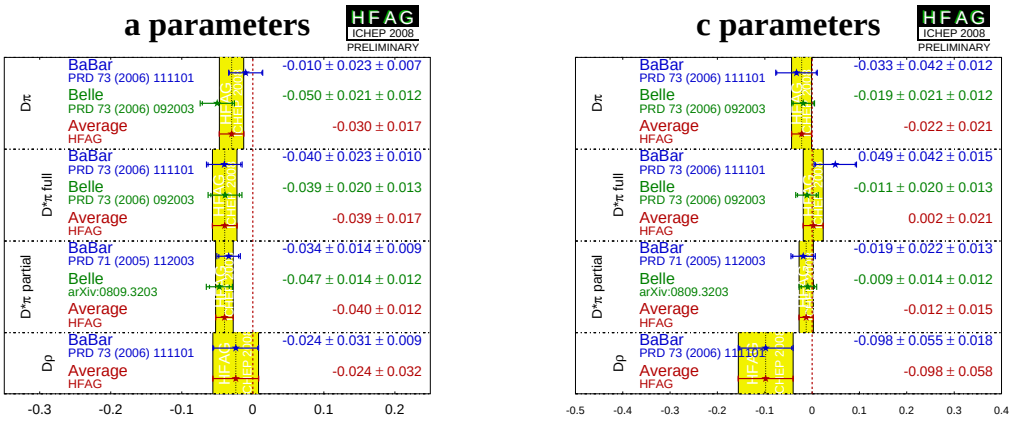

Fig. 73. Measurements of observables in $B \to D\pi$ and similar final states. The parameters used in these compilations are $a = (-1)^{L+1} 2R \sin(2\beta+\gamma)\cos(\delta)$ and $c = (-1)^{L+1} 2R \cos(2\beta+\gamma)\sin(\delta)$, where L is the angular momentum in the decay ($+1$ for $D\pi$ and -1 for $D^*\pi$ and $D\rho$), R is the magnitude of the ratio of the $\overline{b} \to \overline{u}$ and $b \to c$ amplitudes and δ is their relative phase.

into account in the systematic error. This results in the value $2\beta+\gamma = (83 \pm 53 \pm 20)^\circ$ or $(263 \pm 53 \pm 20)^\circ$.

8.3. *Outlook on the γ measurement*

The world average values that include the latest measurements presented in 2008 are reported in Sec. 10.

For an evaluation of the prospect of γ measurement, it is essential to note the fact that for the first time the value of r_B is shown to be significantly non-zero. In previous measurements, poor constraints on r_B caused significantly non-gaussian errors for γ, and made it difficult to predict the future sensitivity of this parameter. Now that r_B is constrained to be of the order 0.1, one can confidently extrapolate the current precision to future measurements at LHCb and Super-B facilities.

The γ precision is mainly dominated by Dalitz analyses. These analyses currently suffer from a hard-to-control uncertainty due to the D^0 decay amplitude description, which is estimated to be 5–10°. At the current level of statistical precision this error starts to influence the total γ uncertainty. A solution to this problem can be the use of quantum-correlated $D\overline{D}$ decays at $\psi(3770)$ resonance available currently at CLEO-c experiment, where the missing information about the strong phase in D^0 decay can be obtained experimentally.

8.3.1. *Model-independent Method*

Giri *et al.* proposed [257] a model-independent procedure for obtaining γ, as follows. The Dalitz plot is divided into $2\mathcal{N}$ bins, symmetrically about the line $m_+^2 = m_-^2$. The bins are indexed from $-i$ to i, excluding zero. The coordinate transformation $m_+^2 \leftrightarrow m_-^2$ thus corresponds to the exchange of bins $i \leftrightarrow -i$. The number of events in the i-th bin

of a flavor-tagged D^0 decay $K^0_S\pi^+\pi^-$ Dalitz plot is then expressed as:

$$K_i = A_D \int_i |f_D(m^2_+, m^2_-)|^2 dm^2_+ dm^2_- = A_D F_i, \tag{382}$$

where A_D is a normalization factor. The coefficients K_i can be obtained precisely from a very large sample of D^0 decays reconstructed in flavor eigenstate, which is accessible at B-factories, for example. The interference between the D^0 and $\bar{D}^0$ amplitudes is parametrized by the quantities c_i and s_i:

$$c_i \equiv \frac{1}{\sqrt{F_i F_{-i}}} \int_i |f_D(m^2_+, m^2_-)||f_D(m^2_-, m^2_+)| \cos[\Delta\delta_D(m^2_+, m^2_-)] dm^2_+ dm^2_-, \tag{383}$$

$$s_i \equiv \frac{1}{\sqrt{F_i F_{-i}}} \int_i |f_D(m^2_+, m^2_-)||f_D(m^2_+, m^2_-)| \sin[\Delta\delta_D(m^2_+, m^2_-)] dm^2_+ dm^2_-, \tag{384}$$

where the integral is performed over a single bin. The quantities c_i and s_i are the amplitude-weighted averages of $\cos\Delta\delta_D$ and $\sin\Delta\delta_D$ over each Dalitz-plot bin. The expected number of events in the bins of the Dalitz plot of the D decay from $B^\pm \to DK^\pm$ is

$$\langle N_i \rangle = A_B[K_i + r^2_B K_{-i} + 2\sqrt{K_i K_{-i}}(x_\pm c_i + y \pm s_i)], \tag{385}$$

where A_B is the normalization constant. As soon as the c_i and s_i coefficients are known, one can obtain $x_\pm$ and $y_\pm$ values (and hence γ and other related quantities) by a maximum likelihood fit using equation (385). In principle, c_i and s_i can be left as free parameters in a $\bar{D}^0 \to K^0_S\pi^+\pi^-$ Dalitz-plot analysis from $B^\pm$ decays. However, it has been shown [1032] that almost infinite statistics of B decays is necessary in that case.

It is important to note that c_i and s_i depend only on the D^0 decay, not the B decay, and therefore these quantities can be measured using the quantum-correlated $D\overline{D}$ decays of the $\psi(3770)$ resonance. For example, the expected number of events in a bin of the Dalitz plot of D_{CP} tagged decays equals

$$\langle M_i \rangle^\pm = A^\pm_{CP}[K_i + K_{-i} \pm 2\sqrt{K_i K_{-i}} c_i], \tag{386}$$

where the $\pm$ indicates whether the CP tag is CP-even or CP-odd. This relation can be used to obtain the c_i coefficients, but obtaining s_i remains a problem. If the binning is fine enough, so that both the phase difference $\Delta\delta_D$ and the amplitude $|f_D|$ remain constant across the area of each bin, the expressions (383,384) reduce to $c_i = \cos(\Delta\delta_D)$ and $s_i = \sin(\Delta\delta_D)$. The s_i coefficients can be obtained as $s_i = \pm\sqrt{1 - c^2_i}$. Using this equality if the amplitude varies across a bin will lead to bias in the $x_\pm, y_\pm$ fit results. Since c_i is obtained directly, and the absolute value of s_i is overestimated, the bias will mainly affect $y_\pm$ determination, resulting in lower absolute values of $y_\pm$.

A unique possibility to find s_i independent of c_i is available in a sample where both D mesons from the $\psi(3770)$ decay into the $K^0_S\pi^+\pi^-$ state [1033]. Since the $\psi(3770)$ is a vector, the two D mesons are produced in a P-wave, and the wave function of the two mesons is antisymmetric. Then the four-dimensional density of the two correlated Dalitz plots is given by:

$$\begin{aligned}\langle M \rangle_{ij} = A_{\rm corr}[&K_i K_{-j} + K_{-i} K_j - \\ &2\sqrt{K_i K_{-i} K_j K_{-j}}(c_i c_j + s_i s_j)].\end{aligned} \tag{387}$$

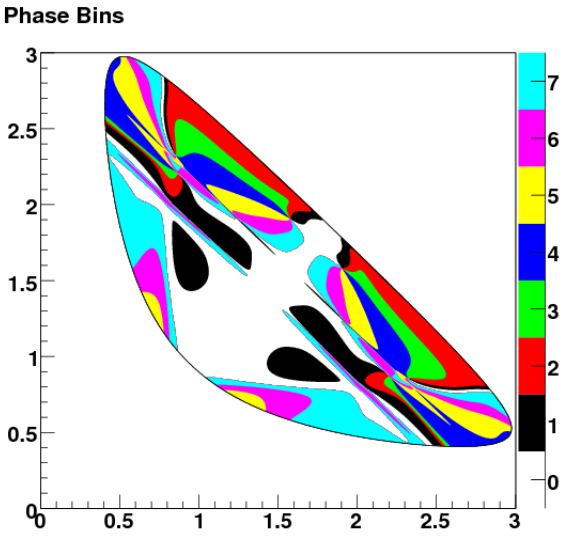

Fig. 74. Phase binning of the $D^0 \to \bar{K}^0_S \pi^+ \pi^-$ Dalitz plot.

The indices i, j correspond to the two D mesons from $\psi(3770)$ decay. This decay is sensitive to both c_i and s_i for the price of having to deal with the four-dimensional phase space.

The original idea of Giri *et al.* was to divide the Dalitz plot into square bins [257]. In case of limited statistics unavoidably the number of the bins could be relatively small. Consequently, a large loss of sensitivity can be expected due to variation of amplitude and phase over the bin. Bondar *et al.* noted [1033] that increased sensitivity can be obtained if the bins are chosen to minimize the variation in $\Delta\delta_D$ over each bin. One can divide the Dalitz phase space into $\mathcal{N}$ bins of equal size with respect to $\Delta\delta_D$ as predicted, for example, by the BaBar isobar model [260]. In the half of the Dalitz plot $m^2_+ < m^2_-$, the i^{th} bin is defined by the condition

$$2\pi(i - 3/2)/\mathcal{N} < \Delta\delta_D(m^2_+, m^2_-) < 2\pi(i - 1/2)/\mathcal{N}, \tag{388}$$

The $-i^{th}$ bin is defined symmetrically in the lower portion of the Dalitz plot. Such a binning with $\mathcal{N} = 8$ is shown in Fig. 74. One might suspect that, since we are using a model to determine our bins, we are not free of model dependence. In fact *any* binning is acceptable in that it will give a correct, unbiased answer for γ, at the cost of larger uncertainties compared to an optimal binning with respect to $\Delta\delta_D$.

Using 818 pb^{-1} of e^+e^- collisions produced at the $\psi(3770)$, the CLEO-c collaboration has made a first determination [1034] of the strong phase parameters, c_i and s_i, which are listed in Tab. 61. From a toy Monte Carlo study with a large sample of $B^\pm \to \tilde{D}^0 K^\pm$ data generated with $\gamma = 60°$, $\delta_B = 130°$ and $r_B = 0.1$, CLEO found that the decay model uncertainty on γ is reduced to about 1.7° due to these new measurements. As a result, the precision of the γ measurement using $B^+ \to \tilde{D}^0 K^+$ decays will not be limited by model-dependent assumptions on strong phase behavior in the $\tilde{D}^0 \to K^0_S \pi^+ \pi^-$ decay.

Table 61
Fit results for c_i and s_i. The first error is statistical, the second error is the systematic uncertainty, the third error is the model uncertainty due to including $K^0_L\pi^+\pi^-$ events in the analysis.

i	c_i	s_i
0	$0.743 \pm 0.037 \pm 0.022 \pm 0.013$	$0.014 \pm 0.160 \pm 0.077 \pm 0.045$
1	$0.611 \pm 0.071 \pm 0.037 \pm 0.009$	$0.014 \pm 0.215 \pm 0.055 \pm 0.017$
2	$0.059 \pm 0.063 \pm 0.031 \pm 0.057$	$0.609 \pm 0.190 \pm 0.076 \pm 0.037$
3	$-0.495 \pm 0.101 \pm 0.052 \pm 0.045$	$0.151 \pm 0.217 \pm 0.069 \pm 0.048$
4	$-0.911 \pm 0.049 \pm 0.032 \pm 0.021$	$-0.050 \pm 0.183 \pm 0.045 \pm 0.036$
5	$-0.736 \pm 0.066 \pm 0.030 \pm 0.018$	$-0.340 \pm 0.187 \pm 0.052 \pm 0.047$
6	$0.157 \pm 0.074 \pm 0.042 \pm 0.051$	$-0.827 \pm 0.185 \pm 0.060 \pm 0.036$
7	$0.403 \pm 0.046 \pm 0.021 \pm 0.002$	$-0.409 \pm 0.158 \pm 0.050 \pm 0.002$

8.3.2. *Prospects for LHCb*

The measurement of the CKM angle γ in tree dominated processes is one of the principal goals of LHCb. Extensive simulation studies have been conducted in a variety of channels. The results summarized here derive from [1035] and references therein.

LHCb will measure γ in tree dominated processes using two main approaches:

(i) **Time-dependent measurements** The extraction of γ has been studied using both $B^0 \to D^{\mp}\pi^{\pm}$ and $B_s \to D_s^{\mp}K^{\pm}$. Although the CP-asymmetries in these modes involve a contribution arising from the mixing diagram, this contribution can be subtracted using the result from complementary measurements in other processes, allowing for a pure tree-level γ determination.

(ii) $\boldsymbol{B \to DK}$ **strategies** The modes that have so far been investigated which have significant weight in the γ measurement include $B^{\mp} \to DK^{\mp}$, with the neutral D reconstructed in the K^+K^-, $\pi^+\pi^-$, $K^{\mp}\pi^{\pm}$, $K^{\mp}\pi^{\pm}\pi^+\pi^-$ and $K^0_S\pi^+\pi^-$ final states, and $B^0 \to D(K^{\pm}\pi^{\pm}, K^+K^-, \pi^+\pi^-)K^{*0}(K^-\pi^+)$ (+c.c.). The fact that no initial-state flavor tagging is required means that the relative sensitivity of the $B \to DK$ method is particularly high at LHCb compared with time-dependent measurements, in which the tagging power is in general lower than is the case at $\Upsilon(4S)$ experiments.

The expected yields in 2 fb^{-1} of data taking in these channels are given in Tab. 62. Note that the goal of the baseline LHCb experiment is to accumulate around 10 fb^{-1} of integrated luminosity. In all modes the selection benefits from the good performance of the $\pi - K$ separation provided by the LHCb RICH system.

The physics processes underlying the event rates and kinematic distributions in the $B \to DK$ channels have many parameters in common. This means that the observables for these channels may be combined in a global fit to achieve the best possible sensitivity to these parameters, most notably γ itself. The power of such a fit has been investigated in a toy Monte Carlo study, taking as input the expected sensitivities on the observables arising from the full simulation. For the two and four body D decay modes the observables are the event rates in each mode; for the $D \to K^0_S\pi^+\pi^-$ decay they are the populations of bins in Dalitz space, as defined by the expected strong-phase difference.

Table 62
Summary of expected LHCb signal and background yields for 2 fb^{-1}. In those rows where more than one channel is specified (eg. $B^{\pm} \to D(K^{\pm}\pi^{\mp})K^{\pm}$ or $B^{+} \to D(K^{+}K^{-} + \pi^{+}\pi^{-})K^{+}$), the yields correspond to the *sum* over all indicated modes. The physics parameters assumed in calculating these numbers can be found in [1035].

Channel	Signal	Background
$B^{\pm} \to D(K^{\pm}\pi^{\mp})K^{\pm}$	56k	35k
$B^{+} \to D(K^{-}\pi^{+})K^{+}$	680	780
$B^{-} \to D(K^{+}\pi^{-})K^{-}$	400	780
$B^{+} \to D(K^{+}K^{-} + \pi^{+}\pi^{-})K^{+}$	3.3k	7.2k
$B^{-} \to D(K^{+}K^{-} + \pi^{+}\pi^{-})K^{-}$	4.4k	7.2k
$B^{\pm} \to D(K^{\pm}\pi^{\mp}\pi^{+}\pi^{-})K^{\pm}$	61k	40k
$B^{+} \to D(K^{-}\pi^{+}\pi^{+}\pi^{-})K^{+}$	470	1.2k
$B^{-} \to D(K^{+}\pi^{-}\pi^{+}\pi^{-})K^{-}$	350	1.2k
$B^{0} \to D(K^{+}\pi^{-})K^{*0}$, $\bar{B^{0}} \to D(K^{-}\pi^{+})\bar{K}^{*0}$	3.4k	1.7k
$B^{0} \to D(K^{-}\pi^{+})K^{*0}$	350	850
$\bar{B^{0}} \to D(K^{+}\pi^{-})\bar{K}^{*0}$	230	850
$B^{0} \to D(K^{+}K^{-} + \pi^{+}\pi^{-})K^{*0}$	150	500
$\bar{B^{0}} \to D(K^{+}K^{-} + \pi^{+}\pi^{-})\bar{K}^{*0}$	550	500
$B^{\pm} \to D(K^{0}_{S}\pi^{+}\pi^{-})K^{\pm}$	5k	4.7k
$B_s, \bar{B}_s \to D_s^{\mp}K^{\pm}$	6.2k	4.3k
$B^{0}, \bar{B^{0}} \to D^{\mp}\pi^{\pm}$	1,300k	290k

Important components of this fit are the external constraints which come from the D decay properties from the quantum-correlated measurements at CLEO-c. These are the measured strong phase difference in $D \to K\pi$ decays [988, 1016], the measured coherence factor [1036] and average strong phase difference in $D \to K\pi\pi\pi$ decays [1023], and the expected sensitivity on the cosine and sine of the strong phase differences in the $D \to K^{0}_{S}\pi^{+}\pi^{-}$ Dalitz plot bins [1034]. [24] The results of this fit have a dependence on the assumed values of the physics parameters; the least well known of these is δ_{B^0}, the strong phase difference between the interfering diagrams in $B^{0} \to DK^{*0}$ decays, and so in Tab. 63 the expected sensitivity on γ is shown as a function of this phase. The CLEO-c inputs allow for a significant improvement on the overall precision.

The results from the global $B \to DK$ fit may be combined with the expected uncertainty on γ from the time-dependent measurements, the most important of which is the analysis of $B_s \to D_s^{\mp}K^{\pm}$ decays. The expected precision on γ from all of these measurements is shown in Tab. 64. It can be seen that with the modes under consideration a sensitivity of $2 - 3^{\circ}$ is expected in the lifetime of the experiment.

[24] Note that the results shown here take as input preliminary estimates of the CLEO-c sensitivity to the D-meson decay properties for both $D \to K\pi\pi\pi$ and $D \to K^{0}_{S}\pi^{+}\pi^{-}$.

Table 63
Expected LHCb sensitivity to γ from $B \to DK$ strategies for data sets corresponding to integrated luminosities of 0.5, 2 and 10 fb^{-1}, with and without CLEO-c constraints.

δ_{B^0} (°)	0	45	90	135	180
0.5 fb^{-1}					
σ_γ without CLEO-c constraints (°)	11.5	12.9	13.1	12.5	9.7
σ_γ with CLEO-c constraints (°)	9.0	12.0	10.7	11.1	8.6
2 fb^{-1}					
σ_γ without CLEO-c constraints (°)	5.8	8.3	7.8	8.4	5.0
σ_γ with CLEO-c constraints (°)	4.6	6.1	5.7	6.0	4.3
10 fb^{-1}					
σ_γ without CLEO-c constraints (°)	2.6	5.4	3.5	4.8	2.4
σ_γ with CLEO-c constraints (°)	2.3	3.5	2.9	3.2	2.2

Table 64
Expected LHCb combined sensitivity to γ from $B \to DK$ and time-dependent measurements for data sets corresponding to integrated luminosities of 0.5, 2 and 10 fb^{-1}.

δ_{B^0} (°)	0	45	90	135	180
σ_γ for 0.5 fb^{-1} (°)	8.1	10.1	9.3	9.5	7.8
σ_γ for 2 fb^{-1} (°)	4.1	5.1	4.8	5.1	3.9
σ_γ for 10 fb^{-1} (°)	2.0	2.7	2.4	2.6	1.9

9. Measurements of the angles of the unitarity triangle in charmless hadronic B decays

9.1. *Theory estimates for hadronic amplitudes*

9.1.1. *Angles, physical amplitudes, topological amplitudes*

Any standard-model (SM) amplitude for a decay $B \to f$ can be written, by integrating out the weak interactions to lowest order in G_F (Sec. 2.1), as a linear combination

$$\mathcal{A}(B \to f) = \sum_{i,U} C_i V_{UD} V_{Ub}^* \langle f|Q_i|B\rangle \tag{389}$$

of matrix elements of local operators Q_i in QCD × QED. Here $D = d, s$ and $U = u, c, t$. By CKM unitarity, one term in the sum over U can be removed. This gives a decomposition into (physical) tree and penguin amplitudes (the names are motivated by Wick contractions of the operators Q_i contributing to them),

$$\begin{aligned}\mathcal{A}(B \to f) &= T_f e^{i\theta_T} + P_f e^{i\theta_P},\\ \mathcal{A}(\overline{B} \to f) &= T_f e^{-i\theta_T} + P_f e^{-i\theta_P},\end{aligned} \tag{390}$$

where T_f and P_f ("strong amplitudes") and θ_T and θ_P ("weak phases") have definite CP transformation properties. For decays into two light mesons, conventionally $U = c$

(or $U = t$) is eliminated, giving $\theta_P = \beta$ ($\theta_P = 0$), and $\theta_T = \gamma$. For decays involving charmonium, the tree is associated with $U = c$ ($\theta_T = 0$), and one of $U = u, t$ is eliminated (both are expected to be negligible). The prototypical angle measurement derives from the time-dependent CP asymmetry

$$A_{\rm CP}(f;t) \equiv \frac{\Gamma(\overline{B}(t) \to f) - \Gamma(B(t) \to f)}{\Gamma(\overline{B}(t) \to f) + \Gamma(B(t) \to f)} \equiv -C_f \cos\Delta m\, t + S_f \sin\Delta m\, t, \qquad (391)$$

where f is a CP eigenstate of eigenvalue $\eta_{\rm CP}(f)$, Δm is the absolute value of the mass difference between the two mass eigenstates in the B^0–$\overline{B}^0$ system, and

$$C_f = \frac{1-|\xi|^2}{1+|\xi|^2}, \qquad S_f = \frac{2{\rm Im}\xi}{1+|\xi|^2}, \qquad \xi = e^{-i2\beta}\frac{\mathcal{A}(\bar{B} \to f)}{\mathcal{A}(B \to f)}. \qquad (392)$$

(We assume CPT conservation, and neglect lifetime differences and CP violation in mixing throughout.) If P_f can be neglected, $|\xi| = 1$, $C_f = 0$, and S_f gives a clean measurement of $\sin 2(\beta + \theta_T)$. This is true to very good approximation for decays into final states containing charmonium such as $B \to J/\psi K_S$ ($\theta_T = 0$, $-\eta_{\rm CP}(f)S_f = \sin 2\beta$). It holds less accurately for $b \to d$ transitions like $B \to (\pi^+\pi^-, \rho^+\pi^-, \rho^+\rho^-)$, where the CKM hierarchy is $[P_f/T_f]_{\rm CKM} = \mathcal{O}(1)$, but some suppression of penguin amplitudes follows from theoretical arguments reviewed below. In these modes, one has approximately $-\eta_{\rm CP}(f)S_f \approx \sin 2(\beta+\gamma) = -\sin 2\alpha$. Conversely, penguin-dominated $b \to s$ modes $B \to (\pi K, \phi K, \eta^{(\prime)}K, \dots)$, where $[T_f/P_f]_{\rm CKM} = \mathcal{O}(\lambda^2)$, probe $\sin 2\beta$.

In view of these considerations, it is clear that the interpretation of the time-dependent CP asymmetries (and more generally, the many charmless B and $\overline{B}$ decay rates) in terms of CKM parameters and possible new-physics contributions requires some information on at least the amplitude ratios P/T, hence on the hadronic matrix elements $\langle f|Q_i|B\rangle$. In principle, the latter are determined by the QCD and electromagnetic coupling and quark masses via (for the case of a two-particle final state) four-point correlation functions involving three operators destroying the B-meson and creating the final-state mesons, as well as one insertion of the operator Q_i. Formally, they are expressible in terms of a path integral

$$\langle M_1 M_2|Q_i|B\rangle \sim \int dA \int d\bar{\psi}\, d\psi\, j_B^\mu(x) j_{M_1}^\nu(y) j_{M_2}^\rho(z) Q_i(w) e^{i(S_{QCD}+Q_{ED})}. \qquad (393)$$

The currents j_B, j_{M_1}, j_{M_2} must have the correct quantum numbers to create/destroy the initial- and final-state particles, for instance $j_B^\mu = \bar{b}\gamma^\mu\gamma_5 d$ for a B^0 decay, but are otherwise arbitrary. In practice, this path integral cannot be evaluated; however, the inner (fermionic) path integral can be represented as a sum of Wick contractions which provide a nonperturbative definition of "topological" amplitudes (Fig. 75). We stress that no expansion of any kind has been made; the lines represent the full inverse Dirac operators, rather than perturbative ("free") propagators, averaged over arbitrary gluon backgrounds by the outer (gluonic) path integral. A complete list has been given in [1037]. Topological amplitudes can also be defined equivalently (and were originally) as matrix elements of the $SU(3)$ decomposition of the weak Hamiltonian [1038, 1039].

Each physical amplitude decomposes into several topological ones. For a tree, in the notation of [1040],

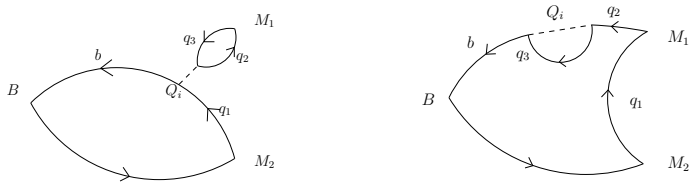

Fig. 75. Examples of Wick contractions. Left: Tree contraction. Right: Penguin contraction. The scheme-independent topological amplitudes correspond to certain sums of contractions of several operators in the weak Hamiltonian. The lines are "dressed" propagators, depending on the gluonic background. Arbitrarily many gluons not shown. From [1037].

$$\begin{aligned} T_{M_1M_2} = |V_{ub}V_{uD}|[&A_{M_1M_2}(\alpha_1(M_1M_2) + \alpha_2(M_1M_2) + \alpha_4^u(M_1M_2)) \\ &+B_{M_1M_2}(b_1(M_1M_2) + b_2(M_1M_2) + b_3^u(M_1M_2) + b_4^u(M_1M_2)) \\ &+\mathcal{O}(\alpha)] \ + (M_1 \leftrightarrow M_2) \ . \end{aligned} \tag{394}$$

The first two terms on the first line are known as the color-allowed and color-suppressed trees, while the third term is due to a set of penguin contractions. The terms on the second lines are due to annihilation topologies, where both fields in the current j_B are contracted with the weak vertex. We have not spelled out $\mathcal{O}(\alpha)$ terms, which include the electroweak penguin terms, as well as long-distance QED effects. [25] Not all topological amplitudes are present for every final state. [26] On the other hand, if both $a_i(M_1M_2)$ and $a_i(M_2M_1)$ are present, they must be summed. For instance [1040],

$$\begin{aligned} T_{\pi^0\rho^0} = \frac{i}{2}|V_{ub}V_{ud}|\frac{G_F}{\sqrt{2}}m_B^2\Bigg[&f_+^{B\pi}(0)f_\rho(\alpha_2(\pi^0\rho^0) - \alpha_4^u(\pi^0\rho^0)) - f_Bf_\pi f_\rho b_1(\pi^0\rho^0) \\ &+A_0^{B\rho}(0)f_\pi(\alpha_2(\rho^0\pi^0) - \alpha_4^u(\rho^0\pi^0)) - f_Bf_\pi f_\rho b_1(\rho^0\pi^0) + \mathcal{O}(\alpha)\Bigg], \end{aligned} \tag{395}$$

where we have also spelled out the normalization factors $A_{M_1M_2}$, which like $B_{M_1M_2}$ consists of form factors, decay constants, G_F, etc. as a convention (and in anticipation of the heavy-quark expansion), neglecting terms $\mathcal{O}(m_\pi/m_B, m_\rho/m_B)$. Moreover, for flavor-singlet mesons M_1 or M_2 there are additional amplitudes.

Similarly, for a penguin, we have the decomposition

$$\begin{aligned} P_{M_1M_1} = |V_{cb}V_{cD}|[&A_{M_1M_2}\alpha_4^c(M_1M_2) + B_{M_1M_2}(b_3^c(M_1M_2) + b_4^c(M_1M_2))] \\ &+(M_1 \leftrightarrow M_2) \ . \end{aligned} \tag{396}$$

The parametrization are general, but we have now fixed a convention where $V_{tb}^*V_{tD}$ has been eliminated.

Present theoretical knowledge on the topological amplitudes derives from expansions (i) in the Wolfenstein parameter λ (see above discussion), (ii) around the $SU(3)$ flavor symmetry limit (i.e., in m_s/Λ), (iii) in the inverse number of colors $1/N_c$, and (iv) the heavy-quark expansion in Λ/m_b and α_s, where $\Lambda \equiv \Lambda_{\rm QCD}$ is the QCD scale parameter. The counting for the various topological amplitudes is shown in Tab. 65. The λ and

[25] These effects include emissions of soft photons from the final-state particles [1041] and are modeled in extracting the two-body rates and asymmetries (which are not infrared safe if soft photons are included) from data.

[26] More precisely, one would write $\alpha_i(M_1M_2) \to c_i(M_1M_2)\alpha_i(M_1M_2)$ where $c_i(M_1M_2) = 0$ if the amplitude is not present and a Clebsch-Gordan coefficient otherwise [1040].

Table 65
Hierarchies among topological amplitudes from expansions in the Cabibbo angle λ, in $1/N_c$, and in $\Lambda_{\rm QCD}/m_b$. Some multiply suppressed amplitudes (e.g. EW penguin amplitudes that are CKM suppressed in $b \to s$ transitions) are omitted.

	T/a_1	C/a_2	P_{ut}/α_4^u	P_{ct}/α_4^c	P_{EW}/α_{3EW}	P_{EW}^C/α_{4EW}	b_3^c	b_4^c	E/b_1	A/b_2
Cabibbo ($b \to d$)	all amplitudes are $\mathcal{O}(\lambda^3)$									
Cabibbo ($b \to s$)	λ^4	λ^4	λ^4	λ^2	λ^2	λ^2	λ^2	λ^2	λ^4	λ^4
$1/N$	1	$\frac{1}{N}$	$\frac{1}{N}$	$\frac{1}{N}$	1	$\frac{1}{N}$	$\frac{1}{N}$	$\frac{1}{N}$	$\frac{1}{N}$	1
Λ/m_b	1	1	1	1	1	1	Λ/m_b	Λ/m_b	Λ/m_b	Λ/m_b

$1/N_c$ counting provide only (rough) hierarchies. Existing $SU(3)$ analyses work at zeroth order, providing relations between topological amplitudes for different final states. (In the case of $\pi^+\pi^-$, $\rho^+\rho^-$, isospin alone provides useful relations. This is the basis for the α determinations reviewed in Sec. 9.3 below.) The virtue is the possibility to completely eliminate some of the theoretically difficult amplitudes from the analysis, removing the need for their theoretical computation. This comes of the expense of eliminating some of the experimental information that is in principle sensitive to short-distance physics (SM and beyond) from the analysis, as well. For instance, in the α determinations, six observables are needed to determine one parameter.

Both the $1/N_c$ expansion and the heavy-quark expansion rely on an expansion in Feynman diagrams. The virtue of the heavy-quark expansion is that, to lowest order in the expansion parameter Λ/m_b, and in some cases to subleading order, the amplitudes themselves are calculable in perturbation theory. More precisely, they factorize into products of form factors and of convolution of a perturbative expression with non-perturbative meson wave functions. Moreover, all the b_i (annihilation) amplitudes are power-suppressed. The theoretical basis of the $1/m_b$ expansion is discussed in Sec. 2.2. The rest of this section is devoted to quantitative results and phenomenology of the topological (and physical) amplitudes.

9.1.2. *Tree amplitudes: results*

The most complete results are available for the topological tree amplitudes, whose factorization at leading power in the $1/m_b$ expansion is pictured in Fig. 76. The gray blobs and the violet 'spring' lines contain the soft and collinear gluon degrees of freedom (virtualities $< \sqrt{\Lambda m_b}$). The hard subgraph, formed by the remaining gluon lines and the pieces of quark lines between their attachments and the weak vertex, connects the quark legs of the weak operators Q_1 and Q_2 with valence quark lines for the external states but not with each other, hence the name "tree". For either operator, the hard scale m_b (wavy lines) can be matched onto two operators $\mathcal{O}^{\rm I,II}$ in $\rm SCET_I$ (see Sec. 2.2). At leading power, all terms at $\mathcal{O}(\alpha_s)$ (NLO) [38–40] and $\mathcal{O}(\alpha_s^2)$ (NNLO) [1042–1046] have been computed. In particular, these results establish the validity of factorization and the good behavior of the perturbation expansion up to NNLO. The hard-collinear scale $\sqrt{\Lambda m_b}$ can also be factorized. This has been performed for the operators of type II in [1044, 1047–1049]. Again, a stable perturbation expansion is observed. Depending on the flavor of the valence quark lines, color factors differ, giving rise to a "color-allowed" amplitude α_1 and a "color-suppressed" one α_2. The type-II (hard-spectator-scattering) contributions then take the form

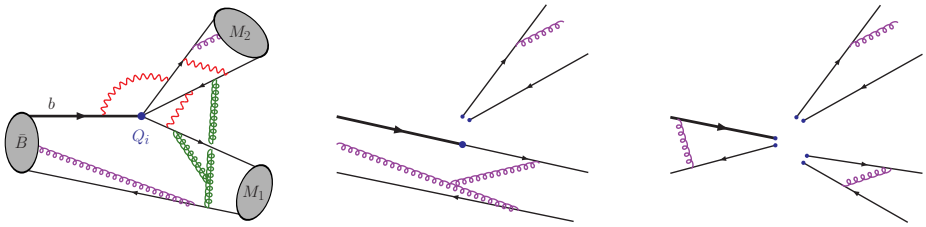

Fig. 76. Factorization of the tree amplitudes. Left: Matrix element of a weak Hamiltonian current-current operator $Q_{1,2}$ in the effective 5-flavor QCD×QED theory. The red, wavy lines close to the vertex have virtualities of order m_b^2; the system of green 'cut-spring' lines connecting to the spectator, of order Λm_b. The purple 'spring' lines entering the mesons indicate the soft gluon background in which the hard subprocess takes place. Middle: Factorization into a product of a wave function and a form factor (to be convoluted with a hard kernel $H^{\rm I}$ or $H^{\rm II}$). Right: The B-type bilocal form factor (convoluted with $H^{\rm II}$) factorizes further into wave functions. (According to the pQCD framework, this is also true for the soft (A-type) form factor.)

$$A_{M_1M_2}\alpha_{1,2}^{\rm II} \propto [H^{\rm II} * \phi_{M_2}] * [\phi_B * J * \phi_{M_1}] \tag{397}$$

of a convolution of hard and hard-collinear scattering kernels $H^{\rm II}$ and J with meson wave functions. An alternative is not to perform the hard-collinear factorization and define a non-local form factor $\zeta_J = \phi_B * J * \phi_M$, information on which has to be extracted from experiment. This works in practice to zeroth order in $\alpha_s(m_b)$ [51]. At higher orders, the kernel $H^{\rm II}$ acquires a dependence on how the momentum is shared between the M_1 valence quarks, i.e. the convolution $H^{\rm II} * \zeta_J$ becomes nontrivial. No higher-order analyses have been performed. [27]

For the type-I operators, in the collinear expansion one encounters divergent convolutions in factorizing the hard-collinear scale already at the leading power, indicating a soft overlap breaking (perturbative) factorization of soft and collinear physics. In this case, however, not performing this factorization is more feasible, as it leaves a single form factor (which can be taken to be an ordinary QCD form factor or the SCET soft form factor) multiplying a convolution of a hard-scattering kernel with one light-meson wave function,

$$A_{M_1M_2}\alpha_{1,2}^{\rm I} \propto f^{BM_1}(0) H^{\rm I} * \phi_{M_2}. \tag{398}$$

[By convention, the form factor is factored out into $A_{M_1M_2}$.] An alternative treatment is k_T factorization ("pQCD") [48], where a transverse-momentum-dependent B-meson wave function is introduced, which regularizes the endpoint divergence. In this case, a convergent convolution arises (at lowest order), and within the uncertainties on the wave function it is generally possible to accommodate the observed data. [28]

Finally, certain power corrections were identified as potentially large in [40]. One class, which is only relevant for final states containing pseudoscalars, consists of "chirally en-

[27] Strictly speaking, the convolution of the ζ_J factor with $H^{\rm II}$ might diverge at the endpoint. Correspondingly, to such a convolution in general a non-perturbative soft rescattering phase should be associated. An endpoint divergence indeed appears in the attempt to perturbatively factorize ζ_J at first subleading power, see below.

[28] Independently of the convergence issue, a perturbative calculation in the k_T (or any other) factorization scheme must demonstrate that the result is dominated by modes which are perturbative.

hanced" terms, which are proportional to the ratio $r_\chi^P = m_P^2/(m_b m_q)$, where P is a pion or Kaon and m_q an average of light quark masses; another class of certain annihilation topologies with large color factors (first pointed out in [48]) is discussed in Sec. 9.1.3 below. Power corrections are of phenomenological relevance in $\alpha_2^{\rm II}$, which contains a chirally-enhanced power correction involving the large Wilson coefficient C_1, where the convolution of $H^{\rm II}$ with the power-suppressed analogue $\zeta_J^{\rm tw3}$ of ζ_J is divergent. These power corrections are therefore not dominated by perturbative gluon exchange. They have been modeled in [40] by introducing an IR cutoff $\mathcal{O}(500\,\text{MeV})$ on the convolutions and associating an arbitrary rescattering phase with the soft dynamics.

Quantitatively, combining the phenomenological analysis in [1050] (where values for hadronic parameters are specified) with the results of [1045, 1046] gives

$$\begin{aligned}\alpha_1(\pi\pi) &= 1.015 + [0.025 + 0.012i]_V + [0.024 + 0.026i]_{VV} \\ &\quad - \left[\frac{r_{\rm sp}}{0.485}\right]\Big\{[0.020]_{\rm LO} + [0.034 + 0.029i]_{HV} + [0.012]_{\rm tw3}\Big\} \\ &= 0.999^{+0.034}_{-0.072} + (0.009^{+0.024}_{-0.051})i, \end{aligned} \tag{399}$$

$$\begin{aligned}\alpha_2(\pi\pi) &= 0.184 - [0.153 + 0.077i]_V - [0.030 + 0.042i]_{VV} \\ &\quad + \left[\frac{r_{\rm sp}}{0.485}\right]\Big\{[0.122]_{\rm LO} + [0.050 + 0.053i]_{HV} + [0.071]_{\rm tw3}\Big\} \\ &= 0.245^{+0.228}_{-0.135} + (-0.066^{+0.115}_{-0.081})i. \end{aligned} \tag{400}$$

In each amplitude, the terms on the first and second lines correspond to the type-I and type-II contributions. These are further split into terms $\mathcal{O}(1)$, $\mathcal{O}(\alpha_s)$ (V, LO), and $\mathcal{O}(\alpha_s^2)$ (VV, HV), and an estimate of a chirally enhanced power correction following a model defined in [40] ("tw3"). The relative normalization factor of the spectator-scattering contributions, $r_{\rm sp} = (9 f_\pi f_B)/(m_b f_+^{B\pi}(0)\lambda_B)$, contains the bulk of the parametric uncertainty of that term. We observe that the color-allowed tree is perturbatively stable and has small uncertainties resulting from the poor knowledge of hadronic input parameters. Moreover, the spectator-scattering contribution is small, including a weak dependence on endpoint-divergent power corrections (labeled "tw3").

Conversely, the color-suppressed tree amplitude is dominated by the type-II contribution, and it exhibits large sensitivity to a chirally enhanced, non-factorizable power correction. It is important to keep in mind that the estimate for the latter, unlike all other pieces, is based on a model. Several phenomenological analyses of the $B \to \pi\pi$ data favor large values $\alpha_2(\pi\pi) = \mathcal{O}(1)$, which is sometimes called a puzzle. In the Standard Model, a large value can come from a large $r_{\rm sp}$, for instance through the moment $\lambda_B^{-1} \equiv \int \mathrm{d}\omega \phi_{B+}(\omega)/\omega$ of the relevant B-meson wave function. Information on λ_B can be obtained by operator product expansions in HQET [1051, 1052] and from QCD sum rules [1053, 1054], but with considerable uncertainties. An interesting possibility is to determine λ_B more directly from radiative semileptonic decay, discussed in Sec. 9.1.5 below. Second, is not inconceivable that a large value originates from the presently incalculable twist-three spectator scattering. Such an interpretation would be consistent with the fact that data suggest a small value of $\alpha_2(\rho\rho)$, which is not sensitive to chiral enhancement.

In the treatment advocated in [51], ζ_J is not factorized. The generic prediction is $\arg \alpha_2/\alpha_1 = \mathcal{O}(\alpha_s)$ (this is set to zero in the analysis). A prediction on the magnitude requires knowledge on ζ and ζ_J from outside sources, in analogy with the results described

above. For more details, see [51, 53, 1055].

In the pQCD approach, the issue of a large α_2/α_1 (possibly with a large phase) has been addressed in [1056] and again in [1057]. The latter paper augments the structure in the original approach by an extra soft rescattering factor which represents an additional non-perturbative parameter that has to be adjusted to experimental data. We note that the computation in [1056] uses the hard (type-I) vertex from [38–40] as a building block to estimate NLO effects in the pQCD approach. Taking, for the sake of the argument, the asymptotic form of the distribution amplitude ϕ_{M_2}, the contribution is proportional to

$$C_2(\mu) + \frac{C_1(\mu)}{N_c}\left[1 + \frac{\alpha_s(\mu)\,C_F}{4\pi}\left(-\frac{37}{2} - 3\,i\,\pi + 12\,\ln\frac{m_b}{\mu}\right)\right], \tag{401}$$

where $C_1(\mu)$ is the large current-current Wilson coefficient. In order to obtain both a large magnitude and phase, one would need to evaluate this expression at a low scale $\mu \ll m_b$, where perturbation theory is questionable. [29] In the pQCD approach the above expression appears inside a convolution integral, where the scale μ is fixed by the internal kinematics of the spectator scattering. The enhancement and the large phase of the color-suppressed tree amplitude found in [1056] therefore has to be associated to a rather low effective renormalization scale (see also the discussion in [1058]). Correspondingly, scale variations or alternative scale-setting procedures in the pQCD approach represent an additional source of potentially large theoretical uncertainties associated to this kind of NLO effects.

Finally, the (physical) tree amplitudes receive contributions from penguin and annihilation contractions as discussed above. The factorization properties of the former are very similar to those of the penguin amplitudes discussed in the following section and give rise to corrections that are subleading with respect to α_1, α_2. For the annihilation amplitudes b_1 and b_2 there is no factorization in the collinear expansion. Both the model of [40] and the k_T factorization of [48] result in small numerical values. [30]

9.1.3. *Penguin amplitudes: results*

The penguin contraction $\alpha_4^c(M_1M_2)$ entering the physical penguin amplitude $P_{M_1M_2}$ decomposes in the heavy-quark expansion as

$$\alpha_4^c = a_4^c + r_\chi a_6 + \text{higher powers and terms not chirally enhanced.} \tag{402}$$

Factorization of a_4^c (as defined here) to leading power has been argued (to one loop) and the hard kernels computed in [38–40] but has been the subject of some controversy over the existence of an extra leading-power long-distance nonrelativistic "charming-penguin" contribution [51, 1060, 1061]. Such an incalculable extra term would, in practice, imply that no prediction for penguin amplitudes can be made. It appears that this theoretical issue has recently been resolved [1062] (in favor of calculability in the sense of [38–40]).

[29] More precisely, the apparent μ-dependence is formally a NNLO effect.

[30] In [1037] it has been noted that b_2 is leading in the $1/N_c$ counting. On the other hand, the diagrams that are leading in the $1/N_c$ counting combine to the product of a decay constant and the matrix element of the divergence of a current that is conserved in the limit $m_{s,d,u} \to 0$. A hard-scattering approach then implies $b_2^{N=\infty} = \mathcal{O}(m_{s,d,u}/m_b)$. This suppression is also found in the QCD light-cone sum rules treatment in [1059]. Nevertheless we do not know a rigorous argument why this amplitude could not be as large as $\mathcal{O}(m_s/\Lambda)$ in $B \to \pi K$ decays.

Again, there are two contributions, labeled I and II as in the case of the trees. The computation of the spectator scattering term $a_4^{\rm II}$ has been performed to $\mathcal{O}(\alpha_s^2)$ [1050,1055]. The "scalar-penguin" term $r_\chi a_6^c$ is again a chirally enhanced power correction, which however is calculable. At $\mathcal{O}(\alpha_s)$ [38–40] it dominates over a_4^c when M_2 is a pseudoscalar (otherwise it is negligible). Finally, the physical penguin amplitudes contain a penguin annihilation term with a large color factor that is not chirally enhanced. Twist-three spectator scattering is unlikely to be very important, as the type-I contributions are significant (similarly to the color-allowed tree). Because the perturbative results for the penguin amplitudes, in comparison to the tree amplitudes, are rather incomplete at this time (only one piece at $\mathcal{O}(\alpha_s^2)$ has been computed, as discussed above), we refrain from giving numerical results; for an exhaustive compendium of $\mathcal{O}(\alpha_s)$ results we refer to [1040]. Rather, we recall the following "anatomy". As just mentioned, physical penguin amplitudes are approximately described in terms of a leading-power piece, a chirally enhanced power correction, and an annihilation term:

$$P_{M_1M_2} \propto a_4^c(M_1M_2) \pm r_\chi^{M_2} a_6^c(M_1M_2) + \frac{B_{M_1M_2}}{A_{M_1M_2}} b_3^c(M_1M_2). \tag{403}$$

The sign in front of a_6 provides for constructive interference in the case of a PP final state and destructive one for a VP final state; moreover the enhancement factor r_χ is absent (or small) for PV final states. This results in a particular pattern for the magnitudes and phases of penguin amplitudes (and P/T ratios) that can be compared to data in $\Delta B = \Delta S = 1$ decays [1040, 1050], with a reasonable agreement within uncertainties. The comparison also indicates the presence of substantial annihilation contributions (as included in the 'S4' scenario favored in [1040]). For instance, a complex annihilation term is essential to account for the observed sign of CP asymmetries in $B^0 \to K^+\pi^-$ and $B^0 \to \pi^+\pi^-$. (A caveat to this is that the $\mathcal{O}(\alpha_s^2)$ contribution to a_6 is currently not known; as it involves the large coefficient C_1 it might make a non-negligible contribution to the phase of P/T.) As with the endpoint divergent twist-three spectator scattering (and with the same caveats) the annihilation term is rendered finite in pQCD (k_T factorization) and one can obtain the "correct" sign of the penguin amplitudes through the annihilation amplitude. A treatment based on the approach of [51], but extended by an a_6 term and a real annihilation amplitude, can be found in [1055]. The phenomenologically required phase is assigned there to a nonperturbative charming-penguin parameter.

9.1.4. *Application to angle measurements*

As explained in Sec. 9.1.1, various time-dependent CP asymmetries measure CKM angles via their S-parameter in the limit of vanishing T or P. The predictions obtained from the heavy-quark expansion can be directly applied to correct for non-vanishing subleading amplitudes. For the case of the angle β in $b \to s$ penguin transition, where

$$\Delta S_f = -\eta_{\rm CP}(f) S_f - \sin(2\beta) \approx 2\cos(2\beta)\sin\gamma\,{\rm Re}\frac{T_f}{P_f}, \tag{404}$$

such analyses have been performed in [53,1063–1066], following the different treatment of hadronic inputs and (divergent) power corrections outlined above. Results are compared in Tab. 66.

Analogous expressions hold for $b \to d$ transitions. This allows a measurement of $S_{\pi^+\pi^-,\pi^+\rho^-,\rho^+\rho^-}$ to be directly turned into one of γ. These determinations are com-

Table 66
Predictions for ΔS defined in the text for several penguin-dominated modes. *Note:* For the QCDF results, we quote the result of a scan over input parameters (conservative). For the SCET results, double results correspond to two solutions of a fit of hadronic parameters, and errors are combined in quadrature. Results for PP final states are from [53], for PV from [1065]; both papers assume $SU(3)$ to reduce the number of theory papers but differ over the inclusion of certain chirally enhanced terms.

mode	QCDF/BBNS [1063]	SCET/BPRS [53, 1065]	pQCD [1066]	experiment
ϕK_S	$0.01 \ldots 0.05$	0 / 0	$0.01 \ldots 0.03$	-0.23 ± 0.18
ωK_S	$0.01 \ldots 0.21$	$-0.25 \ldots -0.14$ / $0.09 \ldots 0.13$	$0.08 \ldots 0.18$	-0.22 ± 0.24
$\rho^0 K_S$	$-0.29 \ldots 0.02$	$0.11 \ldots 0.20$ / $-0.16 \ldots -0.11$	$-0.25 \ldots -0.09$	-0.13 ± 0.20
ηK_S	$-1.67 \ldots 0.27$	$-0.20 \ldots 0.13$ / $-0.07 \ldots 0.21$		
$\eta' K_S$	$0.00 \ldots 0.03$	$-0.06 \ldots 0.10$ / $-0.09 \ldots 0.11$		-0.08 ± 0.07
$\pi^0 K_S$	$0.02 \ldots 0.15$	$0.04 \ldots 0.10$		-0.10 ± 0.17

petitive with the average of isospin-triangle "α" determinations, and in fact even of the global unitarity triangle fit: $\gamma_{\pi\pi} = (70^{+13}_{-10})^\circ$, $\gamma_{\pi\rho} = (69 \pm 7)^\circ$ [1058], and $\gamma_{\rho_L\rho_L} = (73.2^{+7.6}_{-7.7})^\circ$ [1067]. (These involve QCDF calculations of P/T; we have not updated experimental inputs.) For a combination of heavy-quark expansion and $SU(3)$ flavor arguments, see [1068].

9.1.5. *Prospects*

The discovery that predictions for hadronic two-body decay amplitudes can be made in perturbation theory in an expansion in Λ/m_b has led to a lot of activity at the conceptual, technical, and phenomenological level. At the former, it provides a highly nontrivial application of soft-collinear effective theory, while at the latter it bore the promise to discuss many more observables separately than is possible based on isospin and flavor-$SU(3)$ arguments alone. So far, the available technical results are between the NLO and NNLO stage, where they show a good behavior of the perturbation series. The NNLO computations should be completed also for the (topological) penguins, including chirally enhanced power corrections. This means one-loop corrections to $a_6^{\rm II}$ and two-loop corrections to $a_4^{\rm I}$ and $a_6^{\rm II}$, and analogous electroweak amplitudes. Not before then will it be really possible to compare to data (preferably from new-physics-insensitive channels) to assess the importance of certain incalculable power corrections, which will then likely dominate the uncertainties on all amplitudes. A related issue is the status of required nonperturbative inputs – foremost, form factors and moments of the B-meson wave functions. While some progress on the former is expected from improved lattice results, the latter has to be obtained in other ways, such as from QCD light-cone sum rules or from data itself. Most important are the first inverse moments λ_B^{-1} and $\lambda_{B_s}^{-1}$. They are intimately related to the size of spectator-scattering terms, hence to the color-suppressed tree (and electroweak-penguin) amplitudes. Interestingly, in the case of B_d mesons this parameter can already be constrained from the search for the radiative semileptonic decay $B^+ \to \gamma\ell^+\nu$ [1069]. Here, a more sophisticated theoretical analysis taking into account known higher-order and power corrections in that mode would be interesting.

For the non-factorizable power corrections themselves, significant conceptual progress would be necessary before one might gain quantitative control. The fate of soft-collinear factorization is a hard problem but is important. Meanwhile, a comparison of data with

refined theory predictions may give us more (or less) confidence in present models of the power corrections.

9.2. *Measurement of β*

9.2.1. *Theoretical aspects*

Measurements of time-dependent *CP* violation in hadronic $b \to s$ penguin dominated decay modes provide an interesting method to test the SM. Naively, decays to *CP* eigenstate final states f (with *CP* eigenvalues η_f) which are dominated by $V_{tb}V_{ts}^*$ amplitudes should have small values of $\Delta S_f \equiv -\eta_f S_f - S_{J/\psi\, K_S^0}$ since, in the SM, $\arg\left(V_{tb}V_{ts}^*\right) \approx \arg\left(V_{cb}V_{cs}^*\right)$. Although one expects hadronic corrections in these modes to be only of $\mathcal{O}(\lambda^2) \approx 5\%$ [1070, 1071], this is difficult to confirm rigorously. In fact in the past few years many theoretical studies [1063, 1064, 1066, 1072, 1073] of the "pollution" from the amplitude proportional to $V_{ub}V_{us}^*$ to these modes have been undertaken. Recall that the amplitude can be written as

$$A(\bar{B} \to f) = V_{cb}V_{cs}^*\, a_f^c + V_{ub}V_{us}^*\, a_f^u \propto 1 + e^{-i\gamma}\, d_f, \tag{405}$$

where schematically the hadronic amplitude ratio is given by

$$d_f \sim \left|\frac{V_{ub}V_{us}^*}{V_{cb}V_{cs}^*}\right| \frac{\{P^u, C, \ldots\}}{P^c + \ldots}. \tag{406}$$

Since for small d_f, the correction $\Delta S_f \approx 2\,\mathrm{Re}(d_f)\cos(2\beta)\sin\gamma$, these contributions have to be negligibly small for time-dependent CP asymmetry measurements in $b \to s$ transitions to provide a clean and viable test of the SM, or d_f has to be under very good theoretical control. The problem is that precise model independent estimates are rather difficult to make. Most theoretical calculations suggest that the two penguin amplitudes P^c, P^u are similar resulting in a universal positive contribution 0.03 to S_f, while the final-state dependence results mainly from the interference of the color-suppressed tree amplitude C with the dominant penguin amplitude, $\mathrm{Re}(C/P^c)$. For more detailed reviews, see Refs. [1074, 1075].

In fact, it is important to note that there are actually (at least) three ways to determine $\sin 2\beta$ in the SM:

- First, the gold-plated method via $B^0 \to J/\psi\, K_S^0$,
- Via the $b \to s$ penguin-dominated decay modes,
- From the "predicted" value of $\sin 2\beta$, based on the SM CKM Unitarity Triangle fit. Unlike the previous two, which are directly measured values of $\sin 2\beta$, the predicted value is typically obtained by using hadronic matrix elements, primarily from lattice calculations, along with experimental information on *CP* violating and *CP* conserving parameters ϵ_K, $\Delta m_s/\Delta m_d$ and V_{ub}/V_{cb}. In fact, recently it has been shown that the precision in one hadronic matrix element (B_K) has improved so that even without using V_{ub}/V_{cb} a non-trivial constraint can be obtained for the predicted value of $\sin 2\beta$ in the SM [1076]. This is important since there is an appreciable disagreement between inclusive and exclusive determinations of V_{ub} [261].

Differences in the resulting three values of $\sin 2\beta$ may imply new physics and need to be carefully understood.

In the discussion of experimental results below, we see that ten $b \to s$ penguin dominated decay modes have been identified so far. Several theoretical studies find that

three of the modes: ϕK^0_S, $\eta' K^0_S$ and $K^0_S K^0_S K^0_S$ are the cleanest with SM predictions of $\Delta S_f \lesssim 0.05$, since either there is no pollution from the color-suppressed tree amplitude, or the penguin amplitude is large, in which case d_f is estimated to be only a few percent; this also generally means that the uncertainties on these estimates are small. On the other hand, theoretical calculations find appreciably larger tree contributions (with large uncertainties) in several of the other modes, such as ηK^0_S, ρK^0_S, ωK^0_S. It therefore no longer seems useful to average the *CP* asymmetry over all of the penguin modes. Factorization-based calculations suggest that the uncertainty in the case of $\pi^0 K^0_S$ is intermediate between the two sets of final states above. However, for $\pi^0 K^0_S$ additional information is available: a general amplitude parametrization of the entire set of πK final states together with SU(3) flavor symmetry allows to constrain $S_{\pi^0 K^0_S}$ by other πK and $\pi\pi$ observables [1077–1079]. At present this method yields $S_{\pi^0 K^0_S} \simeq 0.8$–1, if one allows for an anomalously large color-suppressed tree amplitude that is suggested by the current πK branching fractions and direct CP asymmetries. Hence improved measurements of the direct and time-dependent asymmetries may still provide useful tests of the SM.

Finally, we note that the current experimental errors of 0.07 ($\eta' K^0_S$) and 0.17 (ϕK^0_S and $K^0_S K^0_S K^0_S$), as shown in Fig. 80, are statistics dominated and are also still large compared to the expected theory uncertainties. At a Super Flavor Factory ($\approx$ 50–75 ab^{-1} of data) the experimental errors will get significantly reduced down to around 0.01–0.03 [167, 1074, 1080–1082]. Looking to the future, another interesting channel is $B_s \to \phi\phi$ [1070,1083], where the naïve Standard Model expectation for S_f is zero, and which will be measured by LHCb. As mentioned above, in the SM it is theoretically quite difficult to explain ΔS_f larger than 0.05 in these modes. Therefore if improved experimental measurements show $\Delta S \gtrsim 0.1$ then that would be an unambiguous sign of a *CP*-odd phase beyond the SM-CKM paradigm.

9.2.2. *Experimental results*

$B^0 \to \eta' K^0$ and $B^0 \to \omega K^0_S$

Both the BaBar and Belle experiments reconstruct seven decay channels of $B^0 \to \eta' K^0$,
$B^0 \to \eta'(\rho\gamma, \eta_{\gamma\gamma}\pi^+\pi^-, \eta_{3\pi}\pi^+\pi^-)K^0_S(\pi^+\pi^-)$,
$B^0 \to \eta'(\rho\gamma, \eta_{\gamma\gamma}\pi^+\pi^-)K^0_S(\pi^0\pi^0)$ and
$B^0 \to \eta'(\eta_{\gamma\gamma}\pi^+\pi^-, \eta_{3\pi}\pi^+\pi^-)K^0_L$.
BaBar identifies the decays with a K^0_S using $m_{\rm ES}$, ΔE and a Fisher discriminant which separates continuum from $B\overline{B}$ events [249]. Similarly, Belle uses $M_{\rm bc}$, ΔE and a likelihood ratio, $\mathcal{R}_{S/B}$, which performs the same task of $q\overline{q}$ discrimination [949]. For K^0_L modes, only the K^0_L direction is measured, so either $m_{\rm ES}$ or ΔE is calculated. BaBar uses ΔE while Belle chooses $M_{\rm bc}$. Fig. 77 shows Δt and asymmetry projections for $B^0 \to \eta' K^0$.

For $B^0 \to \omega K^0_S$, the only useful decay channel is, $B^0 \to \omega(\pi^+\pi^-\pi^0)K^0_S(\pi^+\pi^-)$. BaBar uses $m_{\rm ES}$, ΔE, a Fisher discriminant, the ω mass and its helicity to discriminate between signal and background [249] while Belle uses $M_{\rm bc}$, ΔE, $\mathcal{R}_{S/B}$ and the ω mass [1084]. The fit results are summarized in Tab. 67 and Fig. 80.

In these modes there is no evidence for direct *CP* violation while mixing-induced *CP* violation is consistent with charmonium. The significance of the mixing-induced *CP* violation effect in $B^0 \to \eta' K^0$ is greater than 5σ in both BaBar and Belle analyses.

$B^0 \to K^0\pi^0$, $B^0 \to K^0_S K^0_S K^0_S$ and $B^0 \to K^0_S \pi^0 \pi^0$

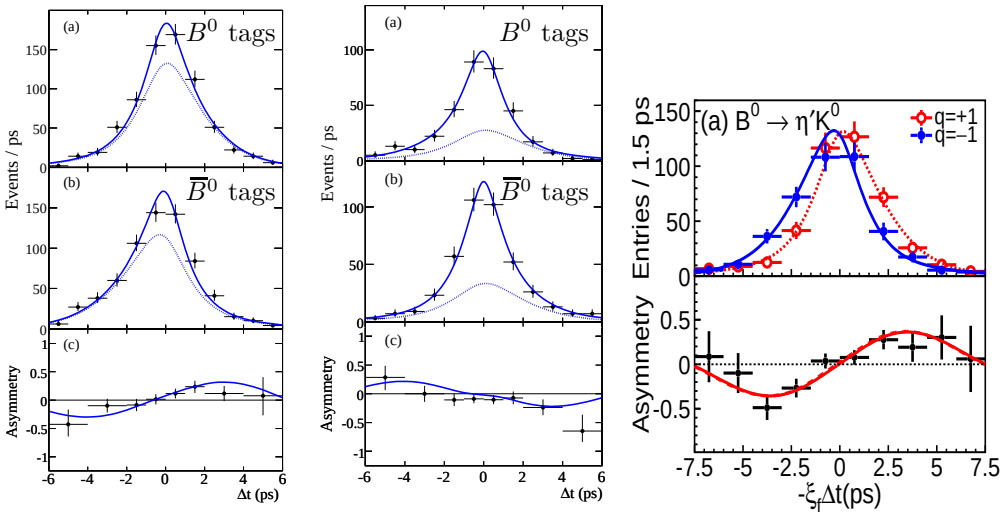

Fig. 77. Signal enhanced Δt projections and asymmetry plots for $B^0 \to \eta' K^0$. The left (middle) plot shows BaBar's fit results for $B^0 \to \eta' K^0_S$ ($B^0 \to \eta' K^0_L$) and the right plot shows Belle's combined fit result.

Table 67
Summary of $B^0 \to \eta' K^0$ and $B^0 \to \omega K^0_S$.

	BaBar	Belle
$B^0 \to \eta' K^0$		
Yield ($N(B\overline{B}) \times 10^6$)	2515 ± 69 (467)	1875 ± 60 (535)
$B^0 \to \omega K^0$		
Yield ($N(B\overline{B}) \times 10^6$)	163 ± 18 (467)	118 ± 18 (535)

These modes are distinguished by the lack of a primary track coming from the reconstructed B vertex. In such cases, the B vertex is determined by extrapolating the K^0_S pseudo-track back to the interaction point. However, due to the relatively long lifetime of the K^0_S meson, the vertex reconstruction efficiency is less than 100% as the charged pion daughters may not be able to register hits in the innermost sub-detector.

For $B^0 \to K^0\pi^0$, BaBar describes signal events with the reconstructed B mass and the mass of the tag-side B calculated from the known beam energy and reconstructed B momentum constrained with the nominal B mass. In addition, the cosine of the polar angle of the B candidate in the $\Upsilon(4S)$ frame and ratio of angular moments, L_2/L_0, which discriminate against continuum are also used [249]. Belle uses $M_{\rm bc}$, ΔE, and $\mathcal{R}_{S/B}$ to describe signal events and additionally considers the $B^0 \to K^0_L\pi^0$ channel for which ΔE cannot be calculated [1085]. Fig. 78 shows Δt and asymmetry projections for $B^0 \to K^0\pi^0$.

For $B^0 \to K^0_S K^0_S K^0_S$ and $B^0 \to K^0_S\pi^0\pi^0$ [1086], BaBar uses $m_{\rm ES}$, ΔE and a neural network (NN) which distinguishes $B\overline{B}$ from $q\overline{q}$ events to describe signal [1087, 1088] and similarly, Belle uses $M_{\rm bc}$, ΔE and $\mathcal{R}_{S/B}$ [949, 1089]. For $B^0 \to K^0_S K^0_S K^0_S$, both experiments include the case where one K^0_S decays to a neutral pion pair. The fit results are summarized in Tab. 68 and Fig. 80.

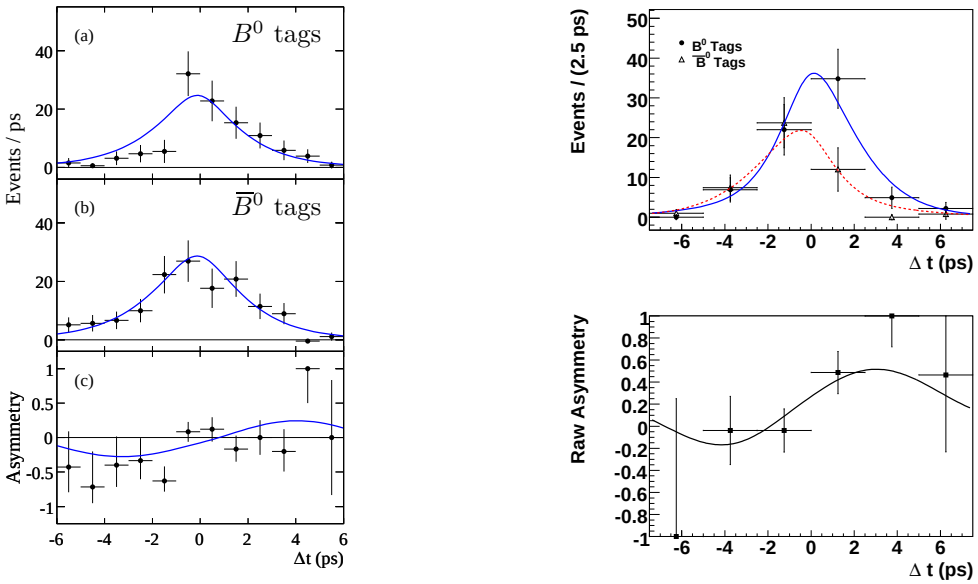

Fig. 78. Signal enhanced and background subtracted Δt projections and asymmetry plots for $B^0 \to K^0\pi^0$. The left plot shows BaBar's fit result and the right plot shows Belle fit result.

Table 68
Summary of $B^0 \to K^0\,\pi^0$, $B^0 \to K^0_S\,K^0_S\,K^0_S$ and $B^0 \to K^0_S\,\pi^0\,\pi^0$.

	BaBar	Belle
$B^0 \to K^0\pi^0$		
Yield ($N(B\overline{B}) \times 10^6$)	556 ± 32 (467)	657 ± 37 (657)
$B^0 \to K^0_S K^0_S K^0_S$		
Yield ($N(B\overline{B}) \times 10^6$)	274 ± 20 (467)	185 ± 17 (535)
$B^0 \to K^0_S \pi^0 \pi^0$		
Yield ($N(B\overline{B}) \times 10^6$)	117 ± 27 (227)	307 ± 32 (657)

In these modes the direct *CP* components are all consistent with Standard Model expectations and the mixing-induced parameters are consistent with charmonium with current statistics. The largest discrepancy, which is not statistically significant, is in the mixing-induced *CP* violation parameter in $B^0 \to K^0_S\pi^0\pi^0$, which appears to have the wrong sign.

$B^0 \to K^0_S\pi^+\pi^-$ and $B^0 \to K^0_S K^+ K^-$

To extract *CP* violation parameters of modes such as $B^0 \to K^0_S\rho^0$ ($\rho^0 \to \pi^+\pi^-$) or $B^0 \to K^0_S\phi$ ($\phi \to K^+K^-$), it is necessary to perform a time-dependent Dalitz plot analysis as interfering resonances in the three-body final states make the results of quasi-two-body analyses difficult to interpret. As the relative amplitudes and phases of each decay channel in the Dalitz plot are determined in such an analysis, the angle $\beta^{\rm eff}$ can be directly obtained, rather than measuring $\mathcal{S}^{\rm eff}_{CP}$.

For $B^0 \to K^0_S\pi^+\pi^-$, the signal model contains the $K^{*+}(892)$, $K^{*+}_0(1430)$, $\rho^0(770)$, $f_0(980)$, $f_2(1270)$, $f_{\rm X}(1300)$ states and a nonresonant component. BaBar describes signal events with $m_{\rm ES}$, ΔE and the output of a neutral network [1090] while Belle just uses ΔE [1091]. Belle finds two solutions given in Tab. 69 with consistent CP parameters but different $K^{*+}_0(1430)\pi^-$ relative fractions due to the interference between $K^{*+}_0(1430)$ and the non-resonant component. The high $K^{*+}\pi^-$ fraction of Solution 1 is in agreement with some phenomenological estimates [1092] and may also be qualitatively favored by the total K–π S-wave phase shift as a function of $m(K\pi)$ when compared with that measured by the LASS collaboration [1020]. The fit results for both experiments are summarized in Tab. 71 and Fig. 79, which includes the preferred solution from Belle.

Table 69
Multiple solutions in $B^0 \to K^0_S\pi^+\pi^-$ at Belle where the first error is statistical, the second systematic and the third is the model uncertainty.

	Sol. 1	Sol. 2
$\beta^{\rm eff}(\rho^0(770)K^0_S)$	$(20.0^{+8.6}_{-8.5} \pm 3.2 \pm 3.5)^\circ$	$(22.8 \pm 7.5 \pm 3.3 \pm 3.5)^\circ$
$\beta^{\rm eff}(f_0(980)K^0_S)$	$(12.7^{+6.9}_{-6.5} \pm 2.8 \pm 3.3)^\circ$	$(14.8^{+7.3}_{-6.7} \pm 2.7 \pm 3.3)^\circ$

The decay $B^0 \to K^0_S K^+K^-$ is also studied with a time-dependent Dalitz plot analysis. The signal model contains the $f_0(980)$, $\phi(1020)$, $f_X(1500)$ and χ_{c0} states and a nonresonant component. The BaBar collaboration additionally uses the K^0_S decay channel to neutral pions and describes signal events with $m_{\rm ES}$ and ΔE [1093]. Similarly, Belle uses $M_{\rm bc}$ and ΔE [1094].

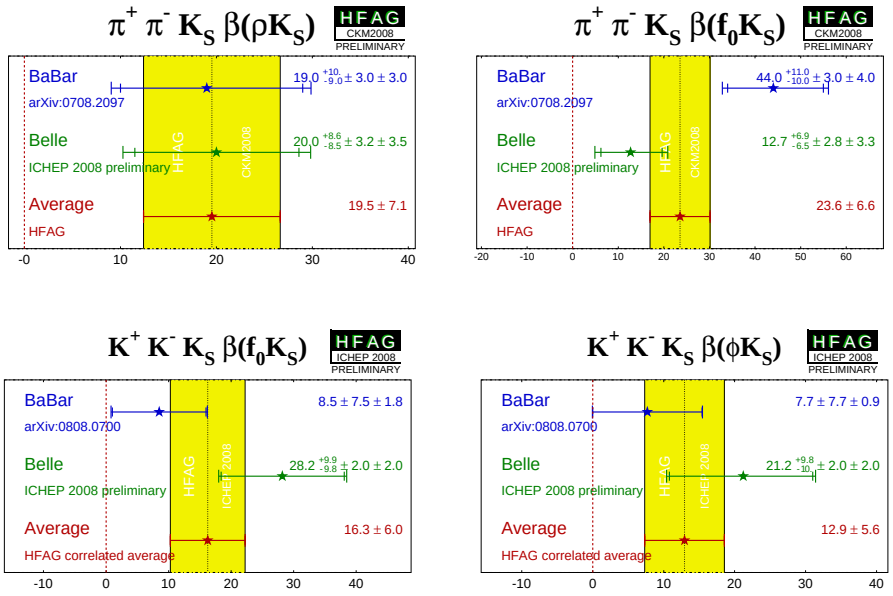

Fig. 79. CP parameters of $B^0 \to K^0_S\pi^+\pi^-$ and $B^0 \to K^0_S K^+K^-$.

Belle finds four solutions as shown in Tab. 70 due to the interference between $f_0(980)$, $f_X(1500)$ and the non-resonant component. Using external information from $B^0 \to K^0_S\pi^+\pi^-$, if the $f_X(1500)$ is the $f_0(1500)$ for both $B^0 \to K^0_S\pi^+\pi^-$ and $B^0 \to K^0_S K^+K^-$, the ratio of branching fractions, $\mathcal{B}(f_0(1500) \to \pi^+\pi^-)/\mathcal{B}(f_0(1500) \to K^+K^-)$, prefers the solution with the low $f_X(1500)K^0_S$ fraction. Similarly other measurements of the relative magnitudes of the $f_0(980) \to \pi^+\pi$ and $f_0(980) \to K^+K^-$ widths prefer the solution with the low $f_0(980)K^0_S$ fraction. The fit results for both experiments are summarized in Tab. 71 and Fig. 79, which includes the preferred solution from Belle, while Fig. 80 gives a summary of these results together with those from other charmless hadronic B decays. In the time-dependent *CP* violation analyses, there is no evidence for direct *CP* violation and $\beta^{\rm eff}$ is consistent with charmonium.

Table 70
Multiple solutions in $B^0 \to K^0_S K^+K^-$ at Belle where the error is statistical only.

	Sol. 1	Sol. 2	Sol. 3	Sol. 4
$\beta^{\rm eff}(f_0(980)K^0_S)$	$(28.2^{+9.8}_{-9.9})^\circ$	$(64.1^{+7.6}_{-8.0})^\circ$	$(61.5^{+6.5}_{-6.5})^\circ$	$(36.9^{+10.9}_{-9.6})^\circ$
$\beta^{\rm eff}(\phi(1020)K^0_S)$	$(21.2^{+9.8}_{-10.4})^\circ$	$(62.1^{+8.3}_{-8.8})^\circ$	$(65.1^{+8.7}_{-8.7})^\circ$	$(44.9^{+13.2}_{-13.6})^\circ$

Table 71
Summary of $B^0 \to K^0_S\pi^+\pi^-$ and $B^0 \to K^0_S K^+K^-$.

	BaBar	Belle
$B^0 \to K^0_S\pi^+\pi^-$		
Yield ($N(B\overline{B}) \times 10^6$)	2172 ± 70 (383)	1944 ± 98 (657)
$B^0 \to K^0_S K^+K^-$		
Yield ($N(B\overline{B}) \times 10^6$)	1428 ± 47 (467)	1269 ± 51 (657)

9.3. *Measurements of α*

9.3.1. *Theoretical aspects*

The $b \to u$ tree amplitude (Fig. 81(a)) is proportional to V_{ub} and, in the usual convention, carries the weak phase γ. Since $B^0\overline{B}^0$ mixing carries the weak phase 2β, at the tree level the time-dependent *CP*-violation measurements in the $B^0 \to \pi^+\pi^-$ and $B^0 \to \rho^+\rho^-$ decays are sensitive to $2\beta + 2\gamma = 2\pi - 2\alpha$.

The decay-time distribution for $B^0 \to \pi^+\pi^-$ is given by

$$\frac{dN}{d\Delta t} = \frac{e^{-|\Delta t|/\tau}}{4\tau} \times \left\{1 - q_{\rm tag}[C_{\pi\pi}\cos(\Delta m_d \Delta t) - S_{\pi\pi}\sin(\Delta m_d \Delta t)]\right\}, \qquad (407)$$

where τ is the neutral B lifetime, Δm_d is the B^0–$\overline{B}^0$ mixing frequency, Δt is the difference in decay times $t_{\pi\pi} - t_{\rm tag}$, and the parameter $q_{\rm tag}$ equals $+1\,(-1)$ when the tag-side B decays as a $B^0(\overline{B}^0)$. The parameter $C_{\pi\pi}$ characterizes direct *CP* violation and is also referred to in the literature as $-\mathcal{A}_{\pi\pi}$. At the tree level, the *CP*-violating asymmetries $S_{\pi\pi} = \sin 2\alpha$ ($\alpha \equiv \arg[-V_{td}V^*_{tb}/V_{ud}V^*_{ub}]$) and $C_{\pi\pi} \equiv -\mathcal{A}_{\pi\pi} = 0$. However, since the leading higher-order $b \to d$ contribution to the $B^0 \to \pi^+\pi^-$ decay amplitude (Fig. 81(b)) is sizable and carries the weak phase $-\beta$, direct *CP* violation $C_{\pi\pi} \neq 0$ becomes possible

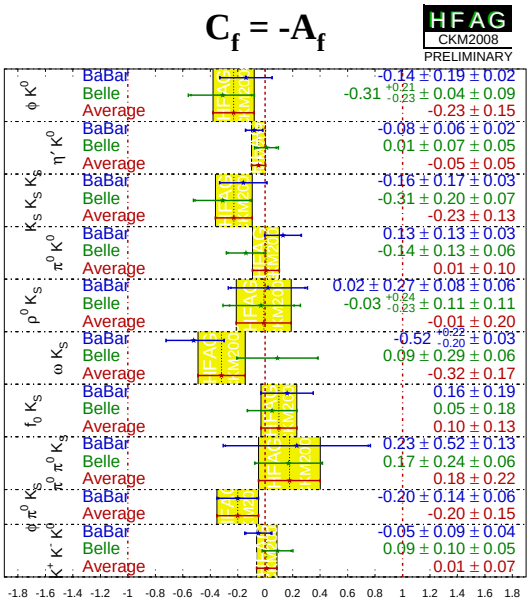

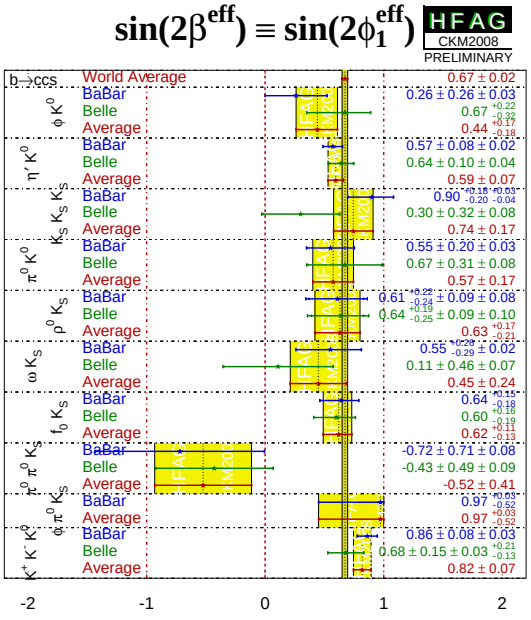

Fig. 80. *CP* parameters of charmless hadronic B decays.

and $S_{\pi\pi} = \sin 2\alpha_{\rm eff}\sqrt{1-C^2_{\pi\pi}}$, where, in general, the phase difference $\alpha - \alpha_{\rm eff} = \Delta\alpha \equiv \delta \neq 0$. Contributions from physics beyond the Standard Model could affect the *CP*-violating asymmetries $S_{\pi\pi}$ and $C_{\pi\pi}$ primarily through additional penguin amplitudes.

The value of δ can be extracted through a model-independent analysis that uses the $SU(2)$ isospin-related decays $B^\pm \to \pi^\pm\pi^0$ and $B^0 \to \pi^0\pi^0$ [37]. Let us denote the $B^{ij} \to \pi^i\pi^j$ and $\overline{B}^{ij} \to \pi^i\pi^j$ decay amplitudes A^{ij} and $\overline{A}^{ij}$, respectively. Assuming isospin symmetry, these amplitudes are related by the equations

$$A^{+-}/\sqrt{2} + A^{00} = A^{+0}, \qquad \overline{A}^{+-}/\sqrt{2} + \overline{A}^{00} = \overline{A}^{-0}, \tag{408}$$

which can be represented graphically in the form of "isospin triangles" (Fig. 81(c)). Neglecting electroweak penguins, $|A^{+0}| = |\overline{A}^{-0}|$ (evidence of direct *CP* violation in $B^\pm \to \pi^\pm\pi^0$ would show that such contributions cannot be neglected, and would be a signal for new physics contributions). If the (arbitrary) global phase of all A^{ij} amplitudes is chosen such that $A^{+0} = \overline{A}^{-0}$, it can be shown that the phase difference between A^{+-} and $\overline{A}^{+-}$ is 2δ. Note that the value of δ extracted in this manner carries an eightfold ambiguity. Moreover, the value of α that is obtained is insensitive to new physics effects, unless they violate isospin. In the $B \to \pi\pi$ system (as in the $B \to \rho\rho$ case, discussed below), knowledge of A^{00} and $\overline{A}^{00}$ is the limiting factor in the extraction of δ.

For $B \to \rho\rho$ decays, the same formalism applies separately to each helicity amplitude (where $CP = +1$ ($L = 0, 2$) and $CP = -1$ ($L = 1$)). Thus, the extraction of α requires knowledge of the polarization. In practise, the fraction of longitudinal polarization (f_L) is measured by fitting the ρ helicity angle distribution. The probability density function (PDF) used is

$$\frac{d^2N}{d\cos\theta_1\, d\cos\theta_2} = 4f_L\cos^2\theta_1\cos^2\theta_2 + (1-f_L)\sin^2\theta_1\sin^2\theta_2\,, \tag{409}$$

where θ_1 (θ_2) is the angle between the daughter π^0 and direction opposite the ρ^- (ρ^+) direction in the ρ^+ (ρ^-) rest frame (see Fig. 82). $B^0 \to \rho^+\rho^-$ is found to be almost purely $f_L = 1$, which implies that the *CP*-odd $L = 1$ component is negligible. This high polarization is fortunate, as it gives a larger *CP* asymmetry and thus greater sensitivity to α. (Conversely, the possibility to resolve some of the ambiguities in the solution for α from the interference between different helicity amplitudes is precluded.) Moreover, the contributions from penguin amplitudes (Fig. 81b) are found to be small for $B \to \rho\rho$, allowing a determination of α with small theoretical uncertainty.

A second complication in $B \to \rho\rho$ decays is that the final state ρ mesons have non-zero decay width, and thus their masses are not necessarily equal. As a consequence, Bose-Einstein symmetry no longer holds, and the $I = 1$ isospin state is allowed [1095]. In this case the isospin relations needed to extract α (Fig. 81c) do not hold. The problem can be studied by restricting the $\pi\pi$ invariant mass window used to select $\rho \to \pi\pi$ candidates

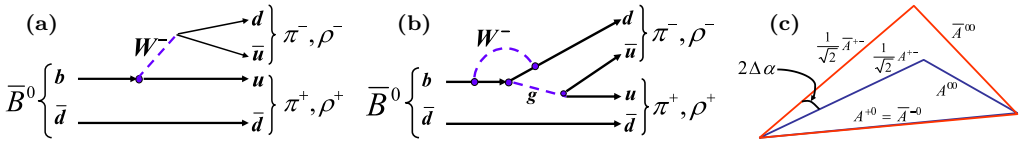

Fig. 81. (a) Tree and (b) gluonic-penguin contributions to $B^0 \to (\pi/\rho)^+(\pi/\rho)^-$. (c) London–Gronau isospin triangles for $B \to \pi\pi$, $B \to \rho\rho$ [37].

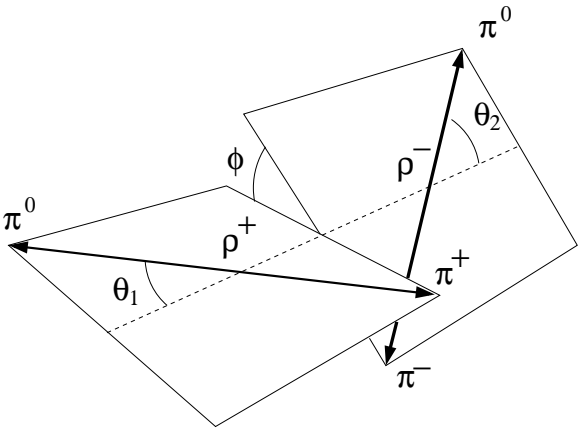

Fig. 82. Definition of helicity angles θ_1 and θ_2 used to fit for f_L, the fraction of longitudinal polarization.

to a narrow range and checking whether the fitted value of sin2α shifts. No such shift has been observed, and hence possible isospin violation is below the sensitivity of current measurements.

The decays $B^0 \to \rho^+\pi^-$, $B^0 \to \rho^-\pi^+$, and $B^0 \to \rho^0\pi^0$ (collectively referred to as $B^0 \to \rho\pi$) are also mediated by the $b \to u\bar{u}d$ transition, and thus the interference between $B^0 \to \rho\pi$ and $\overline{B}^0 \to \rho\pi$ is also sensitive to α. However, these modes have an advantage over $B \to \pi\pi$ and $B \to \rho\rho$ decays, as pointed out in Ref. [1096]: the three-body $\pi^+\pi^-\pi^0$ final state yields a Dalitz plot that can be analyzed to measure all three $B^0 \to (\rho\pi)^0$ modes simultaneously. The decay-time distributions of these three states allows one to resolve the penguin contribution and determine α with very little theoretical uncertainty and only a single unresolvable ambiguity ($\alpha \longrightarrow \alpha + \pi$). In addition, one can use the branching fractions for the charged modes $B^+ \to \rho^+\pi^0$ and $B^+ \to \rho^0\pi^+$ along with isospin relations to improve the determination of α [1097, 1098].

The Dalitz plot has a time dependence

$$|A(t, s_+, s_-)|^2 \;\propto\; e^{-\Gamma|t|}\Bigg\{ (|A_{3\pi}|^2 + |\overline{A}_{3\pi}|^2) \;- \\ q_{\rm tag}\cdot(|A_{3\pi}|^2 - |\overline{A}_{3\pi}|^2)\cos(\Delta m\,\Delta t) \;+ \\ q_{\rm tag}\cdot 2\cdot {\rm Im}\left(\frac{q}{p}A^*_{3\pi}\overline{A}_{3\pi}\right)\sin(\Delta m\,\Delta t)\Bigg\}, \qquad (410)$$

where $A_{3\pi} = \mathcal{A}(B^0 \to \pi\pi\pi)$, $\overline{A}_{3\pi} = \mathcal{A}(\overline{B}^0 \to \pi\pi\pi)$, $s_+ = (p_+ + p_0)^2$, $s_- = (p_- + p_0)^2$, and p_+, p_-, and p_0 are the four-momenta of the π^+, π^-, and π^0, respectively. The parameter $q_{\rm tag}$ equals $+1\,(-1)$ when the tag-side B decays as a $B^0(\overline{B}^0)$, and q/p is the ratio of complex coefficients relating the B^0 and $\overline{B}^0$ flavor eigenstates to the mass eigenstates.

The amplitudes $A_{3\pi}$ and $\overline{A}_{3\pi}$ are further decomposed into

$$A_{3\pi}(s_+, s_-) \;=\; f_+(s_+, s_-)\, A_+ + f_-(s_+, s_-)\, A_- + f_0(s_+, s_-)\, A_0 \qquad (411)$$

$$\left(\frac{q}{p}\right) \overline{A}_{3\pi}(s_+, s_-) \;=\; \bar{f}_+(s_+, s_-)\, \overline{A}_+ + \bar{f}_-(s_+, s_-)\, \overline{A}_- + \bar{f}_0(s_+, s_-)\, \overline{A}_0\,, \qquad (412)$$

where the subscript "+" represents $\rho^+\pi^-$, "−" is for $\rho^-\pi^+$, and "0" is for $\rho^0\pi^0$. The kinematic functions f_i and $\bar{f}_i$ are the products of Breit-Wigner functions to describe the $\pi\pi$ lineshape and an angular function to describe the helicity distribution. The goal of the analysis is to fit the time-dependence of the Dalitz plot to determine the six complex amplitudes A_i and $\overline{A}_i$; from these one determines α via the relationship

$$e^{i2\alpha} = \frac{\overline{A}_+ + \overline{A}_- + 2\overline{A}_0}{A_+ + A_- + 2A_0}\,. \qquad (413)$$

Note that the description of the $\pi\pi$ lineshape introduces some systematic error in the Dalitz plot analysis. This can be checked by changing the lineshape in within a reasonable range or by using an alternative SU(3)-based method to extract α that does not use the tails of $\pi\pi$ lineshapes [1099].

All the above methods use isospin to estimate the penguin pollution. They are thus theoretically limited by isospin breaking. While hard to compute these corrections are expected to be at the degree level, with the smallest impact expected in the $B \to \rho\pi$ extraction [1100–1102].

9.3.2. *Experimental measurements*

$\underline{B \to \pi\pi}$

High-quality separation of charged Kaons and pions is a distinctive experimental challenge in the $B^0 \to \pi^+\pi^-$ and $B^\pm \to \pi^\pm\pi^0$ analyses. Indeed, $\mathcal{B}(B^0 \to K^+\pi^-)/\mathcal{B}(B^0 \to \pi^+\pi^-) \approx 3.8$ and $\mathcal{B}(B^\pm \to K^\pm\pi^0)/\mathcal{B}(B^\pm \to \pi^\pm\pi^0) \approx 2.3$ [560], and the separation between the $K\pi$ and $\pi\pi$ candidates in the kinematic quantity ΔE at e^+e^- B-meson factories is only about 1.5σ. Both Belle and *BABAR* employ sophisticated likelihood-based pion-Kaon separation in the branching-fraction and *CP*-violation analyses in these modes. In addition to the B factories, the CDF experiment, thanks to its 1.4σ $\mathrm{d}E/\mathrm{d}x$-based Kaon-pion separation, aided by the invariant-mass separation of the $K^\pm\pi^\mp$ and $\pi^+\pi^-$ candidates, is able to provide a competitive measurement of the $\mathcal{B}(B^0 \to K^+\pi^-)/\mathcal{B}(B^0 \to \pi^+\pi^-)$ ratio, and thus of the less-well-known $\mathcal{B}(B^0 \to \pi^+\pi^-)$.

The most up-to-date measurements in the $B \to \pi\pi$ modes, along with the September 2008 HFAG averages, are quoted in Tab. 72. With the exception of $C_{\pi^0\pi^0}$, the sensitivities of the *BABAR* and Belle measurements are very similar. Plots of $B^0 \to \pi^+\pi^-$ Δt

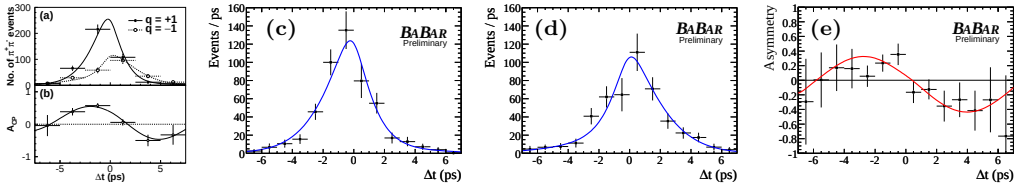

Fig. 83. (a) Distributions of Δt for B^0 ($q = +1$) and $\overline{B}^0$ ($q = -1$) tags and (b) their *CP*-violating asymmetry in $B^0 \to \pi^+\pi^-$ signal events reported by Belle [1105]. Distributions of Δt for (c) B^0 and (d) $\overline{B}^0$ tags and (e) their *CP*-violating asymmetry in $B^0 \to \pi^+\pi^-$ signal events reported by *BABAR* [1104].

Table 72
Branching fractions and *CP* asymmetries in $B \to \pi\pi$. First error is statistical and second systematic. Please note that Belle quotes $\mathcal{A} \equiv -C$. The April 2008 online update of the preliminary CDF result is $\mathcal{B}(\pi^+\pi^-) = (5.02 \pm 0.33 \pm 0.35) \times 10^{-6}$ [1103]. Values given in parentheses are the numbers of $B\overline{B}$ pairs in the datasets used in the analyses, where appropriate.

	BABAR	Belle	HFAG avg.
$S_{\pi\pi}$	$-0.68 \pm 0.10 \pm 0.03$ [1104] (467M)	$-0.61 \pm 0.10 \pm 0.04$ [1105] (535M)	-0.65 ± 0.07
$C_{\pi\pi}$	$-0.25 \pm 0.08 \pm 0.02$ [1104] (467M)	$-0.55 \pm 0.08 \pm 0.05$ [1105] (535M)	-0.38 ± 0.06
$\mathcal{B}(\pi^+\pi^-) \times 10^6$	$5.5 \pm 0.4 \pm 0.3$ [1106] (227M)	$5.1 \pm 0.2 \pm 0.2$ [1107] (449M)	5.16 ± 0.22
$\mathcal{B}(\pi^+\pi^0) \times 10^6$	$5.02 \pm 0.46 \pm 0.29$ [1108] (383M)	$6.5 \pm 0.4^{+0.4}_{-0.5}$ [1107] (449M)	$5.59^{+0.41}_{-0.40}$
$\mathcal{A}(\pi^+\pi^0)$	$0.030 \pm 0.039 \pm 0.010$ [1108] (383M)	$0.07 \pm 0.03 \pm 0.01$ [1109] (535M)	0.050 ± 0.025
$\mathcal{B}(\pi^0\pi^0) \times 10^6$	$1.83 \pm 0.21 \pm 0.13$ [1104] (467M)	$1.1 \pm 0.3 \pm 0.1$ [1110] (535M)	1.55 ± 0.19
$C_{\pi^0\pi^0}$	$-0.43 \pm 0.26 \pm 0.05$ [1104] (467M)	$-0.44^{+0.62\ +0.06}_{-0.73\ -0.04}$ [1110] (535M)	$-0.43^{+0.24}_{-0.25}$

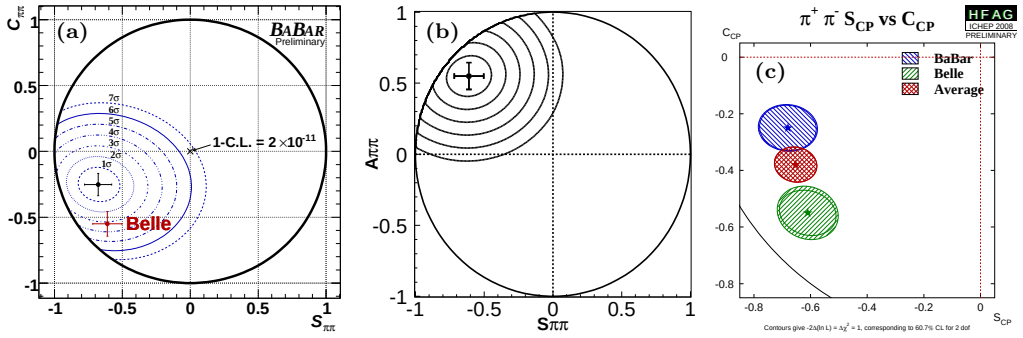

Fig. 84. $S_{\pi\pi}$ and $C_{\pi\pi} \equiv -\mathcal{A}_{\pi\pi}$ in $B^0 \to \pi^+\pi^-$: central values, uncertainties, and confidence-level (C.L.) contours for $1 - \text{C.L.} = 0.317$ (1σ), 4.55×10^{-2} (2σ), 2.70×10^{-3} (3σ), 6.33×10^{-5} (4σ), 5.73×10^{-7} (5σ), 1.97×10^{-9} (6σ) and 2.56×10^{-12} (7σ): (a) *BABAR* [1104], (b) Belle [1105]. (c) *BABAR* and Belle $\Delta\chi^2 = 1$ ($S_{\pi\pi}$, $C_{\pi\pi}$) contours, corresponding to 60.7% C.L., and their HFAG correlated average. *BABAR* and Belle results are consistent at 0.055 (1.9σ) C.L.

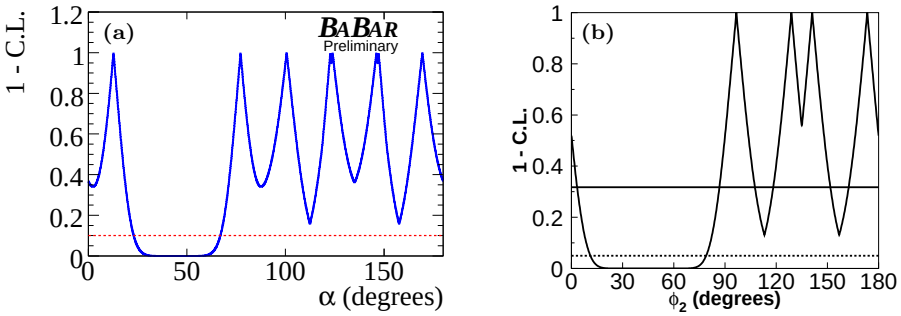

Fig. 85. Constraints on the CKM angle α: (a) from *BABAR* [1104] using only the $B \to \pi\pi$ results from *BABAR*; (b) from Belle [1105], using Belle's measurements of $S_{\pi^+\pi^-}$ and $C_{\pi^+\pi^-}$ and the Summer 2006 HFAG world averages for the branching fractions and *CP*-violating asymmetries in $B^+ \to \pi^+\pi^0$ and $B^0 \to \pi^0\pi^0$.

distributions for the B^0 and $\overline{B}^0$ tags and their *CP*-violating asymmetries are shown in Fig. 83, and the ($S_{\pi\pi}$, $C_{\pi\pi}$) confidence-level contours are shown in Fig. 84. Interpretation of the latest *BABAR* and Belle $B \to \pi\pi$ results in terms of constraints on the angle α is shown in Fig. 85. Only the isospin-triangle relations are used in these constraints. Values of α near 0 or π can be excluded with additional physics input [1108, 1111]. The key point is that the isospin analysis requires no knowledge about either the magnitude or phase of the penguin contribution. However, using CKM unitarity the relative phase between penguin and tree can be chosen to be α, so that the direct CP violation parameter $C_{\pi\pi} \propto \alpha$. Consequently, the observation $C_{\pi\pi} \neq 0$ requires $\alpha \neq 0$ (or alternatively hadronic parameters must unphysically tend to infinity).

Both Belle and *BABAR* observe a non-zero *CP*-violating asymmetry $S_{\pi\pi}$ in the time distribution of $B^0 \to \pi^+\pi^-$ decays, with significances of 5.3σ and 6.3σ, respectively. Belle observes, with a significance of 5.5σ, direct *CP* violation ($C_{\pi\pi} \neq 0$) in $B^0 \to \pi^+\pi^-$; *BABAR* sees 3.0σ evidence of $C_{\pi\pi} \neq 0$.

$\underline{B \to \rho\rho}$

The decay $B^0 \to \rho^+\rho^-$ has been measured by Belle and *BABAR* several times with increasingly larger data samples. Both experiments measure the branching fraction, f_L, and the *CP*-violating parameters $A_{\rho\rho}$ and $S_{\rho\rho}$. The most recent results are listed in Tab. 73. The measured values of $A_{\rho\rho}$ and $S_{\rho\rho}$ are consistent with zero, i.e., there is no evidence for *CP* violation. The decay-time distributions and *CP* asymmetry distribution (A_{CP} in bins of Δt) are shown in Figs. 86 and 87. From the same analysis, Belle has also set a limit on the nonresonant $B^0 \to \rho^0\pi^+\pi^-$ contribution at $\Gamma(\rho^\pm\pi^\mp\pi^0)/\Gamma(\rho^+\rho^-) = 0.063 \pm 0.067$.

Table 73
Belle and *BABAR* results for $B^0 \to \rho^+\rho^-$ decays [1112–1114].

	Data (fb^{-1})	Branching fraction $\times 10^{-6}$	f_L	$A_{\rho\rho}$	$S_{\rho\rho}$
Belle	253/492	$22.8 \pm 3.8^{+2.3}_{-2.6}$	$0.941^{+0.034}_{-0.040} \pm 0.030$	$0.16 \pm 0.21 \pm 0.08$	$0.19 \pm 0.30 \pm 0.08$
BABAR	349	$25.5 \pm 2.1^{+3.6}_{-3.9}$	$0.992 \pm 0.024^{+0.026}_{-0.013}$	$-0.01 \pm 0.15 \pm 0.06$	$-0.17 \pm 0.20^{+0.05}_{-0.06}$

The most recent results from Belle [1115] and *BABAR* [1116] on the decay $B^+ \to \rho^+\rho^0$ are listed in Tab. 74. Both measured values of A_{CP} are consistent with zero, implying that a possible electroweak penguin contribution is small. Belle has also set a limit on the nonresonant $B^+ \to (\rho\pi\pi)^+$ contribution of $\Gamma[(\rho\pi\pi)^+]/\Gamma(\rho^+\rho^0) < 0.17$ at 90% C.L.

Table 74
Belle and *BABAR* results for $B^+ \to \rho^+\rho^0$ decays, from Refs. [1115, 1116].

	Data (fb^{-1})	Branching fraction $\times 10^{-6}$	f_L	A_{CP}
Belle	78	$31.7 \pm 7.1^{+3.8}_{-6.7}$	$0.95 \pm 0.11 \pm 0.02$	$-0.12 \pm 0.13 \pm 0.10$
BABAR	211	$16.8 \pm 2.2 \pm 2.3$	$0.905 \pm 0.042^{+0.023}_{-0.027}$	$0.00 \pm 0.22 \pm 0.03$

The decay $B^0 \to \rho^0\rho^0$ has proved difficult to measure due to its small branching fraction, and has only recently been observed. Measurements from *BABAR* [1117] and

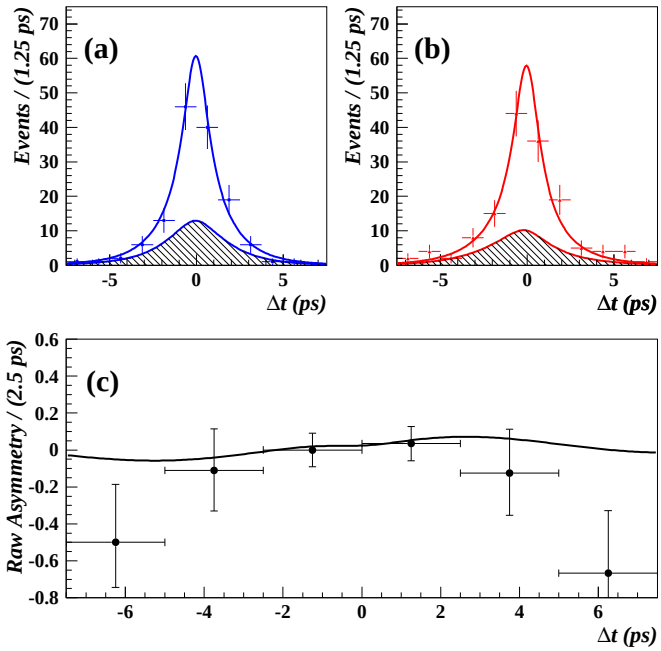

Fig. 86. Decay time distributions from Belle [1112]. *(a)* $\overline{B}^0 \to \rho^+\rho^-$ decays *(b)* $B^0 \to \rho^+\rho^-$ decays, and *(c)* the raw asymmetry $(\overline{N} - N)/(\overline{N} + N)$, where $\overline{N}$ (N) is the number of $\overline{B}^0$ (B^0) candidates including background. The hatched region shows the fit result for the signal component, and the solid curve shows the fit result for the total.

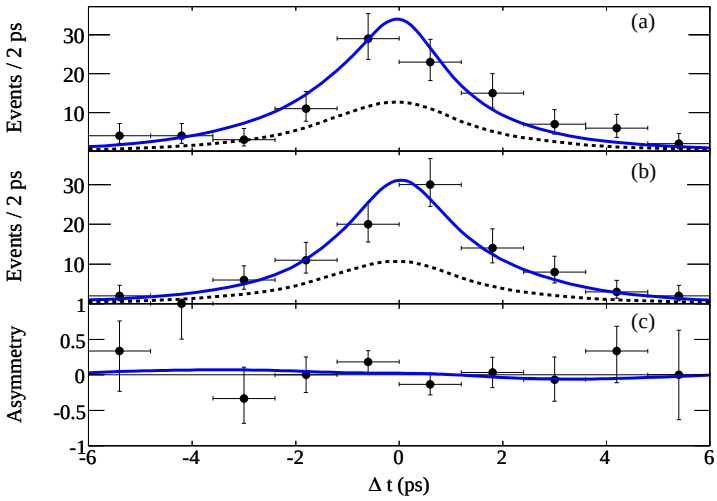

Fig. 87. Decay time distributions from *BABAR* [1113]. *(a)* $\overline{B}^0 \to \rho^+\rho^-$ decays *(b)* $B^0 \to \rho^+\rho^-$ decays, and *(c)* the asymmetry $(\overline{N} - N)/(\overline{N} + N)$, where $\overline{N}$ (N) is the number of signal $\overline{B}^0 \to \rho^+\rho^-$ $(B^0 \to \rho^+\rho^-)$ decays. The dashed curve shows the fit result for all backgrounds, and the solid curve shows the fit result for the total.

Belle [1118] are listed in Tab. 75. Both experiments obtain the signal yield from unbinned maximum likelihood fits to M_{bc} (or $m_{\rm ES} \equiv M_{bc}$), ΔE, and $M_{\pi\pi}$. The fit is complicated by possible contributions from $\rho^0 f_0(980)$, $f_0 f_0$, $f_0\pi^+\pi^-$, and $a_1\pi$ final states, as well as from $B^0 \to \rho^0\pi^+\pi^-$ and $B^0 \to \pi^+\pi^-\pi^+\pi^-$.

The *BABAR* experiment requires that $M_{\pi\pi} \in (0.50, 1.05)\,{\rm GeV}/c^2$; they subsequently fit to variables $m_{\rm ES}$, ΔE, helicity angles $\cos\theta_1$, $\cos\theta_2$, and the decay time difference Δt. Including the helicity angles in the fit yields a measurement of f_L, and including Δt yields a measurement of $A_{\rho\rho}$ and $S_{\rho\rho}$. *BABAR* observes an excess of signal events with 3.1σ significance, and no significant nonresonant contributions. The measured values of $A_{\rho\rho}$ and $S_{\rho\rho}$ are consistent with zero, i.e., there is no evidence for *CP* violation.

The Belle experiment requires $M_{\pi\pi} \in (0.55, 1.70)\,{\rm GeV}/c^2$– a wider window than that used by *BABAR* (see Fig. 88). Belle observes a higher rate of nonresonant $\rho\pi\pi$ and 4π components than *BABAR* does, and the significance of Belle's $\rho^0\rho^0$ signal is only 1.0σ.

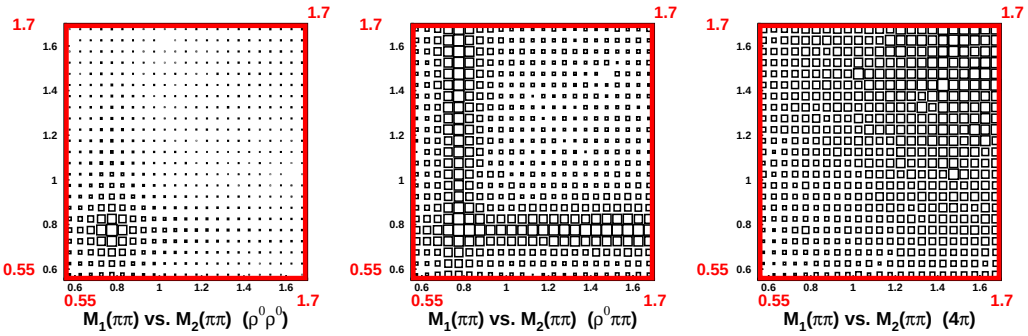

Fig. 88. Monte Carlo simulated $M_{\pi\pi}$ distributions for *(a)* $B^0 \to \rho^0\rho^0$, *(b)* $B^0 \to \rho^0\pi^+\pi^-$, and *(b)* $B^0 \to \pi^+\pi^-\pi^+\pi^-$ decays, from Belle. The plots are symmetrized by randomly choosing the mass combination plotted against the horizontal axis. The fitted region for Belle is $M_{\pi\pi} \in (0.55, 1.70)\,{\rm GeV}/c^2$, whereas that for *BABAR* is $M_{\pi\pi} \in (0.55, 1.05)\,{\rm GeV}/c^2$.

Table 75
Belle and *BABAR* results for $B^0 \to \rho^0\rho^0$ decays [1117, 1118].

Mode	Branching fraction (10^{-6})	f_L	$A_{\rho\rho}$	$S_{\rho\rho}$
		Belle ($605\,{\rm fb}^{-1}$)		
$\rho^0\rho^0$	$0.4 \pm 0.4\,^{+0.2}_{-0.3}$	–	–	–
$\rho^0\pi^+\pi^-$	$5.9\,^{+3.5}_{-3.4} \pm 2.7$	–	–	–
$\pi^+\pi^-\pi^+\pi^-$	$12.4\,^{+4.7\,+2.1}_{-4.6\,-1.9}$	–	–	–
		BABAR ($423\ {\rm fb}^{-1}$)		
$\rho^0\rho^0$	$0.92 \pm 0.32 \pm 0.14$	$0.75\,^{+0.11}_{-0.14} \pm 0.05$	$-0.2 \pm 0.8 \pm 0.3$	$0.3 \pm 0.7 \pm 0.2$
$\rho^0\pi^+\pi^-$	$-1.6\,^{+5.0}_{-4.5} \pm 2.2$	–	–	–
$\pi^+\pi^-\pi^+\pi^-$	$3.0\,^{+11.6}_{-9.9} \pm 4.1$	–	–	–

Both Belle and *BABAR* constrain α using isospin analysis [37]. The fitted observables are the branching fractions and fractions of longitudinal polarization for $B^+ \to \rho^+\rho^0$, $B^0 \to \rho^+\rho^-$, and $B^0 \to \rho^0\rho^0$, the coefficients $A_{\rho\rho}$ and $S_{\rho\rho}$ for $B^0 \to \rho^+\rho^-$ decays, and $A_{\rho\rho}$ for $B^0 \to \rho^0\rho^0$ decays. The fitted parameters are the magnitudes $|\mathcal{A}(B^0 \to \rho^+\rho^0)|$, $|\mathcal{A}(B^0 \to \rho^+\rho^-)|$, and $|\mathcal{A}(B^0 \to \rho^0\rho^0)|$, the average phase of, and phase difference between, amplitudes $\mathcal{A}(B^0 \to \rho^+\rho^-)$ and $\mathcal{A}(\overline{B}^0 \to \rho^+\rho^-)$, and α. To obtain a confidence interval for α, the experiments scan values of α and, for each value, fit the measured observables. The resulting χ^2 is input into the cumulative χ^2 distribution to obtain a confidence level (p-value) for that value of α. Plotting this confidence level (C.L.) versus α allows one to read off a confidence interval.

The most recent Belle result [1118], obtained using world average values [560] for all observables except $B(B^0 \to \rho^0\rho^0)$ for which only the Belle result is used, is shown in Fig. 89 (top). The "flat-top" region results from the fact that no measurement of $A_{\rho\rho}$ for $B^0 \to \rho^0\rho^0$ decays is used. From the plot one reads off three disjoint 68.3% C.L. intervals; the interval consistent with unitarity ($\alpha + \beta + \gamma = 180^\circ$) is $(75.8, 106.2)^\circ$. Requiring symmetric errors gives $\alpha = (91.7 \pm 14.9)^\circ$.

The most recent *BABAR* result [1117], made using *BABAR* results exclusively, is shown in Fig. 89 (bottom). The dotted contour is the nominal solution; however, including in the fit the parameter $S_{\rho\rho}$ from $B^0 \to \rho^0\rho^0$ decays reduces the four-fold ambiguity for α to three solutions (solid contour). The final result is expressed in terms of the shift $\delta \equiv \alpha - \alpha_{\rm eff}$ that results from the penguin contribution (recall that $S_{\rho\rho} = -\sqrt{1 - A^2_{\rho\rho}}\,\sin 2\alpha_{\rm eff}$, see Eq. 407). The upper limit is $|\delta| < 17.6^\circ$ at 90% C.L.

$\underline{B^0 \to \rho\pi}$

The time-dependent Dalitz plot analysis of $B^0 \to \pi^+\pi^-\pi^0$ has been performed by *BABAR* using $346\,\text{fb}^{-1}$ of data [1119] and by Belle using $414\,\text{fb}^{-1}$ [1120]. In principle, one inserts the parametrization (411) and (412) into (410) to obtain the PDF for fitting. However, the resulting PDF is nonlinear in the amplitudes A_i and $\overline{A}_i$, and the fit is not well-behaved for current statistics. To stabilize the fit, one defines new fitting parameters [1121]

$$U_i^\pm = |A_i|^2 \pm |\overline{A}_i|^2 \tag{414}$$

$$U_{ij}^\pm = A_i\,A_j^* \pm \overline{A}_i\,\overline{A}_j^* \tag{415}$$

$$I_i = \text{Im}(\overline{A}_i\,A_i^*) \tag{416}$$

$$\text{Re}(I_{ij}) = \text{Re}(\overline{A}_i\,A_j^* - \overline{A}_j\,A_i^*) \tag{417}$$

$$\text{Im}(I_{ij}) = \text{Im}(\overline{A}_i\,A_j^* + \overline{A}_j\,A_i^*)\,. \tag{418}$$

Eqs. (414)-(418) define 27 real parameters from six complex amplitudes, and thus these parameters are not all independent. The overall normalization is fixed by setting $U_+^+ = 1$, and then there are 26 free parameters in the fit. The fit results for *BABAR* and Belle are listed in Tab. 76.

To constrain α, a χ^2 fit is performed to the 27 measured observables listed in Tab. 76. The χ^2 statistic takes into account all correlations between the observables. There are in principle 12 free parameters in the fit, corresponding to the six complex amplitudes A_i and $\overline{A}_i$. However, the additional parameter α is included along with the (complex) isospin

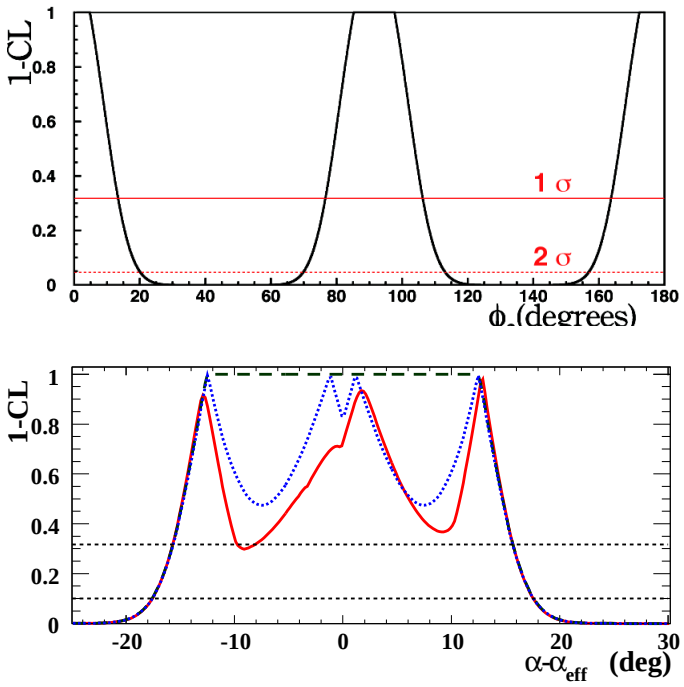

Fig. 89. Plot of $1-CL$ versus α from Belle [1118] (top), and $1-CL$ versus $\alpha - \alpha_{\rm eff}$ from *BABAR* [1117] (bottom). From these plots one reads off confidence intervals. In the top plot, the flat-top region results from not using $A_{\rho\rho}$ from $B^0 \to \rho^0\rho^0$ in the fit; in the bottom plot, the solid curve results from using both $A_{\rho\rho}$ and $S_{\rho\rho}$ from $B^0 \to \rho^0\rho^0$.

relation (413); together these reduce the number of free parameters to 11. The constraint $U_+^+ = 1$ fixes the overall normalization, and a global phase factor can be neglected; thus the final number of free parameters is nine. A scan is performed over values of α, where for each value the other eight parameters are floated in order to minimize the χ^2. The resulting change in the χ^2 from the minimum value is converted into a confidence level (CL) either by using the cumulative χ^2 distribution for one degree of freedom, or by finding the p-value from an ensemble of toy MC experiments.

The resulting plots of $1-CL$ versus α for *BABAR* and Belle are shown in Fig. 90. The values of α that have $(1-CL) > 0.317$ determine 1σ confidence intervals for α. As can be seen from the plots, the $1-CL$ contour has large variations that result in multiple regions, i.e., non-simply-connected intervals. Typically, the experiments quote only the interval consistent with unitarity. Belle obtains a second $1-CL$ contour by including additional observables: the branching fractions for $B^0 \to \rho^+\pi^-$, $\rho^-\pi^+$, $\rho^0\pi^0$ obtained from their analysis, and world average values [560] for the branching fractions and CP asymmetries measured for the charged modes $B^\pm \to \rho^\pm\pi^0$ and $B^\pm \to \rho^0\pi^\pm$. With these four new observables, two additional isospin relations are used; the final number of parameters floated in the fit is 12. The resulting $1-CL$ contour is also shown in Fig. 90. The final result from *BABAR* is $\alpha = (87^{+45}_{-13})^\circ$, whereas the final result from Belle is $\alpha \in (68^\circ, 95^\circ)$ at 68.3% CL.

Table 76
Fit results for the U and I coefficients from Refs. [1119] (*BABAR*) and [1120] (Belle). The first error listed is statistical, and the second is systematic.

Parameter	*BABAR*	Belle
U_+^+	1.0 (fixed)	+1 (fixed)
U_-^+	$1.32 \pm 0.12 \pm 0.05$	$+1.27 \pm 0.13 \pm 0.09$
U_0^+	$0.28 \pm 0.07 \pm 0.04$	$+0.29 \pm 0.05 \pm 0.04$
$U_{+-}^{+,\mathrm{Re}}$	$0.17 \pm 0.49 \pm 0.31$	$+0.49 \pm 0.86 \pm 0.52$
$U_{+0}^{+,\mathrm{Re}}$	$-1.08 \pm 0.48 \pm 0.20$	$+0.29 \pm 0.50 \pm 0.35$
$U_{-0}^{+,\mathrm{Re}}$	$-0.36 \pm 0.38 \pm 0.08$	$+0.25 \pm 0.60 \pm 0.33$
$U_{+-}^{+,\mathrm{Im}}$	$-0.07 \pm 0.71 \pm 0.73$	$+1.18 \pm 0.86 \pm 0.34$
$U_{+0}^{+,\mathrm{Im}}$	$-0.16 \pm 0.57 \pm 0.14$	$-0.57 \pm 0.35 \pm 0.51$
$U_{-0}^{+,\mathrm{Im}}$	$-0.17 \pm 0.50 \pm 0.23$	$-1.34 \pm 0.60 \pm 0.47$
U_+^-	$0.54 \pm 0.15 \pm 0.05$	$+0.23 \pm 0.15 \pm 0.07$
U_-^-	$-0.32 \pm 0.14 \pm 0.05$	$-0.62 \pm 0.16 \pm 0.08$
U_0^-	$-0.03 \pm 0.11 \pm 0.09$	$+0.15 \pm 0.11 \pm 0.08$
$U_{+-}^{-,\mathrm{Re}}$	$2.23 \pm 1.00 \pm 0.43$	$-1.18 \pm 1.61 \pm 0.72$
$U_{+0}^{-,\mathrm{Re}}$	$-0.18 \pm 0.88 \pm 0.35$	$-2.37 \pm 1.36 \pm 0.60$
$U_{-0}^{-,\mathrm{Re}}$	$-0.63 \pm 0.72 \pm 0.32$	$-0.53 \pm 1.44 \pm 0.65$
$U_{+-}^{-,\mathrm{Im}}$	$-0.38 \pm 1.06 \pm 0.36$	$-2.32 \pm 1.74 \pm 0.91$
$U_{+0}^{-,\mathrm{Im}}$	$-1.66 \pm 0.94 \pm 0.25$	$-0.41 \pm 1.00 \pm 0.47$
$U_{-0}^{-,\mathrm{Im}}$	$0.12 \pm 0.75 \pm 0.22$	$-0.02 \pm 1.31 \pm 0.83$
I_+	$-0.02 \pm 0.10 \pm 0.03$	$-0.01 \pm 0.11 \pm 0.04$
I_-	$-0.01 \pm 0.10 \pm 0.02$	$+0.09 \pm 0.10 \pm 0.04$
I_0	$0.01 \pm 0.06 \pm 0.01$	$+0.02 \pm 0.09 \pm 0.05$
I_{+-}^{Re}	$1.90 \pm 2.03 \pm 0.65$	$+1.21 \pm 2.59 \pm 0.98$
I_{+0}^{Re}	$0.41 \pm 1.30 \pm 0.41$	$+1.15 \pm 2.26 \pm 0.92$
I_{-0}^{Re}	$0.41 \pm 1.30 \pm 0.21$	$-0.92 \pm 1.34 \pm 0.80$
I_{+-}^{Im}	$-1.99 \pm 1.25 \pm 0.34$	$-1.93 \pm 2.39 \pm 0.89$
I_{+0}^{Im}	$-0.21 \pm 1.06 \pm 0.25$	$-0.40 \pm 1.86 \pm 0.85$
I_{-0}^{Im}	$1.23 \pm 1.07 \pm 0.29$	$-2.03 \pm 1.62 \pm 0.81$

$B^0 \to a_1^\pm \pi^\mp$

As proposed by Gronau and Zupan [1122], the Δt distribution for $B^0 \to a_1^\pm \pi^\mp$ decays can be fit to determine α. However, there can be a penguin amplitude that substantially shifts the measured α value from the true value, as found for $B \to \pi\pi$ decays. Thus, to determine α from $B^0 \to a_1^\pm \pi^\mp$ requires external input, e.g., assuming $SU(3)$ symmetry and using measurements of $B \to a_1 K$ [1123] and $B^0 \to K_{1A}\pi$ [1124] decays. This method has uncertainties arising from $SU(3)$-breaking corrections and unknown decay constants f_{a_1} and f_{K_1}.

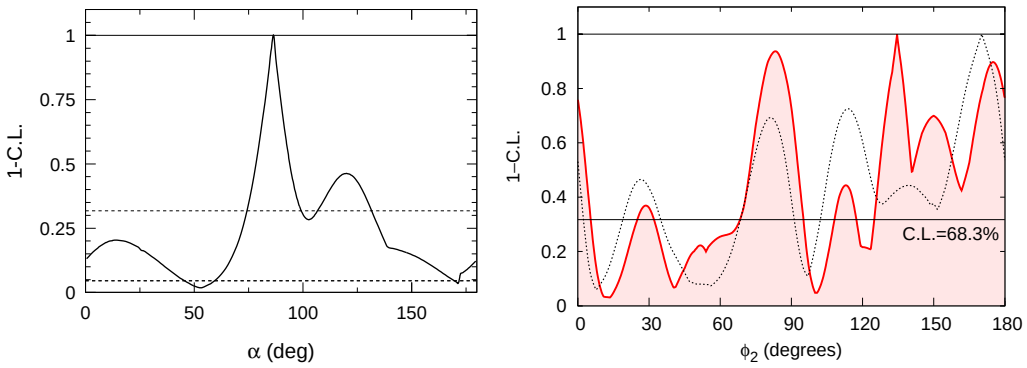

Fig. 90. $1 - CL$ versus α resulting from χ^2 fits to the 27 observables listed in Tab. 76. The left plot is from *BABAR* [1119], and the right plot is from Belle [1120]. The horizontal line at $1 - CL = 0.317$ corresponds to 68.3% CL and is used to determine 1σ confidence intervals for α. For Belle, the dashed contour corresponds to a nine-parameter fit, and the solid contour corresponds to a twelve parameter fit (see text).

Experimentally, one simultaneously fits the four distributions $B^0 \to a_1^\pm \pi^\mp$ and $\overline{B}^0 \to a_1^\pm \pi^\mp$ to the PDF

$$\frac{dN(a_1^\pm \pi^\mp)}{d\Delta t} = (1 \pm \mathcal{A}_{CP}) \frac{e^{-|\Delta t|/\tau}}{8\tau} \times \left\{ 1 - q_{\rm tag} \Big[(C \pm \Delta C) \cos(\Delta m\, \Delta t) - (S \pm \Delta S) \sin(\Delta m\, \Delta t) \Big] \right\}, \tag{419}$$

where $q_{\rm tag} = +1\,(-1)$ when the tag-side B decays as a $B^0\,(\overline{B}^0)$. The parameters $\mathcal{A}_{CP}$, C, and S are *CP*-violating, and the parameters ΔC and ΔS are *CP*-conserving. *BABAR* has performed this fit using $349\,\text{fb}^{-1}$ of data [1125]; the results are listed in Tab. 77. The values obtained are subsequently used to determine $\alpha_{\rm eff} = \alpha - \delta$ within a four-fold ambiguity. The solution closest to the α value favored by $B \to \rho\rho$ and $B \to \pi\pi$ decays is $\alpha_{\rm eff} = (78.6 \pm 7.3)^\circ$. This result differs from α by the unknown penguin contribution δ.

Table 77
BABAR results for $B^0 \to a_1^\pm \pi^\mp$ decays, from Ref. [1125].

Parameter	Value
$\mathcal{A}_{CP}$	$-0.07 \pm 0.07 \pm 0.02$
C	$-0.10 \pm 0.15 \pm 0.09$
S	$0.37 \pm 0.21 \pm 0.07$
ΔC	$0.26 \pm 0.15 \pm 0.07$
ΔS	$-0.14 \pm 0.21 \pm 0.06$

9.4. *Measurements of γ in charmless hadronic B decays*

In this subsection we review the methods to determine the weak phase in the CKM matrix using $\Delta S = 1$ charmless hadronic B decays: $B \to K\pi$, $B \to K\pi\pi$. Conventionally this is rewritten as a constraint on γ, but in many instances it also involves the knowledge of the $B^0\overline{B}^0$ mixing phase. This is taken to be well known as it is measured precisely in $B^0 \to J/\psi K^0_S$. The $B \to K\pi$ and $B \to K\pi\pi$ decays are dominated by QCD penguins and are as such sensitive to new physics effects from virtual corrections entering at 1-loop. Comparing the extracted value of γ with that from a tree level determination using $B \to DK$ constitutes a test of Standard Model.

9.4.1. *Constraints from $B_{(s)} \to hh$*

We can write any amplitude as a sum of two terms

$$A(B \to f) = Pe^{i\delta_P} + Te^{i\gamma}e^{i\delta_T}, \tag{420}$$

where the "penguin" P carries only a strong phase δ_P, while the "tree" T has both strong phase δ_T and a weak phase γ. The latter flips signs for the *CP* conjugated amplitude $A(\overline{B} \to \bar{f})$). The sensitivity to γ comes from the interference of the two contributions. In $\Delta S = 1$ decays the tree contribution is doubly CKM suppressed — it carries the CKM factor $|V^*_{ub}V_{us}|$ – while the penguin contribution has a CKM factor $|V^*_{cb}V_{cs}|$ that is $\sim 1/\lambda^2$ times larger. We can thus expand in T/P, which gives for the direct *CP* asymmetry and branching fraction respectively

$$\begin{aligned} A_{CP} &= 2\frac{T}{P}\sin(\delta_P - \delta_T)\sin\gamma + O\Big(\Big(\frac{T}{P}\Big)^2\Big), \\ \mathcal{B} &= P^2\Big[1 + 2\frac{T}{P}\cos(\delta_P - \delta_T)\cos\gamma + O\Big(\Big(\frac{T}{P}\Big)^2\Big)\Big]. \end{aligned} \tag{421}$$

Using the above expression for $\mathcal{B}(B^0 \to K^+\pi^-)$ one can get a very simple geometric bound on γ, if P is known. Obtaining P from $\mathcal{B}(B^+ \to \pi^+K^0)$ — neglecting very small color suppressed electroweak penguins — one has $|\cos\gamma| > \sqrt{1-R}$ valid for $R < 1$ [1126, 1127] (R is defined in Eq. 422 below). At present this gives $\gamma < 77^\circ$ at 1σ.

The extraction of γ requires more theoretical input. One needs to determine the strong phase difference $\delta_P - \delta_T$ and the ratio T/P. This can be achieved either by relating T/P to $\Delta S = 0$ decays using SU(3) [1077, 1128–1137] or by using the $1/m_b$ expansion and factorization theorems to calculate the T/P ratio [40, 51, 52, 1040, 1056, 1138].

The methods that use SU(3) flavor symmetries exploit the fact that $\Delta S = 0$ decays such as $B \to \pi\pi$ are tree dominated. The CKM factors multiplying the "tree" ($V^*_{ub}V_{ud}$) and "penguin" terms ($V^*_{cb}V_{cd}$) are of comparable size (unlike $\Delta S = 1$ decays where the "tree" is CKM suppressed). From these decays one can then determine the size of T/P and feed it into $\Delta S = 1$ decays to extract γ. In doing this quite often some $1/m_b$ suppressed annihilation or exchange amplitudes need to be neglected. These methods are hard to improve systematically, while already at present the determined value of γ is dominated by theoretical errors due to SU(3) breaking and the neglected amplitudes. These were estimated to be of order $8^\circ - 10^\circ$ in [1132] for the extraction of γ from $B \to \pi\pi$ and $B \to \pi K$. Some improvement can be expected, if one does not need to neglect annihilation amplitudes but rely only on flavor symmetry. One interesting method of this type uses $B_s \to K^+K^-$ and $B \to \pi^+\pi^-$ decays [1137, 1139]. In this analysis, the

theoretical error on the extracted value of γ due to SU(3) breaking was estimated to be of the order of 5° [1136]. This is a promising avenue of investigation for the LHCb experiment.

If instead of extracting γ the goal is to make a precision test of the Standard Model, one can rather take as an input the value of γ determined from $B \to DK$ or from global fits. A theoretically clean prediction of $S_{K^0_S\pi^0}$ is then possible using isospin relations, while theoretical calculations based on the $1/m_b$ expansion are used only for SU(3) breaking terms [1078] (see also [1079]).

If the $1/m_b$ expansion is used to determine γ, a number of different observables can be used, since in principle all the observables are now calculable. At present in the $1/m_b$ expansion calculations γ is taken as an input, but it could of course be extracted from data instead. Different groups treat differently various terms in the expansion, for instance expanding or not expanding in $\alpha_S(\sqrt{\Lambda m_b})$, including different $1/m_b$ suppressed terms in the expansion, etc., and this may lead to slightly different extracted values of γ (but the estimated theoretical errors should account for the differences). The important point is that the expansion is systematically improvable so that the errors could at least in principle be reduced in the future. For instance, the theoretical errors on the value of γ extracted from $S_{\rho\pi}$ are about 5° and about 10° if extracted from $S_{\pi\pi}$ [1040]. Much larger errors can be expected for γ extracted from $\Delta S = 1$ decays, since the interference is CKM suppressed.

As an example let us consider the ratios

$$R = \frac{\mathcal{B}(B^0 \to \pi^\mp K^\pm)\tau_{B^+}}{\mathcal{B}(B^\pm \to \pi^\pm K^0)\tau_{B^0}}, \quad R_c = \frac{2\mathcal{B}(B^\pm \to \pi^0 K^\pm)}{\mathcal{B}(B^\pm \to \pi^\pm K^0)}, \quad R_n = \frac{\mathcal{B}(B^0 \to \pi^\mp K^\pm)}{2\mathcal{B}(B^0 \to \pi^0 K^0)}, \quad (422)$$

for which part of the theoretical and experimental uncertainties cancel [1140]. Tab. 78 summarizes the current experimental measurements of the $B \to K\pi$ branching fractions and *CP* asymmetries [560, 1104, 1106–1108, 1141, 1142], while $\tau_{B^+}/\tau_{B^0} = 1.073 \pm 0.008$ [560]. In Tab. 78 we also quote the resulting world averages for the ratios, ignoring the correlations between the individual branching fraction measurements. These translate into the following bounds on γ at 68% confidence level [1056]

$$R \Rightarrow 55° < \gamma < 95°, \qquad R_c \Rightarrow 55° < \gamma < 80°, \qquad R_n \Rightarrow 40° < \gamma < 75°. \quad (423)$$

The measurements of B_s decays to two light hadrons can provide further constraints on γ [1133]. Following its earlier discovery of $B_s \to K^+K^-$ [1143], the CDF collaboration has recently produced updated measurements of the branching fraction and *CP* asymmetry of the decay $B_s \to K^-\pi^+$ [1144, 1145]:

$$\mathcal{B}(B_s \to K^-\pi^+) = (5.0 \pm 0.7 \pm 0.8) \times 10^{-6}\,, \quad (424)$$

$$A_{CP}(B_s \to K^-\pi^+) = (39 \pm 15 \pm 8)\%\,. \quad (425)$$

It has been recently pointed out that these results have implications for SU(3) and QCD factorization [1146], which prefer a larger value of the branching fraction for the Standard Model value of γ.

9.4.2. *Constraints from $B \to K\pi\pi$ Dalitz-plot analyses*

Three-body decays have an added benefit that quasi-two-body decays such as $B \to K^*\pi$ and $B \to K\rho$ can interfere through the same final $K\pi\pi$ state. Measuring the

Table 78
Summary of $B \to K\pi$ experimental measurements.

Quantity	BaBar Value	Belle Value	World Average Value
$\mathcal{B}(B^\pm \to \pi^\pm K^0)$	$(23.9 \pm 1.1 \pm 1.0) \times 10^{-6}$	$(22.8\,^{+0.8}_{-0.7} \pm 1.3) \times 10^{-6}$	$(23.1 \pm 1.0) \times 10^{-6}$
$\mathcal{B}(B^\pm \to \pi^0 K^\pm)$	$(13.6 \pm 0.6 \pm 0.7) \times 10^{-6}$	$(12.4 \pm 0.5 \pm 0.6) \times 10^{-6}$	$(12.9 \pm 0.6) \times 10^{-6}$
$\mathcal{B}(B^0 \to \pi^\mp K^\pm)$	$(19.1 \pm 0.6 \pm 0.6) \times 10^{-6}$	$(19.9 \pm 0.4 \pm 0.8) \times 10^{-6}$	$(19.4 \pm 0.6) \times 10^{-6}$
$\mathcal{B}(B^0 \to \pi^0 K^0)$	$(10.1 \pm 0.6 \pm 0.4) \times 10^{-6}$	$(9.7 \pm 0.7\,^{+0.6}_{-0.7}) \times 10^{-6}$	$(9.8 \pm 0.6) \times 10^{-6}$
$A_{CP}(B^\pm \to \pi^\pm K^0)$	$(-2.9 \pm 3.9 \pm 1.0)\%$	$(+3 \pm 3 \pm 1)\%$	$(+0.9 \pm 2.5)\%$
$A_{CP}(B^\pm \to \pi^0 K^\pm)$	$(+3.0 \pm 3.9 \pm 1.0)\%$	$(+7 \pm 3 \pm 1)\%$	$(+5.0 \pm 2.5)\%$
$A_{CP}(B^0 \to \pi^\mp K^\pm)$	$(-10.7 \pm 1.6\,^{+0.6}_{-0.4})\%$	$(-9.4 \pm 1.8 \pm 0.8)\%$	$(-9.8\,^{+1.2}_{-1.1})\%$
$A_{CP}(B^0 \to \pi^0 K^0)$	$(-13 \pm 13 \pm 3)\%$	$(+14 \pm 13 \pm 6)\%$	$(-1 \pm 10)\%$
R	...	...	0.90 ± 0.05
R_c	...	...	1.12 ± 0.07
R_n	...	...	0.99 ± 0.07

interference pattern in the Dalitz plot then allows to determine not only the magnitudes of the amplitudes as in the two body decays, but also the relative phases between the amplitudes. This can then be used either to check $1/m_b$ predictions or as an additional input for the determination of the CKM weak phase using flavor symmetries. We will review such a method below [1147, 1148]. The cleanest method requires measurements from the $B^0 \to K^+\pi^-\pi^0$ and $B^0 \to K^0_S\pi^+\pi^-$ Dalitz plots [1147–1149]. Other methods also use $B^+ \to K^0_S\pi^+\pi^0$ [1147], $B^+ \to K^+\pi^+\pi^-$ and $B^0 \to K^0_S\pi^+\pi^-$ [1150], and $B_s \to K^+\pi^-\pi^0$ and $B_s \to K^0_S\pi^+\pi^-$ [1151].

The main idea of the method [1147, 1148] is that by using isospin decomposition one can cancel the QCD penguin contributions ($\Delta I = 0$ reduced amplitudes) in $B \to K^*\pi$ decays. The $I = 3/2$ ($\Delta I = 1$) final state, is for instance given by

$$3A_{3/2} = A(B^0 \to K^{*+}\pi^-) + \sqrt{2}A(B^0 \to K^{*0}\pi^0) \ , \tag{426}$$

with an equivalent definition for the amplitude for charge-conjugated states, $\bar{A}_{3/2}$. Since both magnitudes and relative phases of amplitudes are measurables, this is now an observable quantity — up to an overall phase. In the absence of electroweak penguin (EWP) terms $A_{3/2}$ carries a weak phase γ, so that in this limit

$$\gamma = \Phi_{3/2} \equiv -\frac{1}{2}\arg\left(R_{3/2}\right) \ , \quad \text{where} \quad R_{3/2} \equiv \frac{\bar{A}_{3/2}}{A_{3/2}} \ . \tag{427}$$

The constraint in $\overline{\rho} - \overline{\eta}$ plane in the absence of EWP is a straight line, $\overline{\eta} = \overline{\rho}\,\tan\Phi_{3/2}$. The inclusion of EWP shifts this constraint to [1148]

$$\overline{\eta} = \tan\Phi_{3/2}\left[\overline{\rho} + C[1 - 2\mathrm{Re}(r_{3/2})] + \mathcal{O}(r^2_{3/2})\right] \ , \tag{428}$$

where C is a quantity that depends only on electroweak physics and is well known, with a theoretical error below 1% ($\lambda = 0.227$)

$$C \equiv \frac{3}{2}\frac{C_9 + C_{10}}{C_1 + C_2}\frac{1 - \lambda^2/2}{\lambda^2} = -0.27 \ , \tag{429}$$

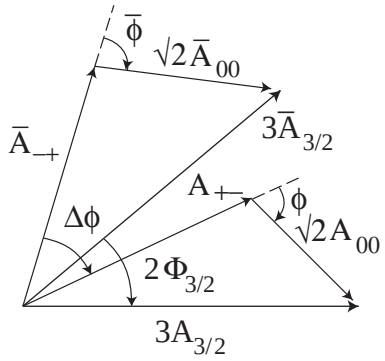

Fig. 91. Geometry for Eq. (426) and its charge-conjugate, using notations $A_{+-} \equiv A(B^0 \to K^{*+}\pi^-)$, $A_{00} = A(B^0 \to K^{*0}\pi^0)$ and similar notations for charge-conjugated modes [1148].

while the nonperturbative QCD effects enter only through a complex parameter

$$r_{3/2} \equiv \frac{(C_1 - C_2)\langle (K^*\pi)_{I=3/2}|\mathcal{O}_1 - \mathcal{O}_2|B^0\rangle}{(C_1 + C_2)\langle (K^*\pi)_{I=3/2}|\mathcal{O}_1 + \mathcal{O}_2|B^0\rangle} \ . \tag{430}$$

Here $\mathcal{O}_1 \equiv (\bar{b}s)_{\mathrm{V-A}}(\bar{u}u)_{\mathrm{V-A}}$ and $\mathcal{O}_2 \equiv (\bar{b}u)_{\mathrm{V-A}}(\bar{u}s)_{\mathrm{V-A}}$ are the V-A current-current operators. In naive factorization $r_{3/2}$ is found to be real and small, $r_{3/2} \leq 0.05$ [1147]. This is in agreement with the estimate using flavor SU(3) from $B \to \rho\pi$, $r_{3/2} = 0.054 \pm 0.045 \pm 0.023$ [1148], where the first error is experimental and the second an estimate of theoretical errors. This then gives the constraint

$$\overline{\eta} = \tan\Phi_{3/2}\,[\overline{\rho} - 0.24 \pm 0.03] \ . \tag{431}$$

The phase $\Phi_{3/2}$ can be determined by measuring the magnitudes and relative phases of the $B^0 \to K^{*+}\pi^-$, $B^0 \to K^{*0}\pi^0$ amplitudes and their charge-conjugates. A graphical representation of the triangle relation Eq. (426) and its charge conjugate is given in Fig. 91. The above four magnitudes of amplitudes and the two relative phases, $\phi \equiv \arg[A(B^0 \to K^{*0}\pi^0)/A(B^0 \to K^{*+}\pi^-)]$ and $\bar{\phi} \equiv \arg[A(\overline{B}^0 \to \overline{K}^{*0}\pi^0)/A(\overline{B}^0 \to K^{*-}\pi^+)]$, determine the two triangles separately. Their relative orientation is fixed by the phase difference $\Delta\phi \equiv \arg[A(B^0 \to K^{*+}\pi^-)/A(\overline{B}^0 \to K^{*-}\pi^+)]$.

A similar analysis is possible using $B \to \rho K$ decays. Although each ρ meson has only a single dipion decay, the relative phase between the amplitudes in Eq. (426) can be determined exploiting the fact that the $K^*\pi$ amplitudes appear in both $K\pi\pi$ Dalitz plots and therefore can be used as a common reference. The same approach could also be applied to $B \to K^*\rho$ decays.

The $B^+ \to K^+\pi^+\pi^-$ Dalitz plot provides the highest signal event yield of the $K\pi\pi$ Dalitz plots and so can be used to establish a working isobar model. This information can be used by the other analyses, leading to smaller systematic uncertainties. The $K^+\pi^+\pi^-$ Dalitz plot also contains the intermediate state $\rho^0(770)K^+$, which is predicted to have a large direct *CP* asymmetry $\sim 40\%$. Measuring this asymmetry, interesting in its own right, tells us that the tree and penguin contributions are of similar order and that we do indeed have sensitivity to γ in these decays. BaBar [1152] and Belle [1153] have recently updated their analyses of this Dalitz plot and both see strong evidence of direct *CP* violation in $B^+ \to \rho^0(770)K^+$. The results are in excellent agreement

and are summarized in Tab. 79. The signal Dalitz-plot model used in these analyses contains contributions from $K^{*0}(892)\pi^+$, $K_0^{*0}(1430)\pi^+$, $\rho^0(770)K^+$, $\omega(782)K^+$, $f_0(980)K^+$, $f_2(1270)K^+$, $f_{\rm X}(1300)K^+$, $\chi_{c0}K^+$, and a nonresonant component; the BaBar model also contains $K_2^{*0}(1430)\pi^+$. The main difference between the approaches of the two experiments concerns the nonresonant model. Belle uses two $e^{-\alpha s}$ distributions, where α is a free parameter, one with $s = m^2_{K^+\pi^-}$ and one with $s = m^2_{\pi^+\pi^-}$. BaBar uses a phase-space component in addition to a parametrization of the low-mass $K^+\pi^-$ S-wave that follows that of the LASS experiment [1020].

Table 79
Summary of results for A_{CP} of $B^+ \to \rho^0(770)K^+$. The uncertainties are statistical, systematic and model-dependent respectively.

Experiment	$A_{CP}(\rho^0(770)K^+)$
BaBar	$(+44 \pm 10 \pm 4\,^{+5}_{-13})\%$
Belle	$(+41 \pm 10 \pm 3\,^{+3}_{-7})\%$
HFAG Average	$(+42\,^{+8}_{-10})\%$

The $B^0 \to K^0_S\pi^+\pi^-$ Dalitz plot is an extremely rich physics environment. As well as providing measurements of the $B^0\overline{B}^0$ mixing phase 2β, discussed in Sec. 9.2.2, it is possible to measure the phase difference $\Delta\phi$ between $B^0 \to K^{*+}\pi^-$ and $\overline{B}^0 \to K^{*-}\pi^+$, one of the crucial ingredients in the determination of γ with the method of Refs. [1147–1149]. Both BaBar [1090] and Belle [1094] have performed time-dependent Dalitz-plot analyses of this mode. Details of the analyses are discussed in Sec. 9.2.2. Belle find two fit solutions that correspond to different interference between the $K_0^{*+}(1430)$ and nonresonant components. These two solutions prefer different values of $\Delta\phi$. The results for $\Delta\phi$ are illustrated in Fig. 92 and summarized in Tab. 80. There is some disagreement between the BaBar and Belle results. The experimentally measured values of $\Delta\phi$ include the $B^0\overline{B}^0$ mixing phase since they come from time-dependent analyses. This has to be removed before the values can be used in the extraction of γ.

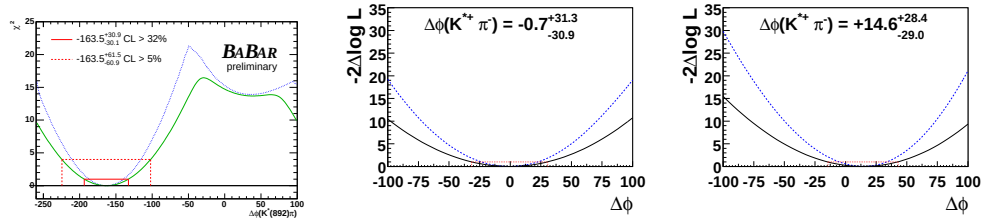

Fig. 92. Likelihood scans of $\Delta\phi$ from Dalitz-plot analyses of $B^0 \to K^0_S\pi^+\pi^-$. The left plot is from BaBar, the middle and right plots are from Belle and represent the scans of the two different solutions.

The other two parameters required to determine γ are ϕ and $\bar{\phi}$. These are the relative phases of $B^0 \to K^{*+}\pi^-$ and $B^0 \to K^{*0}\pi^0$ and $\overline{B}^0 \to K^{*-}\pi^+$ and $\overline{B}^0 \to \overline{K}^{*0}\pi^0$, respectively. Both of these quantities can be determined from a time-integrated Dalitz-plot analysis of $B^0 \to K^+\pi^-\pi^0$ (and its charge conjugate). Such an analysis has not yet been performed by Belle but BaBar has published results based on 232×10^6 $B\overline{B}$ pairs [1154] and has preliminary results based on the full BaBar dataset of 454×10^6 $B\overline{B}$

Table 80
Summary of results for $\Delta\phi(K^{*+}\pi^-)$ from time-dependent Dalitz-plot analyses of $B^0 \to K^0_S\pi^+\pi^-$. The uncertainties are statistical, systematic and model-dependent respectively.

Experiment	$\Delta\phi(K^{*+}\pi^-)$
BaBar	$(-164 \pm 24 \pm 12 \pm 15)^\circ$
Belle Soln. 1	$(-1\,^{+24}_{-23} \pm 11 \pm 18)^\circ$
Belle Soln. 2	$(+15\,^{+19}_{-20} \pm 11 \pm 18)^\circ$

pairs [248]. The published analysis includes contributions from $\rho^-(770)K^+$, $K^{*+}(892)\pi^-$, $K^{*0}(892)\pi^0$, $K_0^{*+}(1430)\pi^-$ and $K_0^{*0}(1430)\pi^0$. The higher K^* resonances are modeled by the LASS parametrization, which also includes a slowly varying nonresonant term. The fit exhibits multiple solutions that are not well separated. This can be seen in the likelihood scans in Fig. 93 and unfortunately leads to a weaker constraint on γ. BaBar's preliminary results on the larger data sample indicate much better separation between solutions, however likelihood scans of ϕ and $\bar{\phi}$ are not yet completed.

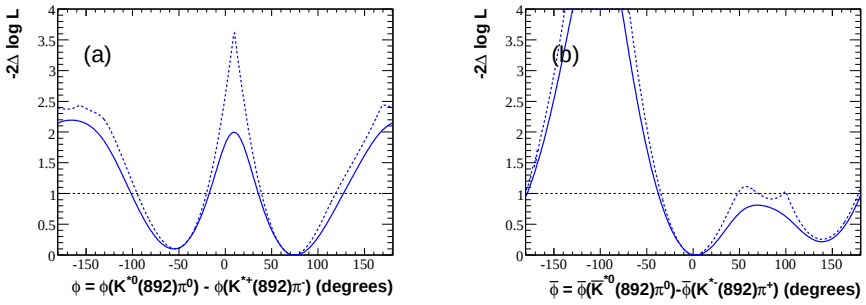

Fig. 93. Likelihood scans of ϕ (left) and $\bar{\phi}$ (right) from BaBar Dalitz-plot analysis of $B^0 \to K^+\pi^-\pi^0$.

The BaBar results on $\Delta\phi$ [1090], ϕ and $\bar{\phi}$ [1154] have been combined [1149] to create a constraint

$$39^\circ < \Phi_{3/2} < 112^\circ \ (68\%\text{CL})\,, \tag{432}$$

which can be converted to a constraint on the $\overline{\rho}-\overline{\eta}$ plane, using the relation (431). Both of these constraints are shown in Fig. 94.

10. Global Fits to the Unitarity Triangle and Constraints on New Physics

The large variety of precise measurements reported so far can be used to place constraints on theoretical models of flavor particles and their interactions. The impact of these constraints has been studied using global fits to the predictions of the Standard Model and other theoretical models.

In this section, results of such studies will be presented. First, the results described in this report are interpreted within the Standard Model (Sec. 10.1). Next, Sec. 10.2 summarizes the constraints imposed by these measurements on deviations from the Standard Model. Discussions of constraints, first in a model independent approach, then for Grand Unified Theories, and for models with Extra Dimensions conclude the report.

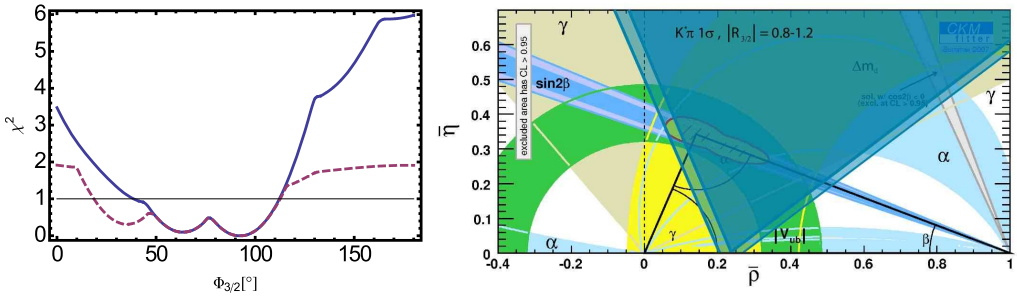

Fig. 94. Constraint on the angle $\Phi_{3/2}$ (left) from combined information from $K\pi\pi$ Dalitz plot analyses. The dashed purple line is for the case when $\left|R_{3/2}\right|$ is unconstrained while the solid blue line is for the case when $0.8 < \left|R_{3/2}\right| < 1.2$. Constraint on the $\overline{\rho} - \overline{\eta}$ plane (right) from combined information from $K\pi\pi$ Dalitz plot analyses. The dark shaded region corresponds to the experimental 1σ range while the light shaded region includes the theoretical error on the contributions from electroweak penguin processes.

10.1. *Constraints on the Unitarity Triangle Parameters*

The measured quantities reported so far are sensitive to different combinations of the parameters of the CKM matrix (see Sec. 1.1.3 for details). Their relations to the angles and sides of the Unitarity Triangle (UT) place constraints on the coordinates of its apex $(\overline{\rho}, \overline{\eta})$ and thus can be used to test the predictions of the Standard Model or any other theory describing flavor physics. The most powerful way to make such tests is to perform global fits comparing the data to theoretical predictions.

To combine a large number of measurements of different quantities performed with different methods and data samples, widely different in size and composition, and thus with different statistical and systematic errors, not all of them Gaussian in nature, is a non-trivial task. Theoretical predictions have uncertainties that are very difficult to assess and that are usually not expected to adhere to Gaussian distributions. Two groups have independently developed global analysis tools to determine the CKM parameters in the framework of the Standard Model and its extensions. The two approaches differ significantly, in particular in the treatment of uncertainties of data and of the theory predictions. The results of this report have been analyzed by the **UT***fit* group. Most of this section therefore discusses their Bayesian approach in detail, the work of the CKMfitter group being summarized for comparison in Sec. 10.1.5.

10.1.1. *Fitting technique*

The Unitarity Triangle analysis developed by the **UT***fit* group relies on the Bayes Theorem. Its specific application is briefly described in the following, more details can be found in elsewhere [1155].

A given constraint c_j relates the coordinates of the apex of the Unitarity Triangle $(\overline{\rho}, \overline{\eta})$ to quantities that have been experimentally determined or theoretically calculated $(\boldsymbol{x} = \{x_1, x_2, ..., x_N\})$, through functional dependencies that are prescribed by the theory that is being tested, $c_j = c_j(\bar{\rho}, \bar{\eta}, \boldsymbol{x})$.

In the case of perfect knowledge of c_j and x_i, each of the constraints would represent a well defined curve in the $(\overline{\rho}, \overline{\eta})$ plane. In the presence of uncertainties, the constraints are represented by distributions of curves, each weighted according to the probability density

derived from the error distributions. Based on Bayes Theorem, the **UT***fit* group derives for M constraints c_j and N free parameters x_i, a *pdf* or probability density function,

$$f(\bar{\rho},\bar{\eta},\boldsymbol{x}|\hat{c_1},...,\hat{c_M}) \propto \prod_{j=1,\mathrm{M}} f_j(\hat{c}_j\,|\,\overline{\rho},\overline{\eta},\boldsymbol{x}) \times \prod_{i=1,\mathrm{N}} f_i(x_i) \times f_\circ(\overline{\rho},\overline{\eta}). \tag{433}$$

By integrating Eq. (433) over $\boldsymbol{x}$, one obtains,

$$f(\overline{\rho},\overline{\eta}\,|\,\hat{\mathbf{c}},\mathbf{f}) \propto \mathcal{L}(\hat{\mathbf{c}}\,|\,\overline{\rho},\overline{\eta},\mathbf{f}) \times f_\circ(\overline{\rho},\overline{\eta})\,, \tag{434}$$

where $\hat{\mathbf{c}}$ stands for the set of measured constraints, and

$$\mathcal{L}(\hat{\mathbf{c}}\,|\,\overline{\rho},\overline{\eta},\mathbf{f}) = \int \prod_{j=1,\mathrm{M}} f_j(\hat{c}_j\,|\,\overline{\rho},\overline{\eta},\boldsymbol{x}) \prod_{i=1,\mathrm{N}} f_i(x_i)\,\mathrm{d}x_i \tag{435}$$

is the effective overall likelihood function which takes into account all possible values of x_j and their weights based on their associated error distributions. This expression underlines the dependence of the likelihood on the best knowledge of all x_i, described by $f(\boldsymbol{x})$. Assuming a flat *a priori* distribution for $\overline{\rho}$ and $\overline{\eta}$, *i.e.* all values are equally likely, the final (unnormalized) *pdf* is,

$$f(\overline{\rho},\overline{\eta}) \propto \int \prod_{j=1,\mathrm{M}} f_j(\hat{c}_j\,|\,\overline{\rho},\overline{\eta},\mathbf{x}) \prod_{i=1,\mathrm{N}} f_i(x_i)\,\mathrm{d}x_i\,. \tag{436}$$

The integration is done by Monte Carlo methods, in which a large sample is extracted for the free parameters and a weight is assigned for each extraction . In this way an *a posteriori pdf* for each parameter is obtained, generally different from the *a priori* one, because of the weighting procedure. The result of each extraction is considered more or less likely, depending on the agreement of the corresponding measured quantities with the actual experimental results or theoretical calculation. The **UT***fit* group treats theoretical and experimental parameters in a uniform way, adopting the error distributions, Gaussian or non-Gaussian, directly as *a priori* probability density functions.

The *a posteriori pdf*s depend by construction on the choice of the *a priori* ones, which are based on - to a certain degree subjective - assessments of systematic uncertainties, experimental and theoretical, on theoretical approximations and assumptions. In many Unitarity Triangle analyses, the precise and abundant measurements and theoretical inputs represent very stringent constraints and the results are not very sensitive to the particular choice of the *a priori* distributions for the parameters. If this is not the case, an assessment of the sensitivity of the result to variations of the prior is required.

As part of the **UT***fit* analysis, the agreement of the measured quantities is quantified in the so-called *compatibility plots* [1156]. An indirect determination of a particular quantity is obtained from a global fit including all the available constraints, except those from the direct measurement of the quantity of interest. This indirectly determined value represents the prediction by the Standard Model or any other theory from which the constraints are derived. The comparison of the prediction and the direct measurement, including their respective uncertainties, can be used to assess the compatibility with the underlying theoretical calculations or model.

Specifically, if $f(x_{th})$ and $f(x_{fit})$ are the *pdf*s for the predicted and the measured values, respectively, their compatibility is evaluated by constructing the *pdf* for the difference, $x_{th} - x_{fit}$, and by estimating the distance of its most probable value from zero,

in units of standard deviations. In the *compatibility plots*, contours of constant distance are shown in two dimensions, $\sigma(x_{fit})$ versus $\bar{x}_{fit}$. The compatibility between x_{th} and x_{fit} can be directly estimated, for any central value and error on x_{fit}. In this way, the compatibility of constraints with the measurements is simply assessed by comparing two different *pdf*s, without any assumption about their shapes. Examples of *compatibility plots* are shown in section 10.1.3.

10.1.2. *Inputs to the Unitarity Triangle Analysis*

Not all measurements have sensitivity to the Unitarity Triangle parameters and there are determinations of the same observable that are equivalent but not identical. A choice has to be made. The best selection of experimental results discussed in this report has been used as input to the CKM analysis using UT fits. They are summarized in Tab. 81. The set of lattice inputs (see Ref. [887] for details) chosen for UT fits is summarized in Tab. 82.

Table 81
Most relevant experimental inputs to the UT fits. Internal references with the details of the choice of the inputs are also included.

Input	Source	Value	Reference
$\|V_{ud}\|$	Nuclear decays	0.97425 ± 0.00022	Eq. 117
$\|V_{us}\|$	SL Kaon decays	0.2259 ± 0.0009	Eq 178
$\|V_{cb}\|incl.$	SL charmed B decays	$(41.54 \pm 0.73) \times 10^{-3}$	Eq. 265
$\|V_{cb}\|excl.$	SL charmed B decays	$(38.6 \pm 1.1) \times 10^{-3}$	Eq. 259
$\|V_{ub}\|$ incl.	SL charmless B decays	$(4.11^{+0.27}_{-0.28}) \times 10^{-3}$	Eq. 280
$\|V_{ub}\|$ excl.	SL charmless B decays	$(3.38 \pm 0.36) \times 10^{-3}$	Eq. 229
$\mathcal{B}(B^+ \to \tau^+\nu)$	Leptonic B decays	$(1.51 \pm 0.33) \times 10^{-4}$	Tab. 44
Δm_d	$B_d\bar{B}_d$ mixing	(0.507 ± 0.005) ps^{-1}	Fig. 58
Δm_s	$B_s\bar{B}_s$ mixing	(17.77 ± 0.12) ps^{-1}	Sec. 7.2.2
$\|\epsilon_K\|$	$K\bar{K}$ mixing	$(2.229 \pm 0.012) \times 10^{-3}$	Eq. 341
$\sin 2\beta$	Charmonium B decays	0.671 ± 0.023	Fig. 60
$\mathcal{B}$ & CP parameters	$B \to \pi\pi$, $\rho\rho$, $\rho\pi$ decays		Sec. 9
$(x^{\pm}, y^{\pm})$, $\mathcal{B}$ & A	$B \to D^{(*)0}K^{(*)\pm}$ (GGSZ, GLW, ADS)		Sec. 8

Table 82
Phenomenological inputs obtained from Lattice QCD calculations

Input	Value
f_{B_s} (MeV)	245 ± 25
$\hat{B}_{B_s}$	1.22 ± 0.12
f_{B_s}/f_{B_d}	1.21 ± 0.04
$\hat{B}_{B_s}/\hat{B}_{B_d}$	1.00 ± 0.03
B_K	0.75 ± 0.07

10.1.3. *Results of Global Fits*

Figure 95 displays the results of the global fit in the $(\bar{\rho}, \bar{\eta})$ plane. A summary of the fitted parameters of the CKM matrix (see Sec. 1 for definitions) is presented in Table 83. The global fits also result in improved determinations of the measured quantities, the

Table 83
Results of the global fit for the parameters of the CKM matrix. Parameters obtained with the CKMfitter approach (see Sec. 10.1.5) are also shown for comparison.

Parameter	Result	CKMfitter
$\bar{\rho}$	0.158 ± 0.021	$0.139^{+0.025}_{-0.027}$
$\bar{\eta}$	0.343 ± 0.013	$0.341^{+0.016}_{-0.015}$
A	0.802 ± 0.015	$0.812^{+0.010}_{-0.024}$
λ	0.2259 ± 0.0016	0.2252 ± 0.0008

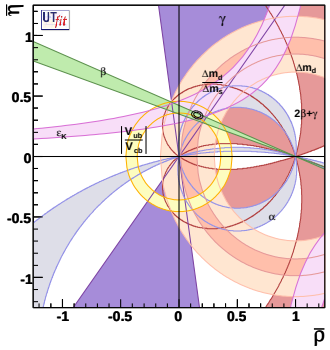

Fig. 95. Individual and global constraints in the $(\bar{\rho}, \bar{\eta})$ plane from the global UT fits. The shaded areas indicate the individual constraints at 95% CL. The contours of the overall constraints defining the apex of the UT triangle correspond to 68% and 95% C.L. .

angles and sides of the Unitarity Triangle which are listed in Tab. 84.

Table 84
Improved measurements of angles and sides of the Unitarity Triangle obtained from the global fits. Results obtained with the CKMfitter approach (see Sec. 10.1.5) are also shown for comparison.

Parameter	Results	CKMfitter
$\alpha(^o)$	92.6 ± 3.2	$90.6^{+3.8}_{-4.2}$
$sin2\beta$	0.698 ± 0.019	$0.684^{+0.023}_{-0.021}$
$\gamma(^o)$	65.4 ± 3.1	$67.8^{+4.2}_{-3.9}$
$\|V_{ub}\|$	0.00359 ± 0.0012	$0.00350^{+0.00015}_{-0.00014}$
$\|V_{cb}\|$	0.0409 ± 0.0005	$0.04117^{+0.00038}_{-0.00115}$
$\|V_{td}\|$	0.00842 ± 0.00021	$0.00859^{+0.00027}_{-0.00029}$

The increasing precision of the measurements and of the theoretical calculations have significantly improved the knowledge of the allowed region for the apex position $(\overline{\rho}, \overline{\eta})$.

Good overall consistency between the various measurements at 95 % C.L. is observed, thus establishing the CKM mechanism as the dominant source of CP violation in B-meson decays.

Furthermore, measurements of CP-violating quantities from the B-factories are now so abundant and precise that the CKM parameters can be constrained by the angles of the Unitarity Triangle alone, as shown in Fig. 96. In addition, $(\overline{\rho}, \overline{\eta})$ can be determined independently using experimental information from CP-conserving processes, $|V_{ub}|/|V_{cb}|$ from semileptonic B decays, Δm_d and Δm_s from the $B_d - \bar{B}_d$ and $B_s - \bar{B}_s$ oscillations) and the direct CP violation measurements in the Kaon sector, ϵ_K (see Fig. 96). Prior to the precise *BABAR* and Belle measurements this was the strategy used to predict the value of $\sin 2\beta$ [1157].

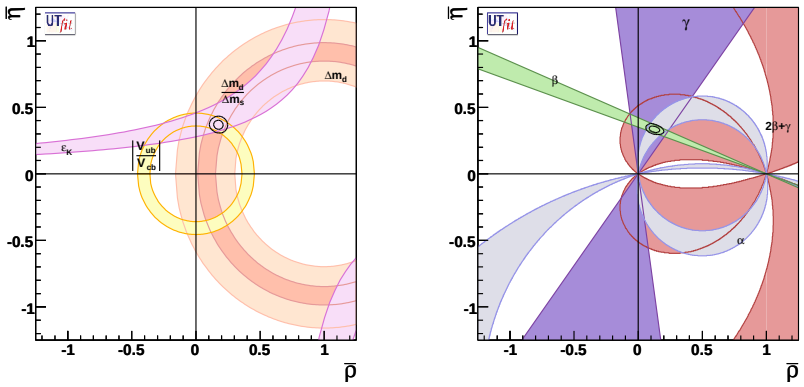

Fig. 96. Allowed regions for $(\overline{\rho}, \overline{\eta})$, as constrained by the measurement of $|V_{ub}|/|V_{cb}|$, Δm_d, Δm_s and ϵ_K (left) and of the angles α, $\sin 2\beta$, γ, $2\beta + \gamma$, β and $\cos 2\beta$ (right) . The closed contours indicate the regions of 68% and 95% C.L. for the triangle apex, while the colored zones mark the 95% C.L. for each constraint.

Although the global fits show very good agreement overall, there are some measurements for which the agreement is less convincing. As described in Sec. 10.1.1, **UT***fit* quantifies the overall agreement of individual measurements with predictions of the global fit by means of *compatibility plots*. Such plots for α, $\sin 2\beta$, γ and Δm_s are shown in Fig. 97. The direct measurements for α and Δm_s are in excellent agreement with the indirect determination from the global fits, although for Δm_s the effectiveness of the comparison is limited by the precision on the theoretical inputs, resulting in sizable uncertainties (compared to the experimental one) for the prediction extracted from the fit. The direct measurement of γ yields a slightly higher value of $(78 \pm 12)^o$ than the indirect one from the overall fit, $(65 \pm 3)^o$, though they are compatible within 1σ. The measurement of $\sin 2\beta$ based on the CP asymmetry in $B^0 \to J/\psi K^0$ is slightly shifted with respect to the indirect determination, but compatible to within 2σ.

It has been observed for several years that the direct measurement of $\sin 2\beta$ favors a value of $|V_{ub}|$ that is more compatible with the direct determination of $|V_{ub}|$ based on exclusive rather than inclusive charmless semileptonic decays. The problem is illustrated in Fig. 98 and reflects the great challenge that the extraction of $|V_{ub}|$ from charmless semileptonic decays represents. Experimentally, these charmless decays are impacted by

very large backgrounds which are difficult to understand in detail and difficult to suppress due to the presence of a neutrino in the final state. Theoretically, the required normalization and corrections for hadronic effects based on QCD calculations are dominating the uncertainties. The QCD calculations and models are different for the two processes and their uncertainties are impacted by the selection of the experimental data. While there are now several calculations available, it remains very difficult to assess the overall theoretical uncertainties for the extraction of $|V_{ub}|$. The fact that the current values of $|V_{ub}|$ from exclusive and inclusive decays are only marginally consistent could be taken as an indication that the uncertainties are larger than stated.

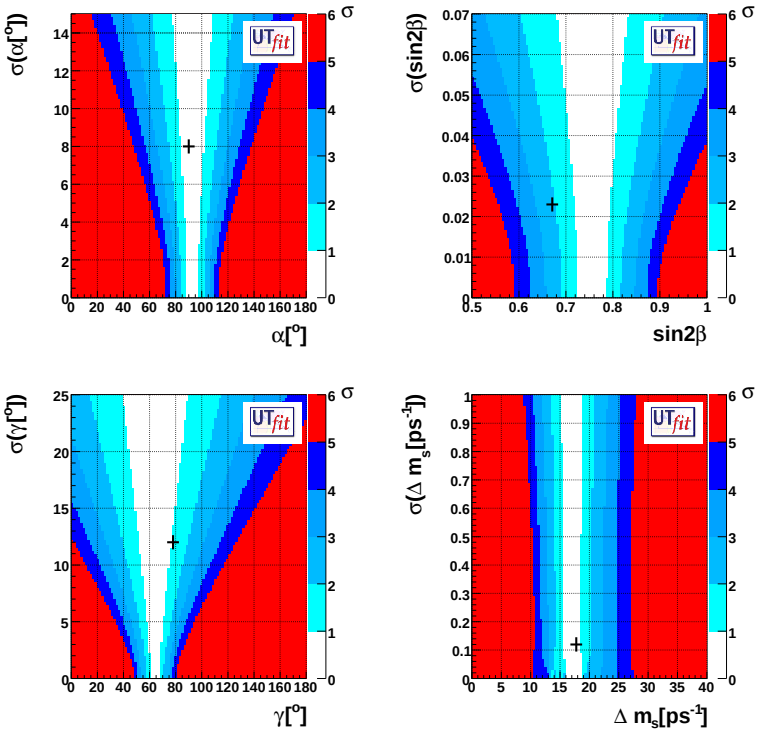

Fig. 97. Compatibility plots for α, $\sin 2\beta$ $\sin 2\beta$ from the measurement of the *CP* asymmetry in $B^0 \to J/\psi K^0$, γ and Δm_s. The color code indicates the compatibility between direct and indirect determinations, given in terms of standard deviations, as a function of the measured value and the experimental uncertainty. The crosses indicate the world averages and errors of the direct measurements.

Given the present experimental measurements, no significant deviation from the CKM picture has been observed. Of course, this statement does not apply to observables that have no or very small impact on $\bar{\rho}$ and $\bar{\eta}$ (for instance the B_s mixing phase).

10.1.4. *Impact of the Uncertainties on Theoretical Quantities*

Given the abundance of constraints now available for the determination of the UT Triangle, $\bar{\rho}$ and $\bar{\eta}$, one can perform the global fit without the hadronic parameters derived

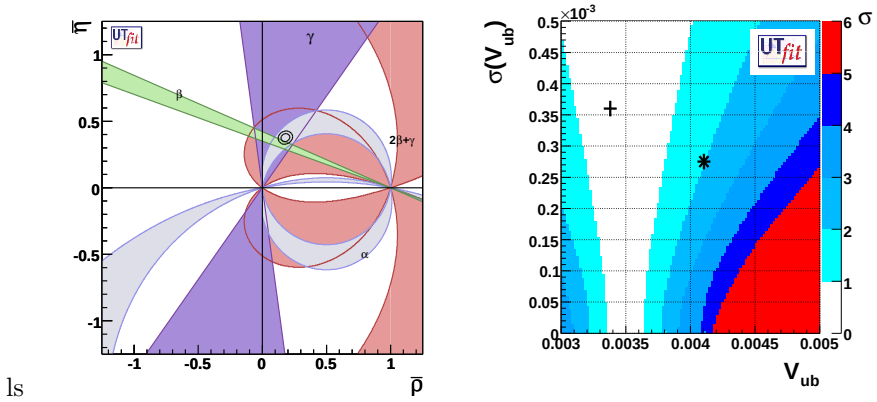

ls

Fig. 98. Left: Allowed regions for $\bar{\rho}$ and $\bar{\eta}$ obtained by using the measurements of $|V_{ub}|/|V_{cb}|$, Δm_d, Δm_s, ϵ_K, The colored zones indicate the 68% and 95% probability regions for the angle measurements, which are not included in the fit. Right: Compatibility plot for V_{ub}. The cross and the star indicate the exclusive and inclusive measurements, respectively.

from lattice calculations as input. In this way, one can quantify the impact that future improvements in the lattice QCD calculation will have on the UT analysis.

Figure 99, shows the 68% and 95% probability regions for different lattice quantities, obtained from a UT fit using the measurements of angles and the constraints from semileptonic B decays. The relations between observables and theoretical quantities used in this fit are obtained assuming the validity of the SM. Numerical results are given in Table 85.

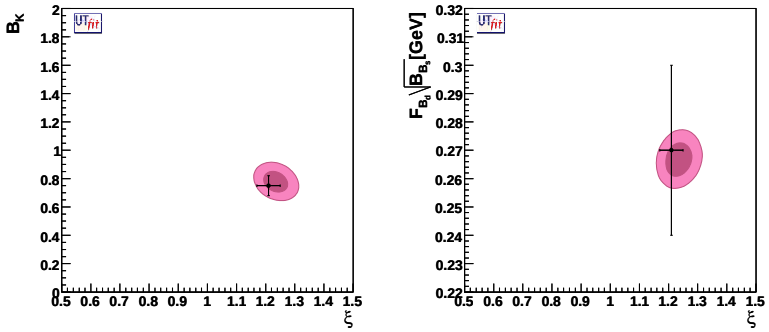

Fig. 99. Comparison of the current lattice calculations (data points) with prediction of the global fit, left: ξ versus B_K and right: $f_{B_s}\sqrt{B_{B_s}}$ versus ξ. The dark and light colored areas show the 68% and 95% probability regions.

10.1.5. *Comparison with the Results of CKMfitter*

Extracting Standard Model best values of parameters from the very large number of different measurements is difficult. It is not trivial to combine measurements with very different statistical errors and extract the best the information. However, it is much more

Table 85
The values obtained for the theoretical parameters from a UT analysis using the angles and V_{ub}/V_{cb} measurements are compared with the results of lattice calculations.

Parameter	UT (angles+V_{ub}/V_{cb})	Lattice QCD results
B_K	0.78 ± 0.05	0.75 ± 0.07
$f_{B_s}\sqrt{B_{B_s}}$ [MeV]	266.8 ± 4.1	270 ± 30
$\xi = \frac{f_{B_s}\sqrt{B_{B_s}}}{f_{B_d}\sqrt{B_{B_d}}}$	1.23 ± 0.03	1.21 ± 0.04
f_{B_d} [MeV]	195 ± 11	200 ± 20

difficult to combine measurements with widely different sources and estimations of the systematic errors, in many cases there is need for case-to-case judgment and margin for interpretation.

For these reasons, it has been extremely important to have more than one approach to fits of the UT Triangle. In this section the results obtained by the **UT***fit* group are compared with the most recent results of the CKMfitter group as summarized in http://ckmfitter.in2p3.fr/. The inputs to the two fitting methods are different, and the choice of the lattice parameters differs and experimental inputs are taken from a slightly different sets of measurements, some of them taken from earlier publications. Nonetheless, the comparison is important, because it shows that different approaches lead to somewhat different results.

Statistical method

The CKMfitter was developed in parallel to **UT***fit* to perform global UT analyses. The most significant difference to the **UT***fit* approach is the treatment of non-Gaussian errors. In particular, the CKMFitter group introduced *RangeFit* [956], a special procedure to deal with uncertainties of theoretical predictions.

The CKMfitter method is described briefly as follows. The experimental input is a set of N_{exp} measurements, $\boldsymbol{x}_{exp}$, related to a set of theoretical expressions or constraints, $\boldsymbol{x}_{theo}$. The theoretical expressions are model-dependent functions of of N_{mod} parameters $\boldsymbol{y}_{mod}$. A subset of N_{theo} parameters in $\boldsymbol{y}_{mod}$ are considered fundamental and free parameters of the theory, *e.g.* the four Wolfenstein parameters in the SM or the top quark mass. These parameters are denoted as $\boldsymbol{y}_{theo}$. The remaining $N_{QCD} = N_{mod} - N_{theo}$ input parameters, which currently are less well known due to the difficulty of computing strong interaction effects, *e.g.* f_{b_d}, B_d,... are denoted as $\boldsymbol{y_{QCD}}$.

The fit is set up to minimize the quantity, $\chi^2 = -2\ln\mathcal{L}(\boldsymbol{y}_{mod})$, with the likelihood function $\mathcal{L}(\boldsymbol{y}_{mod})$, defined as a product two types of contributions,

$$\mathcal{L}(\boldsymbol{y}_{mod}) = \mathcal{L}_{exp}(\boldsymbol{x}_{exp} - \boldsymbol{x}_{theo}(\boldsymbol{y}_{mod})) \times \mathcal{L}_{theo}(\boldsymbol{y}_{QCD}). \tag{437}$$

$\mathcal{L}_{exp}$ depends on the experimental measurements $\boldsymbol{x}_{exp}$, with errors that are Gaussian distributed in general (and correlations, if known, are taken into account), and their theoretical predictions $\boldsymbol{x}_{theo}$, which are functions of the model parameters $\boldsymbol{y}_{mod}$. In the case of a non-Gaussian experimental errors, the exact description of the associated likelihood is used in the fit. $\mathcal{L}_{theo}$ describes the imperfect knowledge of the QCD parameters $\boldsymbol{y}_{QCD} \in \boldsymbol{y}_{mod}$, where the theoretical uncertainties $\boldsymbol{\sigma}_{syst}$ are considered to be bound by a range, $[\boldsymbol{y}_{QCD} - \boldsymbol{\sigma}_{syst}, \boldsymbol{y}_{QCD} + \boldsymbol{\sigma}_{syst}]$. In *RangeFit* the theoretical likelihood functions $\mathcal{L}_{theo}(i)$ do not contribute to the χ^2 of the fit, as long as the $\boldsymbol{y}_{QCD}$ values are within

their range. With these constraints, all results should be understood as valid only if the allowed ranges contain the true values of the $\boldsymbol{y}_{mod}$.

The minimization is performed in two steps. First, the global minimum, $\chi^2_{min,global}$, is determined with respect to all N_{mod} parameters. Due to the systematic uncertainties from experiment and theory, this minimum does in general not correspond to a unique $\boldsymbol{y}_{mod}$. Second, a selected subspace of the parameter space, *e.g.* $a = (\bar{\rho}, \bar{\eta})$ is scanned, to determine the local minimum χ^2, $\chi^2_{min,local}(a)$, for each fixed point on a grid in the parameter space a, with respect to the remaining parameters. The offset-corrected χ^2 is calculated as, $\Delta\chi^2(a) = \chi^2_{min,local}(a) - \chi^2_{min,global}$, where its minimum is equal to zero by construction.

Finally, a confidence level (C.L.) for a is obtained, assuming Gaussian distributions, by using the cumulative χ^2 distribution:

$$1 - \mathrm{CL} = \mathrm{Prob}(\Delta\chi^2(\mathrm{a}), \mathrm{N_{dof}}) \tag{438}$$

$$= \frac{1}{\sqrt{2^{N_{dof}}}\Gamma(N_{dof}/2)} \int_{\chi^2(y_{mod})}^{\infty} e^{-t/2} t^{N_{dof}/2-1} dt. \tag{439}$$

Inputs

The inputs to the fits performed by the CKMfitter group differ slightly from the results of this report and different choices of parameters estimated with lattice QCD calculations have been made. The latter difference is mostly due to the difference in the treatment of systematic errors. These differences are presented in Tables 86 and 87 to be compared with Tables 81 and 82. Identical input values are not included in these tables. The

Table 86
Most relevant experimental inputs used by CKMfitter for the global UT fit that are different from those used by UT fit. The numbers marked in bold are theoretical uncertainties treated using *R*fit (flat likelihood).

Input	Source	Value	Reference
$\|V_{ud}\|$	Nuclear decays	0.97418 ± 0.00026	[275]
$\|V_{us}\|$	SL Kaon decays	0.2246 ± 0.0012	[346]
$\|V_{cb}\|$	SL charmed B decays	$(40.59 \pm 0.38 \pm \mathbf{0.58}) \times 10^{-3}$	[560] [31]
$\|V_{ub}\|$	SL charmless B decays	$(3.87 \pm 0.09 \pm \mathbf{0.46}) \times 10^{-3}$	[560]
$\mathcal{B}(B^+ \to \tau^+\nu)$	Leptonic B decays	$(1.73 \pm 0.35) \times 10^{-4}$	Tab. 44 combined with [1158]

Table 87
Phenomenological inputs from Lattice QCD calculations as adopted by the CKMfitter group. The errors treated according to the *R*fit (see text) prescription are highlighted in bold.

f_{B_s} (MeV)	$228 \pm 3 \pm \mathbf{17}$
$\hat{B}_{B_s}$	$1.196 \pm 0.008 \pm \mathbf{0.023}$
f_{B_s}/f_{B_d}	$1.23 \pm 0.03 \pm \mathbf{0.05}$
$\hat{B}_{B_s}/\hat{B}_{B_d}$	$1.05 \pm 0.02 \pm \mathbf{0.05}$
B_K	$0.721 \pm 0.005 \pm \mathbf{0.040}$

sources of the experimental inputs are given in Tables 86, the different choices of lattice parameter are justified in the following.

First of all, only unquenched lattice calculations with 2 or 2+1 dynamical fermions, published in journals or proceedings are taken into account. The Gaussian and flat components of the errors are separated and the latter is treated according to *R*fit prescription [956].

The Gaussian errors comprise purely statistical errors as well as systematic uncertainties that are expected to also have normal error distributions (*e.g.*interpolation errors). The remaining systematic uncertainties are handled as *R*fit errors. If there are several error sources in the *R*fit category, they are added linearly.

If *R*fit is taken *stricto sensu* and the individual likelihood functions are combined by multiplication, the resulting overall uncertainty might be underestimated. This effect is corrected for by adopting the following procedure: first, the likelihood functions for the Gaussian uncertainties are combined; next this combination is assigned the smallest of the individual *R*fit errors. The underlying idea is as follows: The estimated error should not be smaller than the best of all estimates, but this best estimate should not be impacted by less precise methods, as would be the case if one took the dispersion of the individual central values as a guess of the combined theoretical uncertainty. All this underlines the fact that theoretical uncertainties are often ill-defined, and procedures to combine such errors should be judged critically. The CKMFitter approach is only one among several the alternatives that can be found in the literature.

Results of CKM Fitter

Figure 100 displays the result of global fits performed with the CKMfitter, together with the 96% C.L. contours of the individual constraints. For comparison with UT fit, the results are listed in Tables 83 and 84). The two global fit procedures give comparable results, although they arrive at somewhat different contours for the individual constraints. The results are an excellent proof of robustness of the fit methods, indicating that at present precision the different choices for the treatment of errors do not impact the conclusions significantly.

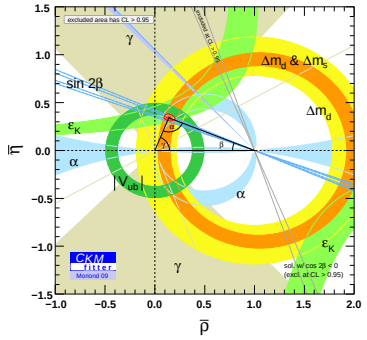

Fig. 100. Individual and global constraints in the $(\bar{\rho}, \bar{\eta})$ plane obtained by the CKMfitter group. The shaded areas indicate the individual constraints at 95% CL. The contours of the overall constraints defining the apex of the UT triangle correspond to 68% and 95% C.L. .

10.2.1. *Model independent constraints on New Physics from global fits*

The Standard Model (SM) of electroweak and strong interactions works beautifully up to the highest energies presently explored at colliders. However, there are several indications that it must be embedded as an effective theory into a more complete model that should, among other things, contain gravity, allow for gauge coupling unification and provide a dark matter candidate and an efficient mechanism for baryogenesis. As discussed in Sec. 2.5, this effective theory can be described by a Lagrangian of the form

$$\mathcal{L}(M_W) = \Lambda^2 H^\dagger H + \mathcal{L}_{\rm SM} + \frac{1}{\Lambda}\mathcal{L}^5 + \frac{1}{\Lambda^2}\mathcal{L}^6 + \dots \,,$$

where the logarithmic dependence on the cutoff Λ has been neglected. Barring the possibility of a conspiracy between physics at scales below and above Λ to give an electroweak symmetry breaking scale $M_w \ll \Lambda$, we assume that the cutoff lies close to M_w. Then the power suppression of higher dimensional operators is not too severe for $\mathcal{L}^{5,6}$ to produce sizable effects in low-energy processes, provided that they do not compete with tree-level SM contributions. Therefore, we should look for new physics effects in quantities that are zero at the tree level in the SM and are finite and calculable at the quantum level. Within the SM, such quantities fall in two categories: i) electroweak precision observables (protected by the electroweak symmetry) and ii) Flavor Changing Neutral Currents (FCNC) (protected by the GIM mechanism). In the SM, all FCNC and CP violating processes are computable in terms of quark masses and of the elements of the Cabibbo-Kobayashi-Maskawa (CKM) matrix [1, 2]. This implies very strong correlations among observables in the flavor sector. NP contributions, or equivalently the operators in $\mathcal{L}^{5,6}$, violate in general these correlations, so that NP can be strongly constrained by combining all the available experimental information on flavor and CP violation.

A very useful tool to combine the available experimental data in the quark sector is the Unitarity Triangle (UT) analysis [956, 1156]. Thanks to the measurements of the Unitarity Triangle (UT) angles recently performed at B factories, the UT fit is overconstrained. Therefore, it has become possible to add NP contributions to all quantities entering the UT analysis and to perform a combined fit of both NP and SM parameters. In general, NP models introduce a large number of new parameters: flavor changing couplings, short distance coefficients and matrix elements of new local operators. The specific list and the actual values of these parameters can only be determined within a given model. Nevertheless, each of the meson-antimeson mixing processes is described by a single amplitude and can be parametrized, without loss of generality, in terms of two parameters, which quantify the difference between the full amplitude and the SM one. Thus, for instance, in the case of $B_q^0 - \bar{B}_q^0$ mixing we define [36]:

$$C_{B_q}\, e^{2i\phi_{B_q}} = \frac{\langle B_q^0 | H_{\rm eff}^{\rm full} | \bar{B}_q^0 \rangle}{\langle B_q^0 | H_{\rm eff}^{\rm SM} | \bar{B}_q^0 \rangle}\,; \quad C_{\Delta m_K} = \frac{{\rm Re}[\langle K^0 | H_{\rm eff}^{\rm full} | \bar{K}^0 \rangle]}{{\rm Re}[\langle K^0 | H_{\rm eff}^{\rm SM} | \bar{K}^0 \rangle]}\,; \quad C_{\epsilon_K} = \frac{{\rm Im}[\langle K^0 | H_{\rm eff}^{\rm full} | \bar{K}^0 \rangle]}{{\rm Im}[\langle K^0 | H_{\rm eff}^{\rm SM} | \bar{K}^0 \rangle]} \tag{440}$$

where $q = d, s$, $H_{\rm eff}^{\rm SM}$ includes only the SM box diagrams, while $H_{\rm eff}^{\rm full}$ includes also the NP contributions. For the $K^0 - \bar{K}^0$ mixing, we find it convenient to introduce two parameters related to the real and imaginary parts of the total amplitude to the SM one. In summary,

all NP effects in $\Delta F = 2$ transitions are parametrized in terms of six real quantities, C_{ϵ_K}, $C_{\Delta m_K}$, C_{B_d}, ϕ_{B_d}, C_{B_s} and ϕ_{B_s} [1155].

To further improve the NP parameter determination in the B_s sector, mainly unconstrained in the classical UT analysis, we include in the NP fit recent results from the Tevatron. We use the following experimental inputs: the semileptonic asymmetry in B_s decays $A^s_{\rm SL}$, the dimuon charge asymmetry $A^{\mu\mu}_{\rm SL}$ from CDF and D0, the measurement of the B_s lifetime from flavor-specific final states, and the two-dimensional likelihood ratio for $\Delta\Gamma_s$ and $\phi_s = 2(\beta_s - \phi_{B_s})$ from the time-dependent tagged angular analysis of $B_s \to J/\psi\phi$ decays by CDF and D0 [32]. The new input parameters used in our analysis are given in Ref. [36] and continuously updated in [1159]. The relevant NLO formulas for $\Delta\Gamma_s$ and for the semileptonic asymmetries in the presence of NP have been discussed in Refs. [36, 1160, 1161].

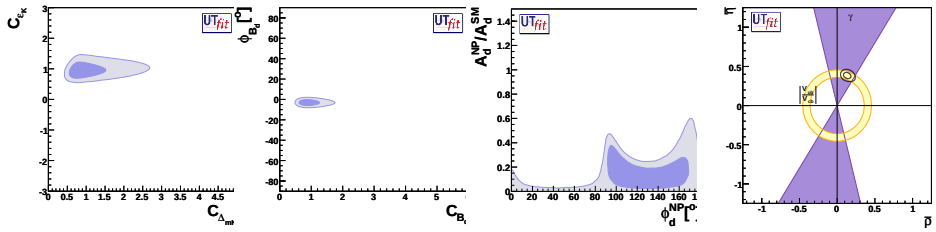

Fig. 101. From left to right, C_{ϵ_K} vs. $C_{\Delta m_K}$, ϕ_{B_d} vs. C_{B_d}, $(A_{\rm NP}/A_{\rm SM})$ vs. $\phi_{\rm NP}$ for NP in the B_d sector and the resulting selected region on the $\bar\rho - \bar\eta$ plane obtained from the NP analysis [36].

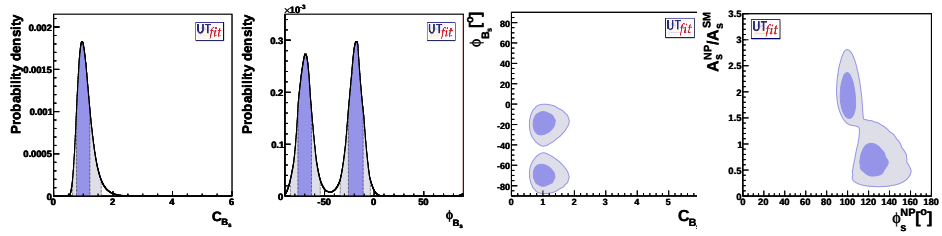

Fig. 102. From left to right, p.d.f.'s for C_{B_s}, ϕ_{B_s}, ϕ_{B_s} *vs.* C_{B_s} and $(A_{\rm NP}/A_{\rm SM})$ vs. $\phi_{\rm NP}$ for NP in the B_s sector [1162].

We also include in the fit NP effects in $\Delta B = 1$ transitions that can also affect some of the measurements entering the UT analysis, in particular the measurements of α, $A_{\rm SL}$ and $\Delta\Gamma_s$ [36, 1160, 1161].

The results obtained in a global fit for the six NP parameters are shown in Fig. 101, together with the corresponding regions in the $\bar\rho$–$\bar\eta$ plane. More details on the analysis can be found in Ref. [1161] (see Ref. [956, 1160] for previous analyses).

Writing $C_{B_q} e^{2i\phi_{B_q}} = (A_{\rm SM} e^{2i\beta_q} + A_{\rm NP} e^{2i(\beta_q + \phi_{\rm NP})})/(A_{\rm SM} e^{2i\beta_q})$ and given the p.d.f. for C_{B_q} and ϕ_{B_q}, we can derive the p.d.f. in the $(A_{\rm NP}/A_{\rm SM})$ vs. $\phi_{\rm NP}$ plane as seen in Fig. 101.

[32] We use the latest D0 results without assumptions on the strong phases

We see that in the B_d system, the NP contribution can be substantial if its phase is close to the SM phase, while for arbitrary phases its magnitude has to be much smaller than the SM one. Notice that, with the latest data, the SM ($\phi_{B_d} = 0$) is disfavored at 68% probability due to the slight disagreement between $\sin 2\beta$ and $|V_{ub}/V_{cb}|$. This requires $A_{\rm NP} \neq 0$ and $\phi_{\rm NP} \neq 0$. For the same reason, $\phi_{\rm NP} > 90^\circ$ at 68% probability and the plot is not symmetric around $\phi_{\rm NP} = 90^\circ$. Assuming that the small but non-vanishing value for ϕ_{B_d} we obtained is just due to a statistical fluctuation, the result of our analysis points either towards models with no new source of flavor and CP violation beyond the ones present in the SM (Minimal Flavor Violation, MFV), or towards models in which new sources of flavor and CP violation are only present in $b \to s$ transitions.

Conversely, from the results of our analysis in the B_s system, we see that the phase ϕ_{B_s} deviates from zero at $\sim 3.0\sigma$. The solution around $\phi_{B_s} \sim -20^\circ$ corresponds to $\phi_s^{\rm NP} \sim -50^\circ$ and $A_s^{\rm NP}/A_s^{\rm SM} \sim 75\%$. The second solution is much more distant from the SM and it requires a dominant NP contribution ($A_s^{\rm NP}/A_s^{\rm SM} \sim 190\%$). In this case the NP phase is thus very well determined. The strong phase ambiguity affects the sign of $\cos\phi_s$ and thus Re $A_s^{\rm NP}/A_s^{\rm SM}$, while Im $A_s^{\rm NP}/A_s^{\rm SM} \sim -0.74$ in any case.

This result shows an hint of discrepancy with respect to the SM expectation in the B_s CP-violating phase. We are eager to see updated measurements using larger data sets from both the Tevatron experiments in order to strengthen the present evidence, waiting for the advent of LHCb for a high-precision measurement of the NP phase.

It is remarkable that to explain the result obtained for ϕ_s, new sources of CP violation beyond the CKM phase are required, strongly disfavoring the MFV hypothesis. These new phases will in general produce correlated effects in $\Delta B = 2$ processes and in $b \to s$ decays. These correlations cannot be studied in a model-independent way, but it will be interesting to analyze them in specific extensions of the SM. In this respect, improving the results on CP violation in $b \to s$ penguins at present and future experimental facilities is of the utmost importance.

If we now consider the most general effective Hamiltonian for $\Delta F = 2$ processes ($\mathcal{H}_{\rm eff}^{\Delta F=2}$ [36]), we can translate the experimental constraints into allowed ranges for the Wilson coefficients of $\mathcal{H}_{\rm eff}^{\Delta F=2}$. These coefficients in general have the form

$$C_i(\Lambda) = \frac{F_i L_i}{\Lambda^2} \tag{441}$$

where F_i is a function of the (complex) NP flavor couplings, L_i is a loop factor that is present in models with no tree-level Flavor Changing Neutral Currents (FCNC), and Λ is the scale of NP, *i.e.* the typical mass of the new particles mediating $\Delta F = 2$ transitions. For a generic strongly-interacting theory with arbitrary flavor structure, one expects $F_i \sim L_i \sim 1$ so that the allowed range for each of the $C_i(\Lambda)$ can be immediately translated into a lower bound on Λ. Specific assumptions on the flavor structure of NP, for example Minimal or Next-to-Minimal Flavor Violation (see Sec. 2.5), correspond to particular choices of the F_i functions. To obtain the p.d.f. for the Wilson coefficients at the NP scale Λ, we switch on one coefficient at a time in each sector and calculate its value from the result of the NP analysis presented above.

The connection between the $C_i(\Lambda)$ and the NP scale Λ depends on the general properties of the NP model, and in particular on the flavor structure of the F_i. Assuming strongly interacting new particles, we have

$$\Lambda = \sqrt{\frac{F_i}{C_i}}\,. \tag{442}$$

In deriving the lower bounds on the NP scale Λ, we assume $L_i = 1$, corresponding to strongly-interacting and/or tree-level NP. Two other interesting possibilities are given by loop-mediated NP contributions proportional to α_s^2 or α_W^2.

Assuming strongly interacting and/or tree-level NP contributions with generic flavor structure (*i.e.* $L_i = |F_i| = 1$), we can translate the upper bounds on C_i into the lower bounds on the NP scale Λ. Conversely, in case of hints of NP effects, an upper bounds on the NP scale Λ is extracted.

Table 88
95% probability lower bounds on the NP scale Λ (in TeV) for several possible flavor structures and loop suppressions from the K and B_d systems.

Scenario	strong/tree	α_s loop	α_W loop
MFV	5.5	0.5	0.2
NMFV	62	6.2	2
General	240000	24000	8000

Table 89
95% probability upper bounds on the NP scale Λ (in TeV) for several possible flavor structures and loop suppressions from the B_s system.

Scenario	strong/tree	α_s loop	α_W loop
NMFV	35	4	2
General	800	80	30

From the lower bound Tab. 88, we could conclude that any model with strongly interacting NP and/or tree-level contributions is beyond the reach of direct searches at the LHC. Flavor and CP violation remain the main tool to constrain (or detect) such NP models. Weakly-interacting extensions of the SM can be accessible at the LHC provided that they enjoy a MFV-like suppression of $\Delta F = 2$ processes, or at least a NMFV-like suppression with an additional depletion of the NP contribution to ϵ_K.

If we consider the current effect in the B_s mixing, we obtain the upper bound Tab. 89 and we notice that the general model is strongly problematic being the upper bound at a much lower scale with respect to the corresponding lower bound resulting from the K and B_d systems. NMFV models are less problematic, but they can hardly reproduce with the current size of the NP effect in the B_s system while keeping small effects in the B_d and even smaller effects in the K system. Finally, MFV models would have possible solutions in this scheme but they cannot generate the effect in the B_s phase. So the current hint suggests some hierarchy in NP mixing which is stronger that the SM one.

10.2.2. *Impact of flavor physics measurements on grand unified*

In a model of physics beyond the Standard Model, it is expected that observables in the flavor physics are affected by the contributions from new particles which couple to the quarks and leptons. Comparing measured values of flavor observables with the Standard Model predictions enables us to obtain information on the new physics contributions. If the measured value of certain observable differs from the Standard Model prediction, the difference shows the magnitude of the new physics contribution. If the measured value is consistent with the Standard Model prediction, that measurement is still useful as a constraint on the new physics.

Here we focus on the cases of supersymmetric grand unified models. For general reviews of supersymmetric models, see Refs. [154, 1163, 1164] and references therein.

In supersymmetric extensions of the Standard Model, there exist superpartners of the Standard Model particles, namely squarks, sleptons, gauginos and higgsinos. Supersym-

metrized interactions include quark-squark-gaugino and quark-squark-higgsino couplings. The mass matrices of the superparticles are different from corresponding ones of the Standard Model particles because of the supersymmetry breaking. Therefore the flavor mixing among the squarks depend on flavor structure of the supersymmetry breaking mechanism. The mismatch between the flavor bases of quarks and squarks generates mixing matrices at the quark-squark-gaugino(higgsino) interactions. These mixing matrices are not necessarily the same as the CKM matrix and affect the flavor changing amplitudes through loop diagrams with squarks in the internal lines.

Importance of the flavor physics in supersymmetric models have been recognized since early 1980's [161, 162]. It was pointed out that squarks of the first and second generations must be almost degenerate in mass, since otherwise too large contribution to the $K - \bar{K}$ mixing would be given by squark-gaugino loops. This requirement, which is known as "SUSY flavor problem", motivates us to build a model of supersymmetry breaking mechanism that controls the squark mass matrices. The minimal supergravity (mSUGRA) model is one of those models. In mSUGRA, it is assumed that the supersymmetry breaking occurs in a hidden sector and its effect is transferred to the observable sector by (super-)gravitational interactions. Consequently, the supersymmetry breaking masses and interactions of the superparticles are generated near the Planck scale and flavor-blind. Mass differences and flavor mixings of the squarks are induced by the (supersymmetrized) Yukawa interactions through radiative corrections. Therefore the degeneracy of the first and the second generation squarks is explained by the smallness of the Yukawa couplings of the light quarks. On the other hand, masses of the third generation squarks, particularly stop, receive significant corrections from large top Yukawa coupling. Squark flavor mixing occurs in left-handed squarks and the mixing matrix is approximately the same as the CKM matrix [1165–1167].

Effects of the superparticles on flavor observables have been studied in the past decades [1168–1170], and it turns out that deviations from the Standard Model predictions are small in the simplest mSUGRA scenario, under the improved constraints from direct searches for the superparticles and the Higgs bosons at LEP and Tevatron experiments. An exception is the $b \to s\,\gamma$ decay. $b \to s\,\gamma$ in supersymmetric models has been studied intensively in 1990's [1171–1174]. It is shown that the contributions from the suparparticle loops can be as large as the Standard Model one, thus the agreement between the measured value of $B(b \to s\,\gamma)$ and its Standard Model prediction gives us an important constraint on the parameter space of a supersymmetric model.

After the existence of the neutrino masses is established by neutrino oscillation experiments, flavor mixing in the lepton sector has been also taken into account. Although the the neutrino masses are very small compared to the quark and charged lepton masses, Yukawa couplings of the neutrinos need not to be small. If the see-saw mechanism [1175–1177] works and the Majorana masses of the right-handed neutrinos are sufficiently large, the Yukawa coupling constants of the neutrinos may be $O(1)$. In the mSUGRA scenario, the neutrino Yukawa coupling generates the flavor mixing in the slepton mass matrices through radiative corrections. The flavor mixing in the sleptons eventually induces the lepton flavor violating processes such as $\mu \to e\,\gamma$ [1178, 1179].

In the supersymmetric grand unified models, the Yukawa interactions of quarks and leptons are unified at the energy scale of the grand unification. Therefore both squark and slepton mass matrices receive flavor off-diagonal contributions due to the unified Yukawa interactions above the GUT scale. In a $SU(5)$ unification model, flavor mixings

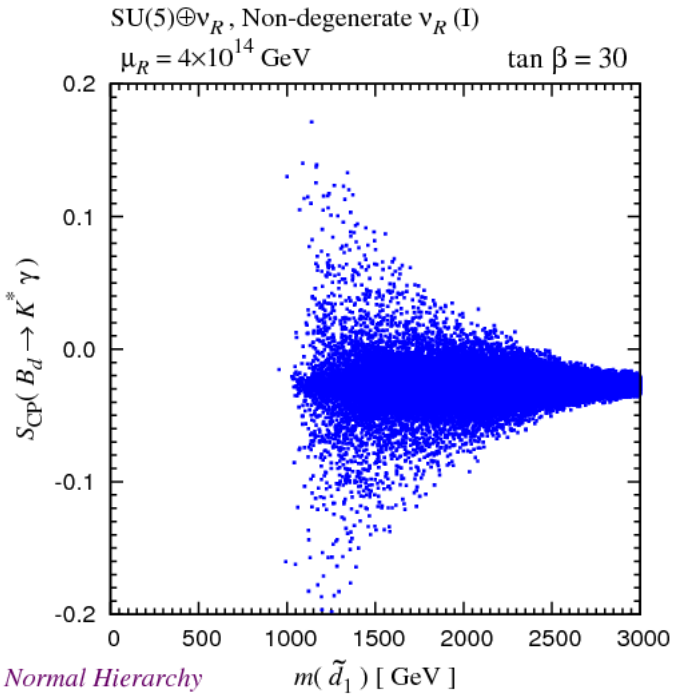

Fig. 103. Mixing-induced CP asymmetry in $B_d \to K^* \gamma$ decay as a function of the lightest down-type squark mass in the $SU(5)$ SUSY GUT with right-handed neutrinos [1186].

of the left-handed squarks and the right-handed charged sleptons are governed by the Yukawa coupling matrix of the up-type quarks that consists of the top Yukawa coupling [1180,1181]. On the other hand, the right-handed down-type squarks and the left-handed sleptons receive contributions form the neutrino Yukawa coupling matrix, which is related to the Maki-Nakagawa-Sakata neutrino mixing matrix [1182]. Since the neutrino mixing angle between the second and the third generations is known to be large, it is expected that significant $\tilde{b}_R - \tilde{s}_R$ mixing is induced when the magnitudes of the neutrino Yukawa couplings are sufficiently large [1183–1185].

The squark flavor mixings, which are generated by the (grand-unified) neutrino Yukawa interactions, contribute to the quark flavor changing amplitudes. Since these additional contributions are independent of the CKM matrix, it is possible that deviations from the Standard Model predictions of the flavor observables in the B decays are sizably large while those in K decays are suppressed. Fig. 103 [1186] shows the mixing-induced CP asymmetry in $B_d \to K^* \gamma$ decay as a function of the lightest down-type squark mass in the $SU(5)$ SUSY GUT with right-handed neutrinos. Each dot in the plot corresponds to a different choice of supersymmetry breaking parameters in the mSUGRA scenario. CKM matrix elements and neutrino parameters are fixed. The neutrino Yukawa coupling matrix is chosen so that the flavor mixing between the second and the third generations is large, whereas the mixing between the first and the second generations is suppressed. With this choice, SUSY contributions to the $K - \bar{K}$ mixing (ε_K) and $\mu \to e\gamma$ are small enough. It is seen that there exist parameter regions where the asymmetry is as

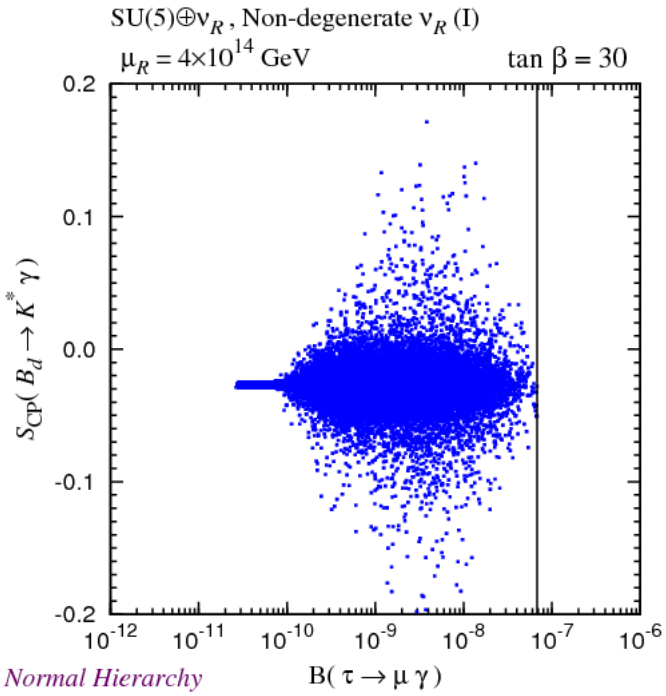

Fig. 104. Correlation between the mixing-induced CP asymmetry in $B_d \to K^* \gamma$ and the branching fraction of $\tau \to \mu \gamma$ [1186].

large as $\pm 20\%$ for the squark mass $\sim$ 1TeV satisfying other experimental constraints. Other observables in $b \to s$ transition, such as the time-dependent CP asymmetries in $B_d \to \phi K_S$ and $B_s \to J/\psi \phi$ are also affected significantly in the same parameter region.

Another characteristic feature is that the SUSY flavor signals in the quark and lepton sectors are correlated with each other [1186]. As can be seen in Fig. 104, the branching fraction of $\tau \to \mu \gamma$ can be as large as 10^{-8} in the parameter region with large corrections to $b \to s$ observables.

The pattern of deviations from the Standard Model predictions depends on the flavor structure of the masses and interactions of the squarks and sleptons. Therefore a combined analysis of many flavor observables provides us with important clue on physics determining the structure of the SUSY breaking sector.

10.2.3. *New physics in extra-dimension models*

In recent years a lot of interest was dedicated to extensions of the Standard Model involving one or more extra dimensions (ED), motivated by the possibility to find a *natural* solution, in this context, of the hierarchy between the electroweak and the Planck scale. ED models can be grouped basically into three classes according to the space-time geometry of the ED and the localization properties of SM fields. In ADD [1187, 1188] models the space-time is extended by one or more large (sub-millimeter) EDs with flat geometry. Only gravity is allowed to propagate in the higher-dimensional bulk, while all gauge and matter fields are confined to a 4d brane. In a different class of models,

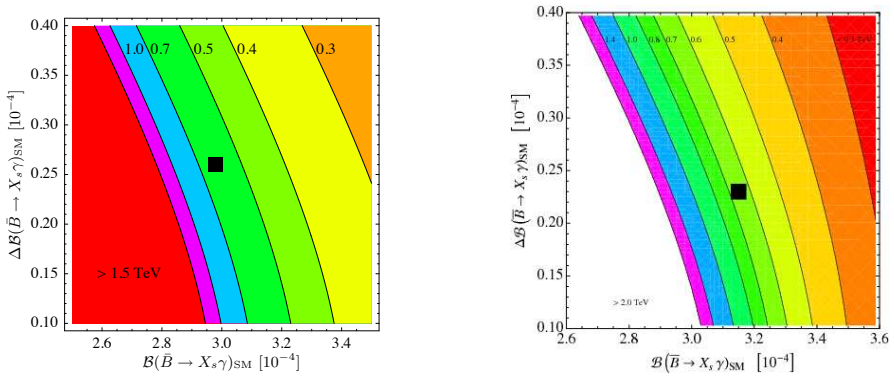

Fig. 105. 95 % C.L. limits on $1/R$ as a function of the SM central value and error on $\mathcal{B}(\bar{B}\to X_s\gamma)$ for the minimal UED5 [662] and UED6 [663] models.

dubbed Universal Extra Dimensions (UED) [1189], the EDs have flat geometry and are compactified, but now the SM fields are free to propagate in the bulk. Finally, in RS [1190, 1191] models, a 5d warped space-time is considered. Nowadays, in most phenomenological applications modifications of the original RS1 setup [1190] are considered, where gauge and matter fields propagate in the 5d bulk [176, 1192, 1193] and only the Higgs boson is confined on or near the IR brane. In the following we will summarize flavor physics constraints on UED and warped models.

10.2.3.1. *Universal extra dimensions (UED).* For what concerns UEDs we consider the so called minimal UED5 [1189] and minimal UED6 [1194–1196] models, characterized by one ED compactified on $S^1/\mathbb{Z}_2$ and two EDs compactified on $T^2/\mathbb{Z}_2$, respectively. The minimality refers to the absence of flavor non-universal boundary terms that would lead to unacceptably large flavor changing neutral currents. With these assumptions the Kaluza-Klein (KK) modes of the SM fields induce new contributions to flavor violating processes. As the models are minimal flavor violating (see Sec. 2.5), those interactions are entirely controlled by the CKM matrix and the relevant free parameters of the models are the compactification radius R and the cut-off scale Λ at which the full (5d/6d) theory becomes non-perturbative. Detailed analyses of FCNC processes in UED5 and UED6 have been presented in [660–662, 842, 1197–1206] and [660, 663], respectively. Lower bounds on $1/R$ come from oblique corrections, $Z\to b\bar{b}$, $(g-2)_\mu$ and $b\to s\gamma$, with the latter providing by far the strongest constraint. It is interesting to note that UED contributions to $b\to s\gamma$ tend always to decrease the branching ratio and, within the 5d (6d) theory, have a negligible (logarithmic) dependence on the cut-off Λ. Utilizing the world average $\mathcal{B}(\bar{B}\to X_s\gamma)_{\rm exp} = (3.55\pm 0.24^{+0.09}_{-0.10}\pm 0.03)\cdot 10^{-4}$ the authors of Refs. [662, 663] find that in both models the inverse compactification radius has to be larger than about 600 GeV, with the exact bound depending quite sensitively on the theoretical prediction for the central value. Their findings are summarized in Fig. 105. A discussion of these models in the context of dark matter and accelerator searches can be found, for instance, in Ref. [1207].

10.2.3.2. *Bulk fermions in a warped ED.* The case of bulk fermions in a warped ED is more interesting from the flavor physics point of view, as the localization of fermion zero modes along the 5^{th} dimension provides an intrinsic explanation of the observed

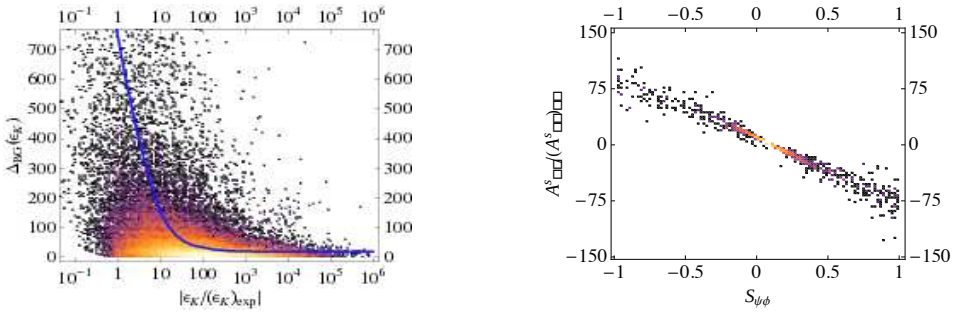

Fig. 106. *left:* Required Barbieri-Giudice [1224] fine-tuning $\Delta_{\rm BG}(\varepsilon_K)$ as a function of ε_K in the custodially protected RS model. The blue curve displays the average fine-tuning [182]. *right:* Correlation between the CP-asymmetries $A^s_{\rm SL}$ and $S_{\psi\phi}$ in the custodially protected RS model, fulfilling all available $\Delta F = 2$ constraints [182].

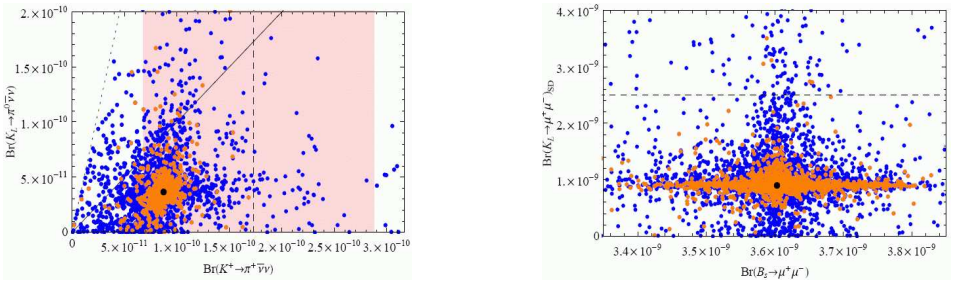

Fig. 107. *left:* $Br(K_L \to \pi^0\nu\bar{\nu})$ as a function of $Br(K^+ \to \pi^+\nu\bar{\nu})$ in the custodially protected RS model [181]. The shaded area represents the experimental 1σ-range for $Br(K^+ \to \pi^+\nu\bar{\nu})$. *right:* $Br(K_L \to \mu^+\mu^-)$ versus $Br(B_s \to \mu^+\mu^-)$ in the custodially protected RS model [181].

hierarchies in fermion masses and mixings [176, 1193, 1208]. Due to the absence of KK parity, here new physics contributions to FCNC observables appear already at the tree level, however they are strongly suppressed thanks to the so-called RS-GIM mechanism [178]. In contrast to the UED models, this class of models goes beyond MFV and many new flavor violating parameters and CP phases are present, in addition to new flavor violating operators beyond the SM ones.

In order to obtain agreement with the electroweak T parameter, usually an enlarged gauge sector $SU(2)_L \times SU(2)_R \times U(1)_X$ is considered [1209, 1210], together with custodially protected fermion representations that avoid large anomalous $Zb_L\bar{b}_L$ [1211–1214] and at the same time also $Zd^i_L\bar{d}^j_L$ [181, 182, 1215] couplings. Consequently the KK mass scale can be as low as $M_{\rm KK} \simeq (2-3)\,$TeV and therefore in the reach of direct LHC searches.

The impact of RS bulk matter on quark flavor violating observables has been discussed extensively in the literature, see e.g. [178, 181, 182, 1216–1223] for details. Here we focus only on the most stringent constraint, coming from the ε_K observable, that measures indirect CP-violation in the neutral K meson sector, and on implications for flavor observables that have not yet been measured with high precision.

In contrast to the SM, the tree level exchange of KK gauge bosons induces amongst others the presence of left-right operators $\mathcal{Q}_{LR}$ contributing to $\Delta F = 2$ processes. These

operators receive large renormalisation group corrections and are in the case of $K^0 - \bar{K}^0$ mixing in addition chirally enhanced. It turns out then that the otherwise so powerful RS-GIM mechanism in this case is not sufficient to suppress the new physics contribution below the experimental limits, so that assuming completely anarchic 5d Yukawa couplings a lower bound on the KK mass scale $M_{\rm KK} \simeq 20\,{\rm TeV}$ is obtained [182,1221]. In [182] it has been shown however that allowing for modest hierarchies in the 5d Yukawas agreement with ε_K can be obtained even without significant fine-tuning (see Fig. 106), so that a natural solution to the "ε_K-problem" even for low KK scales cannot be excluded. Imposing then all available $\Delta F = 2$ constraints on the RS parameter space, large new CP-violating effects in $B_s - \bar{B}_s$ mixing can still be found in this model [182], offering a neat explanation of the recent CDF and D0 data [232, 958, 1225]. In addition slight tensions between CP-violation in K and B_d observables [872,1076] could easily be resolved thanks to the presence of non-MFV interactions [182]. An interesting pattern of deviations from the SM can also be found in the case of rare K and $B_{d,s}$ decays (see Fig. 107) [181]. As the dominant contribution stems from tree level flavor changing couplings of the Z boson to right-handed down-type quarks, generally larger effects are to be expected in rare K decays, e. g. $Br(K_L \to \pi^0 \nu\bar{\nu})$ can be enhanced by up to a factor 5. While the effects in $B_{d,s}$ decays are much more modest (e. g. $\pm 20\%$ in $Br(B_{d,s} \to \mu^+\mu^-)$), flavor universality can be strongly violated, so that interesting deviations from the MFV predictions appear. Striking correlations arise not only between various rare K decays, but also between K and $B_{d,s}$ physics observables, thus allowing to distinguish this framework from other new physics scenarios.

Alternative solutions to solve the "ε_K-problem", based on flavor symmetries, have as well been discussed in the recent literature. One approach is to protect the model from all tree level FCNCs by incorporating a full 5d GIM mechanism [183], in which the bulk respects a full $U(3)^3$ flavor symmetry. Although this model is safe, since its effective theory is MFV, it leaves the origin of the large hierarchies in the flavor sector unanswered. More recent proposals therefore seek to suppress dangerous FCNCs and simultaneously try to explain the hierarchical structure of the flavor sector. One of them is the so called "5d MFV" model [1226]. Here one postulates that the only sources of flavor breaking are two anarchic Yukawa spurions. The low-energy limit is not MFV, and the additional assumption, that brane and bulk terms in the down sector are effectively aligned, is needed to suppress dangerous FCNCs. Recently, an economical model has been proposed [1227] in which one assumes a $U(3)$ flavor symmetry for the 5D fields containing the right handed down quarks. Dangerous contributions to $\mathcal{Q}_{LR}$ are then only generated by suppressed mass insertions on the IR brane where the symmetry is necessarily broken. Another recent approach [184] presents a simple model where the key ingredient are two horizontal $U(1)$ symmetries which induce an alignment of bulk masses and down Yukawas, thus strongly suppressing FCNCs in the down sector. FCNCs in the up sector, however, can be close to experimental limits.

11. Acknowledgements

We would like to thank the Universitá "Sapienza" of Rome and in particular its Department of Physics for the hospitality during the days of the workshop (9-13 September 2008). For the finantial and organizational support to the workshop itself we would like

to thank INFN and in particular its Roma1 Section and the Local Organizing Committee (D. Anzellotti, C. Bulfon, G. Bucci, E. Di Silvestro, R. Faccini, M. Mancini, G. Piredda, and R. Soldatelli) respectively.

The program of the workshop was elaborated by the Programm Committee (P. Ball, G. Cavoto, M. Ciuchini, R. Faccini – chair, R. Forty, S. Giagu, P. Gambino, B. Grinstein, S. Hashimoto, T. Iijima, G. Isidori, V. Luth, G. Piredda, M. Rescigno, and A. Stocchi) under consultation of the International Advisory Committee (I. I. Bigi, C. Bloise, A. Buras, N. Cabibbo, A. Ceccucci, P. Chang, F. Ferroni, A. Golutvin, A. Jawahery, A. S. Kronfeld, Y. Kwon, M. Mangano, W. J. Marciano, G. Martinelli, A. Masiero, T. Nakada, M. Neubert, P. Roudeau, A. I. Sanda, M. D. Shapiro, I. P.J. Shipsey, A. Soni, W. J. Taylor, N. G. Uraltsev, and M. Yamauchi).

This work is supported by Australian Research Council and the Australian Department of Industry Innovation, Science and Research, the Natural Sciences and Engineering Research Council (Canada), the National Science Fundation of China, the Commissariat à l'Energie Atomique and Institut National de Physique Nucléaire et de Physique des Particules (France), the Bundesministerium für Bildung und Forschung and Deutsche Forschungsgemeinschaft (Germany), the Department of Science and Technology of India the Istituto Nazionale di Fisica Nucleare (Italy), the Ministry of Education Culture, Sports, Science, and Technology (Japan), the Japan Society of Promotion of Science, the BK21 program of the Ministry of Education of Korea, the Research Council of Norway, the Ministry of Education and Science of the Russian Federation, the Slovenian Research Agency, Ministerio de Educación y Ciencia (Spain), the Science and Technology Facilities Council (United Kingdom), and the US Department of Energy and National Science Foundation .

Individuals have received support from European Community's Marie-Curie Research Training Networks under contracts MRTN-CT-2006-035505 ('Tools and Precision Calculations for Physics Discoveries at Colliders') and MRTN-CT-2006-035482 ('FLAVIAnet'), from the National Science Fundation of China (grants 10735080 and 10625525), the DFG Cluster of Excellence 'Origin and Structure of the Universe' (grant BU 706/2-1), the Jpan Society for the Promotion of Science (grant 20244037), and the A. von Humboldt Stiftung, from MICINN, Spain (grant FPA2007-60323), from the ITP at University of Zurich, from the US National Science Fundation (grant PHY-0555304) and Department of Energy (grants DE-FG02-96ER41005 and DE-AC02-07CH11359 – Fermi Research Alliance, LLC), and from Generalitat Valenciana (grant PROMETEO/2008/069).

References

[1] N. Cabibbo, Unitary Symmetry and Leptonic Decays, Phys. Rev. Lett. 10 (1963) 531–533.

[2] M. Kobayashi, T. Maskawa, CP Violation in the Renormalizable Theory of Weak Interaction, Prog. Theor. Phys. 49 (1973) 652–657.

[3] L.-L. Chau, W.-Y. Keung, Comments on the Parametrization of the Kobayashi-Maskawa Matrix, Phys. Rev. Lett. 53 (1984) 1802.

[4] C. Amsler, A. Masoni, The $\eta(1405)$, $\eta(1475)$, $f_1(1420)$, and $f_1(1510)$.

[5] L. Wolfenstein, Parametrization of the Kobayashi-Maskawa Matrix, Phys. Rev. Lett. 51 (1983) 1945.

[6] A. J. Buras, M. E. Lautenbacher, G. Ostermaier, Waiting for the top quark mass, K+ $\to$ pi+ neutrino anti-neutrino, B(s)0 - anti-B(s)0 mixing and CP asymmetries in B decays, Phys. Rev. D50 (1994) 3433–3446.

[7] R. Aleksan, B. Kayser, D. London, Determining the quark mixing matrix from CP violating asymmetries, Phys. Rev. Lett. 73 (1994) 18–20.
[8] J. P. Silva, L. Wolfenstein, Detecting new physics from CP-violating phase measurements in B decays, Phys. Rev. D55 (1997) 5331–5333.
[9] C. Jarlskog, Commutator of the Quark Mass Matrices in the Standard Electroweak Model and a Measure of Maximal CP Violation, Phys. Rev. Lett. 55 (1985) 1039.
[10] K. G. Wilson, Nonlagrangian models of current algebra, Phys. Rev. 179 (1969) 1499–1512.
[11] K. G. Wilson, The Renormalization Group and Strong Interactions, Phys. Rev. D3 (1971) 1818.
[12] M. K. Gaillard, B. W. Lee, $\Delta I = 1/2$ Rule for Nonleptonic Decays in Asymptotically Free Field Theories, Phys. Rev. Lett. 33 (1974) 108.
[13] G. Altarelli, L. Maiani, Octet Enhancement of Nonleptonic Weak Interactions in Asymptotically Free Gauge Theories, Phys. Lett. B52 (1974) 351–354.
[14] E. Witten, Short Distance Analysis of Weak Interactions, Nucl. Phys. B122 (1977) 109.
[15] F. J. Gilman, M. B. Wise, Effective Hamiltonian for $\Delta S = 1$ Weak Nonleptonic Decays in the Six Quark Model, Phys. Rev. D20 (1979) 2392.
[16] B. Guberina, R. D. Peccei, Quantum Chromodynamic Effects and CP Violation in the Kobayashi-Maskawa Model, Nucl. Phys. B163 (1980) 289.
[17] A. I. Vainshtein, V. I. Zakharov, M. A. Shifman, A Possible mechanism for the $\Delta T = 1/2$ rule in nonleptonic decays of strange particles, JETP Lett. 22 (1975) 55–56.
[18] M. A. Shifman, A. I. Vainshtein, V. I. Zakharov, Light Quarks and the Origin of the $\Delta I = 1/2$ Rule in the Nonleptonic Decays of Strange Particles, Nucl. Phys. B120 (1977) 316.
[19] M. A. Shifman, A. I. Vainshtein, V. I. Zakharov, Nonleptonic Decays of K Mesons and Hyperons, Sov. Phys. JETP 45 (1977) 670.
[20] F. J. Gilman, M. B. Wise, K0 anti-K0 Mixing in the Six Quark Model, Phys. Rev. D27 (1983) 1128.
[21] J. Bijnens, M. B. Wise, Electromagnetic Contribution to Epsilon-prime/Epsilon, Phys. Lett. B137 (1984) 245.
[22] M. Lusignoli, Electromagnetic corrections to the effective hamiltonian for strangeness changing decays and ϵ'/ϵ, Nucl. Phys. B325 (1989) 33.
[23] K. G. Chetyrkin, M. Misiak, M. Munz, Weak radiative B-meson decay beyond leading logarithms, Phys. Lett. B400 (1997) 206–219.
[24] M. Gorbahn, U. Haisch, Effective Hamiltonian for non-leptonic $|\Delta F| = 1$ decays at NNLO in QCD, Nucl. Phys. B713 (2005) 291–332.
[25] A. J. Buras, M. Jamin, M. E. Lautenbacher, Two loop anomalous dimension matrix for $\Delta S = 1$ weak nonleptonic decays. 2. O(alpha-alpha-s), Nucl. Phys. B400 (1993) 75–102.
[26] M. Ciuchini, E. Franco, G. Martinelli, L. Reina, The $\Delta S = 1$ effective Hamiltonian including next-to- leading order QCD and QED corrections, Nucl. Phys. B415 (1994) 403–462.
[27] C. Bobeth, M. Misiak, J. Urban, Photonic penguins at two loops and m(t)-dependence of $BR(B \to X(s)\ell^+\ell^-)$, Nucl. Phys. B574 (2000) 291–330.
[28] M. Misiak, M. Steinhauser, Three-loop matching of the dipole operators for $b \to s\gamma$ and $b \to sg$, Nucl. Phys. B683 (2004) 277–305.
[29] M. Gorbahn, U. Haisch, M. Misiak, Three-loop mixing of dipole operators, Phys. Rev. Lett. 95 (2005) 102004.
[30] M. Czakon, U. Haisch, M. Misiak, Four-loop anomalous dimensions for radiative flavour- changing decays, JHEP 03 (2007) 008.
[31] A. J. Buras, P. Gambino, M. Gorbahn, S. Jager, L. Silvestrini, Universal unitarity triangle and physics beyond the standard model, Phys. Lett. B500 (2001) 161–167.
[32] A. J. Buras, W. Slominski, H. Steger, B Meson Decay, CP Violation, Mixing Angles and the Top Quark Mass, Nucl. Phys. B238 (1984) 529.
[33] A. J. Buras, M. Jamin, P. H. Weisz, Leading and next-to-leading QCD corrections to ϵ parameter and $B^0 - \bar{B}^0$ mixing in the presence of a heavy top quark, Nucl. Phys. B347 (1990) 491–536.
[34] S. Herrlich, U. Nierste, Enhancement of the K(L) - K(S) mass difference by short distance QCD corrections beyond leading logarithms, Nucl. Phys. B419 (1994) 292–322.
[35] S. Herrlich, U. Nierste, The Complete $|\Delta S| = 2$ Hamiltonian in the Next-To- Leading Order, Nucl. Phys. B476 (1996) 27–88.
[36] M. Bona, et al., Model-independent constraints on $\Delta F = 2$ operators and the scale of new physics, JHEP 03 (2008) 049.

[37] M. Gronau, D. London, Isospin analysis of CP asymmetries in B decays, Phys. Rev. Lett. 65 (1990) 3381–3384.
[38] M. Beneke, G. Buchalla, M. Neubert, C. T. Sachrajda, QCD factorization for $B \to \pi\pi$ decays: Strong phases and CP violation in the heavy quark limit, Phys. Rev. Lett. 83 (1999) 1914–1917.
[39] M. Beneke, G. Buchalla, M. Neubert, C. T. Sachrajda, QCD factorization for exclusive, non-leptonic B meson decays: General arguments and the case of heavy-light final states, Nucl. Phys. B591 (2000) 313–418.
[40] M. Beneke, G. Buchalla, M. Neubert, C. T. Sachrajda, QCD factorization in $B \to \pi K$, $\pi\pi$ decays and extraction of Wolfenstein parameters, Nucl. Phys. B606 (2001) 245–321.
[41] C. W. Bauer, S. Fleming, M. E. Luke, Summing Sudakov logarithms in $B \to X_s + \gamma$ in effective field theory, Phys. Rev. D63 (2000) 014006.
[42] C. W. Bauer, S. Fleming, D. Pirjol, I. W. Stewart, An effective field theory for collinear and soft gluons: Heavy to light decays, Phys. Rev. D63 (2001) 114020.
[43] C. W. Bauer, I. W. Stewart, Invariant operators in collinear effective theory, Phys. Lett. B516 (2001) 134–142.
[44] C. W. Bauer, D. Pirjol, I. W. Stewart, Soft-Collinear Factorization in Effective Field Theory, Phys. Rev. D65 (2002) 054022.
[45] H.-n. Li, H.-L. Yu, Perturbative QCD analysis of B meson decays, Phys. Rev. D53 (1996) 2480–2490.
[46] H.-N. Li, H.-L. Yu, PQCD analysis of exclusive charmless B meson decay spectra, Phys. Lett. B353 (1995) 301–305.
[47] T.-W. Yeh, H.-n. Li, Factorization theorems, effective field theory, and nonleptonic heavy meson decays, Phys. Rev. D56 (1997) 1615–1631.
[48] Y.-Y. Keum, H.-n. Li, A. I. Sanda, Fat penguins and imaginary penguins in perturbative QCD, Phys. Lett. B504 (2001) 6–14.
[49] Y. Y. Keum, H.-N. Li, A. I. Sanda, Penguin enhancement and $B \to K\pi$ decays in perturbative QCD, Phys. Rev. D63 (2001) 054008.
[50] C.-H. Chen, Y.-Y. Keum, H.-n. Li, Perturbative QCD analysis of $B \to \phi K$ decays, Phys. Rev. D64 (2001) 112002.
[51] C. W. Bauer, D. Pirjol, I. Z. Rothstein, I. W. Stewart, $B \to M_1 M_2$: Factorization, charming penguins, strong phases, and polarization, Phys. Rev. D70 (2004) 054015.
[52] C. W. Bauer, I. Z. Rothstein, I. W. Stewart, SCET analysis of $B \to K\pi$, $B \to K\bar{K}$, and $B \to \pi\pi$ decays, Phys. Rev. D74 (2006) 034010.
[53] A. R. Williamson, J. Zupan, Two body B decays with isosinglet final states in SCET, Phys. Rev. D74 (2006) 014003.
[54] K. G. Wilson, Confinement of Quarks, Phys. Rev. D10 (1974) 2445–2459.
[55] J. B. Kogut, A Review of the Lattice Gauge Theory Approach to Quantum Chromodynamics, Rev. Mod. Phys. 55 (1983) 775.
[56] D. Friedan, A proof of the Nielsen-Ninomiya theorem, Commun. Math. Phys. 85 (1982) 481–490.
[57] H. B. Nielsen, M. Ninomiya, Absence of Neutrinos on a Lattice. 1. Proof by Homotopy Theory, Nucl. Phys. B185 (1981) 20.
[58] T. Banks, L. Susskind, J. B. Kogut, Strong Coupling Calculations of Lattice Gauge Theories: (1+1)-Dimensional Exercises, Phys. Rev. D13 (1976) 1043.
[59] L. Susskind, Lattice Fermions, Phys. Rev. D16 (1977) 3031–3039.
[60] K. G. Wilson, Quarks: From Paradox to Myth, Subnucl. Ser. 13 (1977) 13–32.
[61] P. H. Ginsparg, K. G. Wilson, A Remnant of Chiral Symmetry on the Lattice, Phys. Rev. D25 (1982) 2649.
[62] U. J. Wiese, Fixed point actions for Wilson fermions, Phys. Lett. B315 (1993) 417–424.
[63] P. Hasenfratz, V. Laliena, F. Niedermayer, The index theorem in QCD with a finite cut-off, Phys. Lett. B427 (1998) 125–131.
[64] D. B. Kaplan, A Method for simulating chiral fermions on the lattice, Phys. Lett. B288 (1992) 342–347.
[65] Y. Shamir, Chiral fermions from lattice boundaries, Nucl. Phys. B406 (1993) 90–106.
[66] V. Furman, Y. Shamir, Axial symmetries in lattice QCD with Kaplan fermions, Nucl. Phys. B439 (1995) 54–78.
[67] T. Blum, A. Soni, QCD with domain wall quarks, Phys. Rev. D56 (1997) 174–178.

[68] H. Neuberger, Exactly massless quarks on the lattice, Phys. Lett. B417 (1998) 141–144.
[69] H. Neuberger, More about exactly massless quarks on the lattice, Phys. Lett. B427 (1998) 353–355.
[70] M. Luscher, Exact chiral symmetry on the lattice and the Ginsparg- Wilson relation, Phys. Lett. B428 (1998) 342–345.
[71] P. F. Bedaque, Aharonov-Bohm effect and nucleon nucleon phase shifts on the lattice, Phys. Lett. B593 (2004) 82–88.
[72] G. M. de Divitiis, R. Petronzio, N. Tantalo, On the discretization of physical momenta in lattice QCD, Phys. Lett. B595 (2004) 408–413.
[73] G. 't Hooft, A Property of Electric and Magnetic Flux in Nonabelian Gauge Theories, Nucl. Phys. B153 (1979) 141.
[74] M. Luscher, Volume Dependence of the Energy Spectrum in Massive Quantum Field Theories. 1. Stable Particle States, Commun. Math. Phys. 104 (1986) 177.
[75] C. T. Sachrajda, G. Villadoro, Twisted boundary conditions in lattice simulations, Phys. Lett. B609 (2005) 73–85.
[76] M. Luscher, Signatures of unstable particles in finite volume, Nucl. Phys. B364 (1991) 237–254.
[77] L. Lellouch, M. Luscher, Weak transition matrix elements from finite-volume correlation functions, Commun. Math. Phys. 219 (2001) 31–44.
[78] A. S. Kronfeld, Uses of effective field theory in lattice QCD. arXiv:hep-lat/0205021.
[79] J. Gasser, H. Leutwyler, Spontaneously Broken Symmetries: Eeffective Lagrangians at Finite Volume, Nucl. Phys. B307 (1988) 763.
[80] G. Colangelo, C. Haefeli, Finite volume effects for the pion mass at two loops, Nucl. Phys. B744 (2006) 14–33.
[81] K. Symanzik, Continuum Limit and Improved Action in Lattice Theories. 1. Principles and phi**4 Theory, Nucl. Phys. B226 (1983) 187.
[82] K. Symanzik, Continuum Limit and Improved Action in Lattice Theories. 2. O(N) Nonlinear Sigma Model in Perturbation Theory, Nucl. Phys. B226 (1983) 205.
[83] A. S. Kronfeld, Application of heavy-quark effective theory to lattice QCD. I: Power corrections, Phys. Rev. D62 (2000) 014505.
[84] J. Harada, et al., Application of heavy-quark effective theory to lattice QCD. II: Radiative corrections to heavy-light currents, Phys. Rev. D65 (2002) 094513.
[85] J. Harada, S. Hashimoto, A. S. Kronfeld, T. Onogi, Application of heavy-quark effective theory to lattice QCD. III: Radiative corrections to heavy-heavy currents, Phys. Rev. D65 (2002) 094514.
[86] A. S. Kronfeld, Heavy quarks and lattice QCD, Nucl. Phys. Proc. Suppl. 129 (2004) 46–59.
[87] G. M. de Divitiis, M. Guagnelli, F. Palombi, R. Petronzio, N. Tantalo, Heavy-light decay constants in the continuum limit of lattice QCD, Nucl. Phys. B672 (2003) 372–386.
[88] H.-W. Lin, N. Christ, Non-perturbatively determined relativistic heavy quark action, Phys. Rev. D76 (2007) 074506.
[89] E. Marinari, G. Parisi, C. Rebbi, Monte Carlo Simulation of the Massive Schwinger Model, Nucl. Phys. B190 (1981) 734.
[90] D. Weingarten, Monte Carlo Evaluation of Hadron Masses in Lattice Gauge Theories with Fermions, Phys. Lett. B109 (1982) 57.
[91] C. T. H. Davies, et al., High-precision lattice QCD confronts experiment, Phys. Rev. Lett. 92 (2004) 022001.
[92] C. W. Bernard, et al., The QCD spectrum with three quark flavors, Phys. Rev. D64 (2001) 054506.
[93] C. Aubin, et al., Light hadrons with improved staggered quarks: Approaching the continuum limit, Phys. Rev. D70 (2004) 094505.
[94] K. Jansen, Lattice QCD: a critical status report. arXiv:0810.5634.
[95] H. W. Hamber, E. Marinari, G. Parisi, C. Rebbi, Numerical simulations of Quantum Chromodynamics, Phys. Lett. B124 (1983) 99.
[96] M. Creutz, The evil that is rooting, Phys. Lett. B649 (2007) 230–234.
[97] M. Creutz, The author replies. (Chiral anomalies and rooted staggered fermions), Phys. Lett. B649 (2007) 241–242.
[98] M. Creutz, Why rooting fails, PoS LAT2007 (2007) 007.
[99] C. Bernard, M. Golterman, Y. Shamir, S. R. Sharpe, Comment on 'Chiral anomalies and rooted staggered fermions', Phys. Lett. B649 (2007) 235–240.

[100] C. Bernard, M. Golterman, Y. Shamir, S. R. Sharpe, 't Hooft vertices, partial quenching, and rooted staggered QCD, Phys. Rev. D77 (2008) 114504.
[101] Y. Shamir, Locality of the fourth root of the staggered-fermion determinant: Renormalization-group approach, Phys. Rev. D71 (2005) 034509.
[102] Y. Shamir, Renormalization-group analysis of the validity of staggered-fermion QCD with the fourth-root recipe, Phys. Rev. D75 (2007) 054503.
[103] S. Durr, Theoretical issues with staggered fermion simulations, PoS LAT2005 (2006) 021.
[104] S. R. Sharpe, Rooted staggered fermions: Good, bad or ugly?, PoS LAT2006 (2006) 022.
[105] A. S. Kronfeld, Lattice gauge theory with staggered fermions: how, where, and why (not), PoS LAT2007 (2007) 016.
[106] A. Bazavov, et al., Full nonperturbative QCD simulations with 2+1 flavors of improved staggered quarks. arXiv:0903.3598.
[107] S. Aoki, et al., 2+1 Flavor Lattice QCD toward the Physical Point. arXiv:0807.1661.
[108] S. Durr, et al., Ab Initio Determination of Light Hadron Masses, Science 322 (2008) 1224–1227.
[109] P. Boucaud, et al., Dynamical twisted mass fermions with light quarks, Phys. Lett. B650 (2007) 304–311.
[110] C. Allton, et al., Physical Results from 2+1 Flavor Domain Wall QCD and SU(2) Chiral Perturbation Theory, Phys. Rev. D78 (2008) 114509.
[111] S. Aoki, et al., Two-flavor QCD simulation with exact chiral symmetry, Phys. Rev. D78 (2008) 014508.
[112] S. Weinberg, Phenomenological Lagrangians, Physica A96 (1979) 327.
[113] J. Gasser, H. Leutwyler, Chiral Perturbation Theory to One Loop, Ann. Phys. 158 (1984) 142.
[114] J. Gasser, H. Leutwyler, Chiral Perturbation Theory: Expansions in the Mass of the Strange Quark, Nucl. Phys. B250 (1985) 465.
[115] J. Goldstone, Field Theories with Superconductor Solutions, Nuovo Cim. 19 (1961) 154–164.
[116] Y. Nambu, D. Lurie, Chirality conservation and soft pion production, Phys. Rev. 125 (1962) 1429–1436.
[117] S. Weinberg, Nonlinear realizations of chiral symmetry, Phys. Rev. 166 (1968) 1568–1577.
[118] S. R. Coleman, J. Wess, B. Zumino, Structure of phenomenological Lagrangians. 1, Phys. Rev. 177 (1969) 2239–2247.
[119] J. Callan, Curtis G., S. R. Coleman, J. Wess, B. Zumino, Structure of phenomenological Lagrangians. 2, Phys. Rev. 177 (1969) 2247–2250.
[120] M. Gell-Mann, R. J. Oakes, B. Renner, Behavior of current divergences under SU(3) x SU(3), Phys. Rev. 175 (1968) 2195–2199.
[121] M. Gell-Mann, Symmetries of baryons and mesons, Phys. Rev. 125 (1962) 1067–1084.
[122] S. Okubo, Note on Unitary Symmetry in Strong Interaction. II Excited States of Baryons, Prog. Theor. Phys. 28 (1962) 24–32.
[123] J. Bijnens, Chiral meson physics at two loops, AIP Conf. Proc. 768 (2005) 153–159.
[124] A. Roessl, Pion kaon scattering near the threshold in chiral SU(2) perturbation theory, Nucl. Phys. B555 (1999) 507–539.
[125] J. A. Cronin, Phenomenological model of strong and weak interactions in chiral U(3) x U(3), Phys. Rev. 161 (1967) 1483–1494.
[126] J. Kambor, J. H. Missimer, D. Wyler, The Chiral Loop Expansion of the Nonleptonic Weak Interactions of Mesons, Nucl. Phys. B346 (1990) 17–64.
[127] V. Cirigliano, J. F. Donoghue, E. Golowich, Electromagnetic corrections to $K \to \pi\pi$. I: Chiral perturbation theory, Phys. Rev. D61 (2000) 093001.
[128] G. Ecker, G. Isidori, G. Muller, H. Neufeld, A. Pich, Electromagnetism in nonleptonic weak interactions, Nucl. Phys. B591 (2000) 419–434.
[129] M. B. Wise, Chiral perturbation theory for hadrons containing a heavy quark, Phys. Rev. D45 (1992) 2188–2191.
[130] G. Burdman, J. F. Donoghue, Union of chiral and heavy quark symmetries, Phys. Lett. B280 (1992) 287–291.
[131] J. Gasser, M. E. Sainio, A. Svarc, Nucleons with Chiral Loops, Nucl. Phys. B307 (1988) 779.
[132] E. E. Jenkins, A. V. Manohar, Baryon chiral perturbation theory using a heavy fermion Lagrangian, Phys. Lett. B255 (1991) 558–562.
[133] R. Urech, Virtual photons in chiral perturbation theory, Nucl. Phys. B433 (1995) 234–254.

[134] M. Knecht, H. Neufeld, H. Rupertsberger, P. Talavera, Chiral perturbation theory with virtual photons and leptons, Eur. Phys. J. C12 (2000) 469–478.
[135] G. D'Ambrosio, G. F. Giudice, G. Isidori, A. Strumia, Minimal flavour violation: An effective field theory approach, Nucl. Phys. B645 (2002) 155–187.
[136] T. Feldmann, M. Jung, T. Mannel, Sequential Flavour Symmetry Breaking. arXiv:0906.1523.
[137] T. Hurth, G. Isidori, J. F. Kamenik, F. Mescia, Constraints on New Physics in MFV models: A Model- independent analysis of $\Delta F = 1$ processes, Nucl. Phys. B808 (2009) 326–346.
[138] T. Feldmann, T. Mannel, Minimal Flavour Violation and Beyond, JHEP 02 (2007) 067.
[139] T. Feldmann, T. Mannel, Large Top Mass and Non-Linear Representation of Flavour Symmetry, Phys. Rev. Lett. 100 (2008) 171601.
[140] A. L. Kagan, G. Perez, T. Volansky, J. Zupan, General Minimal Flavor Violation. arXiv:0903.1794.
[141] A. J. Buras, Minimal flavor violation, Acta Phys. Polon. B34 (2003) 5615–5668.
[142] L. J. Hall, R. Rattazzi, U. Sarid, The Top quark mass in supersymmetric SO(10) unification, Phys. Rev. D50 (1994) 7048–7065.
[143] T. Blazek, S. Raby, S. Pokorski, Finite supersymmetric threshold corrections to CKM matrix elements in the large tan Beta regime, Phys. Rev. D52 (1995) 4151–4158.
[144] G. Isidori, A. Retico, Scalar flavor changing neutral currents in the large tan beta limit, JHEP 11 (2001) 001.
[145] W.-S. Hou, Enhanced charged Higgs boson effects in B- $\to$ tau anti- neutrino, mu anti-neutrino and b $\to$ tau anti-neutrino + X, Phys. Rev. D48 (1993) 2342–2344.
[146] G. Isidori, P. Paradisi, Hints of large tan(beta) in flavour physics, Phys. Lett. B639 (2006) 499–507.
[147] G. Degrassi, P. Gambino, G. F. Giudice, $B \to X_s\gamma$ in supersymmetry: Large contributions beyond the leading order, JHEP 12 (2000) 009.
[148] M. S. Carena, D. Garcia, U. Nierste, C. E. M. Wagner, $b \to s\gamma$ and supersymmetry with large tan(β), Phys. Lett. B499 (2001) 141–146.
[149] A. J. Buras, P. H. Chankowski, J. Rosiek, L. Slawianowska, $\Delta M_{d,s}, B^0_{d,s} \to \mu^+\mu^-$ and $B \to X_s\gamma$ in supersymmetry at large tan β, Nucl. Phys. B659 (2003) 3.
[150] A. J. Buras, P. H. Chankowski, J. Rosiek, L. Slawianowska, Δ M(s) / Δ M(d), sin 2 Beta and the angle γ in the presence of new $\Delta F = 2$ operators, Nucl. Phys. B619 (2001) 434–466.
[151] C. Hamzaoui, M. Pospelov, M. Toharia, Higgs-mediated FCNC in supersymmetric models with large tan(beta), Phys. Rev. D59 (1999) 095005.
[152] S. R. Choudhury, N. Gaur, Dileptonic decay of B_s meson in SUSY models with large tan(beta), Phys. Lett. B451 (1999) 86–92.
[153] K. S. Babu, C. F. Kolda, Higgs mediated $B^0 \to \mu^+\mu^-$ in minimal supersymmetry, Phys. Rev. Lett. 84 (2000) 228–231.
[154] S. P. Martin, A Supersymmetry Primer. arXiv:hep-ph/9709356.
[155] L. J. Hall, L. Randall, Weak scale effective supersymmetry, Phys. Rev. Lett. 65 (1990) 2939–2942.
[156] G. F. Giudice, R. Rattazzi, Theories with gauge-mediated supersymmetry breaking, Phys. Rept. 322 (1999) 419–499.
[157] P. Paradisi, M. Ratz, R. Schieren, C. Simonetto, Running minimal flavor violation, Phys. Lett. B668 (2008) 202–209.
[158] G. Colangelo, E. Nikolidakis, C. Smith, Supersymmetric models with minimal flavour violation and their running, Eur. Phys. J. C59 (2009) 75–98.
[159] O. Buchmueller, et al., Predictions for Supersymmetric Particle Masses in the CMSSM using Indirect Experimental and Cosmological Constraints, JHEP 09 (2008) 117.
[160] O. Buchmueller, et al., Prediction for the Lightest Higgs Boson Mass in the CMSSM using Indirect Experimental Constraints, Phys. Lett. B657 (2007) 87–94.
[161] J. R. Ellis, D. V. Nanopoulos, Flavor Changing Neutral Interactions in Broken Supersymmetric Theories, Phys. Lett. B110 (1982) 44.
[162] R. Barbieri, R. Gatto, Conservation Laws for Neutral Currents in Spontaneously Broken Supersymmetric Theories, Phys. Lett. B110 (1982) 211.
[163] L. J. Hall, V. A. Kostelecky, S. Raby, New Flavor Violations in Supergravity Models, Nucl. Phys. B267 (1986) 415.
[164] F. Gabbiani, E. Gabrielli, A. Masiero, L. Silvestrini, A complete analysis of FCNC and CP constraints in general SUSY extensions of the standard model, Nucl. Phys. B477 (1996) 321–352.

[165] M. Ciuchini, et al., Next-to-leading order strong interaction corrections to the $\Delta_F = 2$ effective hamiltonian in the MSSM, JHEP 09 (2006) 013.
[166] J. Foster, K.-i. Okumura, L. Roszkowski, Probing the flavour structure of supersymmetry breaking with rare B-processes: A beyond leading order analysis, JHEP 08 (2005) 094.
[167] M. Artuso, et al., B, D and K decays, Eur. Phys. J. C57 (2008) 309–492.
[168] D. Chang, A. Masiero, H. Murayama, Neutrino mixing and large CP violation in B physics, Phys. Rev. D67 (2003) 075013.
[169] M. Ciuchini, et al., Soft SUSY breaking grand unification: Leptons versus quarks on the flavor playground, Nucl. Phys. B783 (2007) 112–142.
[170] A. J. Buras, A. Poschenrieder, S. Uhlig, W. A. Bardeen, Rare K and B Decays in the Littlest Higgs Model without T-Parity, JHEP 11 (2006) 062.
[171] M. Blanke, et al., Rare and CP-Violating K and B Decays in the Littlest Higgs Model with T-Parity, JHEP 01 (2007) 066.
[172] M. Blanke, A. J. Buras, S. Recksiegel, C. Tarantino, S. Uhlig, Correlations between ϵ'/ϵ and rare K decays in the littlest Higgs model with T-parity, JHEP 06 (2007) 082.
[173] T. Goto, Y. Okada, Y. Yamamoto, Ultraviolet divergences of flavor changing amplitudes in the littlest Higgs model with T-parity, Phys. Lett. B670 (2009) 378–382.
[174] M. Blanke, A. J. Buras, B. Duling, S. Recksiegel, C. Tarantino, FCNC processes in the Littlest Higgs model with T-parity: a 2009 LookIn preparation.
[175] N. Arkani-Hamed, M. Schmaltz, Hierarchies without symmetries from extra dimensions, Phys. Rev. D61 (2000) 033005.
[176] T. Gherghetta, A. Pomarol, Bulk fields and supersymmetry in a slice of AdS, Nucl. Phys. B586 (2000) 141–162.
[177] S. J. Huber, Q. Shafi, Fermion Masses, Mixings and Proton Decay in a Randall- Sundrum Model, Phys. Lett. B498 (2001) 256–262.
[178] K. Agashe, G. Perez, A. Soni, Flavor structure of warped extra dimension models, Phys. Rev. D71 (2005) 016002.
[179] K. Agashe, M. Papucci, G. Perez, D. Pirjol, Next to minimal flavor violation. arXiv:hep-ph/0509117.
[180] S. Davidson, G. Isidori, S. Uhlig, Solving the flavour problem with hierarchical fermion wave functions, Phys. Lett. B663 (2008) 73–79.
[181] M. Blanke, A. J. Buras, B. Duling, K. Gemmler, S. Gori, Rare K and B Decays in a Warped Extra Dimension with Custodial Protection, JHEP 03 (2009) 108.
[182] M. Blanke, A. J. Buras, B. Duling, S. Gori, A. Weiler, $\Delta F = 2$ Observables and Fine-Tuning in a Warped Extra Dimension with Custodial Protection, JHEP 03 (2009) 001.
[183] G. Cacciapaglia, et al., A GIM Mechanism from Extra Dimensions, JHEP 04 (2008) 006.
[184] C. Csaki, A. Falkowski, A. Weiler, A Simple Flavor Protection for RS. arXiv:0806.3757.
[185] C. Csaki, G. Perez, Z. Surujon, A. Weiler, Flavor Alignment via Shining in RS. arXiv:0907.0474.
[186] V. Fanti, et al., The Beam and detector for the NA48 neutral kaon CP violations experiment at CERN, Nucl. Instrum. Meth. A574 (2007) 433–471.
[187] A. Alavi-Harati, et al., Measurements of Direct CP Violation, CPT Symmetry, and Other Parameters in the Neutral Kaon System, Phys. Rev. D67 (2003) 012005.
[188] G. D. Barr, et al., A New measurement of direct CP violation in the neutral kaon system, Phys. Lett. B317 (1993) 233–242.
[189] L. K. Gibbons, et al., Measurement of the CP violation parameter Re($\epsilon'/$ *epsilon*), Phys. Rev. Lett. 70 (1993) 1203–1206.
[190] J. R. Batley, et al., Measurement of the Dalitz plot slope parameters of the $K^{\pm} \to \pi^{\pm}\pi^{+}\pi^{-}$ decay, Phys. Lett. B649 (2007) 349–358.
[191] G. Anelli, et al., Proposal to measure the rare decay $K^{+} \to \pi^{+}\nu\bar{\nu}$ at the CERN SPSCERN-SPSC-2005-013.
[192] G. Anelli, et al., NA62/P-326 Status reportCERN-SPSC-2007-035.
[193] I. V. Ajinenko, et al., Study of the $K^{-} \to \pi^{0}e^{-}\nu$ decay, Phys. Atom. Nucl. 65 (2002) 2064–2069.
[194] S. C. Adler, et al., Evidence for the Decay $K^{+} \to \pi^{+}\nu\bar{\nu}$, Phys. Rev. Lett. 79 (1997) 2204–2207.
[195] S. C. Adler, et al., Further Search for the Decay $K^{+} \to \pi^{+}\nu\bar{\nu}$, Phys. Rev. Lett. 84 (2000) 3768–3770.
[196] S. S. Adler, et al., Further search for the decay $K^{+} \to \pi^{+}\nu\bar{\nu}$ in the momentum region P ¡ 195 MeV/c, Phys. Rev. D70 (2004) 037102.

[197] S. Adler, et al., Measurement of the $K^+ \to \pi^+ \nu\bar{\nu}$ Branching Ratio, Phys. Rev. D77 (2008) 052003.
[198] M. Adinolfi, et al., The tracking detector of the KLOE experiment, Nucl. Instrum. Meth. A488 (2002) 51–73.
[199] M. Adinolfi, et al., The KLOE electromagnetic calorimeter, Nucl. Instrum. Meth. A482 (2002) 364–386.
[200] PEP-II: An Asymmetric B Factory. Conceptual Design Report. June 1993SLAC-418.
[201] A. E. Bondar, KEKB performance, Nucl. Instrum. Meth. A462 (2001) 139–145.
[202] D. Andrews, et al., The CLEO Detector, Nucl. Instr. Meth. 211 (1983) 47.
[203] Y. Kubota, et al., The CLEO-II detector, Nucl. Instrum. Meth. A320 (1992) 66–113.
[204] G. Viehhauser, CLEO III operation, Nucl. Instrum. Meth. A462 (2001) 146–151.
[205] D. Peterson, et al., The CLEO III drift chamber, Nucl. Instrum. Meth. A478 (2002) 142–146.
[206] M. Artuso, et al., The CLEO RICH detector, Nucl. Instrum. Meth. A554 (2005) 147–194.
[207] B. Aubert, et al., The BaBar detector, Nucl. Instrum. Meth. A479 (2002) 1–116.
[208] A. Abashian, et al., The Belle detector, Nucl. Instrum. Meth. A479 (2002) 117–232.
[209] R. A. Briere, et al., CLEO-c and CESR-c: A New Frontier of Weak and Strong Interactions, LEPP Report No. CLNS 01/1742.
[210] J. Z. Bai, et al., The BES detector, Nucl. Instrum. Meth. A344 (1994) 319–334.
[211] J. Z. Bai, et al., The BES upgrade, Nucl. Instrum. Meth. A458 (2001) 627–637.
[212] F. A. Harris, Bepcii and Besiii, Int. J. Mod. Phys. A24 (2009) 377–384.
[213] D. E. Acosta, et al., Measurement of the J/ψ meson and $b-$hadron production cross sections in $p\bar{p}$ collisions at $\sqrt{s} = 1960$ GeV, Phys. Rev. D71 (2005) 032001.
[214] T. Aaltonen, et al., Measurement of the b-Hadron Production Cross Section Using Decays to mu^- D^0 X Final States in $p\bar{p}$ Collisions at sqrt s = 1.96 TeV, Phys. Rev. D79 (2009) 092003.
[215] T. Aaltonen, et al., Measurement of Ratios of Fragmentation Fractions for Bottom Hadrons in $p\bar{p}$ Collisions at $\sqrt{s} = 1.96$-TeV, Phys. Rev. D77 (2008) 072003.
[216] V. M. Abazov, et al., The Upgraded D0 Detector, Nucl. Instrum. Meth. A565 (2006) 463–537.
[217] C. S. Hill, Operational experience and performance of the CDFII silicon detector, Nucl. Instrum. Meth. A530 (2004) 1–6.
[218] D. Tsybychev, Status and performance of the new innermost layer of silicon detector at D0, Nucl. Instrum. Meth. A582 (2007) 701–704.
[219] S. Cabrera, et al., The CDF-II time-of-flight detector, Nucl. Instrum. Meth. A494 (2002) 416–423.
[220] A. Abulencia, et al., Observation of $B_s^0 - \bar{B}_s^0$ oscillations, Phys. Rev. Lett. 97 (2006) 242003.
[221] B. Ashmanskas, et al., The CDF silicon vertex trigger, Nucl. Instrum. Meth. A518 (2004) 532–536.
[222] G. Salamanna, Study of B_s mixing at the CDFII experiment with a newly developed opposite side b flavour tagging algorithm using kaonsFERMILAB-THESIS-2006-21.
[223] V. M. Abazov, et al., Measurement of B_d mixing using opposite-side flavor tagging, Phys. Rev. D74 (2006) 112002.
[224] C. Lecci, A neural jet charge tagger for the measurement of the B/s0 $\bar{B}/$ s^0 oscillation frequency at CDFFERMILAB-THESIS-2005-89.
[225] B. Aubert, et al., A study of time dependent CP-violating asymmetries and flavor oscillations in neutral B decays at the $\Upsilon(4S)$, Phys. Rev. D66 (2002) 032003.
[226] G. A. Giurgiu, B Flavor Tagging Calibration and Search for B_s Oscillations in Semileptonic Decays with the CDF Detector at FermilabFERMILAB-THESIS-2005-41.
[227] V. Tiwari, Measurement of the B_s $\bar{B}_s$ oscillation frequency using semileptonic decaysFERMILAB-THESIS-2007-09.
[228] B. Aubert, et al., Measurement of Time-Dependent CP Asymmetry in B0-¿ccbar K(*)0 Decays. arXiv:0902.1708.
[229] K. F. Chen, et al., Time-dependent CP-violating asymmetries in b –¿ s anti-q q transitions, Phys. Rev. D72 (2005) 012004.
[230] T. C. Collaboration, CDF Notes 8235,8241,8460 (2006).
[231] A. Belloni, Observation of Bs0 - anti-Bs0 oscillations and the development and application of same-side-kaon flavor tagging FERMILAB-THESIS-2007-36.
[232] V. M. Abazov, et al., Measurement of B_s^0 mixing parameters from the flavor-tagged decay $B_s^0 \to J/\psi\phi$, Phys. Rev. Lett. 101 (2008) 241801.
[233] T. C. Collaboration, CDF Note 9203 (2008).
[234] G. Sciolla, et al., The BaBar drift chamber, Nucl. Instrum. Meth. A419 (1998) 310–314.

[235] H. Hirano, et al., A high resolution cylindrical drift chamber for the KEK B- factory, Nucl. Instrum. Meth. A455 (2000) 294–304.
[236] A. A. Affolder, et al., CDF central outer tracker, Nucl. Instrum. Meth. A526 (2004) 249–299.
[237] F. Ambrosino, et al., Data handling, reconstruction, and simulation for the KLOE experiment, Nucl. Instrum. Meth. A534 (2004) 403–433.
[238] H. Kichimi, et al., The BELLE TOF system, Nucl. Instrum. Meth. A453 (2000) 315–320.
[239] T. Iijima, et al., Aerogel Cherenkov counter for the BELLE detector, Nucl. Instrum. Meth. A453 (2000) 321–325.
[240] I. Adam, et al., The DIRC particle identification system for the BaBar experiment, Nucl. Instrum. Meth. A538 (2005) 281–357.
[241] B. Aubert, et al., Observation of CP violation in $B^0 \to K^+\pi^-$ and $B^0 \to \pi^+\pi^-$, Phys. Rev. Lett. 99 (2007) 021603.
[242] K. Hanagaki, H. Kakuno, H. Ikeda, T. Iijima, T. Tsukamoto, Electron identification in Belle, Nucl. Instrum. Meth. A485 (2002) 490–503.
[243] C. Bebek, A Cesium Iodide calorimeter with photodiode readout for CLEO-II, Nucl. Instrum. Meth. A265 (1988) 258–265.
[244] D. N. Brown, J. Ilic, G. B. Mohanty, Extracting longitudinal shower development information from crystal calorimetry plus tracking, Nucl. Instrum. Meth. A592 (2008) 254–260.
[245] M. Adinolfi, et al., The KLOE electromagnetic calorimeter, Nucl. Instrum. Meth. A494 (2002) 326–331.
[246] A. Abashian, et al., Muon identification in the Belle experiment at KEKB, Nucl. Instrum. Meth. A491 (2002) 69–82.
[247] D. Bortoletto, et al., A Muon identification detector for B physics near e+ e- → B anti-B threshold, Nucl. Instrum. Meth. A320 (1992) 114–127.
[248] B. Aubert, et al., Amplitude Analysis of the Decay $B^0 \to K^+\pi^-\pi^0$. arXiv:0807.4567.
[249] B. Aubert, et al., Measurement of time dependent CP asymmetry parameters in B^0 meson decays to ωK^0_S, $\eta' K^0$, and $\pi^0 K^0_S$, Phys. Rev. D79 (2009) 052003.
[250] B. Aubert, et al., Measurement of $|V_cb|$ and the form-factor slope for $\bar{B} \to D\ell^-\bar{\nu}_\ell$ decays on the recoil of fully reconstructed B mesons. arXiv:0807.4978.
[251] B. Aubert, et al., Determination of the form-factors for the decay $B^0 \to D^{*-}\ell^+\nu_l$ and of the CKM matrix element $|V_{cb}|$, Phys. Rev. D77 (2008) 032002.
[252] Q. He, et al., Comparison of $D \to K^0_s pi$ and $D \to K^0_L\pi$ Decay Rates, Phys. Rev. Lett. 100 (2008) 091801.
[253] J. Adler, et al., Measurement of the Branching Fractions for $D^0 \to \pi^- e^+\nu_e$ and $D^0 \to K^- e^+\nu_e$ and determination of $(V_{cd}/V_{cs})^2$, Phys. Rev. Lett. 62 (1989) 1821.
[254] S. Dobbs, et al., Measurement of Absolute Hadronic Branching Fractions of D Mesons and $e^+e^- \to D\bar{D}$ Cross Sections at the psi(3770), Phys. Rev. D76 (2007) 112001.
[255] J. Y. Ge, et al., Study of $D^0 \to \pi^- e^+\nu_e$, $D^+ \to \pi^0 e^+\nu_e$, $D^0 \to K^- e^+\nu_e$, and $D^+ \to \bar{K}^0 e^+\nu_e$ in Tagged Decays of the $\psi(3770)$ Resonance. arXiv:0810.3878.
[256] D. M. Asner, W. M. Sun, Time-Independent Measurements of $D^0 - \bar{D}^0$ Mixing and Relative Strong Phases Using Quantum Correlations, Phys. Rev. D73 (2006) 034024.
[257] A. Giri, Y. Grossman, A. Soffer, J. Zupan, Determining gamma using $B^\pm \to DK^\pm$ with multibody D decays, Phys. Rev. D68 (2003) 054018.
[258] J. P. Alexander, et al., Measurement of $BD^+_s \to \ell^+\nu$ and the Decay Constant fD^+_s From 600 $/pb^{-1}$ of $e^\pm$ Annihilation Data Near 4170 MeV, Phys. Rev. D79 (2009) 052001.
[259] R. H. Dalitz, , Phyl. Mag. 44 (1953) 1068.
[260] B. Aubert, et al., Improved measurement of the CKM angle γ in $B^\mp \to D^{(*)}K^{(*\mp)}$ decays with a Dalitz plot analysis of D decays to $K^0_S\pi^+\pi^-)$ and $K^0_S K^+ K^-)$, Phys. Rev. D78 (2008) 034023.
[261] W. M. Yao, et al., Review of particle physics, J. Phys. G33 (2006) 1–1232.
[262] J. M. Blatt, V. F. Weisskopf, Theoretical Nuclear Physics, John Wiley & Sons, New York.
[263] C. Zemach, Three pion decays of unstable particles, Phys. Rev. 133 (1964) B1201.
[264] C. Zemach, Determination of the Spins and Parities of Resonances, Phys. Rev. 140 (1965) B109–B124.
[265] V. Filippini, A. Fontana, A. Rotondi, Covariant spin tensors in meson spectroscopy, Phys. Rev. D51 (1995) 2247–2261.
[266] M. Jacob, G. C. Wick, Annals Phys. 7 (1959) 404.

[267] S. U. Chung, Helicity coupling amplitudes in tensor formalism, Phys. Rev. D48 (1993) 1225–1239.
[268] E. P. Wigner, Resonance Reactions and Anomalous Scattering, Phys. Rev. 70 (1946) 15–33.
[269] I. J. R. Aitchison, K-Matrix formalism for overlapping resonances, Nucl. Phys. A189 (1972) 417–423.
[270] W. J. Marciano, A. Sirlin, On the Renormalization of the Charm Quartet Model, Nucl. Phys. B93 (1975) 303.
[271] D. B. Chitwood, et al., Improved Measurement of the Positive Muon Lifetime and Determination of the Fermi Constant, Phys. Rev. Lett. 99 (2007) 032001.
[272] W. J. Marciano, A. Sirlin, Radiative Corrections to beta Decay and the Possibility of a Fourth Generation, Phys. Rev. Lett. 56 (1986) 22.
[273] J. C. Hardy, I. S. Towner, Superallowed 0+ to 0+ nuclear beta decays: A new survey with precision tests of the conserved vector current hypothesis and the standard model. arXiv:0812.1202.
[274] I. S. Towner, J. C. Hardy, A new analysis of 14O beta decay: branching ratios and CVC consistency, Phys. Rev. C72 (2005) 055501.
[275] I. S. Towner, J. C. Hardy, An improved calculation of the isospin-symmetry-breaking corrections to superallowed Fermi beta decay, Phys. Rev. C77 (2008) 025501.
[276] W. E. Ormand, B. A. Brown, Calculated isospin-mixing corrections to Fermi β- decays in 1s0d-shell nuclei with emphasis on A = 34, Nucl. Phys. A440 (1985) 274–300.
[277] W. E. Ormand, B. A. Brown, Corrections to the Fermi matrix element for superallowed beta decay, Phys. Rev. Lett. 62 (1989) 866–869.
[278] W. E. Ormand, B. A. Brown, Isospin-mixing corrections for fp-shell Fermi transitions, Phys. Rev. C52 (1995) 2455–2460.
[279] G. A. Miller, A. Schwenk, Isospin-symmetry-breaking corrections to superallowed Fermi beta decay: Formalism and schematic models, Phys. Rev. 78 (2008) 035501.
[280] E. Caurier, P. Navratil, W. E. Ormand, J. P. Vary, Ab initio shell model for A=10 nuclei, Phys. Rev. C66 (2002) 024314.
[281] W. J. Marciano, A. Sirlin, Improved calculation of electroweak radiative corrections and the value of V_{ud}, Phys. Rev. Lett. 96 (2006) 032002.
[282] J. D. Jackson, S. B. Treiman, H. W. Wyld, Possible tests of time reversal invariance in Beta decay, Phys. Rev. 106 (1957) 517–521.
[283] D. H. Wilkinson, Analysis of neutron beta decay, Nucl. Phys. A377 (1982) 474–504.
[284] S. Gardner, C. Zhang, Sharpening low-energy, standard-model tests via correlation coefficients in neutron beta-decay, Phys. Rev. Lett. 86 (2001) 5666–5669.
[285] C. Amsler, et al., Review of particle physics, Phys. Lett. B667 (2008) 1.
[286] A. Czarnecki, W. J. Marciano, A. Sirlin, Precision measurements and CKM unitarity, Phys. Rev. D70 (2004) 093006.
[287] H. Abele, The neutron. Its properties and basic interactions, Prog. Part. Nucl. Phys. 60 (2008) 1–81.
[288] P. Bopp, et al., The beta decay asymmetry of the neutron and g_A/g_V, Phys. Rev. Lett. 56 (1986) 919.
[289] B. Erozolimsky, I. Kuznetsov, I. Stepanenko, Y. A. Mostovoi, Corrigendum: Corrected value of the beta-emission asymmetry in the decay of polarized neutrons measured in 1990, Phys. Lett. B412 (1997) 240–241.
[290] P. Liaud, et al., The measurement of the beta asymmetry in the decay of polarized neutrons, Nucl. Phys. A612 (1997) 53–81.
[291] H. Abele, et al., Is the Unitarity of the quark-mixing-CKM-matrix violated in neutron β-decay?, Phys. Rev. Lett. 88 (2002) 211801.
[292] Y. A. Mostovoi, I. A. Kuznetsov, A. P. Serebrov, B. G. Erozolimsky, Effect of taking into account the radiative decay mode in measurements of the antineutrino-spin correlation in neutron decay, Phys. Atom. Nucl. 64 (2001) 151–152.
[293] A. Serebrov, et al., Measurement of the neutron lifetime using a gravitational trap and a low-temperature Fomblin coating, Phys. Lett. B605 (2005) 72–78.
[294] R. W. Pattie, et al., First Measurement of the Neutron β-Asymmetry with Ultracold Neutrons, Phys. Rev. Lett. 102 (2009) 012301.
[295] M. Ademollo, R. Gatto, Nonrenormalization Theorem for the Strangeness Violating Vector Currents, Phys. Rev. Lett. 13 (1964) 264–265.

[296] V. Cirigliano, M. Knecht, H. Neufeld, H. Pichl, The pionic beta decay in chiral perturbation theory, Eur. Phys. J. C27 (2003) 255–262.
[297] S. Descotes-Genon, B. Moussallam, Radiative corrections in weak semi-leptonic processes at low energy: A two-step matching determination, Eur. Phys. J. C42 (2005) 403–417.
[298] D. Pocanic, et al., Precise Measurement of the $\pi^+ \to \pi^0 e^+ \nu$ Branching Ratio, Phys. Rev. Lett. 93 (2004) 181803.
[299] W. J. Marciano, A. Sirlin, Radiative corrections to pi(lepton 2) decays, Phys. Rev. Lett. 71 (1993) 3629–3632.
[300] V. Cirigliano, I. Rosell, $\pi/K \to e\nu$ branching ratios to O(e2 p4) in Chiral Perturbation Theory, JHEP 10 (2007) 005.
[301] A. Sirlin, Current Algebra Formulation of Radiative Corrections in Gauge Theories and the Universality of the Weak Interactions, Rev. Mod. Phys. 50 (1978) 573.
[302] A. Sirlin, Large m(W), m(Z) Behavior of the O(alpha) Corrections to Semileptonic Processes Mediated by W, Nucl. Phys. B196 (1982) 83.
[303] W. J. Marciano, Precise determination of $|V_{us}|$ from lattice calculations of pseudoscalar decay constants, Phys. Rev. Lett. 93 (2004) 231803.
[304] V. Cirigliano, I. Rosell, Two-loop effective theory analysis of pi (K) $\to$ e anti- nu/e [gamma] branching ratios, Phys. Rev. Lett. 99 (2007) 231801.
[305] M. Finkemeier, Radiative corrections to pi(l2) and K(l2) decays, Phys. Lett. B387 (1996) 391–394.
[306] V. Cirigliano, M. Giannotti, H. Neufeld, Electromagnetic effects in Kl3 decays, JHEP 11 (2008) 006.
[307] B. Ananthanarayan, B. Moussallam, Four-point correlator constraints on electromagnetic chiral parameters and resonance effective Lagrangians, JHEP 06 (2004) 047.
[308] V. Cirigliano, M. Knecht, H. Neufeld, H. Rupertsberger, P. Talavera, Radiative corrections to K_{l3} decays, Eur. Phys. J. C23 (2002) 121–133.
[309] J. Gasser, H. Leutwyler, Low-Energy Expansion of Meson Form-Factors, Nucl. Phys. B250 (1985) 517–538.
[310] R. F. Dashen, Chiral SU(3) x SU(3) as a symmetry of the strong interactions, Phys. Rev. 183 (1969) 1245–1260.
[311] H. Neufeld, H. Rupertsberger, Isospin breaking in chiral perturbation theory and the decays eta $\to$ pi lepton neutrino and tau $\to$ eta pi neutrino, Z. Phys. C68 (1995) 91–102.
[312] A. Kastner, H. Neufeld, The Kl3 scalar form factors in the standard model, Eur. Phys. J. C57 (2008) 541–556.
[313] J. F. Donoghue, A. F. Perez, The electromagnetic mass differences of pions and kaons, Phys. Rev. D55 (1997) 7075–7092.
[314] J. Bijnens, J. Prades, Electromagnetic corrections for pions and kaons: Masses and polarizabilities, Nucl. Phys. B490 (1997) 239–271.
[315] G. Amoros, J. Bijnens, P. Talavera, QCD isospin breaking in meson masses, decay constants and quark mass ratios, Nucl. Phys. B602 (2001) 87–108.
[316] J. Bijnens, K. Ghorbani, $\eta \to 3\pi$ at Two Loops In Chiral Perturbation Theory, JHEP 11 (2007) 030.
[317] H. Leutwyler, The ratios of the light quark masses, Phys. Lett. B378 (1996) 313–318.
[318] C. G. Callan, S. B. Treiman, Equal Time Commutators and K Meson Decays, Phys. Rev. Lett. 16 (1966) 153–157.
[319] H. Leutwyler, private communication.
[320] J. Bijnens, K. Ghorbani, Isospin breaking in $K\pi$ vector form-factors for the weak and rare decays $K_{\ell 3}$, $K \to \pi\nu\bar{\nu}$ and $K \to \pi\ell^+\ell^-$. arXiv:0711.0148.
[321] V. Bernard, E. Passemar, Matching Chiral Perturbation Theory and the Dispersive Representation of the Scalar Kpi Form Factor, Phys. Lett. B661 (2008) 95–102.
[322] V. Bernard, M. Oertel, E. Passemar, J. Stern, Dispersive representation and shape of the Kl3 form factors: robustness. arXiv:0903.1654.
[323] R. J. Hill, Constraints on the form factors for $K \to \pi l\nu$ and implications for $|V_{us}|$, Phys. Rev. D74 (2006) 096006.
[324] V. Bernard, M. Oertel, E. Passemar, J. Stern, K(L)(mu3) decay: A stringent test of right-handed quark currents, Phys. Lett. B638 (2006) 480.
[325] K. M. Watson, The Effect of final state interactions on reaction cross- sections, Phys. Rev. 88 (1952) 1163–1171.

[326] E. Passemar, Dispersive representation and shape of K_{l3} form factors, PoS KAON (2008) 012.
[327] H. Leutwyler, M. Roos, Determination of the Elements V(us) and V(ud) of the Kobayashi-Maskawa Matrix, Z. Phys. C25 (1984) 91.
[328] J. Bijnens, P. Talavera, K(l3) decays in chiral perturbation theory, Nucl. Phys. B669 (2003) 341–362.
[329] M. Jamin, J. A. Oller, A. Pich, Order p^6 chiral couplings from the scalar $K\pi$ form-factor, JHEP 02 (2004) 047.
[330] V. Cirigliano, et al., The ¡S P P¿ Green function and SU(3) breaking in K(l3) decays, JHEP 04 (2005) 006.
[331] D. Becirevic, et al., The $K \to \pi$ vector form factor at zero momentum transfer on the lattice, Nucl. Phys. B705 (2005) 339–362.
[332] N. Tsutsui, et al., Kaon semileptonic decay form factors in two-flavor QCD, PoS LAT2005 (2006) 357.
[333] C. Dawson, T. Izubuchi, T. Kaneko, S. Sasaki, A. Soni, Vector form factor in K_{l3} semileptonic decay with two flavors of dynamical domain-wall quarks, Phys. Rev. D74 (2006) 114502.
[334] D. Brommel, et al., Kaon semileptonic decay form factors from $N_f = 2$ non- perturbatively O(a)-improved Wilson fermions, PoS LAT2007 (2007) 364.
[335] P. A. Boyle, et al., Kl3 semileptonic form factor from 2+1 flavour lattice QCD, Phys. Rev. Lett. 100 (2008) 141601.
[336] V. Lubicz, F. Mescia, S. Simula, C. Tarantino, f. t. E. Collaboration, $K \to \pi$ Semileptonic Form Factors from Two-Flavor Lattice QCD. arXiv:0906.4728.
[337] J. M. Flynn, C. T. Sachrajda, SU(2) chiral prturbation theory for Kl3 decay amplitudes, Nucl. Phys. B812 (2009) 64–80.
[338] P. A. Boyle, J. M. Flynn, A. Juttner, C. T. Sachrajda, J. M. Zanotti, Hadronic form factors in lattice QCD at small and vanishing momentum transfer, JHEP 05 (2007) 016.
[339] C. Aubin, et al., Light pseudoscalar decay constants, quark masses, and low energy constants from three-flavor lattice QCD, Phys. Rev. D70 (2004) 114501.
[340] E. Follana, C. T. H. Davies, G. P. Lepage, J. Shigemitsu, High Precision determination of the π, K, D and D_s decay constants from lattice QCD, Phys. Rev. Lett. 100 (2008) 062002.
[341] S. Dürr, f_K/f_π in full QCD, Talk at The XXVI International Symposium on Lattice Field Theory, 2008.
[342] C. Aubin, J. Laiho, R. S. Van de Water, Light pseudoscalar meson masses and decay constants from mixed action lattice QCD. arXiv:0810.4328.
[343] B. Blossier, et al., Pseudoscalar decay constants of kaon and D-mesons from Nf=2 twisted mass Lattice QCD. arXiv:0904.0954.
[344] S. R. Beane, P. F. Bedaque, K. Orginos, M. J. Savage, f_K/f_π in Full QCD with Domain Wall Valence Quarks, Phys. Rev. D75 (2007) 094501.
[345] G. Colangelo, et al., The FLAG working group: making lattice results accessible to phenomenologists Kaon09 `http://kaon09.kek.jp/program.html`.
[346] M. Antonelli, et al., Precision tests of the Standard Model with leptonic and semileptonic kaon decays. arXiv:0801.1817.
[347] T. Alexopoulos, et al., Measurements of KL Branching Fractions and the CP Violation Parameter —eta+-—, Phys. Rev. D70 (2004) 092006.
[348] A. Lai, et al., Measurement of the branching ratio of the decay $K_L \to \pi e \nu$ and extraction of the CKM parameter $|V_{us}|$, Phys. Lett. B602 (2004) 41–51.
[349] F. Ambrosino, et al., Measurements of the absolute branching ratios for the dominant K(L) decays, the K(L) lifetime, and V(us) with the KLOE detector, Phys. Lett. B632 (2006) 43–50.
[350] F. Ambrosino, et al., Measurement of the K(L) meson lifetime with the KLOE detector, Phys. Lett. B626 (2005) 15–23.
[351] F. Ambrosino, et al., Measurement of the branching ratio of the $K_L \to \pi^+\pi^-$ decay with the KLOE detector, Phys. Lett. B638 (2006) 140–145.
[352] A. Lai, et al., Measurement of the ratio $\Gamma(K_L \to \pi^+\pi^-)/\Gamma(K_L \to \pi^\pm e^\mp \nu)$ and extraction of the CP violation parameter $|\eta_\pm|$, Phys. Lett. B645 (2007) 26–35.
[353] F. Ambrosino, et al., Measurement of the branching fraction and charge asymmetry for the decay $K_S \to \pi e \nu$ with the KLOE detector, Phys. Lett. B636 (2006) 173–182.
[354] F. Ambrosino, et al., Precise measurement of $\Gamma(K_S \to \pi^+\pi^-(\gamma))/\Gamma(K_S \to \pi^0\pi^0)$ with the KLOE detector at DAFNE, Eur. Phys. J. C48 (2006) 767–780.

[355] J. R. Batley, et al., Determination of the relative decay rate K(S) → pi e nu / K(L) → pi e nu, Phys. Lett. B653 (2007) 145–150.
[356] J. R. Batley, et al., Measurements of Charged Kaon Semileptonic Decay Branching Fractions $K^{\pm} \to pi0mu^{\pm}$ nu and $K^{\pm} \to pi0e^{\pm}$ nu and Their Ratio, Eur. Phys. J. C50 (2007) 329–340.
[357] F. Ambrosino, et al., Measurement of the absolute branching ratios for semileptonic K+/- decays with the KLOE detector, JHEP 02 (2008) 098.
[358] F. Ambrosino, et al., The measurement of the absolute branching ratio of the K+ to pi+ pi0 (gamma) decay at KLOE. arXiv:0707.2654.
[359] F. Ambrosino, et al., Measurement of the absolute branching ratio for the $K^+ \to \mu^+\nu(\gamma)$ decay with the KLOE detector, Phys. Lett. B632 (2006) 76–80.
[360] M. Antonelli presenatation at La Thuile '09; M. Moulson, communication to FlaviaNet Kaon WG.
[361] E. Goudzovski presenatation at KAON09; M. Sozzi, communication to FlaviaNet Kaon WG.
[362] T. Alexopoulos, et al., Measurements of Semileptonic KL Decay Form Factors, Phys. Rev. D70 (2004) 092007.
[363] F. Ambrosino, et al., Measurement of the form-factor slopes for the decay $K_L \to \pi^{\pm}e^{\mp}\nu$ with the KLOE detector, Phys. Lett. B636 (2006) 166–172.
[364] O. P. Yushchenko, et al., High statistic measurement of the $K^- \to \pi^0 e^-\nu$ decay form-factors, Phys. Lett. B589 (2004) 111–117.
[365] A. Lai, et al., Measurement of K^0_{e3} form factors, Phys. Lett. B604 (2004) 1–10.
[366] F. Ambrosino, et al., Measurement of the $K_L \to \pi\mu\nu$ form factor parameters with the KLOE detector, JHEP 12 (2007) 105.
[367] O. P. Yushchenko, et al., High statistic study of the $K^- \to \pi^0\mu^-\nu$ decay, Phys. Lett. B581 (2004) 31–38.
[368] A. Lai, et al., Measurement of $K^0_{\mu 3}$ form factors, Phys. Lett. B647 (2007) 341–350.
[369] E. Gamiz, M. Jamin, A. Pich, J. Prades, F. Schwab, V_{us} and m_s from hadronic tau decays, Phys. Rev. Lett. 94 (2005) 011803.
[370] E. Gamiz, M. Jamin, A. Pich, J. Prades, F. Schwab, Theoretical progress on the V_{us} determination from tau decays, PoS KAON (2008) 008.
[371] E. Braaten, QCD Predictions for the Decay of the tau Lepton, Phys. Rev. Lett. 60 (1988) 1606–1609.
[372] S. Narison, A. Pich, QCD Formulation of the tau Decay and Determination of Λ_{MS}, Phys. Lett. B211 (1988) 183.
[373] E. Braaten, S. Narison, A. Pich, QCD analysis of the tau hadronic width, Nucl. Phys. B373 (1992) 581–612.
[374] F. Le Diberder, A. Pich, The perturbative QCD prediction to R(tau) revisited, Phys. Lett. B286 (1992) 147–152.
[375] A. Pich, QCD predictions for the tau hadronic width: Determination of $\alpha_s(M_\tau^2)$, Nucl. Phys. Proc. Suppl. 39BC (1995) 326.
[376] B. Aubert, et al., Exclusive branching fraction measurements of semileptonic tau decays into three charged hadrons, $\tau^- \to \phi\pi^-\nu_\tau$ and $\tau^- \to \phi K^-\nu_\tau$, Phys. Rev. Lett. 100 (2008) 011801.
[377] D. Epifanov, et al., Study of $\tau^- \to K_S\pi^-\nu_\tau$ decay at Belle, Phys. Lett. B654 (2007) 65–73.
[378] S. Banerjee, Measurement of $|V_{us}|$ using hadronic tau decays from BaBar and Belle, PoS KAON (2008) 009.
[379] M. Davier, A. Hocker, Z. Zhang, The physics of hadronic tau decays, Rev. Mod. Phys. 78 (2006) 1043–1109.
[380] A. Pich, J. Prades, Strange quark mass determination from Cabibbo-suppressed tau decays, JHEP 10 (1999) 004.
[381] S. Chen, et al., Strange quark mass from the invariant mass distribution of Cabibbo-suppressed tau decays, Eur. Phys. J. C22 (2001) 31–38.
[382] K. G. Chetyrkin, J. H. Kuhn, A. A. Pivovarov, Determining the Strange Quark Mass in Cabibbo Suppressed Tau Lepton Decays, Nucl. Phys. B533 (1998) 473–493.
[383] J. G. Korner, F. Krajewski, A. A. Pivovarov, Determination of the strange quark mass from Cabibbo suppressed tau decays with resummed perturbation theory in an effective scheme, Eur. Phys. J. C20 (2001) 259–269.
[384] K. Maltman, C. E. Wolfe, V_{us} from hadronic tau decays, Phys. Lett. B639 (2006) 283–289.
[385] J. Kambor, K. Maltman, The strange quark mass from flavor breaking in hadronic tau decays, Phys. Rev. D62 (2000) 093023.

[386] K. Maltman, Problems with extracting m(s) from flavor breaking in hadronic tau decays, Phys. Rev. D58 (1998) 093015.
[387] P. A. Baikov, K. G. Chetyrkin, J. H. Kuhn, Strange quark mass from tau lepton decays with $O(\alpha_s^3)$ accuracy, Phys. Rev. Lett. 95 (2005) 012003.
[388] M. Jamin, J. A. Oller, A. Pich, Scalar K pi form factor and light quark masses, Phys. Rev. D74 (2006) 074009.
[389] K. Maltman, J. Kambor, Decay constants, light quark masses and quark mass bounds from light quark pseudoscalar sum rules, Phys. Rev. D65 (2002) 074013.
[390] K. Maltman, A Mixed Tau-Electroproduction Sum Rule for V_{us}, Phys. Lett. B672 (2009) 257–263.
[391] K. Maltman, C. E. Wolfe, S. Banerjee, I. M. Nugent, J. M. Roney, Status of the Hadronic tau Decay Determination of $|V_{us}|$, Nucl. Phys. Proc. Suppl. 189 (2009) 175–180.
[392] M. Testa, Recent results from KLOE. arXiv:0805.1969.
[393] E. Passemar and S. Glazov, communication to FlaviaNet Kaon WG.
[394] O. Yushchenko, communication to FlaviaNet Kaon WG.
[395] S. Fubini, G. Furlan, On the algebraization of some dispersion sum rules, Lett. Nuovo Cim. 3S1 (1970) 168–172.
[396] W. J. Marciano, A. Sirlin, Constraint on additional neutral gauge bosons from electroweak radiative corrections, Phys. Rev. D35 (1987) 1672–1676.
[397] P. L. Anthony, et al., Precision measurement of the weak mixing angle in Moeller scattering, Phys. Rev. Lett. 95 (2005) 081601.
[398] A. Czarnecki, W. J. Marciano, Electrons are not ambidextrous, Nature 435 (2005) 437–438.
[399] A. G. Akeroyd, S. Recksiegel, The effect of $H^\pm$ on $B^\pm \to \tau^\pm \nu_\tau$ and $B\pm \to \mu^\pm \nu_\mu$, J. Phys. G29 (2003) 2311–2317.
[400] R. Barbieri, C. Bouchiat, A. Georges, P. Le Doussal, Quark-lepton nonuniversality in supersymmetric models, Phys. Lett. B156 (1985) 348.
[401] K. Hagiwara, S. Matsumoto, Y. Yamada, Supersymmetric contribution to the quark - lepton universality violation in charged currents, Phys. Rev. Lett. 75 (1995) 3605–3608.
[402] A. Kurylov, M. J. Ramsey-Musolf, Charged current universality in the MSSM, Phys. Rev. Lett. 88 (2002) 071804.
[403] M. E. Peskin, T. Takeuchi, A New constraint on a strongly interacting Higgs sector, Phys. Rev. Lett. 65 (1990) 964–967.
[404] W. J. Marciano, J. L. Rosner, Atomic parity violation as a probe of new physics, Phys. Rev. Lett. 65 (1990) 2963–2966.
[405] A. Masiero, P. Paradisi, R. Petronzio, Probing new physics through $\mu - e$ universality in $K \to l\nu$, Phys. Rev. D74 (2006) 011701.
[406] C. Bourrely, B. Machet, E. de Rafael, Semileptonic decays of pseudoscalar particles ($M \to M' \ell \nu_\ell$) and short distance behavior of Quantum Chromodynamics, Nucl. Phys. B189 (1981) 157.
[407] C. G. Boyd, B. Grinstein, R. F. Lebed, Constraints on form-factors for exclusive semileptonic heavy to light meson decays, Phys. Rev. Lett. 74 (1995) 4603–4606.
[408] L. Lellouch, Lattice-Constrained Unitarity Bounds for $\bar{B}^0 \to \pi^+ \ell^- \bar{\nu}_\ell$ Decays, Nucl. Phys. B479 (1996) 353–391.
[409] C. G. Boyd, M. J. Savage, Analyticity, shapes of semileptonic form factors, and $\bar{B} \to \pi \ell \bar{\nu}$, Phys. Rev. D56 (1997) 303–311.
[410] M. C. Arnesen, B. Grinstein, I. Z. Rothstein, I. W. Stewart, A precision model independent determination of $|V_{ub}|$ from $B \to \pi e \nu$, Phys. Rev. Lett. 95 (2005) 071802.
[411] J. Bailey, et al., The $B \to \pi \ell \nu$ semileptonic form factor from three- flavor lattice QCD: A model-independent determination of $|V_{ub}|$, Phys. Rev. D79 (2009) 054507.
[412] T. Becher, R. J. Hill, Comment on form factor shape and extraction of $|V_{ub}|$ from $B \to \pi \ell \nu$, Phys. Lett. B633 (2006) 61–69.
[413] C. Bourrely, I. Caprini, L. Lellouch, Model-independent description of $B \to \pi \ell \nu$ decays and a determination of $|V_{ub}|$, Phys. Rev. D79 (2009) 013008.
[414] J. M. Flynn, J. Nieves, Extracting $|V_{ub}|$ from $B \to \pi \ell \nu$ decays using a multiply-subtracted Omnes dispersion relation, Phys. Rev. D75 (2007) 013008.
[415] J. M. Flynn, J. Nieves, $|V_{ub}|$ from exclusive semileptonic B to π decays revisited, Phys. Rev. D76 (2007) 031302.
[416] W.-J. Lee, S. R. Sharpe, Partial Flavor Symmetry Restoration for Chiral Staggered Fermions, Phys. Rev. D60 (1999) 114503.

[417] C. Aubin, C. Bernard, Pion and Kaon masses in Staggered Chiral Perturbation Theory, Phys. Rev. D68 (2003) 034014.
[418] O. Bar, G. Rupak, N. Shoresh, Chiral perturbation theory at O(α^2) for lattice QCD, Phys. Rev. D70 (2004) 034508.
[419] S. R. Sharpe, J. M. S. Wu, Twisted mass chiral perturbation theory at next-to-leading order, Phys. Rev. D71 (2005) 074501.
[420] O. Bar, C. Bernard, G. Rupak, N. Shoresh, Chiral perturbation theory for staggered sea quarks and Ginsparg-Wilson valence quarks, Phys. Rev. D72 (2005) 054502.
[421] C. Aubin, C. Bernard, Heavy-Light Semileptonic Decays in Staggered Chiral Perturbation Theory, Phys. Rev. D76 (2007) 014002.
[422] K. C. Bowler, et al., Improved $B \to \pi\ell\nu_\ell$ form factors from the lattice, Phys. Lett. B486 (2000) 111–117.
[423] A. Abada, et al., Heavy $\to$ light semileptonic decays of pseudoscalar mesons from lattice QCD, Nucl. Phys. B619 (2001) 565–587.
[424] S. Aoki, et al., Differential decay rate of $B \to \pi\ell\nu$ semileptonic decay with lattice NRQCD, Phys. Rev. D64 (2001) 114505.
[425] A. X. El-Khadra, A. S. Kronfeld, P. B. Mackenzie, S. M. Ryan, J. N. Simone, The semileptonic decays $B \to \pi\ell\nu$ and $D \to \pi\ell\nu$ from lattice QCD, Phys. Rev. D64 (2001) 014502.
[426] J. Shigemitsu, et al., Semileptonic B decays from an NRQCD/D234 action, Phys. Rev. D66 (2002) 074506.
[427] M. Okamoto, et al., Semileptonic $D \to \pi/K$ and $B \to \pi/D$ decays in 2+1 flavor lattice QCD, Nucl. Phys. Proc. Suppl. 140 (2005) 461–463.
[428] E. Dalgic, et al., B Meson Semileptonic Form Factors from Unquenched Lattice QCD, Phys. Rev. D73 (2006) 074502.
[429] B. Blossier, V. Lubicz, C. Tarantino, S. Simula, Pseudoscalar meson decay constants f_K, f_D and f_{D_s}, from $N_f = 2$ twisted mass Lattice QCD. arXiv:0810.3145.
[430] D. Becirevic, B. Haas, F. Mescia, Semileptonic D-decays and Lattice QCD, PoS LAT2007 (2007) 355.
[431] B. Haas, D-decays with unquenched Lattice QCD. arXiv:0805.2392.
[432] A. A. Khan, et al., Decays of mesons with charm quarks on the lattice, PoS LAT2007 (2007) 343.
[433] I. I. Balitsky, V. M. Braun, A. V. Kolesnichenko, Radiative Decay Sigma+ $\to$ p gamma in Quantum Chromodynamics, Nucl. Phys. B312 (1989) 509–550.
[434] V. M. Braun, I. E. Filyanov, QCD Sum Rules in Exclusive Kinematics and Pion Wave Function, Z. Phys. C44 (1989) 157.
[435] V. L. Chernyak, I. R. Zhitnitsky, B meson exclusive decays into baryons, Nucl. Phys. B345 (1990) 137–172.
[436] M. A. Shifman, A. I. Vainshtein, V. I. Zakharov, QCD and Resonance Physics. Sum Rules, Nucl. Phys. B147 (1979) 385–447.
[437] M. A. Shifman, A. I. Vainshtein, V. I. Zakharov, QCD and Resonance Physics: Applications, Nucl. Phys. B147 (1979) 448–518.
[438] P. Colangelo, A. Khodjamirian, QCD sum rules, a modern perspective. arXiv:hep-ph/0010175.
[439] V. M. Belyaev, A. Khodjamirian, R. Ruckl, QCD calculation of the B $\to$ pi, K form-factors, Z. Phys. C60 (1993) 349–356.
[440] V. M. Belyaev, V. M. Braun, A. Khodjamirian, R. Ruckl, D^* D π and B^* B π couplings in QCD, Phys. Rev. D51 (1995) 6177–6195.
[441] A. Khodjamirian, R. Ruckl, S. Weinzierl, O. I. Yakovlev, Perturbative QCD correction to the $B \to \pi$ transition form factor, Phys. Lett. B410 (1997) 275–284.
[442] E. Bagan, P. Ball, V. M. Braun, Radiative corrections to the decay $B \to \pi e\nu$ and the heavy quark limit, Phys. Lett. B417 (1998) 154–162.
[443] A. Khodjamirian, R. Ruckl, S. Weinzierl, C. W. Winhart, O. I. Yakovlev, Predictions on $B \to \pi\bar{\ell}\nu_\ell$, $D \to \pi\bar{\ell}\nu_\ell$ and $D \to K\bar{\ell}\nu_\ell$ from QCD light-cone sum rules, Phys. Rev. D62 (2000) 114002.
[444] P. Ball, R. Zwicky, New results on $B \to \pi, K, \eta$ decay form factors from light-cone sum rules, Phys. Rev. D71 (2005) 014015.
[445] P. Ball, Testing QCD sum rules on the light-cone in $D \to (\pi, K)\ell\nu$ decays, Phys. Lett. B641 (2006) 50–56.
[446] P. Ball, G. W. Jones, R. Zwicky, $B \to V\gamma$ beyond QCD factorisation, Phys. Rev. D75 (2007) 054004.

[447] P. Ball, G. W. Jones, $B \to \eta^{(\prime)}$ Form Factors in QCD, JHEP 08 (2007) 025.
[448] G. Duplancic, A. Khodjamirian, T. Mannel, B. Melic, N. Offen, Light-cone sum rules for $B \to \pi$ form factors revisited, JHEP 04 (2008) 014.
[449] G. Duplancic, B. Melic, B, $B_s \to K$ form factors: an update of light-cone sum rule results, Phys. Rev. D78 (2008) 054015.
[450] P. Ball, V. M. Braun, A. Lenz, Twist-4 Distribution Amplitudes of the K^* and ϕ Mesons in QCD, JHEP 08 (2007) 090.
[451] M. Jamin, B. O. Lange, f_B and f_{B_s} from QCD sum rules, Phys. Rev. D65 (2002) 056005.
[452] A. Khodjamirian, T. Mannel, N. Offen, Form factors from light-cone sum rules with B-meson distribution amplitudes, Phys. Rev. D75 (2007) 054013.
[453] F. De Fazio, T. Feldmann, T. Hurth, Light-cone sum rules in soft-collinear effective theory, Nucl. Phys. B733 (2006) 1–30.
[454] F. De Fazio, T. Feldmann, T. Hurth, SCET sum rules for $B \to P$ and $B \to V$ transition form factors, JHEP 02 (2008) 031.
[455] B. Aubert, et al., Measurement of the q^2 dependence of the Hadronic Form Factor in $D^0 \to K^- e^+ \nu_e$ decays, Phys. Rev. D76 (2007) 052005.
[456] L. Widhalm, et al., Measurement of $D^0 \to \pi\ell\nu(K\ell\nu)$ form factors and absolute branching fractions, Phys. Rev. Lett. 97 (2006) 061804.
[457] L. Widhalm, Leptonic and semileptonic D and D_s decays at B- factories. arXiv:0710.0420.
[458] S. Dobbs, et al., A Study of the Semileptonic Charm Decays $D^0 \to \pi^- e^+ \nu_e$, $D^+ \to \pi^0 e^+ \nu_e$, $D^0 \to K^- e^+ \nu_e$, and $D^+ \to \bar{K}^0 e^+ \nu_e$, Phys. Rev. D77 (2008) 112005.
[459] . D. Besson, Improved measurements of D meson semileptonic decays to pi and K mesons. arXiv:0906.2983.
[460] B. Aubert, et al., Study of the decay $D_s^+ \to K^+ K^- e^+ \nu_e$, Phys. Rev. D78 (2008) 051101.
[461] J. M. Link, et al., New measurements of the $D_s^+ \to \phi\mu^+\nu$ form factor ratios, Phys. Lett. B586 (2004) 183–190.
[462] C. Bernard, et al., Visualization of semileptonic form factors from lattice QCD. arXiv:0906.2498.
[463] C. Aubin, et al., Semileptonic decays of D mesons in three-flavor lattice QCD, Phys. Rev. Lett. 94 (2005) 011601.
[464] N. E. Adam, et al., A Study of Exclusive Charmless Semileptonic B Decay and $|V_{ub}|$, Phys. Rev. Lett. 99 (2007) 041802.
[465] S. B. Athar, et al., Study of the q^2 dependence of $B \to \pi\ell\nu$ and $B \to \rho(\omega)\ell\nu$ decay and extraction of $|V_{ub}|$, Phys. Rev. D68 (2003) 072003.
[466] B. Aubert, et al., Measurement of the $B^0 \to \pi^- \ell^+ \nu$ form- factor shape and branching fraction, and determination of $|V_{ub}|$ with a loose neutrino reconstruction technique, Phys. Rev. Lett. 98 (2007) 091801.
[467] B. Aubert, et al., Measurements of $B \to \{\pi, \eta, \eta'\}\ell\nu_\ell$ Branching Fractions and Determination of $|V_{ub}|$ with Semileptonically Tagged B Mesons, Phys. Rev. Lett. 101 (2008) 081801.
[468] B. Aubert, et al., Measurement of the $B \to \pi\ell\nu$ Branching Fraction and Determination of $|V_{ub}|$ with Tagged B Mesons, Phys. Rev. Lett. 97 (2006) 211801.
[469] B. Aubert, et al., Measurement of the $B^+ \to \omega\ell^+\nu$ and $B^+ - \to \eta\ell^+\nu$ Branching Fractions. arXiv:0808.3524.
[470] B. Aubert, et al., Study of $B \to \pi\ell\nu$ and $B \to \rho\ell\nu$ decays and determination of $|V_{ub}|$, Phys. Rev. D72 (2005) 051102.
[471] T. Hokuue, et al., Measurements of branching fractions and $q2$ distributions for $B \to \pi\ell\nu$ and $B \to \rho\ell\nu$ Decays with $B \to D^{(*)}\ell\nu$ Decay Tagging, Phys. Lett. B648 (2007) 139–148.
[472] I. Adachi, et al., Measurement of exclusive $B \to X_u\ell\nu$ decays using full- reconstruction tagging at Belle. arXiv:0812.1414.
[473] K. Abe, et al., Evidence for $B^+ \to \omega\ell^+\nu$. arXiv:hep-ex/0307075.
[474] D. Scora, N. Isgur, Semileptonic meson decays in the quark model: An update, Phys. Rev. D52 (1995) 2783–2812.
[475] B. Aubert, et al., Measurement of the $B^+ \to \eta\ell^+\nu$ and $B^+ \to \eta'\ell^+\nu$ branching fractions using $\upsilon_{4S} \to B\bar{B}$ events tagged by a fully reconstructed B meson. arXiv:hep-ex/0607066.
[476] D. Becirevic, A. B. Kaidalov, Comment on the heavy $\to$ light form factors, Phys. Lett. B478 (2000) 417–423.
[477] R. S. Van de Water, P. B. Mackenzie, Unitarity and the heavy quark expansion in the determination of semileptonic form factors, PoS LAT2006 (2006) 097.

[478] G. M. de Divitiis, E. Molinaro, R. Petronzio, N. Tantalo, Quenched lattice calculation of the $B \to D\ell\nu$ decay rate, Phys. Lett. B655 (2007) 45–49.
[479] G. M. de Divitiis, R. Petronzio, N. Tantalo, Quenched lattice calculation of semileptonic heavy-light meson form factors, JHEP 10 (2007) 062.
[480] G. M. de Divitiis, R. Petronzio, N. Tantalo, Quenched lattice calculation of the vector channel $B \to D^*\ell\nu$ decay rate, Nucl. Phys. B807 (2009) 373–395.
[481] E. Eichten, B. R. Hill, An Effective Field Theory for the Calculation of Matrix Elements Involving Heavy Quarks, Phys. Lett. B234 (1990) 511.
[482] J. Heitger, R. Sommer, Non-perturbative heavy quark effective theory, JHEP 02 (2004) 022.
[483] R. Sommer, Non-perturbative QCD: Renormalization, O(a)-improvement and matching to heavy quark effective theory. arXiv:hep-lat/0611020.
[484] B. Sheikholeslami, R. Wohlert, Improved Continuum Limit Lattice Action for QCD with Wilson Fermions, Nucl. Phys. B259 (1985) 572.
[485] A. X. El-Khadra, A. S. Kronfeld, P. B. Mackenzie, Massive Fermions in Lattice Gauge Theory, Phys. Rev. D55 (1997) 3933–3957.
[486] M. B. Oktay, A. S. Kronfeld, New lattice action for heavy quarks, Phys. Rev. D78 (2008) 014504.
[487] M. Guagnelli, F. Palombi, R. Petronzio, N. Tantalo, f_B and two scales problems in lattice QCD, Phys. Lett. B546 (2002) 237–246.
[488] S. Hashimoto, et al., Lattice QCD calculation of $\bar{B} \to D\ell\bar{\nu}$ decay form factors at zero recoil, Phys. Rev. D61 (1999) 014502.
[489] M. E. Luke, Effects of subleading operators in the heavy quark effective theory, Phys. Lett. B252 (1990) 447–455.
[490] M. Okamoto, Full determination of the CKM matrix using recent results from lattice QCD, PoS LAT2005 (2006) 013.
[491] C. Bernard, et al., The $\bar{B} \to D^*\ell\bar{\nu}$ form factor at zero recoil from three-flavor lattice QCD: A Model independent determination of $|V_{cb}|$, Phys. Rev. D78 (2008) 094505.
[492] J. Laiho, R. S. Van de Water, $B \to D^*\ell\nu$ and $B \to D\ell\nu$ form factors in staggered chiral perturbation theory, Phys. Rev. D73 (2006) 054501.
[493] I. Caprini, L. Lellouch, M. Neubert, Dispersive bounds on the shape of $\bar{B} \to D^{(*)}\ell\bar{\nu}$ form factors, Nucl. Phys. B530 (1998) 153–181.
[494] J. E. Duboscq, et al., Measurement of the form-factors for $\bar{B}^0 \to D^{*+}\ell^-\bar{\nu}$, Phys. Rev. Lett. 76 (1996) 3898–3902.
[495] . I. Adachi, Measurement of the form factors of the decay $B_0 \to D^{*-}l^+\nu_l$ and determination of the CKM matrix element $|V_{cb}|$. arXiv:0810.1657.
[496] B. Aubert, et al., Measurement of the Decay $B^- \to$ D*0 $e^-\bar{\nu}(\ e)$, Phys. Rev. Lett. 100 (2008) 231803.
[497] B. Aubert, et al., Measurements of the Semileptonic Decays $\overline{B} \to D\ell\overline{\nu}$ and $\overline{B} \to D^*\ell\overline{\nu}$ Using a Global Fit to $DX\ell\overline{\nu}$ Final States, Phys. Rev. D79 (2009) 012002.
[498] B. Grinstein, Z. Ligeti, Heavy quark symmetry in $B \to D^{(*)}l\bar{\nu}$ spectra, Phys. Lett. B526 (2002) 345–354.
[499] D. Liventsev, et al., Study of $B \to D^{**}\ell\nu$ with full reconstruction tagging, Phys. Rev. D77 (2008) 091503.
[500] B. Aubert, et al., A Measurement of the branching fractions of exclusive $\bar{B} \to D^{(*)}\ (\pi)\ \ell^-\bar{\nu}(\ \ell)$ decays in events with a fully reconstructed B meson, Phys. Rev. Lett. 100 (2008) 151802.
[501] J. Chay, H. Georgi, B. Grinstein, Lepton energy distributions in heavy meson decays from QCD, Phys. Lett. B247 (1990) 399–405.
[502] I. I. Y. Bigi, M. A. Shifman, N. G. Uraltsev, A. I. Vainshtein, QCD predictions for lepton spectra in inclusive heavy flavor decays, Phys. Rev. Lett. 71 (1993) 496–499.
[503] B. Blok, L. Koyrakh, M. A. Shifman, A. I. Vainshtein, Differential distributions in semileptonic decays of the heavy flavors in QCD, Phys. Rev. D49 (1994) 3356–3366.
[504] A. V. Manohar, M. B. Wise, Inclusive semileptonic B and polarized Λ_b decays from QCD, Phys. Rev. D49 (1994) 1310–1329.
[505] A. V. Manohar, M. B. Wise, Heavy quark physics, Camb. Monogr. Part. Phys. Nucl. Phys. Cosmol. 10 (2000) 1–191.
[506] D. Benson, I. I. Bigi, T. Mannel, N. Uraltsev, Imprecated, yet impeccable: On the theoretical evaluation of $\Gamma(B \to X_c\ell\nu)$, Nucl. Phys. B665 (2003) 367–401.

[507] A. F. Falk, M. Neubert, Second order power corrections in the heavy quark effective theory. 1. Formalism and meson form-factors, Phys. Rev. D47 (1993) 2965–2981.
[508] T. Becher, H. Boos, E. Lunghi, Kinetic corrections to $B \to X_c \ell \bar{\nu}$ at one loop, JHEP 12 (2007) 062.
[509] C. W. Bauer, Z. Ligeti, M. Luke, A. V. Manohar, B decay shape variables and the precision determination of $|V_{cb}|$ and m_b, Phys. Rev. D67 (2003) 054012.
[510] C. W. Bauer, Z. Ligeti, M. Luke, A. V. Manohar, M. Trott, Global analysis of inclusive B decays, Phys. Rev. D70 (2004) 094017.
[511] O. Buchmuller, H. Flacher, Fits to moment measurements from $B \to X_c \ell \nu$ and $B \to X_s \gamma$ decays using heavy quark expansions in the kinetic scheme, Phys. Rev. D73 (2006) 073008.
[512] P. Gambino, N. Uraltsev, Moments of semileptonic B decay distributions in the $1/m_b$ expansion, Eur. Phys. J. C34 (2004) 181–189.
[513] M. Gremm, A. Kapustin, Order $1/m_b$ 3 corrections to inclusive semileptonic B decay, Phys. Rev. D55 (1997) 6924–6932.
[514] M. Jezabek, J. H. Kuhn, QCD Corrections to Semileptonic Decays of Heavy Quarks, Nucl. Phys. B314 (1989) 1.
[515] M. Jezabek, J. H. Kuhn, Lepton Spectra from Heavy Quark Decay, Nucl. Phys. B320 (1989) 20.
[516] A. Czarnecki, M. Jezabek, J. H. Kuhn, Hadron spectra from semileptonic decays of heavy quarks, Acta Phys. Polon. B20 (1989) 961.
[517] A. Czarnecki, M. Jezabek, Distributions of leptons in decays of polarized heavy quarks, Nucl. Phys. B427 (1994) 3–21.
[518] M. B. Voloshin, Moments of lepton spectrum in B decays and the m(b) - m(c) quark mass difference, Phys. Rev. D51 (1995) 4934–4938.
[519] M. Trott, Improving extractions of —V(cb)— and m(b) from the hadronic invariant mass moments of semileptonic inclusive B decay, Phys. Rev. D70 (2004) 073003.
[520] A. F. Falk, M. E. Luke, M. J. Savage, Hadron spectra for semileptonic heavy quark decay, Phys. Rev. D53 (1996) 2491–2505.
[521] M. E. Luke, M. J. Savage, M. B. Wise, Perturbative strong interaction corrections to the heavy quark semileptonic decay rate, Phys. Lett. B343 (1995) 329–332.
[522] P. Ball, M. Beneke, V. M. Braun, Resummation of running coupling effects in semileptonic B meson decays and extraction of $|V_{cb}|$, Phys. Rev. D52 (1995) 3929–3948.
[523] M. Gremm, I. W. Stewart, Order $\alpha_s^2 \beta_0$ correction to the charged lepton spectrum in $b \to c \ell \bar{\nu}_\ell$ decays, Phys. Rev. D55 (1997) 1226–1232.
[524] A. F. Falk, M. E. Luke, Hadronic spectral moments in semileptonic B decays with a lepton energy cut, Phys. Rev. D57 (1998) 424–430.
[525] N. Uraltsev, Perturbative corrections to the semileptonic b-decay moments: E_{cut}^{ℓ} dependence and running-α_s effects in the OPE approach, Int. J. Mod. Phys. A20 (2005) 2099–2118.
[526] V. Aquila, P. Gambino, G. Ridolfi, N. Uraltsev, Perturbative corrections to semileptonic b decay distributions, Nucl. Phys. B719 (2005) 77–102.
[527] N. Uraltsev, BLM-resummation and OPE in heavy flavor transitions, Nucl. Phys. B491 (1997) 303–322.
[528] A. H. Hoang, Z. Ligeti, A. V. Manohar, B decays in the Upsilon expansion, Phys. Rev. D59 (1999) 074017.
[529] M. Beneke, A quark mass definition adequate for threshold problems, Phys. Lett. B434 (1998) 115–125.
[530] S. W. Bosch, B. O. Lange, M. Neubert, G. Paz, Factorization and shape-function effects in inclusive B- meson decays, Nucl. Phys. B699 (2004) 335–386.
[531] M. Neubert, Two-loop relations for heavy-quark parameters in the shape-function scheme, Phys. Lett. B612 (2005) 13–20.
[532] M. Neubert, QCD Calculations of Decays of Heavy Flavor Hadrons. arXiv:0801.0675.
[533] K. Melnikov, $O(\alpha_s^2)$ corrections to semileptonic decay $b \to c l \bar{\nu}_l$. arXiv:0803.0951.
[534] A. Pak, A. Czarnecki, Mass effects in muon and semileptonic $b \to c$ decays, Phys. Rev. Lett. 100 (2008) 241807.
[535] A. Czarnecki, K. Melnikov, Two-loop QCD corrections to semileptonic b decays at an intermediate recoil, Phys. Rev. D59 (1999) 014036.
[536] M. Dowling, A. Pak, A. Czarnecki, Semi-Leptonic b-decay at Intermediate Recoil, Phys. Rev. D78 (2008) 074029.

[537] B. M. Dassinger, T. Mannel, S. Turczyk, Inclusive semi-leptonic B decays to order $1/m_b^4$, JHEP 03 (2007) 087.
[538] M. A. Shifman, Quark-hadron duality. arXiv:hep-ph/0009131.
[539] I. I. Y. Bigi, N. Uraltsev, A vademecum on quark hadron duality, Int. J. Mod. Phys. A16 (2001) 5201–5248.
[540] I. I. Bigi, T. Mannel, Parton hadron duality in B meson decays. arXiv:hep-ph/0212021.
[541] I. I. Bigi, N. Uraltsev, R. Zwicky, On the nonperturbative charm effects in inclusive $B \to X_c \ell \nu$ decays, Eur. Phys. J. C50 (2007) 539–556.
[542] C. Breidenbach, T. Feldmann, T. Mannel, S. Turczyk, On the Role of 'Intrinsic Charm' in Semi-Leptonic B-Meson Decays, Phys. Rev. D78 (2008) 014022.
[543] B. M. Dassinger, R. Feger, T. Mannel, Testing the left-handedness of the $b \to c$ transition, Phys. Rev. D75 (2007) 095007.
[544] B. Dassinger, R. Feger, T. Mannel, Complete Michel Parameter Analysis of inclusive semileptonic $b \to c$ transition. arXiv:0803.3561.
[545] B. Aubert, et al., Measurement of the electron energy spectrum and its moments in inclusive $B \to X e \nu$ decays, Phys. Rev. D69 (2004) 111104.
[546] B. Aubert, et al., Measurements of moments of the hadronic mass distribution in semileptonic B decays, Phys. Rev. D69 (2004) 111103.
[547] B. Aubert, et al., Measurement of Moments of the Hadronic-Mass and -Energy Spectrum in Inclusive Semileptonic $\bar{B} \to X_c \ell^- \bar{\nu}$ Decays. arXiv:0707.2670.
[548] P. Urquijo, et al., Moments of the electron energy spectrum and partial branching fraction of $B \to X_c e \nu$ decays at Belle, Phys. Rev. D75 (2007) 032001.
[549] C. Schwanda, et al., Moments of the hadronic invariant mass spectrum in $B \to X_c \ell \nu$ decays at Belle, Phys. Rev. D75 (2007) 032005.
[550] D. E. Acosta, et al., Measurement of the moments of the hadronic invariant mass distribution in semileptonic B decays, Phys. Rev. D71 (2005) 051103.
[551] S. E. Csorna, et al., Moments of the B meson inclusive semileptonic decay rate using neutrino reconstruction, Phys. Rev. D70 (2004) 032002.
[552] J. Abdallah, et al., Determination of heavy quark non-perturbative parameters from spectral moments in semileptonic B decays, Eur. Phys. J. C45 (2006) 35–59.
[553] B. Aubert, et al., Measurement of the branching fraction and photon energy moments of $B \to X_s \gamma$ and $A_{CP}(B \to X_{s+d}\gamma)$, Phys. Rev. Lett. 97 (2006) 171803.
[554] B. Aubert, et al., Measurements of the $B \to X_s \gamma$ branching fraction and photon spectrum from a sum of exclusive final states, Phys. Rev. D72 (2005) 052004.
[555] C. Schwanda, et al., Measurement of the Moments of the Photon Energy Spectrum in $B \to X_s \gamma$ Decays and Determination of $|V_c b|$ and m_b at Belle, Phys. Rev. D78 (2008) 032016.
[556] K. Abe, et al., Improved Measurement of Inclusive Radiative B-meson decays, AIP Conf. Proc. 1078 (2009) 342–344.
[557] S. Chen, et al., Branching fraction and photon energy spectrum for $b \to s\gamma$, Phys. Rev. Lett. 87 (2001) 251807.
[558] A. Hocker, V. Kartvelishvili, SVD Approach to Data Unfolding, Nucl. Instrum. Meth. A372 (1996) 469–481.
[559] D. Benson, I. I. Bigi, N. Uraltsev, On the photon energy moments and their 'bias' corrections in $B \to X_s + \gamma$, Nucl. Phys. B710 (2005) 371–401.
[560] E. Barberio, et al., Averages of $b-$hadron and $c-$hadron Properties at the End of 2007. arXiv:0808.1297.
[561] I. I. Y. Bigi, N. G. Uraltsev, Weak annihilation and the endpoint spectrum in semileptonic B decays, Nucl. Phys. B423 (1994) 33–55.
[562] N. Uraltsev, Theoretical uncertainties in Gamma(sl)(b $\to$ u), Int. J. Mod. Phys. A14 (1999) 4641–4652.
[563] M. B. Voloshin, Nonfactorization effects in heavy mesons and determination of $|V_{ub}|$ from inclusive semileptonic B decays, Phys. Lett. B515 (2001) 74–80.
[564] P. Gambino, G. Ossola, N. Uraltsev, Hadronic mass and q^2 moments of charmless semileptonic B decay distributions, JHEP 09 (2005) 010.
[565] M. Neubert, QCD based interpretation of the lepton spectrum in inclusive anti-B $\to$ X(u) lepton anti-neutrino decays, Phys. Rev. D49 (1994) 3392–3398.

[566] I. I. Y. Bigi, M. A. Shifman, N. G. Uraltsev, A. I. Vainshtein, On the motion of heavy quarks inside hadrons: Universal distributions and inclusive decays, Int. J. Mod. Phys. A9 (1994) 2467–2504.
[567] J. R. Andersen, E. Gardi, Taming the $B \to X_s\gamma$ spectrum by dressed gluon exponentiation, JHEP 06 (2005) 030.
[568] J. R. Andersen, E. Gardi, Inclusive spectra in charmless semileptonic B decays by dressed gluon exponentiation, JHEP 01 (2006) 097.
[569] J. R. Andersen, E. Gardi, Radiative B decay spectrum: DGE at NNLO, JHEP 01 (2007) 029.
[570] E. Gardi, Inclusive B decays from resummed perturbation theory. arXiv:hep-ph/0703036.
[571] Z. Ligeti, I. W. Stewart, F. J. Tackmann, Treating the b quark distribution function with reliable uncertainties, Phys. Rev. D78 (2008) 114014.
[572] B. O. Lange, M. Neubert, G. Paz, A two-loop relation between inclusive radiative and semileptonic B decay spectra, JHEP 10 (2005) 084.
[573] B. O. Lange, Shape-function independent relations of charmless inclusive B-decay spectra, JHEP 01 (2006) 104.
[574] A. K. Leibovich, Z. Ligeti, M. B. Wise, Enhanced subleading structure functions in semileptonic B decay, Phys. Lett. B539 (2002) 242–248.
[575] C. W. Bauer, M. Luke, T. Mannel, Subleading shape functions in $B \to X_u\ell\bar{\nu}$ and the determination of $|V_{ub}|$, Phys. Lett. B543 (2002) 261–268.
[576] S. W. Bosch, M. Neubert, G. Paz, Subleading shape functions in inclusive B decays, JHEP 11 (2004) 073.
[577] P. Gambino, P. Giordano, G. Ossola, N. Uraltsev, Inclusive semileptonic B decays and the determination of $|V_{ub}|$, JHEP 10 (2007) 058.
[578] F. De Fazio, M. Neubert, $B \to X_u\ell\bar{\nu}_\ell$ decay distributions to order α_s, JHEP 06 (1999) 017.
[579] P. Gambino, E. Gardi, G. Ridolfi, Running-coupling effects in the triple-differential charmless semileptonic decay width, JHEP 12 (2006) 036.
[580] R. Bonciani, A. Ferroglia, Two-Loop QCD Corrections to the Heavy-to-Light Quark Decay, JHEP 11 (2008) 065.
[581] H. M. Asatrian, C. Greub, B. D. Pecjak, NNLO corrections to $B \to X_u l\nu$ in the shape-function region, Phys. Rev. D78 (2008) 114028.
[582] M. Beneke, T. Huber, X. Q. Li, Two-loop QCD correction to differential semi-leptonic $b \to u$ decays in the shape-function region, Nucl. Phys. B811 (2009) 77–97.
[583] G. Bell, NNLO corrections to inclusive semileptonic B decays in the shape-function region, Nucl. Phys. B812 (2009) 264–289.
[584] J. L. Rosner, et al., Experimental limits on weak annihilation contributions to $b \to u\ell\nu$ decay, Phys. Rev. Lett. 96 (2006) 121801.
[585] B. Aubert, et al., Measurement of the $B^0 \to X_u^-\ell^+\nu_\ell$ decays near the kinematic endpoint of the lepton spectrum and search for violation of isospin symmetry. arXiv:0708.1753.
[586] B. O. Lange, M. Neubert, G. Paz, Theory of charmless inclusive B decays and the extraction of V_{ub}, Phys. Rev. D72 (2005) 073006.
[587] E. Gardi, Inclusive distributions near kinematic thresholds. arXiv:hep-ph/0606080.
[588] E. Gardi, Radiative and semi-leptonic B-meson decay spectra: Sudakov resummation beyond logarithmic accuracy and the pole mass, JHEP 04 (2004) 049.
[589] U. Aglietti, F. Di Lodovico, G. Ferrera, G. Ricciardi, Inclusive Measure of $|V_{ub}|$ with the Analytic Coupling Model, Eur. Phys. J. C59 (2009) 831–840.
[590] D. V. Shirkov, I. L. Solovtsov, Analytic model for the QCD running coupling with universal alpha(s)-bar(0) value, Phys. Rev. Lett. 79 (1997) 1209–1212.
[591] M. Battaglia, et al., The CKM matrix and the unitarity triangle. Workshop, CERN, Geneva, Switzerland, 13-16 Feb 2002: Proceedings. arXiv:hep-ph/0304132.
[592] N. Gray, D. J. Broadhurst, W. Grafe, K. Schilcher, Three loop relation of quark $\bar{M}S$ and pole masses, Z. Phys. C48 (1990) 673–680.
[593] K. Melnikov, T. v. Ritbergen, The three-loop relation between the MS-bar and the pole quark masses, Phys. Lett. B482 (2000) 99–108.
[594] K. G. Chetyrkin, M. Steinhauser, The relation between the MS-bar and the on-shell quark mass at order α_s^3, Nucl. Phys. B573 (2000) 617–651.
[595] A. H. Hoang, et al., Top-antitop pair production close to threshold: Synopsis of recent NNLO results, Eur. Phys. J. direct C2 (2000) 1.

[596] I. I. Y. Bigi, M. A. Shifman, N. Uraltsev, A. I. Vainshtein, High power n of m(b) in beauty widths and n = 5 → infinity limit, Phys. Rev. D56 (1997) 4017–4030.
[597] I. I. Y. Bigi, M. A. Shifman, N. G. Uraltsev, A. I. Vainshtein, Sum rules for heavy flavor transitions in the SV limit, Phys. Rev. D52 (1995) 196–235.
[598] A. Czarnecki, K. Melnikov, N. Uraltsev, Non-Abelian dipole radiation and the heavy quark expansion, Phys. Rev. Lett. 80 (1998) 3189–3192.
[599] K. Melnikov, A. Yelkhovsky, The b quark low-scale running mass from Upsilon sum rules, Phys. Rev. D59 (1999) 114009.
[600] A. H. Hoang, Z. Ligeti, A. V. Manohar, B decay and the Upsilon mass, Phys. Rev. Lett. 82 (1999) 277–280.
[601] A. H. Hoang, T. Teubner, Top quark pair production close to threshold: Top mass, width and momentum distribution, Phys. Rev. D60 (1999) 114027.
[602] A. H. Hoang, A. Jain, I. Scimemi, I. W. Stewart, Infrared Renormalization Group Flow for Heavy Quark Masses, Phys. Rev. Lett. 101 (2008) 151602.
[603] V. A. Novikov, et al., Sum Rules for Charmonium and Charmed Mesons Decay Rates in Quantum Chromodynamics, Phys. Rev. Lett. 38 (1977) 626.
[604] L. J. Reinders, H. Rubinstein, S. Yazaki, Hadron Properties from QCD Sum Rules, Phys. Rept. 127 (1985) 1.
[605] A. H. Hoang, 1S and MSbar Bottom Quark Masses from Upsilon Sum Rules, Phys. Rev. D61 (2000) 034005.
[606] M. Beneke, A. Signer, The bottom $\bar{\text{M}}$S quark mass from sum rules at next-to-next-to-leading order, Phys. Lett. B471 (1999) 233–243.
[607] A. H. Hoang, Bottom quark mass from Upsilon mesons: Charm mass effects. arXiv:hep-ph/0008102.
[608] M. Eidemuller, QCD moment sum rules for Coulomb systems: the charm and bottom quark masses, Phys. Rev. D67 (2003) 113002.
[609] A. Pineda, A. Signer, Renormalization Group Improved Sum Rule Analysis for the Bottom Quark Mass, Phys. Rev. D73 (2006) 111501.
[610] J. H. Kuhn, M. Steinhauser, Determination of α_s and heavy quark masses from recent measurements of $R(s)$, Nucl. Phys. B619 (2001) 588–602.
[611] J. Bordes, J. Penarrocha, K. Schilcher, Bottom quark mass and QCD duality, Phys. Lett. B562 (2003) 81–86.
[612] G. Corcella, A. H. Hoang, Uncertainties in the MSbar bottom quark mass from relativistic sum rules, Phys. Lett. B554 (2003) 133–140.
[613] A. H. Hoang, M. Jamin, MSbar Charm Mass from Charmonium Sum Rules with Contour Improvement, Phys. Lett. B594 (2004) 127–134.
[614] R. Boughezal, M. Czakon, T. Schutzmeier, Charm and bottom quark masses from perturbative QCD, Phys. Rev. D74 (2006) 074006.
[615] J. H. Kuhn, M. Steinhauser, C. Sturm, Heavy quark masses from sum rules in four-loop approximation, Nucl. Phys. B778 (2007) 192–215.
[616] A. H. Hoang, Three-loop anomalous dimension of the heavy quark pair production current in non-relativistic QCD, Phys. Rev. D69 (2004) 034009.
[617] P. Gambino, P. Giordano, Normalizing inclusive rare B decays, Phys. Lett. B669 (2008) 69–73.
[618] A. Bochkarev, P. de Forcrand, Determination of the renormalized heavy quark mass in lattice QCD, Nucl. Phys. B477 (1996) 489–520.
[619] Q. Mason, H. D. Trottier, R. Horgan, C. T. H. Davies, G. P. Lepage, High-precision determination of the light-quark masses from realistic lattice QCD, Phys. Rev. D73 (2006) 114501.
[620] A. Gray, et al., The Upsilon spectrum and m_b from full lattice QCD, Phys. Rev. D72 (2005) 094507.
[621] J. Heitger, Heavy quark masses from lattice QCD, Nucl. Phys. Proc. Suppl. 181+182 (2008) 156.
[622] I. Allison, et al., High-Precision Charm-Quark Mass from Current-Current Correlators in Lattice and Continuum QCD, Phys. Rev. D78 (2008) 054513.
[623] I. F. Allison, et al., Matching the Bare and MSbar Charm Quark Masses Using Weak Coupling Simulations. arXiv:0810.0285.
[624] A. H. Hoang, A. V. Manohar, Charm Quark Mass from Inclusive Semileptonic B Decays, Phys. Lett. B633 (2006) 526–532.

[625] B. Aubert, et al., Measurement of the inclusive electron spectrum in charmless semileptonic B decays near the kinematic endpoint and determination of $|V_{ub}|$, Phys. Rev. D73 (2006) 012006.
[626] I. Bizjak, et al., Measurement of the inclusive charmless semileptonic partial branching fraction of B mesons and determination of $|V_{ub}|$ using the full reconstruction tag, Phys. Rev. Lett. 95 (2005) 241801.
[627] B. CollaborationPreliminary result shown at CKM2008.
[628] A. Bornheim, et al., Improved Measurement of $|V_{ub}|$ with Inclusive Semileptonic B Decays, Phys. Rev. Lett. 88 (2002) 231803.
[629] B. Aubert, et al., Determination of $|V_{ub}|$ from measurements of the electron and neutrino momenta in inclusive semileptonic B decays, Phys. Rev. Lett. 95 (2005) 111801.
[630] H. Kakuno, et al., Measurement of $|V_{ub}|$ using inclusive $B \to X_u \ell \nu$ decays with a novel X_u reconstruction method, Phys. Rev. Lett. 92 (2004) 101801.
[631] A. Limosani, et al., Measurement of inclusive charmless semileptonic B-meson decays at the endpoint of the electron momentum spectrum, Phys. Lett. B621 (2005) 28–40.
[632] B. Aubert, et al., Measurements of Partial Branching Fractions for $\bar{B} \to X_u \ell \bar{\nu}$ and Determination of $|V_{ub}|$, Phys. Rev. Lett. 100 (2008) 171802.
[633] M. Neubert, Analysis of the photon spectrum in inclusive $B \to X_s + \gamma$ decays, Phys. Rev. D49 (1994) 4623–4633.
[634] A. K. Leibovich, I. Low, I. Z. Rothstein, Extracting V_{ub} without recourse to structure functions, Phys. Rev. D61 (2000) 053006.
[635] V. B. Golubev, Y. I. Skovpen, V. G. Luth, Extraction of $|V_{ub}|$ with Reduced Dependence on Shape Functions, Phys. Rev. D76 (2007) 114003.
[636] B. Aubert, et al., Determinations of $|V_{ub}|$ from inclusive semileptonic B decays with reduced model dependence, Phys. Rev. Lett. 96 (2006) 221801.
[637] M. Bona, et al., The unitarity triangle fit in the standard model and hadronic parameters from lattice QCD: A reappraisal after the measurements of Δm_s and $BR(B \to \tau \nu_\tau)$, JHEP 10 (2006) 081.
[638] A. J. Buras, A. Czarnecki, M. Misiak, J. Urban, Completing the NLO QCD calculation of $\bar{B} \to X_s \gamma$, Nucl. Phys. B631 (2002) 219–238.
[639] K. Melnikov, A. Mitov, The photon energy spectrum in $B \to X_s + \gamma$ in perturbative QCD through $O(\alpha_s^2)$, Phys. Lett. B620 (2005) 69–79.
[640] I. R. Blokland, A. Czarnecki, M. Misiak, M. Slusarczyk, F. Tkachov, The electromagnetic dipole operator effect on $B \to X_s \gamma$ at $\mathrm{O}(\alpha_s^2)$, Phys. Rev. D72 (2005) 033014.
[641] H. M. Asatrian, et al., NNLL QCD contribution of the electromagnetic dipole operator to $\Gamma(B \to X_s \gamma)$, Nucl. Phys. B749 (2006) 325–337.
[642] Z. Ligeti, M. E. Luke, A. V. Manohar, M. B. Wise, The $B \to X_s \gamma$ photon spectrum, Phys. Rev. D60 (1999) 034019.
[643] K. Bieri, C. Greub, M. Steinhauser, Fermionic NNLL corrections to $b \to s\gamma$, Phys. Rev. D67 (2003) 114019.
[644] R. Boughezal, M. Czakon, T. Schutzmeier, NNLO fermionic corrections to the charm quark mass dependent matrix elements in $B \to X_s \gamma$, JHEP 09 (2007) 072.
[645] T. Ewerth, Fermionic corrections to the interference of the electro- and chromomagnetic dipole operators in $B \to X_s \gamma$ at $\mathrm{O}(\alpha_s^2)$, Phys. Lett. B669 (2008) 167–172.
[646] M. Misiak, M. Steinhauser, NNLO QCD corrections to the $B \to X_s \gamma$ matrix elements using interpolation in m_c, Nucl. Phys. B764 (2007) 62–82.
[647] M. Misiak, et al., The first estimate of $BR(\bar{B} \to X_s \gamma)$ at $O(\alpha_s^2)$, Phys. Rev. Lett. 98 (2007) 022002.
[648] S. J. Lee, M. Neubert, G. Paz, Enhanced non-local power corrections to the $B \to X_s + \gamma$ decay rate, Phys. Rev. D75 (2007) 114005.
[649] M. Neubert, Renormalization-group improved calculation of the $B \to X_s + \gamma$ branching ratio, Eur. Phys. J. C40 (2005) 165–186.
[650] T. Becher, M. Neubert, Toward a NNLO calculation of the $B \to X_s + \gamma$ decay rate with a cut on photon energy. I: Two-loop result for the soft function, Phys. Lett. B633 (2006) 739–747.
[651] T. Becher, M. Neubert, Toward a NNLO calculation of the $B \to X_s \gamma$ decay rate with a cut on photon energy. II: Two-loop result for the jet function, Phys. Lett. B637 (2006) 251–259.
[652] T. Becher, M. Neubert, Analysis of $BR(B \to X_s + \gamma)$ at NNLO with a cut on photon energy, Phys. Rev. Lett. 98 (2007) 022003.

[653] M. Ciuchini, G. Degrassi, P. Gambino, G. F. Giudice, Next-to-leading QCD corrections to $B \to X_s + \gamma$: Standard model and two-Higgs doublet model, Nucl. Phys. B527 (1998) 21–43.
[654] F. Borzumati, C. Greub, 2HDMs predictions for $B \to X_s + \gamma$ in NLO QCD, Phys. Rev. D58 (1998) 074004.
[655] C. Bobeth, M. Misiak, J. Urban, Matching conditions for $b \to s\gamma$ and $b \to sg$ in extensions of the standard model, Nucl. Phys. B567 (2000) 153–185.
[656] M. Ciuchini, G. Degrassi, P. Gambino, G. F. Giudice, Next-to-leading QCD corrections to $B \to X_s\gamma$ in supersymmetry, Nucl. Phys. B534 (1998) 3–20.
[657] G. Degrassi, P. Gambino, P. Slavich, QCD corrections to radiative B decays in the MSSM with minimal flavor violation, Phys. Lett. B635 (2006) 335–342.
[658] M. Albrecht, W. Altmannshofer, A. J. Buras, D. Guadagnoli, D. M. Straub, Challenging SO(10) SUSY GUTs with family symmetries through FCNC processes, JHEP 10 (2007) 055.
[659] W. Altmannshofer, D. Guadagnoli, S. Raby, D. M. Straub, SUSY GUTs with Yukawa unification: A Go/no-go study using FCNC processes, Phys. Lett. B668 (2008) 385–391.
[660] K. Agashe, N. G. Deshpande, G. H. Wu, Universal extra dimensions and $b \to s\gamma$, Phys. Lett. B514 (2001) 309–314.
[661] A. J. Buras, A. Poschenrieder, M. Spranger, A. Weiler, The impact of universal extra dimensions on $B \to X_s\gamma$, $B \to X_s g$, $B \to X_s\mu^+\mu^-$, $K_L \to \pi^0 e^+ e^-$, and ϵ'/ϵ, Nucl. Phys. B678 (2004) 455–490.
[662] U. Haisch, A. Weiler, Bound on minimal universal extra dimensions from $B \to X_s\gamma$, Phys. Rev. D76 (2007) 034014.
[663] A. Freitas, U. Haisch, $B \to X_s\gamma$ in two universal extra dimensions, Phys. Rev. D77 (2008) 093008.
[664] B. Aubert, et al., Measurement of $B \to X\gamma$ Decays and Determination of $|V_{td}/V_{ts}|$. arXiv:0807.4975.
[665] A. Ali, H. Asatrian, C. Greub, Inclusive decay rate for $B \to X_d + \gamma$ in next-to- leading logarithmic order and CP asymmetry in the standard model, Phys. Lett. B429 (1998) 87–98.
[666] H. Abe, K.-S. Choi, T. Kobayashi, H. Ohki, Three generation magnetized orbifold models, Nucl. Phys. B814 (2009) 265–292.
[667] A. L. Kagan, M. Neubert, Direct CP violation in $B \to X_s\gamma$ decays as a signature of new physics, Phys. Rev. D58 (1998) 094012.
[668] T. Hurth, E. Lunghi, W. Porod, Untagged $B \to X_{s+d}\gamma$ CP asymmetry as a probe for new physics, Nucl. Phys. B704 (2005) 56–74.
[669] S. Baek, P. Ko, Probing SUSY-induced CP violations at B factories, Phys. Rev. Lett. 83 (1999) 488–491.
[670] K. Kiers, A. Soni, G.-H. Wu, Direct CP violation in radiative b decays in and beyond the standard model, Phys. Rev. D62 (2000) 116004.
[671] B. Aubert, et al., A Measurement of CP Asymmetry in $b \to s\gamma$ using a Sum of Exclusive Final States, Phys. Rev. Lett. 101 (2008) 171804.
[672] S. Nishida, et al., Measurement of the CP asymmetry in $B \to X_s + \gamma$, Phys. Rev. Lett. 93 (2004) 031803.
[673] B. Aubert, et al., Measurement of the $B \to X_s$ gamma Branching Fraction and Photon Energy Spectrum using the Recoil Method, Phys. Rev. D77 (2008) 051103.
[674] K. Abe, et al., A measurement of the branching fraction for the inclusive $B \to X_s + \gamma$ decays with Belle, Phys. Lett. B511 (2001) 151–158.
[675] A. L. Kagan, M. Neubert, QCD anatomy of $B \to X_s + \gamma$ decays, Eur. Phys. J. C7 (1999) 5–27.
[676] A. Kapustin, Z. Ligeti, H. D. Politzer, Leading logarithms of the b quark mass in inclusive $B \to X_s + \gamma$ decay, Phys. Lett. B357 (1995) 653–658.
[677] Z. Ligeti, L. Randall, M. B. Wise, Comment on nonperturbative effects in $B \to X_s + \gamma$, Phys. Lett. B402 (1997) 178–182.
[678] G. P. Korchemsky, G. Sterman, Infrared factorization in inclusive B meson decays, Phys. Lett. B340 (1994) 96–108.
[679] E. Gardi, On the quark distribution in an on-shell heavy quark and its all-order relations with the perturbative fragmentation function, JHEP 02 (2005) 053.
[680] M. Neubert, Advanced predictions for moments of the $B \to X_s\gamma$ photon spectrum, Phys. Rev. D72 (2005) 074025.
[681] C. W. Bauer, M. E. Luke, T. Mannel, Light-cone distribution functions for B decays at subleading order in $1/m_b$, Phys. Rev. D68 (2003) 094001.

[682] K. S. M. Lee, I. W. Stewart, Factorization for power corrections to $B \to X_s\gamma$ and $B \to X_u\ell\bar{\nu}$, Nucl. Phys. B721 (2005) 325–406.
[683] M. Beneke, F. Campanario, T. Mannel, B. D. Pecjak, Power corrections to $B \to X_u\ell\bar{\nu}(X_s\gamma)$ decay spectra in the 'shape-function' region, JHEP 06 (2005) 071.
[684] H. M. Asatrian, T. Ewerth, A. Ferroglia, P. Gambino, C. Greub, Magnetic dipole operator contributions to the photon energy spectrum in $B \to X_s + \gamma$ at O(alpha(s)**2), Nucl. Phys. B762 (2007) 212–228.
[685] G. P. Korchemsky, G. Marchesini, Structure function for large x and renormalization of Wilson loop, Nucl. Phys. B406 (1993) 225–258.
[686] S. Moch, J. A. M. Vermaseren, A. Vogt, The three-loop splitting functions in QCD: The non-singlet case, Nucl. Phys. B688 (2004) 101–134.
[687] M. Misiak, QCD Calculations of Radiative B Decays. arXiv:0808.3134.
[688] A. Ali, C. Greub, Photon energy spectrum in $B \to X_s + \gamma$ and comparison with data, Phys. Lett. B361 (1995) 146–154.
[689] M. Beneke, T. Feldmann, D. Seidel, Systematic approach to exclusive $B \to V\ell^+\ell^-$, $V\gamma$ decays, Nucl. Phys. B612 (2001) 25–58.
[690] S. W. Bosch, G. Buchalla, The radiative decays $B \to V\gamma$ at next-to-leading order in QCD, Nucl. Phys. B621 (2002) 459–478.
[691] A. Ali, A. Y. Parkhomenko, Branching ratios for $B \to \rho\gamma$ decays in next-to- leading order in α_s including hard spectator corrections, Eur. Phys. J. C23 (2002) 89–112.
[692] Y. Y. Keum, M. Matsumori, A. I. Sanda, CP asymmetry, branching ratios and isospin breaking effects of $B \to K^*\gamma$ with perturbative QCD approach, Phys. Rev. D72 (2005) 014013.
[693] C.-D. Lu, M. Matsumori, A. I. Sanda, M.-Z. Yang, CP asymmetry, branching ratios and isospin breaking effects in $B \to \rho\gamma$ and $B \to \omega\gamma$ decays with the pQCD approach, Phys. Rev. D72 (2005) 094005.
[694] M. Matsumori, A. I. Sanda, The mixing-induced CP asymmetry in $B \to K * \gamma$ decays with perturbative QCD approach, Phys. Rev. D73 (2006) 114022.
[695] A. Ali, B. D. Pecjak, C. Greub, $B \to V\gamma$ Decays at NNLO in SCET, Eur. Phys. J. C55 (2008) 577–595.
[696] T. Becher, R. J. Hill, M. Neubert, Factorization in $B \to V\gamma$ decays, Phys. Rev. D72 (2005) 094017.
[697] A. L. Kagan, M. Neubert, Isospin breaking in $B \to K^*\gamma$ decays, Phys. Lett. B539 (2002) 227–234.
[698] S. W. Bosch, G. Buchalla, Constraining the unitarity triangle with $B \to V\gamma$, JHEP 01 (2005) 035.
[699] M. Beneke, T. Feldmann, D. Seidel, Exclusive radiative and electroweak $b \to d$ and $b \to s$ penguin decays at NLO, Eur. Phys. J. C41 (2005) 173–188.
[700] A. Ali, A. Parkhomenko, $B \to (\rho, \omega)\gamma$ decays and CKM phenomenology. arXiv:hep-ph/0610149.
[701] C. Kim, A. K. Leibovich, T. Mehen, Nonperturbative Charming Penguin Contributions to Isospin Asymmetries in Radiative B decays, Phys. Rev. D78 (2008) 054024.
[702] B. Grinstein, Y. Grossman, Z. Ligeti, D. Pirjol, The photon polarization in $B \to X_s + \gamma$ in the standard model, Phys. Rev. D71 (2005) 011504.
[703] Y. Ushiroda, et al., Time-dependent CP asymmetries in $B^0 \to K^0_S\pi^0\gamma$ transitions, Phys. Rev. D74 (2006) 111104.
[704] B. Aubert, et al., Measurement of Time-Dependent CP Asymmetry in $B^0 \to K^0_S\pi^0\gamma$ Decays, Phys. Rev. D78 (2008) 071102.
[705] S. Descotes-Genon, C. T. Sachrajda, Sudakov effects in $B \to \pi\ell\nu_\ell$ form factors, Nucl. Phys. B625 (2002) 239–278.
[706] R. Ammar, et al., Evidence for penguins: First observation of $B \to K^*(892)\gamma$, Phys. Rev. Lett. 71 (1993) 674–678.
[707] M. Nakao, et al., Measurement of the $B \to K^*\gamma$ branching fractions and asymmetries, Phys. Rev. D69 (2004) 112001.
[708] B. Aubert, et al., Measurement of Branching Fractions and CP and Isospin Asymmetries in $B \to K^*\gamma$. arXiv:0808.1915.
[709] H. Yang, et al., Observation of $B^+ \to K_1(1270)^+\gamma$, Phys. Rev. Lett. 94 (2005) 111802.
[710] S. Nishida, et al., Radiative B meson decays into K pi gamma and K pi pi gamma final states, Phys. Rev. Lett. 89 (2002) 231801.

[711] B. Aubert, et al., Measurement of the $B^0 \to K_2^*(1430)0\gamma$ and $B^+ \to K_2^*(1430)^+\gamma$ branching fractions, Phys. Rev. D70 (2004) 091105.
[712] S. Nishida, et al., Observation of $B^+ \to K^+\eta\gamma$, Phys. Lett. B610 (2005) 23–30.
[713] B. Aubert, et al., Branching Fractions and CP-Violating Asymmetries in Radiative B Decays to eta K gamma, Phys. Rev. D79 (2009) 011102.
[714] I. Adachi, et al., Evidence for B to K eta' gamma Decays at Belle. arXiv:0810.0804.
[715] A. Drutskoy, et al., Observation of radiative $B \to \phi K\gamma$ decays, Phys. Rev. Lett. 92 (2004) 051801.
[716] B. Aubert, et al., Measurement of B decays to Phi K gamma, Phys. Rev. D75 (2007) 051102.
[717] M. Z. Wang, et al., Study of $B^+ \to p\bar{\Lambda}\gamma$, $p\bar{\Lambda}\pi 0$ and $B^0 \to p\bar{\Lambda}\pi^-$, Phys. Rev. D76 (2007) 052004.
[718] B. Aubert, et al., Measurement of branching fractions and mass spectra of $B \to K\pi\pi\gamma$, Phys. Rev. Lett. 98 (2007) 211804.
[719] J. Wicht, et al., Observation of $B_s^0 \to \phi\gamma$ and Search for $B_s^0 \to \gamma\gamma$ Decays at Belle, Phys. Rev. Lett. 100 (2008) 121801.
[720] N. Taniguchi, et al., Measurement of branching fractions, isospin and CP- violating asymmetries for exclusive $b \to d\gamma$ modes, Phys. Rev. Lett. 101 (2008) 111801.
[721] B. Aubert, et al., Measurements of Branching Fractions for $B^+ \to \rho^+\gamma$, $B^0 \to \rho 0\gamma$, and $B^0 \to \omega\gamma$, Phys. Rev. D78 (2008) 112001.
[722] D. Atwood, T. Gershon, M. Hazumi, A. Soni, Mixing-induced CP violation in $B \to P_1P_2\gamma$ in search of clean new physics signals, Phys. Rev. D71 (2005) 076003.
[723] Q.-f. Li, J. Steinheimer, H. Petersen, M. Bleicher, H. Stocker, Effects of a phase transition on HBT correlations in an integrated Boltzmann+Hydrodynamics approach, Phys. Lett. B674 (2009) 111–116.
[724] F. Muheim, Y. Xie, R. Zwicky, Exploiting the width difference in $B_s \to \phi\gamma$, Phys. Lett. B664 (2008) 174–179.
[725] A. J. Buras, Relations between $\Delta M_{s,d}$ and $B_{s,d} \to \mu\bar{\mu}$ in models with minimal flavor violation, Phys. Lett. B566 (2003) 115–119.
[726] T. Aaltonen, et al., Search for $B_s^0 \to \mu^+\mu^-$ and $B_d^0 \to \mu^+\mu^-$ decays with $2fb^{-1}$ of $p\bar{p}$ collisions, Phys. Rev. Lett. 100 (2008) 101802.
[727] K. Ikado, et al., Evidence of the purely leptonic decay $B^- \to \tau\bar{\nu}_\tau$, Phys. Rev. Lett. 97 (2006) 251802.
[728] B. Aubert, et al., A Search for $B^+ \to \tau^+\nu$, Phys. Rev. D76 (2007) 052002.
[729] B. Aubert, et al., A Search for $B^+ \to \tau^+\nu$ with Hadronic B tags, Phys. Rev. D77 (2008) 011107.
[730] B. Aubert, et al., Search for $B^+ \to \mu^+\nu\mu$ with inclusive reconstruction at BaBar. arXiv:0807.4187.
[731] N. Satoyama, et al., A search for the rare leptonic decays $B^+ \to \mu^+\nu$ and $B^+ \to e^+\nu$, Phys. Lett. B647 (2007) 67–73.
[732] I. Adachi, et al., Measurement of $B^- \to \tau^-\bar{\nu}_t au$ Decay With a Semileptonic Tagging Method. arXiv:0809.3834.
[733] D. Martinez, J. A. Hernando, F. Teubert, LHCb potential to measure / exclude the branching ratio of the decay $B_s \to \mu^+\mu^-$CERN-LHCB-2007-033.
[734] G. Aad, et al., Expected Performance of the ATLAS Experiment - Detector, Trigger and Physics. arXiv:0901.0512.
[735] V. M. Abazov, et al., Search for $B_s \to \mu^+\mu^-$ at D0, Phys. Rev. D76 (2007) 092001.
[736] T. Aaltonen, et al., Search for the Decays $B0(s) \to e^+\mu^-$ and $B0(s) \to e^+e^-$ in CDF Run. II, Phys. Rev. Lett. 102 (2009) 201801.
[737] B. Aubert, et al., Search for decays of $B^0 \to$ mesons into e^+e^-, $\mu^+\mu^-$, and $e^\pm\mu^\mp$ final states, Phys. Rev. D77 (2008) 032007.
[738] M. C. Chang, et al., Search for $B^0 \to \ell^+\ell^-$ at BELLE, Phys. Rev. D68 (2003) 111101.
[739] U. Nierste, S. Trine, S. Westhoff, Charged-Higgs effects in a new $B \to D\tau\nu$ differential decay distribution, Phys. Rev. D78 (2008) 015006.
[740] J. F. Kamenik, F. Mescia, $B \to D\tau\nu$ Branching Ratios: Opportunity for Lattice QCD and Hadron Colliders, Phys. Rev. D78 (2008) 014003.
[741] D. Eriksson, F. Mahmoudi, O. Stal, Charged Higgs bosons in Minimal Supersymmetry: Updated constraints and experimental prospects, JHEP 11 (2008) 035.
[742] S. Trine, Charged-Higgs effects in $B \to D\tau\nu$ decays. arXiv:0810.3633.
[743] K. Kiers, A. Soni, Improving constraints on $\tan\beta/m_H$ using $B \to D\tau\bar{\nu}$, Phys. Rev. D56 (1997) 5786–5793.

[744] H. H. Asatryan, H. M. Asatrian, C. Greub, M. Walker, Calculation of two loop virtual corrections to $b \to s l^+ l^-$ in the standard model, Phys. Rev. D65 (2002) 074004.
[745] H. H. Asatryan, H. M. Asatrian, C. Greub, M. Walker, Complete gluon bremsstrahlung corrections to the process $b \to s l^+ l^-$, Phys. Rev. D66 (2002) 034009.
[746] A. Ghinculov, T. Hurth, G. Isidori, Y. P. Yao, Forward-backward asymmetry in $B \to X_s l^+ l^-$ at the NNLL level, Nucl. Phys. B648 (2003) 254–276.
[747] H. M. Asatrian, K. Bieri, C. Greub, A. Hovhannisyan, NNLL corrections to the angular distribution and to the forward-backward asymmetries in $b \to X_s l^+ l^-$, Phys. Rev. D66 (2002) 094013.
[748] A. Ghinculov, T. Hurth, G. Isidori, Y. P. Yao, New NNLL QCD results on the decay $B \to X_s l^+ l^-$, Eur. Phys. J. C33 (2004) s288–s290.
[749] A. Ghinculov, T. Hurth, G. Isidori, Y. P. Yao, The rare decay $B \to X_s l^+ l^-$ to NNLL precision for arbitrary dilepton invariant mass, Nucl. Phys. B685 (2004) 351–392.
[750] C. Bobeth, P. Gambino, M. Gorbahn, U. Haisch, Complete NNLO QCD analysis of $\bar{B} \to X_s \ell^+ \ell^-$ and higher order electroweak effects, JHEP 04 (2004) 071.
[751] H. M. Asatrian, H. H. Asatryan, A. Hovhannisyan, V. Poghosyan, Complete bremsstrahlung corrections to the forward- backward asymmetries in $b \to X_s l^+ l^-$, Mod. Phys. Lett. A19 (2004) 603–614.
[752] T. Huber, E. Lunghi, M. Misiak, D. Wyler, Electromagnetic logarithms in $\bar{B} \to X_s \ell^+ \ell^-$, Nucl. Phys. B740 (2006) 105–137.
[753] T. Huber, T. Hurth, E. Lunghi, Logarithmically Enhanced Corrections to the Decay Rate and Forward Backward Asymmetry in $\bar{B} \to X_s \ell^+ \ell^-$, Nucl. Phys. B802 (2008) 40–62.
[754] A. F. Falk, M. E. Luke, M. J. Savage, Nonperturbative contributions to the inclusive rare decays B → X(s) gamma and B → X(s) lepton+ lepton-, Phys. Rev. D49 (1994) 3367–3378.
[755] A. Ali, G. Hiller, L. T. Handoko, T. Morozumi, Power corrections in the decay rate and distributions in $B \to X_s l^+ l^-$ in the standard model, Phys. Rev. D55 (1997) 4105–4128.
[756] J.-W. Chen, G. Rupak, M. J. Savage, Non-$1/m_b^n$ power suppressed contributions to inclusive $B \to X_s l^+ l^-$ decays, Phys. Lett. B410 (1997) 285–289.
[757] G. Buchalla, G. Isidori, S. J. Rey, Corrections of order Λ_{QCD}^2/m_c^2 to inclusive rare B decays, Nucl. Phys. B511 (1998) 594–610.
[758] G. Buchalla, G. Isidori, Nonperturbative effects in $B \to X_s l^+ l^-$ for large dilepton invariant mass, Nucl. Phys. B525 (1998) 333–349.
[759] C. W. Bauer, C. N. Burrell, Nonperturbative corrections to moments of the decay $B \to X_s \ell^+ \ell^-$, Phys. Rev. D62 (2000) 114028.
[760] Z. Ligeti, F. J. Tackmann, Precise predictions for $B \to X_s \ell^+ \ell^-$ in the large q^2 region, Phys. Lett. B653 (2007) 404–410.
[761] T. Huber, T. Hurth, E. Lunghi, The Role of Collinear Photons in the Rare Decay $\bar{B} \to X_s \ell^+ \ell^-$. arXiv:0807.1940.
[762] A. Ali, G. Hiller, Perturbative QCD- and power-corrected hadron spectra and spectral moments in the decay $B \to X_s \ell^+ \ell^-$, Phys. Rev. D58 (1998) 074001.
[763] K. S. M. Lee, Z. Ligeti, I. W. Stewart, F. J. Tackmann, Universality and m_X cut effects in $B \to X_s \ell^+ \ell^-$, Phys. Rev. D74 (2006) 011501.
[764] K. S. M. Lee, Z. Ligeti, I. W. Stewart, F. J. Tackmann, Extracting short distance information from $b \to s \ell^+ \ell^-$ effectively, Phys. Rev. D75 (2007) 034016.
[765] B. Aubert, et al., Measurement of the $B \to X_s \ell^+ \ell^-$ branching fraction with a sum over exclusive modes, Phys. Rev. Lett. 93 (2004) 081802.
[766] M. Iwasaki, et al., Improved measurement of the electroweak penguin process $B \to X_s \ell^+ \ell^-$, Phys. Rev. D72 (2005) 092005.
[767] F. Kruger, J. Matias, Probing new physics via the transverse amplitudes of $B^0 \to K^{*0}(\to K^- \pi^+) \ell^+ \ell^-$ at large recoil, Phys. Rev. D71 (2005) 094009.
[768] B. Grinstein, D. Pirjol, Precise —V(ub)— determination from exclusive B decays: Controlling the long-distance effects, Phys. Rev. D70 (2004) 114005.
[769] J. Charles, A. Le Yaouanc, L. Oliver, O. Pene, J. C. Raynal, Heavy-to-light form factors in the heavy mass to large energy limit of QCD, Phys. Rev. D60 (1999) 014001.
[770] M. Beneke, T. Feldmann, Symmetry-breaking corrections to heavy-to-light B meson form factors at large recoil, Nucl. Phys. B592 (2001) 3–34.

[771] G. Burdman, Short distance coefficients and the vanishing of the lepton asymmetry in $B \to \mathrm{V}\ \ell^+$ lepton-, Phys. Rev. D57 (1998) 4254–4257.
[772] A. Ali, P. Ball, L. T. Handoko, G. Hiller, A Comparative study of the decays $B \to (K,\ K^*)\ell^+\ell^-$ in standard model and supersymmetric theories, Phys. Rev. D61 (2000) 074024.
[773] T. Feldmann, J. Matias, Forward-backward and isospin asymmetry for $B \to K^*\ell^+\ell^-$ decay in the standard model and in supersymmetry, JHEP 01 (2003) 074.
[774] W. Altmannshofer, et al., Symmetries and Asymmetries of $B \to K^*\mu^+\mu^-$ Decays in the Standard Model and Beyond, JHEP 01 (2009) 019.
[775] A. Ali, G. Kramer, G.-h. Zhu, $B \to K^*\ell^+\ell^-$ in soft-collinear effective theory, Eur. Phys. J. C47 (2006) 625–641.
[776] C. Bobeth, G. Hiller, G. Piranishvili, Angular Distributions of $B \to K\ell\ell$ Decays, JHEP 12 (2007) 040.
[777] U. O. Yilmaz, Analysis of $B_s \to \phi\ell^+\ell^-$ decay with new physics effects, Eur. Phys. J. C58 (2008) 555–568.
[778] M. Beneke, T. Feldmann, D. SeidelIn preparation.
[779] F. KrugerChapter 2.17 of Ref. [1228].
[780] E. Lunghi, J. Matias, Huge right-handed current effects in $B \to K^*(K\pi)\ell^+\ell^-$ in supersymmetry, JHEP 04 (2007) 058.
[781] C. Bobeth, G. Hiller, G. Piranishvili, CP Asymmetries in bar $B \to \bar{K}^*(\to \bar{K}\pi)\bar{\ell}\ell$ and Untagged $\bar{B}_s$, $B_s \to \phi(\to K^+K^-)\bar{\ell}\ell$ Decays at NLO, JHEP 07 (2008) 106.
[782] U. Egede, T. Hurth, J. Matias, M. Ramon, W. Reece, New observables in the decay mode $\bar{B} \to \bar{K}^{*0}\ell^+\ell^-$, JHEP 11 (2008) 032.
[783] F. Kruger, L. M. Sehgal, N. Sinha, R. Sinha, Angular distribution and CP asymmetries in the decays $B \to K^-\pi^+e^-e^+$ and $B \to \pi^-\pi^+e^-e^+$, Phys. Rev. D61 (2000) 114028.
[784] D. Melikhov, N. Nikitin, S. Simula, Probing right-handed currents in $B \to K^*\ell^+\ell^-$ transitions, Phys. Lett. B442 (1998) 381–389.
[785] C. S. Kim, Y. G. Kim, C.-D. Lu, T. Morozumi, Azimuthal angle distribution in $B \to K^*(\to K\pi)l^+l^-$ at low invariant m_{l+l-} region, Phys. Rev. D62 (2000) 034013.
[786] C. S. Kim, Y. G. Kim, C.-D. Lu, Possible supersymmetric effects on angular distributions in $B \to K^*(\to K\pi)l^+l^-$ decays, Phys. Rev. D64 (2001) 094014.
[787] A. Faessler, T. Gutsche, M. A. Ivanov, J. G. Korner, V. E. Lyubovitskij, The Exclusive rare decays $B \to \mathrm{K(K^*)}\ \bar{\ell}\ell$ and $B_c \to D(D^*)\bar{\ell}\ell$ in a relativistic quark model, Eur. Phys. J. direct C4 (2002) 18.
[788] K. Abe, et al., Observation of the decay $B \to K\ell^+\ell^-$, Phys. Rev. Lett. 88 (2002) 021801.
[789] B. Aubert, et al., Evidence for the rare decay $B \to K^*\ell^+\ell^-$ and measurement of the $B \to K\ell^+\ell^-$ branching fraction, Phys. Rev. Lett. 91 (2003) 221802.
[790] A. Ishikawa, et al., Observation of the electroweak penguin decay $B \to K^*\ell^+\ell^-$, Phys. Rev. Lett. 91 (2003) 261601.
[791] B. Aubert, et al., Angular Distributions in the Decays $B \to K^*\ell^+\ell^-$, Phys. Rev. D79 (2009) 031102.
[792] B. Aubert, et al., Direct CP, Lepton Flavor and Isospin Asymmetries in the Decays $B \to K^{(*)}\ell^+\ell^-$, Phys. Rev. Lett. 102 (2009) 091803.
[793] and others, Measurement of the Differential Branching Fraction and Forward-Backword Asymmetry for $B \to K^*\ell^+\ell^-$. arXiv:0904.0770.
[794] A. Ali, E. Lunghi, C. Greub, G. Hiller, Improved model independent analysis of semileptonic and radiative rare B decays, Phys. Rev. D66 (2002) 034002.
[795] Q.-S. Yan, C.-S. Huang, W. Liao, S.-H. Zhu, Exclusive semileptonic rare decays $B \to (K,\ K^*)\ell^+\ell^-$ in supersymmetric theories, Phys. Rev. D62 (2000) 094023.
[796] G. Hiller, F. Kruger, More model independent analysis of $b \to s$ processes, Phys. Rev. D69 (2004) 074020.
[797] T. Aaltonen, et al., Search for the Rare Decays $B^+ \to \mu^+\mu^-K^+$, $B^0 \to \mu^+\mu^-K^{*0}(892)$, and $B_s^0 \to \mu^+\mu^-\phi$ at CDF, Phys. Rev. D79 (2009) 011104.
[798] P. Gambino, U. Haisch, M. Misiak, Determining the sign of the $b \to s\gamma$ amplitude, Phys. Rev. Lett. 94 (2005) 061803.
[799] B. Aubert, et al., Search for the rare decay $B \to \pi\ell^+\ell^-$, Phys. Rev. Lett. 99 (2007) 051801.
[800] J. T. Wei, et al., Search for $B \to \pi\ell^+\ell^-$ Decays at Belle, Phys. Rev. D78 (2008) 011101.

[801] T. M. Aliev, M. Savci, Exclusive $B \to \pi\ell^+\ell^-$ and $B \to \rho\ell^+\ell^-$ decays in two Higgs doublet model, Phys. Rev. D60 (1999) 014005.
[802] J. Dickens, V. Gibson, C. Lazzeroni, M. Patel, Selection of the decay $b_d \to k^{*O}\mu^+\mu^-$ at lhcb, Tech. Rep. LHCb-2007-038. CERN-LHCb-2007-038, CERN, Geneva (Apr 2007).
[803] J. Dickens, V. Gibson, C. Lazzeroni, M. Patel, A study of the sensitivity to the forward-backward asymmetry in $b_d \to k^*\mu^+mu^-$ decays at lhcb, Tech. Rep. LHCb-2007-039. CERN-LHCb-2007-039, CERN, Geneva (Jul 2007).
[804] W. Reece, Extracting angular correlations from the rare decay $overline B_d \to \overline{K}^{*0}\mu^+\mu^-$ at lhcb, Tech. Rep. LHCb-2008-021. CERN-LHCb-2008-021, CERN, Geneva (May 2008).
[805] U. Egede, W. Reece, Performing the full angular analysis of $\overline{B}_d \to \overline{K}^{*0}\mu^+\mu^-$ at lhcb, Tech. Rep. LHCb-2008-041. CERN-LHCb-2008-041, CERN, Geneva (Nov 2008).
[806] G. Buchalla, A. J. Buras, QCD corrections to rare K and B decays for arbitrary top quark mass, Nucl. Phys. B400 (1993) 225–239.
[807] M. Misiak, J. Urban, QCD corrections to FCNC decays mediated by Z-penguins and W-boxes, Phys. Lett. B451 (1999) 161–169.
[808] G. Buchalla, A. J. Buras, Two-loop large-m(t) electroweak corrections to K → pi nu anti-nu for arbitrary Higgs boson mass, Phys. Rev. D57 (1998) 216–223.
[809] A. J. Buras, M. Gorbahn, U. Haisch, U. Nierste, The rare decay $K^+ \to \pi^+\nu\bar{\nu}$ at the next-to-next-to-leading order in QCD, Phys. Rev. Lett. 95 (2005) 261805.
[810] A. J. Buras, M. Gorbahn, U. Haisch, U. Nierste, Charm quark contribution to $K^+ \to \pi^+\nu\bar{\nu}$ at next-to-next-to-leading order, JHEP 11 (2006) 002.
[811] J. Brod, M. Gorbahn, Electroweak Corrections to the Charm Quark Contribution to $K^+ \to \pi^+\nu\bar{\nu}$, Phys. Rev. D78 (2008) 034006.
[812] F. Mescia, C. Smith, Improved estimates of rare K decay matrix-elements from K(l3) decays, Phys. Rev. D76 (2007) 034017.
[813] G. Isidori, F. Mescia, C. Smith, Light-quark loops in $K \to \pi\nu\nu$, Nucl. Phys. B718 (2005) 319–338.
[814] G. Isidori, G. Martinelli, P. Turchetti, Rare kaon decays on the lattice, Phys. Lett. B633 (2006) 75–83.
[815] G. Buchalla, A. J. Buras, $K \to \pi\nu\bar{\nu}$ and high precision determinations of the CKM matrix, Phys. Rev. D54 (1996) 6782–6789.
[816] G. Buchalla, A. J. Buras, M. E. Lautenbacher, Weak decays beyond leading logarithms, Rev. Mod. Phys. 68 (1996) 1125–1144.
[817] G. Buchalla, G. D'Ambrosio, G. Isidori, Extracting short-distance physics from $K_{L,S} \to \pi^0 e^+e^-$ decays, Nucl. Phys. B672 (2003) 387–408.
[818] G. Isidori, C. Smith, R. Unterdorfer, The rare decay $K_L \to \pi^0\mu^+\mu^-$ within the SM, Eur. Phys. J. C36 (2004) 57–66.
[819] G. D'Ambrosio, G. Ecker, G. Isidori, J. Portoles, The decays $K \to \pi l^+l^-$ beyond leading order in the chiral expansion, JHEP 08 (1998) 004.
[820] C. Bruno, J. Prades, Rare Kaon Decays in the $1/N_c$-Expansion, Z. Phys. C57 (1993) 585–594.
[821] S. Friot, D. Greynat, E. De Rafael, Rare kaon decays revisited, Phys. Lett. B595 (2004) 301–308.
[822] F. Mescia, C. Smith, S. Trine, $K_L \to \pi^0 e^+e^-$ and $K_L \to \pi^0\mu^+\mu^-$: A binary star on the stage of flavor physics, JHEP 08 (2006) 088.
[823] M. Gorbahn, U. Haisch, Charm quark contribution to $K_L \to \mu^+\mu^-$ at next-to- next-to-leading order, Phys. Rev. Lett. 97 (2006) 122002.
[824] G. Isidori, R. Unterdorfer, On the short-distance constraints from $K_{L,S} \to \mu^+\mu^-$, JHEP 01 (2004) 009.
[825] J.-M. Gerard, C. Smith, S. Trine, Radiative kaon decays and the penguin contribution to the $\Delta I = 1/2$ rule, Nucl. Phys. B730 (2005) 1–36.
[826] G. Isidori, F. Mescia, P. Paradisi, C. Smith, S. Trine, Exploring the flavour structure of the MSSM with rare K decays, JHEP 08 (2006) 064.
[827] G. Isidori, A. Retico, $B_{s,d} \to \ell^+\ell^-$ and $K_L \to \ell^+\ell^-$ in SUSY models with nonminimal sources of flavor mixing, JHEP 09 (2002) 063.
[828] G. Isidori, P. Paradisi, Higgs-mediated $K \to \pi\nu\bar{\nu}$ in the MSSM at large $\tan(\beta)$, Phys. Rev. D73 (2006) 055017.
[829] E. Nikolidakis, C. Smith, Minimal Flavor Violation, Seesaw, and R-parity, Phys. Rev. D77 (2008) 015021.

[830] C. Bobeth, et al., Upper bounds on rare K and B decays from minimal flavor violation, Nucl. Phys. B726 (2005) 252–274.
[831] U. Haisch, A. Weiler, Determining the Sign of the Z^- Penguin Amplitude, Phys. Rev. D76 (2007) 074027.
[832] Y. Grossman, Y. Nir, $K_L \to \pi^0 \nu\bar{\nu}$ beyond the standard model, Phys. Lett. B398 (1997) 163–168.
[833] Y. Nir, M. P. Worah, Probing the flavor and CP structure of supersymmetric models with $K \to \pi\nu\bar{\nu}$ decays, Phys. Lett. B423 (1998) 319–326.
[834] A. J. Buras, A. Romanino, L. Silvestrini, $K \to \pi\nu\bar{\nu}$: A model independent analysis and supersymmetry, Nucl. Phys. B520 (1998) 3–30.
[835] G. Colangelo, G. Isidori, Supersymmetric contributions to rare kaon decays: Beyond the single mass-insertion approximation, JHEP 09 (1998) 009.
[836] A. J. Buras, P. Gambino, M. Gorbahn, S. Jager, L. Silvestrini, epsilon'/epsilon and Rare K and B Decays in the MSSM, Nucl. Phys. B592 (2001) 55–91.
[837] A. J. Buras, T. Ewerth, S. Jager, J. Rosiek, $K^+ \to \pi^+ \nu\bar{\nu}$ and $K_L \to \pi^0 \nu\bar{\nu}$ decays in the general MSSM, Nucl. Phys. B714 (2005) 103–136.
[838] Y. Grossman, G. Isidori, H. Murayama, Lepton flavor mixing and $K \to \pi\nu\bar{\nu}$ decays, Phys. Lett. B588 (2004) 74–80.
[839] N. G. Deshpande, D. K. Ghosh, X.-G. He, Constraints on new physics from $K \to \pi\nu\bar{\nu}$, Phys. Rev. D70 (2004) 093003.
[840] A. Deandrea, J. Welzel, M. Oertel, $K \to \pi\nu\bar{\nu}$ from standard to new physics, JHEP 10 (2004) 038.
[841] M. Blanke, A. J. Buras, B. Duling, S. Recksiegel, C. Tarantino, FCNC Processes in the Littlest Higgs Model with T-Parity: a 2009 Look. arXiv:0906.5454.
[842] A. J. Buras, M. Spranger, A. Weiler, The Impact of Universal Extra Dimensions on the Unitarity Triangle and Rare K and B Decays, Nucl. Phys. B660 (2003) 225–268.
[843] P. L. Cho, M. Misiak, D. Wyler, $K_L \to \pi\ 0e^+e^-$ and $B \to X_s \ell^+\ell^-$ Decay in the MSSM, Phys. Rev. D54 (1996) 3329–3344.
[844] C. Bobeth, A. J. Buras, F. Kruger, J. Urban, QCD corrections to $\bar{B} \to X_{d,s}\nu\bar{\nu}$, $\bar{B}_{d,s} \to \ell^+\ell^-$, $K \to \pi\nu\bar{\nu}$ and $K_L \to \mu^+\mu^-$ in the MSSM, Nucl. Phys. B630 (2002) 87–131.
[845] A. J. Buras, G. Colangelo, G. Isidori, A. Romanino, L. Silvestrini, Connections between epsilon'/epsilon and rare kaon decays in supersymmetry, Nucl. Phys. B566 (2000) 3–32.
[846] A. V. Artamonov, et al., New measurement of the $K^+ \to \pi^+ \nu\bar{\nu}$ branching ratio, Phys. Rev. Lett. 101 (2008) 191802.
[847] J. Appel, et al., Physics with a High Intensity Proton Source at Fermilab `http://www.fnal.gov/directorate/Longrange/Steering_Public/P5/GoldenBook-2008-02-03.pdf`.
[848] J. K. Ahn, et al., Search for the Decay $K_L^0 \to \pi 0 \nu\bar{\nu}$, Phys. Rev. Lett. 100 (2008) 201802.
[849] S. L. Glashow, J. Iliopoulos, L. Maiani, Weak Interactions with Lepton-Hadron Symmetry, Phys. Rev. D2 (1970) 1285–1292.
[850] G. Burdman, E. Golowich, J. L. Hewett, S. Pakvasa, Rare Charm Decays in the Standard Model and Beyond, Phys. Rev. D66 (2002) 014009.
[851] Q. He, et al., Search for Rare and Forbidden Decays $D^+ \to h^\pm e^\mp e^+$, Phys. Rev. Lett. 95 (2005) 221802.
[852] V. M. Abazov, et al., Measurement of the $t\bar{t}$ production cross section in $p\bar{p}$ collisions at $\sqrt{s} =$ 1.96-TeV using kinematic characteristics of lepton + jets events, Phys. Rev. D76 (2007) 092007.
[853] K. Kodama, et al., Upper limits of charm hadron decays to two muons plus hadrons, Phys. Lett. B345 (1995) 85–92.
[854] J. M. Link, et al., Search for rare and forbidden 3-body di-muon decays of the charmed mesons D^+ and D_s^+, Phys. Lett. B572 (2003) 21–31.
[855] E. M. Aitala, et al., Search for rare and forbidden dilepton decays of the D^+, D_s^+, and D^0 charmed mesons, Phys. Lett. B462 (1999) 401–409.
[856] P. L. Frabetti, et al., Search for rare and forbidden decays of the charmed meson D+, Phys. Lett. B398 (1997) 239–244.
[857] T. E. Coan, et al., First search for the flavor changing neutral current decay $D^0 \to \gamma\gamma$, Phys. Rev. Lett. 90 (2003) 101801.
[858] B. Aubert, et al., Search for flavor-changing neutral current and lepton flavor violating decays of $D^0 \to \ell^+\ell^-$, Phys. Rev. Lett. 93 (2004) 191801.
[859] A. Freyberger, et al., Limits on flavor changing neutral currents in D^0 meson decays, Phys. Rev. Lett. 76 (1996) 3065–3069.

[860] E. M. Aitala, et al., Search for rare and forbidden charm meson decays $D^0 \to V\ell^+\ell^-$ and $hh\ell\ell$, Phys. Rev. Lett. 86 (2001) 3969–3972.
[861] C. Aubin, et al., Charmed meson decay constants in three-flavor lattice QCD, Phys. Rev. Lett. 95 (2005) 122002.
[862] K. M. Ecklund, et al., Measurement of the Absolute Branching Fraction of $D_s^+ \to \tau^+\nu_\tau$ Decay, Phys. Rev. Lett. 100 (2008) 161801.
[863] B. I. Eisenstein, et al., Precision Measurement of $BR(D^+ \to \mu^+\nu)$ and the Pseudoscalar Decay Constant f_{D^+}, Phys. Rev. D78 (2008) 052003.
[864] L. Zhang, Measurements of D and Ds decay constants at CLEO. arXiv:0810.2328.
[865] B. Aubert, et al., Measurement of the pseudoscalar decay constant f_{D_s} using charm-tagged events in e+ e- collisions at $s^{1/2} = 10.58$-GeV, Phys. Rev. Lett. 98 (2007) 141801.
[866] E. Follana, et al., Highly Improved Staggered Quarks on the Lattice, with Applications to Charm Physics, Phys. Rev. D75 (2007) 054502.
[867] B. A. Dobrescu, A. S. Kronfeld, Accumulating evidence for nonstandard leptonic decays of D_s mesons, Phys. Rev. Lett. 100 (2008) 241802.
[868] C. T. H. Davies, et al., Precision charm physics, m_c and α_s from lattice QCD. arXiv:0810.3548.
[869] P. U. E. Onyisi, et al., Improved Measurement of Absolute Branching Fraction of Ds to tau nu, Phys. Rev. D79 (2009) 052002.
[870] S. Faller, R. Fleischer, T. Mannel, Precision Physics with $B_s^0 \to J/\psi\phi$ at the LHC: The Quest for New Physics, Phys. Rev. D79 (2009) 014005.
[871] J. Bijnens, J. M. Gerard, G. Klein, The K(L) - K(S) mass difference, Phys. Lett. B257 (1991) 191–195.
[872] A. J. Buras, D. Guadagnoli, Correlations among new CP violating effects in $\Delta F = 2$ observables, Phys. Rev. D78 (2008) 033005.
[873] T. Inami, C. S. Lim, Effects of Superheavy Quarks and Leptons in Low-Energy Weak Processes K(L) → mu anti-mu, K+ → pi+ Neutrino anti-neutrino and K0 ↔ anti-K0, Prog. Theor. Phys. 65 (1981) 297.
[874] D. J. Antonio, et al., Neutral kaon mixing from 2+1 flavor domain wall QCD, Phys. Rev. Lett. 100 (2008) 032001.
[875] C. Aubin, J. Laiho, R. S. Van de Water, The neutral kaon mixing parameter B_K from unquenched mixed-action lattice QCD. arXiv:0905.3947.
[876] E. Gamiz, et al., Unquenched determination of the kaon parameter B_K from improved staggered fermions, Phys. Rev. D73 (2006) 114502.
[877] S. Aoki, et al., B_K with two flavors of dynamical overlap fermions, Phys. Rev. D77 (2008) 094503.
[878] P. Dimopoulos, et al., K-meson vector and tensor decay constants and BK-parameter from Nf=2 tmQCD, PoS LATTICE2008 (2008) 271.
[879] W. A. Bardeen, A. J. Buras, J. M. Gerard, The B Parameter Beyond the Leading Order of 1/n Expansion, Phys. Lett. B211 (1988) 343.
[880] J. Bijnens, J. Prades, The B(K) parameter in the 1/N(c) expansion, Nucl. Phys. B444 (1995) 523–562.
[881] J. Bijnens, E. Gamiz, J. Prades, The B(K) kaon parameter in the chiral limit, JHEP 03 (2006) 048.
[882] J. Prades, C. A. Dominguez, J. A. Penarrocha, A. Pich, E. de Rafael, The K0 - anti-K0 B factor in the QCD hadronic duality approach, Z. Phys. C51 (1991) 287–296.
[883] S. Aoki, et al., Kaon B parameter from quenched lattice QCD, Phys. Rev. Lett. 80 (1998) 5271–5274.
[884] Y. Aoki, et al., The kaon B-parameter from quenched domain-wall QCD, Phys. Rev. D73 (2006) 094507.
[885] Y. Nakamura, S. Aoki, Y. Taniguchi, T. Yoshie, Precise determination of B_K and right quark masses in quenched domain-wall QCD, Phys. Rev. D78 (2008) 034502.
[886] C. Dawson, progress in kaon phenomenology from lattice QCD, PoS LAT2005 (2006) 007.
[887] V. Lubicz, C. Tarantino, Flavour physics and Lattice QCD: averages of lattice inputs for the Unitarity Triangle Analysis, Nuovo Cim. 123B (2008) 674–688.
[888] L. Lellouch, Kaon physics: a lattice perspective. arXiv:0902.4545.
[889] A. J. Buras, Weak Hamiltonian, CP violation and rare decays. arXiv:hep-ph/9806471.
[890] C. W. Bernard, T. Draper, A. Soni, H. D. Politzer, M. B. Wise, Application of Chiral Perturbation Theory to K → 2 pi Decays, Phys. Rev. D32 (1985) 2343–2347.

[891] J. I. Noaki, et al., Calculation of non-leptonic kaon decay amplitudes from $K \to \pi$ matrix elements in quenched domain-wall QCD, Phys. Rev. D68 (2003) 014501.
[892] T. Blum, et al., Kaon Matrix Elements and CP-violation from Quenched Lattice QCD: (I) the 3-flavor case, Phys. Rev. D68 (2003) 114506.
[893] S. Li, N. H. Christ, Chiral perturbation theory, K to pi pi decays and 2+1 flavor domain wall QCD. arXiv:0812.1368.
[894] L. Giusti, et al., On $K \to \pi\pi$ amplitudes with a light charm quark, Phys. Rev. Lett. 98 (2007) 082003.
[895] K. Hagiwara, et al., Review of particle physics, Phys. Rev. D66 (2002) 010001.
[896] J. R. Batley, et al., A precision measurement of direct CP violation in the decay of neutral kaons into two pions, Phys. Lett. B544 (2002) 97–112.
[897] T. Yamanaka, Review on epsilon'/epsilon. arXiv:0807.1418.
[898] E. T. Worcester, Measurements of Direct CP Violation, CPT Symmetry, and Other Parameters in the Neutral Kaon SystemFERMILAB-THESIS-2007-51.
[899] M. S. Sozzi, On the direct CP violation parameter epsilon prime, Eur. Phys. J. C36 (2004) 37–42.
[900] F. Ambrosino, et al., A direct search for the CP-violating decay $K_S \to 3\pi^0$ with the KLOE detector at DAPHNE, Phys. Lett. B619 (2005) 61–70.
[901] F. Ambrosino, et al., Determination of CP and CPT violation parameters in the neutral kaon system using the Bell-Steinberger relation and data from the KLOE experiment, JHEP 12 (2006) 011.
[902] I. I. Y. Bigi, B. Blok, M. A. Shifman, N. Uraltsev, A. I. Vainshtein, Nonleptonic decays of beauty hadrons: From phenomenology to theory. arXiv:hep-ph/9401298.
[903] M. B. Voloshin, Inclusive weak decay rates of heavy hadrons. arXiv:hep-ph/0004257.
[904] M. Neubert, C. T. Sachrajda, Spectator effects in inclusive decays of beauty hadrons, Nucl. Phys. B483 (1997) 339–370.
[905] J. L. Rosner, Enhancement of the Λ_b decay rate, Phys. Lett. B379 (1996) 267–271.
[906] M. Ciuchini, E. Franco, V. Lubicz, F. Mescia, Next-to-leading order QCD corrections to spectator effects in lifetimes of beauty hadrons, Nucl. Phys. B625 (2002) 211–238.
[907] E. Franco, V. Lubicz, F. Mescia, C. Tarantino, Lifetime ratios of beauty hadrons at the next-to-leading order in QCD, Nucl. Phys. B633 (2002) 212–236.
[908] M. Beneke, G. Buchalla, C. Greub, A. Lenz, U. Nierste, The B+ - B/d0 lifetime difference beyond leading logarithms, Nucl. Phys. B639 (2002) 389–407.
[909] F. Gabbiani, A. I. Onishchenko, A. A. Petrov, Λ_b lifetime puzzle in heavy-quark expansion, Phys. Rev. D68 (2003) 114006.
[910] F. Gabbiani, A. I. Onishchenko, A. A. Petrov, Spectator effects and lifetimes of heavy hadrons, Phys. Rev. D70 (2004) 094031.
[911] A. Badin, F. Gabbiani, A. A. Petrov, Lifetime difference in B_s mixing: Standard model and beyond, Phys. Lett. B653 (2007) 230–240.
[912] M. A. Shifman, M. B. Voloshin, Preasymptotic Effects in Inclusive Weak Decays of Charmed Particles, Sov. J. Nucl. Phys. 41 (1985) 120.
[913] B. Guberina, S. Nussinov, R. D. Peccei, R. Ruckl, D Meson Lifetimes and Decays, Phys. Lett. B89 (1979) 111.
[914] N. Bilic, B. Guberina, J. Trampetic, Pauli Interference Effect in D+ Lifetime, Nucl. Phys. B248 (1984) 261.
[915] B. Guberina, R. Ruckl, J. Trampetic, Charmed Baryon Lifetime Differences, Z. Phys. C33 (1986) 297.
[916] B. Guberina, B. Melic, H. Stefancic, Lifetime-difference pattern of heavy hadrons, Phys. Lett. B484 (2000) 43–50.
[917] M. Di Pierro, C. T. Sachrajda, A lattice study of spectator effects in inclusive decays of B mesons, Nucl. Phys. B534 (1998) 373–391.
[918] M. Di Pierro, C. T. Sachrajda, C. Michael, An exploratory lattice study of spectator effects in inclusive decays of the Λ_b baryon, Phys. Lett. B468 (1999) 143.
[919] M. Di Pierro, C. T. Sachrajda, Spectator effects in inclusive decays of beauty hadrons, Nucl. Phys. Proc. Suppl. 73 (1999) 384–386.
[920] D. Becirevic, Theoretical progress in describing the B meson lifetimes. arXiv:hep-ph/0110124.
[921] A. Ali Khan, et al., Decay constants of B and D mesons from improved relativistic lattice QCD with two flavours of sea quarks, Phys. Rev. D64 (2001) 034505.

[922] A. Ali Khan, et al., B meson decay constant from two-flavor lattice QCD with non-relativistic heavy quarks, Phys. Rev. D64 (2001) 054504.
[923] C. Bernard, et al., Lattice calculation of heavy-light decay constants with two flavors of dynamical quarks, Phys. Rev. D66 (2002) 094501.
[924] S. Aoki, et al., $B^0 - \bar{B}^0$ mixing in unquenched lattice QCD, Phys. Rev. Lett. 91 (2003) 212001.
[925] M. Wingate, C. T. H. Davies, A. Gray, G. P. Lepage, J. Shigemitsu, The B/s and D/s decay constants in 3 flavor lattice QCD, Phys. Rev. Lett. 92 (2004) 162001.
[926] A. Gray, et al., The B Meson Decay Constant from Unquenched Lattice QCD, Phys. Rev. Lett. 95 (2005) 212001.
[927] E. Gamiz, C. T. H. Davies, G. P. Lepage, J. Shigemitsu, M. Wingate, Neutral B Meson Mixing in Unquenched Lattice QCD. arXiv:0902.1815.
[928] C. Bernard, et al., The decay constants f_B and f_{D^+} from three-flavor lattice QCD, PoS LAT2007 (2007) 370.
[929] L. Lellouch, C. J. D. Lin, Standard model matrix elements for neutral B meson mixing and associated decay constants, Phys. Rev. D64 (2001) 094501.
[930] D. Becirevic, V. Gimenez, G. Martinelli, M. Papinutto, J. Reyes, B-parameters of the complete set of matrix elements of $\Delta B = 2$ operators from the lattice, JHEP 04 (2002) 025.
[931] S. Aoki, et al., $B^0 - \bar{B}^0$ mixing in quenched lattice QCD. ((U)) ((W)), Phys. Rev. D67 (2003) 014506.
[932] E. Dalgic, et al., $B_s^0 - \bar{B}_s^0$ mixing parameters from unquenched lattice QCD, Phys. Rev. D76 (2007) 011501.
[933] C. Albertus, et al., B - $\bar{B}$ mixing with domain wall fermions in the static approximation, PoS LAT2007 (2007) 376.
[934] M. Beneke, G. Buchalla, C. Greub, A. Lenz, U. Nierste, Next-to-leading order QCD corrections to the lifetime difference of B_s mesons, Phys. Lett. B459 (1999) 631–640.
[935] M. Beneke, G. Buchalla, A. Lenz, U. Nierste, CP asymmetry in flavour-specific B decays beyond leading logarithms, Phys. Lett. B576 (2003) 173–183.
[936] M. Ciuchini, E. Franco, V. Lubicz, F. Mescia, C. Tarantino, Lifetime differences and CP violation parameters of neutral B mesons at the next-to-leading order in QCD, JHEP 08 (2003) 031.
[937] M. Beneke, G. Buchalla, I. Dunietz, Width Difference in the $B_s - \bar{B}_s$ System, Phys. Rev. D54 (1996) 4419–4431.
[938] A. Lenz, U. Nierste, Theoretical update of $B_s - \bar{B}_s$ mixing, JHEP 06 (2007) 072.
[939] C. Tarantino, B-meson mixing and lifetimes, Nucl. Phys. Proc. Suppl. 156 (2006) 33–37.
[940] V. V. Kiselev, Decays of the B_c meson. arXiv:hep-ph/0308214.
[941] T. C. Collaboration, CDF Note 9458 (2008).
[942] H. Albrecht, et al., Observation of B0 - anti-B0 Mixing, Phys. Lett. B192 (1987) 245.
[943] H. G. Moser, A. Roussarie, Mathematical methods for B0 anti-B0 oscillation analyses, Nucl. Instrum. Meth. A384 (1997) 491–505.
[944] D0 B_s oscillation combination for summer 2007.D0 note 5618 `http://www-d0.fnal.gov/Run2Physics/WWW/results/prelim/B/B54/B54.pdf`.
[945] V. M. Abazov, et al., First direct two-sided bound on the B_s^0 oscillation frequency, Phys. Rev. Lett. 97 (2006) 021802.
[946] I. I. Y. Bigi, A. I. Sanda, Notes on the Observability of CP Violations in B Decays, Nucl. Phys. B193 (1981) 85.
[947] A. B. Carter, A. I. Sanda, CP Violation in B Meson Decays, Phys. Rev. D23 (1981) 1567.
[948] B. Aubert, et al., Update of Time-Dependent CP Asymmetry Measurements in $b \to c\bar{c}s$ Decays. arXiv:0808.1903.
[949] K. F. Chen, et al., Observation of time-dependent CP violation in $B^0 \to \eta' K^0$ decays and improved measurements of CP asymmetries in $B^0 \to \phi K^0, K_S^0 K_S^0 K_S^0$ and $B^0 \to J/\psi K^0$ decays, Phys. Rev. Lett. 98 (2007) 031802.
[950] H. Sahoo, et al., Measurements of time-dependent CP violation in $B^0 \to \psi(2S) K_S$ decays, Phys. Rev. D77 (2008) 091103.
[951] B. Aubert, et al., Ambiguity-free measurement of $\cos(2\beta)$: Time- integrated and time-dependent angular analyses of $B \to J/\psi K\pi$, Phys. Rev. D71 (2005) 032005.
[952] R. Itoh, et al., Studies of CP violation in $B \to J/\psi K^*$ decays, Phys. Rev. Lett. 95 (2005) 091601.
[953] B. Aubert, et al., Evidence for CP violation in $B^0 \to J/\psi \pi^0$ decays, Phys. Rev. Lett. 101 (2008) 021801.

[954] S. E. Lee, et al., Improved measurement of time-dependent CP violation in $B^0 \to J/\psi\pi^0$ decays, Phys. Rev. D77 (2008) 071101.
[955] M. Ciuchini, E. Franco, G. Martinelli, L. Reina, L. Silvestrini, An Upgraded analysis of epsilon-prime epsilon at the next- to-leading order, Z. Phys. C68 (1995) 239–256.
[956] J. Charles, et al., CP violation and the CKM matrix: Assessing the impact of the asymmetric B factories, Eur. Phys. J. C41 (2005) 1–131.
[957] I. Dunietz, R. Fleischer, U. Nierste, In pursuit of new physics with B_s decays, Phys. Rev. D63 (2001) 114015.
[958] T. Aaltonen, et al., First Flavor-Tagged Determination of Bounds on Mixing- Induced CP Violation in $B_s^0 \to J/\psi\phi$ Decays, Phys. Rev. Lett. 100 (2008) 161802.
[959] B. Aubert, et al., Measurement of decay amplitudes of $B \to J/\psi K^*, \psi(2S)K^*$, and $\chi_{c1}K^*$ with an angular analysis, Phys. Rev. D76 (2007) 031102.
[960] T. Aaltonen, et al., Measurement of lifetime and decay-width difference in $B_s^0 \to J/\psi\phi$ decays, Phys. Rev. Lett. 100 (2008) 121803.
[961] K. S. Cranmer, Frequentist hypothesis testing with background uncertainty. arXiv:physics/0310108.
[962] G. Punzi, Ordering algorithms and confidence intervals in the presence of nuisance parameters. arXiv:physics/0511202.
[963] H.-Y. Cheng, CP Violating Effects in Heavy Meson Systems, Phys. Rev. D26 (1982) 143.
[964] A. Datta, D. Kumbhakar, $D^0 - \bar{D}^0$ Mixing: A Possible Test of Physics Beyond the Standard Model, Z. Phys. C27 (1985) 515.
[965] H. Georgi, D - anti-D mixing in heavy quark effective field theory, Phys. Lett. B297 (1992) 353–357.
[966] E. Golowich, A. A. Petrov, Short distance analysis of $D^0 - \bar{D}^0$ mixing, Phys. Lett. B625 (2005) 53–62.
[967] T. Ohl, G. Ricciardi, E. H. Simmons, D - anti-D mixing in heavy quark effective field theory: The Sequel, Nucl. Phys. B403 (1993) 605–632.
[968] I. I. Y. Bigi, N. G. Uraltsev, $D^0 - \bar{D}^0$ oscillations as a probe of quark-hadron duality, Nucl. Phys. B592 (2001) 92–106.
[969] R. Aleksan, A. Le Yaouanc, L. Oliver, O. Pene, J. C. Raynal, Estimation of $\Delta\Gamma$ for the $B_s - \bar{B}_s$ system: Exclusive decays and the parton model, Phys. Lett. B316 (1993) 567–577.
[970] F. Buccella, M. Lusignoli, G. Miele, A. Pugliese, P. Santorelli, Nonleptonic weak decays of charmed mesons, Phys. Rev. D51 (1995) 3478–3486.
[971] J. F. Donoghue, E. Golowich, B. R. Holstein, J. Trampetic, Dispersive Effects in $D^0 - \bar{D}^0$ Mixing, Phys. Rev. D33 (1986) 179.
[972] L. Wolfenstein, $D^0 - \bar{D}^0$ Mixing, Phys. Lett. B164 (1985) 170.
[973] A. F. Falk, Y. Grossman, Z. Ligeti, A. A. Petrov, SU(3) breaking and $D^0 - \bar{D}^0$ mixing, Phys. Rev. D65 (2002) 054034.
[974] A. F. Falk, Y. Grossman, Z. Ligeti, Y. Nir, A. A. Petrov, The $D^0 - \bar{D}^0$ mass difference from a dispersion relation, Phys. Rev. D69 (2004) 114021.
[975] E. Golowich, S. Pakvasa, A. A. Petrov, New physics contributions to the lifetime difference in $D^0 - \bar{D}^0$ mixing, Phys. Rev. Lett. 98 (2007) 181801.
[976] A. A. Petrov, G. K. Yeghiyan, Lifetime difference in D_0 - $\bar{D_0}$ mixing within R- parity-violating SUSY, Phys. Rev. D77 (2008) 034018.
[977] E. Golowich, J. Hewett, S. Pakvasa, A. A. Petrov, Implications of $D^0 - \bar{D}^0$ Mixing for New Physics, Phys. Rev. D76 (2007) 095009.
[978] B. Aubert, et al., Evidence for $D^0 - \bar{D}^0$ Mixing, Phys. Rev. Lett. 98 (2007) 211802.
[979] M. Staric, et al., Evidence for $D^0 - \bar{D}^0$ Mixing, Phys. Rev. Lett. 98 (2007) 211803.
[980] B. Aubert, et al., Measurement of $D^0 - \bar{D}^0$ mixing using the ratio of lifetimes for the decays $D^0 \to K^-\pi^+$, K^-K^+, and $\pi^-\pi^+$, Phys. Rev. D78 (2008) 011105.
[981] B. Aubert, et al., Measurement of $D^0 - \bar{D}^0$ mixing from a time- dependent amplitude analysis of $D^0 \to K^+\pi^-\pi^0$ decays. arXiv:0807.4544.
[982] G. Burdman, I. Shipsey, $D^0 - \bar{D}^0$ mixing and rare charm decays, Ann. Rev. Nucl. Part. Sci. 53 (2003) 431–499.
[983] A. A. Petrov, Charm mixing in the Standard Model and beyond, Int. J. Mod. Phys. A21 (2006) 5686–5693.

[984] G. Blaylock, A. Seiden, Y. Nir, The Role of CP violation in $D^0 - \bar{D}^0$ mixing, Phys. Lett. B355 (1995) 555–560.
[985] Staric, Marko, *CP violation from B factories*, this workshop.
[986] T. Aaltonen, et al., Evidence for $D^0 - \bar{D}^0$ mixing using the CDF II Detector, Phys. Rev. Lett. 100 (2008) 121802.
[987] Donati, Simone, $D^0 - \overline{D}^0$ *mixing and CP violation from Hadron Colliders*, this workshop.
[988] D. M. Asner, et al., Determination of the $D^0 \to K^+\pi^-$ Relative Strong Phase Using Quantum-Correlated Measurements in $e^+e^- \to D^0D^0$ bar at CLEO, Phys. Rev. D78 (2008) 012001.
[989] D. M. Asner, et al., Search for D_0 - $\bar{D}_0$ Mixing in the Dalitz Plot Analysis of $D_0 \to K^0_S\pi^+\pi^-$, Phys. Rev. D72 (2005) 012001.
[990] K. Abe, et al., Measurement of $D^0 - \bar{D}^0$ mixing in $D^0 \to K_s\pi^+\pi^-$ decays, Phys. Rev. Lett. 99 (2007) 131803.
[991] T.-h. T. Liu, The $D^0 - \bar{D}^0$ mixing search: Current status and future prospects. arXiv:hep-ph/9408330.
[992] I. Adachi, et al., Measurement of y_{CP} in D meson decays to CP eigenstates. arXiv:0808.0074.
[993] A. S. Dighe, I. Dunietz, R. Fleischer, Extracting CKM phases and $B_s - \bar{B}_s$ mixing parameters from angular distributions of nonleptonic B decays, Eur. Phys. J. C6 (1999) 647–662.
[994] T. L. Collaboration, The lhcb rich tdr, CERN/LHCC 2000-037.
[995] A. A. Alves, et al., The LHCb Detector at the LHC, JINST 3 (2008) S08005.
[996] P. M. Spradlin, G. Wilkinson, F. Xing, Selection of tagged wrong sign $D^0 \to \pi^-K^+$ candidates for $D^0\bar{D}^0$ mixing measurementsCERN-LHCB-2007-049.
[997] I. I. Y. Bigi, A. I. Sanda, On direct CP violation in $B \to D^0(\bar{D}^0)K\pi's$ versus $\bar{B} \to D^0(\bar{D}^0)\bar{K}\pi's$ decays, Phys. Lett. B211 (1988) 213.
[998] M. Gronau, D. London., How to determine all the angles of the unitarity triangle from $B^0_d \to DK_S$ and $B^0_s \to D^0$, Phys. Lett. B253 (1991) 483–488.
[999] M. Gronau, D. Wyler, On determining a weak phase from CP asymmetries in charged B decays, Phys. Lett. B265 (1991) 172–176.
[1000] D. Atwood, I. Dunietz, A. Soni, Enhanced CP violation with $B \to KD^0(\bar{D}^0)$ modes and extraction of the CKM angle γ, Phys. Rev. Lett. 78 (1997) 3257–3260.
[1001] D. Atwood, I. Dunietz, A. Soni, Improved methods for observing CP violation in $B^\pm \to KD$ and measuring the CKM phase gamma, Phys. Rev. D63 (2001) 036005.
[1002] Y. Grossman, Z. Ligeti, A. Soffer, Measuring γ in $B^\pm \to K^pm(KK^*)(D)$ decays, Phys. Rev. D67 (2003) 071301.
[1003] A. Bondar, proceedings of BINP Special Analysis Meeting on Dalitz Analysis (2002).
[1004] A. Poluektov, et al., Measurement of ϕ_3 with Dalitz plot analysis of $B^\pm \to D^{(*)}K^\pm$ decay, Phys. Rev. D70 (2004) 072003.
[1005] Y. Grossman, A. Soffer, J. Zupan, The effect of D anti-D mixing on the measurement of gamma in $B \to DK$ decays, Phys. Rev. D72 (2005) 031501.
[1006] M. Gronau, Y. Grossman, N. Shuhmaher, A. Soffer, J. Zupan, Using untagged $B^0 \to DK_S$ to determine γ, Phys. Rev. D69 (2004) 113003.
[1007] M. Gronau, Y. Grossman, Z. Surujon, J. Zupan, Enhanced effects on extracting γ from untagged B^0 and B_s decays, Phys. Lett. B649 (2007) 61–66.
[1008] A. Bondar, T. Gershon, On ϕ_3 measurements using $B^- \to D^*K^-$ decays, Phys. Rev. D70 (2004) 091503.
[1009] M. Gronau, Improving bounds on gamma in $B^\pm \to DK^\pm$ and $B^{\pm,0} \to DX^{\pm,0}_s$, Phys. Lett. B557 (2003) 198–206.
[1010] T. Gershon, On the Measurement of the Unitarity Triangle Angle γ from $B^0 \to DK^{*0}$ Decays, Phys. Rev. D79 (2009) 051301.
[1011] B. Aubert, et al., Measurement of CP observables in $B^\pm \to D^0_{CP}K^\pm$ decays, Phys. Rev. D77 (2008) 111102.
[1012] K. Abe, et al., Study of $B^\pm \to D_{CP}K^\pm$ and $D^*_{CP}K^\pm$ decays, Phys. Rev. D73 (2006) 051106.
[1013] K. Gibson, Measurement of CP Observables in $B^- \to D^0K^-$ Decays at CDF. arXiv:0809.4809.
[1014] B. Aubert, et al., Search for $b \to u$ transitions in $B^- \to D^0K^-$ and $B^- \to D^{*0}K^-$, Phys. Rev. D72 (2005) 032004.
[1015] Y. Horii, et al., Study of the Suppressed B meson Decay $B^- \to DK^-$, $D \to K^+\pi^-$, Phys. Rev. D78 (2008) 071901.

[1016] J. L. Rosner, et al., Determination of the Strong Phase in $D^0 \to K^+\pi^-$ Using Quantum-Correlated Measurements, Phys. Rev. Lett. 100 (2008) 221801.
[1017] A. Poluektov, et al., Measurement of ϕ_3 with Dalitz plot analysis of $B^+ \to D^{(*)}K^{(*)+}$ decay, Phys. Rev. D73 (2006) 112009.
[1018] K. Abe, et al., Updated Measurement of phi_3 with a Dalitz Plot Analysis of $B \to D^{(*)}K$ Decay. arXiv:0803.3375.
[1019] V. V. Anisovich, A. V. Sarantsev, K-matrix analysis of the ($IJ^{PC} = 00^{++}$)-wave in the mass region below 1900 MeV, Eur. Phys. J. A16 (2003) 229–258.
[1020] D. Aston, et al., A Study of K- pi+ Scattering in the Reaction K- p → K- pi+ n at 11-GeV/c, Nucl. Phys. B296 (1988) 493.
[1021] I. Dunietz, CP violation with selftagging B(d) modes, Phys. Lett. B270 (1991) 75–80.
[1022] B. Aubert, et al., Search for $b \to u$ transitions in $B^0 \to D^0K^{*0}$ decays. arXiv:0904.2112.
[1023] N. Lowrey, et al., Determination of the $D^0 \to K^-\pi^+\pi^0$ and $D^0 \to K^-\pi^+\pi^+\pi^-$ Coherence Factors and Average Strong-Phase Differences Using Quantum-Correlated Measurements. arXiv:0903.4853.
[1024] B. Aubert, et al., Measurement of the CKM angle gamma in $B^0 \to \bar{D}^0(D^0)K^{*0}$ with a Dalitz analysis of $D^0 \to K_S\pi^+\pi^-$. arXiv:0805.2001.
[1025] B. Aubert, et al., Measurement of time-dependent CP-violating asymmetries and constraints on $\sin(2\beta+\gamma)$ with partial reconstruction of $B \to D^{*\mp}\pi^\pm$ decays, Phys. Rev. D71 (2005) 112003.
[1026] B. Aubert, et al., Measurement of time-dependent CP asymmetries in $B^0 \to D^{(*)}$ +- $\pi^\mp$ and $B^0 \to D^\pm\rho^\mp$ decays, Phys. Rev. D73 (2006) 111101.
[1027] I. Adachi, et al., Measurements of time-dependent CP Asymmetries in $B \to D^{*\mp}\pi^\pm$ decays using a partial reconstruction technique. arXiv:0809.3203.
[1028] F. J. Ronga, et al., Measurements of CP violation in $B^0 \to D^{*-}\pi^+$ and $B^0 \to D^-\pi^+$ decays, Phys. Rev. D73 (2006) 092003.
[1029] R. Aleksan, T. C. Petersen, A. Soffer, Measuring the weak phase gamma in color allowed $B \to DK\pi$ decays, Phys. Rev. D67 (2003) 096002.
[1030] F. Polci, M. H. Schune, A. Stocchi, Feasibility study for a model independent measurement of $2\beta+\gamma$ in B^0 decays using $D^-K^0\pi^+$ final states. arXiv:hep-ph/0605129.
[1031] B. Aubert, et al., Time-dependent Dalitz plot analysis of $B^0 \to D^\mp K^0\pi^\pm$ decays, Phys. Rev. D77 (2008) 071102.
[1032] A. Bondar, A. Poluektov, Feasibility study of model-independent approach to ϕ_3 measurement using Dalitz plot analysis, Eur. Phys. J. C47 (2006) 347–353.
[1033] A. Bondar, A. Poluektov, The use of quantum-correlated D^0 decays for ϕ_3 measurement, Eur. Phys. J. JC55 (2008) 51.
[1034] R. A. Briere, First model-independent determination of the relative strong phase between D^0 and $\bar{D}^0 \to K_S\pi^+\pi^-$ and its impact on the CKM Angle gamma/phi3 measurement. arXiv:0903.1681.
[1035] K. Akiba, et al., Determination of the CKM-angle gamma with tree-level processes at LHCbCERN-LHCB-2008-031.
[1036] D. Atwood, A. Soni, Role of charm factory in extracting CKM-phase information via $B \to DK$, Phys. Rev. D68 (2003) 033003.
[1037] A. J. Buras, L. Silvestrini, Non-leptonic two-body B decays beyond factorization, Nucl. Phys. B569 (2000) 3–52.
[1038] D. Zeppenfeld, SU(3) Relations for B Meson Decays, Zeit. Phys. C8 (1981) 77.
[1039] M. Gronau, O. F. Hernandez, D. London, J. L. Rosner, Decays of B mesons to two light pseudoscalars, Phys. Rev. D50 (1994) 4529–4543.
[1040] M. Beneke, M. Neubert, QCD factorization for $B \to PP$ and $B \to PV$ decays, Nucl. Phys. B675 (2003) 333–415.
[1041] E. Baracchini, G. Isidori, Electromagnetic corrections to non-leptonic two-body B and D decays, Phys. Lett. B633 (2006) 309–313.
[1042] M. Beneke, S. Jager, Spectator scattering at NLO in non-leptonic B decays: Tree amplitudes, Nucl. Phys. B751 (2006) 160–185.
[1043] N. Kivel, Radiative corrections to hard spectator scattering in $B \to \pi\pi$ decays, JHEP 05 (2007) 019.
[1044] V. Pilipp, Hard spectator interactions in $B \to \pi\pi$ at order α_s^2, Nucl. Phys. B794 (2008) 154–188.
[1045] G. Bell, NNLO Vertex Corrections in charmless hadronic B decays: Imaginary part, Nucl. Phys. B795 (2008) 1–26.

[1046] G. Bell, NNLO vertex corrections in charmless hadronic B decays: Real part. arXiv:0902.1915.
[1047] T. Becher, R. J. Hill, Loop corrections to heavy-to-light form factors and evanescent operators in SCET, JHEP 10 (2004) 055.
[1048] M. Beneke, D. Yang, Heavy-to-light B meson form factors at large recoil energy: Spectator scattering corrections, Nucl. Phys. B736 (2006) 34–81.
[1049] G. G. Kirilin, Loop corrections to the form factors in $B \to \pi\ell\nu$ decay. arXiv:hep-ph/0508235.
[1050] M. Beneke, S. Jager, Spectator scattering at NLO in non-leptonic B decays: Leading penguin amplitudes, Nucl. Phys. B768 (2007) 51–84.
[1051] S. J. Lee, M. Neubert, Model-independent properties of the B-meson distribution amplitude, Phys. Rev. D72 (2005) 094028.
[1052] H. Kawamura, K. Tanaka, Operator product expansion for B-meson distribution amplitude and dimension-5 HQET operators, Phys. Lett. B673 (2009) 201–207.
[1053] P. Ball, E. Kou, $B \to \gamma e\nu$ transitions from QCD sum rules on the light-cone, JHEP 04 (2003) 029.
[1054] V. M. Braun, D. Y. Ivanov, G. P. Korchemsky, The B-Meson Distribution Amplitude in QCD, Phys. Rev. D69 (2004) 034014.
[1055] A. Jain, I. Z. Rothstein, I. W. Stewart, Penguin Loops for Nonleptonic B-Decays in the Standard Model: Is there a Penguin Puzzle?. arXiv:0706.3399.
[1056] H.-n. Li, S. Mishima, A. I. Sanda, Resolution to the $B \to \pi K$ puzzle, Phys. Rev. D72 (2005) 114005.
[1057] H.-n. Li, S. Mishima, Resolution of the $B \to \pi\pi,\ \pi K$ puzzles. arXiv:0901.1272.
[1058] M. Beneke, Hadronic B decays, ECONF C0610161 (2006) 030.
[1059] A. Khodjamirian, T. Mannel, M. Melcher, B. Melic, Annihilation effects in $B \to \pi\pi$ from QCD light-cone sum rules, Phys. Rev. D72 (2005) 094012.
[1060] M. Beneke, G. Buchalla, M. Neubert, C. T. Sachrajda, Comment on '$B \to M_1 M_2$: Factorization, charming penguins, strong phases, and polarization', Phys. Rev. D72 (2005) 098501.
[1061] C. W. Bauer, D. Pirjol, I. Z. Rothstein, I. W. Stewart, On differences between SCET and QCDF for $B \to \pi\pi$ decays, Phys. Rev. D72 (2005) 098502.
[1062] M. Beneke, G. Buchalla, M. Neubert, C. T. Sachrajda, Penguins with Charm and Quark-Hadron Duality. arXiv:0902.4446.
[1063] M. Beneke, Corrections to $\sin(2\beta)$ from CP asymmetries in $B^0 \to (\pi^0, \rho^0, \eta, \eta', \omega, \phi)K_S$ decays, Phys. Lett. B620 (2005) 143–150.
[1064] H.-Y. Cheng, C.-K. Chua, A. Soni, Effects of Final-state Interactions on Mixing-induced CP Violation in Penguin-dominated B Decays, Phys. Rev. D72 (2005) 014006.
[1065] W. Wang, Y.-M. Wang, D.-S. Yang, C.-D. Lu, Charmless Two-body $B(B_s) \to VP$ decays In Soft-Collinear-Effective-Theory, Phys. Rev. D78 (2008) 034011.
[1066] H.-n. Li, S. Mishima, Penguin-dominated $B \to PV$ decays in NLO perturbative QCD, Phys. Rev. D74 (2006) 094020.
[1067] M. Beneke, J. Rohrer, D. Yang, Branching fractions, polarisation and asymmetries of $B \to VV$ decays, Nucl. Phys. B774 (2007) 64–101.
[1068] M. Beneke, M. Gronau, J. Rohrer, M. Spranger, A precise determination of α using $B^0 \to \rho^+\rho^-$ and $B^+ \to K^{*0}\rho^+$, Phys. Lett. B638 (2006) 68–73.
[1069] B. Aubert, et al., Search for the radiative leptonic decay $B^+ \to \gamma\ell^+\nu_l$. arXiv:0704.1478.
[1070] Y. Grossman, M. P. Worah, CP asymmetries in B decays with new physics in decay amplitudes, Phys. Lett. B395 (1997) 241–249.
[1071] D. London, A. Soni, Measuring the CP angle beta in hadronic $b \to s$ penguin decays, Phys. Lett. B407 (1997) 61–65.
[1072] G. Buchalla, G. Hiller, Y. Nir, G. Raz, The pattern of CP asymmetries in $b \to s$ transitions, JHEP 09 (2005) 074.
[1073] H.-Y. Cheng, C.-K. Chua, A. Soni, CP-violating asymmetries in B^0 decays to $K^+K^-K^0_{(S,L)}$ and $K^0_S K^0_S K^0_{(S,L)}$, Phys. Rev. D72 (2005) 094003.
[1074] T. E. Browder, T. Gershon, D. Pirjol, A. Soni, J. Zupan, New Physics at a Super Flavor Factory. arXiv:0802.3201.
[1075] L. Silvestrini, Searching for new physics in $b \to s$ hadronic penguin decays, Ann. Rev. Nucl. Part. Sci. 57 (2007) 405–440.

[1076] E. Lunghi, A. Soni, Possible Indications of New Physics in B_d -mixing and in $\sin(2\beta)$ Determinations, Phys. Lett. B666 (2008) 162–165.
[1077] M. Ciuchini, E. Franco, G. Martinelli, M. Pierini, L. Silvestrini, Searching For New Physics With B to K pi Decays, Phys. Lett. B674 (2009) 197–203.
[1078] R. Fleischer, S. Jager, D. Pirjol, J. Zupan, Benchmarks for the New-Physics Search through CP Violation in $B^0 \to \pi^0 K_S$, Phys. Rev. D78 (2008) 111501.
[1079] M. Gronau, J. L. Rosner, Implications for CP asymmetries of improved data on $B \to K^0\pi^0$, Phys. Lett. B666 (2008) 467–471.
[1080] e. . Hashimoto, S., et al., Letter of intent for KEK Super B FactoryKEK-REPORT-2004-4.
[1081] M. Bona, et al., Superb: A high-luminosity heavy flavour factory. conceptual design reportPisa, Italy: INFN (2007) 453 p. www.pi.infn.it/SuperB/?q=CDR.
[1082] T. Browder, et al., On the Physics Case of a Super Flavour Factory, JHEP 02 (2008) 110.
[1083] M. Raidal, CP asymmetry in B –¿ Phi K(S) decays in left-right models and its implications on B/s decays, Phys. Rev. Lett. 89 (2002) 231803.
[1084] K. Abe, et al., Measurements of time-dependent CP violation in $B^0 \to \omega K^0_S, f_0(980)K^0_S, K^0_S\pi^0$ and $K^+K^-K^0_S$ decays, Phys. Rev. D76 (2007) 091103.
[1085] I. Adachi, et al., Measurement of CP asymmetries in $B^0 \to K^0\pi^0$ decays. arXiv:0809.4366.
[1086] T. Gershon, M. Hazumi, Time-dependent CP violation in $B^0 \to P^0P^0X^0$ decays, Phys. Lett. B596 (2004) 163–172.
[1087] B. Aubert, et al., cKM Preliminary (2008).
[1088] B. Aubert, et al., Measurement of CP Asymmetry in $B^0 \to K_s\pi^0\pi^0$ Decays, Phys. Rev. D76 (2007) 071101.
[1089] K. Abe, et al., Measurements of CP Violation Parameters in $B^0 \to K_S\pi^0\pi^0$ and $B^0 \to K_SK_S$ Decays. arXiv:0708.1845.
[1090] B. Aubert, et al., Time-dependent Dalitz Plot Analysis of $B^0 \to K^0_s\pi^+\pi^-$. arXiv:0708.2097.
[1091] J. Dalseno, et al., Time-dependent Dalitz Plot Measurement of CP Parameters in $B^0 \to K_s\pi^+\pi^-$ Decays. arXiv:0811.3665.
[1092] V. Chernyak, Estimates of flavoured scalar production in B decays, Phys. Lett. B509 (2001) 273–276.
[1093] B. Aubert, et al., Measurement of CP-Violating Asymmetries in the $B^0 \to K^+K^-K^0_s$ Dalitz Plot. arXiv:0808.0700.
[1094] J. Dalseno, Measurements of CKM angle phi1 with charmless penguins at Belle. arXiv:0810.2628.
[1095] A. F. Falk, Z. Ligeti, Y. Nir, H. Quinn, Comment on extracting alpha from $B \to \rho\rho$, Phys. Rev. D69 (2004) 011502.
[1096] A. E. Snyder, H. R. Quinn, Measuring CP asymmetry in $B \to \rho\pi$ decays without ambiguities, Phys. Rev. D48 (1993) 2139–2144.
[1097] H. J. Lipkin, Y. Nir, H. R. Quinn, A. Snyder, Penguin trapping with isospin analysis and CP asymmetries in B decays, Phys. Rev. D44 (1991) 1454–1460.
[1098] M. Gronau, Elimination of penguin contributions to CP asymmetries in B decays through isospin analysis, Phys. Lett. B265 (1991) 389–394.
[1099] M. Gronau, J. Zupan, On measuring alpha in $B(t) \to \rho^\pm\pi^\mp$, Phys. Rev. D70 (2004) 074031.
[1100] S. Gardner, How isospin violation mocks *new* physics: $\pi^0 - \eta, \eta'$ mixing in $B \to \pi\pi$ decays, Phys. Rev. D59 (1999) 077502.
[1101] M. Gronau, J. Zupan, Isospin-breaking effects on alpha extracted in $B \to \pi\pi, \rho\rho, \rho\pi$, Phys. Rev. D71 (2005) 074017.
[1102] J. Zupan, Penguin pollution estimates relevant for ϕ_2/α extraction, Nucl. Phys. Proc. Suppl. 170 (2007) 33–38.
[1103] M. Morello, Branching fractions and direct CP asymmetries of charmless decay modes at the Tevatron, Nucl. Phys. Proc. Suppl. 170 (2007) 39–45.
[1104] B. Aubert, et al., Measurement of CP Asymmetries and Branching Fractions in $B^0 \to\to \pi^+\pi^-$, $B^0 \to K^+\pi^-$, $B^0 \to \pi^0\pi^0$, $B^0 \to K^0\pi^0$ and Isospin Analysis of $B \to \pi\pi$ Decays. arXiv:0807.4226.
[1105] H. Ishino, et al., Observation of Direct CP-Violation in $B^0 \to \pi^+\pi^-$ Decays and Model-Independent Constraints on ϕ_2, Phys. Rev. Lett. 98 (2007) 211801.
[1106] B. Aubert, et al., Improved Measurements of the Branching Fractions for $B^0 \to \pi^+\pi^-$ and $B^0 \to K^+\pi^-$, and a Search for $B^0 \to K^+K^-$, Phys. Rev. D75 (2007) 012008.
[1107] K. Abe, et al., Measurements of branching fractions for $B \to K\pi$ and $B \to \pi\pi$ decays with 449 million B anti-B pairs, Phys. Rev. Lett. 99 (2007) 121601.

[1108] B. Aubert, et al., Study of $B^0 \to \pi^0\pi^0$, $B^\pm \to \pi^\pm\pi^0$, and $B^\pm \to K^\pm\pi^0$ Decays, and Isospin Analysis of $B \to \pi\pi$ Decays, Phys. Rev. D76 (2007) 091102.
[1109] Difference in direct charge-parity violation between charged and neutral B meson decays, Nature 452 (2008) 332–335.
[1110] K. Abe, et al., Improved measurement of $B^0 \to \pi^0\pi^0$. arXiv:hep-ex/0610065.
[1111] M. Bona, et al., Improved determination of the CKM angle α from $B \to \pi\pi$ decays, Phys. Rev. D76 (2007) 014015.
[1112] A. Somov, et al., Improved measurement of CP-violating parameters in $\rho^+\rho^-$ decays, Phys. Rev. D76 (2007) 011104.
[1113] B. Aubert, et al., A Study of $B^0 \to \rho^+\rho^-$ Decays and Constraints on the CKM Angle alpha, Phys. Rev. D76 (2007) 052007.
[1114] A. Somov, et al., Measurement of the branching fraction, polarization, and CP asymmetry for $B^0 \to \rho^+\rho^-$ decays, and determination of the CKM phase phi(2), Phys. Rev. Lett. 96 (2006) 171801.
[1115] J. Zhang, et al., Observation of $B^+ \to \rho^+\rho^0$, Phys. Rev. Lett. 91 (2003) 221801.
[1116] B. Aubert, et al., Measurements of branching fraction, polarization, and charge asymmetry of $B^\pm \to \rho^\pm\rho 0$ and a search for $B^\pm \to \rho^\pm$ f0(980), Phys. Rev. Lett. 97 (2006) 261801.
[1117] B. Aubert, et al., Measurement of the Branching Fraction, Polarization, and CP Asymmetries in $B^0 \to \rho^0\rho^0$ Decay, and Implications for the CKM Angle alpha, Phys. Rev. D78 (2008) 071104.
[1118] C. C. Chiang, et al., Measurement of $B^0 \to \pi^+\pi^-\pi^+\pi^-$ Decays and Search for $B^0 \to \rho^0\rho^0$, Phys. Rev. D78 (2008) 111102.
[1119] B. Aubert, et al., Measurement of CP-violating asymmetries in $B^0 \to \rho\pi^0$ using a time-dependent Dalitz plot analysis, Phys. Rev. D76 (2007) 012004.
[1120] A. Kusaka, et al., Measurement of CP Asymmetries and Branching Fractions in a Time-Dependent Dalitz Analysis of $B^0 \to (\rho\pi)^0$ and a Constraint on the Quark Mixing Angle ϕ_2, Phys. Rev. D77 (2008) 072001.
[1121] H. R. Quinn, J. P. Silva, The Use of early data on $B \to \rho\pi$ decays, Phys. Rev. D62 (2000) 054002.
[1122] M. Gronau, J. Zupan, Weak phase α from $B^0 \to a_1(1260)^\pm\pi^\mp$, Phys. Rev. D73 (2006) 057502.
[1123] B. Aubert, et al., Observation of B^+ Meson Decays to $a_1(1260)^+K0$ and B^0 to $a_1(1260) - K^+$, Phys. Rev. Lett. 100 (2008) 051803.
[1124] B. Aubert, et al., Measurement of branching fractions of B^0 decays to $K_1(1270)^+\pi^-$ and $K_1(1400)^+\pi^-$. arXiv:0807.4760.
[1125] B. Aubert, et al., Measurements of CP-Violating Asymmetries in $B^0 \to a_1 \pm (1260)\pi^\mp$ decays, Phys. Rev. Lett. 98 (2007) 181803.
[1126] R. Fleischer, T. Mannel, Constraining the CKM angle gamma and penguin contributions through combined $B \to \pi K$ branching ratios, Phys. Rev. D57 (1998) 2752–2759.
[1127] M. Neubert, J. L. Rosner, New bound on gamma from $B^\pm \to \pi K$ decays, Phys. Lett. B441 (1998) 403–409.
[1128] M. Neubert, J. L. Rosner, Determination of the weak phase gamma from rate measurements in $B^\pm \to \pi K$, $\pi\pi$ decays, Phys. Rev. Lett. 81 (1998) 5076–5079.
[1129] A. J. Buras, R. Fleischer, A general analysis of gamma determinations from $B \to \pi K$ decays, Eur. Phys. J. C11 (1999) 93–109.
[1130] A. J. Buras, R. Fleischer, Constraints on the CKM Angle γ and Strong Phases from $B \to \pi K$ Decays, Eur. Phys. J. C16 (2000) 97–104.
[1131] A. J. Buras, R. Fleischer, S. Recksiegel, F. Schwab, Anatomy of prominent B and K decays and signatures of CP- violating new physics in the electroweak penguin sector, Nucl. Phys. B697 (2004) 133–206.
[1132] M. Gronau, J. L. Rosner, Systematic Error on Weak Phase γ from $B \to \pi^+\pi^-$ and $B \to K\pi$, Phys. Lett. B651 (2007) 166–170.
[1133] M. Gronau, J. L. Rosner, The Role of $B_s \to K\pi$ in determining the weak phase γ, Phys. Lett. B482 (2000) 71–76.
[1134] C.-W. Chiang, M. Gronau, J. L. Rosner, D. A. Suprun, Charmless $B \to PP$ decays using flavor SU(3) symmetry, Phys. Rev. D70 (2004) 034020.
[1135] C.-W. Chiang, M. Gronau, Z. Luo, J. L. Rosner, D. A. Suprun, Charmless $B \to VP$ decays using flavor SU(3) symmetry, Phys. Rev. D69 (2004) 034001.
[1136] R. Fleischer, $B_{s,d} \to \pi\pi, \pi K, KK$: Status and Prospects, Eur. Phys. J. C52 (2007) 267–281.

[1137] R. Fleischer, New strategies to extract beta and gamma from $B_d \to \pi^+\pi^-$ and $B_s \to K^+K^-$, Phys. Lett. B459 (1999) 306–320.
[1138] C. W. Bauer, I. Z. Rothstein, I. W. Stewart, A new method for determining gamma from $B \to \pi\pi$ decays, Phys. Rev. Lett. 94 (2005) 231802.
[1139] I. Dunietz, Extracting CKM parameters from B decaysPresented at Summer Workshop on B Physics at Hadron Accelerators, Snowmass, CO, 21 Jun - 2 Jul 1993.
[1140] A. J. Buras, R. Fleischer, S. Recksiegel, F. Schwab, The $B \to \pi\pi$, πK puzzles in the light of new data: Implications for the standard model, new physics and rare decays, Acta Phys. Polon. B36 (2005) 2015–2050.
[1141] B. Aubert, et al., Observation of $B^+ \to \bar{K}^0 K^+$ and $B^0 \to K^0\bar{K}^0$, Phys. Rev. Lett. 97 (2006) 171805.
[1142] K. Abe, et al., Observation of B decays to two kaons, Phys. Rev. Lett. 98 (2007) 181804.
[1143] A. Abulencia, et al., Observation of B^0 $(s) \to K^+K^-$ and Measurements of Branching Fractions of Charmless Two-body Decays of B^0 and B_s^0 Mesons in $\bar{p}p$ Collisions at $\sqrt{s} = 1.96$-TeV, Phys. Rev. Lett. 97 (2006) 211802.
[1144] T. Aaltonen, et al., Observation of New Charmless Decays of Bottom Hadrons. arXiv:0812.4271.
[1145] M. J. Morello, Charmless $b-$hadrons decays at CDF. arXiv:0810.3258.
[1146] C.-W. Chiang, M. Gronau, J. L. Rosner, Examination of Flavor SU(3) in B, $B_s \to K\pi$ Decays, Phys. Lett. B664 (2008) 169–173.
[1147] M. Ciuchini, M. Pierini, L. Silvestrini, New bounds on the CKM matrix from $B \to K\pi\pi$ Dalitz plot analyses, Phys. Rev. D74 (2006) 051301.
[1148] M. Gronau, D. Pirjol, A. Soni, J. Zupan, Improved method for CKM constraints in charmless three- body B and B_s decays, Phys. Rev. D75 (2007) 014002.
[1149] M. Gronau, D. Pirjol, A. Soni, J. Zupan, Constraint on rho-bar, eta-bar from B to K*pi, Phys. Rev. D77 (2008) 057504.
[1150] I. Bediaga, G. Guerrer, J. M. de Miranda, Extracting the quark mixing phase gamma from $B^\pm \to K^\pm\pi^+\pi^-$, $B^0 \to K_S\pi^+\pi^-$, and $\bar{B}^0 \to K_S\pi^+\pi^-$, Phys. Rev. D76 (2007) 073011.
[1151] M. Ciuchini, M. Pierini, L. Silvestrini, Hunting the CKM weak phase with time-integrated Dalitz analyses of $B_s \to KK\pi$ and $B_s \to K\pi\pi$ decays, Phys. Lett. B645 (2007) 201–203.
[1152] B. Aubert, et al., Evidence for Direct CP Violation from Dalitz-plot analysis of $B^\pm \to K^\pm\pi^\mp\pi^\pm$, Phys. Rev. D78 (2008) 012004.
[1153] A. Garmash, et al., bELLE-CONF-0827.
[1154] B. Aubert, et al., Dalitz Plot Analysis of the Decay $B^0(\bar{B}^0) \to K^\pm\pi^\mp\pi^0$, Phys. Rev. D78 (2008) 052005.
[1155] M. Ciuchini, et al., 2000 CKM triangle analysis: A Critical review with updated experimental inputs and theoretical parameters, JHEP 07 (2001) 013.
[1156] M. Bona, et al., The 2004 UTfit Collaboration report on the status of the unitarity triangle in the standard model, JHEP 07 (2005) 028.
[1157] F. Parodi, P. Roudeau, A. Stocchi, Constraints on the parameters of the V(CKM) matrix by end 1998, Nuovo Cim. A112 (1999) 833–854.
[1158] B. Aubert, et al., A Search for $B^+ \to \ell^+\nu_\ell$ Recoiling Against $B^- \to D^0\ell^-\bar{\nu}$. arXiv:0809.4027.
[1159] M. Bona, et al., www.utfit.org web site.
[1160] M. Bona, et al., The UTfit collaboration report on the status of the unitarity triangle beyond the standard model. I: Model- independent analysis and minimal flavour violation, JHEP 03 (2006) 080.
[1161] M. Bona, et al., Constraints on new physics from the quark mixing unitarity triangle, Phys. Rev. Lett. 97 (2006) 151803.
[1162] M. Bona, et al., First Evidence of New Physics in $b \to s$ Transitions. arXiv:0803.0659.
[1163] H. P. Nilles, Supersymmetry, Supergravity and Particle Physics, Phys. Rept. 110 (1984) 1–162.
[1164] D. J. H. Chung, et al., The soft supersymmetry-breaking Lagrangian: Theory and applications, Phys. Rept. 407 (2005) 1–203.
[1165] J. F. Donoghue, H. P. Nilles, D. Wyler, Flavor Changes in Locally Supersymmetric Theories, Phys. Lett. B128 (1983) 55.
[1166] A. Bouquet, J. Kaplan, C. A. Savoy, On Flavor Mixing in Broken Supergravity, Phys. Lett. B148 (1984) 69.
[1167] A. Bouquet, J. Kaplan, C. A. Savoy, Low-Energy Constraints on Supergravity Parameters, Nucl. Phys. B262 (1985) 299.

[1168] F. Gabbiani, A. Masiero, FCNC in Generalized Supersymmetric Theories, Nucl. Phys. B322 (1989) 235.
[1169] I. I. Y. Bigi, F. Gabbiani, Impact of different classes of supersymmetric models on rare B decays, $B^0 - \bar{B}^0$ mixing and CP violation, Nucl. Phys. B352 (1991) 309–341.
[1170] S. Bertolini, F. Borzumati, A. Masiero, G. Ridolfi, Effects of supergravity induced electroweak breaking on rare B decays and mixings, Nucl. Phys. B353 (1991) 591–649.
[1171] N. Oshimo, Radiative B meson decay in supersymmetric models, Nucl. Phys. B404 (1993) 20–41.
[1172] J. L. Hewett, Can $b \to s\gamma$ close the supersymmetric Higgs production window?, Phys. Rev. Lett. 70 (1993) 1045–1048.
[1173] V. D. Barger, M. S. Berger, R. J. N. Phillips, Implications of b $\to$ s gamma decay measurements in testing the MSSM Higgs sector, Phys. Rev. Lett. 70 (1993) 1368–1371.
[1174] R. Barbieri, G. F. Giudice, b $\to$ s gamma decay and supersymmetry, Phys. Lett. B309 (1993) 86–90.
[1175] P. Minkowski, $\mu \to e\gamma$ at a Rate of One Out of 1-Billion Muon Decays?, Phys. Lett. B67 (1977) 421.
[1176] T. Yanagida, Horizontal gauge symmetry and masses of neutrinosIn Proceedings of the Workshop on the Baryon Number of the Universe and Unified Theories, Tsukuba, Japan, 13-14 Feb 1979.
[1177] M. Gell-Mann, P. Ramond, R. Slansky, Complex spinors and unified theoriesPrint-80-0576 (CERN).
[1178] J. Hisano, D. Nomura, T. Yanagida, Atmospheric neutrino oscillation and large lepton flavour violation in the SUSY SU(5) GUT, Phys. Lett. B437 (1998) 351–358.
[1179] J. Hisano, D. Nomura, Solar and atmospheric neutrino oscillations and lepton flavor violation in supersymmetric models with the right- handed neutrinos, Phys. Rev. D59 (1999) 116005.
[1180] R. Barbieri, L. J. Hall, Signals for supersymmetric unification, Phys. Lett. B338 (1994) 212–218.
[1181] R. Barbieri, L. J. Hall, A. Strumia, Violations of lepton flavor and CP in supersymmetric unified theories, Nucl. Phys. B445 (1995) 219–251.
[1182] Z. Maki, M. Nakagawa, S. Sakata, Remarks on the unified model of elementary particles, Prog. Theor. Phys. 28 (1962) 870.
[1183] S. Baek, T. Goto, Y. Okada, K.-i. Okumura, Neutrino oscillation, SUSY GUT and B decay, Phys. Rev. D63 (2001) 051701.
[1184] T. Moroi, Effects of the right-handed neutrinos on $\Delta S = 2$ and $\Delta B = 2$ processes in supersymmetric SU(5) model, JHEP 03 (2000) 019.
[1185] T. Moroi, CP violation in $B_d \to \phi K_S$ in SUSY GUT with right- handed neutrinos, Phys. Lett. B493 (2000) 366–374.
[1186] T. Goto, Y. Okada, T. Shindou, M. Tanaka, Patterns of flavor signals in supersymmetric models, Phys. Rev. D77 (2008) 095010.
[1187] N. Arkani-Hamed, S. Dimopoulos, G. R. Dvali, The hierarchy problem and new dimensions at a millimeter, Phys. Lett. B429 (1998) 263–272.
[1188] N. Arkani-Hamed, S. Dimopoulos, G. R. Dvali, Phenomenology, astrophysics and cosmology of theories with sub-millimeter dimensions and TeV scale quantum gravity, Phys. Rev. D59 (1999) 086004.
[1189] T. Appelquist, H.-C. Cheng, B. A. Dobrescu, Bounds on universal extra dimensions, Phys. Rev. D64 (2001) 035002.
[1190] L. Randall, R. Sundrum, A large mass hierarchy from a small extra dimension, Phys. Rev. Lett. 83 (1999) 3370–3373.
[1191] L. Randall, R. Sundrum, An alternative to compactification, Phys. Rev. Lett. 83 (1999) 4690–4693.
[1192] S. Chang, J. Hisano, H. Nakano, N. Okada, M. Yamaguchi, Bulk standard model in the Randall-Sundrum background, Phys. Rev. D62 (2000) 084025.
[1193] Y. Grossman, M. Neubert, Neutrino masses and mixings in non-factorizable geometry, Phys. Lett. B474 (2000) 361–371.
[1194] B. A. Dobrescu, E. Ponton, Chiral compactification on a square, JHEP 03 (2004) 071.
[1195] M. Hashimoto, D. K. Hong, Topcolor breaking through boundary conditions, Phys. Rev. D71 (2005) 056004.
[1196] B. A. Dobrescu, D. Hooper, K. Kong, R. Mahbubani, Spinless photon dark matter from two universal extra dimensions, JCAP 0710 (2007) 012.

[1197] D. Chakraverty, K. Huitu, A. Kundu, Effects of Universal Extra Dimensions on $B^0 - \bar{B}^0$ Mixing, Phys. Lett. B558 (2003) 173–181.
[1198] G. Devidze, A. Liparteliani, U.-G. Meissner, $B_{s,d} \to \gamma\gamma$ decay in the model with one universal extra dimension, Phys. Lett. B634 (2006) 59–62.
[1199] P. Colangelo, F. De Fazio, R. Ferrandes, T. N. Pham, Exclusive $B \to K^{(*)} l^+ l^-$, $B \to K^{(*)} \nu\bar{\nu}$ and $B \to K^* \gamma$ transitions in a scenario with a single universal extra dimension, Phys. Rev. D73 (2006) 115006.
[1200] P. Colangelo, F. De Fazio, R. Ferrandes, T. N. Pham, Spin effects in rare $B \to X_s \tau^+ \tau^-$ and $B \to K^* \tau^+ \tau^-$ decays in a single universal extra dimension scenario, Phys. Rev. D74 (2006) 115006.
[1201] R. Mohanta, A. K. Giri, Study of FCNC mediated rare B_s decays in a single universal extra dimension scenario, Phys. Rev. D75 (2007) 035008.
[1202] P. Colangelo, F. De Fazio, R. Ferrandes, T. N. Pham, FCNC B_s and Λ_b transitions: Standard model versus a single universal extra dimension scenario, Phys. Rev. D77 (2008) 055019.
[1203] R. Ferrandes, $B \to K^* \ell^+ \ell^-$ as a probe of Universal Extra Dimensions. arXiv:0710.2040.
[1204] I. Ahmed, M. A. Paracha, M. J. Aslam, Exclusive $B \to K_1 l^+ l^-$ decay in model with single universal extra dimension, Eur. Phys. J. C54 (2008) 591–599.
[1205] V. Bashiry, K. Zeynali, Exclusive $B \to \pi \ell^+ \ell^-$ and $B \to \rho \ell^+ \ell^-$ Decays in the Universal Extra Dimension, Phys. Rev. D79 (2009) 033006.
[1206] I. I. Bigi, G. G. Devidze, A. G. Liparteliani, U. G. Meissner, $B \to \gamma\gamma$ in an ACD model, Phys. Rev. D78 (2008) 097501.
[1207] D. Hooper, S. Profumo, Dark matter and collider phenomenology of universal extra dimensions, Phys. Rept. 453 (2007) 29–115.
[1208] S. J. Huber, Flavor violation and warped geometry, Nucl. Phys. B666 (2003) 269–288.
[1209] K. Agashe, A. Delgado, M. J. May, R. Sundrum, RS1, custodial isospin and precision tests, JHEP 08 (2003) 050.
[1210] C. Csaki, C. Grojean, L. Pilo, J. Terning, Towards a realistic model of Higgsless electroweak symmetry breaking, Phys. Rev. Lett. 92 (2004) 101802.
[1211] K. Agashe, R. Contino, L. Da Rold, A. Pomarol, A custodial symmetry for Z b anti-b, Phys. Lett. B641 (2006) 62–66.
[1212] R. Contino, L. Da Rold, A. Pomarol, Light custodians in natural composite Higgs models, Phys. Rev. D75 (2007) 055014.
[1213] G. Cacciapaglia, C. Csaki, G. Marandella, J. Terning, A New Custodian for a Realistic Higgsless Model, Phys. Rev. D75 (2007) 015003.
[1214] M. S. Carena, E. Ponton, J. Santiago, C. E. M. Wagner, Electroweak constraints on warped models with custodial symmetry, Phys. Rev. D76 (2007) 035006.
[1215] A. J. Buras, B. Duling, S. Gori, The Impact of Kaluza-Klein Fermions on Standard Model Fermion Couplings in a RS Model with Custodial Protection. arXiv:0905.2318.
[1216] G. Burdman, Constraints on the bulk standard model in the Randall- Sundrum scenario, Phys. Rev. D66 (2002) 076003.
[1217] G. Burdman, Flavor violation in warped extra dimensions and CP asymmetries in B decays, Phys. Lett. B590 (2004) 86–94.
[1218] K. Agashe, G. Perez, A. Soni, B-factory signals for a warped extra dimension, Phys. Rev. Lett. 93 (2004) 201804.
[1219] G. Moreau, J. I. Silva-Marcos, Flavour physics of the RS model with KK masses reachable at LHC, JHEP 03 (2006) 090.
[1220] S. Chang, C. S. Kim, J. Song, Constraint of $B_{d,s} - \bar{B}_{d,s}$ mixing on warped extra- dimension model, JHEP 02 (2007) 087.
[1221] C. Csaki, A. Falkowski, A. Weiler, The Flavor of the Composite Pseudo-Goldstone Higgs, JHEP 09 (2008) 008.
[1222] K. Agashe, A. Azatov, L. Zhu, Flavor Violation Tests of Warped/Composite SM in the Two- Site Approach. arXiv:0810.1016.
[1223] M. E. Albrecht, M. Blanke, A. J. Buras, B. Duling, K. Gemmler, Electroweak and Flavour Structure of a Warped Extra Dimension with Custodial Protection. arXiv:0903.2415.
[1224] R. Barbieri, G. F. Giudice, Upper Bounds on Supersymmetric Particle Masses, Nucl. Phys. B306 (1988) 63.

[1225] G. Brooijmans, Mixing and CP Violation at the Tevatron. arXiv:0808.0726.
[1226] A. L. Fitzpatrick, G. Perez, L. Randall, Flavor from Minimal Flavor Violation and a Viable Randall- Sundrum Model. arXiv:0710.1869.
[1227] J. Santiago, Minimal Flavor Protection: A New Flavor Paradigm in Warped Models, JHEP 12 (2008) 046.
[1228] E. . Hewett, Joanne L., et al., The Discovery potential of a Super B Factory. Proceedings, SLAC Workshops, Stanford, USA, 2003. arXiv:hep-ph/0503261.